

AN INTRODUCTION TO COMPUTATIONAL FLUID MECHANICS BY EXAMPLE

AN INTRODUCTION TO COMPUTATIONAL FLUID MECHANICS BY EXAMPLE

Sedat Biringen and Chuen-Yen Chow



JOHN WILEY & SONS, INC.

This book is printed on acid-free paper.[∞]

Copyright © 2011 by John Wiley & Sons, Inc. All rights reserved

Published by John Wiley & Sons, Inc., Hoboken, New Jersey

Published simultaneously in Canada

No part of this publication may be reproduced, stored in a retrieval system, or transmitted in any form or by any means, electronic, mechanical, photocopying, recording, scanning, or otherwise, except as permitted under Section 107 or 108 of the 1976 United States Copyright Act, without either the prior written permission of the Publisher, or authorization through payment of the appropriate per-copy fee to the Copyright Clearance Center, 222 Rosewood Drive, Danvers, MA 01923, (978) 750-8400, fax (978) 646-8600, or on the web at www.copyright.com. Requests to the Publisher for permission should be addressed to the Permissions Department, John Wiley & Sons, Inc., 111 River Street, Hoboken, NJ 07030, (201) 748-6011, fax (201) 748-6008, or online at www.wiley.com/go/permissions.

Limit of Liability/Disclaimer of Warranty: While the publisher and the author have used their best efforts in preparing this book, they make no representations or warranties with respect to the accuracy or completeness of the contents of this book and specifically disclaim any implied warranties of merchantability or fitness for a particular purpose. No warranty may be created or extended by sales representatives or written sales materials. The advice and strategies contained herein may not be suitable for your situation. You should consult with a professional where appropriate. Neither the publisher nor the author shall be liable for any loss of profit or any other commercial damages, including but not limited to special, incidental, consequential, or other damages.

For general information about our other products and services, please contact our Customer Care Department within the United States at (800) 762-2974, outside the United States at (317) 572-3993 or fax (317) 572-4002.

Wiley also publishes its books in a variety of electronic formats. Some content that appears in print may not be available in electronic books. For more information about Wiley products, visit our web site at www.wiley.com.

Library of Congress Cataloging-in-Publication Data:

Biringen, Sedat.

An introduction to computational fluid mechanics by example/ Sedat Biringen, Chuen-Yen Chow.

p. cm.

Includes index.

ISBN 978-0-470-10226-8 (hardback); ISBN 978-0-470-91515-8 (ebk); ISBN 978-0-470-91516-5 (ebk); ISBN 978-0-470-91517-2 (ebk); ISBN 978-0-470-95155-2 (ebk); ISBN 978-0-470-95172-9 (ebk)

1. Fluid mechanics. 2. Fluid mechanics—Data processing. I. Chow, Chuen-Yen, 1932- II. Title.

TA357.C475 2011

532—dc22

2010054180

Printed in the United States of America

10 9 8 7 6 5 4 3 2 1

To our spouses,
to our children,

and to the memory of our parents, who gave us the spirit for intellectual
and creative pursuit

CONTENTS

Preface

ix

**1 Flow Topics Governed by Ordinary Differential Equations:
Initial-Value Problems**

1

- 1.1 Numerical Solution of Ordinary Differential Equations:
Initial-Value Problems / 1
- 1.2 Free Falling of a Spherical Body / 5
- 1.3 Computer Simulation of Some Restrained Motions / 13
- 1.4 Fourth-Order Runge-Kutta Method for Computing
Two-Dimensional Motions of a Body through a Fluid / 22
- 1.5 Ballistics of a Spherical Projectile / 24
- 1.6 Flight Path of a Glider—A Graphical Presentation / 32
- 1.7 Rolling Up of the Trailing Vortex Sheet behind
a Finite Wing / 35
- Appendix / 44

2 Inviscid Fluid Flows

50

- 2.1 Incompressible Potential Flows / 51
- 2.2 Numerical Solution of Second-Order Ordinary Differential
Equations: Boundary-Value Problems / 55
- 2.3 Radial Flow Caused by Distributed Sources and Sinks / 60
- 2.4 Inverse Method I: Superposition of Elementary Flows / 61
- 2.5 von Kármán's Method for Approximating Flow Past Bodies
of Revolution / 69
- 2.6 Inverse Method II: Conformal Mapping / 76
- 2.7 Classification of Second-Order Partial Differential
Equations / 87
- 2.8 Numerical Methods for Solving Elliptic Partial Differential
Equations / 90
- 2.9 Potential Flows in Ducts or around Bodies—Irrregular
and Derivative Boundary Conditions / 96

vii

2.10	Numerical Solution of Hyperbolic Partial Differential Equations / 105
2.11	Propagation and Reflection of a Small-Amplitude Wave / 110
2.12	Propagation of a Finite-Amplitude Wave: Formation of a Shock / 120
2.13	An Application to Biological Fluid Dynamics: Flow in an Elastic Tube / 128
	Appendix / 143

3 Viscous Fluid Flows **145**

3.1	Governing Equations for Viscous Flows / 145
3.2	Self-Similar Laminar Boundary-Layer Flows / 147
3.3	Flat-Plate Thermometer Problem—Ordinary Boundary-Value Problems Involving Derivative Boundary Conditions / 157
3.4	Pipe and Open-Channel Flows / 163
3.5	Explicit Methods for Solving Parabolic Partial Differential Equations—Generalized Rayleigh Problem / 168
3.6	Implicit Methods for Solving Parabolic Partial Differential Equations—Starting Flow in a Channel / 173
3.7	Numerical Solution of Biharmonic Equations—Stokes Flows / 179
3.8	Flow Stability and Pseudo-Spectral Methods / 185
	Appendix / 207

4 Numerical Solution of the Incompressible Navier-Stokes Equation **215**

4.1	Flow around a Sphere at Finite Reynolds Numbers—Galerkin Method / 216
4.2	Upwind Differencing and Artificial Viscosity / 229
4.3	Bénard and Taylor Instabilities / 234
4.4	Primitive Variable Formulation: Algorithmic Considerations / 249
4.5	Primitive Variable Formulation: Numerical Integration of the Navier-Stokes Equation / 258
4.6	Flow Past a Circular Cylinder: An Example for the Vorticity-Stream Function Formulation / 280
	Appendix / 297

Bibliography **298****Index** **303**

PREFACE

This book is based on the original textbook by C.-Y. Chow entitled *An Introduction to Computational Fluid Mechanics*, adopted and used by both authors in Computational Fluid Dynamics/Mechanics (CFDM) courses they have taught at the University of Colorado at Boulder and at the University of New Hampshire at Durham (SB). The original text was written in a highly accessible manner with senior undergraduate and first-year graduate students in mind and occasionally has been benefited by researchers in mechanical and aerospace engineering disciplines. Over the 25 years since the original publication, the field of CFDM has seen many changes, evolutions, and advances in algorithmic developments as well as in computer software/hardware. The new book incorporates some of the modern algorithmic developments into the solution techniques implemented in the vast number of examples provided in the text. Concurrently, we tried to widen the scope of the applications to include examples relevant to other engineering disciplines to make the text attractive and useful for a larger audience. We revised the computer programs included in the original text and converted all the programs to MATLAB, one of the most widely adopted computer languages in engineering education. The new MATLAB programs are available on line on the book's web site (www.wiley.com/go/Biringen). The reader is expected to have a working knowledge of MATLAB programming basics. The core-scope of the new book was expanded to include more up-to-date solution methods for the Navier-Stokes equations, including fractional step time-advancement and pseudo-spectral methods. In summary, we expect the new text to create a unique niche because of its hands-on approach and practical content and to have wide appeal in the classroom as well as in the research environment.

The pedagogical approach used in this book follows the path of the original and focuses on teaching by the study of actual examples from fluid mechanics. It is our belief that building up from worked examples and providing a hands-on approach allows students to implement simple codes as a very effective means of teaching complex material. This approach is the unique aspect of our book, primarily as a teaching instrument. In addition, more advanced solution procedures can be constructed based on the provided solvers.

The contents of the current book follow closely the contents of Chow's book, with additions relevant to the solution of the full Navier-Stokes equations.

Almost all solution methods presented are based on finite differences. The book should be suitable for a two-semester course in computational fluid mechanics, or topics can be selected for a one-semester course at the beginning graduate level. There is sufficient material for a more advanced course, or selected topics can be included as a supplement to traditional textbooks for courses in fluid mechanics at undergraduate or graduate levels.

We emphasize that this is predominantly an introductory book that teaches how to implement computational methods in fluid mechanics applications and not a book on numerical computation/analysis. It deals with flow problems that either have to be solved numerically or can be made much simpler with the help of computational tools. Numerical methods and algorithms are presented simply as tools implemented to solve physical problems; detailed analyses and critical evaluation of these techniques are not attempted. Of course, several methods exist for numerically integrating a given ordinary or partial differential equation; the numerical methods adopted in this book are only the simpler ones or the commonly used ones with which the authors have intimate experience and are by no means the complete spectrum of available methods. The book also does not cover in detail more advanced topics such as mesh generation and solution methods for the full compressible Navier-Stokes equation; also omitted are more advanced techniques such as multigrid methods, and other elliptic solvers.

The authors have benefited from interactions with many bright and capable students who have contributed to this book in various ways to improve the content. Particularly we (SB) thank Dr. Gökhan Danabaşoğlu for his many contributions when he was a teaching assistant for Advanced Computational Fluid Mechanics at the University of Colorado many years ago, Dr. Manuel Barcelos for his assistance in translating the FORTRAN codes from Chow's book to MATLAB codes available on the web site for the book (www.wiley.com/go/biringen), and Scott Waggy for his programming assistance.

The first author (SB) would like to emphasize that the authorship order was designated alphabetically by the graceful insistence of C.-Y. Chow, who came out of his comfortable retirement to play a very active role to complete this project. All the successes of this book belong to him, and the first author will willingly shoulder the responsibility for all the potential shortcomings.

1

FLOW TOPICS GOVERNED BY ORDINARY DIFFERENTIAL EQUATIONS: INITIAL-VALUE PROBLEMS

The numerical solution of initial-value problems that involve nonlinear ordinary differential equations is considered in this chapter. In Section 1.1 some numerical methods, especially the Runge-Kutta methods, are introduced for solving the first- and second-order equations. They are applied in Section 1.2 for finding the motion of a free-falling sphere through air and in Section 1.3 to simulate the motions of a simple pendulum and an aeroelastic system.

To extend the applications from one-dimensional to two-dimensional motions, Runge-Kutta formulas for solving simultaneous second-order equations are deduced in Section 1.4. Simultaneously, we have implemented MATLAB initial value solver ODE45 in the programs developed in this chapter and elsewhere in the book. After the motion of a spherical projectile in the presence of a fluid has been computed, the numerical integration procedure of Section 1.5 is combined with the half-interval method to find the maximum range of such a body. Section 1.6 deals with the computation of the trajectory of a glider, and Section 1.7 is an example from aerodynamics concerning the vortex sheet trailing behind a finite wing.

1.1 NUMERICAL SOLUTION OF ORDINARY DIFFERENTIAL EQUATIONS: INITIAL-VALUE PROBLEMS

Consider the simplest case of a first-order ordinary differential equation having the general form

$$\frac{dx}{dt} = f(x, t) \quad (1.1.1)$$

where f is an analytic function. If, at a starting point $t = t_0$, the function x has a given value x_0 , it is desired to find $x(t)$ for $t > t_0$ that satisfies both (1.1.1)

2 FLOW TOPICS GOVERNED BY ORDINARY DIFFERENTIAL EQUATIONS

and the prescribed initial condition. Such a problem is called an *initial-value problem*.

To solve the problem numerically, the axis of the independent variable is usually divided into evenly spaced small intervals of width h whose end points are situated at

$$t_i = t_0 + ih, \quad i = 0, 1, 2, \dots \quad (1.1.2)$$

The solution evaluated at the point t_i is denoted by x_i . Thus, by using a numerical method, the continuous function $x(t)$ is approximated by a set of discrete values x_i , $i = 0, 1, 2, \dots$, as sketched in Fig. 1.1.1. Since h is small and f is an analytic function, the solution at any point can be obtained by means of a Taylor's series expansion about the previous point:

$$\begin{aligned} x_{i+1} &\equiv x(t_{i+1}) = x(t_i + h) \\ &= x_i + h \left(\frac{dx}{dt} \right)_i + \frac{h^2}{2!} \left(\frac{d^2x}{dt^2} \right)_i + \frac{h^3}{3!} \left(\frac{d^3x}{dt^3} \right)_i + \dots \\ &= x_i + hf_i + \frac{h^2}{2!}f'_i + \frac{h^3}{3!}f''_i + \dots \end{aligned} \quad (1.1.3)$$

where f_i^n denotes $d^n f / dt^n$ evaluated at (x_i, t_i) . f is generally a function of both x and t , so that the first-order derivative is obtained according to the formula

$$\frac{df}{dt} = \frac{\partial f}{\partial t} + \frac{dx}{dt} \frac{\partial f}{\partial x}$$

Higher-order derivatives are obtained by using the same chain rule.

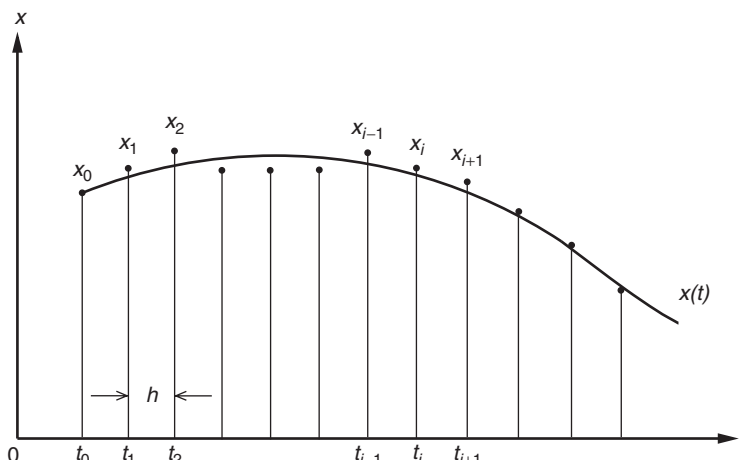


FIGURE 1.1.1 Numerical solution of an ordinary initial-value problem.

Alternatively (1.1.3) can be rewritten as

$$x_{i+1} = x_i + \Delta x_i \quad (1.1.4)$$

where

$$\Delta x_i = h f_i + \frac{h^2}{2!} f'_i + \frac{h^3}{3!} f''_i + \dots \quad (1.1.5)$$

Starting from $i = 0$ with x_0 given and Δx_0 computed based on any desired number of terms in (1.1.5), the value of x_1 is first calculated. Then, by letting $i = 1, 2, \dots$, in (1.1.4), the values of x_2, x_3, \dots are obtained successively. Theoretically, if the number of terms retained in (1.1.5) increases indefinitely, the numerical result from this marching scheme approaches the exact solution. In reality, however, it is not permissible to do so, and the series has to be cut off after a certain finite number of terms. For example, if two terms are retained on the right-hand side of (1.1.5) in computing Δx_i , the value of x_{i+1} so obtained is smaller than the exact value by an amount $(h^3/3!)f''_i + (h^4/4!)f'''_i + \dots$. For small h the first term is dominant. We may say that the error involved in this numerical calculation is of the order of $h^3 f''_i$, or simply $O(h^3 f''_i)$. This is the *truncation error* that results from taking a finite number of terms in an infinite series.

It is termed *Euler's method* when only one term is used on the right-hand side of (1.1.5). The truncation error is $O(h^2 f'_i)$, and the method should not be used if accuracy is demanded in the result.

It is impractical to use Taylor's series expansion method if f is a function that has complicated derivatives. Furthermore, because of the dependence of the series on the derivatives of f , a generalized computer program cannot be constructed for this method. The n th-order *Runge-Kutta method* is a commonly used alternative. Computations in this method require the evaluation of the function, f , instead of its derivatives, with properly chosen arguments; the accuracy is equivalent to that with n terms retained in the series expansion (1.1.5). The second-order Runge-Kutta formulas are

$$x_{i+1} = x_i + hf\left(x_i + \frac{1}{2}\Delta_1 x_i, t_i + \frac{1}{2}h\right) \quad (1.1.6)$$

where

$$\Delta_1 x_i = hf(x_i, t_i) \quad (1.1.7)$$

For better results the following fourth-order Runge-Kutta formulas are usually employed:

$$x_{i+1} = x_i + \frac{1}{6}(\Delta_1 x_i + 2\Delta_2 x_i + 2\Delta_3 x_i + \Delta_4 x_i) \quad (1.1.8)$$

in which the increments are computed in the following order:

$$\begin{aligned} \Delta_1 x_i &= hf(x_i, t_i) \\ \Delta_2 x_i &= hf\left(x_i + \frac{1}{2}\Delta_1 x_i, t_i + \frac{1}{2}h\right) \\ \Delta_3 x_i &= hf\left(x_i + \frac{1}{2}\Delta_2 x_i, t_i + \frac{1}{2}h\right) \\ \Delta_4 x_i &= hf(x_i + \Delta_3 x_i, t_i + h) \end{aligned} \quad (1.1.9)$$

The derivation of these formulas can be found, for instance, in Kuo (1972, p. 137). In the fourth-order method the dominant term in the truncation error is $(h^5/5!)f_i^{iv}$. Unless the slope of the solution is very steep, satisfactory results are usually obtained with reasonably small h . Stability and step-size control in Runge-Kutta methods are referred to in the book by Carnahan, Luther, and Wilkes (1969, p. 363) and are not discussed here.

Runge-Kutta methods can be extended to solve higher-order or simultaneous ordinary differential equations. Consider a second-order equation of the general form

$$\frac{d^2x}{dt^2} = F\left(x, \frac{dx}{dt}, t\right) \quad (1.1.10)$$

accompanied by the initial conditions that $x = x_0$ and $dx/dt = p_0$ when $t = t_0$. By calling the first-order derivative a new variable p , the equation (1.1.10) can be written in the form of two simultaneous first-order equations:

$$\begin{aligned} \frac{dx}{dt} &= p \\ \frac{dp}{dt} &= F(x, p, t) \end{aligned} \quad (1.1.11)$$

with initial values $x(t_0) = x_0$ and $p(t_0) = p_0$. The fourth-order Runge-Kutta formulas for marching from t_i to t_{i+1} are

$$\begin{aligned} x_{i+1} &= x_i + \frac{1}{6}(\Delta_1 x_i + 2\Delta_2 x_i + 2\Delta_3 x_i + \Delta_4 x_i) \\ p_{i+1} &= p_i + \frac{1}{6}(\Delta_1 p_i + 2\Delta_2 p_i + 2\Delta_3 p_i + \Delta_4 p_i) \end{aligned} \quad (1.1.12)$$

in which the individual terms are computed in the following order:

$$\begin{aligned} \Delta_1 x_i &= h p_i \\ \Delta_1 p_i &= h F(x_i, p_i, t_i) \\ \Delta_2 x_i &= h(p_i + \frac{1}{2}\Delta_1 p_i) \\ \Delta_2 p_i &= h F(x_i + \frac{1}{2}\Delta_1 x_i, p_i + \frac{1}{2}\Delta_1 p_i, t_i + \frac{1}{2}h) \\ \Delta_3 x_i &= h(p_i + \frac{1}{2}\Delta_2 p_i) \\ \Delta_3 p_i &= h F(x_i + \frac{1}{2}\Delta_2 x_i, p_i + \frac{1}{2}\Delta_2 p_i, t_i + \frac{1}{2}h) \\ \Delta_4 x_i &= h(p_i + \Delta_3 p_i) \\ \Delta_4 p_i &= h F(x_i + \Delta_3 x_i, p_i + \Delta_3 p_i, t_i + h) \end{aligned} \quad (1.1.13)$$

Most of the programs included in this chapter have utilized MATLAB initial-value solvers, ODE23 and ODE45; however, we also provide explicit function subprograms that contain fourth-order Runge-Kutta solvers. These subprograms can be easily substituted for the MATLAB solvers by the user.

1.2 FREE FALLING OF A SPHERICAL BODY

As the first application of the Runge-Kutta methods, the motion of a free-falling body is to be studied. This problem is an example in which a solution cannot be obtained without using a numerical method.

It is said that Galileo released simultaneously two objects of different masses from the Leaning Tower of Pisa and found that they touched the ground at the same instant. If Galileo did perform such an experiment, is the conclusion stated in the story correct? Certainly it is true in a vacuum. In the atmosphere, however, forces are exerted on a body by the surrounding air that are determined by the size and motion of the body, and the conclusion seems doubtful. If it is not correct, which body should touch the ground first, the larger one or the smaller one?

To answer these questions, we will not repeat the experiment in a laboratory. Instead, we will first formulate the body motion, including the forces caused by the surrounding fluid, and then perform the experiment numerically on a digital computer. Because of its available drag data, a spherical body is preferred for our analysis.

The z -axis is chosen in the direction of gravitational acceleration g ; its origin coincides with the center of the sphere at the initial instant $t = 0$, as shown in Fig. 1.2.1. At time $t > 0$, the sphere of diameter d and mass m is at a distance z from the origin and has a velocity v . It is surrounded by a fluid of density ρ_f and kinematic viscosity ν . In a vacuum the only external force acting on the body is the gravitational pull, mg , in the positive z direction. While moving through a fluid it is acted on by the following additional forces:

1. *The buoyant force.* According to Archimedes' principle, the buoyant force is equal to the weight of the fluid displaced by the body. It has the expression $-m_f g$, where

$$m_f = \frac{1}{6}\pi d^3 \rho_f \quad (1.2.1)$$

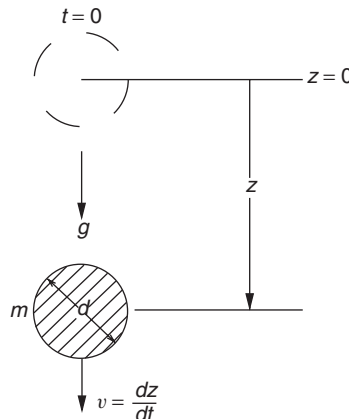


FIGURE 1.2.1 A free-falling spherical body.

and the negative sign means that the force is in the direction of the negative z -axis.

2. The force on an accelerating body. When a body immersed in a stationary fluid is suddenly set in motion, a flow field is induced in the fluid. The kinetic energy associated with the fluid motion is generated by “doing work,” or moving the body against a drag force. This drag exists even if the fluid is frictionless, and it has the value $-\frac{1}{2}m_f dv/dt$, derived from an inviscid theory (Lamb, 1932, p. 124).

3. The forces caused by viscosity. Around a body moving through a real fluid, a region of rapid velocity change exists adjacent to the surface. The velocity gradient causes a shear stress on the surface; the force resulting from integrating the shear stresses throughout the body is termed the *skin friction*. In addition, in a viscous fluid the pressure at the rear of the body becomes lower than that at the front. The pressure difference gives rise to a *pressure* or *form drag* on the body. The total viscous force, or the sum of skin friction and form drag, is sometimes expressed in a dimensionless form called a *drag coefficient*, which is a function of the body shape and the *Reynolds number*. Except for a few simple shapes and at very low Reynolds numbers, this function is difficult to find analytically, and it is usually determined through experiment. Figure 1.2.2 shows a typical experimental curve for smooth spheres (Goldstein, 1938, p. 16) in which the drag coefficient c_d , defined as the total viscous force divided by $\frac{1}{2}\rho_f v^2 \frac{1}{4}\pi d^2$, is plotted against the Reynolds number Re , defined as $v d / \nu$.

4. The wave drag. When the body speed is comparable to the speed of sound in a fluid medium, shock waves may develop on or ahead of the body, causing a *wave drag*.

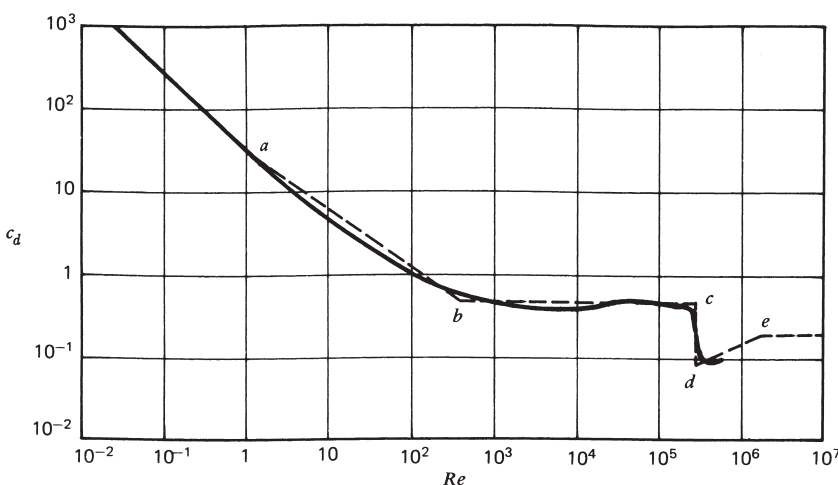


FIGURE 1.2.2 Drag coefficient for smooth spheres.

If we consider only low subsonic speeds, the wave drag can be safely omitted. Including all the other forces discussed, Newton's law of motion, when applied to a spherical body, has the form

$$m \frac{dv}{dt} = mg - m_f g - \frac{1}{2} m_f \frac{dv}{dt} - \frac{1}{2} \rho_f v |v| \frac{\pi}{4} d^2 c_d(v)$$

$v|v|$ is used instead of v^2 , so that the direction of viscous drag is always opposite to the direction of v . After rearranging, it can be written as

$$\left(m + \frac{1}{2} m_f \right) \frac{dv}{dt} = (m - m_f)g - \frac{\pi}{8} \rho_f v |v| d^2 c_d(v) \quad (1.2.2)$$

The left-hand side indicates that in an accelerating or decelerating motion through a fluid, the body behaves as if its mass were increased. The term $\frac{1}{2} m_f$ is sometimes referred to as the *added mass*. Upon substitution from (1.2.1) and from $m = \frac{1}{6} \pi d^3 \rho$, ρ being the density of the body, (1.2.2) becomes

$$\frac{dv}{dt} = \frac{1}{A} [B - C v |v| c_d(v)] \quad (1.2.3)$$

with

$$\frac{dz}{dt} = v \quad (1.2.4)$$

where $A = 1 + \frac{1}{2} \bar{\rho}$, $B = (1 - \bar{\rho})g$, and $C = 3\bar{\rho}/4d$; $\bar{\rho}$ stands for the density ratio ρ_f/ρ . These equations fit the general form (1.1.11) and can be solved by applying Runge-Kutta methods.

Special care is needed for the empirical function $c_d(v)$ in numerical computation. To present it in a form suitable for the computer, the curve is replaced by several broken lines, as shown in Fig. 1.2.2. To the left of the point a , where $Re \leq 1$, the *Stokes formula*

$$c_d = \frac{24}{Re} \quad (1.2.5)$$

is used, which coincides well with the experimental curve for Reynolds numbers that are much less than unity and deviates only slightly from it in the neighborhood of the point a (where $Re = 1$, $c_d = 24$). On the log-log plot a straight line is drawn between points a and b (where $Re = 400$, $c_d = 0.5$) to approximate the actual curve, which gives

$$c_d = 24/Re^{0.646} \quad \text{for } 1 < Re \leq 400 \quad (1.2.6)$$

Between b and c (where $Re = 3 \times 10^5$), we assume that the drag coefficient has a constant value of 0.5. The abrupt drop of drag coefficient around c is an indication of transition from laminar to turbulent boundary layer before flow separates from the body surface (see Kuethe and Chow, 1998, Section 17.11). Another straight line is drawn between d (where $Re = 3 \times 10^5$, $c_d = 0.08$) and e (where $Re = 2 \times 10^6$, $c_d = 0.18$). Thus,

$$c_d = 0.000366 \times Re^{0.4275} \quad \text{for } 3 \times 10^5 < Re \leq 2 \times 10^6 \quad (1.2.7)$$

Finally, in the high-Reynolds number region beyond e , a constant value of 0.18 is assumed for the drag coefficient.

Here we have chosen a simple way to approximate a complicated function. Better results can be expected by dividing the curve into a larger number of broken lines. Alternatively, the drag coefficient can be fed into the computer as a tabulated function from which the value at any Reynolds number can be interpolated or extrapolated.

Now let us return to the numerical experiment. Suppose steel spheres are dropped in air under standard atmospheric conditions at sea level; we have $\rho = 8000 \text{ kg/m}^3$, $\rho_f = 1.22 \text{ kg/m}^3$, $v = 1.49 \times 10^{-5} \text{ m}^2/\text{s}$, and $g = 9.8 \text{ m/s}^2$. Because of the low value of $\bar{\rho}$ in this particular example, the effects of buoyancy and added mass are negligible, as can be seen in (1.2.3). They become significant if the experiment is repeated in water or in any fluid whose density is comparable to that of the body. However, for generality these terms are still kept in our computer program.

The result for a sphere 0.01 m in diameter will be shown. Its motion is to be compared with that of the same body when dropped in a vacuum. In the latter case $\bar{\rho} = 0$, (1.2.3) and (1.2.4) can be integrated directly to give the solution in the vacuum:

$$v_v = v_0 + gt$$

$$z_v = z_0 + v_0 t + \frac{1}{2} g t^2$$

where z_0 and v_0 are, respectively, the initial position and velocity of the sphere at $t_0 = 0$. We will choose the initial values $z_0 = 0$ and $v_0 = 0$ in the computation.

Since the right-hand side of (1.2.3) does not explicitly contain z or t , let us call it $F(v)$, which has a form simpler than the general expression shown in (1.1.11). We compute the position and velocity at time t_{i+1} based on those at t_i according to the following formulas simplified from (1.1.12) and (1.1.13).

The eight increments are first calculated.

$$\Delta_1 z_i = h v_i$$

$$\Delta_1 v_i = h F(v_i)$$

$$\Delta_2 z_i = h(v_i + \frac{1}{2} \Delta_1 v_i)$$

$$\Delta_2 v_i = h F(v_i + \frac{1}{2} \Delta_1 v_i)$$

$$\Delta_3 z_i = h(v_i + \frac{1}{2} \Delta_2 v_i)$$

$$\Delta_3 v_i = h F(v_i + \frac{1}{2} \Delta_2 v_i)$$

$$\Delta_4 z_i = h(v_i + \Delta_3 v_i)$$

$$\Delta_4 v_i = h F(v_i + \Delta_3 v_i)$$

They enable us to compute the new values:

$$z_{i+1} = z_i + \frac{1}{6}(\Delta_1 z_i + 2\Delta_2 z_i + 2\Delta_3 z_i + \Delta_4 z_i)$$

$$v_{i+1} = v_i + \frac{1}{6}(\Delta_1 v_i + 2\Delta_2 v_i + 2\Delta_3 v_i + \Delta_4 v_i)$$

According to the above formulas, the variables t_i , z_i , and v_i are one-dimensional arrays whose elements consist of their individual values at t_0, t_1, t_2, \dots . However, if instead of printing the complete set of data at the last time step we print out the time, position, and velocity at every time step t_i , the same variable names may be used for the quantities evaluated at t_{i+1} . In this way the subscripts i and $i + 1$ can be dropped from the variables to simplify the appearance of the program.

In Program 1.1 the instantaneous Reynolds number is shown in addition to the position and velocity for our reference. A time limit TMAX is introduced in the program. The numerical integration is stopped when t exceeds this value.

In Program 1.1 a time step of 0.1 s is used. To check the accuracy, the same program has been repeated with step sizes of 0.02 and 0.2 s. Since no appreciable difference can be found between the three sets of data, it can be concluded that the result is reliable. Keeping $h = 0.1$ s, more data are obtained by varying the diameter while doubling the maximum time of integration. They are plotted in Figs. 1.2.3 and 1.2.4.

We have thus obtained some results from the numerical experiment of a free-falling steel sphere. The displacement curves in Fig. 1.2.3 indicate that to travel through a given distance, a larger body takes less time than a smaller one. For two spheres of comparable sizes, the difference in arrival times at a distance of 56 m (the height of the Tower of Pisa) is only a small fraction of a second. Such a time difference is difficult to detect without the help of some instruments.

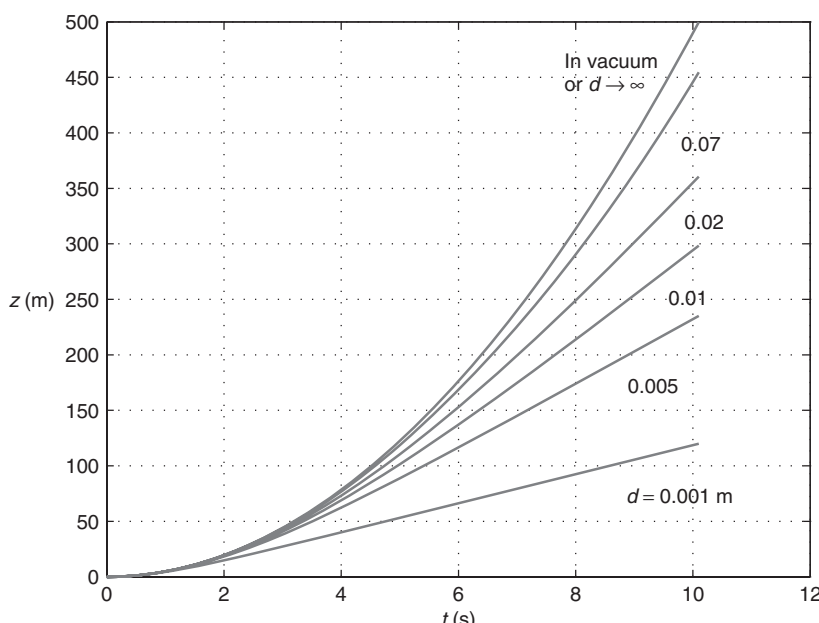


FIGURE 1.2.3 Displacement of steel spheres falling in air.

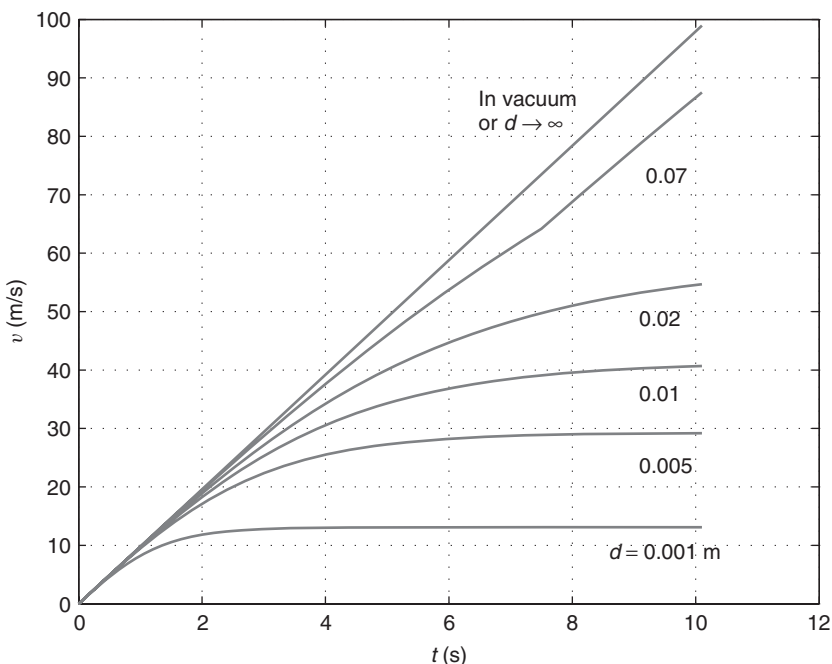


FIGURE 1.2.4 Velocity of steel spheres falling in air.

A body falling through a fluid always reaches a constant velocity, called the *terminal velocity*, which increases with the diameter of a spherical body, as shown in Fig. 1.2.4. For a small sphere the Reynolds number is relatively low and the boundary layer always remains laminar before the point of separation. At a sufficiently high Reynolds number, when the transition from a laminar to a turbulent boundary layer occurs on a larger sphere, the abrupt decrease in drag shown in Fig. 1.2.2 will cause a sudden acceleration of the body. This phenomenon can be observed in Fig. 1.2.4 on the curve for a sphere with $d = 0.07$ m around $t = 7.5$ s. For an extremely large sphere the effect of the surrounding fluid becomes negligible in comparison with body inertia, so that the sphere behaves as if it were moving in a vacuum. In this case the velocity increases indefinitely with time, and a terminal velocity can never be reached.

When traveling at the terminal velocity, the gravitational force is balanced by the sum of buoyancy and viscous drag, so that the acceleration is zero. From (1.2.2) an expression is derived for the terminal velocity:

$$v_t = \sqrt{\frac{4(1 - \bar{\rho})gd}{3\bar{\rho}c_d(v_t)}} \quad (1.2.8)$$

Based on the numerical result for the steel sphere of 0.01 m diameter, the terminal Reynolds number is estimated to be not much higher than 2.73×10^4 . According

to the approximation shown in Fig. 1.2.2, the drag coefficient at the terminal velocity is $c_d(v_t) = 0.5$. Substitution of this together with other given values into (1.2.8) gives $v_t = 41.4$ m/s.

In general, $c_d(v_t)$ is not known a priori, and the terminal velocity cannot be obtained unless the time history of the motion is computed first. However, from the data computed for steel spheres falling through air, it is concluded that the terminal Reynolds number exceeds 2×10^6 if the diameter of a sphere is greater than 0.12 m. $c_d(v_t)$ has a constant value of 0.18 for such a sphere according to our approximation, and v_t can readily be calculated. On the other hand, for tiny particles whose terminal Reynolds numbers are in the Stokes flow regime, the Stokes formula (1.2.5) is used in (1.2.8) to obtain

$$v_t = \frac{(1 - \bar{\rho})g d^2}{18\bar{\rho}\nu} \quad \text{for } \text{Re} < 1 \quad (1.2.9)$$

Let us now estimate the minimum diameter of a steel sphere whose terminal velocity in air can exceed the speed of sound, 340 m/s at sea level. The terminal Reynolds number of such a body is well beyond 2×10^6 , so that the value 0.18 is used for $c_d(v_t)$. By assigning the sound speed to v_t , (1.2.8) gives $d = 0.243$ m. Remember that before reaching sonic speed, a transonic region appears on the body, causing a wave drag that should also be included in the drag coefficient. Furthermore, because of the limited drag data available for high Reynolds numbers, the constant c_d assumption is doubtful. The minimum diameter estimated here is expected to be too low.

In the atmosphere or in an ocean, if the displacement of a body is so large that the variations in fluid density and kinematic viscosity are significant, the program must be modified by specifying the dependence of these quantities on the height z . In this case the function $F(v)$ in Program 1.1 should be changed to $F(v, z)$.

Problem 1.1 Find the motion of a Ping-Pong ball 0.036 m in diameter released at the bottom of a water tank. The density of water is 1000 kg/m^3 and the kinematic viscosity is $1 \times 10^{-6} \text{ m}^2/\text{s}$. Assume that the shell of the ball is so thin that the density of the body is the same as that of the filling air, or 1.22 kg/m^3 .

Hint

Because of the large buoyant force, the stationary ping-pong ball initially experiences a large acceleration. You may verify that the numerical solution diverges if $h = 0.1$ s is still used. The value $h = 0.01$ s is recommended in this problem. Since the ball reaches an upward steady motion within a fraction of a second, a maximum time of 0.5 s is sufficient for the computation.

Problem 1.2 For a given body falling in a specified fluid, the terminal velocity is fixed independent of the initial velocity of the body. If the initial velocity is slower than or in a direction opposite to the terminal velocity, the body will accelerate toward the terminal value. On the other hand, if the initial velocity is faster

than the terminal velocity, it will decelerate and finally reach the same velocity. Verify this phenomenon by assigning several values to v_0 in Program 1.1.

On a rainy day it can be observed that the larger raindrops come down faster than the smaller ones. If a raindrop is considered to be a rigid ball of water, its motion can be computed from Program 1.1 by assigning the numerical value of water density to the variable name RHO. The resulting terminal velocities for drops of various diameters are plotted in Fig. 1.2.5 in comparison with the measured data taken from Blanchard (1967, p. 12). Good agreements between computed and measured values are obtained for drops whose diameters are less than 3.5 mm.

The difference in terminal velocity between a liquid drop and a rigid sphere occurs because the binding surface of the liquid drop moves with the surrounding fluid and, at the same time, it is deformed. At small Reynolds numbers a liquid drop is approximately spherical in shape. The tangential motion of the interior

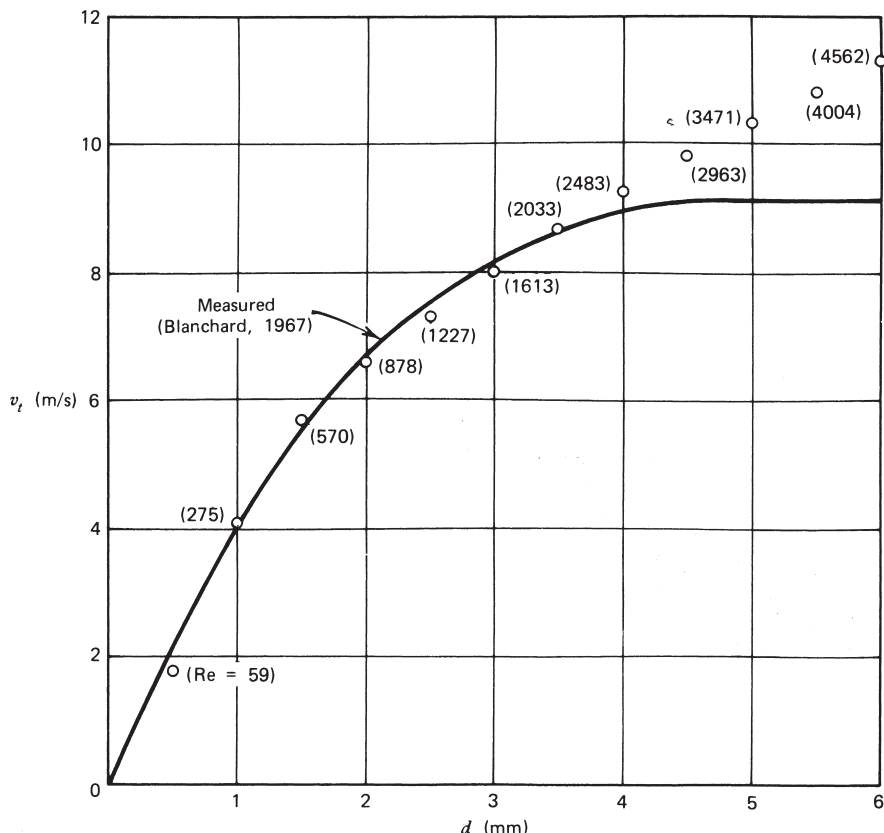


FIGURE 1.2.5 Measured terminal velocity of a raindrop in comparison with that computed for a rigid sphere. Numbers in parentheses are Reynolds numbers at the points indicated.

fluid at the interface reduces the skin friction and delays flow separation from the surface. Thus, a small spherical liquid drop has a smaller drag than a rigid sphere of the same size and density and, therefore, has a faster terminal velocity. When the Reynolds number is large, however, the drop is deformed by the external flow into a shape that is flattened in the vertical direction (see Blanchard, 1967, Plate III, for a photograph of a water drop in an airflow). This shape causes an early flow separation and results in a tremendous increase in form drag. This explains the phenomenon that the terminal velocity of a large liquid drop is slower than that computed for a rigid sphere, as shown by the flattening portion of the measured curve. Certain instabilities grow in very large liquid drops, causing them to break into smaller droplets. Because of this, raindrops having diameters greater than 6 mm are rarely observed.

For Reynolds numbers that are much less than unity, the nonlinear inertia terms in the equations of motion can be ignored, and both the internal and external flow fields can be found analytically. The drag of a liquid sphere so derived has the expression (Happel and Brenner, 1965, p. 127)

$$\text{Drag} = 3\pi\mu_e dv \frac{1 + 2\mu_e/3\mu_i}{1 + \mu_e/\mu_i} \quad (1.2.10)$$

where μ_i and μ_e are, respectively, the coefficients of viscosity of the internal and external fluid media. For a raindrop falling in air, $\mu_i = 1 \times 10^{-3}$ and $\mu_e = 1.818 \times 10^{-5}$ kg/ms, the drag of a liquid sphere is only slightly lower than $3\pi\mu_e dv$, which is the drag of a rigid sphere in the Stokes flow regime.

The expression (1.2.10) has been modified by Taylor and Acrivos (1964) to include the inertial effect under the restriction that $\text{Re} \ll 1$. Because of the nonlinearity of the governing equations, a closed-form solution cannot be found for a liquid drop at a Reynolds number much higher than unity.

When a raindrop freezes, its diameter increases because of the lower density. You may verify that at a low Reynolds number a freezing raindrop experiences a deceleration while falling.

1.3 COMPUTER SIMULATION OF SOME RESTRAINED MOTIONS

In the previous example of a free-falling body the physical system was first replaced by a system of mathematical equations that describes approximately the body motion. The algorithm for solving this system of equations was then programmed in Program 1.1 under a set of specified conditions. By varying the input data in the same program, one can find the motion of a spherical body of an arbitrary material falling through a given fluid starting from any desired initial conditions. Thus, instead of measuring the real motion, which is usually tedious and in some cases extremely difficult, one can perform the experiment numerically on a computer, which is a simple process once the physical laws have

been correctly formulated. In this respect the motion of a free-falling sphere is said to have been simulated numerically by Program 1.1.

Discrepancies certainly exist between the real and the simulated motions because of the approximations used in deriving the governing equations and the errors involved in numerical computations. However, numerical simulation gives an approximate outcome before an experiment is actually conducted, and the result can be used as a guide in designing the experiment and in choosing the right instruments for measurements. For example, such a practice has been used in predicting the orbit of a spacecraft or the landing site of a reentry vehicle.

In this section some restrained body motions in a fluid are simulated. We first consider the oscillatory motion of a simple pendulum whose small-amplitude motion in vacuum is well known. The weight of the pendulum is a spherical body of diameter d and mass m suspended on a weightless thin cord of length $(l - \frac{1}{2}d)$. At time t the displacement angle is θ , the tangential velocity is v , and the body is acted on by forces shown in Fig. 1.3.1. Fluid dynamic forces consist of the viscous drag and the force caused by acceleration. For the motion in tangential direction, the governing equations are

$$v = l \frac{d\theta}{dt}$$

and

$$m \frac{dv}{dt} = -(m - m_f)g \sin \theta - \frac{1}{2}m_f \frac{dv}{dt} - \frac{1}{2}\rho_f v|v| \frac{\pi}{4} d^2 c_d(v)$$

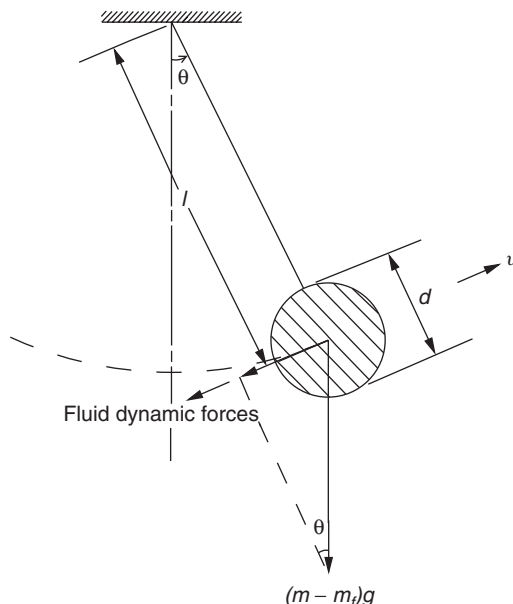


FIGURE 1.3.1 A simple pendulum.

where m_f , ρ_f , g , and c_d have the same meanings as defined in the previous section. By letting $y = l\theta$ and defining A , B , and C in the same manner as shown in (1.2.3), the above equations become

$$\frac{dy}{dt} = v \quad (1.3.1)$$

$$\frac{dv}{dt} = \frac{1}{A} \left[-B \sin \frac{y}{l} - C v |v| c_d(v) \right] \quad (1.3.2)$$

The general initial conditions are that $y = y_0$ (or $l\theta_0$) and $v = v_0$ at time $t = t_0$. For the motion in a vacuum the equations reduce to

$$\frac{dy_v}{dt} = v_v \quad (1.3.3)$$

$$\frac{dv_v}{dt} = -g \sin \left(\frac{y_v}{l} \right) \quad (1.3.4)$$

obtained by setting $\rho_f = 0$ in (1.3.2). Even in this simplified case, analytical solution is not straightforward if the amplitude of oscillation is large. The fourth-order Runge-Kutta formulas (1.1.12) and (1.1.13) will be used in solving the preceding two systems of equations.

For numerical computations a glass sphere ($\rho = 2500 \text{ kg/m}^3$) with $d = 0.01 \text{ m}$ and $l = 2 \text{ m}$ is considered. At $t = 0$ the sphere is released from a stationary position of the cord with 45° angular displacement. Its motions in the vacuum and in the air are computed and compared in Program 1.2.

As mentioned previously, in all the subsequent programs dealing with ordinary differential equations, we have simultaneously implemented the MATLAB solver ODE45 as an alternative to the direct implementation of the Runge-Kutta method presented in this section. ODE45 is based on a fourth- and fifth-order Runge-Kutta approximation and keeps the error within a given error tolerance by adjusting the step size (see, for example, Harman, Dabney, and Richert, 2000).

In the above formulation the angular displacement θ is expressed in radians, but we prefer degree as the unit of θ in Program 1.2. It has to be multiplied by the factor $\pi/180$ to convert back to radians.

From the plot of angular displacement in Fig. 1.3.2 based on the output of Program 1.2, we can see that the pendulum swings undamped in a vacuum with a constant amplitude of 45° . The period is approximately 2.95 s compared to 2.838 s, calculated from the well-known expression $2\pi\sqrt{l/g}$ for the period, assuming small amplitudes. The time history of angular displacement is no longer a cosine curve, as predicted by the linearized theory. In the presence of air the amplitude is slowly damped by air resistance and, in the meantime, the period is shortened.

Parameters can be varied in Program 1.2 to simulate the motions of a pendulum that has any combination of size and material in different fluid media. For example, the motion of the same pendulum in water is obtained by changing the

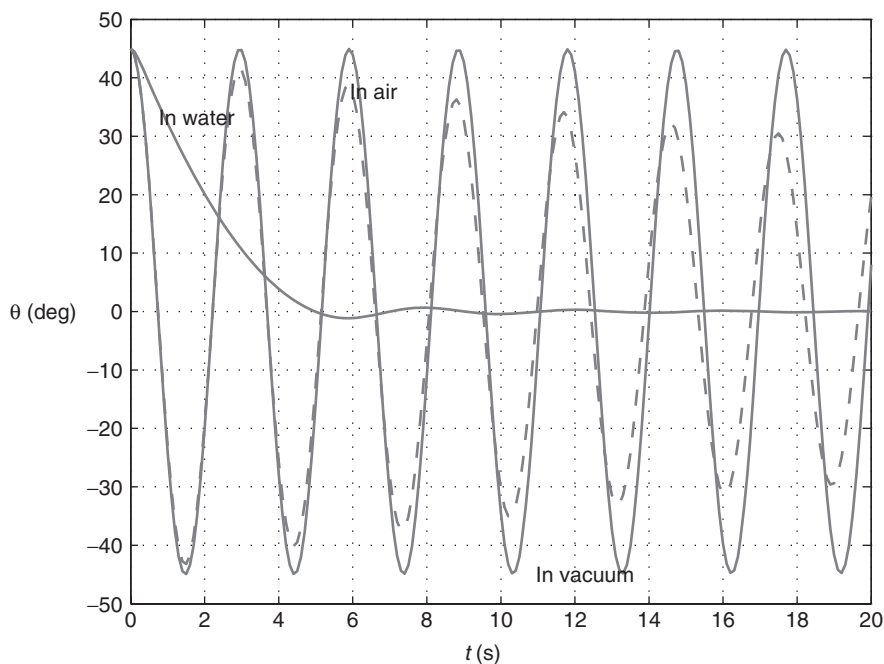


FIGURE 1.3.2 Angular displacements of a suspended glass sphere in different fluid media.

input values of ρ_f and v and is plotted in Fig. 1.3.2 for comparison. In this case the density of water is comparable to that of the glass sphere. The influence of fluid is so large that the displacement curve is far different from that in a vacuum. Starting from the same inclination, it takes 5 s to reach the vertical position in water compared with 0.74 s in a vacuum or in air. After that it oscillates at a small but decreasing amplitude with a period approximately equal to 4 s.

Problem 1.3 Find the variation of period with amplitude for a simple pendulum swinging in a vacuum.

Problem 1.4 If the body in Program 1.2 is replaced by a thin spherical shell containing air, and the cord is rigid but weightless and frictionless, find the angular motion of the shell in water, starting from a stationary position of 5° inclination. Assume that the shell is so thin that its weight is negligible, and that the rigid arm can rotate freely about the hinge.

An elastically restrained wing vibrates under certain flight conditions. Instead of studying the problem analytically, which is usually done by the use of linearized theories, we will simulate a simplified aeroelastic system and study on the computer the response of a wing to various wind conditions. By analytical methods such a study is difficult and, in some cases, it is impossible if a high degree of accuracy is required.

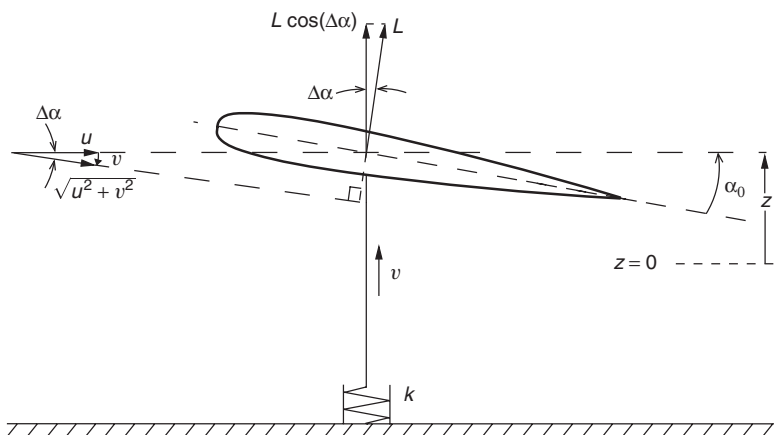


FIGURE 1.3.3 Vertical motion of a wing in a wind tunnel.

Figure 1.3.3 shows schematically a wing installed in a wind tunnel. The weight of the wing, mg , is supported by a spring of spring constant k , which is equivalent to the stiffness of a wing on an airplane. The cross section of the wing is a symmetric airfoil. In the absence of a wind, the airfoil makes an angle α_0 with the horizontal and its center of mass under a state of equilibrium is at a height $z = 0$. Assume that the wing is so installed that it can move only vertically. The displacement of the center of mass is z , considered positive when going upward. The wind tunnel supplies a uniform horizontal wind of speed u at the test section. When the wing moves upward at a speed v , the surrounding air moves downward relative to the wing at the same speed, as shown in the velocity diagram. To the oncoming air flow, the angle of attack of the wing is

$$\begin{aligned}\alpha &= \alpha_0 - \Delta\alpha \\ &= \alpha_0 - \tan^{-1}(v/u)\end{aligned}\quad (1.3.5)$$

The lift of the wing, in the direction normal to the flow, has the expression

$$L = \frac{1}{2} \rho_f (u^2 + v^2) S c_l \quad (1.3.6)$$

where ρ_f is air density, S the projected wing area, and c_l the *lift coefficient* of the wing. According to the *thin-airfoil theory* for a wing of large aspect ratio, the lift coefficient is a linear function of the angle of attack, which has the following form for a symmetric airfoil (Kuethe and Chow, 1998. Section 5.5):

$$c_l = 2\pi\alpha \quad (1.3.7)$$

The theory agrees with the experiment if α is within a certain limit. Beyond the limit the wing no longer behaves like a thin body, and the flow separates from the surface. The sudden decrease of lift associated with this phenomenon causes the wing to stall. For simplicity let us assume that the formula (1.3.7) holds for the wing if $-18^\circ \leq \alpha \leq +18^\circ$, and that beyond this range the lift is zero.

The equations of motion for the center of mass are

$$\frac{dz}{dt} = v \quad \text{and} \quad m \frac{dv}{dt} = -kz + L \cos(\Delta\alpha) \quad (1.3.8)$$

Upon substitution of the value $\cos(\Delta\alpha) = u / \sqrt{u^2 + v^2}$ and L from (1.3.6), the second equation becomes

$$m \frac{dv}{dt} = -kz + \frac{1}{2} \rho_f S c_l u \sqrt{u^2 + v^2} \quad (1.3.9)$$

As in previous examples, this problem also contains several parameters, and each of them may vary. Instead of solving the equations in the present form for each set of parameters, it is usually more economical to solve them in a nondimensionalized form. In this way we need only to vary the values of a reduced number of dimensionless parameters, so that a class of problems can be solved through a single computation.

The procedure in nondimensionalizing the governing equations is first to find the basic reference quantities for the problem. For instance, in kinematics they are the reference time, length, and velocity.

In the present case of a spring-supported wing, we may use the period of free oscillation of the system, $2\pi\sqrt{m/k}$, as the reference time; the deformation of spring due to the weight of wing, mg/k , as the reference length; and the ratio of the two as the reference velocity. Based on these reference quantities, the following dimensionless variables are defined:

$$\begin{aligned} T &= \frac{t}{2\pi\sqrt{m/k}} & Z &= \frac{z}{mg/k} \\ U &= \frac{u}{(g/2\pi)\sqrt{m/k}} & V &= \frac{v}{(g/2\pi)\sqrt{m/k}} \end{aligned} \quad (1.3.10)$$

After being expressed in terms of these new variables, (1.3.8) and (1.3.9) become

$$\frac{dZ}{dT} = V \quad (1.3.11)$$

$$\frac{dV}{dT} = -(2\pi)^2 Z + \beta c_l U \sqrt{U^2 + V^2} \quad (1.3.12)$$

where $\beta = \rho_f g S / 2k$ is a dimensionless parameter. Thus, the six parameters, ρ_f , g , m , S , k , and u , are reduced to only two dimensionless groups, β and U . Each set of values of β and U represents a large number of combinations of the dimensional parameters. For our numerical computations, the following conditions are assumed:

$$\rho_f = 1.22 \text{ kg/m}^3 \quad g = 9.8 \text{ m/s}^2$$

$$m = 3 \text{ kg} \quad S = 0.3 \text{ m}^2$$

$$k = 980 \text{ kg/s}^2 \quad \alpha_0 = 10^\circ$$

Corresponding to these assumptions, $\beta = 0.00183$, the reference time is 0.348 s, the reference length is 0.03 m, and the reference velocity is 0.0862 m/s. Thus, $U = 100$ means that the horizontal wind speed is 8.62 m/s. The numerical result in dimensionless form applies to other problems under a variety of conditions, for example, if m , S , and k are multiplied by the same factor.

In Program 1.3, (1.3.11) and (1.3.12) can be solved either by using the function subprogram RUNGE (borrowed from Program 1.2), or by the implementation of MATLAB program ODE45. The lift coefficient is defined in the function subprogram CL(V) according to (1.3.7) under the assumed limitations, and the angle of attack that appears in the function is expressed by (1.3.5). Program 1.3 computes the displacement, velocity, and angle of attack of the wing, initially stationary at its equilibrium position, after an airflow of various speeds is passed through the wind tunnel.

The computed displacement of the wing is plotted in Fig. 1.3.4 for five different wind speeds. After the wind is turned on, the aerodynamic force raises the wing upward from its static equilibrium position and the wing starts to oscillate; meanwhile, the motion of the wing causes the lift to change. At a low wind speed the wing oscillates at the natural frequency of the mass–spring system, and the amplitude of oscillation damps with time at a slow rate. As the wind speed increases, there is a slow increase in period in contrast with a faster damping in amplitude. In each case the wing will finally settle at a new state of equilibrium

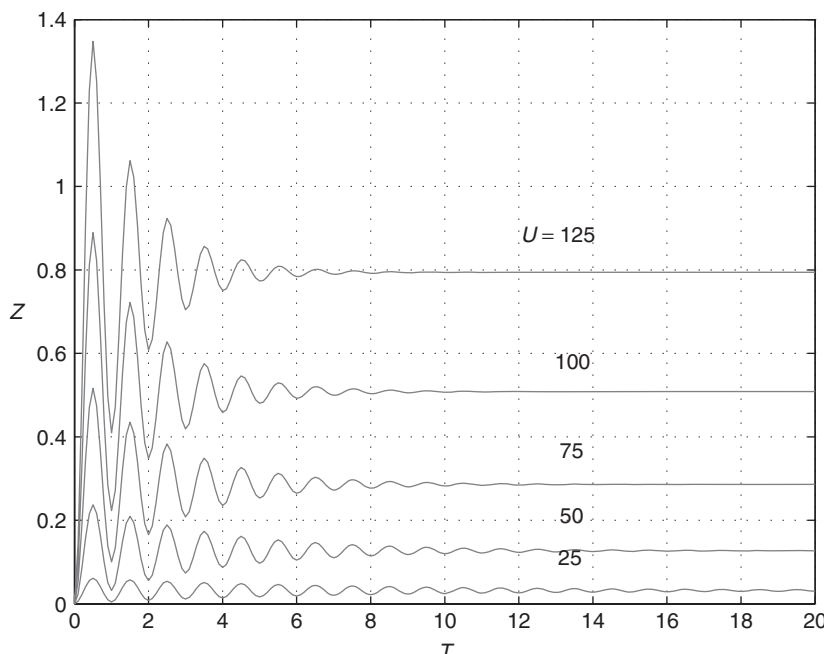


FIGURE 1.3.4 Displacement of a wing under five different wind speeds.

under which the lift is just balanced by the force from the stretched spring. You may verify that in a much stronger wind the wing may approach the equilibrium position without going through any oscillatory motion.

In Program 1.3 the lift coefficient is calculated only approximately from the steady-state formula (1.3.7), with α defined as the instantaneous angle between the resultant wind velocity and the chordline. Finding the actual lift on a wing in an unsteady motion is quite involved (Theodorsen, 1935; Bisplinghoff and Ashley, 1962, Chapter 4) and will not be discussed here. Furthermore, the angular displacement of the wing plays an important role in causing the wing to flutter. With the rotational degree of freedom omitted in the present formulation, the wing–spring system becomes stable; that is, the amplitude of oscillation cannot grow indefinitely with time.

Before an airplane is built, the designer would like to know the response of the wing to a gusty wind. Such motions of the wing may also be simulated by using our simplified model based on a quasisteady approximation. Suppose that superimposed on the uniform flow there is a fluctuating horizontal velocity component, so that the total velocity can be expressed in dimensionless form as $U(1 + a \sin \omega T)$. The fluctuation has an amplitude aU , and its frequency is ω times the natural frequency of the wing.

Computations have been performed after replacing U by the present form and changing the function $CL(V)$ to $CL(V, T)$ in Program 1.3. The results for $U = 100$, $a = 0.2$, and $\omega = 0.5, 1, 2$ are presented in Fig. 1.3.5. In response to a gust of any frequency, the wing initially tries to vibrate at its natural frequency, but finally sets into a periodical (*not* sinusoidal) motion whose frequency is smaller than both the natural frequency and the frequency of the fluctuating wind.

It is interesting to examine also the response to a fluctuating wind in the vertical direction. Figure 1.3.6 shows the results for $U = 100$ and $a = 0.2$, under the assumption that the dimensionless vertical velocity is described by $-aU \sin \omega T$. Data were obtained from Program 1.3 after replacing V by $V + aU \sin \omega T$ in the function F . In all three cases computed for $\omega = 0.5, 1$, and 2 , the wing finally vibrates approximately at its natural frequency with an amplitude varying in time. After some initial adjustment the seemingly irregular motion actually repeats the pattern every definite period of time. This period increases with decreasing ω , and it is equal to the period of the final oscillatory motion shown in Fig. 1.3.5 for the same value of ω .

In both examples resonance does not occur when the frequency of the gust coincides with the natural frequency of the wing. In a wind with horizontal fluctuations, the final amplitude of the wing motion increases with ω , while the opposite is true in a wind with vertical fluctuations. You may experiment with the program to find the value of ω that causes a maximum amplitude of oscillation for each case.

Program 1.3 can easily be generalized for computing the motion of a wing in a turbulent atmosphere with fluctuating velocities in both horizontal and vertical

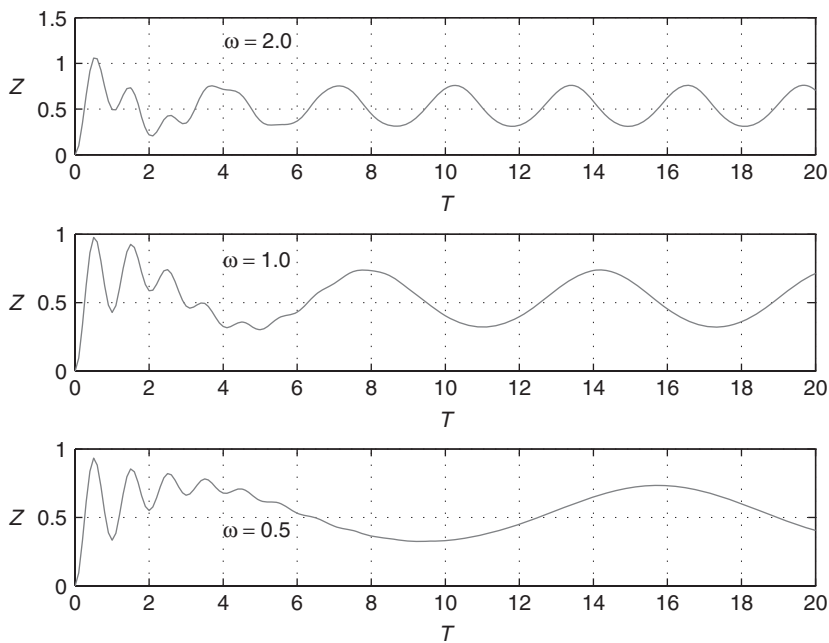


FIGURE 1.3.5 Response of a wing to an unsteady wind of speed $U(1 + a \sin \omega T)$, where $U = 100$ and $a = 0.2$.

directions. The fluctuations may be expressed as functions of time in the form of Fourier series.

Problem 1.5 If a horizontal oscillatory wind is added and the sphere is replaced by a circular cylinder in Fig. 1.3.1, the arrangement may be used as a crude model for studying the motion of a power transmission line in time-varying winds.

Consider a copper wire ($\rho = 8950 \text{ kg/m}^3$) of diameter $d = 0.005 \text{ m}$, initially stationary at its lowest sagging position with $l = 0.3 \text{ m}$. Simulate numerically its motion in a wind of speed

$$u = 30(1 + 0.2 \sin \omega t) \text{ m/s}$$

with $\omega = 0, 0.5, 1$, and 2 .

The drag coefficient of a circular cylinder is defined by

$$c_d = (\text{drag per unit length}) / \left(\frac{1}{2} \rho_f v_r^2 d\right),$$

where v_r is the *total* velocity of the fluid *relative* to the body. The drag coefficient of a long circular cylinder varies with Reynolds number, as does that of a sphere. For simplicity let us assume that $c_d = 1.2$, which is the approximate value for Reynolds numbers between 10^4 and 1.5×10^5 (Lindsey, 1938).

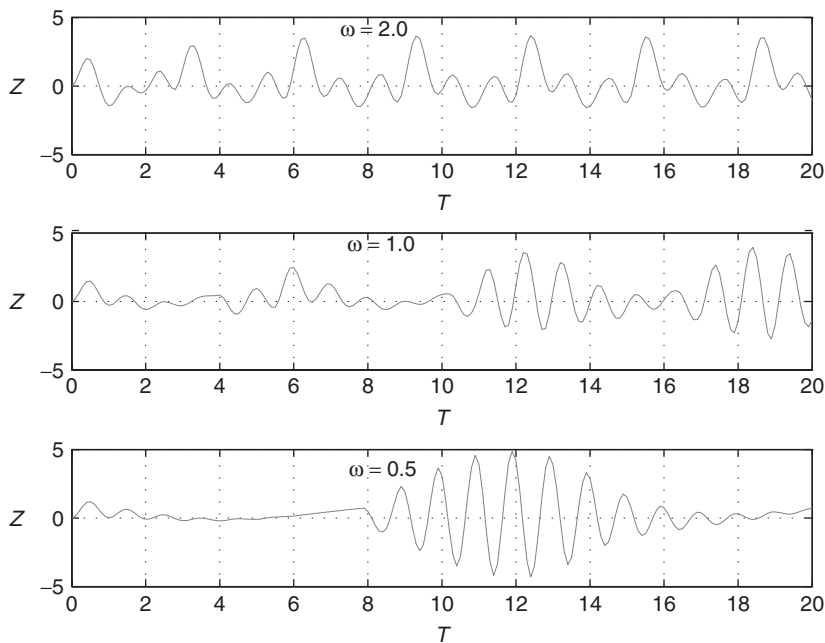


FIGURE 1.3.6 Response of a wing to gusty wind with a uniform horizontal speed $U = 100$ and an unsteady vertical speed of $0.2U \sin \omega T$.

Hint

Since the density of copper is much higher than that of air, the buoyancy and added mass can be neglected in the equations of motion. It can be shown that the component of viscous force in the direction of v is

$$\frac{1}{2} \rho_f d c_d (u \cos \theta - v) \sqrt{(u \sin \theta)^2 + (u \cos \theta - v)^2}$$

where θ and v are indicated in Fig. 1.3.1. The direction of this force component is controlled by the sign of $(u \cos \theta - v)$.

1.4 FOURTH-ORDER RUNGE-KUTTA METHOD FOR COMPUTING TWO-DIMENSIONAL MOTIONS OF A BODY THROUGH A FLUID

Consider the translation motion of a body through a fluid in the x - y plane, where y is in the direction opposite to that of the gravitational acceleration, as sketched in Fig. 1.4.1. The velocity vector of the body relative to the stationary coordinate system is \mathbf{w} , which has components u and v . In general the fluid is in motion and, at the location of the body, its velocity, \mathbf{w}_f has components u_f and v_f . The fluid dynamic forces are determined by the velocity $\mathbf{w}_r (= \mathbf{w}_f - \mathbf{w})$ of the fluid relative to that of the body.

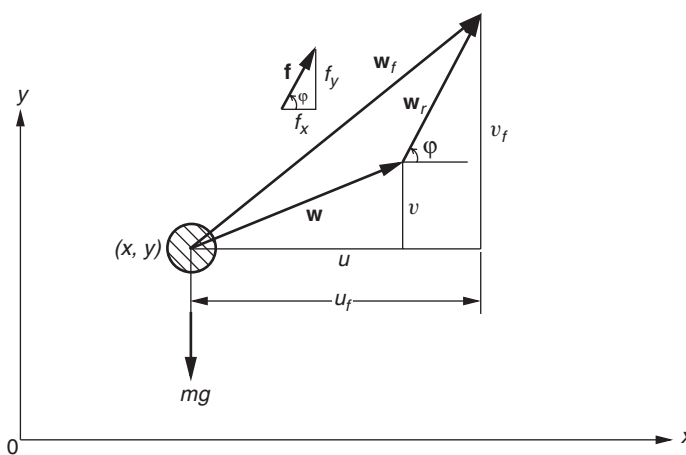


FIGURE 1.4.1 Two-dimensional motion of a body through a fluid.

If the resultant fluid dynamic force acting on the body is \mathbf{f} , with components f_x and f_y , which excludes the force associated with the added mass m' , the equations of motion of the body of mass m are

$$\begin{aligned} (m + m') \frac{d^2x}{dt^2} &= f_x \\ (m + m') \frac{d^2y}{dt^2} &= -(m - m_f)g + f_y \end{aligned} \quad (1.4.1)$$

where x, y are the coordinates of the projectile and m_f is the mass of fluid displaced by the body.

Since \mathbf{f} is generally a function of position, velocity, and time, the simultaneous ordinary differential equations (1.4.1) can be expressed in the following functional form, with each second-order equation replaced by two simultaneous equations of the first order:

$$\begin{aligned} \frac{dx}{dt} &= u & \frac{du}{dt} &= F_1(x, y, u, v, t) \\ \frac{dy}{dt} &= v & \frac{dv}{dt} &= F_2(x, y, u, v, t) \end{aligned} \quad (1.4.2)$$

The forms of the functions F_1 and F_2 vary in different problems. Suppose at an initial instant t_0 the position (x_0, y_0) and velocity (u_0, v_0) are given, the trajectory and motion of the body for $t > t_0$ are to be sought as functions of time.

The initial-value problem can again be solved numerically by use of Runge-Kutta methods. Similar to (1.1.12) and (1.1.13), with h representing the size of increments in time and subscripts i and $i + 1$ respectively denoting the values

evaluated at time steps t_i and $t_{i+1}(= t_i + h)$, the fourth-order formulas are

$$\begin{aligned}
 \Delta_1 x_i &= h u_i \\
 \Delta_1 y_i &= h v_i \\
 \Delta_1 u_i &= h F_1(x_i, y_i, u_i, v_i, t_i) \\
 \Delta_1 v_i &= h F_2(x_i, y_i, u_i, v_i, t_i) \\
 \Delta_2 x_i &= h(u_i + \frac{1}{2} \Delta_1 u_i) \\
 \Delta_2 y_i &= h(v_i + \frac{1}{2} \Delta_1 v_i) \\
 \Delta_2 u_i &= h F_1\left(x_i + \frac{1}{2} \Delta_1 x_i, y_i + \frac{1}{2} \Delta_1 y_i, u_i + \frac{1}{2} \Delta_1 u_i, v_i + \frac{1}{2} \Delta_1 v_i, t_i + \frac{1}{2} h\right) \\
 \Delta_2 v_i &= h F_2\left(x_i + \frac{1}{2} \Delta_1 x_i, y_i + \frac{1}{2} \Delta_1 y_i, u_i + \frac{1}{2} \Delta_1 u_i, v_i + \frac{1}{2} \Delta_1 v_i, t_i + \frac{1}{2} h\right) \\
 \Delta_3 x_i &= h(u_i + \frac{1}{2} \Delta_2 u_i) \\
 \Delta_3 y_i &= h(v_i + \frac{1}{2} \Delta_2 v_i) \\
 \Delta_3 u_i &= h F_1\left(x_i + \frac{1}{2} \Delta_2 x_i, y_i + \frac{1}{2} \Delta_2 y_i, u_i + \frac{1}{2} \Delta_2 u_i, v_i + \frac{1}{2} \Delta_2 v_i, t_i + \frac{1}{2} h\right) \\
 \Delta_3 v_i &= h F_2\left(x_i + \frac{1}{2} \Delta_2 x_i, y_i + \frac{1}{2} \Delta_2 y_i, u_i + \frac{1}{2} \Delta_2 u_i, v_i + \frac{1}{2} \Delta_2 v_i, t_i + \frac{1}{2} h\right) \\
 \Delta_4 x_i &= h(u_i + \Delta_3 u_i) \\
 \Delta_4 y_i &= h(v_i + \Delta_3 v_i) \\
 \Delta_4 u_i &= h F_1(x_i + \Delta_3 x_i, y_i + \Delta_3 y_i, u_i + \Delta_3 u_i, v_i + \Delta_3 v_i, t_i + h) \\
 \Delta_4 v_i &= h F_2(x_i + \Delta_3 x_i, y_i + \Delta_3 y_i, u_i + \Delta_3 u_i, v_i + \Delta_3 v_i, t_i + h) \\
 x_{i+1} &= x_i + \frac{1}{6}(\Delta_1 x_i + 2\Delta_2 x_i + 2\Delta_3 x_i + \Delta_4 x_i) \\
 y_{i+1} &= y_i + \frac{1}{6}(\Delta_1 y_i + 2\Delta_2 y_i + 2\Delta_3 y_i + \Delta_4 y_i) \\
 u_{i+1} &= u_i + \frac{1}{6}(\Delta_1 u_i + 2\Delta_2 u_i + 2\Delta_3 u_i + \Delta_4 u_i) \\
 v_{i+1} &= v_i + \frac{1}{6}(\Delta_1 v_i + 2\Delta_2 v_i + 2\Delta_3 v_i + \Delta_4 v_i)
 \end{aligned} \tag{1.4.3}$$

Based on these formulas, a subprogram named KUTTA will be constructed in Program 1.4 in the next section. To use the subprogram, one needs only to attach it to the main program and define in two separate subprograms the functions F_1 and F_2 . The usage will be demonstrated in some of the following programs.

1.5 BALLISTICS OF A SPHERICAL PROJECTILE

It is well known that in small-scale motions a projectile traces out a parabola when shooting upward in a direction not perpendicular to the earth's surface. But this conclusion is derived by considering trajectories in a vacuum. To study the

effect of the surrounding fluid on the motion of a spherical projectile, let us go back to the equations of motion (1.4.1). If the sphere does not rotate, \mathbf{f} becomes the viscous drag in the direction of the relative velocity \mathbf{w}_r , which makes an angle φ with the x axis. From Fig. 1.4.1 we have $\sin \varphi = (v_f - v)/w_r$, where $w_r = \sqrt{(u_f - u)^2 + (v_f - v)^2}$. Thus,

$$f_x = |\mathbf{f}| \cos \varphi = \frac{1}{8} \pi \rho_f d^2 c_d (u_f - u) w_r$$

and

$$f_y = |\mathbf{f}| \sin \varphi = \frac{1}{8} \pi \rho_f d^2 c_d (v_f - v) w_r$$

The directions of f_x and f_y are determined by the signs of $(u_f - u)$ and $(v_f - v)$, respectively, and c_d is the drag coefficient of the sphere moving at the speed w_r , described in Fig. 1.2.2.

As discussed in Section 1.2, the added mass m' for a sphere is $m_f/2$. With m and m_f expressed in terms of densities ρ and ρ_f , and f_x , f_y replaced by the above expressions, (1.4.1) becomes, after some rearrangement,

$$\frac{d^2x}{dt^2} = \frac{3\bar{\rho}}{4d} c_d (u_f - u) w_r \left/ \left(1 + \frac{1}{2}\bar{\rho} \right) \right. \quad (1.5.1)$$

and

$$\frac{d^2y}{dt^2} = \left[-(1 - \bar{\rho})g + \frac{3\bar{\rho}}{4d} c_d (v_f - v) w_r \right] \left/ \left(1 + \frac{1}{2}\bar{\rho} \right) \right. \quad (1.5.2)$$

Since the fluid velocity components are generally functions of location and time, the right-hand sides of (1.5.1) and (1.5.2) will be called $\text{FX}(x, y, u, v, t)$ and $\text{FY}(x, y, u, v, t)$, respectively. They are the special forms of the functions F_1 and F_2 in (1.4.2).

We consider a steel sphere 0.05 m in diameter moving in air. Initially, when $t = 0$, the sphere shoots from the origin of the coordinate system with a speed w_0 at an elevation of θ_0° . Elevation is the angle between the initial velocity of a projectile and the x axis. The motions of the body for a fixed initial speed $w_0 = 50$ m/s are to be computed under the conditions that $\theta_0 = 30^\circ$, 45° , and 60° . For numerical computations in Program 1.4, we implement MATLAB initial value solver, ODE45 (Program 1.4), or solve (1.5.1) and (1.5.2) using subprogram KUTTA outlined above (Program 1.4_RK4).

Instead of setting a time limit to terminate the computation, we stop it when the projectile falls back to or below its initial height, in other words, when $y \leq 0$ for a negative v . The drag coefficient of the spherical body is still approximated by the function described already in the subprogram CD attached to Program 1.2. The program is constructed so that the fluid velocity components u_f and v_f are specified in the function subprograms FX and FY instead of in the main program. In the present problem both components are zero. The subprograms can easily be modified to describe any steady or unsteady wind fields.

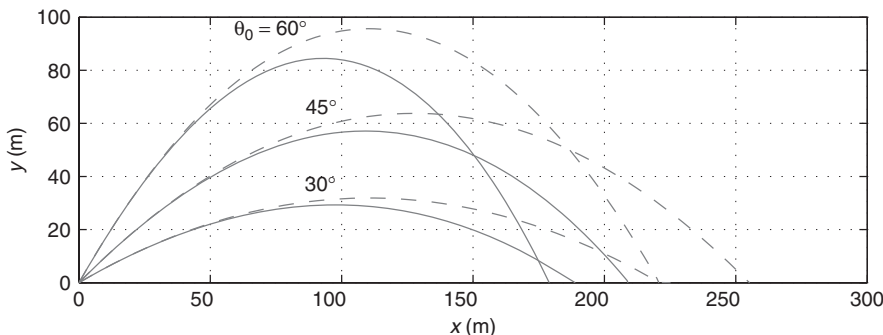


FIGURE 1.5.1 Trajectories of a sphere in air (solid lines) and those in vacuum (dashed lines).

The motions in a vacuum are obtained when the value zero is assigned to ρ_f in Program 1.4, and the resultant trajectories are plotted in Fig. 1.5.1 for comparison. It shows that air resistance reduces both the range and the maximum height of a projectile. The data also reveal that the flight time is also reduced in the presence of air. It is interesting to note that the ranges are the same for $\theta_0 = 30^\circ$ and 60° in a vacuum; while in air, because of the longer flight time for the trajectory with $\theta_0 = 60^\circ$, its range becomes shorter due to the longer action of air resistance.

Problem 1.6 Find the effect of a 20-m/s wind on the trajectory of a sphere described in Program 1.4. The wind may either be in the direction of the x axis or against it.

By examining Fig. 1.5.1 a question naturally arises. It is known that in a vacuum the range of a projectile becomes maximum when $\theta_0 = 45^\circ$. Is this still true in the presence of a fluid?

Modifications to Program 1.4 are needed before we can do some calculations to find an answer to this question. Position and velocity of the body are computed in Program 1.4 according to a constant time increment; therefore, the range is not specifically shown in the output. Furthermore, an algorithm has to be found so that the maximum of a function can be located automatically by the computer.

The range can be found approximately by using Fig. 1.5.2. Suppose that in the numerical integration the point Q is the *first* computed point at which the body falls back on or below the horizon. Tracing back to the previous time step, the body was at the point P . The path connecting P and Q is, in general, a curve, but can be approximated by a straight line if the time interval is small. The range x_r is the distance between the origin and the point where the line PQ intersects the x axis. Similarity of the two shaded triangles gives

$$\frac{y_P}{x_r - x_P} = \frac{-y_Q}{x_Q - x_r}$$

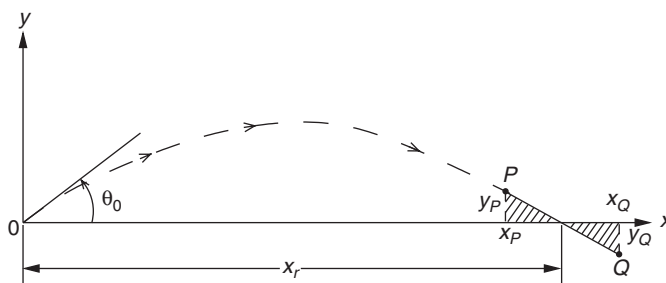


FIGURE 1.5.2 Finding the range of a projectile.

or, after solving for x_r ,

$$x_r = \frac{x_Q y_P - x_P y_Q}{y_P - y_Q} \quad (1.5.3)$$

In this equation y_Q is either negative or zero.

Q is the last point on a trajectory at which numerical computation is performed in Program 1.4. When this point is reached, the data associated with the previous points have been erased from the computer memory according to the way the Runge-Kutta formulas are programmed. The position of P , which is one time step ahead of Q , can be obtained at this stage by calling the subprogram KUTTA (or ODE45) with the argument DT replaced by $-DT$. By doing so it is equivalent to integrating the equations of motion backward through one time step.

If one keeps integrating backward from the point P until time returns to its initial value, the deviations between the computed and the assumed conditions at $t = 0$ will show the accuracy of the numerical method. A test on Program 1.4 reveals that the error in position is only of the order of 10^{-9} m and that in velocity cannot be detected when printed according to the present field specification.

The range computed from (1.5.3) is a function of the elevation of a projectile. If the variation is described by the curve sketched in Fig. 1.5.3, we would like to locate the angle θ_0 at which the range is maximum.

Let us choose an arbitrary point a on the curve and locate a second point b according to the relation

$$(\theta_0)_b = (\theta_0)_a + \delta_1$$

where δ_1 is an arbitrary incremental quantity. If $(x_r)_a < (x_r)_b$ as shown in the sketch, the maximum is to the right of this interval, and a third point c is located that is a distance δ_1 to the right of b . If $(x_r)_b < (x_r)_c$, we repeat the process by locating points successively at a constant pace δ_1 to the right. However, if $(x_r)_b \geq (x_r)_c$ as shown, the maximum should appear to the left of c . This time we change the increment to $\delta_2 (= -\delta_1/2)$ and find the next point d according to

$$(\theta_0)_d = (\theta_0)_c + \delta_2$$

Now $(x_r)_c < (x_r)_d$; that is, the range at the “old” point c is less than that at the “new” point d . Following the previous rule, we should go to a point whose

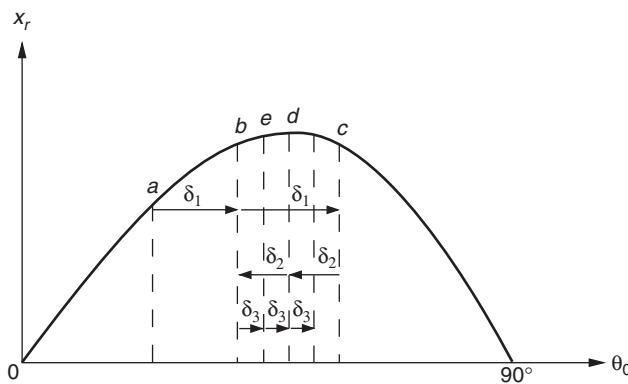


FIGURE 1.5.3 Finding maximum range by the use of a half-interval method.

abscissa is $(\theta_0)_d + \delta_2$, which is essentially point b , although the maximum lies on the other side of d in the present case. But the condition that $(x_r)_d \geq (x_r)_b$, or that the range at the old point is greater than or equal to that at the new point, demands the change of increment to $\delta_3 (= -\delta_2/2)$. This increment brings the next point e back to the right of b . Two steps later we end up at a point between d and c . Repeating the same process, we can arrive at a point that is as close as desired to the point where the range is maximum.

To make it convenient for computer calculation, the process for finding maximum range is generalized as follows. At any step in this method we have a point on the curve whose coordinates are called $(\theta_0)_{\text{old}}$ and $(x_r)_{\text{old}}$, and an increment called δ . A new point is found by using the relation

$$(\theta_0)_{\text{new}} = (\theta_0)_{\text{old}} + \delta \quad (1.5.4)$$

at which the range is $(x_r)_{\text{new}}$. The ranges at these two points are then compared. The increment keeps the same value if $(x_r)_{\text{new}} > (x_r)_{\text{old}}$; otherwise, δ is replaced by $-\delta/2$. At this stage the old point is no longer needed, so we call the new point an old one and, in the meantime, rename its coordinates as $(\theta_0)_{\text{old}}$ and $(x_r)_{\text{old}}$. A new point is then located according to (1.5.4). The process is repeated until $|\delta|$ becomes less than a specified small quantity ε . At this final step the two ranges $(x_r)_{\text{new}}$ and $(x_r)_{\text{old}}$ are again compared. The greater one is the approximated maximum range, and the corresponding θ_0 is the optimum elevation. The accuracy of the result is controlled by the magnitude of ε .

Because the increment δ is consecutively reduced by half in the preceding method, it is called the *half-interval* or *interval halving method*. With some modifications the method can be used to find the minimum or the zeros of a function.

The formula (1.5.3) and the half-interval method are included in Program 1.5 to find the optimum shooting angle of a spherical projectile causing a maximum range. To emphasize the effect of air resistance, a smaller steel sphere of 1 cm diameter is considered instead of the 5-cm-diameter projectile examined

in Program 1.4. The conclusion that the surrounding fluid has less influence on the motion of larger spheres has been drawn from the result of Program 1.1 for free-falling bodies. The initial speed is still kept at 50 m/s.

Three wind conditions are assumed in Program 1.5 with horizontal wind speeds of 20, 0, and -20 m/s, respectively. Because of the variable wind speed, u_f can no longer be defined in the subprograms FX and FY as in Program 1.4. Instead, the wind components are defined in the main program and transmitted into subprograms by defining these variables as “global.”

The computer output (Table 1.A.1) shows that for the 1-cm-diameter projectile the optimum shooting angles are all below 45° . The optimum angle in a favorable wind is the highest, and that in an adverse wind is the lowest among the three. The result can be explained as follows. Shooting a projectile in a vacuum at a 45° angle gives a range longer than the one that resulted from a lower shooting angle, and the flight time of the projectile in the former is longer than that in the latter case. In the presence of air without a wind, because of the shorter action of air resistance on the body, less kinetic energy is dissipated from the projectile shooting at a lower angle and, under appropriate conditions, the loss in horizontal distance because of air friction can be less. The plot of trajectories for $\theta_0 = 30^\circ$ and 60° in Fig. 1.5.1 is such an example. By shooting the body at a properly chosen angle below 45° , the frictional loss can be minimized to give a maximum range. A wind blowing in the direction of the body motion carries the body with it. To aim the projectile higher increases the contact time with air and therefore increases the range. On the other hand, in an adverse wind, the optimum angle should be lower than that in a quiet atmosphere in order to reduce the retarding effect of the wind. The computed results are in agreement with the experiences of a golfer.

The optimum angles are not always below 45° , however, if the size of the projectile is changed. The variations of the optimum angle with diameter under three wind conditions are plotted in Fig. 1.5.4. The data are obtained by varying the value of D in Program 1.5. Figure 1.5.4 shows that for small projectiles in a favorable wind, the optimum angle can be higher than 45° . The influence of air on the motion of a projectile is diminishing with increasing diameter, and the optimum angle finally approaches 45° .

On the curve for the adverse-wind case a sharp dip appears in a region where the Reynolds number starts to exceed the value 3×10^5 . The phenomenon is caused by the abrupt decrease of drag at that particular Reynolds number (see Fig. 1.2.2).

Problem 1.7 Contrary to common sense, under certain conditions the maximum range of a projectile can be made longer when it is thrown against the wind instead of in the wind direction. To prove that this is possible, run Program 1.5 for a steel sphere 0.09 m in diameter while keeping the other conditions the same. The result will show that among the three cases the maximum range is the longest for $u_f = -20$ m/s. Print out the Reynolds numbers and give an explanation of this phenomenon.

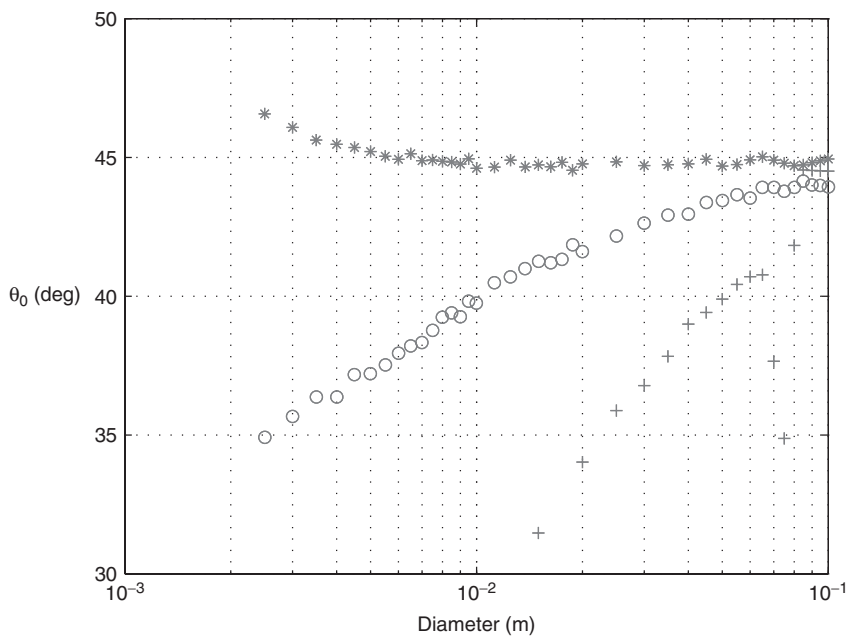


FIGURE 1.5.4 Optimum shooting angle for a steel spherical projectile having an initial speed of 50 m/s. *, $u_f = 20$ m/s; °, $u_f = 0$ m/s; +, $u_f = -20$ m/s.

Problem 1.8 It was discovered accidentally during World War I that aiming a cannon at an angle higher than what had previously been believed to give maximum range resulted in a great increase in the range of the shell. The reason is that the projectile reaches a higher altitude by aiming the gun higher, and the smaller air resistance there may cause a longer range for certain angles. To verify this phenomenon, let us consider a cannon shell whose muzzle velocity is 800 m/s. At a supersonic speed the drag coefficient is a function of Mach number and of Reynolds number, and it varies with the shape of the projectile. For the sake of simplicity we assume that the shell is equivalent to a steel sphere of 0.3 m diameter having a drag coefficient of a constant value of 0.4 throughout the flight. Find the optimum shooting angle and the maximum range of the shell in an atmosphere of constant density of 1.22 kg/m^3 ; then find the angle and range in an atmosphere whose density is described by the exponential law

$$\rho_f = 1.22 \exp(-0.000118y) \text{ kg/m}^3$$

where y is the height above sea level measured in meters. The result will show a higher optimum shooting angle and a longer range in the case of the variable-density atmosphere.

Project for Further Study: Consider the cannon shell and the stratified atmosphere described in Problem 1.8. Write a computer program that computes the

angle at which the cannon should be aimed in order to hit a target a distance x_t away. To make the program more general, the wind components are to be included. Test the program for $x_t = 8000$ m and 15,000 m in the absence of a wind.

Hint

The half-interval method can again be applied to this problem. Let the curve in Fig. 1.5.5 represent the variation of range with shooting angle. There are in general two angles at which the range is x_t , if x_t is within the maximum range. Let the lower one be θ_t . Similar to what we did in finding the maximum range, two arbitrary points whose ordinates are called $(x_r)_{\text{old}}$ and $(x_r)_{\text{new}}$, respectively, are chosen on the curve at a distance δ apart. When the abscissas of both points are on the left side of θ_t , we will choose a new point a distance δ to the right of the second point. If they end up on two sides of θ_t as shown in Fig. 1.5.5, the new point has just passed the location we are looking for, and the next new point will be located midway between the present new and old points. Thus, an algorithm has been obtained. We start from the left end of the curve with two points and a positive value of δ . At each step the product of $[x_t - (x_r)_{\text{old}}]$ and $[x_t - (x_r)_{\text{new}}]$ is examined. δ keeps the same value if the product is positive; it is replaced by $-\delta/2$ otherwise. By adding δ to $(x_r)_{\text{new}}$, the next point is located. Repeat the process until the absolute value of δ is within a specified small quantity; the approximate value of θ_t is then obtained. Proceed to the right from there with the initially assumed value of δ ; the second value of the aiming angle is then found. If no value of θ_t can be found within 90° , the searching should be stopped, because the target is out of the maximum range of the cannon. Print a statement in the output for such a case.

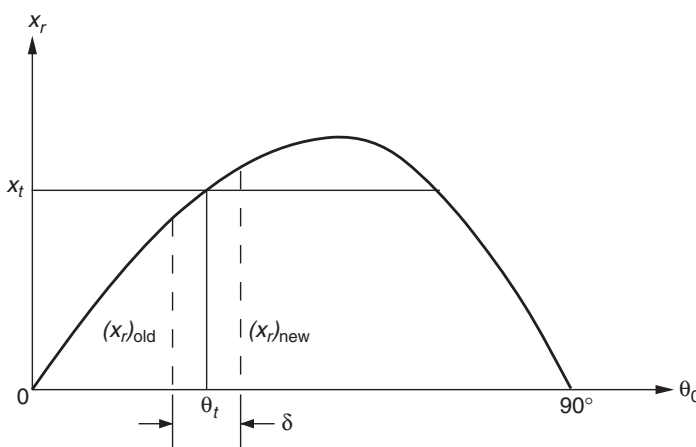


FIGURE 1.5.5 Finding the aiming angles of a cannon for hitting a target at a distance x_t away.

1.6 FLIGHT PATH OF A GLIDER – A GRAPHICAL PRESENTATION

In this section, we will present the numerical result for the flight paths of a glider. Figure 1.6.1 shows a glider of mass m flying at a velocity w , which makes an angle θ with the horizontal x axis. The aerodynamic forces acting on the glider in the directions normal and parallel to the flight path are called the lift L and drag D , respectively. If u and v are the velocity components, the equations of motion of the center of mass, ignoring the added mass and the angular motion about the mass center, are

$$m \frac{du}{dt} = -L \sin \theta - D \cos \theta \quad (1.6.1)$$

$$m \frac{dv}{dt} = -mg + L \cos \theta - D \sin \theta \quad (1.6.2)$$

in which $\sin \theta = v/w$ and $\cos \theta = u/w$. The lift and drag of the aircraft as a whole can be expressed in terms of a lift coefficient c_l and a drag coefficient c_d , so that

$$\begin{aligned} L &= c_l \frac{1}{2} \rho w^2 S \\ D &= c_d \frac{1}{2} \rho w^2 S \end{aligned} \quad (1.6.3)$$

where ρ is the density of air and S is the projected wing area.

Suppose at an initial instant $t = 0$ the velocity is w_0 and the inclination angle is θ_0 . Using w_0 as the reference velocity, w_0/g as the reference time, and w_0^2/g as the reference length, we can construct dimensionless velocity components U, V ,

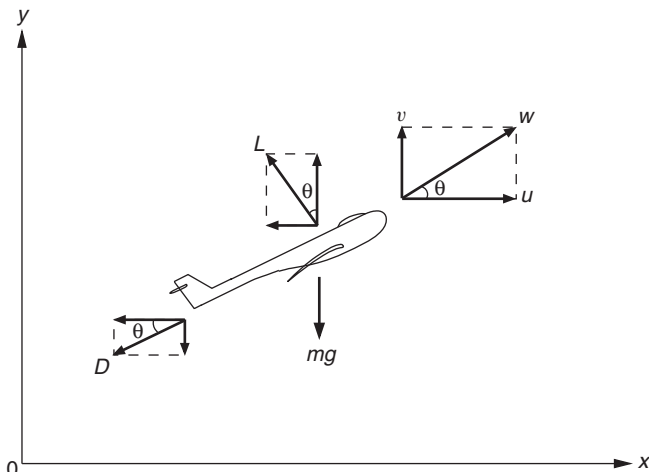


FIGURE 1.6.1 Forces on a glider.

dimensionless time T , and dimensionless coordinates X, Y . Upon substitution from (1.6.3) and by using trigonometric relations, (1.6.1) and (1.6.2), expressed in dimensionless form, become

$$\frac{d^2X}{dT^2} = -A(U^2 + V^2)^{1/2}(BU + V) \quad (1.6.4)$$

$$\frac{d^2Y}{dT^2} = -1 + A(U^2 + V^2)^{1/2}(U - BV) \quad (1.6.5)$$

where $U = dX/dT$ and $V = dY/dT$. The two dimensionless parameters A and B represent the ratios $c_l \frac{1}{2} \rho w_0^2 S / mg$ and c_d / c_l , respectively. Since the lift and drag coefficients are functions of angle of attack controlled by the pilot, both A and B are generally variables. In the following computation A and B are assumed to be constant. An example for such a case is a model glider that has wings fixed at a constant angle of attack.

A glider having $A = 1.5$ and $B = 0.06$ is considered in Program 1.6. Starting from the origin of the coordinate system with the same initial velocity, flight paths are computed for $\theta_0 = -90^\circ$ and 180° by using the fourth-order Runge-Kutta method. At $\theta_0 = -90^\circ$ the glider dives vertically, and at $\theta_0 = 180^\circ$ it flies upside down in the negative x direction. To be used in the plotting subprograms, the coordinates of the glider have to be stored as the elements of some one-dimensional arrays. At the n th time step the coordinates on the first flight path are called $x_1(n)$ and $y_1(n)$, and those on the second flight path are called $x_2(n)$ and $y_2(n)$.

The two flight paths are plotted in Fig. 1.6.2 by using standard MATLAB plotting programs. If there were no drag and the glider were weightless, the lift would

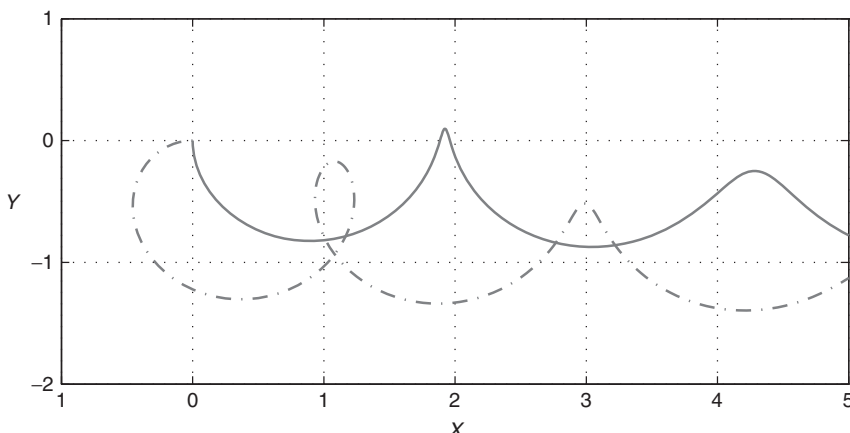


FIGURE 1.6.2 Flight path a glider starting from the origin having $A = 1.5$, $B = 0.06$, $W_0 = 1.0$. —, $\text{THETA0} = -90$ degrees; ..., $\text{THETA0} = 180$ degrees.

always be perpendicular to the flight direction resulting in a circular path. The weight changes the path into a coil-shaped curve drifting along the x axis with an undamped amplitude. These are analogous to the paths of a charged particle moving in a uniform magnetic field with and without a body force normal to the field lines. In the presence of a drag force the kinetic energy is dissipated continuously, and the average altitude of the glider is a decreasing function of time.

In the case $\theta = -90^\circ$, the glider first dives and then climbs upward. When it reaches a position slightly higher than its original height, most of the kinetic energy has been used up in overcoming the frictional and gravitational forces. The low speed cannot generate enough lift to support the weight, so that the glider stalls and then turns itself into a diving position to pick up speed again. Such a trajectory is often observed when a schoolchild tries out a paper glider. On the other hand, in the case $\theta_0 = 180^\circ$, the initial lift force is in the same direction as that of the weight and thus helps to accelerate the glider. When the glider reaches the first horizontal position, it has gained such a high speed that it has sufficient kinetic energy to go through a loop.

When a thrust force is added to (1.6.1) and (1.6.2), they become the equations of motion for an airplane. With some modifications Program 1.6 can be used to simulate taking off, climbing, and other two-dimensional aircraft maneuvers.

Problem 1.9 Flight of a Rocket Equations that define the motion of a rocket are

$$\frac{dz}{dt} = v$$

$$(m_c + m_p) \frac{dv}{dt} = -(m_c + m_p)g + m_p v_e - \frac{1}{2} \rho v |v| A C_D$$

In these equations,

z is the vertical coordinate

weight of rocket casing, $m_c g = 500$ N

gravitational acceleration, $g = 9.8$ m/s 2

air density, $\rho = 1.23$ kg/m 3

maximum cross-sectional area, $A = 0.1$ m 2

exhaust speed, $v_e = 360$ m/s

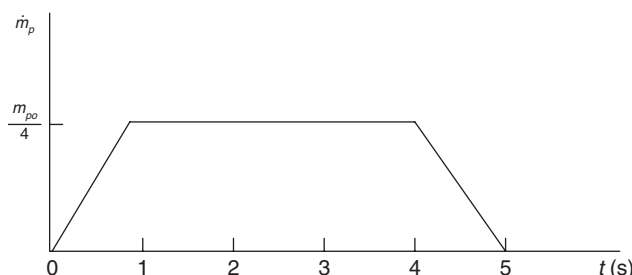
drag coefficient, $C_D = 0.15$

m_p , the instantaneous mass of the propellant at time t , is given by

$$m_p = m_{po} - \int_0^5 \dot{m}_p dt$$

where $m_{po}g$, the initial weight of the propellant at $t = 0$, is 1000 N, and the time-varying burn rate is given below: Write a MATLAB program for computing the height and velocity of the rocket using a second-order Runge-Kutta method with $\Delta t = 0.1$ s. Plot the height (z) and velocity (v) as a function of time, t . From the plots determine, approximately,

- The maximum speed of the rocket, and the time and height at which it occurs.
- The maximum height the rocket can reach, and the time at which it occurs.
- The time and velocity when the rocket hits the ground.
- Check your results with those that you will obtain by using MATLAB ODE45 solver.



1.7 ROLLING UP OF THE TRAILING VORTEX SHEET BEHIND A FINITE WING

In computing the lift for a wing of infinite span, the wing can be replaced by a vortex sheet coinciding with the mean camber line of the airfoil. If the total circulation of the vortex sheet is Γ and the wing flies at a constant speed U through air of density ρ , the lift per unit span is, according to the *Kutta-Joukowski theorem* (Kuethe and Chow, 1998, Chapter 4),

$$L' = \rho U \Gamma \quad (1.7.1)$$

The circulation is defined as

$$\Gamma = \oint \mathbf{V} \cdot d\mathbf{s} \quad (1.7.2)$$

in which \mathbf{V} is the fluid velocity and $d\mathbf{s}$ is a line element along any closed curve enclosing the vortex sheet. The integration is performed in the clockwise direction. Thus, as far as the sectional lift is concerned, the wing may be treated as an infinitely long *bound vortex* of circulation Γ whose axis is parallel to the span. A bound vortex is one that does not move with the fluid like a free vortex.

When a bound vortex is used to approximate a finite wing, the vortex cannot end at the wing tips according to Helmholtz vortex laws; its ends are carried downstream by the fluid motion to form a pair of oppositely revolving vortices trailing behind the wing. Such a form of the vortex line, with the middle portion fixed to the wing and the remaining parts extending to infinity in the downstream direction, is called a *horseshoe vortex*.

The lift per unit span on a finite wing actually varies along the span, so that the circulation of the bound vortex is a function of the spanwise location. A finite wing symmetrical about its midplane is usually constructed by a superposition of horseshoe vortex elements of various strengths, as sketched schematically in Fig. 1.7.1. An infinite number of these vortices lead to a continuous distribution of circulation $\Gamma(x)$ and therefore of the lift per unit span $\rho U \Gamma(x)$ on a wing of span $2a$. The infinite number of trailing vortices then form a vortex sheet on the $x-z$ plane of strength $\gamma(x)$, which is defined as the circulation of vortices contained within unit spanwise length of the sheet. From Fig. 1.7.1 we have

$$\gamma(x) = \frac{d\Gamma}{dx} \quad (1.7.3)$$

The trailing vortices induce at the wing a velocity field pointing in the negative y direction, called the downwash, causing an induced drag that is a characteristic of a wing of finite span. Detailed analyses of finite wings appear in Chapter 6 of Kuethe and Chow (1998) and are not elaborated on here.

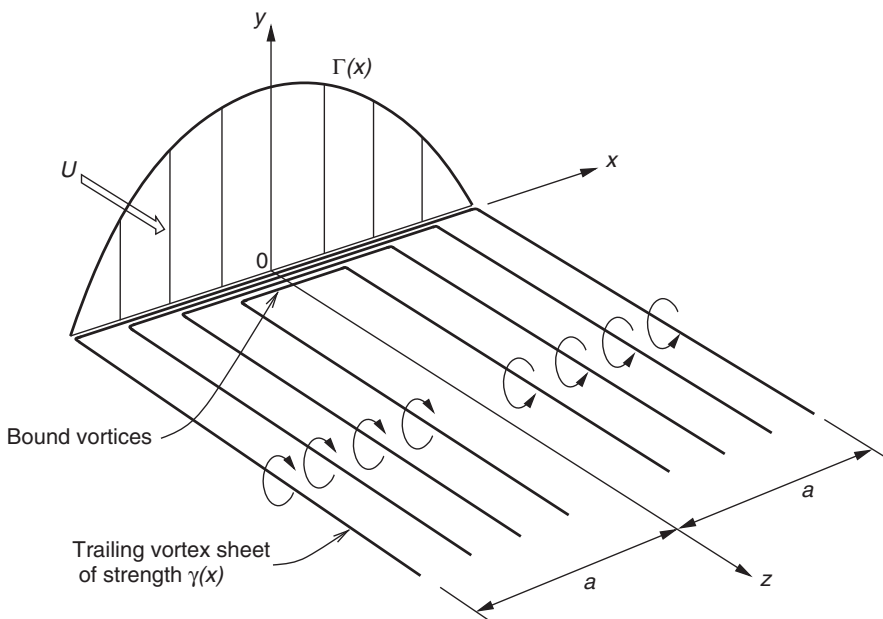


FIGURE 1.7.1 Vortex system for a finite wing.

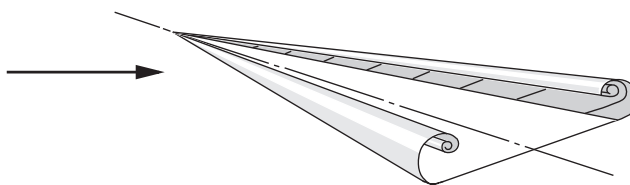


FIGURE 1.7.2 Roll-up of trailing vortex sheet behind a delta wing.

The trailing vortex sheet shown in Fig. 1.7.1 cannot always remain on the x - z plane, as assumed for the convenience of theoretical analyses. Each line vortex moves under the influence of the others, and the motion differs from one vortex to another, depending on the instantaneous geometry of the sheet. In reality the vortex sheet is found to roll up, forming two well-defined column vortices trailing behind an airplane. Figure 1.7.2 shows the rolling up of the vortex sheet behind a delta wing, whose horseshoe-vortex arrangement is somewhat different from that shown in Fig. 1.7.1.

The roll-up of a vortex sheet is a three-dimensional phenomenon, as exhibited by Fig. 1.7.2. Instead of dealing with this realistic but extremely cumbersome situation, we examine a simplified two-dimensional problem by considering the deformation of a vortex sheet of width $2a$ that extends to infinity in either direction along the z -axis. In this way the constraint that one end of the sheet must be attached to the bound vortices inside the wing is removed. The configurations of the two-dimensional vortex sheet at various times closely resemble those at different downstream sections along the deforming three-dimensional sheet.

For an elliptically loaded wing with circulation Γ_0 in the plane of symmetry, the variation of circulation with spanwise location is written

$$\Gamma = \frac{(a^2 - x^2)^{1/2}}{a} \Gamma_0 \quad (1.7.4)$$

and, from (1.7.3), the strength of the initially planar trailing vortex sheet is

$$\gamma = -\frac{\Gamma_0 x}{a(a^2 - x^2)^{1/2}} \quad (1.7.5)$$

It can easily be shown that the total circulation of the vortices of positive strength on the left half of the sheet is Γ_0 , and that of the vortices of negative strength on the right is $-\Gamma_0$. To study the evolution of this continuous vortex distribution, the sheet is discretized by subdividing it into spanwise intervals and replacing each subdivision by a point vortex of circulation equal to the circulation of all vortices within that subdivision. The velocity of each point vortex can be obtained as a function of the position of the others, from which the displacement of that vortex at a short time period later is computed. The deformation of the sheet with respect to time is thus traced by repeatedly integrating forward in time.

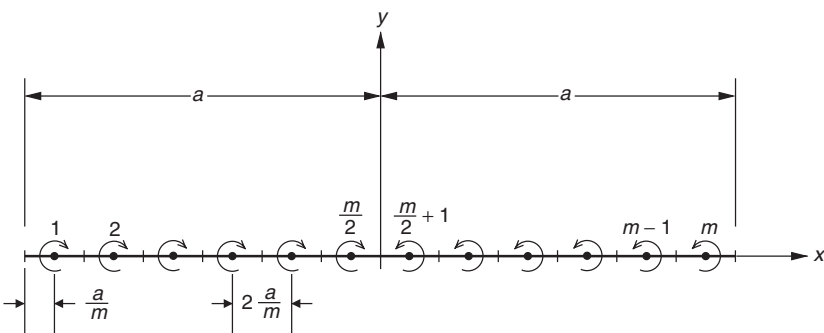


FIGURE 1.7.3 Replacement of a vortex sheet by m equally spaced discrete point vortices.

Suppose that at time $t = 0$ the initially flat vortex sheet is divided into m equally spaced intervals, as shown in Fig. 1.7.3, m being a reasonably large even integer. If each subdivision is replaced by a discrete vortex at the middle, the distance between any two neighboring vortices is $2a/m$, and each of the two outermost vortices is at a distance of a/m from the wing tip. These m discrete vortices are named in an ascending order starting from the left end, as marked in the figure. By substitution from (1.7.5) for γ , the circulation or the strength of the i th vortex located at (x_i, y_i) is

$$\begin{aligned} g_i &= \int_{x_i - a/m}^{x_i + a/m} \gamma \, dx \\ &= \Gamma_0 \left[\sqrt{1 - \left(\frac{x_i}{a} + \frac{1}{m} \right)^2} - \sqrt{1 - \left(\frac{x_i}{a} - \frac{1}{m} \right)^2} \right] \end{aligned} \quad (1.7.6)$$

where x_i is the initial abscissa of the point vortex and $y_i = 0$ at the same time.

The Biot-Savart law (Kuethe and Chow, 1998 Section 2.14) is applied to compute the velocity \mathbf{W}_i of the i th vortex induced by the j th vortex at (x_j, y_j) , with both vortices at two arbitrary positions, as depicted in Fig. 1.7.4.

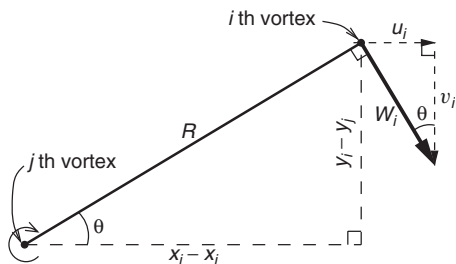


FIGURE 1.7.4 Velocity of the i th vortex induced by the j th vortex.

If $R[=\sqrt{(x_i - x_j)^2 + (y_i - y_j)^2}]$ is the distance between the two concerned vortices, the magnitude of the induced velocity is $W_i = g_j / (2\pi R)$. When it is decomposed into x and y directions, this velocity has the components

$$u_i = W_i \sin \theta = \frac{y_i - y_j}{R} W_i$$

$$v_i = -W_i \cos \theta = -\frac{x_i - x_j}{R} W_i$$

Adding the contributions from all vortices other than the i th vortex itself and replacing u by dx/dt and v by dy/dt , we obtain

$$\frac{dx_i}{dt} = \sum_{j \neq i}^m \frac{g_j}{2\pi} \frac{y_i - y_j}{(x_i - x_j)^2 + (y_i - y_j)^2} \quad (1.7.7)$$

$$\frac{dy_i}{dt} = -\sum_{j \neq i}^m \frac{g_j}{2\pi} \frac{x_i - x_j}{(x_i - x_j)^2 + (y_i - y_j)^2} \quad (1.7.8)$$

It is more convenient to work with dimensionless quantities. In terms of dimensionless variables defined by

$$X = \frac{x}{a}, \quad Y = \frac{y}{a}, \quad G = \frac{g}{\Gamma_0}, \quad T = \frac{t}{2\pi a^2} / \Gamma_0$$

(1.7.6) to (1.7.8) become

$$G_i = \sqrt{1 - \left(X_i + \frac{1}{m}\right)^2} - \sqrt{1 - \left(X_i - \frac{1}{m}\right)^2} \quad (1.7.9)$$

$$\frac{dX_i}{dt} = \sum_{j \neq i}^m G_j \frac{Y_i - Y_j}{(X_i - X_j)^2 + (Y_i - Y_j)^2} \quad (1.7.10)$$

$$\frac{dY_i}{dt} = -\sum_{j \neq i}^m G_j \frac{X_i - X_j}{(X_i - X_j)^2 + (Y_i - Y_j)^2} \quad (1.7.11)$$

The dimensionless distance between any two neighboring vortices at the initial instant is then $2/m$.

Equations (1.7.10) and (1.7.11) form a system of two simultaneous first-order ordinary differential equations. If the system is written in the general form that

$$\frac{dx}{dt} = F_1(x, y), \quad \frac{dy}{dt} = F_2(x, y), \quad (1.7.12)$$

the solution can be obtained using the fourth-order Runge-Kutta method. The formulas for computing the solution x' and y' at $t + h$ based on the solution

x and y at t are, simplified from (1.4.3) for solving simultaneous second-order equations,

$$\begin{aligned}\Delta_1x &= hF_1(x, y) \\ \Delta_1y &= hF_2(x, y) \\ \Delta_2x &= hF_1\left(x + \frac{1}{2}\Delta_1x, y + \frac{1}{2}\Delta_1y\right) \\ \Delta_2y &= hF_2\left(x + \frac{1}{2}\Delta_1x, y + \frac{1}{2}\Delta_1y\right) \\ \Delta_3x &= hF_1\left(x + \frac{1}{2}\Delta_2x, y + \frac{1}{2}\Delta_2y\right) \\ \Delta_3y &= hF_2\left(x + \frac{1}{2}\Delta_2x, y + \frac{1}{2}\Delta_2y\right) \\ \Delta_4x &= hF_1(x + \Delta_3x, y + \Delta_3y) \\ \Delta_4y &= hF_2(x + \Delta_3x, y + \Delta_3y) \\ x' &= x + \frac{1}{6}(\Delta_1x + 2\Delta_2x + 2\Delta_3x + \Delta_4x) \\ y' &= y + \frac{1}{6}(\Delta_1y + 2\Delta_2y + 2\Delta_3y + \Delta_4y)\end{aligned}\tag{1.7.13}$$

This numerical integration procedure is programmed in a subprogram named RUNNTA, in which the names XNEXT and YNEXT are used, respectively, for x' and y' . As an alternative, we also implement ODE45 MATLAB initial value solver for this problem. Plots of numerical results are obtained by using MATLAB plotting routines.

In Program 1.7 the right-hand sides of (1.7.10) and (1.7.11) are respectively called $U(XI, YI)$ and $V(XI, YI)$ for obvious reasons, and are defined in two separate function subprograms.

When marching in time, the step size dT cannot be large in order to avoid numerical instabilities caused by the closeness of some neighboring vortices. Moore (1974), in studying the same problem, found that the restriction on the time step is, after being rewritten in our notation,

$$dT \ll \frac{8\pi}{m^2}\tag{1.7.14}$$

The value $m = 40$ is used in Program 1.7. By choosing the value $1/(25m)$ for dT this inequality is satisfied. The results based on some even smaller step sizes exhibit only minor changes near the wing tips.

Because the vortex sheet is symmetric about the y axis at all times, computations are needed only for discrete vortices on the left half of the sheet, with i running from 1 to $m/2$. The k th vortex, where $k = m + 1 - i$, on the right half of the sheet is the mirror image of the i th vortex about the y axis.

In Fig. 1.7.5 the shape of the vortex sheet at eight representative time instants is plotted. Initially the tip vortex starts to move upward as a result of its peculiarity that vortices are on its one side whereas none on the other. The rest of

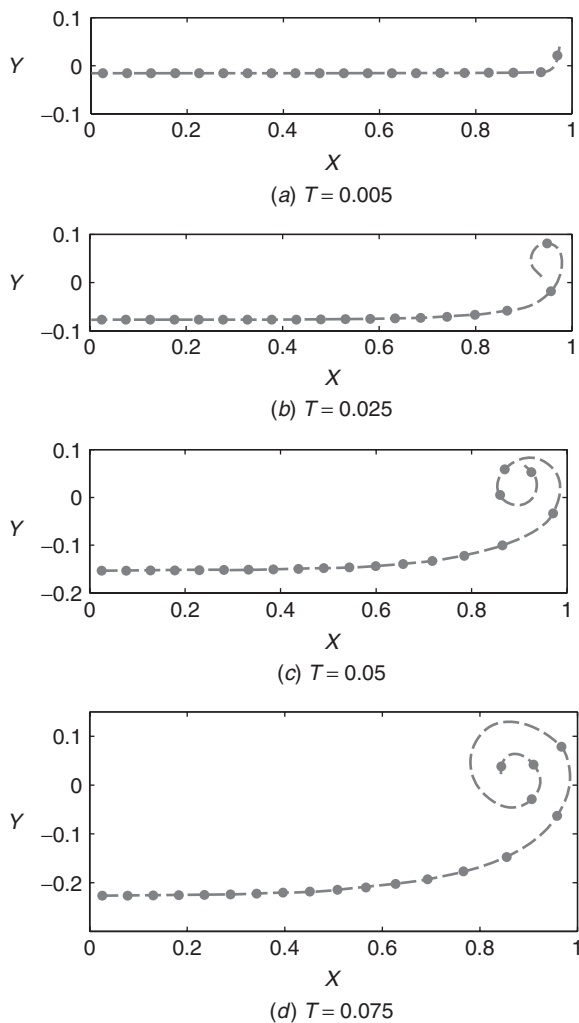


FIGURE 1.7.5 Evolution of an initially flat vortex sheet at different values of T .

the vortices move downward at approximately equal speeds. The mutual interactions among vortices in the tip region cause the sheet to curve up and be rolled into a spiral. As more and more vortices are drawn into the ever-expanding spiral region, the vortex sheet is continuously stretched, leaving longer distances between neighboring vortices along the sheet. Finally, the originally flat vortex sheet will be evolved into two tightly rolled spirals revolving in opposite directions. The situation is similar to what is observed behind an aircraft.

Using 40 discrete vortices to replace the vortex sheet does not give accurate results at large values of T , since the constituent vortices are separated far apart. For example, at $T = 0.35$, irregularities start to appear on the sheet in the spiral

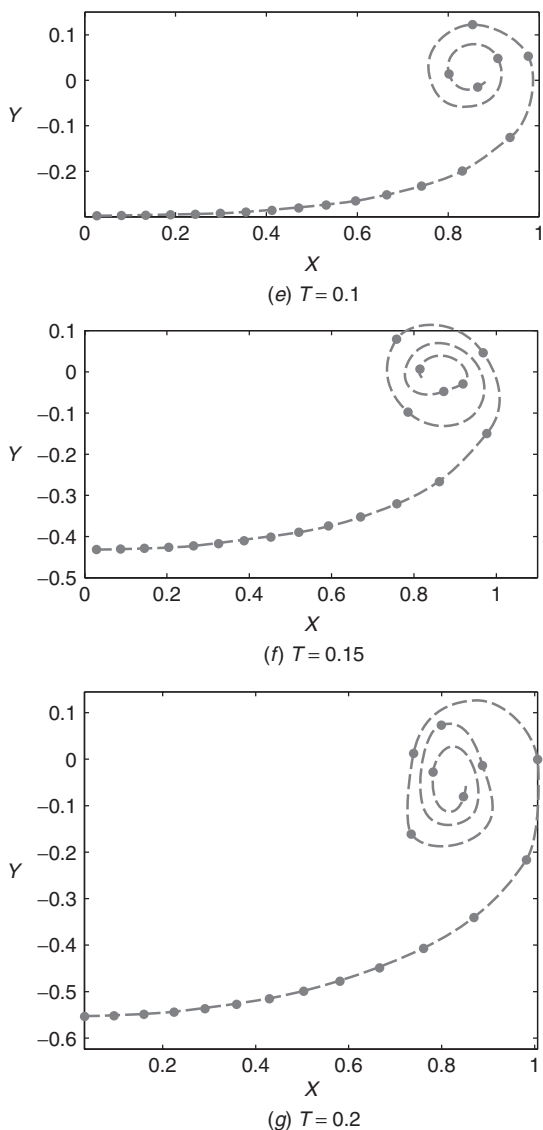


FIGURE 1.7.5 (continued)

region. Results at later time steps show that the paths of some vortices in that region are contorted, and certain parts of the vortex sheet may become crossed. The computation should actually be terminated before this unrealistic situation has developed. The chaotic motion of the spiral has been found by several authors. A brief description of some previous research works is referred to in Moore (1974). To eliminate the chaotic motion, Moore successfully used a concentrated tip vortex to represent the tightly rolled portion of the vortex sheet.

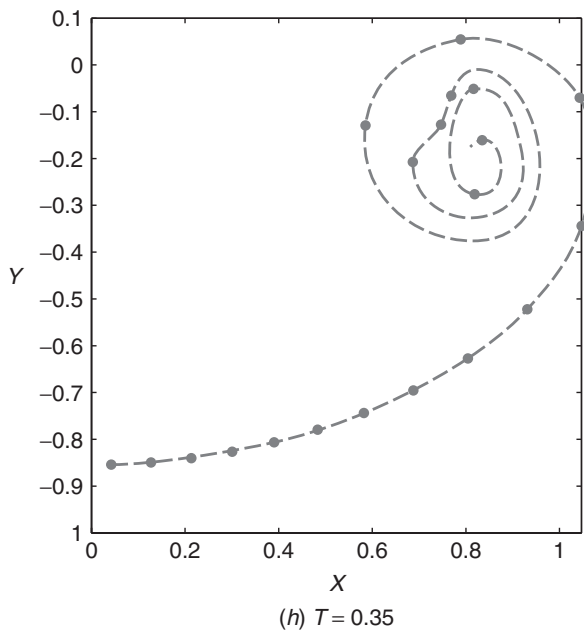


FIGURE 1.7.5 (continued)

Results of higher accuracies can be obtained by choosing larger values for m . However, the computing time increases roughly with m^2 . Let us now apply our result to a realistic problem. For a Boeing 747 with half-span $a = 30$ m and a total weight of 4×10^6 N, the circulation averaged along the span is $815 \text{ m}^2/\text{s}$ during take off at sea level at a speed of 67 m/s. Assuming an elliptical distribution of circulation along the span, as described by (1.7.4),

$$\begin{aligned} 2a \cdot (815) &= \int_{-a}^a \frac{\Gamma_0}{a} (a^2 - x^2)^{1/2} dx \\ &= \frac{1}{2}\pi a \Gamma_0 \end{aligned}$$

giving $\Gamma_0 = 1038 \text{ m}^2/\text{s}$. The characteristic time $2\pi a^2 / \Gamma_0$ is about 5.45 s, and therefore the last plot for $T = 0.35$ in Fig. 1.7.5 shows the vortex sheet configuration at $t = 1.91$ s. For a take-off speed of 67 m/s, this is the approximate configuration of the three-dimensional trailing vortex sheet at a distance of 128 m behind the airplane. The plot also shows that after the sheet has been rolled up, the centers of the two spirals are separated by a distance shorter than the wing span b .

Figure 1.7.5 also reveals that the tip region of the vortex sheet descends slower than the middle region. The vertical position of the midpoint of the sheet descends initially with speed $\Gamma_0/2a$, and slows down toward a constant speed approximately equal to half of that value.

The analysis on which Program 1.7 was based may be improved. In that analysis we subdivide a vortex sheet into small spanwise intervals and replace each one by a point vortex at the center. Since the sheet strength γ is not uniform, the vortices within each subdivision will generally induce a velocity at its center. Thus, the discrete vortex placed there will move under its own influence. This motion was not taken into account, although its magnitude may be small compared with the sum of those induced there by other point vortices. To be more realistic, when a vortex sheet segment is replaced by a discrete vortex, it should be placed at a point on that segment at which the self-induced velocity is zero. The computation for determining the position of such a point for a straight segment can be carried out without any difficulty. However, after the segment is deformed into a curve, the location of the point of vanishing self-induced velocity changes. The determination of its position on an arbitrary curve becomes too involved to be considered practical.

Instead of being replaced by initially equispaced vortices, as demonstrated here, the vortex sheet may also be replaced by discrete vortices of equal strength. Moore's results based on these two approximations show remarkable agreement.

Project for Further Study: Replace the vortex sheet considered in Program 1.7 by 40 discrete vortices of equal strength. Plot the initial configuration of the sheet, and compare the shapes of the sheet with those shown in Fig. 1.7.5 at the same time instants.

APPENDIX

List of Principal Variables in Program 1.1

Program Symbol	Definition
(MAIN PROGRAM)	
A	$1 + \bar{\rho}/2$
B	$(1 - \bar{\rho})g$
C	$3\bar{\rho}/4d$
D	Diameter of sphere, d , m
D1V, D2V, etc.	Velocity increments, $\Delta_1 v_i, \Delta_2 v_i$, etc.
D1Z, D2Z, etc.	Displacement increments, $\Delta_1 z_i, \Delta_2 z_i$, etc.
G	Gravitational acceleration, g , m/s ²
H	Time increment, h , s
NU	Kinematic viscosity of fluid, ν , m ² /s
PI	π
RE	Reynolds number vd/ν
RHO	Density of body, ρ , kg/m ³
RHOBAR	Density ratio, $\bar{\rho}$, or ρ_f/ρ

(continues)

List of Principal Variables in Program 1.1 (continued)

Program Symbol	Definition
RHOF	Density of fluid, ρ_f , kg/m ³
T, T0	Time, t_i , and initial time, t_0 , respectively, s
TMAX	Maximum time of integration, s
V, VO	Velocity, v_i , and initial velocity, v_0 , respectively, of the sphere, m/s
VV	Velocity of sphere in vacuum, v_v , m/s
Z, Z0	Position, z , and initial position, z_0 , respectively, of the sphere, m
ZV	Position of sphere in vacuum, z_v , m
(FUNCTION F)	
CD	Drag coefficient, c_d
F	$(B - CW W c_d)/A$
R	Dummy name for Reynolds number
W	Dummy name for velocity

List of Principal Variables in Program 1.2 Motion of a Simple Pendulum

Program Symbol	Definition
(MAIN PROGRAM)	
A	$1 + \bar{\rho}/2$
B	$(1 - \bar{\rho})g$
C	$3\bar{\rho}/4d$
D	Diameter of sphere, d , m
DT	Time increment, s
G	Gravitational acceleration, g , m/s ²
L	Distance between the pivot axis and the center of sphere, l , m
NU	Kinematic viscosity of fluid, ν , m ² /s
PI	π
RHO	Density of spherical body, ρ , kg/m ³
RHOBAR	Density ratio, $\bar{\rho}$, or ρ_f/ρ
RHOF	Density of fluid, ρ_f , kg/m ³
T, T0	Time, t_i , and initial time, t_0 , respectively, s
THETA, THETA0	Angular displacement of pendulum, θ , and its initial value, θ_0 , respectively, degrees
THETAV	Angular displacement in vacuum, θ_v , degrees
TMAX	Maximum time of integration, s
V, VO	Tangential velocity, v , and its initial value, v_0 , respectively, m/s
VV	Tangential velocity in vacuum, v_v , m/s

(continues)

List of Principal Variables in Program 1.2 Motion of a Simple Pendulum (continued)

Program Symbol	Definition
Y, Y0	Circumferential displacement, y or $l\theta$, and its initial value, y_0 , respectively, m
YV	Circumferential displacement in vacuum, y_v , m
(SUBPROGRAM RUNGE)	
D1P, D2P, etc.	Increments $\Delta_1 p_i, \Delta_2 p_i$, etc. in (1.1.13)
D1X, D2X, etc.	Increments $\Delta_1 x_i, \Delta_2 x_i$, etc. in (1.1.13)
(FUNCTION CD)	
RE	Reynolds number, Re

List of Principal Variables in Program 1.3 Vertical Motion of an Airfoil

Program Symbol	Definition
(MAIN PROGRAM)	
ALPHA, ALPHAD	Angle of attack, α , in radians and that in degrees, respectively
ALPHAO	Angle of attack of a stationary wing, α_0 , rad.
BETA	β , the dimensionless parameter $\rho_f g S / 2k$
DT	Dimensionless time increment
DU	Increment in dimensionless horizontal velocity
PI	π
T, T0	Dimensionless time, T , and its initial value, respectively
TMAX	Maximum time of integration, dimensionless
U	Dimensionless horizontal wind velocity, U
V, V0	Dimensionless vertical velocity of wing, V , and its initial value, respectively
Z, Z0	Dimensionless displacement of the wing, Z , and its initial value, respectively
(FUNCTION CL)	
CL	Lift coefficient of the wing, c_l

List of Principal Variables in Program 1.4 Motion of a Spherical Projectile

Program Symbol	Definition
(MAIN PROGRAM)	
A	$1 + \bar{\rho}/2$
B	$(1 - \bar{\rho})g$
C	$3\bar{\rho}/4d$
D	Diameter of sphere, d , m
DT	Size of time steps, s
G	Gravitational acceleration, g , m/s ²
H	Size of increment in T
I	Step counter
IFRPRT	Frequency of printing
J	Counter for different cases
NU	Kinematic viscosity of fluid, ν , m ² /s
PI	π
RHO	Density of body, ρ , kg/m ³
RHOBAR	Density ratio, $\bar{\rho}$, or ρ_f/ρ
RHOF	Density of fluid, ρ_f , kg/m ³
T, T0	Time, t_i , and initial time, t_0 , respectively, s
THETA0	Elevation of the projectile, θ_0 , deg
U	Horizontal component of body velocity, u , m/s
V	Vertical component of body velocity, v , m/s
W0	Initial speed of body, w_0 , m/s
X, X0	Horizontal position of body, x , and its initial value x_0 , respectively, m
Y, Y0	Vertical position of body, y , and its initial value, y_0 , respectively, m
(FUNCTIONS FX, FY IN [RES])	
UF	Horizontal component of fluid velocity, u_f , m/s
VF	Vertical component of fluid velocity, v_f , m/s
WR	Speed of fluid relative to body, w_r , m/s
CD	Drag coefficient of a sphere

List of Principal Variables in Program 1.5 Maximum Range of a Spherical Projectile

Program Symbol	Definition
DELTA	Increment δ in half - interval method, deg
EPSLON	ε , used to control the accuracy of the optimum shooting angle, deg
M	A counter for different wind conditions
N	Number of steps used in the half-interval method
THENEW, THEOLD	$(\theta_0)_{\text{new}}$ and $(\theta_0)_{\text{old}}$, respectively, deg
THETA	Optimum shooting angle at which range is maximum, deg
XP, XQ, YP, YQ	x_P, x_Q, y_P , and y_Q , respectively, m
XRMAX	Maximum range, m
XRNEW, XROLD	$(x_r)_{\text{new}}$ and $(x_r)_{\text{old}}$, respectively, m

TABLE 1.A.1 Program 1.5 Output

CONSIDER A STEEL SPHERICAL PROJECTILE OF 0.01 M DIAMETER
SHOOTING IN AIR WITH AN INITIAL SPEED OF 50M/SEC.

SYMBOLS USED IN THE FOLLOWING TABLE ARE :

UF = HORIZONTAL WIND SPEED

THETA = THE OPTIMUM SHOOTING ANGLE

XRMAX = THE MAXIMUM RANGE

N = NUMBER OF STEPS USED IN HALF-INTERNAL METHOD TO
OBTAIN THE PRINTED RESULT

THE ERROR IN THETA IS OF THE ORDER OF 0.001DEGREES.

UF (M/SEC)	THETA (DEG)	XRMAX (M)	N
2.0000e+01	4.4611e+01	1.8976e+02	2.4000e+01
0	3.9745e+01	1.3020e+02	2.3000e+01
-2.0000e+01	2.7371e+01	7.5615e+01	2.6000e+01

List of Principal Variables in Program 1.6 Flight Paths of a Glider

Program Symbol	Definition
A	Ratio of initial lift to weight of the glider
B	Ratio of drag to lift of the glider
DT	Dimensionless time increment
F1, F2	Right-hand sides of (1.6.4) and (1.6.5), respectively
M	A counter for changing angle θ_0
N	A counter for time steps
PI	π
T	Dimensionless time
THETA0	Initial angle between flight path and x -axis, θ_0 , radians
U, U0	Dimensionless horizontal velocity of glider and its initial value, respectively
V, V0	Dimensionless vertical velocity of glider and its initial value, respectively
W0	Dimensionless initial velocity of glider
X, Y	Coordinates of glider
X1, Y1	Coordinates of glider for $\theta_0 = -90^\circ$
X2, Y2	Coordinates of glider for $\theta_0 = 180^\circ$

2

INVISCID FLUID FLOWS

All the problems in this chapter are concerned with flows in the absence of viscosity. The justification for ignoring viscosity and a brief review of incompressible irrotational flows can be found in Section 2.1. The numerical solution of boundary-value problems involving linear second-order ordinary differential equations is taken up in Section 2.2, and its application to a radial flow is discussed in Section 2.3.

To solve the problem of flow past a body, two different approaches may be taken. Bodies of various shapes can be generated either by superimposing elementary flows or by transforming from known flow patterns using the conformal mapping technique. These inverse methods are described in Sections 2.4 and 2.6, respectively. On the other hand, direct methods are used to solve for the flow around a body of prescribed shape. The von Karman method, in which singularities are placed along the centerline of an axisymmetric body is introduced in Section 2.5.

The following six sections deal specifically with the second-order partial differential equations with two independent variables. These equations are first classified in Section 2.7. Numerical methods are devised in Section 2.8 for solving elliptic equations, and their computational stabilities are examined. An example is shown to compute the flow induced by a concentrated vorticity in a rectangular domain. In Section 2.9, techniques for handling irregular and derivative boundary conditions are illustrated. The numerical solution of linear hyperbolic equations and its stability criterion are considered in Section 2.10, and an application to solve the problem of propagation and reflection of a sound wave is given in Section 2.11. The propagation of a finite-amplitude wave is studied in Section 2.12 using a numerical scheme constructed for solving nonlinear hyperbolic equations. Finally, in Section 2.13, we present a formulation of blood flow

in elastic arteries modeled by a system of nonlinear hyperbolic partial differential equations. We also introduce multistep methods for numerically integrating hyperbolic partial differential equations.

2.1 INCOMPRESSIBLE POTENTIAL FLOWS

Real fluids are all viscous. Viscosity is caused by the redistribution of excessive momenta among neighboring fluid molecules through the action of intermolecular collisions. Thus, a viscous force is exerted on the surface of a fluid element where a local velocity gradient is present. It may be either a shearing force tangent to the surface, such as the one found in a boundary layer, or a normal force that exists, for example, within a shock wave.

The importance of the viscous force in comparison with the inertial force is represented by the Reynolds number, which is the ratio of a characteristic inertial force to a characteristic viscous force in a flow field. Because of the low viscosity of air and water, the Reynolds numbers of most flows of practical interest are usually very high; in other words, in these flows the viscous forces are very small compared with the inertia.

For a high-Reynolds number flow past a streamlined body from which the flow does not separate, Prandtl (1904) postulated that the influence of viscosity is confined to a very thin boundary layer in the immediate neighborhood of the solid wall, and that in the region outside of the boundary layer the flow behaves as if there were no viscosity. Prandtl's postulation has been proven to be a powerful tool in solving many practical flow problems. For instance, the inviscid flow theory predicts extremely well the lift and pressure distribution on an airfoil for angles of attack below the value at which the flow starts to separate from the body, although the drag has to be found by solving the boundary-layer equations.

It is known that vorticities are generated by the shearing viscous forces, so that the boundary-layer flow is a rotational one. On the other hand, in the absence of viscous and other rotational forces, the originally irrotational flow far upstream will remain so in the region outside the boundary layer. Letting \mathbf{V} denote the velocity field in this region, the irrotationality condition states that the vorticity vanishes; that is,

$$\nabla \times \mathbf{V} = 0 \quad (2.1.1)$$

The preceding equation is automatically satisfied if a *velocity potential* ϕ is introduced such that

$$\mathbf{V} = \nabla\phi \quad (2.1.2)$$

For this reason irrotational flows are also called *potential flows*. As a result of introducing the velocity potential, the velocity vector generally having three components is replaced by a single scalar quantity ϕ .

Furthermore, if the fluid is assumed incompressible, the velocity field must also satisfy the *continuity equation* for such a fluid:

$$\nabla \cdot \mathbf{V} = 0 \quad (2.1.3)$$

Upon substitution from (2.1.2), (2.1.3) becomes

$$\nabla^2 \phi = 0 \quad (2.1.4)$$

where $\nabla^2 \equiv \nabla \cdot \nabla$ is the *Laplacian operator*, and (2.1.4) is called the *Laplace equation*.

Using Prandtl's postulation, the problem of an incompressible flow past a given streamlined body at high Reynolds numbers is to be solved as follows. For the external region a velocity potential is to be found by solving the Laplace equation (2.1.4), which satisfies both the boundary condition prescribed far upstream and the requirement that the fluid velocity be tangent to the body surface. The latter condition is justified by the fact that the boundary layer around the body is thin. The velocity distribution of the external flow along the body surface is then used as the outer boundary condition for the boundary-layer flow. This inner flow satisfies the no-slip condition at the rigid wall and is a solution to the governing boundary-layer equations to be shown in the next chapter.

In the present chapter the boundary-layer flow is disregarded completely. Once the velocity field in the external region is determined from the kinematic considerations just described, the pressure field p can be computed from a dynamic relation, called the *Euler equation*:

$$\rho \frac{D\mathbf{V}}{Dt} = -\nabla p \quad (2.1.5)$$

It is the equation of motion for inviscid fluids with body forces omitted. In this equation ρ is the density, and the operator

$$\frac{D}{Dt} \equiv \frac{\partial}{\partial t} + \mathbf{V} \cdot \nabla \quad (2.1.6)$$

is the *total or substantial derivative* that gives the rate of change by following a fluid particle.

It is easier to compute the pressure from the integrated form of the Euler equation (i.e., the *Bernoulli equation*) than from the Euler equation itself. Under the conditions of incompressible fluid and irrotational velocity field, the Bernoulli equation has the form

$$\rho \frac{\partial \phi}{\partial t} + p + \frac{1}{2} \rho V^2 = H \quad (2.1.7)$$

where the constant of integration, H , is the *Bernoulli constant*. For a steady flow, (2.1.7) simply states that the sum of the hydrostatic pressure, p , and the dynamic

pressure, $\frac{1}{2}\rho V^2$, is a constant at any point in the flow. In this case H is the stagnation pressure, or the pressure measured at a point where the fluid velocity vanishes.

For two-dimensional planar flows, (2.1.2) and (2.1.4) can be expressed in Cartesian coordinates as

$$u = \frac{\partial \phi}{\partial x}, \quad v = \frac{\partial \phi}{\partial y} \quad (2.1.8)$$

and

$$\frac{\partial^2 \phi}{\partial x^2} + \frac{\partial^2 \phi}{\partial y^2} = 0 \quad (2.1.9)$$

where u and v are, respectively, the velocity components along the x and y axes. In polar coordinates, however, they have the expressions

$$u_r = \frac{\partial \phi}{\partial r}, \quad u_\theta = \frac{1}{r} \frac{\partial \phi}{\partial \theta} \quad (2.1.10)$$

and

$$\frac{\partial^2 \phi}{\partial r^2} + \frac{1}{r} \frac{\partial \phi}{\partial r} + \frac{1}{r^2} \frac{\partial^2 \phi}{\partial \theta^2} = 0 \quad (2.1.11)$$

where u_r is the velocity component in the radial direction and u_θ is the velocity component in the azimuthal direction.

Instead of velocity potential, *stream function* is sometimes used for analyzing planar or axisymmetric incompressible flows. The continuity equation (2.1.3) suggests that the velocity vector can also be derived from a vector potential through the relationship

$$\mathbf{V} = \nabla \times (\mathbf{i}_z \psi) \quad (2.1.12)$$

where \mathbf{i}_z is a unit vector along the z axis, which is perpendicular to the plane of fluid motion, and ψ is called the stream function, which represents the volume of fluid passing per unit time between a given point and a reference streamline (see, for example, Kuethe and Chow, 1998, Section 2.6). *Streamlines*, to which the instantaneous velocity vectors are tangent, are described by the equations $\psi = \text{constant}$. In terms of stream function, the irrotationality relation (2.1.1) becomes

$$\nabla \times \nabla \times (\mathbf{i}_z \psi) = 0 \quad (2.1.13)$$

(2.1.12) and (2.1.13), when written in Cartesian coordinates, have the expressions

$$u = \frac{\partial \psi}{\partial y}, \quad v = -\frac{\partial \psi}{\partial x} \quad (2.1.14)$$

$$\frac{\partial^2 \psi}{\partial x^2} + \frac{\partial^2 \psi}{\partial y^2} = 0 \quad (2.1.15)$$

or, in polar coordinates, the expressions

$$u_r = \frac{1}{r} \frac{\partial \psi}{\partial \theta}, \quad u_\theta = -\frac{\partial \psi}{\partial r} \quad (2.1.16)$$

$$\frac{\partial^2 \psi}{\partial r^2} + \frac{1}{r} \frac{\partial \psi}{\partial r} + \frac{1}{r^2} \frac{\partial^2 \psi}{\partial \theta^2} = 0 \quad (2.1.17)$$

It turns out that, similar to the velocity potential, the stream function for planar incompressible flows is also governed by the Laplace equation. However, the nonsteady term in the Bernoulli equation cannot be written in terms of ψ in a simple form similar to that shown in (2.1.7) in terms of ϕ .

The continuity equation (2.1.3) does not apply in regions where fluid mass is created or destroyed. The formulation is now generalized to include the possible sources and sinks in the flow field. Consider an infinitesimal control volume $\Delta x \Delta y \Delta z$ fixed in the Cartesian coordinate system as sketched in Fig. 2.1.1, in which the z dimension is not shown for the purpose of simplicity. The distribution of sources is represented by $q(x, y, z, t)$, which is the volume of fluid created per unit time from a unit volume located at the point (x, y, z) . A simple arithmetic procedure computing the volume fluxes across the surfaces, as indicated in Fig. 2.1.1 (the fluxes in the z direction can easily be added), shows that the net volume of fluid flowing out of the control volume per unit time is

$$\left(\frac{\partial u}{\partial x} + \frac{\partial v}{\partial y} + \frac{\partial w}{\partial z} \right) \Delta x \Delta y \Delta z$$

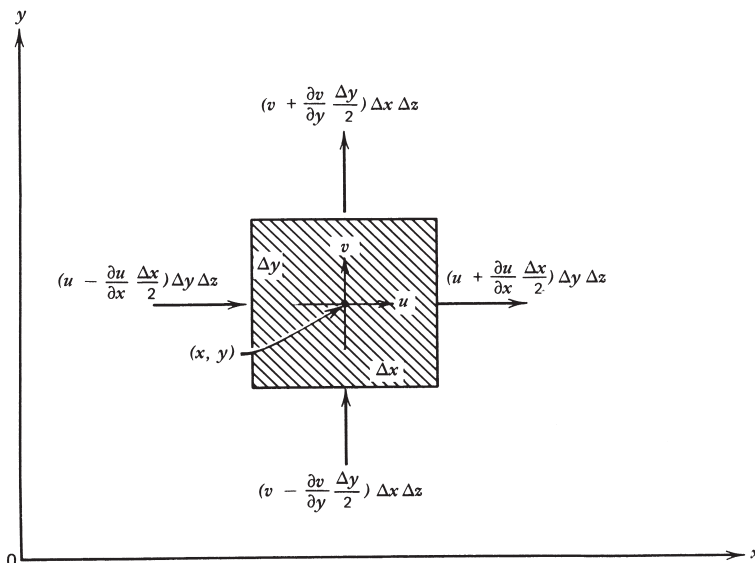


FIGURE 2.1.1 Flow through a control volume.

For an incompressible fluid, this amount of fluid must be equal to $q \Delta x \Delta y \Delta z$, or the amount produced by all the sources contained within the volume. Thus, the resulting continuity equation is

$$\frac{\partial u}{\partial x} + \frac{\partial v}{\partial y} + \frac{\partial w}{\partial z} = q(x, y, z, t) \quad (2.1.18)$$

or, in vector notation,

$$\nabla \cdot \mathbf{V} = q \quad (2.1.19)$$

Sinks are represented by negative values of q . In the absence of sources or sinks, $q = 0$, and the continuity equation (2.1.3) is recovered.

When the velocity vector is expressed in terms of velocity potential, (2.1.19) becomes

$$\nabla^2 \phi = q \quad (2.1.20)$$

which is in the form of a *Poisson equation*.

Despite the fact that both Laplace and Poisson equations are linear, analytical solution for flow past a body of arbitrary shape is by no means simple. Various numerical and seminumerical solution techniques will be introduced in the following sections.

An extensive discussion on potential flows is out of the scope of this book. Such a task can be found in any introductory book on fluid dynamics.

2.2 NUMERICAL SOLUTION OF SECOND-ORDER ORDINARY DIFFERENTIAL EQUATIONS: BOUNDARY-VALUE PROBLEMS

In connection with the numerical solution of ordinary differential equations, various initial-value problems were treated in Chapter 1. In another class of fluid dynamic problems a solution is to be found that satisfies not only the differential equation throughout some domain of its independent variable, but also some conditions on boundaries of that domain. These problems are called *boundary-value problems*. We consider here the numerical solution of a *linear* second-order ordinary differential equation of the form

$$\frac{d^2 f}{dx^2} + A(x) \frac{df}{dx} + B(x)f = D(x) \quad (2.2.1)$$

for the domain $x_{\min} \leq x \leq x_{\max}$, subject to the boundary conditions that the values of f are given at the end points of that range, at $x = x_{\min}$ and x_{\max} . The method developed here will be modified later for solving problems involving derivative boundary conditions.

As the first step in our numerical method, the differential equation is to be approximated by an equation of the finite-difference form. Similar to what was done in solving the initial-value problems, the axis of the independent variable is again subdivided into small intervals of constant width h . If the number of intervals in the given range of x is $n + 1$, and if the end points of the intervals

are labeled according to the index notation shown in Fig. 2.2.1, starting with x_0 at the left end of the range, then the following relations hold:

$$x_i = x_0 + ih, \quad i = 0, 1, 2, \dots, n + 1 \quad (2.2.2)$$

in which $x_o = x_{\min}$ and $x_{n+1} = x_{\max}$. Values of the function f evaluated at these end points are also named in index notation according to the definition $f_i \equiv f(x_i)$. It is desired to approximate the derivatives of f at an arbitrary point x_i by expressions containing values of f evaluated in the neighborhood of x_i .

Let x_j be such a neighboring point with $j = i + m$, where m is a positive or negative integer. For small values of h the function evaluated at x_i may be expanded in a Taylor's series about x_i :

$$\begin{aligned} f_j &\equiv f(x_i + mh) \\ &= f_i + mh f'_i + \frac{(mh)^2}{2!} f''_i + \frac{(mh)^3}{3!} f'''_i + \dots \end{aligned} \quad (2.2.3)$$

where a prime denotes a differentiation with respect to x . By assigning the values -1 and $+1$ to m in (2.2.3), we obtain two expressions for $f(x)$ at immediate neighboring points of x_i .

$$f_{i-1} = f_i - h f'_i + \frac{1}{2} h^2 f''_i - \frac{1}{6} h^3 f'''_i + \dots \quad (2.2.4)$$

$$f_{i+1} = f_i + h f'_i + \frac{1}{2} h^2 f''_i + \frac{1}{6} h^3 f'''_i + \dots \quad (2.2.5)$$

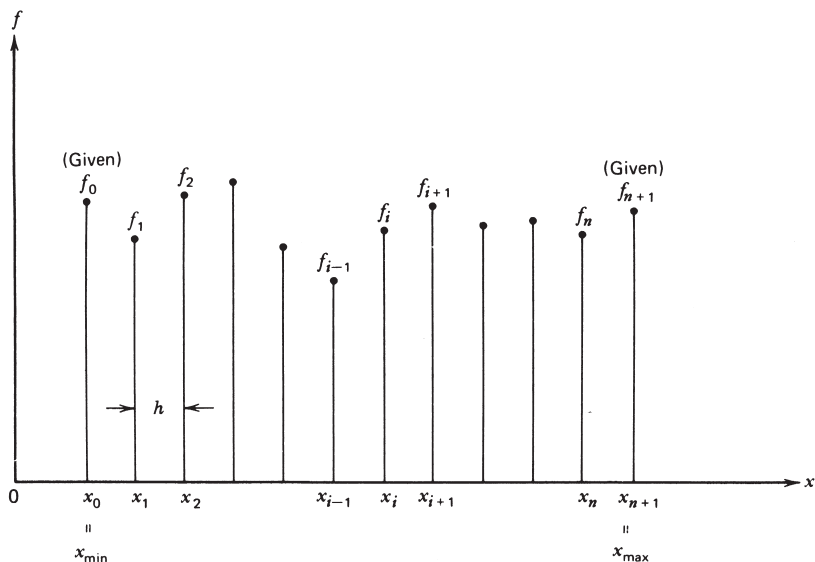


FIGURE 2.2.1 Numerical solution of an ordinary boundary-value problem.

There are many different ways of computing a particular derivative. For example, f'_i may be solved for from (2.2.5) to give

$$f'_i = \frac{1}{h}(f_{i+1} - f_i) - \frac{1}{2}hf''_i - \frac{1}{6}h^2f'''_i - \dots$$

With a truncation error $O(hf''_i)$, it is approximated by

$$f'_i \doteq \frac{1}{h}(f_{i+1} - f_i) \quad (2.2.6)$$

This a *forward-difference formula* for the first-order derivative, so named because it involves the values of the function at x_i and at a point ahead of it. On the other hand, if we use (2.2.4), a *backward-difference formula* of the form

$$f'_i \doteq \frac{1}{h}(f_i - f_{i-1}) \quad (2.2.7)$$

is obtained whose truncation error is of the same order of magnitude as the one associated with the previous formula, except for a difference in sign. Thus, the approximations (2.2.6) and (2.2.7) will give similar accuracies in a numerical computation. A more accurate approximation, having an error of $O(h^2f'''_i)$, is obtained by subtracting (2.2.4) from (2.2.5); this has the form

$$f'_i \doteq \frac{1}{2h}(f_{i+1} - f_{i-1}) \quad (2.2.8)$$

Because of its appearance on the right-hand side, it is called a *central-difference formula* for f' . Formulas giving any desired accuracies can be obtained by assigning additional values to m in (2.2.3) and using the same technique just demonstrated.

To approximate the second-order derivative of f , we show only a central-difference formula

$$f''_i \doteq \frac{1}{h^2}(f_{i+1} - 2f_i + f_{i-1}) \quad (2.2.9)$$

having an error $O(h^2f_i^{iv})$. It is obtained by adding (2.2.4) and (2.2.5) to eliminate f'_i . Formulas of various truncation errors for computing derivatives up to the fourth order are tabulated by McCormick and Salvadori (1964, Section 3.2).

We now return to the differential equation (2.2.1). To allow errors of the same order of magnitude in the two derivatives shown in that equation, we use the central-difference formulas (2.2.8) and (2.2.9). Thus, at a point x_i , the differential equation (2.2.1) is approximated by the difference equation

$$\frac{1}{h^2}(f_{i+1} - 2f_i + f_{i-1}) + \frac{1}{2h}A_i(f_{i+1} - f_{i-1}) + B_if_i = D_i$$

where A_i , B_i , and D_i denote, respectively, $A(x_i)$, $B(x_i)$, and $D(x_i)$. Multiplying the equation by h^2 and grouping similar terms, we obtain

$$\left(1 - \frac{h}{2}A_i\right)f_{i-1} + (-2 + h^2B_i)f_i + \left(1 + \frac{h}{2}A_i\right)f_{i+1} = h^2D_i$$

It can be written in a more convenient form

$$C_{i1}f_{i-1} + C_{i2}f_i + C_{i3}f_{i+1} = C_{i4} \quad (2.2.10)$$

by calling

$$\begin{aligned} C_{i1} &= 1 - \frac{h}{2}A_i \\ C_{i2} &= -2 + h^2B_i \\ C_{i3} &= 1 + \frac{h}{2}A_i \\ C_{i4} &= h^2D_i \end{aligned} \quad (2.2.11)$$

The preceding coefficients are known constants at any *interior* point in the specified range of x . Equation (2.2.10), applied at $i = 1, 2, \dots, n$, gives the set of n linear algebraic equations to be solved simultaneously for the n unknowns f_i .

Special attention is needed when $i = 1$ and n are assigned in (2.2.10). These two equations are

$$C_{11}f_0 + C_{12}f_1 + C_{13}f_2 = C_{14}$$

and

$$C_{n1}f_{n-1} + C_{n2}f_n + C_{n3}f_{n+1} = C_{n4}$$

Since f_0 and f_{n+1} are known from boundary conditions, the two involved terms on the left side are constant and therefore are moved to the right. To simplify the appearance of our program, we assign the value of $(C_{14} - C_{11}f_0)$ to C_{14} and the value of $(C_{n4} - C_{n3}f_{n+1})$ to C_{n4} . This action may be expressed symbolically as

$$\begin{aligned} C_{14} &\leftarrow (C_{14} - C_{11}f_0) \\ C_{n4} &\leftarrow (C_{n4} - C_{n3}f_{n+1}) \end{aligned} \quad (2.2.12)$$

After this rearrangement, C_{11} and C_{n3} disappear from the left side and the set of n simultaneous equations becomes, when expressed in matrix notation,

$$\begin{bmatrix} C_{12} & C_{13} & 0 & 0 & \cdots & 0 & 0 & 0 \\ C_{21} & C_{22} & C_{23} & 0 & \cdots & 0 & 0 & 0 \\ 0 & C_{31} & C_{32} & C_{33} & \cdots & 0 & 0 & 0 \\ \vdots & \vdots & \vdots & \vdots & \cdots & \vdots & \vdots & \vdots \\ 0 & 0 & 0 & 0 & \cdots & C_{n-1,1} & C_{n-1,2} & C_{n-1,3} \\ 0 & 0 & 0 & 0 & \cdots & 0 & C_{n1} & C_{n2} \end{bmatrix} \begin{pmatrix} f_1 \\ f_2 \\ f_3 \\ \vdots \\ f_{n-1} \\ f_n \end{pmatrix} = \begin{pmatrix} C_{14} \\ C_{24} \\ C_{34} \\ \vdots \\ \vdots \\ C_{n-1,4} \\ C_{n4} \end{pmatrix} \quad (2.2.13)$$

The coefficient matrix on the left-hand side of (2.2.13) is called a *tridiagonal matrix*, whose nonvanishing elements form a band, three elements wide along the diagonal. This particular set of equations can be solved by using the *Gaussian elimination method*. According to this method, we multiply the second equation in (2.2.13) by C_{12} and the first by C_{21} and then take the difference of the two to eliminate f_1 . The resulting equation is

$$(C_{22}C_{12} - C_{21}C_{13})f_2 + C_{23}C_{12}f_3 = C_{24}C_{12} - C_{21}C_{14}$$

In this equation, if we call the coefficient of f_2 by the name C_{22} , that of f_3 by the name C_{23} , and the group on the right-hand side by the name C_{24} , and if the final equation is used to replace the second equation in (2.2.13), the form of (2.2.13) will remain unchanged except that C_{21} is replaced by zero. Working with the new second equation and the third equation in (2.2.13), C_{31} can be eliminated by using the same technique. The same process is repeated until $C_{n-1,1}$ is eliminated. In summary, the eliminating processes are achieved by successively renaming the coefficients according to the following assignments:

$$\left. \begin{array}{l} C_{i2} \leftarrow (C_{i2}C_{i-1,2} - C_{i1}C_{i-1,3}) \\ C_{i3} \leftarrow C_{i3}C_{i-1,2} \\ C_{i4} \leftarrow (C_{i4}C_{i-1,2} - C_{i1}C_{i-1,4}) \end{array} \right\} i = 2, 3, \dots, n-1 \quad (2.2.14)$$

At this stage, all the equations in (2.2.13) are in the simple form of having only two terms on the left-hand side. The value of f_n can immediately be found by solving simultaneously the last two equations in (2.2.13). Thus,

$$f_n = \frac{C_{n4}C_{n-1,2} - C_{n1}C_{n-1,4}}{C_{n2}C_{n-1,2} - C_{n1}C_{n-1,3}} \quad (2.2.15)$$

It can easily be verified that the remaining unknowns can be calculated, in a backward order, from the recurrence formula

$$f_j = \frac{C_{j4} - C_{j3}f_{j+1}}{C_{j2}}, \quad j = n-1, n-2, \dots, 2, 1 \quad (2.2.16)$$

The numerical method just described is now summarized as follows. The differential equation (2.2.1) is first replaced by a set of difference equations (2.2.10), whose coefficients are calculated according to (2.2.11). Boundary conditions are taken care of by executing the actions shown in (2.2.12). Finally, the unknowns f_i , with $i = 1, 2, \dots, n$, are computed by following the procedure represented by (2.2.14) to (2.2.16). The last part of the computation will be programmed under a subroutine named TRID, which will appear in the next program.

Later in Chapter 4, we introduce other efficient methods for solving tridiagonal equations, i.e., the compact-storage Thomas algorithm based on Gaussian elimination, and the LU decomposition, which is especially useful when many systems have to be solved with the same coefficient matrix but with different right-hand-sides, such as in parabolic partial differential equations with constant coefficients.

2.3 RADIAL FLOW CAUSED BY DISTRIBUTED SOURCES AND SINKS

The numerical method just described for solving boundary-value problems is applied in this section to solve a flow problem with a known solution, so that the accuracy of the method can be tested. The method will be used later in Section 3.3 on problems whose solutions cannot be obtained analytically.

Consider a radial flow in the domain $r_0 \leq r \leq 4r_0$, within which there is an axisymmetric distribution of sources whose strength increases linearly with r . For such a problem the governing equation (2.1.20) becomes

$$\left(\frac{d^2}{dr^2} + \frac{1}{r} \frac{d}{dr} \right) \phi = q_0 \frac{r}{r_0} \quad (2.3.1)$$

where q_0 is the source strength at $r = r_0$. The radial velocity is computed from (2.1.10):

$$u_r = \frac{d\phi}{dr} \quad (2.3.2)$$

It is always more convenient to work with dimensionless equations. If u_0 represents a characteristic velocity, the following dimensionless variables can be introduced.

$$R = \frac{r}{r_0}, \quad \Phi = \frac{\phi}{r_0 u_0}, \quad U = \frac{u_r}{u_0} \quad (2.3.3)$$

It follows that in the domain $1 \leq R \leq 4$, the flow is described by the dimensionless equations

$$\left(\frac{d^2}{dR^2} + \frac{1}{R} \frac{d}{dR} \right) \Phi = \alpha R \quad (2.3.4)$$

and

$$U = \frac{d\Phi}{dR} \quad (2.3.5)$$

in which $\alpha = q_0 r_0 / u_0$ is a dimensionless source strength. Equation (2.3.4) has a general solution of the form

$$\Phi = \frac{1}{9} \alpha R^3 + \beta \ln R + \gamma$$

The first term on the right-hand side is the particular solution representing the flow caused by the source distribution. The homogeneous solution consists of two terms: the first represents a line source located at $R = 0$ having strength β , and the second is just a constant. Since the velocity field is not affected by the constant term in Φ , γ may conveniently be set to zero. Thus, for $\alpha = 9$ and $\beta = -24$, the expression

$$\Phi = R^3 - 24 \ln R \quad (2.3.6)$$

is the exact solution of the equation

$$\frac{d^2\Phi}{dR^2} + \frac{1}{R} \frac{d\Phi}{dR} = 9R \quad (2.3.7)$$

satisfying the boundary conditions

$$\begin{aligned}\Phi &= 1 & \text{at } R = 1 \\ \Phi &= 64 - 24 \ln 4 & \text{at } R = 4\end{aligned} \quad (2.3.8)$$

The corresponding dimensionless radial velocity is, from (2.3.5),

$$U = 3R^2 - \frac{24}{R} \quad (2.3.9)$$

To solve numerically the boundary-value problem consisting of the differential equation (2.3.7) and boundary conditions (2.3.8), the equation is first compared with the standard form (2.2.1) to obtain

$$\begin{aligned}A(R) &= \frac{1}{R} \\ B(R) &= 0 \\ D(R) &= 9R\end{aligned} \quad (2.3.10)$$

The independent variable in these relations has already been changed from the original x to R . The details of the numerical computation are depicted in Program 2.1, in which the range of R between 1 and 4 is divided equally into 30 intervals. Once the values of Φ evaluated at the interior points are obtained following the procedure described in the previous section, the radial velocity, which is the first-order derivative of Φ according to (2.3.5), is computed using the central-difference formula

$$U_i = \frac{\Phi_{i+1} - \Phi_{i-1}}{2h} \quad (2.3.11)$$

The numerical results for Φ and U are then printed out to compare with the exact solutions represented by (2.3.6) and (2.3.9).

The output of Program 2.1 (Table 2.A.1, see Appendix) shows that the errors of the numerical solution are less than 1% in ϕ and 0.2% in U , which may be considered satisfactory in most engineering problems. Results of higher accuracies can be obtained by increasing the number of intervals at the cost of longer computing time. You may verify this statement by comparing the data obtained by varying the number of intervals in Program 2.1.

2.4 INVERSE METHOD I: SUPERPOSITION OF ELEMENTARY FLOWS

In the previous numerical example, we look directly for a solution to the governing equation that satisfies a set of assumed boundary conditions. Such boundary-value problems are common in studying potential flows. For example, in the problem of a uniform flow past a body of given shape, a solution to the

Laplace equation is to be found that satisfies both the uniform flow condition far away, and the condition that the flow be tangent to the surface of the body. However, to solve such a problem utilizing a *direct method* is not always simple, despite the fact that the governing differential equation is linear. A numerical technique for solving two-dimensional problems directly will be introduced in Section 2.8, but an *inverse method* is described here that solves the flow problems using a different approach.

The Laplace equation, (2.1.15) or (2.1.17), governing the stream function for two-dimensional potential flows is in such a simple form that some elementary solutions to this equation can easily be found. Each of these solutions represents a physically possible elementary potential flow. Because the sum of a linear combination of any number of solutions to a linear differential equation is also a solution to the same equation, infinitely many solutions can thus be generated. Some of the flows represented by the linear combination of solutions may simulate those caused by moving bodies of various shapes through a fluid. Thus, in the inverse method, instead of finding the solution for the flow past a body of a prescribed shape, flows around different bodies are constructed through various combinations of elementary flows and are filed. Based on these typical flow patterns, a body close to the desired shape can generally be constructed through an appropriate combination of elementary flows. The inverse method is also often used in solving problems in electromagnetism and heat conduction whose governing equations are in the form of either the Laplace or the Poisson equation.

There are four elementary two-dimensional flows that are commonly encountered in fluid mechanics: the *uniform flow*, the *line source* (or *sink*), the *line vortex*, and the *doublet*. Their stream functions are listed below, and the corresponding flow patterns are sketched in Fig. 2.4.1.

a. Uniform flow $\psi = U(y \cos \alpha - x \sin \alpha)$ (2.4.1)

b. Line source
$$\begin{aligned} \psi &= \frac{\Lambda}{2\pi} \tan^{-1} \frac{y - y_0}{x - x_0} \\ &= \frac{\Lambda}{2\pi} \theta' \end{aligned}$$
 (2.4.2)

c. Line vortex
$$\begin{aligned} \psi &= \frac{\Gamma}{2\pi} \ln [(x - x_0)^2 + (y - y_0)^2]^{1/2} \\ &= \frac{\Gamma}{2\pi} \ln r' \end{aligned}$$
 (2.4.3)

d. Doublet
$$\begin{aligned} \psi &= -\frac{\kappa}{2\pi} \frac{y - y_0}{(x - x_0)^2 + (y - y_0)^2} \\ &= -\frac{\kappa}{2\pi} \frac{\sin \theta'}{r'} \end{aligned}$$
 (2.4.4)

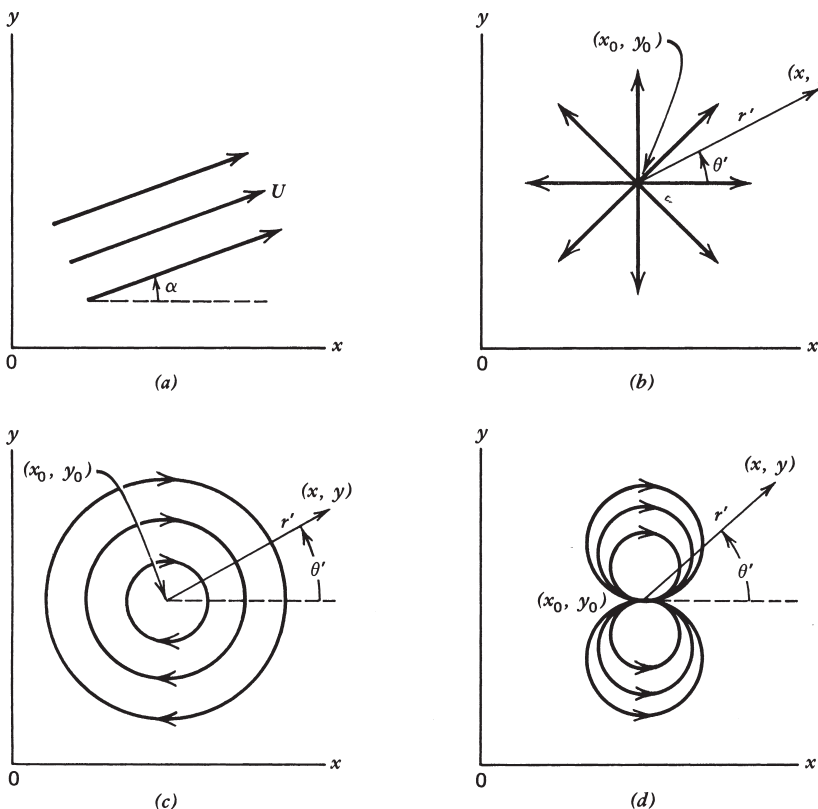


FIGURE 2.4.1 Elementary flows: (a) uniform flow, (b) line source, (c) line vortex, (d) doublet.

Expression (2.4.1) is the stream function for a uniform flow of speed U that makes an angle α with the x axis. Special cases of horizontal and vertical uniform flows are deduced by letting $\alpha = 0^\circ$ and 90° , respectively.

Stream function (2.4.2) describes a source situated at (x_0, y_0) having a strength Λ , which represents the volume of fluid per unit time streaming from a unit length of the line source. Thus, a negative value of Λ corresponds to a line sink. Fluid velocity along a streamline radiating away from the source center has the magnitude $\Lambda/2\pi r'$, where r' is the radial distance from that center. It follows that the flow speed becomes infinity as r' approaches zero.

The stream function shown in (2.4.3) gives the circular flow pattern of a line vortex centered at (x_0, y_0) . The tangential velocity has the magnitude $\Gamma/2\pi r'$, which is a constant along a given streamline. The product of the circumference of a circular streamline and the speed along it is equal to the *circulation* Γ , which is used to denote the strength of a vortex flow. In aerodynamics the clockwise circulation is considered positive. Again, the speed at the vortex center is unbounded.

When a source of strength Λ at $(x_0 - \Delta x, y_0)$ is added to a sink of strength $-\Lambda$ at $(x_0 + \Delta x, y_0)$, a new flow field is obtained. Furthermore, by letting Δx approach zero while keeping the product $2\Delta x\Lambda$ a constant κ , the stream function (2.4.4) for a doublet at (x_0, y_0) is obtained. The streamlines are circles passing through the point (x_0, y_0) with centers on the straight line $x = x_0$. The same flow pattern can be produced by superimposing a vortex $(x_0, y_0 + \Delta y)$ to a vortex of opposite circulation at $(x_0, y_0 - \Delta y)$, and then letting Δy approach zero. κ is called the strength of the doublet. The velocity at the center of a doublet is infinitely large.

Except the uniform flow, the other three elementary flows just discussed have the same property, that the velocity becomes infinity when the center is approached. Because of this property, they are sometimes called *singularities*. They do not cause any mathematical difficulties if each of the singular points is within a domain that is considered to be occupied by a body. For example, when a source is placed in a uniform stream, a half-body is generated in the flow. If the source is replaced by a doublet, a circular cylinder is generated instead. The singularity in each case is enclosed within the boundary of a rigid body, and the flow outside the body is therefore free of singularities. Detailed descriptions of elementary flows and their syntheses can be found in most textbooks on fluid mechanics (e.g., Chapter 4 of Kuethe and Chow, 1998).

In general, bodies of infinite extension are generated by sources or sinks. On the other hand, doublets or a group of sources and sinks of vanishing total strength are used to form bodies of closed boundary. The inverse method of superposition of elementary flows is simple in principle, and the body shape and the flow pattern can be effectively obtained by computing and plotting some representative streamlines of a flow that consists of any number of elementary flows.

Consider a two-dimensional stream function of the general form

$$\psi = f(x, y) \quad (2.4.5)$$

The flow pattern within a rectangular space bounded between x_{\min} and x_{\max} in the x direction and between y_{\min} and y_{\max} in the y direction is to be plotted. The space is subdivided, as shown in Fig. 2.4.2, by vertical lines at a constant distance Δx apart, and by horizontal lines at a distance Δy apart. The sizes of Δx and Δy are not necessarily the same. Grid points that are formed at the intersections of these two sets of perpendicular lines have coordinates (x_i, y_j) , where $i = 1, 2, \dots, m$ and $j = 1, 2, \dots, n$ according to the notation of Fig. 2.4.2. The values of the stream function evaluated at the grid points are called $\psi_{i,j}$, which are computed for all values of i and j from the relation

$$\psi_{i,j} = f(x_i, y_j) \quad (2.4.6)$$

In the output of the program, a graph will be shown that displays the points where the *vertical* grid lines intersect certain particular streamlines. If the number of

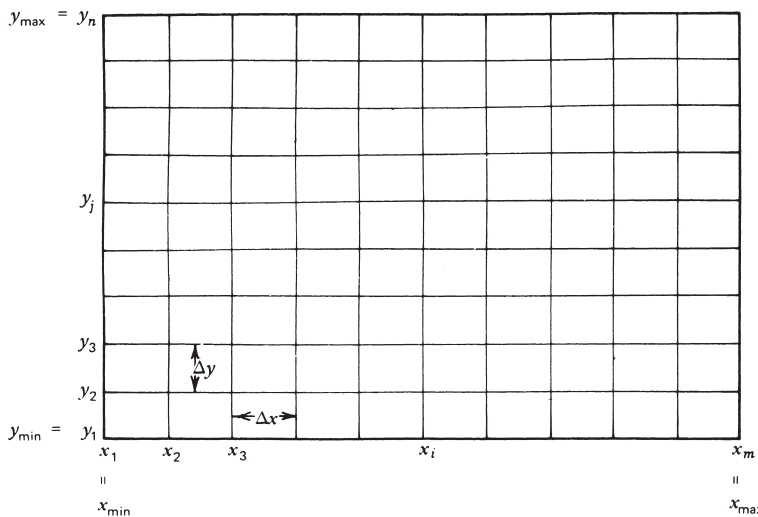


FIGURE 2.4.2 Rectangular grid system.

vertical lines is reasonably large, the printed points will trace out the approximate shape of the flow pattern. The exact coordinates of all the points that appear on the graph will also be tabulated in the output.

To search for all the points at which a vertical grid line intersects with the streamline $\psi = \psi_a$, let us consider an arbitrary distribution of the stream function along the grid line at x_i , as sketched in Fig. 2.4.3. If the height of each spike represents the local value of the stream function, the streamline $\psi = \psi_a$ will go through an interval so that at one end of the interval the spike is higher than ψ_a , and at the other end the spike is shorter than ψ_a . In other words, if P represents the difference between the stream function at the left end of an interval and ψ_a , and Q represents the difference at the right end, the streamline $\psi = \psi_a$ goes through the interval if the product of P and Q is negative. The y coordinate of the intersection point is obtained approximately by subtracting $\Delta y |Q| / (|P| + |Q|)$ from the y coordinate of the point on the right end of that interval, if the variation of ψ within the small interval is approximated by a straight line (see Fig. 2.4.3). All intersection points on the grid line can be located after every interval on that line has been examined.

The searching process along a specified streamline is executed by calling the subroutine **SEARCH**, which performs the previously mentioned action one vertical line after another, starting from the first one at x_1 . The counter k is used to indicate the order of the points thus found. xx_k and yy_k are the coordinates of the k th point, and the total number of points found on a streamline within the given domain is k_{\max} .

For flows having streamlines nearly parallel to the y axis, it is more convenient to show the intersection points of those streamlines and the horizontal grids. This can easily be achieved by changing a few statements in the present subroutine.

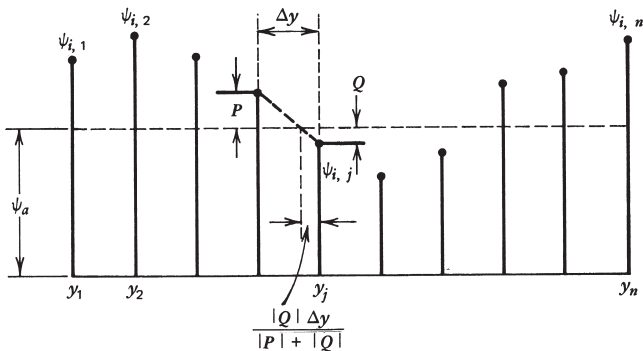


FIGURE 2.4.3 Distribution of stream function along a vertical grid line at x_i .

The example shown in Program 2.2 deals with a flow constructed by adding to a uniform horizontal stream five doublets of different strengths placed on the x -axis at $x/l = -1.0, -0.5, 0, 0.5$, and 1.0 , respectively, where l is a reference length. The stream function of the resultant flow is, from (2.4.1) and (2.4.4),

$$\psi = Uy - \sum_{i=1}^5 \frac{\kappa_i}{2\pi} \frac{y}{(x - d_il)^2 + y^2} \quad (2.4.7)$$

where κ_i are the strengths of the five doublets, and the five values of d_i are, in order, $-1.0, -0.5, 0, 0.5$, and 1.0 . This expression can be made dimensionless in the simpler form

$$\Psi = Y - \sum_{i=1}^5 \frac{c_i Y}{(X - d_i)^2 + Y^2} \quad (2.4.8)$$

in which $\Psi = \psi/Ul$, $X = x/l$, $Y = y/l$, and $c_i = \kappa_i/2\pi l^2 U$. The shape of the body and the flow around it are plotted on the dimensionless spatial coordinates for the five dimensionless strengths $0.15, 0.3, 0.2, 0.1$, and 0.05 , assigned in order to c_i . The right-hand side of (2.4.8) represents the function f in (2.4.5). Remember that a doublet is a singularity having not only an infinite velocity, but also an infinitely large value of stream function at its center. In the present case, the centers of the assumed doublets coincide with five grid points at which the stream function will be evaluated. The computational difficulty can be avoided by shifting the doublets to the right from their original positions through a tiny dimensionless distance of 10^{-6} , as shown in the function subprogram of Program 2.2. By doing so the effects on flow pattern are so small that they cannot be observed.

An egg-shaped body having all of the singularities enclosed within its body boundary is generated in Fig. 2.4.4 by Program 2.2. The body is wider at the section where the stronger doublets are located. This result provides some guide for the construction of bodies symmetric about the x axis, for example, symmetric airfoils at zero angle of attack.

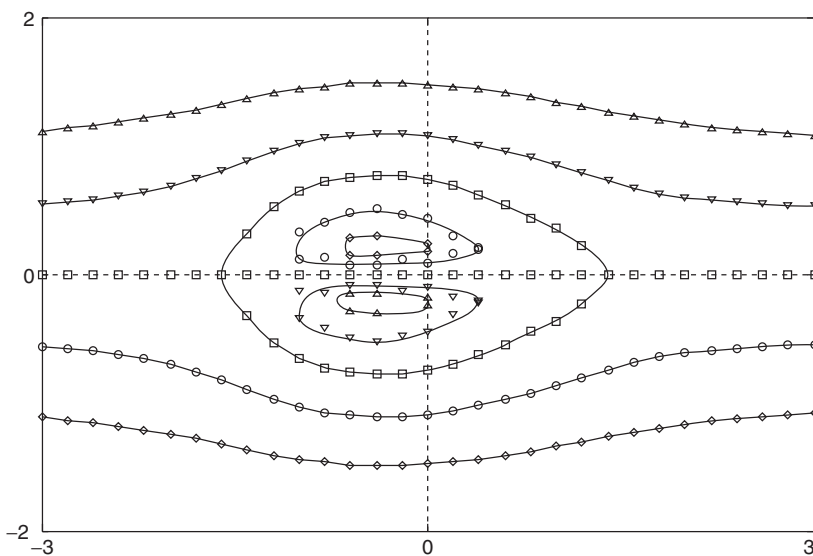


FIGURE 2.4.4 Flow generated by a uniform stream and five doublets. \square , PSI = 0; \circ , PSI = -0.5; \diamond , PSI = -1; ∇ , PSI = 0.5; Δ , PSI = 1.

Program 2.2 may be extended further to compute the pressure distribution around a body or along any streamline in a flow field. Once the positions of the points along that curve are located, the velocity components there can be calculated using either (2.1.14) or (2.1.16). Pressure is finally obtained after substituting the velocity components into the steady Bernoulli equation.

Superposition of elementary flows does not always end up with flow past a rigid body. In the previously mentioned example of a flow past a circular cylinder obtained by adding a doublet to a uniform stream, if the horizontal uniform stream is replaced by one making a 30° angle with the x axis, the resultant flow has the pattern shown in Fig. 2.4.5. The figure is an output of Program 2.2 with the function F modified accordingly. In this flow a well-defined body containing the doublet cannot be found.

Problem 2.1 To become familiar with the inverse method of superposition of elementary flows, plot, by modifying Program 2.2, the flow consisting of

1. A uniform stream and a source
2. A uniform stream and a sink
3. A source on the negative x -axis and a doublet at the origin of the coordinate system
4. A horizontal uniform stream and two doublets of equal strengths on the x -axis separated by a distance d

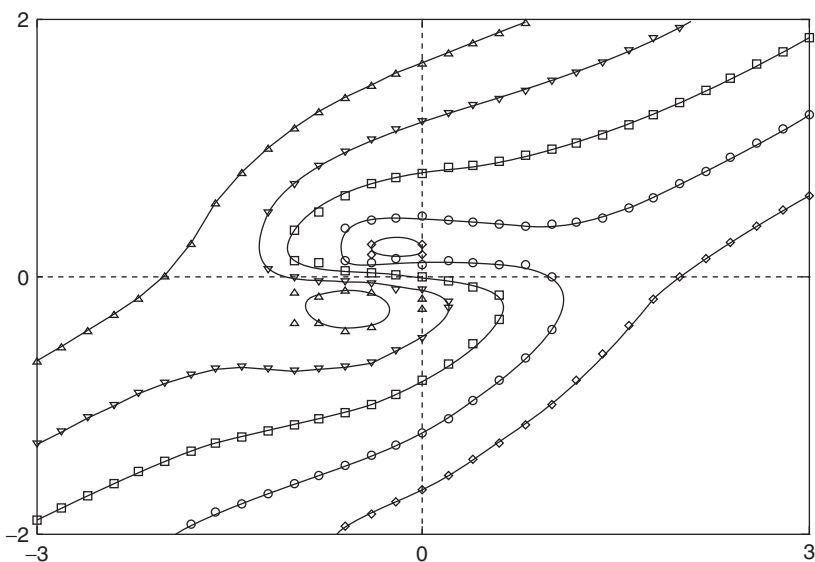


FIGURE 2.4.5 Superposition of a doublet at the origin and a uniform stream making a 30° angle with the x axis. Symbols as in Fig. 2.4.4.

Verify that a smooth oval-shaped body is generated in the flow for a small value of d , the body has the form of a dumbbell for a larger value of d and, finally, the body degenerates into two separate bodies when d is further increased.

Hint

Special care must be taken when sources or sinks appear in a flow whose stream function contains a function in the general form of $\tan^{-1}(y/x)$ by noting that this function must vary from 0 to π in the first and second quadrants and from $-\pi$ to -0 in the third and fourth quadrants. It is more convenient to normalize such a function by dividing it by π . The stream function of the combined flow should be examined to determine which streamline or streamlines may form a body.

Problem 2.2 Plot the streamlines of a flow formed by the combination of a vortex of circulation Γ at $(0, d)$ and another of circulation $-\Gamma$ at $(0, -d)$. The flow pattern will show symmetry about the x -axis, with its upper half describing the streamlines of a vortex distorted by a flat surface at $y = 0$.

This result demonstrates the following. The flow around a vortex in the presence of a flat plane can be obtained by adding to the original vortex its mirror image with respect to the plane surface. As another example, the flow field caused by a source at $(-d, 0)$ in the presence of a vertical wall formed by the y axis is constructed by combining the stream function of the original source and that of its mirror image, which is a source of the same strength situated at $(d, 0)$.

This technique for constructing flows near a flat surface is called the *method of images*.

Problem 2.3 Plot the upper half of the flow consisting of a horizontal uniform stream, a doublet on the y axis, and its image with respect to the plane $y = 0$. It simulates the flow around a closed body in the presence of a plate parallel to the flow far ahead.

Compute the pressure distribution along the upper surface of the flat plate, which shows that the plate is acted on by a net force in a direction toward the body. It follows that the same net force is exerted on the body but in an opposite direction.

2.5 VON KÁRMÁN'S METHOD FOR APPROXIMATING FLOW PAST BODIES OF REVOLUTION

Although the method of superposition of elementary flows described in Section 2.4 is a powerful tool for generating bodies of various shapes in a flow field. Using this method to construct the flow around a given body may require an effort to adjust the positions and strengths of the elementary flows so that the shape of the resulting body is close to what is desired. To avoid this difficulty, a numerical technique was developed by von Kármán (1927) that provides a systematic means for calculating the strengths of a group of sources placed at fixed locations. Even though the method was originally devised for computing the flow around the axisymmetric hull of a dirigible, it can also be applied to planar two-dimensional flow problems. von Kármán's method will be derived in this section and its usage will be illustrated by solving a flow problem with a known analytical solution.

It is natural to adopt the cylindrical coordinate system shown in Fig. 2.5.1 for analyzing axisymmetric flows. For a steady incompressible flow a stream function ψ can still be defined whose value at a given point is proportional to the volume of fluid flowing per unit time through the circular tube whose surface passes through that point. Velocity components are related to the stream function through the following equations:

$$u_r = -\frac{1}{r} \frac{\partial \psi}{\partial z}, \quad u_z = \frac{1}{r} \frac{\partial \psi}{\partial r} \quad (2.5.1)$$

In terms of stream function, the irrotationality condition has the form

$$\frac{\partial^2 \psi}{\partial r^2} - \frac{1}{r} \frac{\partial \psi}{\partial r} + \frac{\partial^2 \psi}{\partial z^2} = 0 \quad (2.5.2)$$

which, unlike the planar flows described in Section 2.1, is not a Laplace equation. Elementary solutions to the preceding linear equation can again be sought and

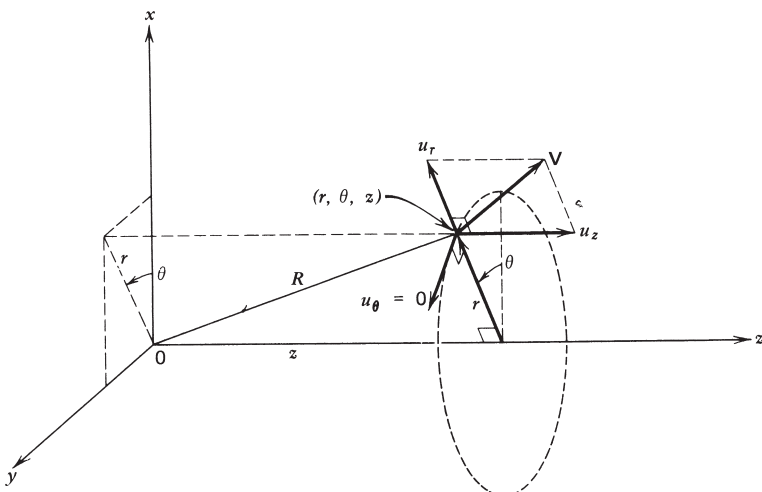


FIGURE 2.5.1 Cylindrical coordinate system for axisymmetric flows.

examined. For example,

$$\psi = \frac{1}{2} Ur^2 \quad (2.5.3)$$

represents a uniform stream of speed U flowing along the z axis, and the solution

$$\psi = -\frac{mz}{\sqrt{r^2 + z^2}} \quad (2.5.4)$$

is the stream function of a point source at the origin of the coordinate system. By using (2.5.1), it can easily be shown that, corresponding to the stream function (2.5.4), the total velocity \mathbf{V} is pointed radially outward from the origin and its magnitude is equal to m/R^2 , where $R = \sqrt{r^2 + z^2}$ is the radial distance from the origin. Thus, the constant $m (= VR^2)$ is proportional to the volume of fluid originating from the source per unit time, and therefore is called the strength of the point source. A negative value of m represents the strength of a point sink. Similar to the two-dimensional case, a doublet can be constructed for the axisymmetric flow by letting a point source–sink pair approach each other along the z axis while keeping the product of the strength and the distance in between a constant μ . The doublet so formed at the origin has the stream function

$$\psi = -\frac{\mu r^2}{(r^2 + z^2)^{3/2}} \quad (2.5.5)$$

Various bodies of revolution can be generated in a flow by linear combinations of elementary flows with proper strengths and at proper locations.

To approximate the flow resulting from a uniform axial stream of speed U past a given body of revolution, point sources or sinks are distributed uniformly

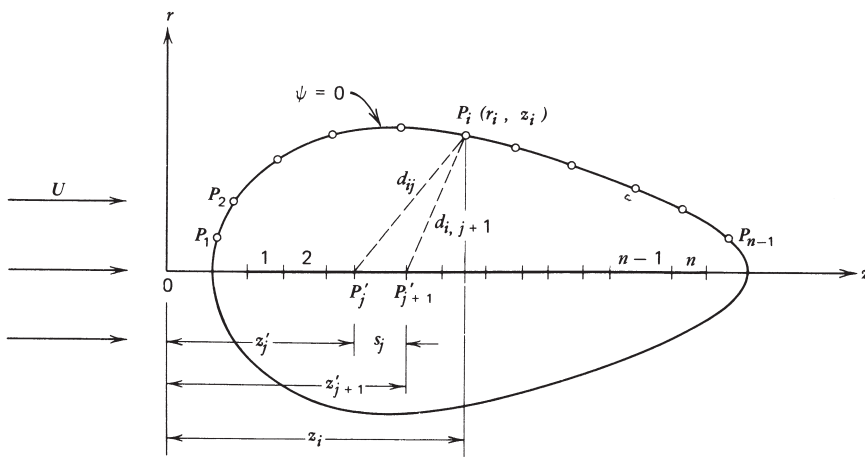


FIGURE 2.5.2 Uniform flow past a body of revolution.

within each of the n properly chosen segments inside the body along the axis of symmetry. The segments, labeled $1, 2, \dots, n$, as shown in Fig. 2.5.2, generally have different lengths and contain sources or sinks of different densities. The number of segments that are employed depends on the desired degree of accuracy. The end points of segment j are designated $P_j'(0, z'_j)$ and $P_{j+1}'(0, z'_{j+1})$, respectively. The length of this segment is $s_j (= z'_{j+1} - z'_j)$, along which sources of a constant strength q_j per unit length are distributed. The stream function of the flow induced at any point (r, z) by the sources within a small interval $d\xi$ located at $(0, \xi)$ on this segment is, from (2.5.4),

$$d\psi = -\frac{q_j(z - \xi) d\xi}{\sqrt{r^2 + (z - \xi)^2}}$$

Integration of the right-hand side from z'_j to z'_{j+1} gives the induced stream function at (r, z) caused by the whole source distribution on segment j , which is of the form

$$q_j \left[\sqrt{r^2 + (z - z'_{j+1})^2} - \sqrt{r^2 + (z - z'_j)^2} \right]$$

The stream function at a point (r, z) in the flow field consists of two parts, one caused by the uniform stream and the other by the source distributions. Thus,

$$\psi(r, z) = \frac{1}{2} Ur^2 + \sum_{j=1}^n q_j \left[\sqrt{r^2 + (z - z'_{j+1})^2} - \sqrt{r^2 + (z - z'_j)^2} \right] \quad (2.5.6)$$

Now $n - 1$ points P_1, P_2, \dots, P_{n-1} are selected on the surface of the prescribed body. At a surface point $P_i(r_i, z_i)$ the stream function is, from the general

expression (2.5.6),

$$\psi(r_i, z_i) = \frac{1}{2} Ur_i^2 + \sum_{j=1}^n q_j \left[\sqrt{r_i^2 + (z_i - z'_{j+1})^2} - \sqrt{r_i^2 + (z_i - z'_j)^2} \right] \quad (2.5.7)$$

The left-hand side of the above equation is zero because the point P_i is on the body surface. And, from Fig. 2.5.2, the two terms contained within the brackets in (2.5.7) represent the two distances $d_{i,j+1}$ and d_{ij} , measured respectively from the surface point P_i to the end points P'_{j+1} and P'_j of segment j . With the notation that

$$\Delta d_{ij} = d_{ij} - d_{i,j+1} = \sqrt{r_i^2 + (z_i - z'_j)^2} - \sqrt{r_i^2 + (z_i - z'_{j+1})^2} \quad (2.5.8)$$

and after replacing q_j/U by Q_j , (2.5.7) becomes

$$\sum_{j=1}^n \Delta d_{ij} Q_j = \frac{1}{2} r_i^2 \quad (2.5.9)$$

in which all quantities but the Q_j 's are known for specified locations of both the source segments and surface points.

Since Q is proportional to the volume of fluid produced per unit time from sources within a unit length of a segment, it requires that the total strength of the sources or sinks must be zero in order to form a closed body. That is,

$$\sum_{j=1}^n s_j Q_j = 0 \quad (2.5.10)$$

Combining the $n - 1$ equations obtained by evaluating (2.5.9) at all surface points and the equation (2.5.10), we have a complete set of n simultaneous algebraic equations for the unknown source strengths:

$$\begin{bmatrix} \Delta d_{11} & \Delta d_{12} & \cdots & \Delta d_{1n} \\ \Delta d_{21} & \Delta d_{22} & \cdots & \Delta d_{2n} \\ \vdots & \vdots & \cdots & \vdots \\ \Delta d_{n-1,1} & \Delta d_{n-1,2} & \cdots & \Delta d_{n-1,n} \\ s_1 & s_2 & \cdots & s_n \end{bmatrix} \begin{pmatrix} Q_1 \\ Q_2 \\ \vdots \\ Q_{n-1} \\ Q_n \end{pmatrix} = \begin{pmatrix} r_1^2/2 \\ r_2^2/2 \\ \vdots \\ r_{n-1}^2/2 \\ 0 \end{pmatrix} \quad (2.5.11)$$

Once Q_j 's are known, the stream function expressed by (2.5.6) becomes determined. According to (2.5.1), the corresponding velocity components are

$$u_r = - \sum_{j=1}^n \frac{U Q_j}{r} \left[\frac{z - z'_{j+1}}{\sqrt{r^2 + (z - z'_{j+1})^2}} - \frac{z - z'_j}{\sqrt{r^2 + (z - z'_j)^2}} \right] \quad (2.5.12)$$

$$u_z = U \left\{ 1 + \sum_{j=1}^n Q_j \left[\frac{1}{\sqrt{r^2 + (z - z'_{j+1})^2}} - \frac{1}{\sqrt{r^2 + (z - z'_j)^2}} \right] \right\} \quad (2.5.13)$$

They show that the velocities induced by the source distributions are diminishing far away from the body.

The pressure field can be computed from the Bernoulli equation (2.1.7) with the nonsteady term dropped. If P is used to denote the pressure far away from the body, the Bernoulli constant can be evaluated, and (2.1.7) becomes

$$p + \frac{1}{2}\rho(u_r^2 + u_z^2) = P + \frac{1}{2}\rho U^2$$

Instead of the pressure, it is sometimes more convenient to use the dimensionless *pressure coefficient* c_p , defined as the excess pressure over the free-stream value divided by the free-stream dynamic pressure. Thus,

$$c_p = \frac{p - P}{\frac{1}{2}\rho U^2} = 1 - \left(\frac{u_r}{U}\right)^2 - \left(\frac{u_z}{U}\right)^2 \quad (2.5.14)$$

and its value at any point can be computed after substitution of the velocity components at that point obtained from (2.5.12) and (2.5.13).

The solution of (2.5.11) can be obtained by Gaussian elimination or by finding the inverse of the coefficient matrix. Defining \mathbf{d} as the coefficient matrix, \mathbf{Q} as the vector of unknowns, and \mathbf{r} as the right-hand-side vector, the latter method can be written as

$$\mathbf{d}\mathbf{Q} = \mathbf{r} \quad (2.5.15)$$

$$\mathbf{d}^{-1}\mathbf{d}\mathbf{Q} = \mathbf{d}^{-1}\mathbf{r} \quad (2.5.16)$$

with $\mathbf{d}^{-1}\mathbf{d} = \mathbf{I}$ (identity matrix),

$$\mathbf{Q} = \mathbf{d}^{-1}\mathbf{r} \quad (2.5.17)$$

In Program 2.3, the inverse matrix is calculated by MATLAB function `inv(d)`.

To test the accuracy of von Kármán's method, it will be applied to a problem having a known solution. Such a problem can be formed by adding a uniform flow to a point doublet, described respectively by (2.5.3) and (2.5.5). By assigning the value $Ua^3/2$ to the strength μ of the doublet, the stream function of the combined flow becomes

$$\psi = \frac{1}{2}Ur^2 \left(1 - \frac{a^3}{R^3} \right) \quad (2.5.18)$$

where $R (= \sqrt{r^2 + z^2})$ is the radial distance from the origin. This shows that the streamline (actually the stream surface) $\psi = 0$ consists of the z axis, along which $r = 0$, and the surface of a sphere of radius a . It can be verified, with the help

of (2.5.1), that the magnitude of the velocity at a point (r, z) on the sphere is

$$|\mathbf{V}| = \frac{3}{2}U \frac{r}{a} \quad (2.5.19)$$

The pressure coefficient at that point is, according to (2.5.14),

$$c_p = 1 - \frac{9}{4} \left(\frac{r}{a} \right)^2 \quad (2.5.20)$$

For the numerical scheme of Program 2.3, sources are distributed within ten segments of equal lengths on the z -axis between $z = \pm 0.8a$, and nine equally spaced points are chosen on the upper surface of the sphere, as shown in Fig. 2.5.3. If φ_i denotes the angle between the z -axis and the radial position of the surface point $P_i(r_i, z_i)$, the nine values of φ_i are

$$\varphi_i = (10 - i) \frac{\pi}{10}, \quad i = 1, 2, \dots, 9 \quad (2.5.21)$$

from which the coordinates are computed through the relationships

$$r_i = a \sin \varphi_i \quad \text{and} \quad z_i = a \cos \varphi_i \quad (2.5.22)$$

After the source strengths are determined, the velocities and pressure coefficients at the surface points will be calculated and compared with the exact values represented by (2.5.19) and (2.5.20).

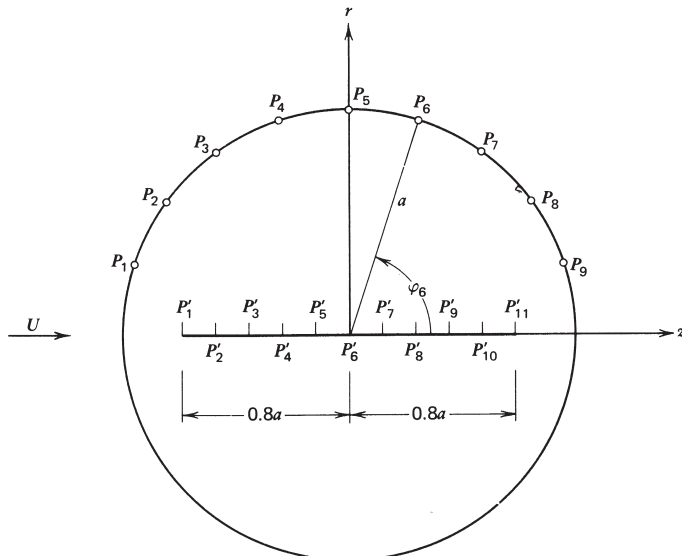


FIGURE 2.5.3 Source segments and surface points used in Program 2.3.

It is more convenient to nondimensionalize length and velocity by using the characteristic quantities a and U , respectively. This is achieved by letting $a = 1$ and $U = 1$ in Program 2.3.

The output of Program 2.3 shows that the velocity and pressure coefficient obtained by using von Kármán's method are almost identical to those computed from the exact solution, except at a few points where discrepancies appear at the fourth decimal place. In von Kármán's original work (1927) the body of a ZR III dirigible was generated in a uniform flow by using a group of sources near the bow and a separate group of sinks near the stern. The tacit assumption was that the contributions of the bow sources to the pressure distribution over the aft section and that of the stern sinks over the forward section would be negligible. The calculated pressure coefficient was in good agreement with the measured pressure coefficient without counting the discrepancy in the neighborhood of the gondola. Program 2.3 can be modified to compute the flow around a body of revolution of any shape. The user needs only to re-specify the positions of both source segments and surface points and to change the affected statements if the number of source segments is different from 10, the number presently used in that program.

Problem 2.4 It works as well if the source segments of Fig. 2.5.2 are replaced by discrete point sources of unknown strengths. Write a program for this purpose and use it to solve the sphere problem stated in Program 2.3.

Project for Further Study: Extend von Karman's method to solve the problem of uniform flow past a two-dimensional closed body of arbitrary shape, which is symmetric about its centerline parallel to the oncoming flow. In this case line sources and sinks described by (2.4.2) will be distributed within small intervals along the centerline. In the evaluation of the integral over a source segment to find the stream function at a point, it is easier to replace the integrand $\tan^{-1}[(y - y_0)/(x - x_0)]$ by $\cot^{-1}[(x - x_0)/(y - y_0)]$. After a procedure has been developed for the numerical computation, it is to be applied to calculate the fluid speed, V , and pressure coefficient, c_p , on the surface of a two-dimensional wing at zero angle of attack, whose cross section is a symmetric NACA 0009 airfoil. The shapes and characteristics of this and many other airfoils designated by the National Advisory Committee for Aeronautics are described in the book by Abbott and von Doenhoff (1949). The following table shows the dimensionless coordinates of some selected points on the airfoil and the dimensionless speeds there, in which c is the chord length of the wing and U is the free-stream speed in the x direction.

x/c	0	0.050	0.100	0.200	0.300	0.400	0.500	0.600	0.700	0.800	0.900	1.000
y/c	0	0.027	0.035	0.043	0.045	0.044	0.040	0.034	0.027	0.020	0.011	0
V/U	0	1.140	1.144	1.137	1.119	1.100	1.082	1.061	1.043	1.018	0.982	0

The tabulated values of V/U , obtained by employing a different method, are included for comparison with the numerical result.

2.6 INVERSE METHOD II: CONFORMAL MAPPING

In considering steady two-dimensional potential flows in Section 2.1, it was shown that the velocity components could be derived from either the velocity potential or the stream function, both of which satisfy the Laplace equation. The relationships involved there are repeated as follows:

$$u = \frac{\partial \phi}{\partial x} = \frac{\partial \psi}{\partial y} \quad (2.6.1)$$

$$v = \frac{\partial \phi}{\partial y} = -\frac{\partial \psi}{\partial x} \quad (2.6.2)$$

$$\frac{\partial^2 \phi}{\partial x^2} + \frac{\partial^2 \phi}{\partial y^2} = 0 \quad (2.6.3)$$

$$\frac{\partial^2 \psi}{\partial x^2} + \frac{\partial^2 \psi}{\partial y^2} = 0 \quad (2.6.4)$$

The $\phi = \text{constant}$ and $\psi = \text{constant}$ curves are called, respectively, the *equipotential lines* and the *streamlines* of the flow. At a point where an equipotential line intersects a streamline, the vectors that are respectively normal to the two curves are perpendicular to each other, since

$$\begin{aligned} \nabla \phi \cdot \nabla \psi &= \frac{\partial \phi}{\partial x} \frac{\partial \psi}{\partial x} + \frac{\partial \phi}{\partial y} \frac{\partial \psi}{\partial y} \\ &= (u)(-v) + (u)(v) = 0 \end{aligned}$$

Thus, the equipotential lines and the streamlines of a two-dimensional flow form two families of mutually orthogonal curves in the x - y plane, except at stagnation points where the directions of the normal vectors are not defined.

We now introduce a complex variable, $z = x + iy$, where $i = \sqrt{-1}$ is called the imaginary unit, and construct with velocity potential and stream function a complex function

$$w(z) = \phi(x, y) + i\psi(x, y) \quad (2.6.5)$$

If w is a single-valued function of z , as assumed in the above form, and if its derivative of the first order, dw/dz , exists throughout the region occupied by the fluid, then the derivative at any point in that region can be computed regardless of the way in which the increment in z tends to zero. Let $\Delta z = \Delta x + i\Delta y$ be such an increment. To find the derivative we may choose to let Δy equal zero and then let Δx approach zero (see Churchill, 1948, Section 18). By choosing

such a path, $\Delta z = \Delta x$ and

$$\begin{aligned}\frac{dw}{dz} &= \lim_{\Delta x \rightarrow 0} \frac{\phi(x + \Delta x, y) - \phi(x, y) + i\psi(x + \Delta x, y) - i\psi(x, y)}{\Delta x} \\ &= \frac{\partial \phi}{\partial x} + i \frac{\partial \psi}{\partial x}\end{aligned}\quad (2.6.6)$$

Alternatively, we may choose to let Δx equal zero and then let Δy approach zero. Thus, $\Delta z = i\Delta y$ and

$$\begin{aligned}\frac{dw}{dz} &= \lim_{\Delta y \rightarrow 0} \frac{\phi(x, y + \Delta y) - \phi(x, y) + i\psi(x, y + \Delta y) - i\psi(x, y)}{i\Delta y} \\ &= -i \frac{\partial \phi}{\partial y} + \frac{\partial \psi}{\partial y}\end{aligned}\quad (2.6.7)$$

Equating the right-hand members of (2.6.6) and (2.6.7) results in

$$\frac{\partial \phi}{\partial x} = \frac{\partial \psi}{\partial y} \quad \text{and} \quad \frac{\partial \phi}{\partial y} = -\frac{\partial \psi}{\partial x}\quad (2.6.8)$$

These equations are called the *Cauchy-Riemann conditions*, which are the necessary conditions for the existence of the derivative of the function $w(z)$. But these conditions are satisfied automatically by (2.6.1) and (2.6.2) derived for a potential flow. This means that $\phi + i\psi$, the function on the right-hand side of (2.6.5), is an *analytic function* of z , that is, a function that is differentiable for the values of z in a region of the z plane. If a function is analytic in the neighborhood of a point but not at the point itself, this point is called a singular point, or a singularity, of that function. Furthermore, (2.6.3) and (2.6.4) are obtained after eliminating either ϕ or ψ from the Cauchy-Riemann conditions (2.6.8), indicating that both real and imaginary parts of an analytic function satisfy the Laplace equation.

Conversely, if we choose an arbitrary analytic function $w(z)$, the real and imaginary parts of the function then automatically qualify as the velocity potential and the stream function, respectively, of a potential flow in the x - y plane. The function w shown in (2.6.5) is called the *complex potential*, whose derivative is related to the velocity components through the following relationship, derived from either (2.6.6) or (2.6.7):

$$\frac{dw}{dz} = u - iv\quad (2.6.9)$$

Hence, the magnitude of the velocity vector is obtained by taking the absolute value of the above expression.

As an example, let us consider a simple analytic function

$$w(z) = Uz e^{-i\alpha}\quad (2.6.10)$$

in which U and α are constants. After being separated into real and imaginary parts, (2.6.10) becomes

$$w = U(x \cos \alpha + y \sin \alpha) + iU(y \cos \alpha - x \sin \alpha)$$

The imaginary part is precisely the stream function of the uniform flow described by (2.4.1) and Fig 2.4.1a. It follows that the real part represents the velocity potential and the right side of (2.6.10) represents the complex potential of that uniform flow. To find the fluid velocity components, we simply use (2.6.9) to obtain $u = U \cos \alpha$ and $v = U \sin \alpha$. It can also be shown in a similar fashion that the functions $(\Lambda/2\pi) \log(z - z_0)$, $(i\Gamma/2\pi) \log(z - z_0)$, and $\kappa/2\pi(z - z_0)$ are, respectively, the complex potentials of the source, vortex, and doublet described by (2.4.2) to (2.4.4), where $z_0 = x_0 + iy_0$. Each of these three functions has a singular point at z_0 , where the first derivative of the function (or the velocity) is unbounded.

We have thus arrived at another inverse method, through which we can generate as many potential flows as we can write analytic functions. The principle of superposition of elementary flows can still be applied in generating new flows. For example, the sum of Uz , the complex potential of a uniform horizontal flow, and $\kappa/2\pi z$, the complex potential of a doublet at the origin, represents the complex potential of a uniform flow past a circular cylinder of radius $\sqrt{\kappa/2\pi U}$ centered at the origin.

There exists another powerful method, called the *method of conformal mapping*, that is used to generate new flow patterns by mapping a known flow in the x - y plane into a new x' - y' plane through various transformations between the two sets of coordinates. Suppose that the complex potential $w(z)$ in (2.6.5) is known for a given flow. Let the variable $z' (= x' + iy')$ be related to z through the relationship

$$z = f(z') \quad (2.6.11)$$

where f is an analytic function of z' . Upon the use of (2.6.11), w becomes an analytic function of z' because the derivative

$$\frac{dw}{dz'} = \frac{dw}{dz} \frac{df}{dz'} \quad (2.6.12)$$

exists, due to the existence of the two derivatives on the right-hand side of (2.6.12). After being transformed into the z' plane, the complex potential may be grouped into real and imaginary parts according to the new coordinates, so that

$$w[f(z')] = \phi'(x', y') + i\psi'(x', y') \quad (2.6.13)$$

It follows from the properties of analytic functions that ϕ' and ψ' must satisfy the Cauchy-Riemann conditions

$$\frac{\partial^2 \phi'}{\partial x'^2} + \frac{\partial^2 \phi'}{\partial y'^2} = 0$$

$$\frac{\partial^2 \psi'}{\partial x'^2} + \frac{\partial^2 \psi'}{\partial y'^2} = 0$$

Thus, the $\phi' = \text{constant}$ and $\psi' = \text{constant}$ lines remain mutually orthogonal in the x' - y' plane after the transformation, and (2.6.13) represents the complex potential of a flow in the x' - y' plane.

Furthermore, because (2.6.5) and (2.6.13) represent the same complex function, we must have

$$\phi(x, y) = \phi'(x', y')$$

$$\psi(x, y) = \psi'(x', y')$$

except that some additive constants may appear in these equations. Hence, under the transformation (2.6.11), a streamline $\psi = c$ and a perpendicular equipotential line $\phi = k$ in the x - y plane map, respectively, into a streamline $\psi' = c$ and an equipotential line $\phi' = k$ in the x' - y' plane. The two curves, although distorted in shape, remain perpendicular to each other after the transformation. For this reason the mapping is said to be conformal. Theorems related to conformal mapping and their proofs are found in Chapter 8 of the book by Churchill (1948).

To illustrate the use of this method, we consider the complex potential

$$\begin{aligned} w(z) &= Uz \\ &= Ux + iUy \end{aligned} \tag{2.6.14}$$

of a uniform stream with speed U flowing along the positive x direction. By choosing a specific form

$$z = z'^2 \tag{2.6.15}$$

for the transformation (2.6.11), the complex potential becomes

$$\begin{aligned} w(z') &= Uz'^2 \\ &= U(x'^2 - y'^2) + i2Ux'y' \end{aligned} \tag{2.6.16}$$

Thus, the streamlines $y = c$ and the equipotential lines $x = k$ in the x - y plane are mapped into streamlines $2x'y' = c$ and equipotential lines $x'^2 - y'^2 = k$ in the x' - y' plane, as shown, respectively, by the solid and dashed lines in Fig. 2.6.1. The pattern describes the flow past a 90° corner.

In general, the function on the right side of (2.6.11) may be expanded in a series of positive and negative powers of z' and, in this respect, the transformation (2.6.15) is merely a special case of the series expansion. If two terms of the following particular form are retained in the series, the relation

$$z = z' + \frac{a^2}{z'} \tag{2.6.17}$$

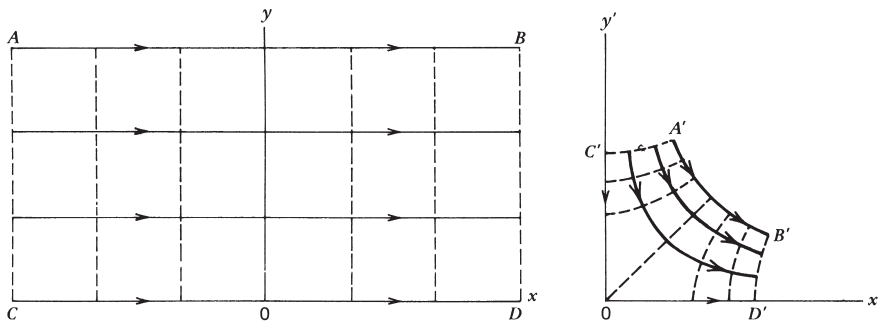


FIGURE 2.6.1 Mapping of a uniform flow in the x - y plane into the x' - y' plane by the transformation $z = z'^2$.

is called the *Joukowski transformation*. Under this transformation the complex potential of a uniform flow, (2.6.14), becomes

$$w(z') = U \left(z' + \frac{a^2}{z'} \right) \quad (2.6.18)$$

which is the complex potential for a uniform flow past a circular cylinder of radius a . The same result was obtained earlier by adding the complex potential of a uniform flow to that of a doublet.

The Joukowski transformation is probably one of the most widely used transformations in solving potential flow problems. For instance, the transformation

$$z = z' + \frac{b^2}{z'} \quad (2.6.19)$$

where $b^2 < a^2$, maps a circle of radius a with center at the origin of the x' , y' coordinates into an ellipse in the x - y plane (Fig. 2.6.2). The same transformation maps two circles intersecting the positive x' axis at $x' = b$, with the center of one circle on the y' axis and that of the other off the coordinate axes, into a circular arc and a so-called *Joukowski airfoil* in the x - y plane (Fig. 2.6.3). The detailed description of these mappings can be found in Chapter 4 of Yih (1969).

Suppose that the flow about the elliptic cylinder of Fig. 2.6.2 is to be sought. A relationship that expresses z' as a function of z may first be obtained by taking the inverse of (2.6.19). Upon substitution of this relationship into the expression (2.6.18) for the complex potential of the flow about a circular cylinder, we obtain the complex potential of the flow about the elliptic cylinder. Streamlines can then be plotted by assigning various constant values to the stream function or the imaginary part of the transformed complex potential. This procedure, however, involves tedious analytical work, especially when separating a complicated function into real and imaginary parts. For this reason we will choose a different approach by solving the problem numerically.

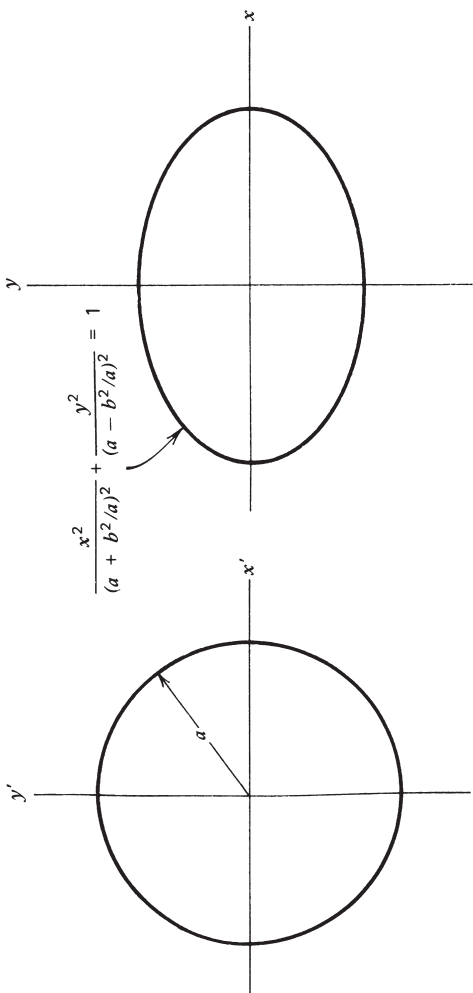


FIGURE 2.6.2 Mapping of a circle in the $x-y$ plane into an ellipse in the $x'-y'$ plane by the Joukowski transformation $z = z' + b^2/z$.

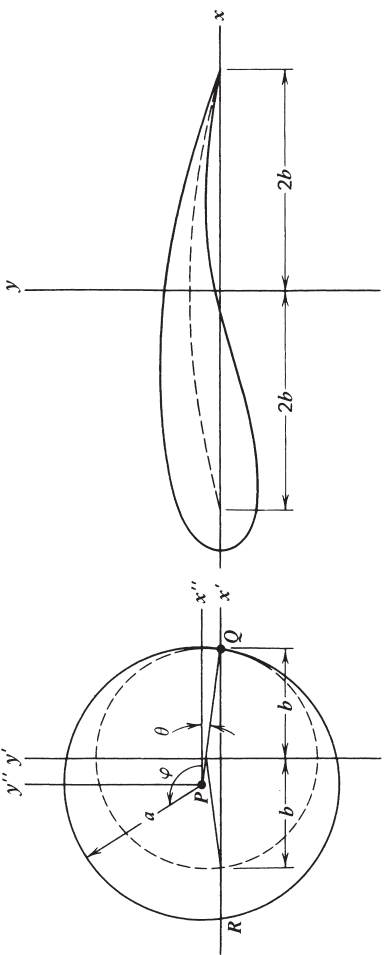


FIGURE 2.6.3 Mapping of two circles in the $x'-y'$ plane into a circular arc and an airfoil in the $x-y$ plane by the Joukowski transformation
$$z = z' + b^2/z'.$$

In the computer program to be constructed, we will find the coordinates of points along some streamlines of the flow before the mapping. This given flow is usually in a relatively simple form, and its characteristics are well known. Some common examples are the uniform flow and the flow around a circle. These points will be mapped according to the specified transformation and will be plotted on the transformed plane. Such a plot will display the pattern of the transformed flow if the number of points is large. In a similar fashion the equipotential lines, velocity, or pressure distribution of the transformed flow may also be plotted.

Our illustrative example is concerned with a uniform flow U in the positive x direction past the Joukowski airfoil shown in Fig. 2.6.3. The airfoil is the image in the x - y plane of the circle of radius a centered at the point P in the x' - y' plane and, in particular, its sharp trailing edge at $x = 2b$ is the image of the point Q at $x' = b$. The flow about the airfoil is obtained from the flow of uniform speed U past the circle using the transformation (2.6.19).

The magnitude of the velocity \mathbf{V} in the x - y plane is related to that of \mathbf{V}' in the x' - y' plane through the equation

$$\left| \frac{dw}{dz} \right| = \left| \frac{dw}{dz'} \right| / \left| \frac{dz}{dz'} \right|$$

By the use of (2.6.9) and (2.6.19), it becomes

$$V = \frac{V'}{\sqrt{1 - \left(\frac{b}{z'} \right)^2}} \quad (2.6.20)$$

This equation shows that the flow speed at the trailing edge of the airfoil becomes infinite if the speed at Q (where $z' = b$) is of a finite magnitude. Physically such a situation is not allowed. Based on observations of bodies with a sharp trailing edge moving through a fluid, the *Kutta condition* states that the flow speed at the trailing edge must be zero if the trailing-edge angle is finite, or the speed there must be finite if the trailing-edge angle is zero. In the present case of a Joukowski airfoil, the Kutta condition is fulfilled only when the speed at Q vanishes. In other words, the airfoil will create about itself a clockwise circulation Γ whose strength is just sufficient to make the point Q a stagnation point on the circular cylinder in the x' - y' plane. Let $z'_P (= x'_P + iy'_P)$ be the position of the point P in the x' - y' plane and let θ be the angle between the line PQ and the direction of the free stream, as indicated in Fig. 2.6.3. The magnitude of the circulation is (Kuethe and Chow, 1998, Section 4.7)

$$\Gamma = 4\pi a U \sin \theta$$

Since $\sin \theta = y'_P/a$, this equation becomes

$$\Gamma = 4\pi y'_P U \quad (2.6.21)$$

The flow about the circle is then constructed by adding to the uniform stream a doublet and a line vortex. In the x'', y'' coordinate system whose origin coincides with P , the complex potential of the resultant flow is

$$w = U \left[z'' + \frac{a^2}{z''} + i2y'_P \log \left(\frac{z''}{a} \right) \right] \quad (2.6.22)$$

where $z'' = x'' + iy''$, and a constant $-i2y'_P \log a$ has been added so that the value of the stream function on the circle remains unchanged after the introduction of the vortex. The complex potential can easily be expressed in terms of z' by using the transformation

$$z'' = z' - z'_P \quad (2.6.23)$$

The shape of the airfoil is controlled by varying a, b and the coordinates of the center P ; a and b determine the thickness envelope and chord length, respectively, while the height of P determines the maximum camber of the airfoil. By inspecting Fig. 2.6.3, these variables are related through the equation

$$a^2 = y'^2_P + (b - x'_P)^2$$

For a given value of a , we may assume a set of values for two of the quantities on the right-hand side of the previous equation, say, for b and y'_P , and compute the value of the third, or

$$x'_P = b - \sqrt{a^2 - y'^2_P} \quad (2.6.24)$$

x'_P must be negative to produce an airfoil having its sharp edge on the downstream side, similar to the one shown in Fig. 2.6.3. If y'_P is chosen to be zero, the circle will be mapped into an uncambered airfoil symmetric about the x axis.

The values $U = 1$ m/s, $a = 1$ m, $b = 0.8$ m, and $y'_P = 0.199$ m are used in Program 2.4. A rectangular grid system is first defined in the $x'-y'$ plane bounded by x'_{\min} , x'_{\max} , y'_{\min} , and y'_{\max} . Stream function is computed at all the grid points using the imaginary part of (2.6.22). The subroutine SEARCH, which was constructed in Program 2.2, is then called to locate the points along some representative streamlines. Another subroutine named MAPPNG is constructed for the purpose of mapping these points from the $x'-y'$ plane into the $x-y$ plane through Joukowski transformation (2.6.19). This subroutine also serves the purpose of throwing away the points falling inside the circle in the $x'-y'$ plane and those outside of the space bounded by x_{\min} , x_{\max} , y_{\min} , and y_{\max} in the $x-y$ plane, which are the boundaries of the region to be plotted. As an alternative, we have also employed MATLAB routines for obtaining these plots, as shown in the program listing.

In addition to the flow pattern, we are also interested in the forces acting on the airfoil. The net pressure force is a lift in the direction of the positive y axis, and its magnitude per unit span is $\rho U \Gamma$ or $4\pi\rho y'_P U^2$ after using (2.6.21). The

surface pressure, however, varies with location and will be computed and plotted on a separate graph according to the following procedure.

One hundred evenly spaced points are selected on the circular cylinder of Fig. 2.6.3. The coordinates of these surface points in the x'' - y'' plane are calculated by varying the angle φ , starting from the value zero, in the expression

$$z'' = ae^{i\varphi}$$

By using the transformations $z' = z'' + z'_p$ and (2.6.19), these points are mapped successively into the x - y plane. In this way the exact positions of the points on the airfoil are obtained, whereas the subroutine SEARCH would return only the approximate positions. Another advantage of using this method is that the points that are on the streamline $\psi = 0$ but not on the airfoil are automatically excluded.

To find the speed V at the surface of the airfoil, we use the formula

$$V = \left| \frac{dw}{dz} \right| = \left| \frac{dw}{dz''} \right| \left| \frac{dz''}{dz'} \right| \left| \frac{dz'}{dz} \right|$$

Upon substitution from (2.6.19), (2.6.22), and (2.6.23), it reduces to

$$V = U \left| \frac{1 - (a/z'')^2 + i2y'_p/z''}{1 - (b/z')^2} \right| \quad (2.6.25)$$

Once the speed at a point becomes known, the pressure coefficient (or the dimensionless pressure difference) at that point can be computed according to

$$c_p = \frac{p - P}{\frac{1}{2}\rho U^2} = 1 - \left(\frac{V}{U} \right)^2 \quad (2.6.26)$$

which is obtained by using (2.5.14) and the Bernoulli equation. The values of c_p are plotted as a function of the x -coordinate of the 100 surface points.

Figure 2.6.4 shows the shape of the airfoil, which is described by the streamline $\psi = 0$. The coordinates of the surface points can easily be printed out if so desired. The plot reveals that the space between the body and the streamline $\psi = 0.5$ is narrower than that between the body and the streamline $\psi = -0.5$, indicating that the speed on the upper surface is higher than that on the lower. The corresponding pressure distributions on the upper and lower surfaces of the airfoil are represented, respectively, by the lower and upper branches of the curve plotted in Fig. 2.6.5. At the forward stagnation point where $V = 0$, the pressure coefficient takes on the maximum value of unity according to (2.6.26). At the sharp trailing edge the speed is finite but not zero, although it is transformed from the stagnation point Q in the x' - y' plane. The area enclosed by the pressure distribution curve is proportional to the total lift of the airfoil. This program may be used not only to generate airfoils of different shapes by varying the values assigned to b and y'_p , but also, with some modifications, to plot

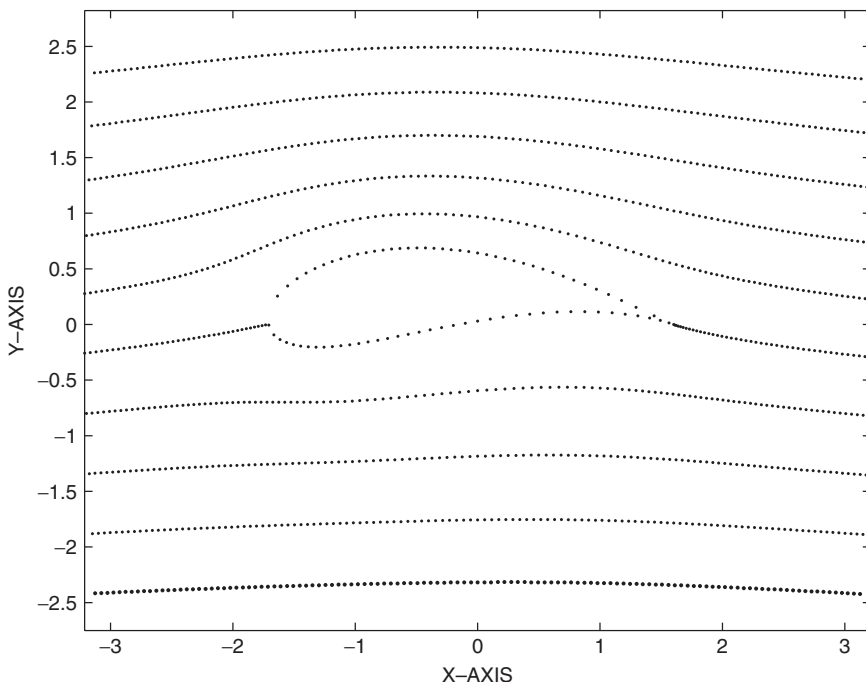


FIGURE 2.6.4 Flow around a Joukowski airfoil.

flow patterns obtained by mapping from various known flows through arbitrary transformations.

Problem 2.5 The transformation

$$z = z' + \frac{1}{z'} \quad (2.6.27)$$

maps the circle $|z'| = 1$ into the line segment on the x axis between the points $x = -2$ and $x = 2$, and the region outside the circle into the entire x - y plane. It is known that

$$w = U \left(z' e^{-i\alpha} + \frac{e^{i\alpha}}{z'} \right) \quad (2.6.28)$$

represents the complex potential for a uniform flow of speed U past a cylinder of unit radius centered at $z' = 0$. The flow makes an angle α with the x' axis at an infinite distance from the cylinder. Under the transformation (2.6.27), the complex potential (2.6.28) then becomes that for a uniform flow past a flat plate at an angle of attack α . Plot the streamlines of this transformed flow and the

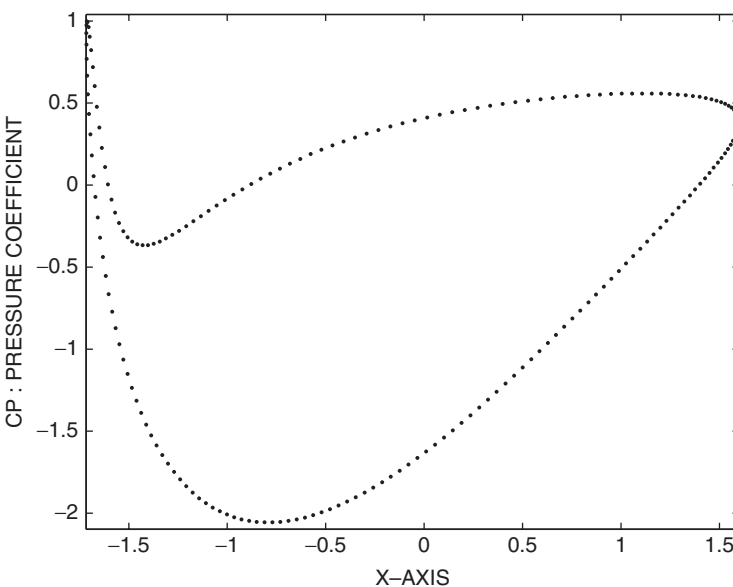


FIGURE 2.6.5 Pressure distribution around the airfoil.

pressure distribution on the upper and lower surfaces of the plate. Note that the velocity and therefore the pressure is unbounded at the edges of the plate.

Problem 2.6 If the Kutta condition is to be satisfied on the flat plate described in the previous problem, a circulation is required to move the rear stagnation point on the circle in the x' - y' plane to the point $(1,0)$, which maps into the trailing edge of the plate. Plot the streamlines and pressure distribution and compare them with those obtained for the case without a circulation.

2.7 CLASSIFICATION OF SECOND-ORDER PARTIAL DIFFERENTIAL EQUATIONS

Consider a body moving through a compressible inviscid fluid. The disturbances originating from the body are propagating away in all directions at the speed of sound. If the body moves at a speed much slower than the sonic speed, these disturbances will finally reach infinity in all directions, and the flow pattern will resemble that of an incompressible potential flow past that body. In a coordinate system attached to the body, the originally uniform oncoming flow is deformed upstream as well as downstream from it. However, if the body moves at a supersonic speed, it overtakes the forward propagating disturbances so that all the disturbances created by the body are left behind. The flow pattern as

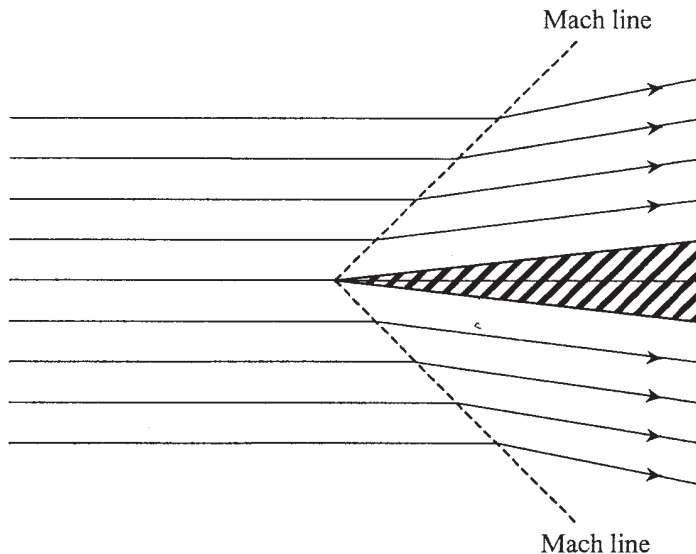


FIGURE 2.7.1 Supersonic flow past a thin wedge.

seen by an observer moving with the body (e.g., a thin wedge of an infinitesimal wedge angle) is sketched in Fig. 2.7.1. The pattern is radically different from that around a body moving subsonically in that the flow upstream from the wedge is undisturbed and remains uniform. This undisturbed region is separated from the disturbed region along two straight lines called the Mach lines or, in mathematical terms, the characteristics. Such lines do not exist in a subsonic flow.

In fact, the governing equations for these two flows are of different forms. About a thin body that produces only weak disturbances, the governing equation for a two-dimensional subsonic flow is (Kuethe and Chow, 1998, Section 11.3)

$$(1 - M^2) \frac{\partial^2 \phi}{\partial x^2} + \frac{\partial^2 \phi}{\partial y^2} = 0 \quad (2.7.1)$$

in which ϕ is the velocity potential and M , the Mach number, is the ratio of flow speed to the speed of sound and is treated in the linearized theory as a constant. The equation takes the following form when the flow is supersonic.

$$(M^2 - 1) \frac{\partial^2 \phi}{\partial x^2} - \frac{\partial^2 \phi}{\partial y^2} = 0 \quad (2.7.2)$$

Notice that in (2.7.1) the two coefficients have the same sign, whereas in (2.7.2) their signs are opposite. These two partial differential equations are said to be of two different types.

The type of an equation is determined by examining the existence of characteristics along which two different solutions to the same equation may be patched

(as demonstrated in Fig. 2.7.1). For a general discussion let us assume that the velocity potential of a two-dimensional flow is governed by a representative equation

$$A\phi_{xx} + 2B\phi_{xy} + C\phi_{yy} = D \quad (2.7.3)$$

in which A , B , C , and D may be functions of x , y , ϕ , ϕ_x , and ϕ_y . Here the subscripts are used to denote partial derivatives, so that ϕ_x represents $\partial\phi/\partial x$, ϕ_{xy} represents $\partial^2\phi/\partial x\partial y$, and so forth. If the velocity components ϕ_x and ϕ_y are both continuous functions of x and y , their changes when going from (x, y) to a neighboring point $(x + dx, y + dy)$ are, respectively,

$$dx \cdot \phi_{xx} + dy \cdot \phi_{xy} + 0 \cdot \phi_{yy} = d\phi_x \quad (2.7.4)$$

$$0 \cdot \phi_{xx} + dx \cdot \phi_{xy} + dy \cdot \phi_{yy} = d\phi_y \quad (2.7.5)$$

Equations (2.7.3) to (2.7.5) may be solved simultaneously for the three second-order derivatives of ϕ . For instance, by applying Cramer's rule, we find

$$\phi_{xy} = \frac{\begin{vmatrix} A & D & C \\ dx & d\phi_x & 0 \\ 0 & d\phi_y & dy \end{vmatrix}}{\begin{vmatrix} A & 2B & C \\ dx & dy & 0 \\ 0 & dx & dy \end{vmatrix}} \quad (2.7.6)$$

However, if dx and dy are the components of a displacement along a Mach line (i.e., a characteristic), the derivatives of velocity components in the direction of that line may be discontinuous because along it two different solutions may be patched. Accordingly, along a characteristic, the second-order derivatives of ϕ are indeterminate. Setting the denominator of (2.7.6) equal to zero gives

$$A \left(\frac{dy}{dx} \right)^2 - 2B \frac{dy}{dx} + C = 0 \quad (2.7.7)$$

where dy/dx is the slope of a characteristic. Its expression is obtained by solving the preceding equation:

$$\left(\frac{dy}{dx} \right)_{\text{char}} = \frac{B \pm \sqrt{B^2 - AC}}{A} \quad (2.7.8)$$

Similarly, by setting the numerator of (2.7.6) equal to zero, the slope of a characteristic is determined in the hodograph plane using velocity components as the coordinates.

There are three possible results for the slope of a characteristic in the physical plane, depending on the magnitude of the expression under the radical of (2.7.8). They are stated separately as follows.

If $B^2 - AC > 0$, there exist two characteristics at a point whose slopes are represented by the two real values computed from the right-hand side of (2.7.8). The partial differential equation is then classified as being of *hyperbolic* type. The equations governing steady or unsteady wave motions usually belong to

this category. One example is (2.7.2), the equation describing perturbations in a supersonic flow, in which $A = M^2 - 1$, $B = 0$, and $C = -1$, so that $B^2 - AC = M^2 - 1 > 0$. The slopes of the two characteristics are $\pm 1/\sqrt{M^2 - 1}$ according to (2.7.8), which are exactly the slopes of Mach lines in a supersonic flow (Kuethe and Chow, 1998, p. 273).

If $B^2 - AC > 0$, the right-hand side of (2.7.8) becomes complex. The existence of characteristics is impossible, and the corresponding partial differential equation is classified as being of *elliptic* type. Examples are the Laplace and Poisson equations introduced in Section 2.1 for incompressible potential flows, and the governing subsonic equation (2.7.1). In the latter case $A = 1 - M^2$, $B = 0$, and $C = 1$ and, therefore, $B^2 - 4AC = -(1 - M^2) < 0$.

Finally, if $B^2 - 4AC = 0$, there is only one real value for the slope, and such a partial differential equation is called of *parabolic* type. The following example is the equation governing the unsteady thermal conduction in a one-dimensional conductor:

$$\frac{\partial T}{\partial t} = k \frac{\partial^2 T}{\partial x^2} \quad (2.7.9)$$

where T denotes temperature, x and t represent, respectively, spatial coordinate and time, and k is the thermal diffusivity of the conducting medium. A comparison between (2.7.9) and the standard form (2.7.3) gives $A = k$, $B = C = 0$, so that $B^2 - AC = 0$. It will be shown in the next chapter that the equation describing diffusion of vorticity in a viscous fluid also belongs to this class.

These three types of partial differential equations may be solved using different numerical techniques, which will be introduced in this and the following chapters.

2.8 NUMERICAL METHODS FOR SOLVING ELLIPTIC PARTIAL DIFFERENTIAL EQUATIONS

Suppose that the Poisson equation

$$\frac{\partial^2 f}{\partial x^2} + \frac{\partial^2 f}{\partial y^2} = q(x, y) \quad (2.8.1)$$

which is an elliptic partial differential equation, is to be solved in a rectangular region subject to the condition that the values of f are prescribed on the boundary of that domain. To introduce a commonly used numerical technique, we refer to the rectangular grid system shown in Fig. 2.8.1. We use the notation (i, j) to indicate the intersecting point of the vertical grid line passing through x_i and the horizontal grid line through y_j . Our first step is to approximate the partial differential equation (2.8.1) by a finite difference equation at the representative interior point (i, j) .

Let $f_{i,j}$ and $q_{i,j}$ represent $f(x_i, y_j)$ and $q(x_i, y_j)$, respectively. Applying the central-difference formula (2.2.9) for computing second-order derivatives and

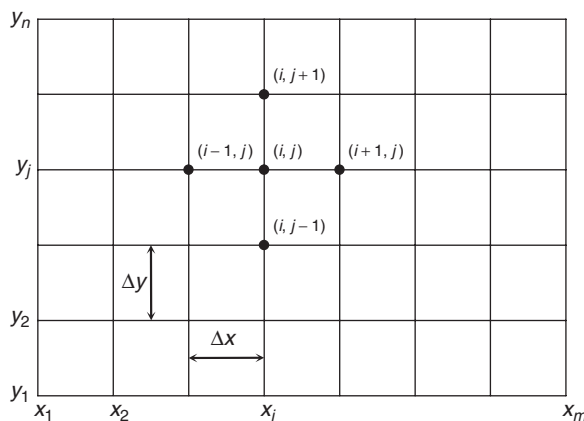


FIGURE 2.8.1 Rectangular domain.

referring to the five neighboring points as shown in Fig. 2.8.1, we have

$$\frac{\partial^2 f}{\partial x^2} = \frac{1}{(\Delta x)^2} (f_{i+1,j} - 2f_{i,j} + f_{i-1,j}) - O\left[(\Delta x)^2 \left(\frac{\partial^4 f}{\partial x^4}\right)_{i,j}\right]$$

$$\frac{\partial^2 f}{\partial y^2} = \frac{1}{(\Delta y)^2} (f_{i,j+1} - 2f_{i,j} + f_{i,j-1}) - O\left[(\Delta y)^2 \left(\frac{\partial^4 f}{\partial y^4}\right)_{i,j}\right]$$

The differential equation (2.8.1) may then be replaced by the finite-difference form

$$\frac{1}{(\Delta x)^2} (f_{i+1,j} - 2f_{i,j} + f_{i-1,j}) + \frac{1}{(\Delta y)^2} (f_{i,j+1} - 2f_{i,j} + f_{i,j-1}) = q_{i,j} \quad (2.8.2)$$

with a truncation error of the order of $(\Delta x)^2 + (\Delta y)^2$.

For a square grid we let $\Delta x = \Delta y = h$, so that the preceding equation becomes

$$f_{i,j} = \frac{1}{4} (f_{i-1,j} + f_{i+1,j} + f_{i,j-1} + f_{i,j+1}) - \frac{1}{4} h^2 q_{i,j} \quad (2.8.3)$$

Vanishing of q reduces (2.8.1) to the Laplace equation, and (2.8.3) states that the value of f at an interior point is equal to the average of the values of f at the four adjoining points. This statement is called the *mean value theorem* for harmonic functions that satisfy the Laplace equation.

When (2.8.2) or (2.8.3) is applied at all interior points bounded within the domain of Fig. 2.8.1, we obtain $(m-2)(n-2)$ algebraic equations that automatically include the boundary conditions. Solving these equations simultaneously, we can, theoretically, find the unknown values of f at the interior grid points.

However, practically, this direct procedure is tedious and time-consuming, especially when the number of grid points is large, although for a small number of grid points (on the order of 10^2) and for two-dimensional problems the use of direct solvers can be feasible (see Section 4.5). It is therefore necessary to develop some methods of solution that can conveniently be carried out on a computer for a large number of grid points.

One of these numerical techniques, using an iterative scheme, is called *Liebmann's method*. In this method values of f are first guessed at all interior points in addition to those prescribed at the boundary points on the edges of the given domain. These values are represented by $f_{i,j}^{(0)}$, with the superscript 0 indicating the zeroth iteration. To facilitate the following discussion, the square mesh is chosen so that the simplified difference equation (2.8.3) will be used. The values of f are computed for the next iteration by executing (2.8.3) at every interior point based on the values of f at the present iteration. The sequence of computation starts from the interior point situated at the lower left corner, proceeds upward until reaching the top, and then goes to the bottom of the next vertical line on the right. This process is repeated until the new value of f at the last interior point at the upper right corner has been obtained. Variations of this point-iteration technique and other line-iteration techniques are given in Tannehill, Anderson, and Pletcher (1997).

Applying (2.8.3) at the first point gives

$$f_{2,2}^{(1)} = \frac{1}{4} \left[f_{1,2}^{(0)} + f_{3,2}^{(0)} + f_{2,1}^{(0)} + f_{2,3}^{(0)} \right] - \frac{1}{4} h^2 q_{2,2} \quad (2.8.4)$$

in which $f_{1,2}^{(0)}$ and $f_{2,1}^{(0)}$ are the constant boundary values and therefore do not vary with the number of iterations. They may be replaced, respectively, by $f_{1,2}^{(1)}$ and $f_{2,1}^{(1)}$ in (2.8.4). The computation at the next point involves $f_{2,2}^{(0)}$. Since an improved value $f_{2,2}^{(1)}$ is available at this time, it will be used instead. Thus,

$$f_{2,3}^{(1)} = \frac{1}{4} \left[f_{1,3}^{(1)} + f_{3,3}^{(0)} + f_{2,2}^{(1)} + f_{2,4}^{(0)} \right] - \frac{1}{4} h^2 q_{2,3} \quad (2.8.5)$$

where $f_{1,3}^{(1)}$ is used to replace the constant boundary value $f_{1,3}^{(0)}$. Repeating this argument, we deduce a general formula for computing values of f at the $(n+1)$ th iteration:

$$f_{i,j}^{(n+1)} = \frac{1}{4} \left[f_{i-1,j}^{(n+1)} + f_{i+1,j}^{(n)} + f_{i,j-1}^{(n+1)} + f_{i,j+1}^{(n)} \right] - \frac{1}{4} h^2 q_{i,j} \quad (2.8.6)$$

This equation applies to any interior point, no matter whether it is next to some boundary points or not. It holds for the former case, as already shown by (2.8.4) and (2.8.5). If (i,j) is a deep interior point, the first and third terms on the right-hand side of (2.8.6) represent, respectively, the values of f at the grid points to the left of and below that point. These values have already been recalculated according to our sequence and, therefore, carry the superscript $(n+1)$. Equation (2.8.6) is named *Liebmann's iterative formula* (also known as the *Gauss-Seidel* formula).

We now need to prove that as $n \rightarrow \infty$, $f_{i,j}^{(n)}$ approaches $f_{i,j}$, the solution to the finite difference equation. For a simpler analysis we will examine, instead of (2.8.6), an iterative scheme called *Richardson's iterative formula* (or the *Jacobi* formula)

$$f_{i,j}^{(n+1)} = \frac{1}{4} \left[f_{i-1,j}^{(n)} + f_{i+1,j}^{(n)} + f_{i,j-1}^{(n)} + f_{i,j+1}^{(n)} \right] - \frac{1}{4} h^2 q_{i,j} \quad (2.8.7)$$

which, as will be shown later, converges slower than (2.8.6) toward the final solution. Subtracting (2.8.3) from (2.8.7) and defining the error at (i,j) during the n th iteration as

$$e_{i,j}^{(n+1)} = f_{i,j}^{(n)} - f_{i,j} \quad (2.8.8)$$

we obtain

$$e_{i,j}^{(n+1)} = \frac{1}{4} \left[e_{i-1,j}^{(n)} + e_{i+1,j}^{(n)} + e_{i,j-1}^{(n)} + e_{i,j+1}^{(n)} \right]$$

which implies that

$$\left| e_{i,j}^{(n+1)} \right| \leq \frac{1}{4} \left[\left| e_{i-1,j}^{(n)} \right| + \left| e_{i+1,j}^{(n)} \right| + \left| e_{i,j-1}^{(n)} \right| + \left| e_{i,j+1}^{(n)} \right| \right] \quad (2.8.9)$$

If $E^{(n)}$ represents the highest value among the absolute errors at all grid points during the n th iteration, (2.8.9) leads to the conclusion that

$$E^{(n+1)} \leq E^{(n)} \quad (2.8.10)$$

This relationship is not sufficient, however, to prove that $E^{(n)} \rightarrow 0$ as $n \rightarrow \infty$. The way in which $E^{(n)}$ shrinks can be estimated as follows.

Referring to Fig. 2.8.1, let the points adjoining at least one boundary point be called the first-layer points, those adjoining at least one first-layer point be called the second-layer points, and so forth. When (2.8.9) is applied at a first-layer point, at least one of the four adjoining points is a boundary point where the error is zero. Therefore,

$$\left| e_{i,j}^{(n+1)} \right| \leq \frac{3}{4} E^{(n)} = \left(1 - \frac{1}{4} \right) E^{(n)} \quad (2.8.11)$$

At a second-layer point, at least one of the adjoining points is a first-layer point. Applying (2.8.9) at such a point gives, by using (2.8.11),

$$\begin{aligned} \left| e_{i,j}^{(n+1)} \right| &\leq \frac{1}{4} \left[3E^{(n)} + \left(1 - \frac{1}{4} \right) E^{(n-1)} \right] \\ &\leq \frac{1}{4} \left[3E^{(n-1)} + \left(1 - \frac{1}{4} \right) E^{(n-1)} \right] = \left(1 - \frac{1}{4^2} \right) E^{(n-1)} \end{aligned}$$

Similarly, we deduce a generalized expression for the absolute error at an m th-layer point.

$$\left| e_{i,j}^{(n+1)} \right| \leq \left(1 - \frac{1}{4^m} \right) E^{(n-m+1)}$$

If the total number of layers in the grid system is M , the maximum absolute error during an iteration should occur on this innermost layer according to the preceding expression. Thus, we have

$$E^{(n+1)} \leq \left(1 - \frac{1}{4^M}\right) E^{(n-M+1)}$$

which gives, by assigning appropriate values to n ,

$$\begin{aligned} E^{(M)} &\leq \left(1 - \frac{1}{4^M}\right) E^{(0)} \\ E^{(2M)} &\leq \left(1 - \frac{1}{4^M}\right) E^{(M)} \end{aligned}$$

and so forth. In other words, if N is any positive integer, the maximum error at the (NM) th iteration is

$$E^{(NM)} \leq \left(1 - \frac{1}{4^M}\right)^N E^{(0)} \quad (2.8.12)$$

The right-hand side approaches zero as $N \rightarrow \infty$; that is, after a large number of iterations, the values of f computed from (2.8.7) will approach the solution to the finite-difference equation (2.8.3). Because of the condition (2.8.10), Liebmann's iterative formula (2.8.6) will converge toward the final solution faster than Richardson's iterative formula (2.8.7).

An improved numerical technique, called the *successive overrelaxation (S.O.R.) method*, gives an even faster convergence than Liebmann's method in solving the Poisson equation. This method used the following iteration scheme for a rectangular domain of square meshes:

$$f_{i,j}^{(n+1)} = f_{i,j}^{(n)} + \frac{\omega}{4} \left[f_{i-1,j}^{(n+1)} + f_{i+1,j}^{(n+1)} + f_{i,j-1}^{(n+1)} + f_{i,j+1}^{(n+1)} - 4f_{i,j}^{(n)} - h^2 q_{i,j} \right] \quad (2.8.13)$$

in which ω is a constant to be determined. The formula is equivalent to (2.8.6) for $\omega = 1$. The iterated result converges for $1 \leq \omega < 2$, and it converges most rapidly when ω is assigned the optimum value

$$\omega_{\text{opt}} = \frac{8 - 4\sqrt{4 - \alpha^2}}{\alpha^2} \quad (2.8.14)$$

with $\alpha = \cos(\pi/m) + \cos(\pi/n)$, where m and n are, respectively, the total number of increments into which the horizontal and vertical sides of the rectangular region are divided. The expression for ω must be modified for nonuniform grid sizes or nonrectangular domains. A more general formulation for the overrelaxation method and its discussions can be found in Chapter III of the book by Roache (1972).

As the first application of Liebmann's formula (2.8.6), we consider the flow caused by a distribution of vorticity within a rectangular domain. Vorticity vector ζ is defined as the curl of the velocity vector, or

$$\nabla \times \mathbf{V} = \zeta \quad (2.8.15)$$

For two-dimensional fluid motion on the x - y plane, the velocity components may be derived from the stream function ψ according to (2.1.14), and the vorticity is a vector in the z direction whose magnitude is designated by ζ . Thus, (2.8.15) can be written in the form of a scalar equation,

$$\frac{\partial^2 \psi}{\partial x^2} + \frac{\partial^2 \psi}{\partial y^2} = -\zeta(x, y) \quad (2.8.16)$$

which belongs to the class of (2.8.1). Based on (2.8.6), the numerical scheme for solving (2.8.16) is

$$\psi_{i,j} = \frac{1}{4} [\psi_{i-1,j} + \psi_{i+1,j} + \psi_{i,j-1} + \psi_{i,j+1} + h^2 \zeta_{i,j}] \quad (2.8.17)$$

Here the superscripts used to denote the number of iterations have been omitted, because they are automatically taken care of if this equation is applied successively at interior points in the same order as that described prior to (2.8.4).

In Program 2.5, we examine how the circular streamlines of a line vortex deform when it is confined within a finite domain defined by $-3 \leq x \leq 3$ and $-2 \leq y \leq 2$. The location of the line vortex of finite vorticity ζ_0 is fixed at (x_0, y_0) . With the value 0.25 assigned to h , which is the size of increments in both x and y directions, there will be 425 grid points corresponding to $m = 25$ and $n = 17$ in the notation of Fig. 2.8.1.

Since the stream function may take on an arbitrary additive constant, the value zero will be assigned to the bounding streamline coinciding with the boundary of the rectangular region. To start the iteration, a constant value of 0.5 is guessed for the stream function at all interior points. After a new value of ψ is computed from (2.8.17) at an interior point, the absolute value of the difference between this and the previous value of ψ at the same point is calculated and is added to the value of a variable called **ERROR**, whose starting value at the beginning of an iteration is zero. At the end of one iteration, when the values of ψ at all interior points have been updated, the value of **ERROR** is compared with **ERRMAX**, which is the maximum allowable value of the total error. If **ERROR** is less than or equal to **ERRMAX**, the desired accuracy has been reached, so the iterating process can be stopped. Otherwise, the iteration counter **ITER** is increased by 1 and a new iteration is started. In our program we let **ERRMAX** = 0.001. In other words, on the average, the maximum error allowed at each of the 345 interior points is approximately 3×10^{-6} . The iteration process stops when the iteration counter reaches this maximum value of 200 even if the result has not yet reached the desired accuracy.

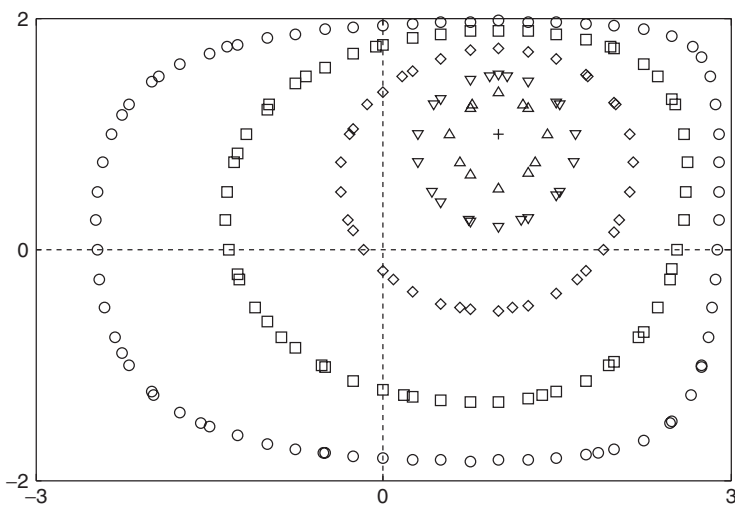


FIGURE 2.8.2 Streamlines of a vortex bounded by a rectangular wall. \circ , $\text{PSI} = 0.05$; \square , $\text{PSI} = 0.2$; \diamond , $\text{PSI} = 0.5$; ∇ , $\text{PSI} = 1$; Δ , $\text{PSI} = 1.5$.

The final values of ψ are printed only at some selected grid points on several $\psi = \text{constant}$ curves which are located by searching through both vertical and horizontal grid lines. This is achieved by calling a subroutine named **SEARCH2**, a modified version of subroutine **SEARCH** used in Program 2.2 that searches only through the vertical grid lines for such points. As before, the program is written using MATLAB plot programs as an alternative. The resulting flow pattern is shown in Fig. 2.8.2.

Problem 2.7 Rerun Program 2.5 after replacing Liebmann's iterative formula (2.8.6) by the successive overrelaxation formula (2.8.13). Compare the efficiency of these two methods in view of the number of iterations required to obtain a solution of the same accuracy.

Problem 2.8 Run Program 2.5 with another concentrated vorticity added in the rectangular domain. If the two vorticities are of opposite signs, the result will show that the two vortices are confined within two regions separated by a branch of the $\psi = 0$ streamline. However, if the vorticities are of the same sign, the two regions containing the vortices are connected by a streamline having the shape of an 8, which is encircled by other streamlines.

2.9 POTENTIAL FLOWS IN DUCTS OR AROUND BODIES – IRREGULAR AND DERIVATIVE BOUNDARY CONDITIONS

The flow considered in Section 2.8 is bounded by a rectangular wall along which the stream function assumes a constant value. In many flow problems, however,

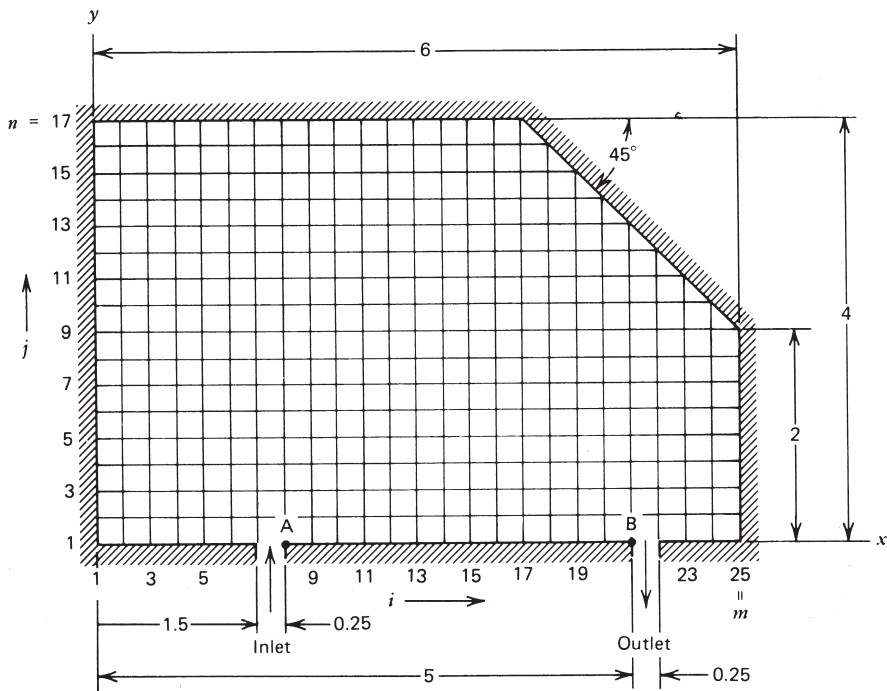


FIGURE 2.9.1 A chamber with irregular boundaries.

the surfaces of a body or wall may be of complicated geometries, or there may exist surfaces along which the derivatives of stream function instead of the function itself are known. Two examples are shown in this section to demonstrate the techniques used for handling irregular and derivative boundary conditions.

The first example is concerned with a rectangular chamber whose upper right corner is blocked off by a plate, making a 45° angle with the x axis. A two-dimensional flow field is established when an inviscid incompressible fluid is flowing steadily through the chamber between an inlet and an outlet, both situated on the bottom wall. Dimensions of the chamber are specified in Fig. 2.9.1. When a square mesh of size $h = 0.25$ is laid, as shown in the figure, the slant surface intersects grid lines exactly at some grid points, which are naturally the boundary points on that surface. The more general case, in which boundary points do not coincide with grid points, will be taken up in the next example.

In the absence of vorticity, the governing equation is deduced from (2.8.16):

$$\frac{\partial^2 \psi}{\partial x^2} + \frac{\partial^2 \psi}{\partial y^2} = 0 \quad (2.9.1)$$

To solve this equation the successive overrelaxation scheme (2.8.13) will be employed in the present example. For computer calculations the iteration formula

can be written as

$$\psi_{i,j} = (1 - \omega)\psi_{i,j} + \frac{\omega}{4} [\psi_{i-1,j} + \psi_{i+1,j} + \psi_{i,j-1} + \psi_{i,j+1}] \quad (2.9.2)$$

in which the $\psi_{i,j}$ on the right-hand side represents its value at the n th iteration and that on the left-hand side represents the value at the next iteration. The optimum value of ω given by (2.8.14) will be used in the computation.

It is known that stream function represents the volume flow rate passing between a point and a reference streamline. Let it be normalized so that the net flow rate through the chamber is unity. In Fig. 2.9.1 the line AB between the inlet and outlet is chosen to be the base streamline along which $\psi = 0$. Then $\psi = 1$ is the streamline described by the remaining part of the chamber wall. Having specified the boundary conditions, we can now apply (2.9.2) at interior points following exactly the same iterative procedure as that adopted for executing (2.8.17) in Program 2.5, except that the interior domain is now redefined to accommodate the slant surface. The numerical solution is considered satisfactory when the sum of errors at all interior points is less than or equal to 0.001.

Figure 2.9.2, the output of Program 2.6, is actually a plot of stream tubes in the flow field. Thus, a wider cross section along a stream tube indicates a region of slower flow speed. In this flow, fast speeds are found at the inlet and outlet openings. To obtain the final solution, 41 iterations were performed. However, tests show that if Liebmann's method is used instead, the number of interactions is increased to 256 for a solution having the same accuracy! The saving in computing time by using the successive overrelaxation method is amazing. Better efficiency can be obtained by implementing multigrid acceleration (see, e.g., Moin 2001; Tannehill et al., 1997).

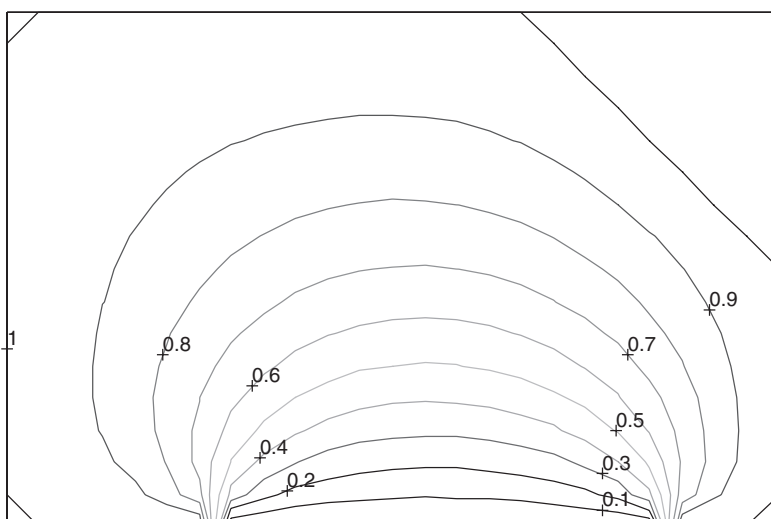


FIGURE 2.9.2 Pattern of flow through a chamber.

As a second example of dealing with various boundary conditions, we consider a channel flow past a circular cylinder, described in Fig. 2.9.3. The flow enters the channel from a small central opening and leaves it at a section downstream from the cylinder. Assume that buffers are installed at the exit so that the flow there becomes horizontal. In this problem it is more convenient to place the origin of the coordinate system at the center of the circular cylinder. Because of its symmetry about the x -axis, only the upper half of the flow will be computed. Again, a square mesh of size $h = 0.25$ is used to cover the region of interest. The governing equation (2.9.1) will be solved numerically using Liebmann's iterative formula:

$$\psi_{i,j} = \frac{1}{4} (\psi_{i-1,j} + \psi_{i+1,j} + \psi_{i,j-1} + \psi_{i,j+1}) \quad (2.9.3)$$

The boundary conditions are (1) $\psi = 0$ on the cylinder surface and on the x -axis outside the body; (2) ψ is a constant, say 1, on the upper wall of the channel; and (3) $v = -\partial\psi/\partial x = 0$ at the exit section.

Two problems arise when specifying these boundary conditions. Boundary points on the cylinder are defined as the intersections of the body surface and the horizontal and vertical grid lines. These points, as marked by small solid circles in Fig. 2.9.3, do not usually coincide with the grid points. Thus, the formula (2.9.3) cannot be used at some grid points in the immediate neighborhood of the cylinder. On the other hand, a numerical technique is needed to incorporate the derivative boundary condition at the exit.

Equation (2.9.3) is a finite difference approximation of the Laplace equation (2.9.1), based on the assumption that point (i,j) is at equal distances from its four neighboring grid points. To solve the first problem, the difference equation

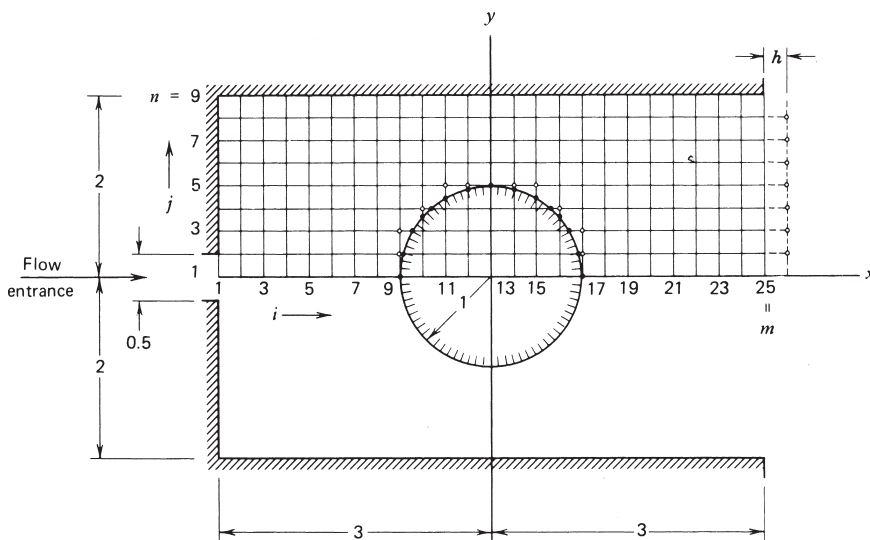
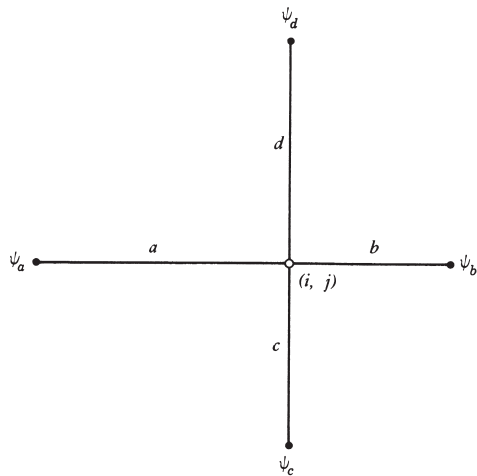


FIGURE 2.9.3 Circular cylinder inside a channel.

FIGURE 2.9.4 Evaluation of $\psi_{i,j}$.

(2.9.3) has to be generalized for an arbitrary situation, shown in Fig. 2.9.4, in which the four neighboring points are at different distances a, b, c , and d from point (i, j) . We let the stream functions evaluated at these neighboring points be denoted ψ_a, ψ_b, ψ_c , and ψ_d respectively, and then approximate the left-hand side of (2.9.1) at (i, j) by the following linear function:

$$\left(\frac{\partial^2 \psi}{\partial x^2} + \frac{\partial^2 \psi}{\partial y^2} \right)_{i,j} = \alpha_0 \psi_{i,j} + \alpha_a \psi_a + \alpha_b \psi_b + \alpha_c \psi_c + \alpha_d \psi_d \quad (2.9.4)$$

where the α 's are coefficients to be determined. Each of the four stream functions can be expanded in Taylor's series about (i, j) . For example,

$$\begin{aligned} \psi_a &= \psi_{i,j} - a \left(\frac{\partial \psi}{\partial x} \right)_{i,j} + \frac{1}{2} a^2 \left(\frac{\partial^2 \psi}{\partial x^2} \right)_{i,j} - O(a^3) \\ \psi_d &= \psi_{i,j} + d \left(\frac{\partial \psi}{\partial y} \right)_{i,j} + \frac{1}{2} d^2 \left(\frac{\partial^2 \psi}{\partial y^2} \right)_{i,j} + O(d^3) \end{aligned}$$

and so forth. Substitution of these equations into (2.9.4) gives, after rearrangement and dropping the cubic and higher-order terms,

$$\begin{aligned} \left(\frac{\partial^2 \psi}{\partial x^2} + \frac{\partial^2 \psi}{\partial y^2} \right)_{i,j} &= (\alpha_0 + \alpha_a + \alpha_b + \alpha_c + \alpha_d) \psi_{i,j} + (b \alpha_b - a \alpha_a) \left(\frac{\partial \psi}{\partial x} \right)_{i,j} \\ &\quad + (d \alpha_d - c \alpha_c) \left(\frac{\partial \psi}{\partial y} \right)_{i,j} + \frac{1}{2} (a^2 \alpha_a + b^2 \alpha_b) \left(\frac{\partial^2 \psi}{\partial x^2} \right)_{i,j} \\ &\quad + \frac{1}{2} (c^2 \alpha_c + d^2 \alpha_d) \left(\frac{\partial^2 \psi}{\partial y^2} \right)_{i,j} \end{aligned}$$

Equating corresponding coefficients on the two sides results in five simultaneous algebraic equations whose solution is

$$\begin{aligned}\alpha_0 &= -2 \left(\frac{1}{ab} + \frac{1}{cd} \right), & \alpha_a &= \frac{2}{a(a+b)}, & \alpha_b &= \frac{2}{b(a+b)}, \\ \alpha_c &= \frac{2}{c(c+d)}, & \alpha_d &= \frac{2}{d(c+d)}\end{aligned}$$

Vanishing of the right-hand side of (2.9.4) gives the desired difference approximation of the Laplace equation:

$$\psi_{i,j} = \left[\frac{\psi_a}{a(a+b)} + \frac{\psi_b}{b(a+b)} + \frac{\psi_c}{c(c+d)} + \frac{\psi_d}{d(c+d)} \right] / \left(\frac{1}{ab} + \frac{1}{cd} \right) \quad (2.9.5)$$

It can easily be shown that (2.9.5) is equivalent to (2.9.3) when $a = b = c = d = h$.

We now return to Fig. 2.9.3. At the boundary points on the cylinder the value $\psi = 0$ is assigned. By inspection we have picked out 10 grid points, marked by hollow circles in the neighborhood of the cylinder, at which the generalized formula (2.9.5) must apply. These grid points can be divided into two groups, depending on whether they are on the left or on the right side of the cylinder. A representative point (i, j) on the left side of the cylinder is sketched in Fig. 2.9.5. At such a point $\psi_a = \psi_{i-1,j}$, $\psi_d = \psi_{i,j+1}$ and $a = d = h$. If within a distance h to the right there is a boundary point on the cylinder, we let

$$b = (13 - i)h - \sqrt{1 - [(j - 1)h]^2} \quad \text{and} \quad \psi_b = 0 \quad (2.9.6)$$

Otherwise, we let $b = h$ and $\psi_b = \psi_{i+1,j}$. However, to simplify the algorithm, the second equation in (2.9.6) will still be written as $\psi_b = \psi_{i+1,j}$ but the value zero will be assigned to stream function at all grid points inside the cylinder. Thus, if a boundary point appears below the point (i, j) within a distance h , we need only to set

$$c = (j - 1)h - \sqrt{1 - [(13 - i)h]^2} \quad (2.9.7)$$

while $\psi_c = \psi_{i,j-1}$ is automatically equal to zero. Similarly, at a point on the right side of the cylinder, $b = d = h$, the modification for c is still (2.9.7), and that for a is

$$a = (i - 13)h - \sqrt{1 - [(j - 1)h]^2} \quad (2.9.8)$$

In this way the curved boundary is taken care of by defining the four lengths a, b, c , and d at each of the points where formula (2.9.5) is to be used. ψ_a, ψ_b, ψ_c , and ψ_d are the values of ψ at the four neighboring grid points of (i, j) and therefore need not be redefined in the computer program.

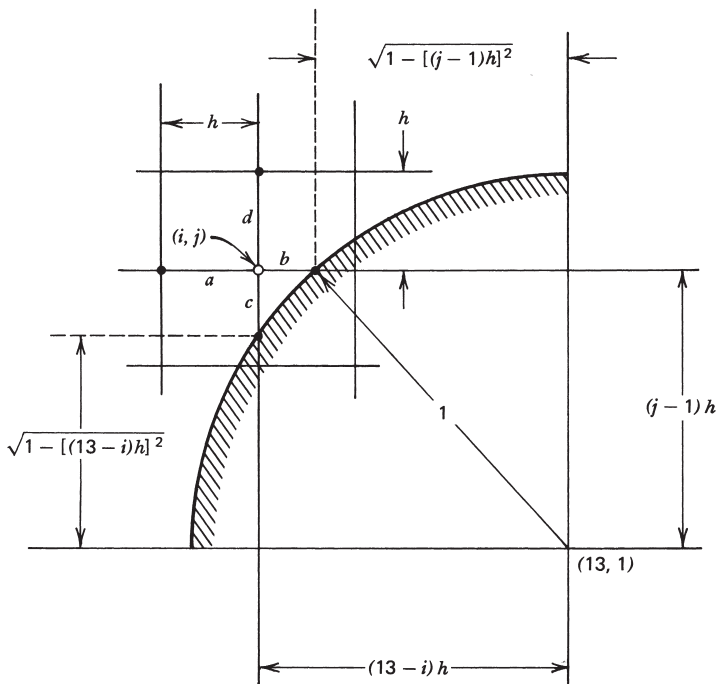


FIGURE 2.9.5 A grid point (i, j) near the left surface of the circular cylinder.

Next we consider the derivative boundary condition that $\partial\psi/\partial x = 0$ at the exit. By using the central-difference formula (2.2.8), the condition becomes

$$\psi_{i+1,j} = \psi_{i-1,j} \quad \text{for } i = 25 \text{ and } j = 2, \dots, 8 \quad (2.9.9)$$

This suggests that an additional column of fictitious grid points is needed at a distance h to the right of the exit section, as indicated in Fig. 2.9.3. These fictitious points do not show specifically in the computation, because with substitution of (2.9.9) the iterative formula (2.9.3) at $i = 25$ becomes

$$\psi_{i,j} = \frac{1}{4} (2\psi_{i-1,j} + \psi_{i,j-1} + \psi_{i,j+1}) \quad (2.9.10)$$

In summary, there are three types of grid points besides the boundary points: (1) the points in the close neighborhood of the cylinder, (2) those at the exit section of the channel, and (3) the remaining grid points inside the fluid. To classify the type, we introduce an identification number ID at each of the interior points and assign to it the integer value of 1, -1, or 0 according to the location of that point as specified in the order just mentioned.

After the numerical solution for ψ has been obtained, the flow pattern is plotted following the same procedure as that described in Program 2.6. The flow

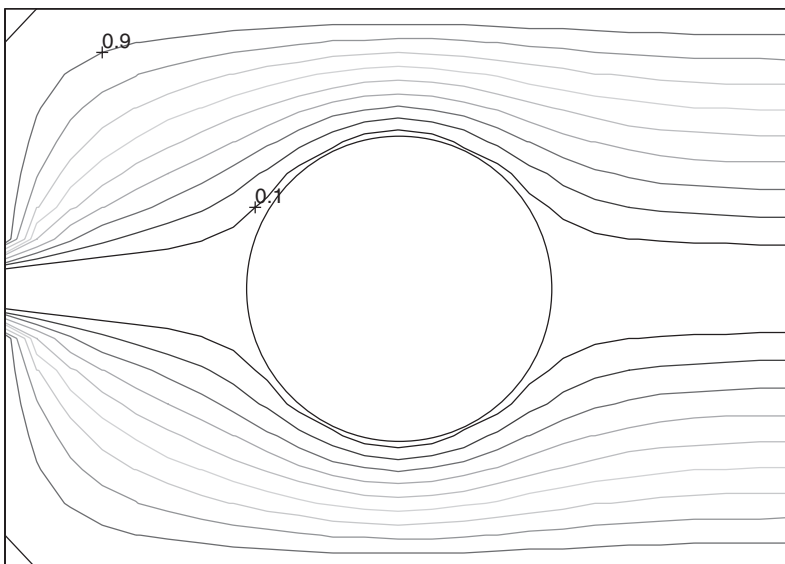


FIGURE 2.9.6 Channel flow past a circular cylinder.

pattern below the centerline of the channel is the mirror image of that above. In the program listing, we also provide an alternative way of plotting selected ψ values by the use of MATLAB contour plotting routines.

Most of the variable names used in Program 2.7 are exactly the same as those used in Program 2.6. New names are listed as follows: ID, A, B, C, and D have just been defined, and JFIRST(i) is the value of j at the lowest interior grid point on the i th grid line.

The output of Program 2.7, Fig. 2.9.6, shows that the flow speed on the right side of the cylinder is slower than that on the left. The pressure difference has a tendency to push the body upstream.

Problem 2.9 Compute and plot the channel flow past a cylinder of rectangular cross section shown in Fig. 2.9.7. The potential flow pattern is assumed to be symmetric about both the x and y axes, so that only the upper left quarter of the flow needs to be computed. It is further assumed that the flow entering the section AB is approximately uniform and the speed there is unity.

The boundary conditions are that $\psi = 0$ along AFED, $\psi = 1$ along BC, $\psi = y/4$ along AB, and $\partial\psi/\partial x = 0$ along CD. In the computation let $h = 0.25$.

Problem 2.10 The equation governing the stream function of an axisymmetric potential flow was derived previously as (2.6.2) having the form

$$\frac{\partial^2 \psi}{\partial r^2} - \frac{1}{r} \frac{\partial \psi}{\partial r} + \frac{\partial^2 \psi}{\partial z^2} = 0$$

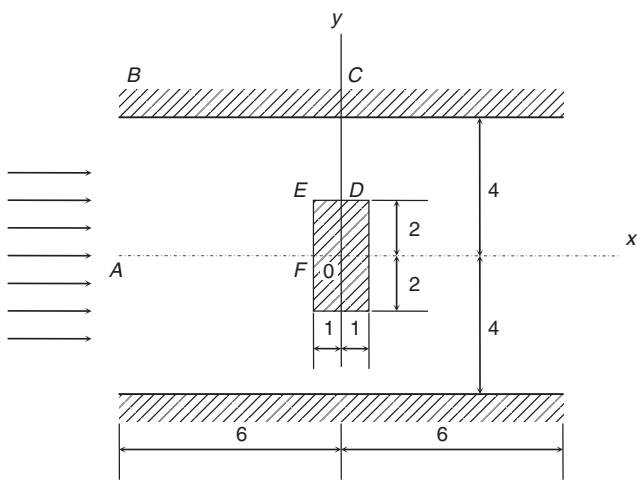


FIGURE 2.9.7 Channel flow past a rectangular cylinder.

Show that for a square mesh of size h , this partial differential equation may be solved numerically by using the following iterative formula:

$$\psi_{i,j} = \frac{1}{4} \left[\psi_{i-1,j} + \psi_{i+1,j} + \left(1 + \frac{h}{2r_j}\right) \psi_{i,j-1} + \left(1 - \frac{h}{2r_j}\right) \psi_{i,j+1} \right] \quad (2.9.11)$$

where r_j is the radial distance of point (i,j) from the z axis. Using this numerical scheme, compute and then plot the flow in the region bounded by $OABCDO$ within an axisymmetric tube containing repeated partitions (see Fig. 2.9.8). Choose a square mesh of size $h = 0.1$ for numerical computation.

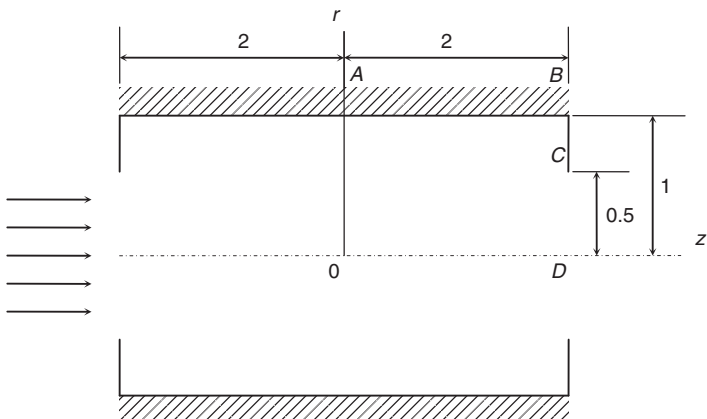


FIGURE 2.9.8 Axisymmetric flow through a tube containing repeated partitions.

Around the boundary of this region, $\psi = 0$ along OD , $\psi = 1$ along ABC , and $\partial\psi/\partial z = 0$ along both OA and CD . The derivative boundary conditions are the result of symmetry of stream function about these two sections.

2.10 NUMERICAL SOLUTION OF HYPERBOLIC PARTIAL DIFFERENTIAL EQUATIONS

Problems concerning wave motions in fluid mechanics are governed by hyperbolic partial differential equations. One example mentioned in Section 2.7 is the supersonic flow past a thin body whose governing equation is (2.7.2). Another commonly cited example is the propagation of a one-dimensional sound wave of small amplitude, described by (see Liepmann and Roshko, 1957, p. 68)

$$\frac{\partial^2 u}{\partial t^2} = a^2 \frac{\partial^2 u}{\partial x^2} \quad (2.10.1)$$

in which t is time, x is the coordinate in the direction of wave propagation, a is the speed of sound treated as constant in the linearized analysis, and u is the fluid speed. It can be shown that density, pressure, and temperature are all governed by equations of the same form.

In this section a numerical technique is developed for solving (2.10.1) to find u at any time $t > 0$ in the spatial domain $0 \leq x \leq L$, provided that the initial conditions of u are given at $t = 0$ and are expressed in the following form, with functions f and g to be specified for a particular problem:

$$u(x, 0) = f(x) \quad (2.10.2)$$

$$\frac{\partial u}{\partial t}(x, 0) = g(x) \quad (2.10.3)$$

Boundary conditions are to be specified at both ends of the gaseous domain, say within a channel of constant cross-sectional area. If one end of the channel is enclosed by a rigid wall, then u must be zero there at all times. On the other hand, at an end that opens to the atmosphere, the pressure there must be a constant or, alternatively, $\partial u/\partial x$ must vanish at that section.

To solve this mixed initial-boundary-value problem numerically, we divide the spatial range of the domain into small intervals of length h and the time axis into intervals of size τ . The total number of vertical grid lines is m , whereas that of horizontal grid lines can be as many as needed in a particular computation. Lines and points in the grid system are named according to Fig. 2.10.1.

A difference equation can be derived following exactly the same procedure as that used to obtain the numerical scheme (2.8.2) for solving the Poisson equation. Using the central-difference formula to approximate the derivatives in (2.10.1), we obtain, after regrouping,

$$u_{i,j+1} = 2u_{i,j} + C^2(u_{i-1,j} - 2u_{i,j} + u_{i+1,j}) - u_{i,j-1} \quad (2.10.4)$$

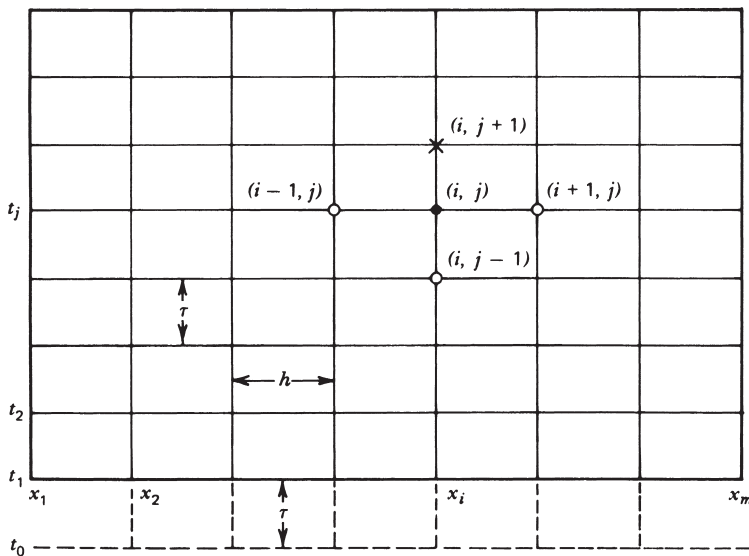


FIGURE 2.10.1 Grid system for numerical computation.

where C is a dimensionless parameter called the *Courant number*, defined by

$$C = \frac{a\tau}{h} \quad (2.10.5)$$

(2.10.4) computes the solution at a certain time level based on the solutions at two previous time levels.

Actually, various numerical schemes can be constructed for solving the same partial differential equation by using different finite-difference approximations. In Section 2.13, we will introduce a multistep explicit method, the MacCormack explicit method (1969), which can be easily extended to nonlinear hyperbolic systems. The applicability of a numerical scheme is determined by whether it is stable, that is, whether the numerical solution grows and becomes unbounded after repeatedly applying the scheme. In a way, we have proved in Section 2.8 that Richardson's iterative formula is stable, and so is Liebmann's. Here we will use a different approach to find the conditions under which (2.10.4) is computationally stable. It turns out that the stability of this numerical scheme is determined by the magnitude of C .

Following *von Neumann's stability analysis*, we assume that time and space variables are separable and that the solution to (2.10.4) can be expanded in the form of a Fourier series. A representative Fourier component may be written

$$u_{i,j} = U_j e^{i k h} \quad (2.10.6)$$

where U_j is the amplitude at t_j of the wave component whose wave number is k , and $I = \sqrt{-1}$. Similarly,

$$u_{i,j\pm 1} = U_{j\pm 1} e^{Ikh}, \quad u_{i\pm 1,j} = U_j e^{I(i\pm 1)kh}$$

Substituting these into (2.10.4) gives, after canceling the common factor e^{Ikh} ,

$$U_{j+1} = 2U_j + C^2 U_j (e^{-Ikh} + e^{Ikh} - 2) - U_{j-1}$$

By using the identity that $(e^{I\theta} + e^{-I\theta})/2 = \cos \theta$, it becomes

$$U_{j+1} = AU_j - U_{j-1} \quad (2.10.7)$$

where $A \equiv 2[1 - C^2(1 - \cos kh)]$. By introduction of an *amplification factor* λ such that

$$U_j = \lambda U_{j-1} \quad \text{and} \quad U_{j+1} = \lambda U_j = \lambda^2 U_{j-1} \quad (2.10.8)$$

(2.10.7) is reduced to

$$\lambda^2 - A\lambda + 1 = 0 \quad (2.10.9)$$

whose roots are

$$\lambda = \frac{A}{2} \pm \sqrt{\left(\frac{A}{2}\right)^2 - 1} \quad (2.10.10)$$

For $|A| \geq 2$, the roots are real, but their magnitudes are $|\lambda| \geq 1$; for $|A| < 2$ the magnitudes of the complex roots are equal to 1. An inspection of (2.10.8) concludes that the amplitude grows indefinitely with increasing time unless $|\lambda| \leq 1$. Thus, the inequality that $|A| \leq 2$ or $A^2 \leq 4$ determines the condition for stability; that is, for stability,

$$[1 - C^2(1 - \cos kh)]^2 \leq 1$$

After expanding the left side and rearranging, we obtain

$$C^2 \leq \frac{2}{1 - \cos kh}$$

When $\cos kh$ varies from -1 to $+1$, the function on the right-hand side varies from 1 to infinity, of which the lowest value is chosen to insure stability. Therefore, the stability criterion for the numerical scheme (2.10.4) is $C^2 \leq 1$, or

$$\frac{a\tau}{h} \leq 1 \quad (2.10.11)$$

To arrive at this expression, we have used the fact that each of the three variables on its left is positive. This relationship implies that τ and h cannot be chosen independently.

If the Courant number is chosen to be

$$\frac{a\tau}{h} = 1 \quad (2.10.12)$$

then (2.10.4) takes an especially simple form:

$$u_{i,j+1} = u_{i-1,j} + u_{i+1,j} - u_{i,j-1} \quad (2.10.13)$$

As shown in Fig. 2.10.1, this equation states that the value of u at a grid point marked by a cross is computed from the values already computed at three circled grid points at two previous time steps. The numerical scheme (2.10.13) is commonly referred to as the *leapfrog method*. It will now be proved that this numerical method actually gives the exact solution to the differential equation (2.10.1).

It is well known that the solution to (2.10.1) satisfying initial conditions (2.10.2) and (2.10.3) is

$$u(x, t) = \frac{1}{2} [f(x + at) + f(x - at)] + \frac{1}{2a} \int_{x-at}^{x+at} g(v) dv \quad (2.10.14)$$

which can be verified by substituting it back into each of those equations. The solution may be written in the simpler functional form

$$u(x, t) = F(x - at) + G(x + at) \quad (2.10.15)$$

where the functions F and G represent simple waves propagating without changing shape along the positive and negative x directions at constant speed a . The lines of slope $dx/dt = \pm a$ in the $x - t$ plane, which trace the progress of the waves, are called the characteristics of the wave equation (see Liepmann and Roshko, 1957, p. 69).

When applied at a grid point (x_i, t_j) , (2.10.15) becomes

$$u_{i,j} = F(x_i - at_j) + G(x_i + at_j)$$

From Fig. 2.10.1 we have

$$x_i = x_1 + (i - 1)h \quad \text{and} \quad t_j = t_1 + (j - 1)\tau$$

so that

$$u_{i,j} = F(\alpha + ih - ja\tau) + G(\beta + ih + ja\tau)$$

in which $\alpha \equiv (x_1 - h) - a(t_1 - \tau)$ and $\beta \equiv (x_1 - h) + a(t_1 - \tau)$. With $a\tau = h$, obtained from the condition that $C = 1$, it reduces to

$$u_{i,j} = F[\alpha + (i - j)h] + G[\beta + (i + j)h]$$

According to this relation, the right-hand side of (2.10.13) is rewritten

$$\begin{aligned}
 u_{i-1,j} + u_{i+1,j} - u_{i,j-1} &= F[\alpha + (i-j-1)h] + G[\beta + (i+j-1)h] \\
 &\quad + F[\alpha + (i-j+1)h] + G[\beta + (i+j+1)h] \\
 &\quad - F[\alpha + (i-j+1)h] - G[\beta + (i+j-1)h] \\
 &= F[\alpha + (i-j-1)h] + G[\beta + (i+j+1)h]
 \end{aligned}$$

which is exactly $u_{i,j+1}$ or the left-hand side of (2.10.13). It follows that the exact solution is computed for (2.10.1) by the leapfrog scheme (2.10.13).

Having introduced the concept of characteristics, we are now in a position to interpret the physical meaning of the stability criterion (2.10.11) by use of Fig. 2.10.2. An examination of (2.10.4) reveals that the solution at the grid point P is influenced by the solution at each of the grid points at previous time steps contained within two diagonals PQ and PR of slope $(dx/dt)_n = \pm h/\tau$. Thus, the region $PQRP$ is the domain of dependence of point P in the numerical computation. If Pq and Pr are the backward characteristics of slope $(dx/dt)_c = \pm a$ passing through P , and if $a < h/\tau$ or, equivalently, if then $|(dx/dt)_c| < |(dx/dt)_n|$, these lines will lie between PQ and PR , as shown in the figure. However, from the theory of characteristics, it is known that point P can receive signals only from the region $PqrP$, which is its physical domain of dependence. In the present case of $a\tau/h < 1$, in which the computational domain of dependence contains the physical domain of dependence, all the information required to determine the condition at P is included in the computation so that the numerical scheme is stable. The result is inaccurate because of the inclusion of some unnecessary information originating from the region between PQ and Pq and the region between PR and Pr . If $a\tau/h > 1$, the characteristics Pq and Pr would be drawn outside of PQ and PR . In this case only a part of the needed information is used to determine the solution at P , and the computation is unstable. It becomes

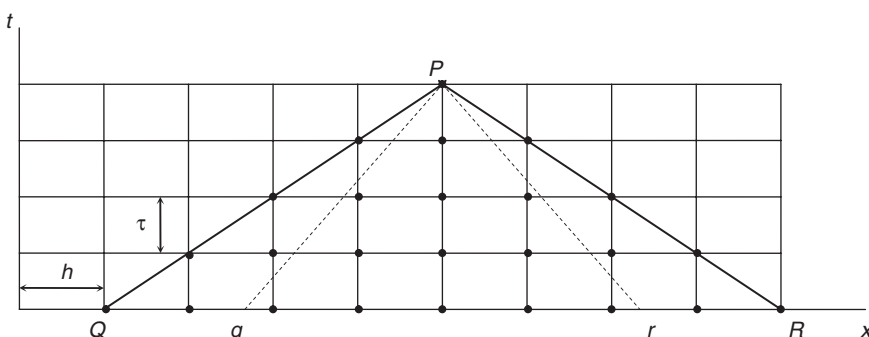


FIGURE 2.10.2 Physical interpretation of the stability criterion (2.10.11).

obvious that when $a\tau/h = 1$ (i.e., when the computational and physical domains of dependence coincide), the numerical solution is the exact solution.

In using the formula (2.10.13) information is needed at two previous time steps. It cannot be used directly at the initial stage to compute the solution at t_2 , since conditions are specified only at the initial instant $t_1 = 0$. To help start the numerical procedure, we construct in Fig. 2.10.1 a row of fictitious grid points $t_0 = t_1 - \tau$, and then rewrite the initial conditions (2.10.2) and (2.10.3) in index notation:

$$u_{i,1} = f_i \quad (2.10.16)$$

$$u_{i,0} = u_{i,2} - 2\tau g_i \quad (2.10.17)$$

in which f_i and g_i represent, respectively, $f(x_i)$ and $g(x_i)$. In obtaining the second expression we have approximated $\partial u / \partial t$ by the central-difference form (2.2.8). For $j = 1$ and with substitution from the preceding equations, (2.10.13) becomes

$$\begin{aligned} u_{i,2} &= u_{i-1,1} + u_{i+1,1} - u_{i,0} \\ &= f_{i-1} + f_{i+1} - u_{i,2} + 2\tau g_i \end{aligned}$$

or

$$u_{i,2} = \frac{1}{2}(f_{i-1} + f_{i+1}) + \tau g_i, \quad i = 2, \dots, m-1 \quad (2.10.18)$$

This is called the starting formula for (2.10.13).

2.11 PROPAGATION AND REFLECTION OF A SMALL-AMPLITUDE WAVE

Although exact solutions of the linear partial differential equation (2.10.1) can be written out in the form of (2.10.14), the work is still tedious when waves interact or reflect from boundaries. In this section these phenomena are examined numerically by using the leapfrog method just derived.

We consider a one-dimensional tube 1 m in length, with the left end closed and the right end open (Fig. 2.11.1). At $t = 0$ a sinusoidal wavelet of 0.4-m wavelength is somehow generated in the tube at a distance 0.2 m from the left end. Let the amplitude of the wavelet be 1 m/s, and let the functions f and g used in (2.10.2) and (2.10.3) to describe the initial conditions be defined as follows:

$$f(x) = \sin\left(2\pi \frac{x - 0.2}{0.4}\right) \text{ for } 0.2 \leq x \leq 0.6 \quad (2.11.1)$$

$$= 0 \text{ elsewhere}$$

$$g(x) = 0 \quad \text{for } 0 \leq x \leq 1 \quad (2.11.2)$$

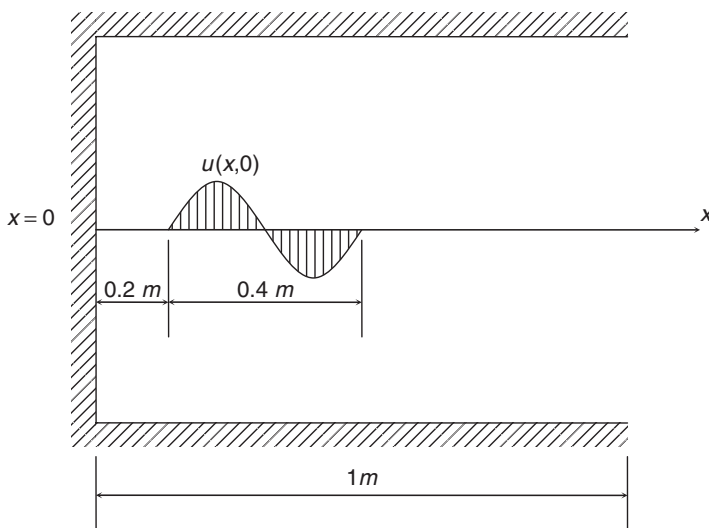


FIGURE 2.11.1 Sinusoidal wavelet in a one-dimensional tube.

The boundary conditions are

$$u(0, t) = 0 \quad (2.11.3)$$

$$\frac{\partial u}{\partial x}(1, t) = 0 \quad (2.11.4)$$

Under sea level conditions, the speed of sound is $a = 340\text{ m/s}$.

For numerical computation we choose $h = 0.02\text{ m}$, so that the number of vertical grid lines is $m = 51$ and the space occupied initially by the wavelet is between grid lines $11 \leq i \leq 31$. Thus, the nonvanishing f_i values for these values of i are given by

$$f_i = \sin \{5\pi [(i - 1)h - 0.2]\} \quad (2.11.5)$$

and $g_i = 0$ for all values of i .

The boundary condition (2.11.3) when written in index notation is

$$u_{1,j} = 0 \quad \text{for all } j \quad (2.11.6)$$

To handle the condition (2.11.4), which contains a derivative with respect to x , we construct a column of fictitious grid points in the x - t plane along the grid line $i = m + 1$, in the same fashion as shown in Fig. 2.9.3. Consequently,

we obtain

$$u_{m+1,j} = u_{m-1,j} \quad \text{for all } j \quad (2.11.7)$$

Under this condition the iterative formula (2.10.13) is modified at $i = m$ by

$$u_{m,j+1} = 2u_{m-1,j} - u_{m,j-1} \quad \text{for } j > 2 \quad (2.11.8)$$

while the starting formula (2.10.18) at the same location becomes

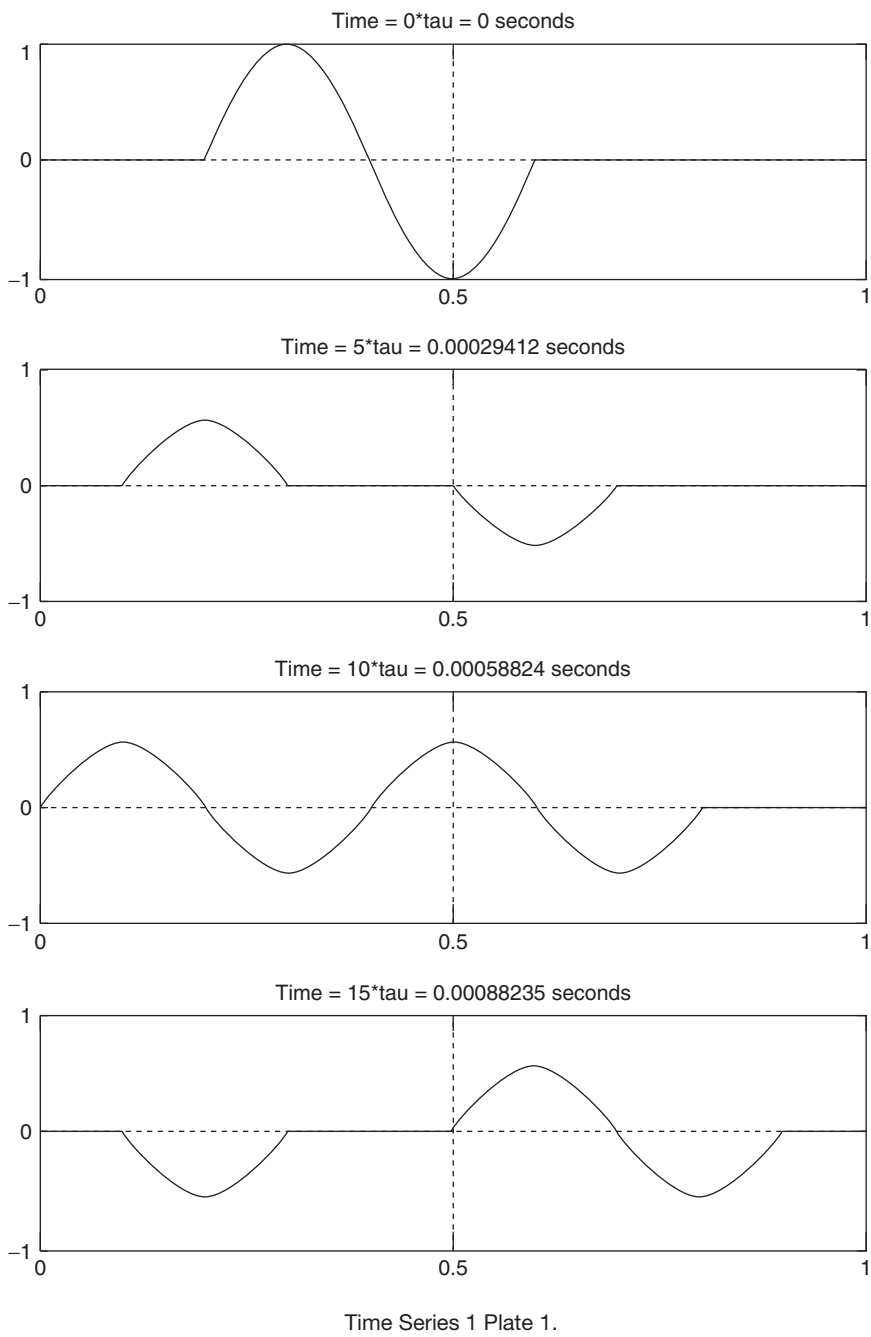
$$u_{m,2} = f_{m-1} + \tau g_m \quad (2.11.9)$$

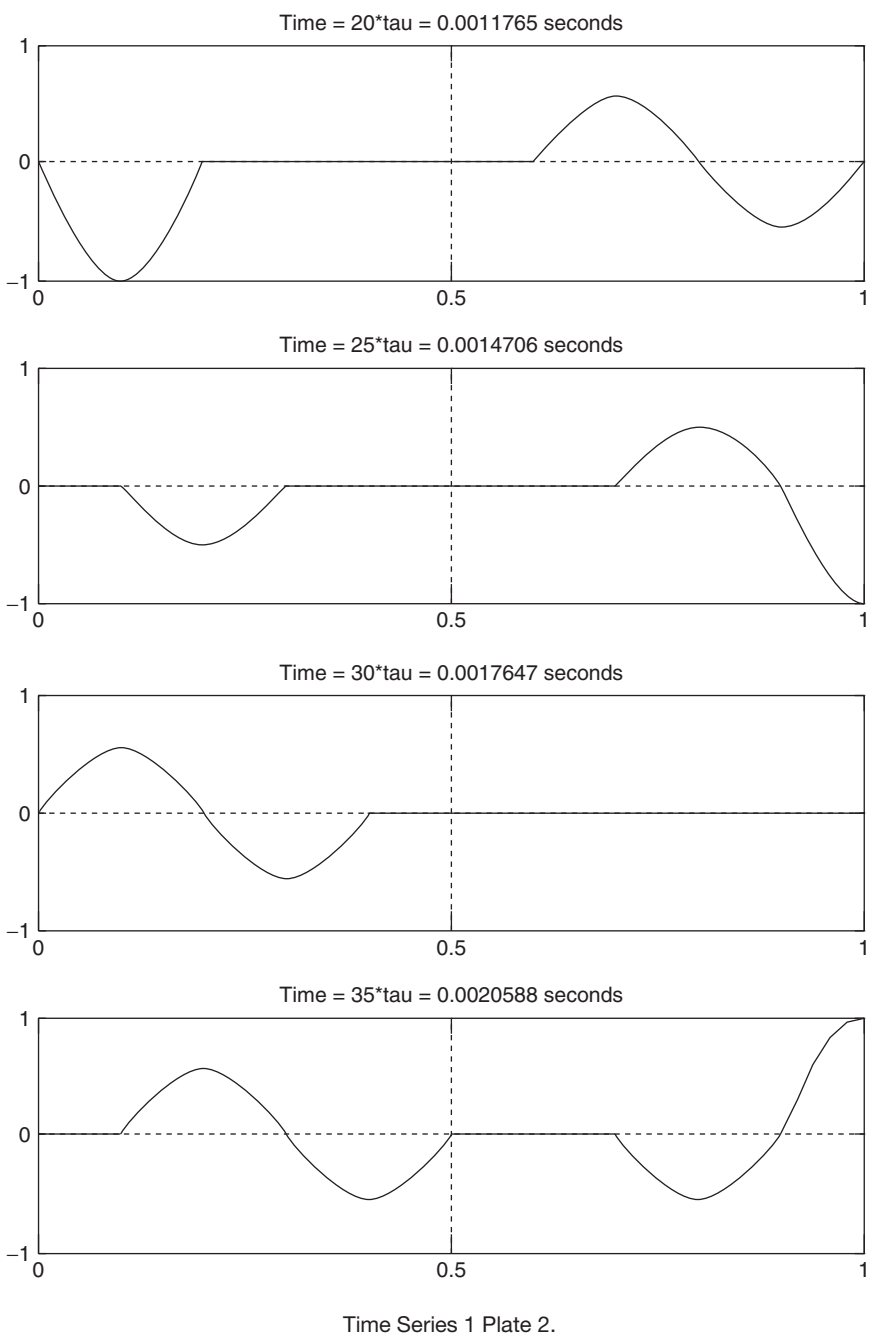
Finally, the size of time steps is computed from $\tau = h/a$. This is the time required for the wave to travel through the distance h . Thus, it takes a time period of 10τ for the left-propagating wave to reach the closed end starting from its initial position.

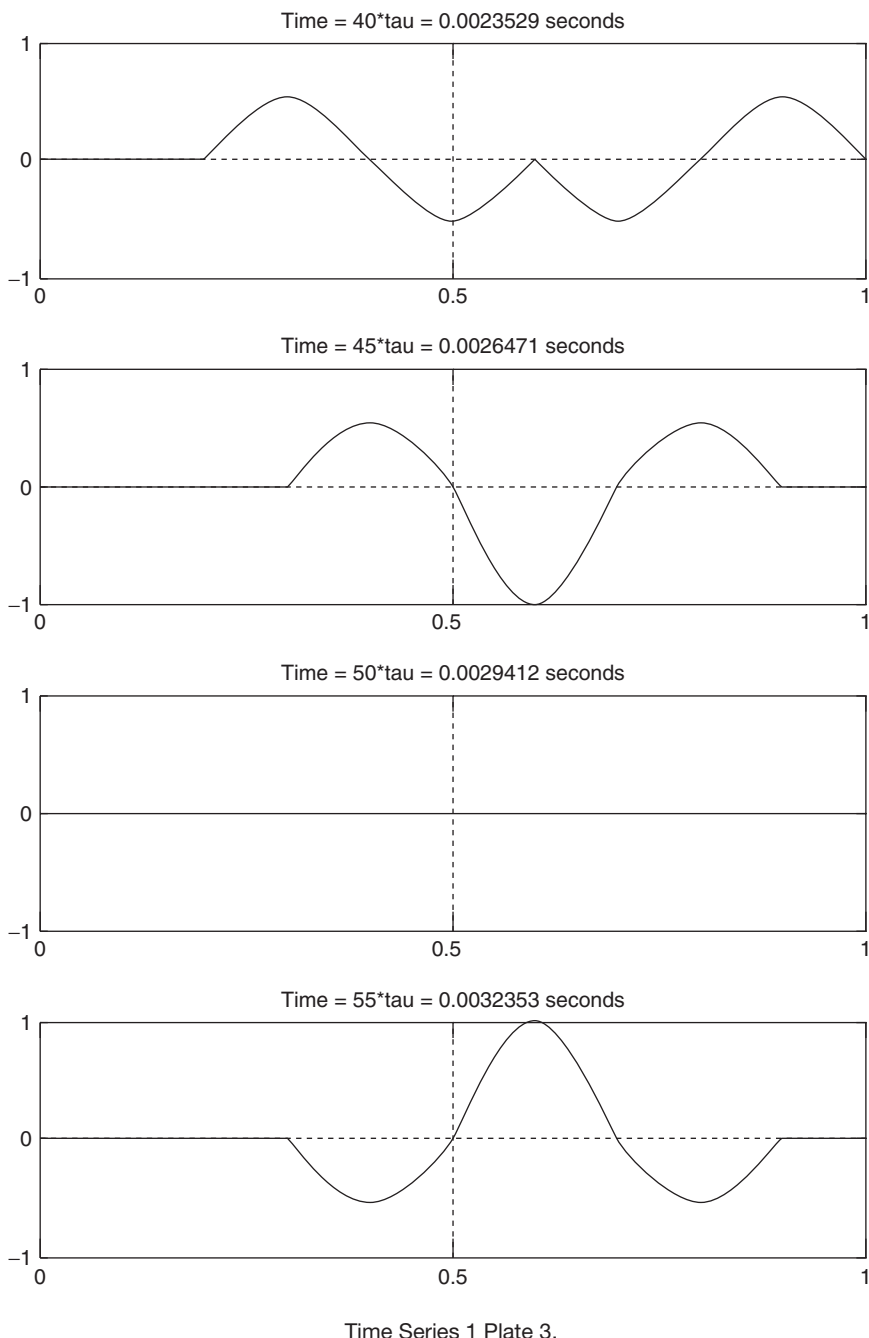
After the solution $u_{i,j}$ has been obtained for $j \leq j_{\max}$, the result is plotted in the form of time-sequential pictures (Time Series 1). The wave shape at one instant is shown in a frame, with the abscissa representing the spatial coordinate of the tube and the ordinate the value of u . One frame is plotted every NT time steps, which is equal to 5 in Program 2.8.

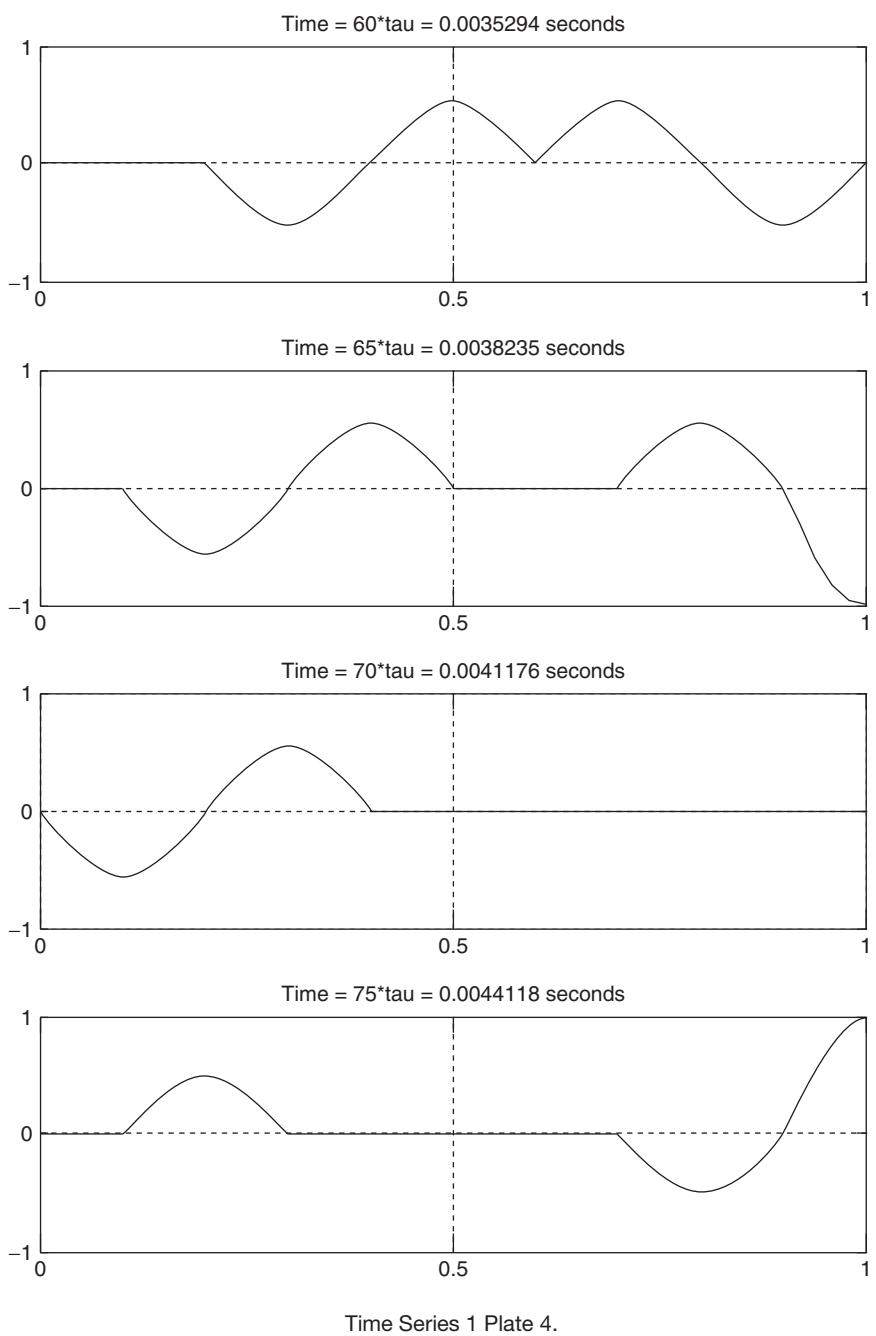
The first picture shows the initial state of the wavelet having an amplitude of 1 m/s and a wavelength of 0.4 m. It decomposes into two identical wavelets of amplitude 0.5 m/s, but of the original wavelength propagating in opposite directions. Let us call the one traveling toward the left the L wave and that toward the right the R wave. At $t = 5\tau$, when each of the two waves have traveled through a distance equal to one-quarter of the wavelength, the trailing halves of them coincide to cancel each other so that only the leading halves are shown. At $t = 10\tau$, these two waves have just come out of each other, but the L wave starts to impinge on the closed end. Numerical computations show that after being reflected from the rigid wall, the L wave reverses not only its direction of propagation, but also the sign of u . As can be observed from the figures plotted respectively at 10τ and 30τ , the incidental wave is led by positive u , whereas the reflected one is led by negative u . The three figures in between describe the interaction of the reflected portion with the oncoming part of the L wave.

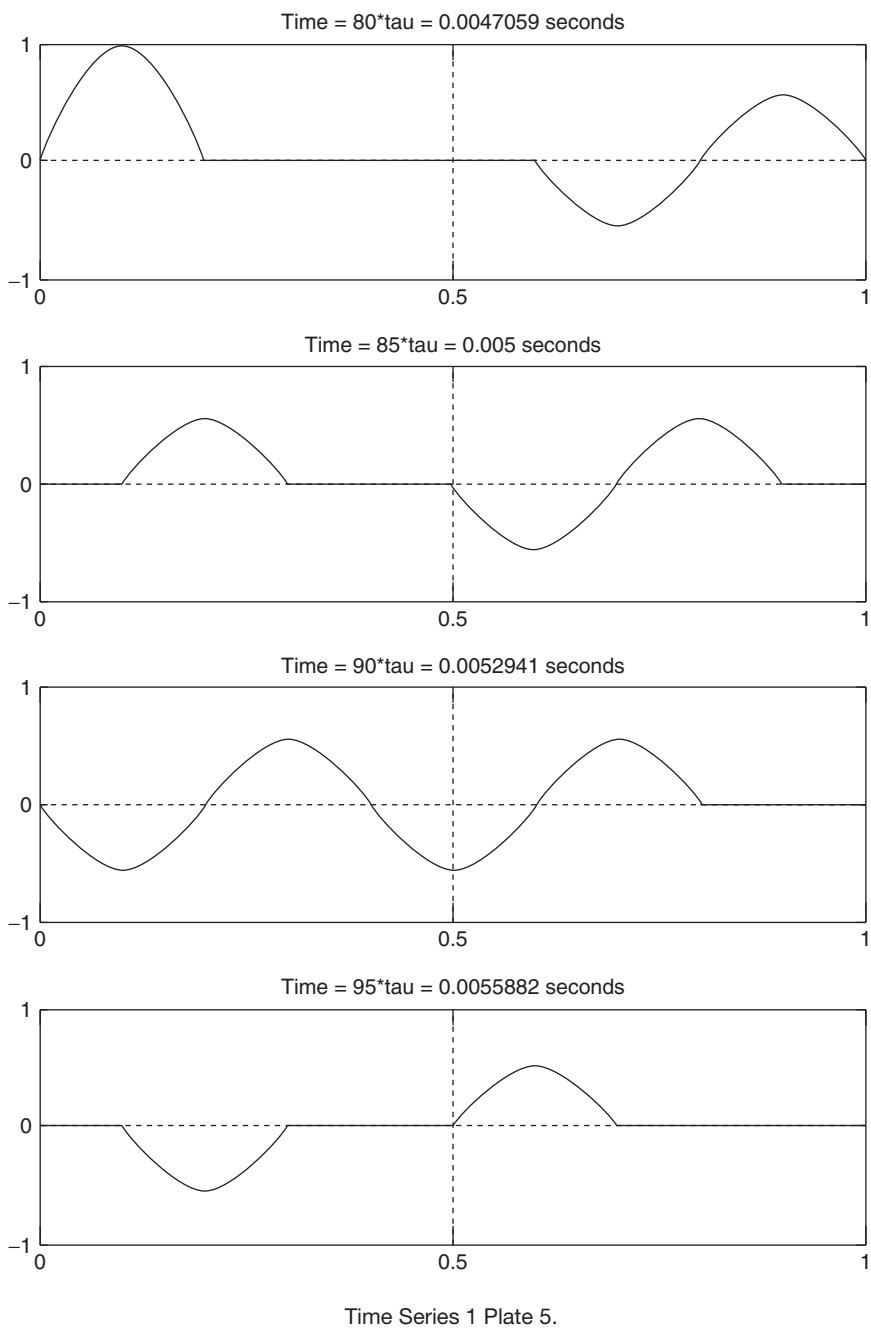
To find the effect of the open end on the R wave, let us examine the figures plotted between 20τ and 40τ . The conclusion is that after being reflected from an open end, the wave reverses only its direction of propagation, but not the sign of u . Thus, the reflected R wave is still led by negative u , as it was before reaching the open end. The four plots after 40τ show the interaction of the two reflected waves when passing each other. At $t = 50\tau$ they just cancel each other, and the tube becomes quiet momentarily. Further reflections and interactions are described in the remaining figures, and the process may go on forever—in an inviscid fluid.

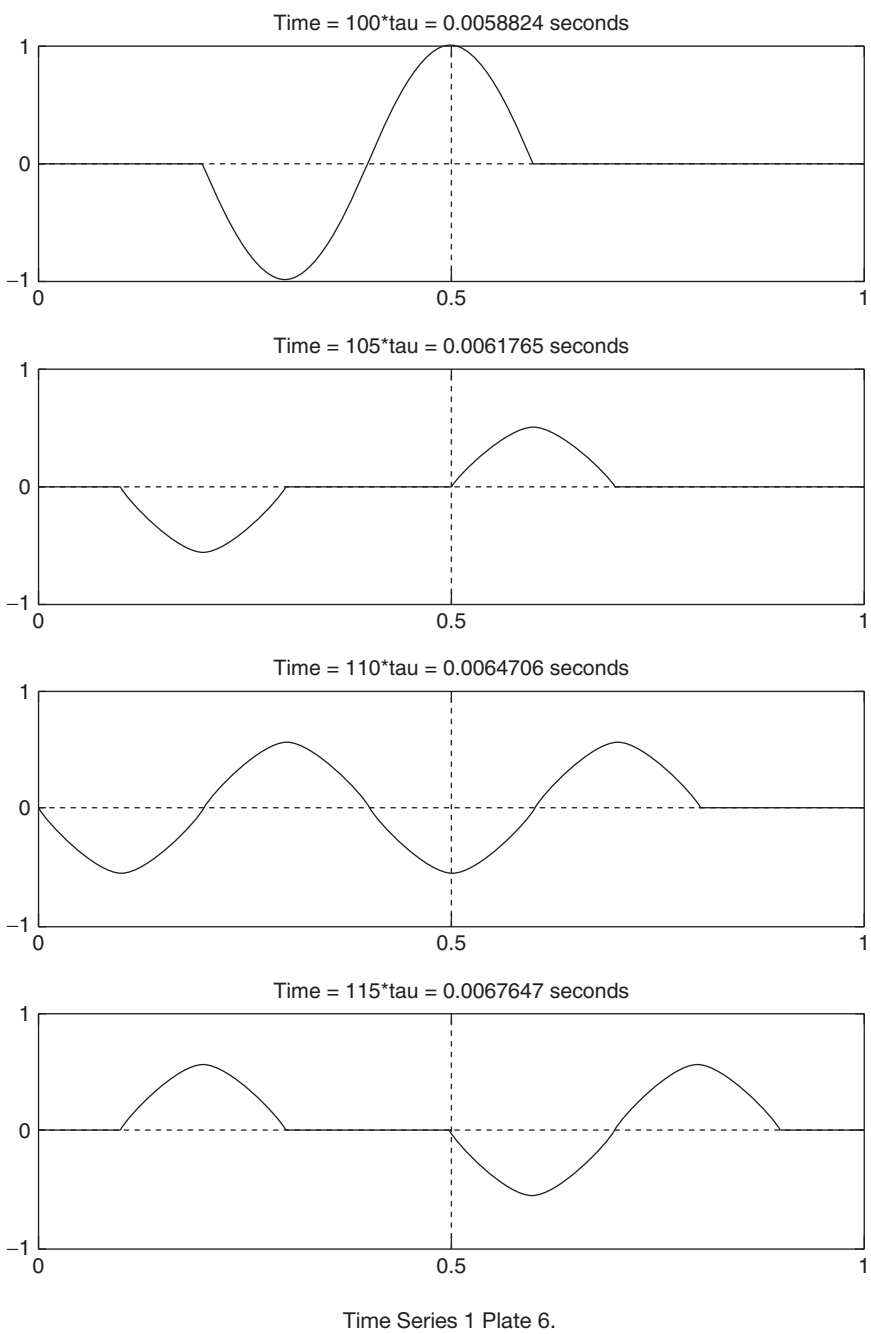












Time Series 1 Plate 6.

Project for Further Study: When a compressible fluid of density ρ_0 is disturbed in such a way that its density becomes $\rho_0 + \rho'(x, t)$, where $\rho' \ll \rho_0$, the density fluctuation, similar to the fluid speed, is also governed by a wave equation

$$\frac{\partial^2 \rho'}{\partial t^2} = a^2 \frac{\partial^2 \rho'}{\partial x^2} \quad (2.11.10)$$

This can readily be proved by combining the Euler equation (2.1.5) and the continuity equation

$$\frac{\partial \rho}{\partial t} + \nabla \cdot (\rho \mathbf{V}) = 0 \quad (2.11.11)$$

linearizing them for one-dimensional flow, and then introducing the speed of sound $a = \sqrt{dp/d\rho}$ under the isentropic condition. For details consult, for example, Section 3.4 of Liepmann and Roshko (1957).

Consider a 1-m-long tube of uniform cross section with both ends closed. The tube is divided into two chambers by a diaphragm at the middle section across which the densities are slightly different. Suppose ρ' is normalized so that it is 1 at and to the right of the diaphragm, and 0 to the left. At $t = 0$ when $\partial \rho'/\partial t = 0$, the diaphragm is suddenly removed and a wave system is set up in the tube. Solve this linearized shock tube problem by finding $\rho'(x, t)$ numerically with the leapfrog method. Density distributions along the tube at some representative time levels are to be plotted.

Boundary conditions for density fluctuation in this problem are determined as follows. At a closed end u vanishes regardless of time; thus, $\partial u/\partial t = 0$ there. This implies that $\partial p/\partial x = 0$ and, therefore, $\partial \rho'/\partial x = 0$ at the closed end by considering the linearized Euler equation. On the other hand, if there were an end open to the atmosphere, ρ' should vanish there because the density at that location is always the same as that outside.

Computer results should show that two waves are generated at the center after the eruption of the diaphragm: an expansion wave propagating toward the right and a compression wave propagating toward the left. A wave is classified as expansive or compressive, depending on whether the wave is traveling into a region of higher or lower density. The result should also show that at a rigid wall, an incidental expansion wave reflects as an expansion wave and an incidental compression wave reflects as a compression wave. It can also be shown that the type of a wave is changed after being reflected from an open end.

The conclusion on wave reflection from a closed or open end seems to contradict the conclusion obtained from the output of Program 2.8. However, when the type of a wave is defined in terms of the sign of u in combination with the direction of propagation, as shown in Fig. 3.3, p. 72 of Liepmann and Roshko (1957), the contradiction is automatically resolved.

2.12 PROPAGATION OF A FINITE-AMPLITUDE WAVE: FORMATION OF A SHOCK

The numerical solution obtained for the preceding example shows that a sound wave propagates at a constant velocity without changing its shape. This property of the wave is the result of linearization of the governing equations, assuming small perturbations about an equilibrium state of the gas. For a wave whose amplitude is not small, its properties are expected to change (see Zucrow and Hoffman, 1977, Section 19.5). This section offers a numerical study of such a wave.

To derive the equations governing nonlinear wave motions, we rewrite the continuity equation (2.11.11) and Euler equation (2.1.5) for unsteady one-dimensional flow:

$$\frac{\partial \rho}{\partial t} + u \frac{\partial \rho}{\partial x} + \rho \frac{\partial u}{\partial x} = 0 \quad (2.12.1)$$

$$\frac{\partial u}{\partial t} + u \frac{\partial u}{\partial x} + \frac{a^2}{\rho} \frac{\partial \rho}{\partial x} = 0 \quad (2.12.2)$$

In (2.12.2) the expression $a^2 \partial \rho / \partial x$ has been used to replace $\partial p / \partial x$, where the speed of sound, a , is also a function of x and t . We assume that the particle speed, u , is less than the sonic speed. Under isentropic conditions one of the three dependent variables, ρ , can be eliminated from the above equations. Let the subscript 0 indicate the undisturbed conditions and γ be the ratio of specific heats of the gas; then

$$\begin{aligned} \frac{p}{p_0} &= \left(\frac{\rho}{\rho_0} \right)^\gamma \\ a^2 &= \frac{dp}{d\rho} = \gamma \frac{p}{\rho} = \gamma \frac{p_0}{\rho_0} \left(\frac{\rho}{\rho_0} \right)^{\gamma-1} = a_0^2 \left(\frac{\rho}{\rho_0} \right)^{\gamma-1} \end{aligned}$$

or

$$\rho = \rho_0 \left(\frac{a}{a_0} \right)^{2/(\gamma-1)} \quad (2.12.3)$$

Substituting (2.12.3) into (2.12.1) and (2.12.2), we obtain

$$\begin{aligned} \frac{2}{\gamma-1} \left(\frac{\partial a}{\partial t} + u \frac{\partial a}{\partial x} \right) + a \frac{\partial u}{\partial x} &= 0 \\ \frac{\partial u}{\partial t} + u \frac{\partial u}{\partial x} + \frac{2a}{\gamma-1} \frac{\partial a}{\partial x} &= 0 \end{aligned}$$

Adding and subtracting, respectively, give the following equations

$$\left[\frac{\partial}{\partial t} + (u + a) \frac{\partial}{\partial x} \right] \left(u + \frac{2a}{\gamma-1} \right) = 0 \quad (2.12.4)$$

$$\left[\frac{\partial}{\partial t} + (u - a) \frac{\partial}{\partial x} \right] \left(u - \frac{2a}{\gamma - 1} \right) = 0 \quad (2.12.5)$$

Equation (2.12.4) states that the quantity $P = u + 2a/(\gamma - 1)$ is constant along a curve in the $x-t$ plane. On this curve $dP = (\partial P/\partial t) dt + (\partial P/\partial x) dx = 0$, or, equivalently,

$$\left(\frac{\partial}{\partial t} + \frac{dx}{dt} \frac{\partial}{\partial x} \right) P = 0$$

Comparing this equation with (2.12.4), we obtain $dx/dt = u + a$, which is the expression for the slope of that curve. Equation (2.12.5) can be similarly interpreted. Thus, (2.12.4) and (2.12.5) exhibit a salient property that the quantities P and $Q = u - 2a/(\gamma - 1)$ are constant on curves that have slopes $dx/dt = u + a$ and $dx/dt = u - a$, respectively. These curves are called the *characteristics*; P and Q are called the *Riemann invariants*. Since both u and a vary with x and t , the characteristics are generally curved lines in the $x-t$ plane.

The *method of characteristics* is developed based on the previously mentioned property. Referring to Fig. 2.12.1, suppose the initial data at $t = 0$ are given and the conditions at an arbitrary point C at $t_C > 0$ are to be computed. Through this point there are two characteristics, one of slope $u + a$ and the other of slope $u - a$, which intersect the x axis at points A and B , respectively. Since $P_C = P_A$ and $Q_C = Q_B$ or, specifically,

$$u_C + \frac{2a_C}{\gamma - 1} = u_A + \frac{2a_A}{\gamma - 1}$$

$$u_C - \frac{2a_C}{\gamma - 1} = u_B - \frac{2a_B}{\gamma - 1}$$

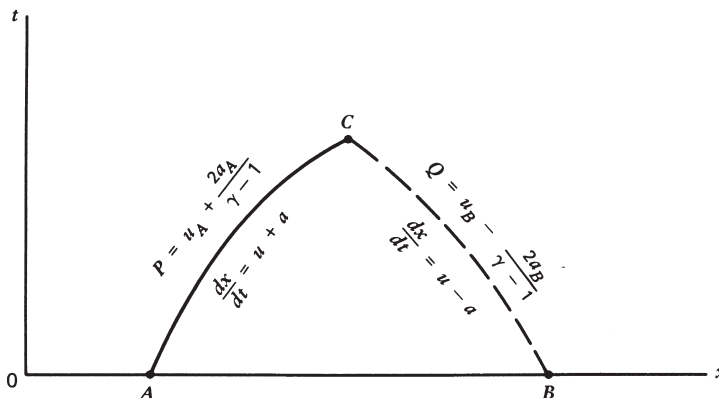


FIGURE 2.12.1 Method of characteristics.

u_C and a_C are computed immediately by adding and subtracting the above equations. Thus,

$$u_C = \frac{1}{2}(u_A + u_B) + \frac{1}{\gamma-1}(a_A - a_B) \quad (2.12.6)$$

$$a_C = \frac{\gamma-1}{4}(u_A - u_B) + \frac{1}{2}(a_A + a_B) \quad (2.12.7)$$

Although the exact shape of the characteristics cannot be determined unless u and a are both known in the region below point C , the solution may be computed approximately if the distance between points A and B is small. Under this condition the curved characteristics can be treated as two straight lines of slopes $u_A + a_A$ and $u_B - a_B$, respectively, and the conditions at point C , which is the intersection of these two straight lines, are described approximately by (2.12.6) and (2.12.7).

Thus, when a row of points is selected at small distances apart on the x axis at $t = 0$, the solution can be computed step by step at later times by constructing a network using the local slopes of the characteristics, shown in Fig. 2.12.2. This method, however, is not practical for machine calculation, because the locations of data points in the network are not known a priori. Many finite-difference techniques have been developed for solving the same problem on a predetermined rectangular mesh. The one chosen to be used here, suggested by Courant, Isaacson, and Rees (1952), is convenient for programming and yet is physically interpretable.

Let us adopt a grid system, exactly the same as that sketched in Fig. 2.10.1, for numerical solution of the simultaneous nonlinear equations (2.12.4) and (2.12.5). Suppose u and a have already been computed at all grid points on time level t_j ; we now proceed to find the conditions at the grid points on the next time level t_{j+1} , for example, at point C , or $(i, j + 1)$, as shown in Fig. 2.12.3. If the

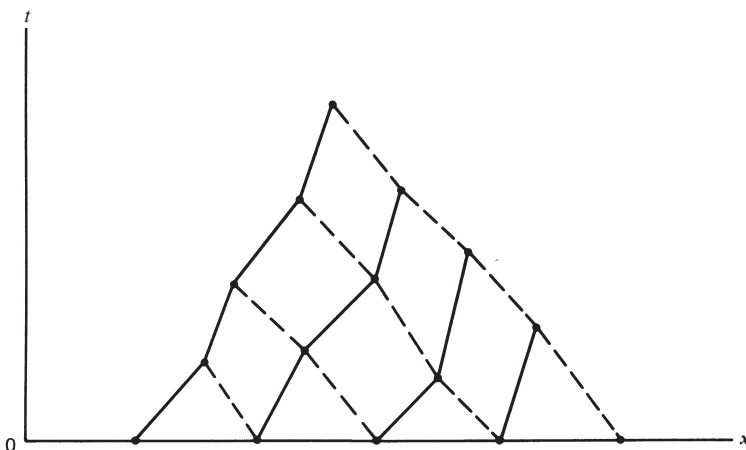


FIGURE 2.12.2 Characteristic network.

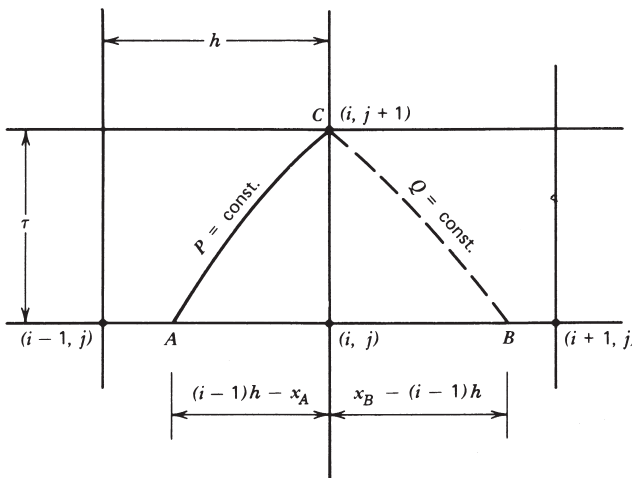


FIGURE 2.12.3 Finite-difference scheme for a rectangular mesh.

characteristics through this point intersect with the back horizontal grid line at points A and B , respectively, then, according to the method of characteristics described in Fig. 2.12.1, the condition at C is determined approximately from those at A and B by using formulas (2.12.6) and (2.12.7). The location and condition at points A and B are to be interpolated from the known information at grid points on that same time level.

Treating the characteristics as straight lines and approximating their slopes by $u_{i,j} + a_{i,j}$ and $u_{i,j} - a_{i,j}$ respectively, we find, from Fig. 2.12.3,

$$x_A = (i-1)h - \tau (u_{i,j} + a_{i,j}) \quad (2.12.8)$$

$$x_B = (i-1)h - \tau (u_{i,j} - a_{i,j}) \quad (2.12.9)$$

After points A and B have been located, linear interpolations are then used to find u_A and a_A within the interval between x_{i-1} and x_i . Thus,

$$u_A = u_{i,j} + \frac{\tau}{h} (u_{i,j} + a_{i,j}) (u_{i-1,j} - u_{i,j}) \quad (2.12.10)$$

$$a_A = a_{i,j} + \frac{\tau}{h} (u_{i,j} + a_{i,j}) (a_{i-1,j} - a_{i,j}) \quad (2.12.11)$$

Similarly, at B ,

$$u_B = u_{i,j} - \frac{\tau}{h} (u_{i,j} - a_{i,j}) (u_{i+1,j} - u_{i,j}) \quad (2.12.12)$$

$$a_B = a_{i,j} - \frac{\tau}{h} (u_{i,j} - a_{i,j}) (a_{i+1,j} - a_{i,j}) \quad (2.12.13)$$

u_C and a_C or, in fact, $u_{i,j+1}$ and $a_{i,j+1}$ are computed immediately following the substitution of (2.12.10) to (2.12.13) into (2.12.6) and (2.12.7).

Detailed analysis of this numerical method has been made by Courant et al. for a more general system of equations. The result is accurate to the first order of h . For computational stability it requires that the ratio τ/h be so chosen that the numerical domain of dependence of any point in the mesh is not less than the physical domain of dependence determined by the characteristics. In other words, the stability condition is that both

$$\frac{\tau}{h} |u + a| \leq 1 \quad \text{and} \quad \frac{\tau}{h} |u - a| \leq 1 \quad (2.12.14)$$

are satisfied everywhere in the domain of computation.

An improved numerical scheme with second-order accuracy was outlined by Hartree (1958). In his method the curved characteristics through C are approximated by two straight lines whose slopes are, respectively, the average of the values at C and A and the average of those at C and B instead of the values at (i, j) . The improved accuracy is paid for by the increased effort in computing the conditions at points A and B by iteration. In the following example the simpler method of Courant et al. will be used for the purpose of illustration.

A 2-m-long tube is considered whose left end is closed and right end is open, similar to the tube shown in Fig. 2.11.1. The length of the tube is again divided into 0.02-m intervals, resulting in 101 vertical grid lines for the numerical work. Let a_0 be the speed of sound in the tube in an undisturbed state. At $t = 0$ a rightward-propagating wavelet of 1-m wavelength is produced in the left half of the tube. To exaggerate the effect of finite amplitude and to show an easily recognized distortion in wave shape, we assume that the initial amplitude of the wavelet is $a_0/2$ and that its initial shape is described by a set of broken straight lines defined by

$$u_{i,1} = \begin{cases} \frac{a_0}{2} \frac{i-1}{12} & \text{for } 1 \leq i \leq 13 \\ \frac{a_0}{2} \frac{26-i}{13} & \text{for } 13 < i \leq 39 \\ \frac{a_0}{2} \frac{i-51}{12} & \text{for } 39 < i \leq 51 \\ 0 & \text{elsewhere} \end{cases}$$

The initial condition for a is determined by that for u through

$$a = a_0 \pm \frac{\gamma - 1}{2} u \quad (2.12.15)$$

which relates the local speed of sound to the local particle velocity (same sign as x) in an isentropic wave. The negative sign is to be taken only if the wave is traveling in the negative x direction. The derivation of (2.12.15) can be found in Section 3.9 of Liepmann and Roshko (1957) and therefore is not repeated here.

The boundary conditions at the ends can be derived with the help of Fig. 2.12.3. At the left end of the tube where $i = 1$, only one backward characteristic can be drawn through a grid point along which $Q = \text{constant}$. Combining this with the condition that particle velocity vanishes at a closed end gives

$$u_{1,j+1} = 0 \quad (2.12.16)$$

$$a_{1,j+1} = a_B - \frac{\gamma - 1}{2} u_B \quad (2.12.17)$$

where u_B and a_B are computed for $i = 1$ from (2.12.12) and (2.12.13). At a grid point at the right end of the tube open to the atmosphere, the density and therefore the sonic speed is the same as that outside. Furthermore, through such a point there is only one backward characteristic along which $P = \text{constant}$. Thus, the boundary conditions there are

$$u_{m,j+1} = u_A + \frac{2}{\gamma - 1} (a_A - a_0) \quad (2.12.18)$$

$$a_{m,j+1} = a_0 \quad (2.12.19)$$

where m is the maximum value of i and u_A, a_A are computed from (2.12.10) and (2.12.11) for $i = m$.

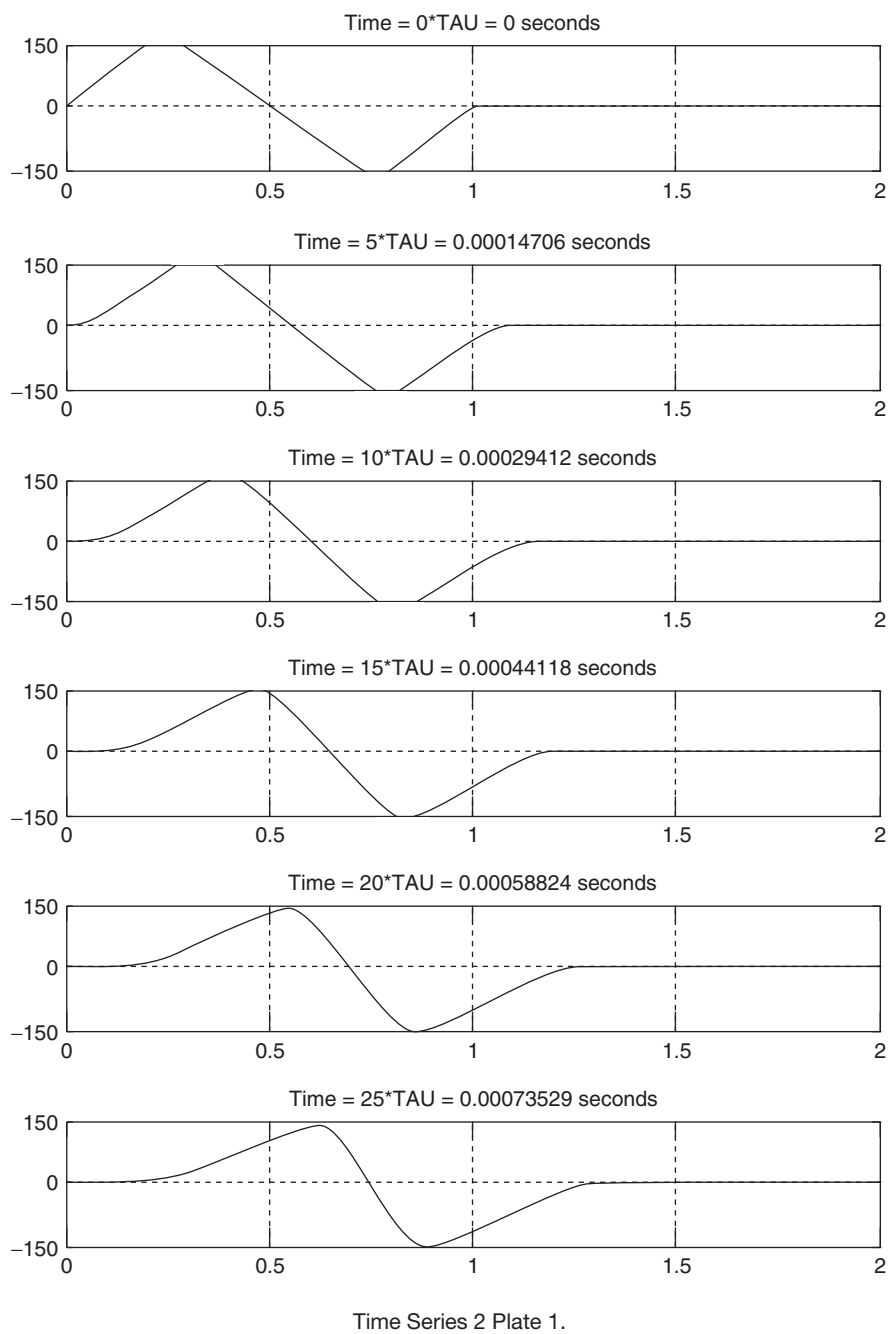
The variables in Program 2.9 are named according to their original form. For example, UA, UB, AA, and AB represent, respectively, u_A, u_B, a_A , and a_B . We use AMPLTD for the initial amplitude of the velocity distribution, RATIO for τ/h , and COEFF for $(\gamma - 1)/2$.

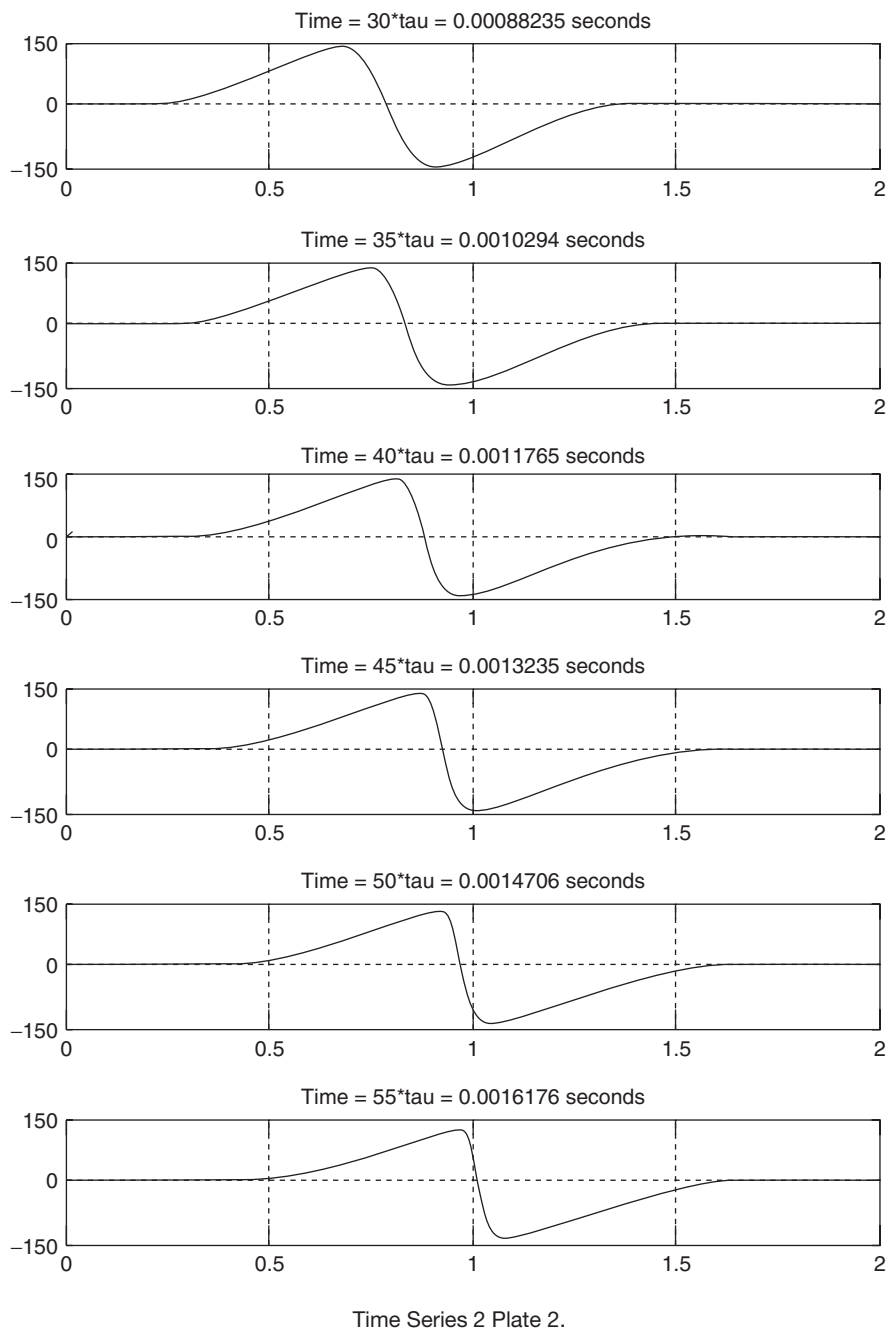
γ is chosen to be 1.4 for air at sea level. For the fixed value of $h = 0.02$ m, the size of time steps is determined from the stability condition (2.12.14). It involves u and a , which are both unknown before the problem is solved. In the program a trial value $\tau = 0.5h/a_0$ is used. Before computing the solution at a grid point, we check (2.12.14) and discontinue the computation whenever this condition is violated. The result shows that this trial value is satisfactory for the present problem at all grid points.

The output of Program 2.9 displays the velocity distributions at increasing time steps (Time Series 2). It is now examined to find the effects of keeping the nonlinear terms in the governing equations.

In the central part of the wave $\partial u / \partial x$ is negative; that is, the right-moving velocity of a gas particle is faster than that of a particle ahead of it. Thus, in this region gas particles are catching up with those ahead; this is called a compression region. The time sequence plots show that the width of this region decreases with time, so that the wave profile is steepening in the central portion. On the other hand, in the leading and trailing parts of the wave where $\partial u / \partial x$ is positive, gas particles ahead are moving faster than those behind. In each of these expansion regions the width increases and the profile flattens with increasing time.

As the wave propagates its profile is no longer antisymmetric about the node. The left portion, within which u is positive, becomes shorter than that on the right portion, within which u is negative, while the total length of the wave is





kept constant. In addition, the amplitude of the wave on the left side of the node diminishes faster in time than that on the right.

When $t = 40\tau$, the wave profile in the compression region becomes almost a vertical line. In other words, at this time a drastic change in u can be found across a very short distance. This is, in fact, a shock wave.

Actually, as explained by Liepmann and Roshko (1957, Section 3.10), before this situation is reached, the velocity gradient becomes so great that viscous and heat transfer effects can no longer be neglected and the governing equations (2.12.4) and (2.12.5) break down. Even if it is numerically feasible, the computation should be stopped before any part of the wave becomes too steep.

The development of a finite-amplitude wave into a shock is analogous to the breaking of a water wave to form a bore. A description of the latter phenomenon can be found in Section 10.10 of Stoker (1957).

Problem 2.11 In the computation of Program 2.9, the wave has not yet been affected by the boundary conditions unless more time steps are added. To study the nonlinear effects on wave reflection, run Program 2.9, which is modified for the following two waves.

1. A left-propagating wave having the same initial velocity distribution as that specified in Program 2.9.
2. A right-propagating wave of the same initial velocity profile, but shifted one wavelength to the right.

2.13 AN APPLICATION TO BIOLOGICAL FLUID DYNAMICS: FLOW IN AN ELASTIC TUBE

In this section we present a one-dimensional analysis of flow in an elastic tube that can be used as a model for arterial blood flow in humans and in animals. The governing equations are based on the inviscid, one-dimensional (area-averaged) form of the equations for mass and momentum, as well as an equation between the vessel cross-sectional area and pressure (Anliker, Rockwell, and Ogden, 1971). This model was extended to coronary arterial blood flow in horses by Rumberger and Nerem (1977) using the method of characteristics. Because of its ease of implementation, here we propose to use the two-step explicit MacCormack (1969) finite-difference method for the numerical integration of the resulting nonlinear hyperbolic system of equations.

The one-dimensional model equations that we adopt from Anliker et al. (1971) are

$$\frac{\partial S}{\partial t} + \frac{\partial SV}{\partial z} + \psi = 0 \quad (2.13.1)$$

$$\frac{\partial V}{\partial t} + V \frac{\partial V}{\partial z} + \frac{1}{\rho} \frac{\partial p}{\partial z} = f \quad (2.13.2)$$

$$S = S(p, z) \quad (2.13.3)$$

$V(z, t)$ is the instantaneous, area-averaged flow velocity, $p(z, t)$ is the local pressure, and the effect of wall friction is parameterized in terms of the force term, f (force per unit mass of fluid in the axial z direction). Fluid density is ρ , and (2.13.3) is an equation of state expressing the cross-sectional area of the vessel, S , as a function of the pressure in the vessel, p , and the axial coordinate, z . Because we consider an elastic tube with no branches and therefore with no leakage, the volumetric outflow term is set to $\psi = 0$.

Once the equation of state (2.13.3) and the friction term f are specified, the computational problem reduces to integrating the system of equations comprising (2.13.1) and (2.13.2) for the variables S and V ; p is calculated from the equation of state.

Before specifying the various inputs into the computer code necessary to integrate this system of equations, we will outline the multilevel (predictor–corrector) explicit second-order finite difference scheme that was developed by MacCormack (1969) for the numerical integration of nonlinear hyperbolic partial differential equations. The original method and its variations have been used in many applications in computational aerodynamics and fluid mechanics.

Consider the one-dimensional linear convection equation,

$$\frac{\partial u}{\partial t} + a \frac{\partial u}{\partial x} = 0 \quad (2.13.4)$$

where a is a constant convection velocity, and u is a flow function, $u = u(x, t)$, that is being convected. The application of the MacCormack scheme to this hyperbolic partial differential equation can be written as

$$\bar{u}_i = u_i^n - \frac{a \Delta t}{\Delta x} (u_{i+1}^n - u_i^n) \quad (2.13.5)$$

$$\bar{\bar{u}}_i = u_i^n - \frac{a \Delta t}{\Delta x} (\bar{u}_i - \bar{u}_{i-1}) \quad (2.13.6)$$

$$u_i^{n+1} = \frac{1}{2} (\bar{u}_i + \bar{\bar{u}}_i) \quad (2.13.7)$$

In (2.13.5)–(2.13.7), the index n refers to time level and the index i represents position in space. The scheme will be stable for Courant number, $C = |a(\Delta t / \Delta x)| \leq 1$; highest accuracy will be obtained when $C = 1$, which is generally possible for linear equations. It is apparent from the fact that the characteristic direction for this problem is the line whose slope is $dx/dt = a$, and when the solution advances on this characteristic, which is the case when $C = 1$, then it is exact. In many cases, when the equation is nonlinear, e.g., if $a = u$, then generally $C < 1$ will be required, so that one would have to sacrifice accuracy for numerical stability. For example, in Problem 2.15, it will be necessary to maintain $C < 0.2$, otherwise the solution rapidly becomes unstable.

Let us now consider the nonlinear convection equation,

$$\frac{\partial u}{\partial t} + u \frac{\partial u}{\partial x} = 0 \quad (2.13.8)$$

We can rewrite this equation in conservative form with the flux term $F = u^2/2$:

$$\frac{\partial u}{\partial t} = -\frac{\partial F}{\partial x}$$

Application of the MacCormack explicit method to this problem consists of the predictor step (forward in space), which reads

$$\bar{u}_i = u_i^n - \frac{\Delta t}{\Delta x} (F_{i+1}^n - F_i^n) \quad (2.13.9)$$

and combining (2.13.6) and (2.13.7), the corrector step (backward in space) can be written as

$$\begin{aligned} u_i^{n+1} &= \frac{1}{2} \left[u_i^n + \bar{u}_i - \frac{\Delta t}{\Delta x} (\bar{F}_i - \bar{F}_{i-1}) \right] \\ \bar{F} &= \bar{u}^2/2 \end{aligned} \quad (2.13.10)$$

In most cases, alternating forward–backward space differencing with backward–forward differencing avoids the inherent bias in one-sided differences. The stability of this scheme requires

$$C = \left| u_{\max} \frac{\Delta t}{\Delta x} \right| \leq 1 \quad (2.13.11)$$

but for nonlinear problems one would have to sacrifice from accuracy for numerical stability and use values for C much less than 1. A generalization of this method to fourth-order accuracy in space (two–four method) was derived by Gottlieb and Turkel (1976).

Another method that has seen widespread popularity for the numerical integration of the Navier-Stokes equations is the implicit Beam and Warming method based on Crank-Nicolson time advancement. However, when applied to the nonlinear convection equation (2.13.8), the resulting finite difference scheme is dispersive, and does not have any inherent numerical dissipation (Tannehill et al. 1997, p. 121). Consequently, to maintain numerical stability, it is often necessary to add artificial dissipation to smooth numerical instabilities. How this term modifies the ensuing results is controversial but, nevertheless, in practice, artificial dissipation has been used often. For the one-dimensional convection equation (2.13.8), this term is written as (Tannehill et al. 1997, p. 193)

$$D = -\frac{\mu_e}{8} (u_{i+2}^n - 4u_{i+1}^n + 6u_i^n - 4u_{i-1}^n + u_{i-2}^n) \quad (2.13.12)$$

Stability will be maintained with

$$0 < \mu_e \leq 1 \quad (2.13.13)$$

For a discussion of artificial viscosity and dissipation see Section 4.2. We also refer the reader to Laney (1998), Tannehill et al. (1997), and Anderson (1995).

The Beam and Warming method advances (2.13.8) in time using the implicit Crank-Nicolson (trapezoidal) differencing such that

$$u_i^{n+1} = u_i^n - \frac{\Delta t}{2} \left[\left(\frac{\partial F}{\partial x} \right)^n + \left(\frac{\partial F}{\partial x} \right)^{n+1} \right] \quad (2.13.14)$$

From (2.13.14), it is apparent that the finite difference equation is nonlinear and we must either use iteration or linearization. Beam and Warming (1976) obtained the following linearization:

$$F^{n+1} \approx F^n + A^n(u^{n+1} - u^n) \quad (2.13.15)$$

For equation (2.13.8), the Jacobian A is defined as

$$A = \frac{\partial F}{\partial u} = \frac{\partial(u^2/2)}{\partial u} = u \quad (2.13.16)$$

Substituting (2.13.15) and (2.13.16) into (2.13.14), we obtain

$$u_i^{n+1} = u_i^n - \frac{\Delta t}{2} \left\{ 2 \left(\frac{\partial F}{\partial x} \right)^n + \frac{\partial}{\partial x} \left[u^n (u_i^{n+1} - u_i^n) \right] \right\} \quad (2.13.17)$$

Using second-order central differences in space,

$$\frac{\partial}{\partial x} [u^n (u_i^{n+1} - u_i^n)] = \frac{u_{i+1}^n u_{i+1}^{n+1} - u_{i-1}^n u_{i-1}^{n+1}}{2\Delta x} - \frac{u_{i+1}^n u_{i+1}^n - u_{i-1}^n u_{i-1}^n}{2\Delta x} \quad (2.13.18)$$

Substituting (2.13.18) into (2.13.17), we obtain the tridiagonal form of the finite-difference equation, which reads

$$\begin{aligned} & -\frac{(\Delta t)u_{i-1}^n}{4\Delta x} u_{i-1}^{n+1} + u_i^{n+1} + \frac{(\Delta t)u_{i+1}^n}{4\Delta x} u_{i+1}^{n+1} \\ & = -\frac{\Delta t}{2\Delta x} (F_{i+1}^n - F_{i-1}^n) + \frac{\Delta t}{4\Delta x} u_{i+1}^n u_{i+1}^n - \frac{\Delta t}{4\Delta x} u_{i-1}^n u_{i-1}^n + u_i^n + O(\Delta t^2, \Delta x^2) \end{aligned} \quad (2.13.19)$$

The method is unconditionally stable in the von Neumann sense, but generally for nonlinear equations stability will be obtained only with artificial viscosity, such as adding (2.13.12) directly to the right-hand-side of (2.13.19).

A more general model equation is the viscous Burgers equation, given as

$$\frac{\partial u}{\partial t} + u \frac{\partial u}{\partial x} = v \frac{\partial^2 u}{\partial x^2} \quad (2.13.20)$$

where v is a transport coefficient. Defining $F = u^2/2$, and $d = v\Delta t/(\Delta x)^2$, MacCormack explicit method can be applied to (2.13.20) with the following

predictor step:

$$\bar{u}_i = u_i^n - \frac{\Delta t}{\Delta x} (F_{i+1}^n - F_i^n) + d (u_{i+1}^n - 2u_i^n + u_{i-1}^n) \quad (2.13.21)$$

followed by the corrector step:

$$u_i^{n+1} = \frac{1}{2} \left[u_i^n + \bar{u}_i - \frac{\Delta t}{\Delta x} (\bar{F}_i - \bar{F}_{i-1}) + d (\bar{u}_{i+1} - 2\bar{u}_i + \bar{u}_{i-1}) \right] \quad (2.13.22)$$

Stability of this scheme can be maintained by the use of an empirical formula (Tannehill et al. 1997),

$$\Delta t \leq \frac{(\Delta x)^2}{|u_{\max}| \Delta x + 2\nu} \quad (2.13.23)$$

Using the Beam and Warming time differencing for (2.13.20), we obtain

$$\frac{u_i^{n+1} - u_i^n}{\Delta t} + \frac{1}{2} \left[\left(\frac{\partial F}{\partial x} \right)_i^n + \left(\frac{\partial F}{\partial x} \right)_i^{n+1} \right] = \frac{1}{2} \nu \left[\left(\frac{\partial^2 u}{\partial x^2} \right)_i^n + \left(\frac{\partial^2 u}{\partial x^2} \right)_i^{n+1} \right] \quad (2.13.24)$$

Then the resulting finite difference equation, which is second-order in both time and space, can be written as

$$\begin{aligned} & \frac{u_i^{n+1} - u_i^n}{\Delta t} + \frac{F_{i+1}^n - F_{i-1}^n}{2\Delta x} + \frac{u_{i+1}^n (u_{i+1}^{n+1} - u_{i+1}^n) - u_{i-1}^n (u_{i-1}^{n+1} - u_{i-1}^n)}{4\Delta x} \\ &= \frac{\nu}{2(\Delta x)^2} [\delta_x^2 u_i^n + \delta_x^2 u_i^{n+1}] \end{aligned} \quad (2.13.25)$$

In (2.13.25), δ_x^2 is the second-order, central difference operator:

$$\delta_x^2 u_i = u_{i+1} - 2u_i + u_{i-1} \quad (2.13.26)$$

As an example, let us consider the nonlinear convection equation (2.13.8), with the following boundary and initial conditions:

$$\begin{aligned} & \frac{\partial u}{\partial t} + u \frac{\partial u}{\partial x} = 0 \\ & u(x, 0) = 10.0 \quad 0 \leq x \leq 20; \quad u(x, 0) = 0 \quad 20 < x \leq 40 \quad (\text{initial condition}) \\ & u(0) = 1; \quad u(40) = 0 \quad (\text{Dirichlet boundary conditions}) \end{aligned} \quad (2.13.27)$$

We will integrate this equation using 101 grid points up to a total time of 4 s. Program 2.10 accomplishes this task with the MacCormack explicit method (2.13.9)–(2.13.10). For right-moving discontinuities such as (2.13.27), it is recommended to use only forward differences in the direction of discontinuity

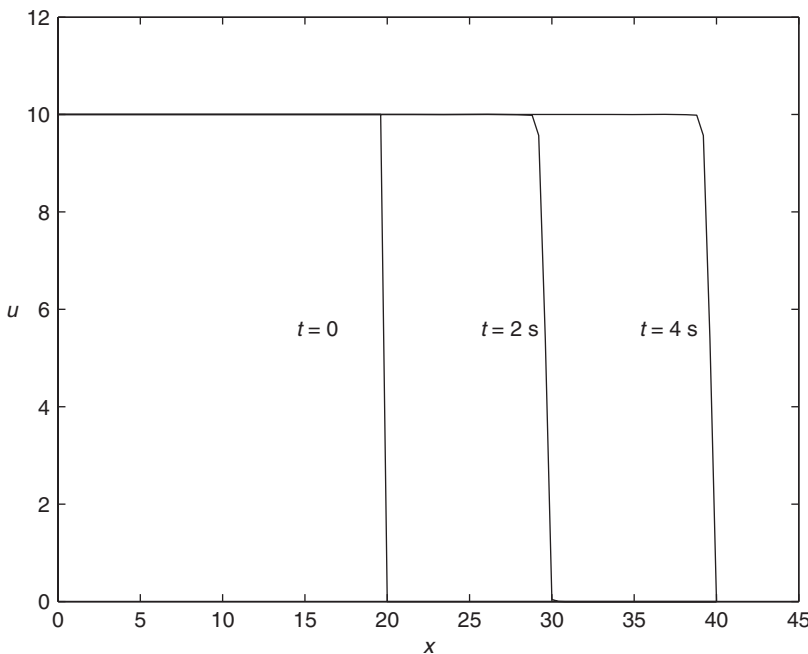


FIGURE 2.13.1 MacCormack explicit scheme for the nonlinear convection equation; $C = 1.0$.

propagation (Tennehill et al., 1997, p. 187). Hence, in Program 2.10, difference switching was not implemented. Results are plotted in Figs. 2.13.1–2.13.3 at various time levels for three different values of C . For $C = 1$ (Fig. 2.13.1) the solution is completely free of dispersion and dissipation errors as it progresses on the characteristics. However, as we observe in Fig. 2.13.2, when the Courant number is reduced to 0.75, numerical stability is maintained, but the solution displays significant dispersion errors in the vicinity of the discontinuity. Finally, when $C = 1.1$ (Fig. 2.13.3), which violates the linear stability limit of $C \leq 1$, the solution deteriorates and, as expected, becomes unstable.

Next, in Program 2.11 the same equation (2.13.27) is solved with the implicit Beam and Warming method (2.13.19), for $C = 1$. We note that (2.13.19) written for all the interior grid points results in a system of linear equations where the coefficient matrix is triadiagonal. A very efficient compact storage algorithm for solving such systems is the Thomas algorithm (see Section 4.4) included as a MATLAB function script in Program 2.11. It is also possible to solve the resulting linear system using the MATLAB “backslash” multiplication function (which we provide as an option in Program 2.11). We also note that in this program, the equations have been modified by the inclusion of the artificial dissipation term (2.13.12) to stabilize the solution, with $\omega = 0.8$. Figure 2.13.4 displays the results for $C = 1$. Although the solution is stable and does not have significant

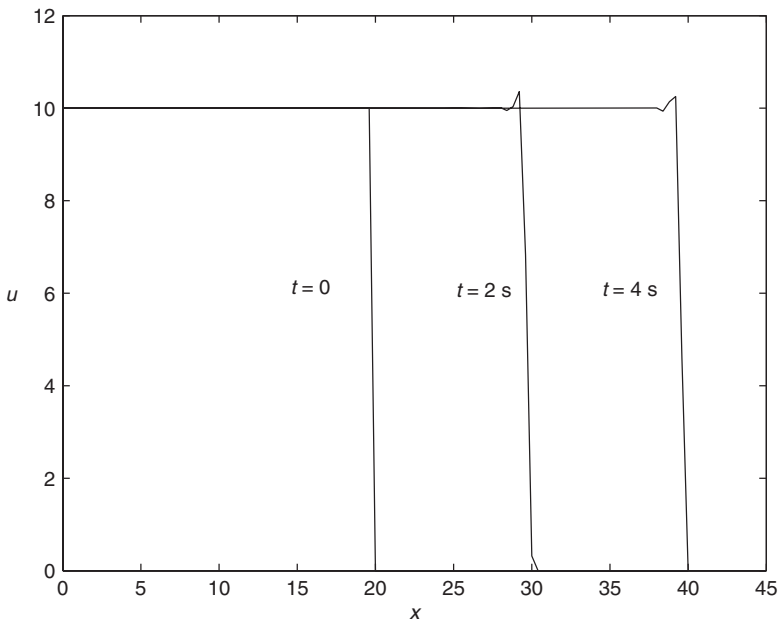


FIGURE 2.13.2 MacCormack explicit scheme for the nonlinear convection equation; $C = 0.75$.

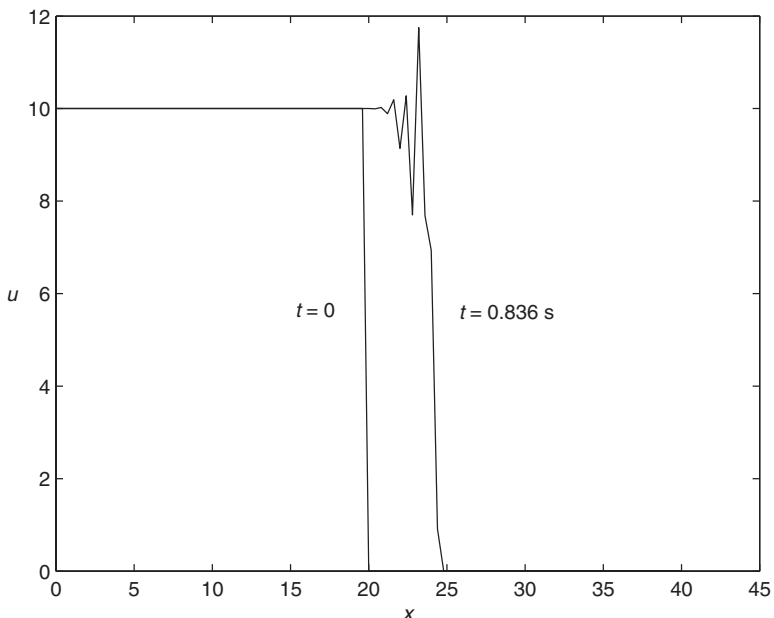


FIGURE 2.13.3 MacCormack explicit scheme for the nonlinear convection equation; $C = 1.1$.

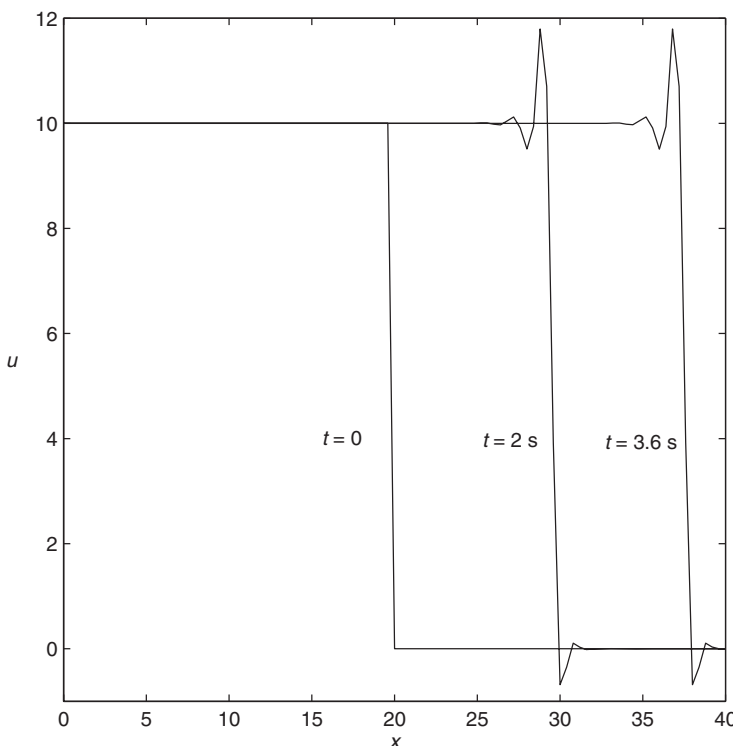


FIGURE 2.13.4 Beam and Warming solution for the nonlinear convection equation; $\omega = 0.8$.

dissipation errors, it is degraded by the existence of significant dispersion errors in the vicinity of the discontinuity. When $\omega = 0$, Fig. 2.13.5. shows that the solution becomes unstable and numerical errors amplify exponentially. Hence, for the inviscid, nonlinear convection equation, the implicit Beam and Warming method may not be the best choice.

Problem 2.12 The one-dimensional Burgers equation (2.13.20) with ν as the kinematic viscosity serves as a model equation for physical problems in fluid dynamics ranging from strong shock waves to spectral dynamics of turbulence. It has also several exact (closed form) solutions for highly viscous, low Reynolds number flows. For such flows, we can use nondimensional variables by making the substitutions:

$$x/L \rightarrow x, \quad vt/L^2 \rightarrow t, \quad uL/\nu \rightarrow u \quad (2.13.28)$$

With this scaling, (2.13.20) becomes

$$\frac{\partial u}{\partial t} + u \frac{\partial u}{\partial x} = \frac{\partial^2 u}{\partial x^2} \quad (2.13.29)$$

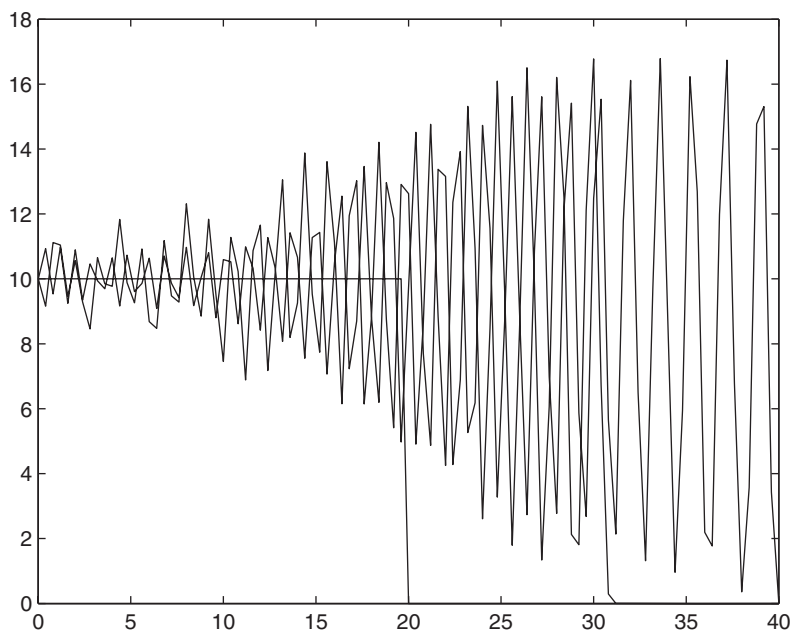


FIGURE 2.13.5 Beam and Warming solution for the nonlinear convection equation; $\omega = 0$.

A family of solutions for this equation is obtained by Benton and Platzman (1972), one of which is given as

$$u(x, t) = \frac{-2 \sinh x}{\cosh x - e^{-t}} \quad (2.13.30)$$

As $t \rightarrow 0$, (2.13.30) gives

$$u(x, 0) = \frac{-2 \sinh x}{\cosh x - 1} \quad (2.13.31)$$

and as $t \rightarrow \infty$ (steady state), one obtains

$$u(x, t) = -2 \tanh x \quad (2.13.32)$$

The exact solution, (2.13.30), is discontinuous at $x = 0$ at $t = 0$ and, owing to the second-order diffusion term in (2.13.29), the discontinuity is rapidly smoothed in time. The exact solution (2.13.30) is valid for the initial value problem for $-\infty \leq x \leq +\infty$ and to use it for testing numerical schemes, we will define initial/boundary conditions for finite x . Consequently, the numerical solution will be approximate.

Initial conditions can be gotten directly from (2.13.31) and we can define the integration domain as $-6 \leq x \leq +6$ with boundary conditions of either Dirichlet

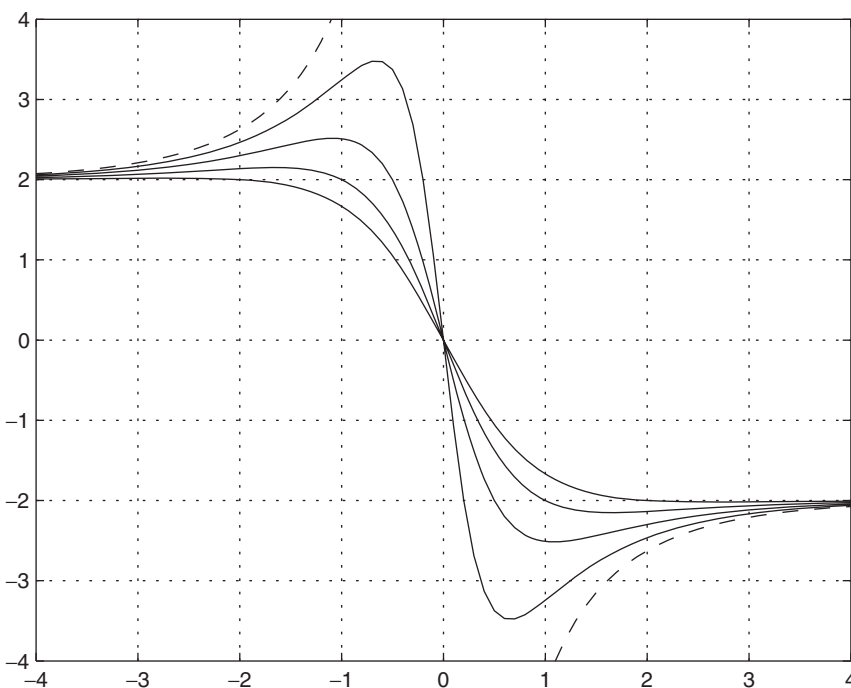


FIGURE 2.13.6 Exact solution (2.13.30) for the Burgers equation: $t = 0$ (dash), 0.2, 0.5, 1, 2.

or Neumann type. At these boundary points, Dirichlet boundary conditions are $u(x, 0) = \mp 2.0$ at $x = \pm 6$. Neumann boundary conditions are prescribed on the gradient of u , and will be given below.

Problem 2.13 Integrate (2.13.29) using the fully explicit MacCormack method. Generate the initial conditions from (2.13.31). Use 100 evenly spaced grid points within $-6 \leq x \leq +6$, and implement Neumann boundary conditions, i.e.,

$$\frac{\partial u}{\partial x} = 0 \quad \text{at} \quad x = \pm 6. \quad (2.13.33)$$

It is sufficient to approximate the gradient boundary conditions using first-order one-sided differences. The fully explicit MacCormack scheme must satisfy $u_{\max} \Delta t / \Delta x \leq 1$ (convective stability) and $\Delta t / \Delta x^2 \leq 1/2$ (viscous stability) restrictions in choosing the allowable time step, Δt . Choose your time step so that both conditions will be satisfied. Here, u_{\max} is the maximum velocity at $t = 0$. Compare your solution with the exact solution at $t = 0.2, 0.5, 1, 2$.

Problem 2.14 Use the fully implicit Beam and Warming method to obtain a numerical solution to (2.13.29), with the same boundary-initial conditions as in Problem 2.13 with 100 grid points. Note that there is no stability restriction because we are using the fully implicit formula. Perform this calculation with Dirichlet boundary conditions $u(x, 0) = \mp 2.0$ at $x = \pm 6$. Compare the numerical results with the exact solution at $t = 0.2, 0.5, 1, 2$. What is the effect of adding artificial viscosity such as (2.13.12)? What is the effect of $C > 1$? How does the solution compare with the MacCormack solution for this problem?

We now return to the elastic tube problem, and write (2.13.1) and (2.13.2) in conservative vector–matrix form:

$$\frac{\partial \mathbf{U}}{\partial t} + \frac{\partial \mathbf{F}}{\partial z} = \mathbf{Q} \quad (2.13.34)$$

where the vectors \mathbf{U} , \mathbf{F} , and \mathbf{Q} are defined as

$$\mathbf{U} = \begin{bmatrix} S \\ V \end{bmatrix}, \quad \mathbf{F} = \begin{bmatrix} SV \\ \frac{1}{2}V^2 \end{bmatrix}, \quad \mathbf{Q} = \begin{bmatrix} -\psi \\ f - \frac{1}{\rho} \frac{\partial p}{\partial z} \end{bmatrix}$$

Using the MacCormack explicit method consisting of a forward-difference predictor step and a backward-difference corrector, (2.13.34) can be advanced in time in the following manner:

$$\bar{\mathbf{U}}_i = \mathbf{U}_i^n - \frac{\Delta t}{\Delta z} (\mathbf{F}_{i+1}^n - \mathbf{F}_i^n) + \Delta t \mathbf{Q}_i^n \quad (2.13.35)$$

$$\bar{\bar{\mathbf{U}}}_i = \mathbf{U}_i^n - \frac{\Delta t}{\Delta z} (\bar{\mathbf{F}}_i - \bar{\mathbf{F}}_{i-1}) + \Delta t \bar{\mathbf{Q}}_i \quad (2.13.36)$$

The value of the unknowns at the advanced time level then can be calculated from

$$\mathbf{U}_i^{n+1} = \frac{1}{2} (\bar{\mathbf{U}}_i + \bar{\bar{\mathbf{U}}}_i) \quad (2.13.37)$$

In (2.13.35)–(2.13.37), index i represents position in space, and the index n is for the time level. For this problem, we recommend implementing operator switching in space, alternating from backward/forward to forward/backward during consecutive time steps. As the equation is hyperbolic, numerical stability requires Courant number (C) to be less than one, such that the computation must obey

$$C = \left| \frac{V_{\max} \Delta t}{\Delta z} \right| \leq 1 \quad (2.13.38)$$

where V_{\max} is the maximum velocity at a given time step.

It should be noted that although the algorithm is written in the compact vector–matrix form of (2.13.35)–(2.13.37), in practice, time advancement is done

separately for each equation in a sequential manner. The application that we consider here consists of a generic elastic tube of reference length $L = 25$ cm. We use fluid properties relevant to human blood, such as density, $\rho = 1.06$ g/cm³; viscosity, $\mu = 0.049$ poise. The reference pressure is set to $p_0 = 80$ mmHg.

The proximal boundary condition for pressure, $p_L(t)$, is time varying while the distal boundary condition is fixed at 15 mmHg. The reference pressure p_0 represents the approximate maximum pressure in the system. Velocity boundary conditions are obtained by zeroth-order extrapolation at both ends of the vessel.

We adopt an approximate equation of state, $S(p, z)$:

$$S(p, z) = 7.07e^{-0.25z + (p - p_0)/\rho c(p, z)c(p_0, z)} \quad (2.13.39)$$

It is apparent that this expression depends on c , the wave speed in the fluid. Assuming that c is a product of linear functions of both z and p and is in units of cm/s, an equation for this quantity can be written as (Anliker et al., 1971)

$$c(p, z) = (97 + 2.03p)(1 + 0.02z) \quad (2.13.40)$$

The pulsating flow in the elastic tube is assumed to be laminar and unsteady, so that the friction term, f , can be written using Poiseuille's formula for circular pipes:

$$f_{\text{laminar}} = -8\pi \frac{\mu}{\rho} \frac{V}{S} \quad (2.13.41)$$

This equation will approximate viscous effects in the vessel and is assumed valid for both steady and unsteady flow.

Initial conditions are less important because after a few initial cycles driven by the proximal boundary conditions, the solution reaches quasi-steady state independent of the initial conditions. If the initial conditions are not too different than the final solution, the computation time to reach quasi steady state will decrease. For this computation, we implemented the following initial conditions:

$$V = V_L e^{\left(\frac{z}{25} \ln \frac{V_R}{V_L}\right)} \quad (2.13.42)$$

$$p = p_L e^{\left(\frac{z}{25} \ln \frac{V_R}{V_L}\right)} \quad (2.13.43)$$

Here, $V_R = 0.1$ cm/s, $V_L = 3.0$ cm/s, $p_R = 15$ mmHg, and p_L is obtained from the proximal boundary condition for pressure.

The axial z direction is discretized with 100 points, corresponding to a grid spacing of $\Delta z = 0.25$. We impose a forcing pressure pulse of about 86 beats per minute through the proximal boundary condition. The signal is interpolated by a cubic spline to provide the value of the left boundary condition for pressure

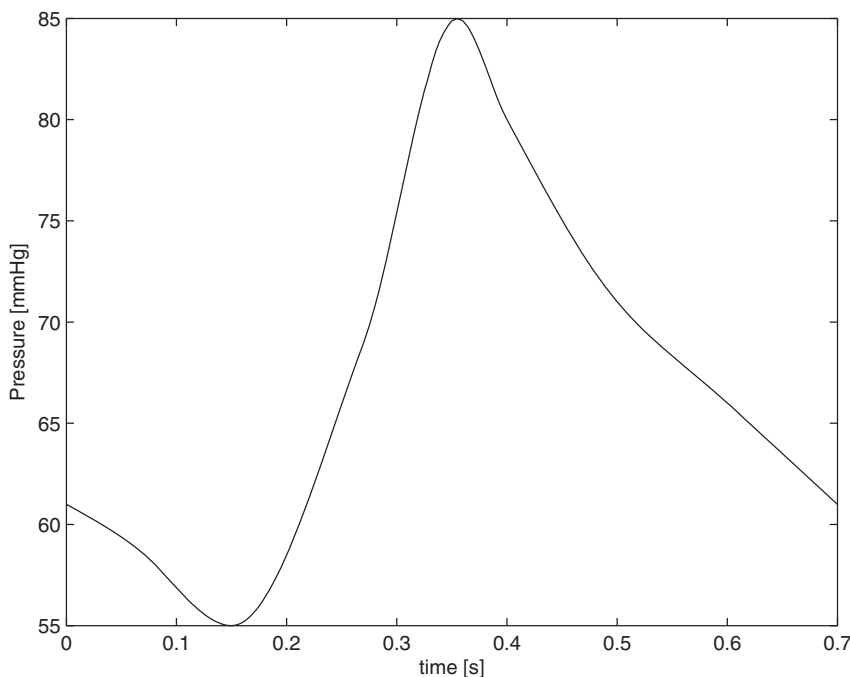


FIGURE 2.13.7 Proximal pressure boundary condition.

at each time step. Figure 2.13.7 shows a typical input signal for the proximal pressure boundary condition and Fig. 2.13.8 displays the calculated pressure and velocity at several locations along the axial direction, z . Closer to the left boundary (Fig. 2.13.8a), the velocity plot indicates reverse flow in the vessel, which disappears downstream. Localized regions of backflow have been observed in other studies as well. As we advance downstream (Fig. 2.13.8 b, c), both the local maximum and minimum velocity magnitudes increase and the velocity is completely synchronous with the pressure. Both quantities remain periodic, although they produce higher harmonics of the forcing pressure. All these qualitative observations are compatible with other models for various arterial simulations, but we stress the fact that the example we are presenting here is for a generic elastic tube; it has to be adapted to real life arterial blood flow by matching all the constants in the mathematical model to actual measured values, and many other factors have to be considered to improve the model for applicability to realistic simulations concerning arterial blood flow. For example, what is the effect of viscosity? Is the Poiseuille friction factor adequate? Should turbulence be considered? Is the wall elasticity modeled with sufficient accuracy? Are the proximal and distal boundary conditions sufficiently accurate to model the physical problem? Regardless, the model outlined in this section should serve as a starting point for simulating arterial blood flow (Akman, Biringen, and Waggy, 2011).

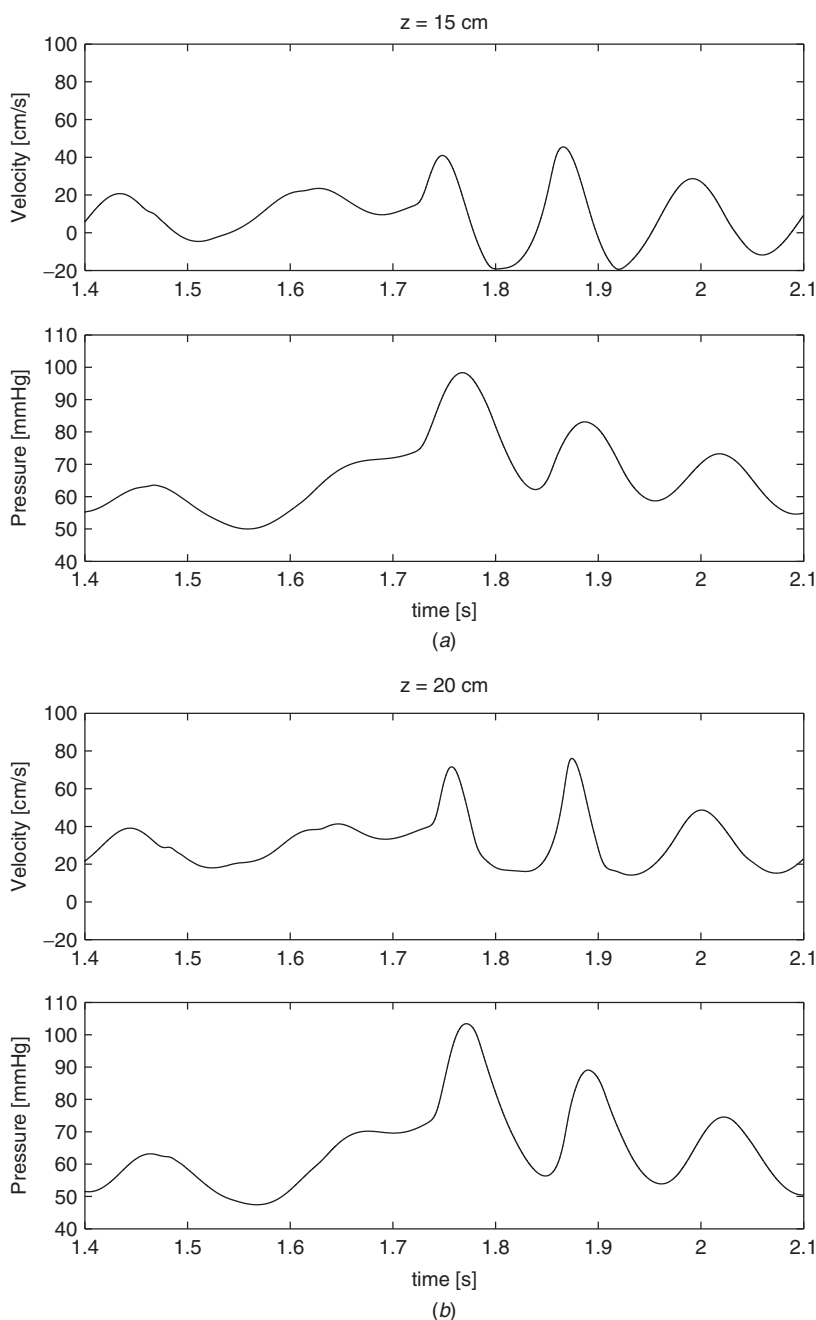


FIGURE 2.13.8 Pressure and velocity signals over one period of the proximal pressure cycle. (a) $z = 15 \text{ cm}$; (b) $z = 20 \text{ cm}$; (c) $z = 22 \text{ cm}$.

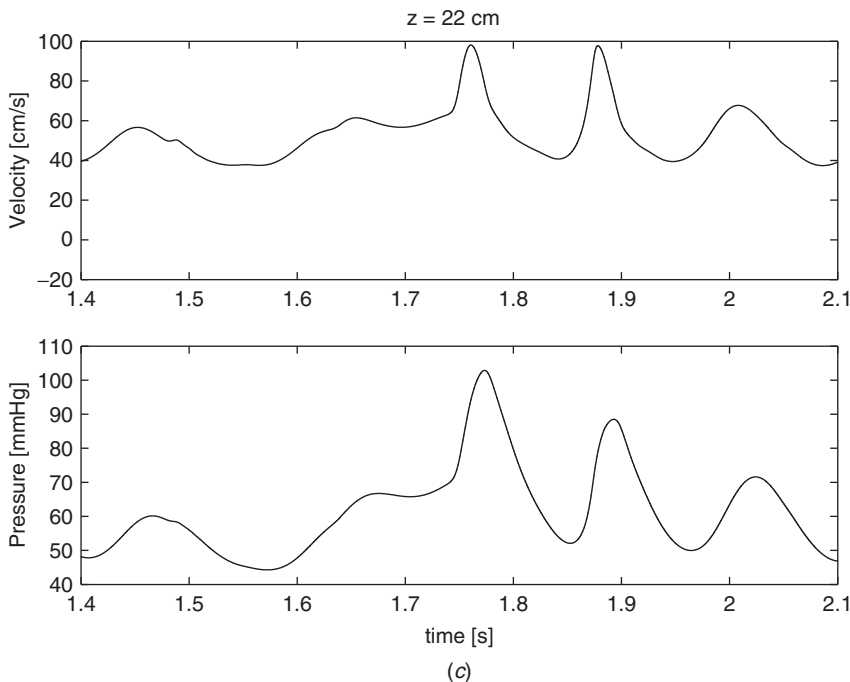


FIGURE 2.13.8 (continued).

We should also note that although the signal propagating in the elastic tube converges to a quasi-steady periodic state, the initial transients in the solution can have very steep fronts necessitating the implementation of artificial dissipation. As we explained above, smoothing irregular and sharp signals with such measures is not uncommon in the applications of computational models to fluid flow problems, as the governing equations are nonlinear and would interact through the advection terms (e.g., $V(\partial V/\partial z)$), resulting in energy accumulating in higher harmonics, which are not resolved by the given finite difference mesh. If the physical dissipation is not sufficient to dampen out these growing numerical errors, or if the integration scheme, i.e., the finite difference formula is not sufficiently dissipative, then one would have to explicitly add an artificial dissipation term to the finite difference equations. For finite difference formulas that are second-order accurate in space, the addition of a fourth-order artificial dissipation term is generally sufficient, and will not decrease the formal accuracy of the method if the coefficient ω is small. In this problem, we add (2.13.12) to the right-hand side of the finite difference equations, which, for the velocity component of (2.13.35), can be written as

$$D = -\frac{\mu_e}{8}(\Delta z)^4 \frac{\partial^4 V}{\partial z^4} = -\frac{\mu_e}{8}(V_{i+2} - 4V_{i+1} + 6V_i - 4V_{i-1} + V_{i-2}) \quad (2.13.44)$$

The negative sign ensures that positive dissipation is produced. The artificial dissipation coefficient was set to $\mu_e = 0.04$, so that the effect of this parameter is not significant on solution accuracy.

Problem 2.15 Construct a MATLAB code to solve the system of equations (2.13.35)–(2.13.37) using the MacCormack explicit method, with the information provided in this section to investigate the influence of the following parameters on the solution: (a) double the frequency of the forcing (proximal boundary condition for pressure); (b) halve the frequency of the forcing; (c) double the amplitude of the forcing; (d) halve the amplitude of the forcing. For all these cases, plot pressure and velocity as a function of time at specified locations along the vessel.

A formula for turbulent flow for the friction function f is given by Anliker and Rockwell (1971). This expression is written as

$$f_{\text{turbulent}} = -0.1360 \left(\frac{\mu}{\rho} \right)^{1/4} \frac{|V|^{7/4}}{S^{5/8}} \operatorname{sgn} V \quad (2.13.45)$$

Use this expression instead of the laminar formula (2.13.41). Compare the amplitude and frequency responses of the pressure and velocity at several locations along the axis of the vessel.

In all these calculations, it is important to run the code at least three periods of the forcing frequency. For example, if the period is 0.7 s, then the total time should be about 2.1–3.8 s. It is also important to note that if the solutions become unstable for some combination of these parameters, it is generally due to the steep front of the initial transients that produce large-amplitude higher harmonics in the pressure. These oscillations can be controlled by increasing the artificial viscosity coefficient or by reducing the time step.

APPENDIX

TABLE 2.A.1 Output of Program 2.1

I	R(I)	PHI(I)	EXPHI(I)	U(I)	EXU(I)
1.0000e+00	1.1000e+00	-9.5430e-01	-9.5644e-01	-1.8220e+01	-1.8188e+01
2.0000e+00	1.2000e+00	-2.6440e+00	-2.6477e+00	-1.5702e+01	-1.5680e+01
3.0000e+00	1.3000e+00	-4.0948e+00	-4.0997e+00	-1.3407e+01	-1.3392e+01
4.0000e+00	1.4000e+00	-5.3254e+00	-5.3313e+00	-1.1274e+01	-1.1263e+01
5.0000e+00	1.5000e+00	-6.3496e+00	-6.3562e+00	-9.2579e+00	-9.2500e+00
6.0000e+00	1.6000e+00	-7.1770e+00	-7.1841e+00	-7.3253e+00	-7.3200e+00
7.0000e+00	1.7000e+00	-7.8147e+00	-7.8221e+00	-5.4511e+00	-5.4476e+00
8.0000e+00	1.8000e+00	-8.2672e+00	-8.2749e+00	-3.6153e+00	-3.6133e+00
9.0000e+00	1.9000e+00	-8.5377e+00	-8.5455e+00	-1.8025e+00	-1.8016e+00

(continues)

TABLE 2.A.1 (continued)

I	R(I)	PHI(I)	EXPHI(I)	U(I)	EXU(I)
1.0000e+01	2.0000e+00	-8.6277e+00	-8.6355e+00	-5.2788e-05	1.5987e-14
1.1000e+01	2.1000e+00	-8.5377e+00	-8.5455e+00	1.8020e+00	1.8014e+00
1.2000e+01	2.2000e+00	-8.2673e+00	-8.2750e+00	3.6120e+00	3.6109e+00
1.3000e+01	2.3000e+00	-7.8153e+00	-7.8228e+00	5.4368e+00	5.4352e+00
1.4000e+01	2.4000e+00	-7.1800e+00	-7.1872e+00	7.2819e+00	7.2800e+00
1.5000e+01	2.5000e+00	-6.3590e+00	-6.3660e+00	9.1521e+00	9.1500e+00
1.6000e+01	2.6000e+00	-5.3495e+00	-5.3563e+00	1.1052e+01	1.1049e+01
1.7000e+01	2.7000e+00	-4.1486e+00	-4.1550e+00	1.2984e+01	1.2981e+01
1.8000e+01	2.8000e+00	-2.7528e+00	-2.7589e+00	1.4951e+01	1.4949e+01
1.9000e+01	2.9000e+00	-1.1584e+00	-1.1641e+00	1.6957e+01	1.6954e+01
2.0000e+01	3.0000e+00	6.3853e-01	6.3331e-01	1.9003e+01	1.9000e+01
2.1000e+01	3.1000e+00	2.6421e+00	2.6373e+00	2.1091e+01	2.1088e+01
2.2000e+01	3.2000e+00	4.8567e+00	4.8524e+00	2.3223e+01	2.3220e+01
2.3000e+01	3.3000e+00	7.2867e+00	7.2829e+00	2.5400e+01	2.5397e+01
2.4000e+01	3.4000e+00	9.9367e+00	9.9334e+00	2.7624e+01	2.7621e+01
2.5000e+01	3.5000e+00	1.2812e+01	1.2809e+01	2.9896e+01	2.9893e+01
2.6000e+01	3.6000e+00	1.5916e+01	1.5914e+01	3.2216e+01	3.2213e+01
2.7000e+01	3.7000e+00	1.9255e+01	1.9253e+01	3.4586e+01	3.4584e+01
2.8000e+01	3.8000e+00	2.2833e+01	2.2832e+01	3.7007e+01	3.7004e+01
2.9000e+01	3.9000e+00	2.6656e+01	2.6656e+01	3.9479e+01	3.9476e+01

3

VISCOUS FLUID FLOWS

The viscous effects ignored in the previous chapter are examined in this chapter. The governing equations for viscous flows are first summarized in Section 3.1. The numerical techniques, devised previously for solving ordinary initial-value and boundary-value problems, are then used or modified to be used in the next two sections to study a velocity boundary layer and a thermal boundary layer. In Section 3.4, an open-channel flow problem is solved utilizing a numerical method constructed in Section 2.8 for solving elliptic partial differential equations.

There are two different approaches in solving parabolic equations. The explicit methods and their computational stabilities are discussed in Section 3.5, with an example given on the unsteady flow caused by a suddenly accelerated plane wall. The computationally stable implicit methods are introduced in Section 3.6. The illustrative example used there is the starting flow in a channel caused by the application of a constant pressure gradient.

Section 3.7 deals with Stokes flows, which are governed by a biharmonic equation. Such an equation is solved by first rewriting it in the form of two coupled elliptic equations and then by applying twice an appropriate iterative method derived in Section 2.8. This numerical scheme is used to solve for the cavity flow caused by a moving surface. The last section, Section 3.8, concerns the linear stability of viscous flows where we also introduce the basic ideas of pseudo-spectral methods.

3.1 GOVERNING EQUATIONS FOR VISCOUS FLOWS

Before solving viscous flow problems, the equations governing the unsteady motion of a viscous compressible fluid having variable physical properties are summarized. Derivation of these equations can be found in many texts on fluid

dynamics, for example, in Schlichting (1968). The equations are expressed here in vector notation. Their specific forms in Cartesian, cylindrical, and spherical coordinates are shown in the book by Hughes and Gaylord (1964).

No matter whether the fluid is viscous or inviscid, the continuity equation (2.11.11) remains in the same form, so that

$$\frac{\partial \rho}{\partial t} + \nabla \cdot (\rho \mathbf{V}) = 0 \quad (3.1.1)$$

However, viscous forces appear in a real fluid, as discussed in Section 2.1. The equation of motion, constructed by adding to Euler's equation (2.1.5) the forces per unit volume caused by viscosity, is of the form

$$\rho \frac{D\mathbf{V}}{Dt} = -\nabla p - \nabla \times [\mu(\nabla \times \mathbf{V})] + \nabla[(2\mu + \lambda)\nabla \cdot \mathbf{V}] \quad (3.1.2)$$

The operator on the left side, defined previously in (2.1.6), is the substantial derivative. μ is the coefficient of viscosity, and λ is the second coefficient of viscosity of the fluid; both are functions of temperature. For a monatomic gas $\lambda = -\frac{2}{3}\mu$. Equation (3.1.2) is generally referred to as the *Navier-Stokes equation*. The addition of viscous forces increases the order of the differential equation by one. The extra constant of integration to appear in the solution is determined from the additional boundary condition required for a viscous fluid that the velocity component tangent to a stationary rigid surface must also be zero. The boundary condition for an inviscid fluid is that the component normal to such a surface vanishes.

The energy equation may be written in several alternative forms. The following form is often used for an ideal gas in terms of specific enthalpy h ($= c_p T$):

$$\rho \frac{Dh}{Dt} = \frac{Dp}{Dt} + \nabla \cdot (k \nabla T) + \Phi \quad (3.1.3)$$

in which c_p and k are, respectively, the constant-pressure specific heat and the thermal conductivity of the gas, T is the absolute temperature, and Φ is the *dissipation function* defined in Cartesian coordinates as

$$\begin{aligned} \Phi = & 2\mu \left[\left(\frac{\partial u}{\partial x} \right)^2 + \left(\frac{\partial v}{\partial y} \right)^2 + \left(\frac{\partial w}{\partial z} \right)^2 \right] + \mu \left(\frac{\partial u}{\partial y} + \frac{\partial v}{\partial x} \right)^2 \\ & + \mu \left(\frac{\partial v}{\partial z} + \frac{\partial w}{\partial y} \right)^2 + \mu \left(\frac{\partial w}{\partial x} + \frac{\partial u}{\partial z} \right)^2 + \lambda(\nabla \cdot \mathbf{V})^2 \end{aligned} \quad (3.1.4)$$

It represents the time rate at which energy of the ordered fluid motion per unit volume is dissipated into heat through the action of viscosity.

Finally, the equation of state for an ideal gas is

$$p = \rho RT \quad (3.1.5)$$

where R is the gas constant.

We now have six scalar equations, (3.1.1) to (3.1.3) and (3.1.5), with (3.1.2) written in component form, which form a complete set of equations for the six unknowns ρ , p , T , u , v , and w . To find solutions to this system is extremely difficult because not only are the equations nonlinear, but also the unknowns are related in such a way that all six equations must be solved simultaneously.

Great simplifications are obtained by assuming that the fluid is incompressible and the temperature variation is not too large so that fluid properties are constant. In this case ρ becomes a constant, the equation of state is not needed, and the energy equation is uncoupled from the continuity equation and the equation of motion. The latter two are simplified in Cartesian coordinates to

$$\nabla \cdot \mathbf{V} = 0 \quad (3.1.6)$$

$$\rho \frac{D\mathbf{V}}{Dt} = -\nabla p + \mu \nabla^2 \mathbf{V} \quad (3.1.7)$$

The procedure for solving the problem is first to obtain p and \mathbf{V} from simultaneous equations (3.1.6) and (3.1.7), and then to find T after substituting the result into the simplified version of (3.1.3).

It is still possible to introduce the stream function defined in Section 2.1; the velocity potential can no longer be used because the flow is generally rotational in the presence of rotational viscous forces.

3.2 SELF-SIMILAR LAMINAR BOUNDARY-LAYER FLOWS

A very important example that exhibits self-similarity is the high Reynolds number flow past a streamline body discussed in Section 2.1. In this case effects of viscosity and conductivity are confined within a thin boundary layer next to the body surface.

The governing equations for boundary-layer flows are deduced from Navier-Stokes equations under the assumption that the boundary-layer thickness δ is small compared with the characteristic length L of the body. Considering a thin, two-dimensional boundary layer around a body having its surface parallel to the x axis and normal to the y -axis, Kuethe and Chow (1998, Appendix B), using an order-of-magnitude analysis, found that $v \ll u$ and $\partial/\partial x \ll \partial/\partial y$ when operating on either velocity or temperature. If the x component of the equation of motion is of order unity, then the y component is of order δ/L . When the latter is ignored completely, with $\partial p/\partial y$ approximated by zero, the resulting Navier-Stokes and energy equations are, respectively,

$$\rho \left(\frac{\partial u}{\partial t} + u \frac{\partial u}{\partial x} + v \frac{\partial u}{\partial y} \right) = -\frac{\partial p}{\partial x} + \frac{\partial}{\partial y} \left(\mu \frac{\partial u}{\partial y} \right) \quad (3.2.1)$$

$$\rho c_p \left(\frac{\partial T}{\partial t} + u \frac{\partial T}{\partial x} + v \frac{\partial T}{\partial y} \right) = \frac{\partial p}{\partial t} + u \frac{\partial p}{\partial x} + \frac{\partial}{\partial y} \left(k \frac{\partial T}{\partial y} \right) + \mu \left(\frac{\partial u}{\partial y} \right)^2 \quad (3.2.2)$$

They are called the *boundary-layer equations* for two-dimensional compressible flow. These, together with the continuity equation (3.1.1) and the equation of state (3.1.5), form a system of four scalar equations for the four unknowns ρ , T , u , and v . The pressure p in a thin boundary layer is no longer treated as an unknown. Instead, it is considered to be constant across the boundary layer, while its x dependence is obtained by solving the problem of an inviscid flow past the same body. The previously mentioned approximations form the basis of *Prandtl's boundary-layer theory*.

If we consider the simple problem of a semi-infinite flat plate aligned with a uniform flow of constant speed U and of constant physical properties, including density ρ , as sketched in Fig. 3.2.1, the governing equations for a steady flow are further simplified to

$$u \frac{\partial u}{\partial x} + v \frac{\partial u}{\partial y} = v \frac{\partial^2 u}{\partial y^2} \quad (3.2.3)$$

$$\frac{\partial u}{\partial x} + \frac{\partial v}{\partial y} = 0 \quad (3.2.4)$$

where $v = \mu/\rho$ is the kinematic viscosity of the fluid. These two equations are sufficient for computing the velocity field. The use of the decoupled energy equation will be demonstrated in Section 3.3. This formulation closely describes the thin laminar boundary layer on the surface of a two-dimensional streamlined body that moves in an incompressible fluid, or in a compressible fluid but at a speed much slower than the speed of sound.

At any fixed x on the plate, three boundary conditions are needed, two for the first equation and one for the second. They are the no-slip condition at the surface and the condition of uniform flow at infinity; that is,

$$u = v = 0 \quad \text{at} \quad y = 0 \quad (3.2.5)$$

$$u \rightarrow U \quad \text{as} \quad y \rightarrow \infty \quad (3.2.6)$$

Finding a solution to the system consisting of (3.2.3) to (3.2.6) is called the *Blasius problem* (Blasius, 1908). In terms of stream function ψ defined in (2.1.14),

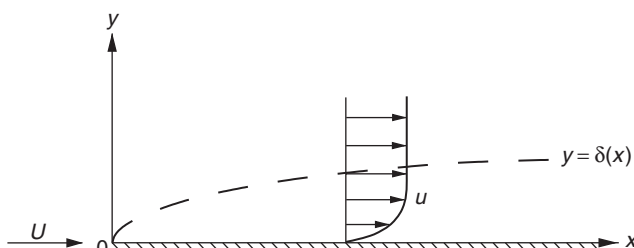


FIGURE 3.2.1 Boundary layer on a flat plate.

that is, $u = \partial\psi/\partial y$ and $v = -\partial\psi/\partial x$, (3.2.4) is satisfied automatically and (3.2.3) becomes

$$\frac{\partial\psi}{\partial y} \frac{\partial^2\psi}{\partial x \partial y} - \frac{\partial\psi}{\partial x} \frac{\partial^2\psi}{\partial y^2} = v \frac{\partial^3\psi}{\partial y^3} \quad (3.2.7)$$

Experiments show that by stretching the vertical coordinate according to the law y/\sqrt{x} , the dimensionless velocity profiles u/U measured in a laminar boundary layer at different distances x from the leading edge collapse into one. In other words, these velocity profiles are similar to one another, and the boundary layer flow is said to be *self-similar*. This evidence suggests a great simplification for our mathematical analysis of the Blasius problem. If the independent variables x and y were combined according to the stretching law just mentioned to form a new single independent variable η , we would expect that the governing partial differential equation (3.2.7) could be transformed into an ordinary differential equation and that the boundary conditions (3.2.5) and (3.2.6) would contain neither x nor y explicitly.

Let us try the following transformations, in which η is nondimensionalized and f is a dimensionless function:

$$\eta = y \left(\frac{U}{vx} \right)^{1/2} \quad (3.2.8)$$

$$\psi = (vUx)^{1/2} f(\eta) \quad (3.2.9)$$

In terms of the new variables, and with a prime denoting differentiation with respect to η , the velocity components become

$$u = Uf' \quad (3.2.10)$$

$$v = \frac{1}{2} \left(\frac{vU}{x} \right)^{1/2} (\eta f' - f) \quad (3.2.11)$$

and the governing equation becomes

$$f''' + \frac{1}{2}ff'' = 0 \quad (3.2.12)$$

with boundary conditions

$$f = f' = 0 \quad \text{at} \quad \eta = 0 \quad (3.2.13)$$

$$f' \rightarrow 1 \quad \text{as} \quad \eta \rightarrow \infty \quad (3.2.14)$$

Sure enough we have reduced our problem to solving an ordinary differential equation, although it is still a nonlinear equation. η is called the *similarity variable*, and the solution to the transformed system is called the *similarity solution* of the original formulation.

It should be pointed out that the transformations (3.2.8) and (3.2.9) are not valid at the leading edge where $x = 0$, and that x (or y) must appear on the

right-hand side of (3.2.9) if u/U is to be a function of η alone. Actually, these two transformations would also be derived if we started with the general form that $\eta = Ax^m y$ and $\psi = Bx^n f(\eta)$, and if we then required that after transformation x and y could not appear explicitly.

The solution of (3.2.12) satisfying accompanying boundary conditions was obtained by Blasius (1908) in the form of a power series expansion about $\eta = 0$ and an asymptotic expansion for $\eta \rightarrow \infty$, the two being matched at an intermediate point. Here we will find the solution using a numerical approach.

If f , f' , and f'' are all known at a certain dimensionless height η_i , the fourth-order Runge-Kutta method may be utilized to find the solution $\eta_{i+1} = \eta_i + h$ and at stations thereafter step by step. To prepare for using the method, the third-order equation (3.2.12) is first written as three first-order simultaneous equations:

$$\frac{df}{d\eta} = p, \quad \frac{dp}{d\eta} = q, \quad \frac{dq}{d\eta} = -\frac{1}{2}fq \quad (3.2.15)$$

Then the Runge-Kutta formulas (1.1.9) are applied to each of them to get

$$\begin{aligned} \Delta_1 f_i &= hp_i \\ \Delta_1 p_i &= hq_i \\ \Delta_1 q_i &= -\frac{1}{2}hf_i q_i \\ \Delta_2 f_i &= h(p_i + \frac{1}{2}\Delta_1 p_i) \\ \Delta_2 p_i &= h(q_i + \frac{1}{2}\Delta_1 q_i) \\ \Delta_2 q_i &= -\frac{1}{2}h(f_i + \frac{1}{2}\Delta_1 f_i)(q_i + \frac{1}{2}\Delta_1 q_i) \\ \Delta_3 f_i &= h(p_i + \frac{1}{2}\Delta_2 p_i) \\ \Delta_3 p_i &= h(q_i + \frac{1}{2}\Delta_2 q_i) \\ \Delta_3 q_i &= -\frac{1}{2}h(f_i + \frac{1}{2}\Delta_2 f_i)(q_i + \frac{1}{2}\Delta_2 q_i) \\ \Delta_4 f_i &= h(p_i + \Delta_3 p_i) \\ \Delta_4 p_i &= h(q_i + \Delta_3 q_i) \\ \Delta_4 q_i &= -\frac{1}{2}h(f_i + \Delta_3 f_i)(q_i + \Delta_3 q_i) \end{aligned} \quad (3.2.16)$$

Finally, the values of f , f' , and f'' are computed at η_{i+1} by analogy with (1.1.8):

$$\begin{aligned} f_{i+1} &= f_i + \frac{1}{6}(\Delta_1 f_i + 2\Delta_2 f_i + 2\Delta_3 f_i + \Delta_4 f_i) \\ p_{i+1} &= p_i + \frac{1}{6}(\Delta_1 p_i + 2\Delta_2 p_i + 2\Delta_3 p_i + \Delta_4 p_i) \\ q_{i+1} &= q_i + \frac{1}{6}(\Delta_1 q_i + 2\Delta_2 q_i + 2\Delta_3 q_i + \Delta_4 q_i) \end{aligned} \quad (3.2.17)$$

However, numerical integration of (3.2.15) cannot be started at $\eta = 0$ because q (i.e., f'') is not known there. Boundary conditions (3.2.13) and (3.2.14) provide

only two of the three values, f and p (or f'), that are required at $\eta = 0$, but provide another value of p at infinity. If the problem is to be solved by the Runge-Kutta method, it may be combined with the half-interval method already introduced in Section 1.5, as follows.

First, the boundary condition (3.2.14) at infinity is not convenient for programming, since every value specified or computed in a program must be finite. Instead of extending to infinity, we limit our range of numerical integration up to a reasonably large height η_{\max} and approximate (3.2.14) by

$$1 - p \leq \epsilon \quad \text{at} \quad \eta = \eta_{\max} \quad (3.2.18)$$

where ϵ represents a positive value much less than unity whose magnitude controls the accuracy of the solution. ϵ must be positive because p is the dimensionless parallel velocity component in the boundary layer that approaches the free-stream value of 1 from below.

At the beginning of our numerical computation a value q_0 is arbitrarily guessed and a positive increment $\Delta_1 q_0$ is picked. By letting $f = p = 0$ and $q = q_0$ at $\eta = 0$, (3.2.15) are integrated using Runge-Kutta formulas until η reaches η_{\max} . The last value of p so computed is designated p_{\max} and is represented by the leftmost point on the q_0 versus p_{\max} plot of Fig. 3.2.2. If the ordinate of this point is below the value 1, as shown, we replace the starting value q_0 of q by $q_0 + \Delta_1 q_0$ and repeat the numerical integration from $\eta = 0$. The process would be repeated again if the same final situation were encountered at η_{\max} . Suppose at the end of the third time a point above the dashed horizontal line of unit height is obtained; we know that the starting value of q is now too large. To reverse the direction, we let $\Delta_2 q_0 = -\Delta_1 q_0/2$ and then replace q_0 by $q_0 + \Delta_2 q_0$. Repeat with this negative value of $\Delta_2 q_0$ until the data point in Fig. 3.2.2 comes below the horizontal dashed line. Then we reverse the direction again by letting $\Delta_3 q_0 = -\Delta_2 q_0/2$ and

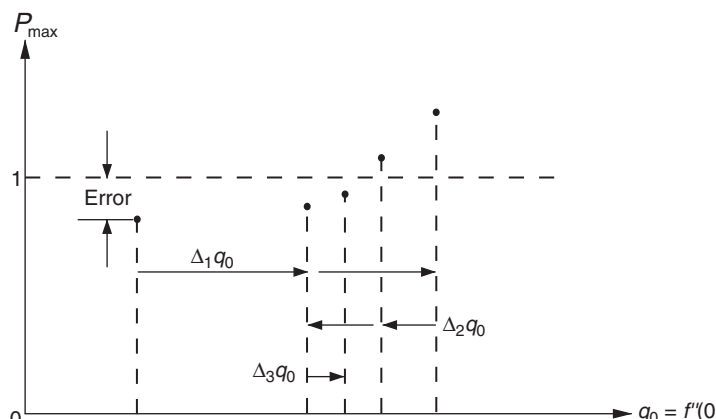


FIGURE 3.2.2 Half-interval method for the Blasius problem.

replacing q_0 by $q_0 + \Delta_3 q_0$. In programming for such computations the subscripts to Δ are actually not needed. The conclusion of this discussion is that the value of Δq_0 is to be changed to $-\Delta q_0/2$ for the next iteration either when p_{\max} is greater than 1 while Δq_0 is positive, or when p_{\max} is less than 1 while Δq_0 is negative.

At the end of each iteration we define $(1 - p_{\max})$ as the error as indicated in Fig. 3.2.2, and we check to see if error is positive and also if it is less than or equal to the assumed ε . When both are true, the approximate boundary condition (3.2.18) is satisfied, and the iterative process is terminated.

Having obtained f and its derivatives as functions of η , we can now compute the dimensionless velocity components in the boundary layer from (3.2.10) and (3.2.11):

$$\frac{u}{U} = f' \quad (3.2.19)$$

$$v \left/ \left(\frac{\nu U}{x} \right)^{1/2} \right. = \frac{1}{2}(\eta f' - f) \quad (3.2.20)$$

It is demonstrated in Program 3.1 that a boundary-value problem can be solved by using a numerical technique for solving an initial-value problem in combination with the half-interval method. This is not an efficient procedure for solving the present problem, however. An improved technique is presented later in Problem 3.1.

The tabulated numerical result (Table 3.A.1) agrees with that obtained by Howarth (1938) using series expansion to integrate the boundary layer equations. Solutions of higher accuracy can easily be computed by reducing both the value of ϵ and the size of h . The curve showing the variation of u/U in the boundary layer would coincide very well with Nikuradse's measured data points if they were also plotted. See Fig. 7.9 of Schlichting (1968).

Solution shows that the parallel velocity component u approaches the free-stream value following a smooth curve; thus, the edge of a boundary layer is actually an artificial terminology. If the boundary layer thickness δ is defined as the height where $u = 0.994 U$, which occurs around $\eta = 5.2$, we have

$$\delta = 5.2 \left(\frac{\nu x}{U} \right)^{1/2} \quad (3.2.21)$$

The edge of the boundary layer is therefore represented by a parabola, as sketched in Fig. 3.2.1.

Figure 3.2.3 displays the interesting phenomenon that the normal velocity component approaches a constant value when going away from the plate into the free stream. This may be explained by reasoning that the retardation of flow speed by viscosity causes a negative $\partial u / \partial x$ in the boundary layer, with which a positive $\partial v / \partial y$ is associated in virtue of the continuity equation. Integration of $\partial v / \partial y$ across the boundary layer results in a finite v in the region far above the plate. Thus, the presence of a thin plate can be detected, theoretically, by

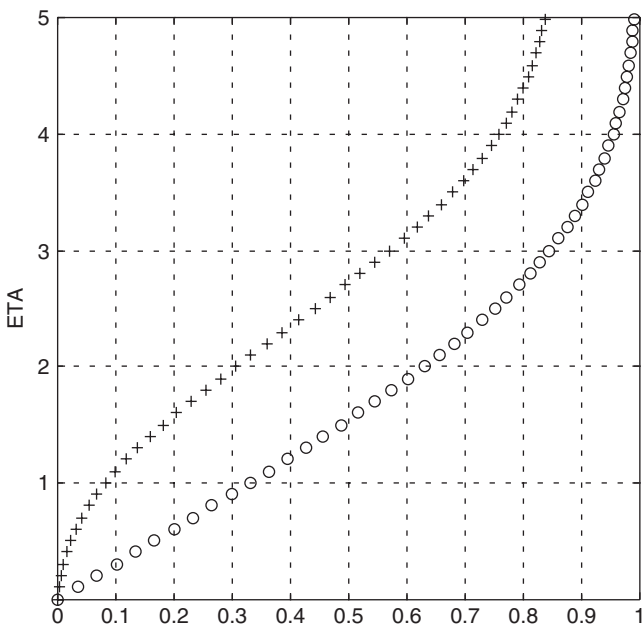


FIGURE 3.2.3 Distribution of dimensionless velocity components. +, V ; \circ , U .

a person right above it by measuring the upcoming velocity component. Notice that the dimensionless velocity components plotted in Fig. 3.2.3 are not based on the same reference velocities. If plotted in dimensional form v would be much smaller than u . That v is finite at infinity clarifies why only the parallel velocity component is specified in the boundary condition (3.2.6) away from the plate.

Let us consider a specific numerical example of an air flow traveling at 30 m/s. At sea level the kinematic viscosity of air is $\nu = 1.49 \times 10^{-5}$ m²/s. At a station 1 m downstream from the leading edge of an aligned plate, the boundary-layer thickness is 0.37 cm according to (3.2.21), and the normal velocity far above the plate is 0.018 m/s according to (3.2.20), which is a negligibly small fraction of the free-stream speed. The Reynolds number at that station based on the distance from the leading edge is Ux/ν , or 2.01×10^6 . A large Reynolds number is a requirement for the validation of the boundary-layer theory.

The shear stress in the fluid is

$$\tau = \mu \frac{\partial u}{\partial y} = \mu U \left(\frac{U}{\nu x} \right)^{1/2} f'' \quad (3.2.22)$$

Thus, f'' describes the dimensionless shear stress distribution in the boundary layer, and the particular value of f'' at $\eta = 0$, which is the q_0 we looked for using half-interval method in Program 3.1, represents the dimensionless shear stress on the flat plate.

Problem 3.1 Program 3.1 shows that 31 iterations are needed to obtain a solution having the desired accuracy, and most of the computational effort has been wasted in the trial-and-error process. The reason for following such a time-consuming scheme is that f'' is not given at the beginning of the numerical integration.

A better method can be derived for finding f'' at $\eta = 0$. Let us introduce a linear transformation for the independent variable, $\eta = kz$, where k is a constant to be determined; in the meantime, we introduce a function g such that $f(\eta) = g(z)/k$. It can easily be verified that

$$\frac{d^n f}{d\eta^n} = \frac{1}{k^{n+1}} \frac{d^n g}{dz^n} \quad \text{for } n \geq 1 \quad (3.2.23)$$

If a prime is used to denote differentiation with respect to the argument, the foregoing relations transform the system consisting of (3.2.12) to (3.2.14) into

$$g''' + \frac{1}{2}gg'' = 0 \quad (3.2.24)$$

$$g = g' = 0 \quad \text{at } z = 0 \quad (3.2.25)$$

$$g' \rightarrow k^2 \quad \text{as } z \rightarrow \infty \quad (3.2.26)$$

Since k is arbitrary and appears only in the condition at infinity, there is no restriction on the magnitude of g'' at the plate. Let us choose a convenient value of unity for $g''(0)$:

$$g'' = 1 \quad \text{at } z = 0 \quad (3.2.27)$$

This assumed condition transforms, according to (3.2.23), into

$$f'' = k^{-3} \quad \text{at } \eta = 0 \quad (3.2.28)$$

Write a computer program for integration of (3.2.24) starting at $z = 0$ with the prescribed initial conditions (3.2.25) and (3.2.27) up to a reasonably large value of z . The value of k is calculated by taking the square root of the last value of g' according to (3.2.26). The solution is obtained by using the transformations $f(\eta) = g(z)/k$ and $\eta = kz$.

However, if the solution for f is to be evaluated only at specific locations separated by $\Delta\eta$, an alternative procedure may be followed. Now f'' at $\eta = 0$ becomes known after substitution of k into (3.2.28). This value, together with $f = f' = 0$ at $\eta = 0$, enables us to integrate (3.2.12) immediately, and the solution will automatically satisfy the boundary condition (3.2.14) far away from the plate.

Problem 3.2 Injection or suction of fluid through the body surface is one of the techniques used to alter the structure of the boundary layer along a body. As a consequence, the drag of the body and the heat exchange rate between the body and the surrounding fluid are modified and, furthermore, the boundary-layer flow may be made to separate or attach to the body surface. A boundary-layer

flow in the presence of injection may become self-similar if the injection speed is properly distributed. As mentioned before, a flow is called self-similar if both the governing equation and the boundary conditions can be transformed into such a form that there is only one similarity parameter as the sole independent variable. Suppose a *uniform* flow is injected into the boundary layer from Blasius' semi-infinite plate. Using the transformations (3.2.8) and (3.2.9), we still obtain the same ordinary differential equation (3.2.12). However, the boundary condition that v be a constant on the plate transforms into one containing x explicitly. It implies mathematically that a solution cannot be found containing η alone and, physically, that the velocity profiles measured at different stations along the plate can no longer be collapsed into one profile no matter how the y -axis is stretched. In this case a similarity solution does not exist and the flow is not self-similar.

Now, if the injection speed v_0 is a function of the distance from the leading edge and is described by the law

$$v_0 = C \left(\frac{vU}{x} \right)^{1/2} \quad (3.2.29)$$

where C is a constant (Fig. 3.2.4), then the transformed boundary conditions at the plate become, in virtue of (3.2.20),

$$f' = 0 \quad \text{and} \quad f = -2C \quad \text{at} \quad \eta = 0 \quad (3.2.30)$$

The governing equation and the boundary condition at infinity remain the same form as (3.2.12) and (3.2.14), respectively. In this case we have found another self-similar flow. The dimensionless injection speed C is used to control the strength and direction of the normal flow. Positive and negative C imply injection and suction, respectively.

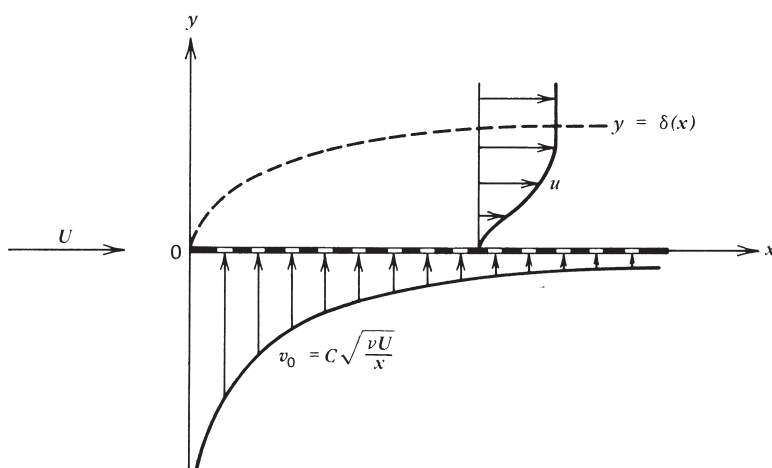


FIGURE 3.2.4 Flat plate with injection of speed v_0 .

To study the effects of injection and suction on velocity profile, boundary-layer thickness, and shear stress, write a program and then run it for C varying from -0.6 to $+0.6$ at intervals of size 0.1 .

From the printed data estimate the boundary layer thickness δ . What is the conclusion after plotting δ and $f''(0)$ as functions of C , and what is the physical interpretation when $f''(0)$ vanishes? Explain why difficulties develop in the computation if a value of C greater than 0.6 is assigned. The result will show that for any positive C an inflection point exists in the velocity profile at which $\partial^2 u / \partial y^2 = 0$ or, equivalently, $f''' = 0$. Such a velocity profile would have a general appearance of the one sketched in Fig. 3.2.4. The presence of an inflection point in the profile is an indication of flow instability (Lin, 1955, Section 4.3), and turbulence is expected to develop in the boundary layer when fluid is injected from the plate.

The transformation described in Problem 3.1 does not work for the problem at hand, because the undetermined constant k appears in one of the boundary conditions at the plate as well as in the condition at infinity, and therefore $g''(0)$ can no longer be chosen arbitrarily.

When the half-interval method is used to find $f''(0)$, the algorithm must be modified from that used previously in Program 3.1. For the Blasius problem we assume in Fig. 3.2.2 (correctly by a mere coincidence) that p_{\max} increases with increasing q_0 . This is not always true, however. To insure that any arbitrary situation can be handled, the following technique is suggested. If at the end of a certain iteration the difference $(1 - p_{\max})$ is computed and is named error, let the difference evaluated in the previous iteration be called error'. By examining every possible situation, you may conclude that the half-interval method is used (i.e., to replace Δq_0 by $-\Delta q_0/2$) when either the product (error)(error') or the difference $|\text{error}'| - |\text{error}|$ becomes negative.

Problem 3.3 A class of self-similar boundary-layer flows in the presence of a pressure gradient was found by Falkner and Skan (1930). If the flow parallel to a semi-infinite flat plate outside the boundary layer is given by

$$U(x) = U_0 x^m \quad (3.2.31)$$

the pressure gradient along the plate can be computed from Euler's equation so that

$$\frac{\partial p}{\partial x} = -m \rho U_0^2 x^{2m-1} \quad (3.2.32)$$

In a region of decreasing pressure along the flow direction, the net pressure force acting on a fluid element tends to accelerate it; the pressure gradient is called a favorable one. In a region in which pressure increases along the flow direction, it is called an adverse pressure gradient. Equation (3.2.32) states that the pressure gradient on the flat plate can be made either favorable or adverse by assigning either positive or negative values to m . With positive values of m , (3.2.31) represents a realistic two-dimensional potential flow at the surface of

a wedge of wedge angle $2m\pi/(m+1)$ placed symmetrically in an originally uniform stream. Negative values of m correspond to flow over a flat plate that is inclined away from the flow far upstream, although it is nonrealistic at $x = 0$ where flow speed becomes unbounded.

Adding the missing term $\rho^{-1}\partial p/\partial x$ on the right side of (3.2.3) and using the transformations that

$$\eta = y \left(\frac{m+1}{2} \frac{U_0}{v} x^{m-1} \right)^{1/2} \quad (3.2.33)$$

$$\psi = \left(\frac{2vU_0}{m+1} x^{m+1} \right)^{1/2} f(\eta) \quad (3.2.34)$$

one can show that the resulting governing equation is

$$f''' + ff'' + \frac{2m}{m+1}(1-f'^2) = 0 \quad (3.2.35)$$

and the boundary conditions are exactly the same as those for Blasius problem, namely, (3.2.13) and (3.2.14).

Construct a computer program for solving the Falkner-Skan problem. Obtain solutions for $m = 0, 0.5$, and 1.0 and then for $m = -0.05$ and -0.09 . The inflection point shows in the dimensionless velocity profiles $f' (= u/U)$ for negative values of m . Note that $f''(0)$ is nearly zero when $m = -0.0904$.

3.3 FLAT-PLATE THERMOMETER PROBLEM – ORDINARY BOUNDARY-VALUE PROBLEMS INVOLVING DERIVATIVE BOUNDARY CONDITIONS

Let us consider the energy aspect of the boundary-layer flow over a flat plate. Converted from the work done by frictional forces, heat is generated within the boundary layer. This heat is diffused away from a fluid element by thermal conductivity and, at the same time, is convected downstream by the fluid motion. If the flat plate is originally at the same temperature as that of the fluid far upstream, it will be heated up and its surface temperature will finally approach a constant value when a steady state is reached; under a steady state there is no heat transfer from the fluid to the wall, or $(\partial T/\partial y)_{y=0} = 0$. The steady-state temperature, T_w , of the equivalently insulated plate is called the *adiabatic* or *recovery temperature*. Because in a boundary layer fluid particles decelerate through an irreversible process, the temperature T_w at the wall where velocity is zero is generally not the stagnation temperature of the free stream. Furthermore, the variation of temperature from T_w at the plate to T_1 in the free stream takes place within a short distance, forming a thermal boundary layer in addition to the velocity boundary layer on the plate.

If the structure of the thermal boundary layer is known, the flat plate just described will serve the purpose of a thermometer when mounted on a moving

body such as a flying aircraft, because then the ambient temperature T_1 can be calculated from T_w measured on the plate. For low speeds the density and physical properties of the fluid may be treated as constants. In addition, we postulate that the thermal boundary layer is also thin and its behavior is similar to that of the velocity boundary layer, so that $\partial T/\partial x \ll \partial T/\partial y$. In the absence of a pressure gradient, the governing boundary-layer equations at steady state are

$$\frac{\partial u}{\partial x} + \frac{\partial v}{\partial y} = 0 \quad (3.3.1)$$

$$u \frac{\partial u}{\partial x} + v \frac{\partial u}{\partial y} = v \frac{\partial^2 u}{\partial y^2} \quad (3.3.2)$$

$$\rho c_p \left(u \frac{\partial T}{\partial x} + v \frac{\partial T}{\partial y} \right) = k \frac{\partial^2 T}{\partial y^2} + \mu \left(\frac{\partial u}{\partial y} \right)^2 \quad (3.3.3)$$

The boundary conditions for velocity and temperature fields are

$$u = v = \frac{\partial T}{\partial y} = 0 \quad \text{at} \quad y = 0 \quad (3.3.4)$$

$$u \rightarrow U, \quad T \rightarrow T_1 \quad \text{as} \quad y \rightarrow \infty \quad (3.3.5)$$

As already mentioned at the end of Section 3.1, the assumption of incompressibility decouples the energy equation from continuity and momentum equations. To solve the energy equation we first obtain expressions for velocity components from the Blasius solution, which is the solution to simultaneous equations (3.3.1) and (3.3.2), subject to their three boundary conditions stated in (3.3.4) and (3.3.5). Substituting u and v into (3.3.3) in terms of the similarity variables η and f , and introducing a dimensionless temperature difference $\theta(\eta)$ defined by

$$\theta = \frac{T - T_1}{U^2/2c_p} \quad (3.3.6)$$

we obtain

$$\frac{d^2\theta}{d\eta^2} + \frac{1}{2}\text{Pr} f \frac{d\theta}{d\eta} = -2\text{Pr}(f'')^2 \quad (3.3.7)$$

where $\text{Pr} = \mu c_p/k$ is the Prandtl number. The transformed boundary conditions are

$$\frac{d\theta}{d\eta} = 0 \quad \text{at} \quad \eta = 0 \quad (3.3.8)$$

$$\theta \rightarrow 0 \quad \text{as} \quad \eta \rightarrow \infty \quad (3.3.9)$$

The result shows that the temperature field is also self-similar.

We now have a boundary-value problem consisting of a second-order ordinary differential equation, whose coefficients contain tabulated functions f and f'' , and two boundary conditions specified across the boundary layer. The solution could

be obtained using the Runge-Kutta method again by guessing the starting value of θ at $\eta = 0$ and then modifying it following the interval-halving technique used in solving the Blasius problem. In so doing the boundary-value problem is treated as if it were an initial-value problem. Here we prefer to solve the problem using the numerical method developed in Section 2.2 for boundary-value problems, which is to be modified to handle the derivative boundary condition involved in this case.

Once more, a reasonably large η_{\max} is chosen to approximate infinity so that the condition (3.3.9) becomes

$$\theta = 0 \quad \text{at} \quad \eta = \eta_{\max} \quad (3.3.10)$$

We let the range between 0 and η_{\max} of the independent variable be divided into n equally spaced intervals of size h , and name the end points consecutively $\eta_1, \eta_2, \dots, \eta_{n+1}$, starting at the lower end. To represent the present problem in Fig. 2.2.1, x in that figure is to be replaced by η and f by θ . Recall that the original figure was used to describe a boundary-value problem with f known at the ends x_0 and x_{n+1} of the physical space, and that range of x was divided into $n + 1$ intervals of size h . When the same figure is used for the present case with a derivative boundary condition at $\eta = 0$, the physical space, divided into n intervals, is contained between η_1 and η_{n+1} , and η_0 becomes a fictitious point at a distance h to the left of η_1 .

Comparing the differential equation (3.3.7) with the standard form (2.2.1), we obtain $A = \frac{1}{2}\Pr f$, $B = 0$, and $D = -2\Pr(f'')^2$. Their known values at η_i enable us to evaluate the coefficients C_{i1}, C_{i2}, C_{i3} , and C_{i4} from (2.2.11). When the finite-difference equation (2.2.10), used to replace the original differential equation, is applied at η_n it becomes

$$C_{n1}\theta_{n-1} + C_{n2}\theta_n + C_{n3}\theta_{n+1} = C_{n4}$$

in which the third term is known from the boundary condition at η_{\max} . This boundary condition is incorporated in the numerical scheme, as already shown in Section 2.2 by the following assignments:

$$C_{n4} \leftarrow (C_{n4} - C_{n3}\theta_{n+1}) \quad (3.3.11)$$

$$C_{n3} \leftarrow 0 \quad (3.3.12)$$

Applying (2.2.10) at η_1 gives

$$C_{11}\theta_0 + C_{12}\theta_1 + C_{13}\theta_2 = C_{14}$$

where θ_0 at the fictitious point is not prescribed but, instead, its value can be related to those at some interior points through the boundary condition at $\eta = 0$. After replacing $d\theta/d\eta$ by the central-difference approximation (2.2.8), (3.3.8) states that $\theta_0 = \theta_2$, so that this derivative boundary condition is incorporated by the following assignments:

$$C_{13} \leftarrow (C_{11} + C_{13}) \quad (3.3.13)$$

$$C_{11} \leftarrow 0 \quad (3.3.14)$$

Having modified four of the coefficients C_{ij} according to (3.3.11) to (3.3.14), we can compute the solution $\theta_1, \theta_2, \dots, \theta_n$ by solving n simultaneous equations arranged in the tridiagonal matrix form of (2.2.13) with the help of subroutine TRID, which was constructed in Section 2.3 for this particular purpose.

In Program 3.2 the functions f and f'' are first computed. Starting with the value $f''(0) = 0.3320572$ taken from the result of Program 3.1, these functions are obtained immediately after integrating (3.2.12) from $\eta = 0$ to $\eta = \eta_{\max}$. Here $\eta_{\max} = 10$ is still used in order to be consistent with Program 3.1.

Three cases are considered for three different fluid media—water, air, and mercury—whose Prandtl numbers are 6.750, 0.714, and 0.044, respectively. The variable names used in Program 3.2 in connection with the Blasius solution are exactly the same as those in Program 3.1.

The numerical value of θ at $\eta = 0$ has a special physical meaning. Consider for the moment a steady isentropic flow. In the absence of viscosity and conductivity, by combining the energy equation (3.1.3) with an equation resulting from the dot product of velocity vector and the momentum equation (3.1.2), we obtain a simple energy relation: the sum of enthalpy and kinetic energy per unit mass is constant following a fluid particle; that is,

$$c_p T + \frac{1}{2} V^2 = \text{constant along a streamline} \quad (3.3.15)$$

If a fluid particle, originally in the free stream of temperature T_1 and speed U , were decelerated isentropically to zero speed at the surface of a plate where its temperature rose to $(T_w)_{\text{isen}}$, which is, in fact, the stagnation temperature of the flow, according to (3.3.15), the total energy per unit mass of the fluid at the wall would be the same as that in the free stream of magnitude

$$c_p (T_w)_{\text{isen}} = c_p T_1 + \frac{1}{2} U^2 \quad (3.3.16)$$

It shows that the kinetic energy would be fully recovered at the wall after an isentropic deceleration. In a real fluid with nonvanishing k and μ , however, the fluid temperature at the surface is T_w and the total energy per unit mass there becomes, according to (3.3.6),

$$c_p T_w = c_p T_1 + \theta(0) \cdot \frac{1}{2} U^2 \quad (3.3.17)$$

The interpretation is that when a free-stream fluid particle slows down through an irreversible process in the boundary layer and finally becomes stationary at the wall, $\theta(0)$ times its original kinetic energy is recovered there and is converted into thermal energy. $\theta(0)$ is therefore called the *recovery factor*.

Program 3.2 reveals that the recovery factor is less than unity for air and mercury, whose Prandtl numbers are below 1, and it is greater than unity for water, whose Prandtl number is above 1. A sketchy explanation of this phenomenon

is that for a fluid with a smaller Prandtl number, the thermal conductivity is relatively large; more heat is conducted out of a fluid element than is produced within it by friction, so that its energy becomes lower. The opposite is true for a fluid of larger Prandtl number, and the energy of a fluid particle at the wall may become higher than that outside of the boundary layer.

What would happen to the wall temperature if the Prandtl number of the fluid were unity? When this value is used in Program 3.2, its output gives a rounded figure $\theta(0) = 1$. In this particular case the energy and temperature at the wall are equal to the energy and stagnation temperature of the free stream, respectively, even if the transition has gone through an irreversible process. Following the preceding reasoning, it may be said that for $\text{Pr} = 1$, the heat produced just balances the heat diffused away.

You may verify by using Program 3.2 that $\theta(0)$ approximately equals $\sqrt{\text{Pr}}$ for Prandtl numbers in the neighborhood of unity. The present result for air is a good example. This agrees with the conclusion obtained by Pohlhausen (1921). The numerical result of Program 3.2 shows that the thermal boundary-layer thickness increases with decreasing Prandtl number due to the increased conductivity (Table 3.A.2). The height $\eta_{\max} = 10$ is barely enough in the computation for air, but is definitely not sufficient for mercury. The accuracy for these two cases can be improved by choosing a larger η_{\max} .

Problem 3.4 We have seen that the total fluid energy at the wall may be lower or higher than that in the free stream, depending on whether the Prandtl number is less than or greater than unity. One may compute to find out how the total energy is distributed across the boundary layer when either of the two situations occurs.

Let H denote the total energy or the total enthalpy of the fluid per unit mass, which is the sum of specific enthalpy and kinetic energy per unit mass. H_1 in the free stream has the magnitude given by (3.3.16). In a boundary layer the enthalpy can be expressed in terms of free-stream conditions and θ through (3.3.6), and the kinetic energy is contributed mainly from the motion parallel to the plate. Thus, in the boundary layer on an aligned, semi-infinite flat plate, the total energy is

$$\begin{aligned} H &= (c_p T_1 + \frac{1}{2} U^2 \theta) + \frac{1}{2} u^2 \\ &= c_p T_1 + \frac{1}{2} U^2 (\theta + f'^2) \end{aligned}$$

A dimensionless energy difference may be defined as

$$\frac{H - H_1}{U^2/2} = \theta + f'^2 - 1$$

Plot this quantity as a function of η for water, air, and mercury, and then give a physical interpretation of the result.

Problem 3.5 Consider a layer of fluid around an infinitely long circular cylinder of radius r_b . Radial gravitational forces hold the fluid in a state of static equilibrium, forming a free surface of radius r_a , as shown in Fig. 3.3.1. The fluid has a constant density ρ and viscosity coefficient μ . When the cylinder is given a rotational motion about its axis, a fluid motion v_θ is induced in the azimuthal direction. The θ component of the Navier-Stokes equation in cylindrical coordinates is (from Hughes and Gaylord, 1964, p. 25)

$$\begin{aligned} \rho \left(\frac{\partial v_\theta}{\partial t} + v_r \frac{\partial v_\theta}{\partial r} + \frac{v_\theta}{r} \frac{\partial v_\theta}{\partial \theta} + v_z \frac{\partial v_\theta}{\partial z} + \frac{v_r v_\theta}{r} \right) \\ = -\frac{1}{r} \frac{\partial p}{\partial \theta} + \mu \left(\frac{\partial^2 v_\theta}{\partial r^2} + \frac{1}{r} \frac{\partial v_\theta}{\partial r} + \frac{1}{r^2} \frac{\partial^2 v_\theta}{\partial \theta^2} + \frac{\partial^2 v_\theta}{\partial z^2} + \frac{2}{r^2} \frac{\partial v_r}{\partial \theta} - \frac{v_\theta}{r^2} \right) \end{aligned} \quad (3.3.18)$$

Because of the axisymmetry of the flow on the r - θ plane, derivatives with respect to θ and z are all zero, and there are no motions in radial and axial directions. When a steady state is reached, all terms in (3.3.18) vanish, except the first two and the last one in the parentheses on the right-hand side.

If the constant tangential speed at the surface of the cylinder is v_b , we may introduce a dimensionless radial distance $R = r/r_b$ and a dimensionless speed $V = v_\theta/v_b$, so that the resultant equation becomes

$$\frac{d^2 V}{dR^2} + \frac{1}{R} \frac{dV}{dR} - \frac{V}{R^2} = 0 \quad (3.3.19)$$

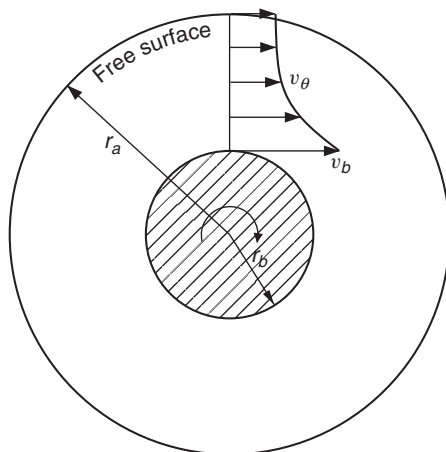


FIGURE 3.3.1 Fluid motion around a rotating cylinder.

The boundary conditions are, with R_a representing r_a/r_b ,

$$V = 1 \quad \text{at} \quad R = 1 \quad (3.3.20)$$

$$\frac{dV}{dR} = 0 \quad \text{at} \quad R = R_a \quad (3.3.21)$$

The second condition simply states that shear stress must vanish at the free surface. If such a stress did exist, no tangential force could be generated above the free surface to balance it, and the equilibrium condition could never be attained.

Divide the fluid region into 50 equally spaced radial intervals and find the velocity distribution for $R_a = 2$ by use of the subroutine TRID. Compute local percent errors from the exact solution that

$$V = \frac{R_a}{1 + R_a^2} \left(\frac{R}{R_a} + \frac{R_a}{R} \right) \quad (3.3.22)$$

Notice that if a diagram similar to Fig. 2.2.1 is constructed, the fluid region should be contained between R_0 and R_n , leaving R_{n+1} as a fictitious point to handle the derivative boundary condition at the free surface.

It is interesting to see that, from (3.3.22) or the numerical result, the fluid layer will not rotate with the cylinder like a solid body under the steady state. This result analogously explains why, even in the absence of differential solar heating and many other factors, our atmosphere can never achieve a solid-body rotation with the earth.

3.4 PIPE AND OPEN-CHANNEL FLOWS

With properly chosen geometries, the equations governing some viscous flows may become linearized. One example is given by Problem 3.5 in the preceding section; it concerns the angular motion of fluid between two concentric circles. In this section a class of flows is considered whose governing equation is linear but involves two independent variables.

We consider the general problem of steady incompressible flow through a straight pipe of uniform but arbitrary cross section. The flow may be caused by either an applied pressure gradient, the gravitational force, the motion of a part of the pipe wall relative to the rest, or any combination of these factors. The flow may be enclosed by a rigid wall or it may have a free surface. Moreover, the flow may contain multiply connected regions formed by axial inner tubes.

Let the infinitely long pipe be parallel to the x -axis along which $\partial \mathbf{V}/\partial x = 0$. Because of this particular geometry, the flow has only one nonvanishing velocity component u in the axial direction, so that the continuity equation (3.1.6) is satisfied automatically and the nonlinear terms on the left side of momentum

equation (3.1.7) disappear. There is only one equation governing u of the form

$$\frac{\partial^2 u}{\partial y^2} + \frac{\partial^2 u}{\partial z^2} = \frac{1}{\mu} \left(\frac{dp}{dx} - f_x \right) \quad (3.4.1)$$

where the x component of the gravitational force per unit volume, f_x , has been added. It turns out that we have a Poisson equation to which the iteration methods developed in Section 2.8 apply.

If $f_x = 0$ and the pipe cross section is circular, (3.4.1) describes the classical problem of the *Poiseuille flow*, whose analytical solution can be obtained immediately. Although (3.4.1) is a linear equation, to find its analytical solution satisfying a set of arbitrary boundary conditions is still a difficult task. Numerical solution of (3.4.1) is generally required except for a few cases in which the cross-sectional shape can be described by some simple geometries.

As an illustrative example for solving this class of problems, we consider a tilted open channel of square cross section making an angle θ with the horizontal (Fig. 3.4.1). The x axis is still chosen to be parallel to the channel, and the angle θ is assumed to be so small that the free surface is everywhere parallel to the channel base. Since there is no applied pressure gradient along the channel, the only forcing function on the right side of (3.4.1) is that due to $f_x = \rho g \sin \theta$, g being the gravitational acceleration. With the introduction of dimensionless variables

$$Y = \frac{y}{L}, \quad Z = \frac{z}{L}, \quad U = \frac{u}{L^2 \rho g \sin \theta / \mu} \quad (3.4.2)$$

where L is the width or height of the square cross section, (3.4.1) becomes

$$\frac{\partial^2 U}{\partial Y^2} + \frac{\partial^2 U}{\partial Z^2} = -1 \quad (3.4.3)$$

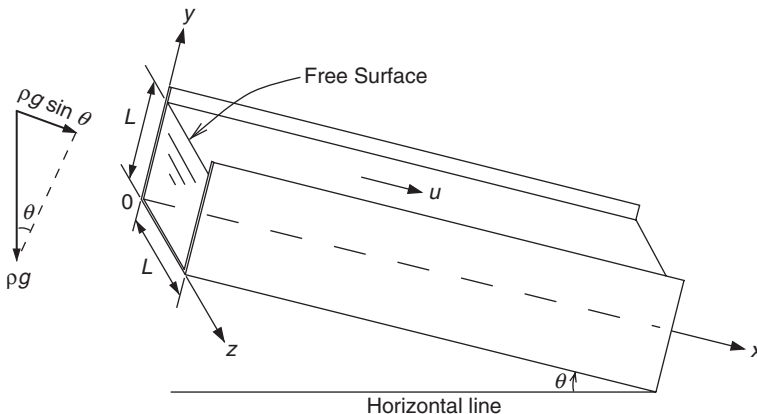


FIGURE 3.4.1 An open-channel flow.

Boundary conditions require that velocity vanishes at solid walls and shear stress is zero at the free surface, or, mathematically,

$$U = 0 \quad \text{at} \quad Y = 0 \quad \text{and at} \quad Z = 0 \text{ and } 1 \quad (3.4.4)$$

$$\frac{\partial U}{\partial Y} = 0 \quad \text{at} \quad Y = 1 \quad (3.4.5)$$

For a numerical solution a square grid system is set up to cover the region occupied by the fluid in the Y - Z plane. With the grid size $h = 0.05$, we obtain $21 (= m)$ vertical grid lines and $21 (= n)$ horizontal grid lines. Because of the derivative boundary condition (3.4.5), a fictitious horizontal line is needed at a distance h above the free surface. Comparing (3.4.3) with the generalized form (2.8.1) of the Poisson equation, we can write down its finite-difference computational scheme based on the successive overrelaxation formula (2.8.13):

$$U_{i,j} = (1 - \omega)U_{i,j} + \frac{\omega}{4} (U_{i-1,j} + U_{i+1,j} + U_{i,j-1} + U_{i,j+1} + h^2) \quad (3.4.6)$$

Here the superscripts used in (2.8.13) to indicate the number of iterations are omitted; they are not needed if in each iteration (3.4.6) is applied successively at interior points starting from the lower left corner of the grid. The optimum value for the relaxation parameter ω is determined according to (2.8.14).

In index notation the boundary conditions (3.4.4) become

$$U_{i,1} = 0, \quad i = 1, 2, \dots, m \quad (3.4.7)$$

$$U_{1,j} = U_{m,j} = 0, \quad j = 1, 2, \dots, n \quad (3.4.8)$$

After replacing the derivative in (3.4.5) by its central-difference approximation, the derivative boundary condition is reduced to

$$U_{i,n+1} = U_{i,n-1}, \quad i = 2, 3, \dots, m - 1 \quad (3.4.9)$$

In the program to follow the conditions (3.4.7) and (3.4.8) are assigned at the beginning and are kept the same for all iterations, while (3.4.9) is used in the computation of (3.4.6) in every iteration whenever j reaches the value n .

Knowing the velocity distribution across a section, we can calculate the volume of fluid passing through the channel per unit time. Let the solid lines in Fig. 3.4.2 represent schematically the grid system covering the channel cross section. Dashed vertical and horizontal lines are then drawn to bisect the solid-line square meshes.

At each of the grid points marked at the intersections of solid lines, the dimensionless velocity U is either given or computed. These points may be grouped into three categories according to their locations: the interior points, the boundary points, and the corner points, as indicated in Fig. 3.4.2. For small mesh sizes we may assume that the velocity in the shaded area containing a grid point is approximately the same as that at the point itself. As shown in the figure, the shaded small area for an interior point is of magnitude h^2 , that for a boundary

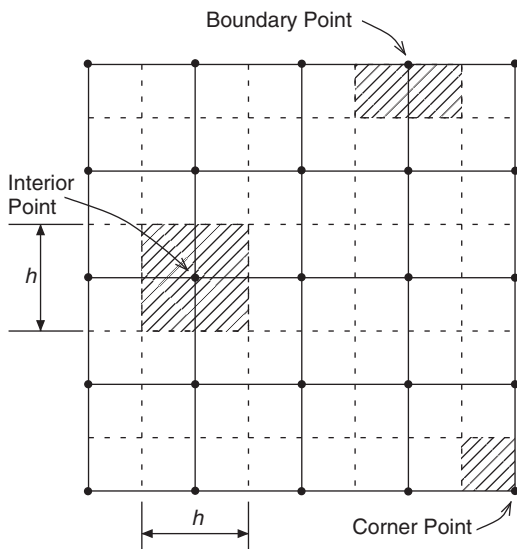


FIGURE 3.4.2 Evaluation of volume flow rate.

point is $h^2/2$, and that for a corner point is $h^2/4$. The volume flow rate is calculated approximately by summing the products of local velocity and area at all grid points.

In the output of Program 3.3 some of the numerical values of U are tabulated (Table 3.A.3) and, in addition, velocity contours are plotted in Fig. 3.4.3. Variables used in this program are named according to their original forms; the name VOLRAT is used for the volume flow rate.

The result shows that the maximum velocity occurs at the middle of the free surface having the magnitude $0.114 L^2 \rho g \sin \theta / \mu$, and the volume flow rate is $0.0569 L^4 \rho g \sin \theta / \mu$. It is interesting to compare this result with the analytical result obtained for the same free-surface flow with the two side walls removed. The velocity profile and volume flow rate in such a channel of width L are, from Batchelor (1967, p. 183), expressed in our notation,

$$u = \frac{\rho g \sin \theta}{2\mu} y(2L - y) \quad (3.4.10)$$

$$Q = \frac{\rho g \sin \theta}{3\mu} L^4 \quad (3.4.11)$$

The maximum velocity at the free surface is then $0.5 L^2 \rho g \sin \theta / \mu$, which is 4.4 times the value in the presence of two side walls separated by a distance equal to the fluid depth, and the flow rate becomes 5 times bigger. The comparison reveals that the side walls have a tremendous retardative effect on channel flows.

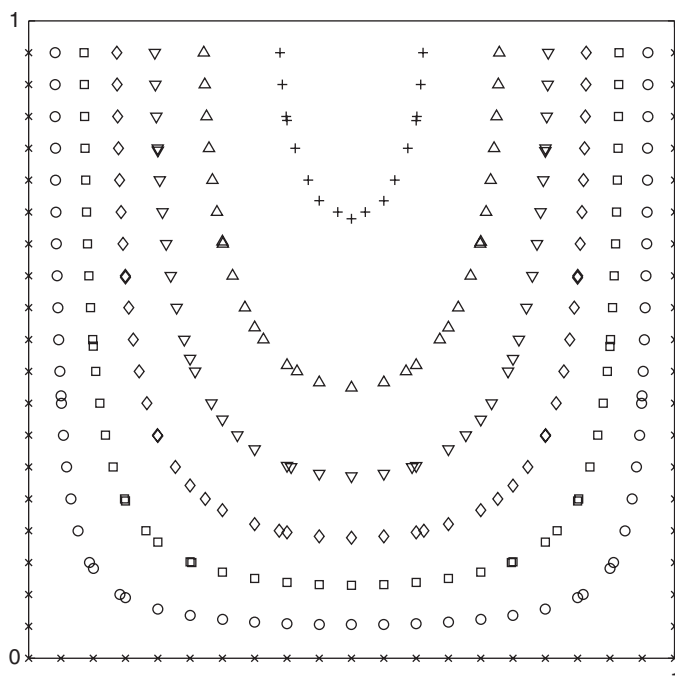


FIGURE 3.4.3 Velocity distribution across an open channel of square cross section. \times , $U = 0$; \circ , $U = 0.018$; \square , $U = 0.036$; \diamond , $U = 0.054$; ∇ , $U = 0.072$; Δ , $U = 0.09$; $+$, $U = 0.108$.

Problem 3.6 Consider a channel with a square cross section of area L^2 having a movable upper wall. Find the velocity distribution and the volume flow rate of the steady flow caused by moving the upper wall at a constant velocity u_0 in the direction parallel to the channel length.

Assume that the gaps between the moving and the stationary side walls are smaller than the grid width h . The boundary condition on the uppermost grid line is that the velocity is u_0 at all grid points except those at the corners, where the velocity is zero.

Problem 3.7 Solve the problem in which the upper movable wall described in Problem 3.6 is replaced by one of width $L/2$, leaving the uncovered portion of the leveled upper fluid surface free. Study the variation of flow rate with the horizontal position of the upper plate whose axial velocity is kept at the same value u_0 .

Project for Further Study: A steady flow is established in a long pipe after a constant pressure gradient dp/dx has been applied along the axis for a long time. Compute the velocity distribution and the volume flow rate of an incompressible fluid in pipes of the cross-sectional shapes described in Fig. 3.4.4.

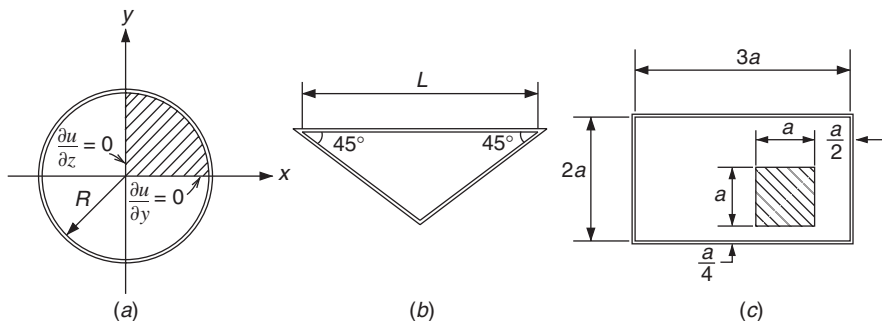


FIGURE 3.4.4 Various tube cross sections.

1. A circular tube of radius R . From symmetry only the first quadrant is needed for the numerical computation. The boundary conditions at the two straight edges of the fan-shaped domain are that the variations of velocity normal to the edges are zero. To handle the curved boundary, the method of Program 2.7 may be used.

Compare the numerical result with the analytical solution for Poiseuille flow (Batchelor, 1967, p. 180) that

$$u = -\frac{1}{4\mu} \frac{dp}{dx} (R^2 - r^2)$$

$$Q = -\frac{\pi R^4}{8\mu} \frac{dp}{dx}$$

2. A triangular tube whose two slant walls make 45° angles with the third.
3. A rectangular tube containing a square inner tube.

3.5 EXPLICIT METHODS FOR SOLVING PARABOLIC PARTIAL DIFFERENTIAL EQUATIONS – GENERALIZED RAYLEIGH PROBLEM

In studying the development of a boundary layer on a body moving through an incompressible fluid, Rayleigh (1911) considered the unsteady motion of an infinitely extended fluid in response to an infinite flat plate suddenly set in motion along its own plane. If the plate is normal to the y axis and the motion is in the x direction, the continuity equation (3.1.6) is satisfied automatically and the incompressible Navier-Stokes equation (3.1.7) is simplified to

$$\frac{\partial u}{\partial t} = \nu \frac{\partial^2 u}{\partial y^2} \quad (3.5.1)$$

Sometimes this equation, governing arbitrary unsteady planar fluid motions, is expressed in terms of vorticity $\zeta (= -\partial u / \partial y)$ in the form

$$\frac{\partial \zeta}{\partial t} = v \frac{\partial^2 \zeta}{\partial y^2} \quad (3.5.2)$$

which describes the diffusion of vorticity through a one-dimensional space. According to the discussions of Section 2.7, both (3.5.1) and (3.5.2) are classified as parabolic partial differential equations. Here we will construct a numerical scheme for solving (3.5.1), examine its computational stability, and then apply it to a particular physical problem.

In numerical computations the space coordinates must be finite. Let us assume that the fluid above the plate at $y = 0$ is bounded below a finite depth that is divided into $m - 1$ equally spaced intervals of size h . If the time axis is divided into steps of size τ , a grid system is formed, as shown in Fig. 3.5.1. To approximate (3.5.1) by a finite difference equation at the grid point (i, j) , the second-order spatial derivative is replaced by the central-difference formula (2.2.9) and the time derivative is replaced by the forward-difference formula (2.2.6). After rearrangement the equation has the final form

$$u_{i,j+1} = u_{i,j} + R(u_{i-1,j} - 2u_{i,j} + u_{i+1,j}) \quad (3.5.3)$$

in which $R = v\tau/h^2$ is a dimensionless parameter. The equation states that the solution at a certain height at time interval τ later can be computed based on the present information at the local and two neighboring stations. For given boundary conditions expressed as known functions of time, the solution at time level t_2 is computed explicitly from the initial condition at t_1 by using (3.5.3). Repeating the procedure for the successive time steps, the solution at any desired time level can be obtained. For this property the method in which (3.5.3) is applied is called an *explicit method* for solving the parabolic equation (3.5.1).

Playing a similar role as the Courant number C in (2.10.4), the parameter R in (3.5.3) cannot be arbitrarily chosen, and the limitation imposed on its magnitude

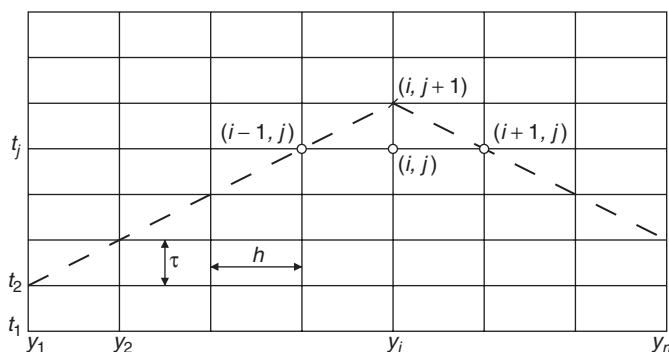


FIGURE 3.5.1 An explicit method for solving parabolic equations.

is to be determined from a stability analysis of the numerical scheme. Following the technique illustrated in Section 2.10, we assume

$$u_{i,j} = U_j e^{Iikh} \quad (3.5.4)$$

and obtain, after substituting into (3.5.3),

$$U_{j+1} = [1 - 2R(1 - \cos kh)]U_j \quad (3.5.5)$$

The quantity contained within the brackets is the amplification factor λ . If $|\lambda| > 1$, $|U_{j+1}| > |U_j|$ and the amplitude of the solution becomes unbounded as $j \rightarrow \infty$. This is called an unstable situation. Thus, for stability we require $\lambda^2 \leq 1$ or, consequently, after expanding the left-hand side,

$$R \leq \frac{1}{1 - \cos kh}$$

Since the lowest value of the expression on the right-hand side is $1/2$ when $\cos kh = -1$, the stability criterion derived for (3.5.3) is

$$\frac{v\tau}{h^2} \leq \frac{1}{2} \quad (3.5.6)$$

When the upper limiting value is used for this parameter, (3.5.3) has a particularly simple form:

$$u_{i,j+1} = \frac{1}{2}(u_{i-1,j} + u_{i+1,j}) \quad (3.5.7)$$

This is called the *Bender-Schmidt recurrence equation*, which determines the solution at (y_i, t_{j+1}) as the average of the values right and left of y_i at a time t_j . However, more accurate results are obtained by using (3.5.3) for $R < 1/2$.

The differential equation (3.5.1) and its finite-difference approximation (3.5.3) apply to any unsteady planar flows bounded by two parallel infinite plates performing arbitrary parallel motions along their own planes. One of the plates may be replaced by a free surface. Furthermore, with modifications to suit cylindrical coordinates, the resulting equations apply to flows between concentric cylinders. Solving for the velocity and the related fields of these flows may be classified as the generalized Rayleigh problem.

For illustrative purposes we consider water contained between two originally stationary flat plates separated by a distance of 1 m. At an initial instant $t = 0$, the upper plate has suddenly acquired a constant speed $u_0 (= 1 \text{ m/s})$ while the lower plate is kept stationary all the time. The sudden motion of the upper plate creates a sharp velocity change there, forming a concentrated vortex sheet right below the plate. The vorticity is diffused downward, according to (3.5.2), into

a region practically free of vorticity, and the velocity is redistributed accordingly. We like to find numerically the velocity distribution across the channel at different times.

In terms of the notation of Fig. 3.5.1, the initial velocity distribution is

$$\begin{aligned} u_{i,1} &= 0 \quad \text{for } 1 = 1, 2, \dots, m - 1 \\ u_{m,1} &= u_0 \end{aligned}$$

and the boundary conditions are

$$\begin{aligned} u_{1,j} &= 0 \quad \text{for } j > 1 \\ u_{m,j} &= u_0 \quad \text{for } j > 1 \end{aligned}$$

For water $\nu = 1 \times 10^{-6}$ m²/s, approximately. If the space between plates is divided into 20 equal intervals, then $m = 21$ and $h = 0.05$ m. Let us choose $R = 1/4$, which determines the time interval $\tau = Rh^2/\nu$ or 625 s. This time step size seems to be rather large. But it is a reasonable size for a laminar shear flow in which vorticity or velocity gradient is diffused purely by intermolecular activities characterized by a small kinematic viscosity.

In the form shown in (3.5.3), the velocity field is a two-dimensional array. This is not necessary, however, in programming for the computation. In Program 3.4 we use one-dimensional arrays UOLD(l) and UNEW(l) to denote $u_{i,j}$ and $u_{i,j+1}$, respectively and overwrite them at successive time steps for efficient use of computer memory. The solution for U is shown in Fig. 3.5.2 for the first five curves.

The output (Table 3.A.4) shows that a velocity discontinuity cannot exist in a viscous fluid and is smoothed out immediately by viscous diffusion. As time progresses the velocity profile approaches a linear distribution that varies from 0 at the lower plate to 1 m/s at the upper and corresponds to the solution for the Couette flow between two parallel plates in a steady shear motion.

Problem 3.8 Assign a value to R that is greater than 0.5, and then run Program 3.4 to watch the growth of the solution to some unrealistic magnitudes. The result proves the validity of the stability criterion (3.5.6).

Problem 3.9 Find the velocity distribution at increasing times in the originally stationary fluid around a circular cylinder with a free surface (Fig. 3.3.1) after the cylinder is suddenly given a rotation of tangential speed v_b at the surface. As time approaches a very large value, the solution should approach that for Problem 3.6.

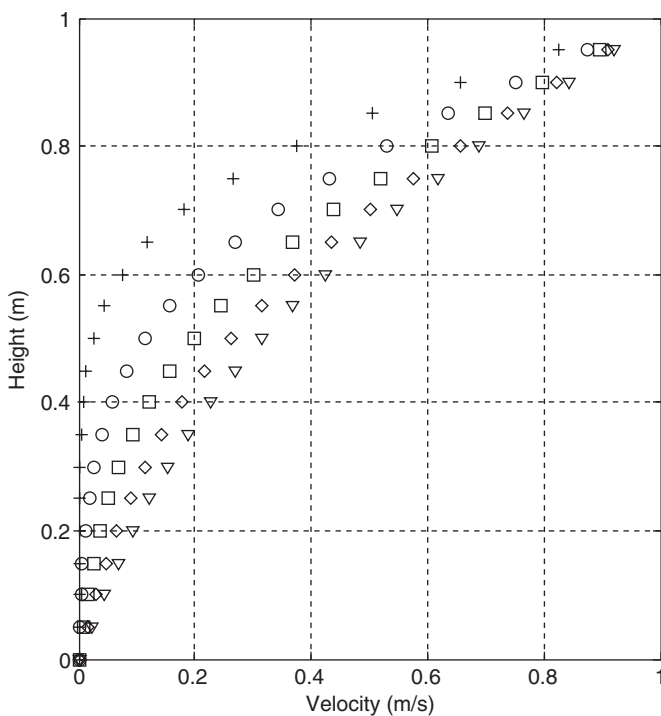


FIGURE 3.5.2 Velocity distribution at different times (in seconds). +, $T = 25,000$; \circ , $T = 50,000$; \square , $T = 75,000$; \diamond , $T = 100,000$; ∇ , $T = 125,000$.

Problem 3.10 Find the velocity distribution in the channel described in Program 3.4 with the upper plate replaced by one oscillating at the speed $u_0 \sin \omega t$, where $u_0 = 1$ m/s and $\omega = 1/1000$ s⁻¹.

Problem 3.11 In approximating the differential equation (3.5.1) by the finite-difference equation (3.5.3), we used forward difference in time and central difference in space, so that the truncation error of the approximation is $O(\tau, h^2)$. An improved explicit scheme with truncation error of $O(\tau^2, h^2)$ can be constructed by also using central difference in time and by replacing the second $u_{i,j}$ on the right side of (3.5.3) by the time-average $(u_{i,j-1} + u_{i,j+1})/2$. Thus,

$$\frac{u_{i,j+1} - u_{i,j-1}}{2\tau} = v \frac{u_{i-1,j} - u_{i,j-1} - u_{i,j+1} + u_{i+1,j}}{h^2} \quad (3.5.8)$$

$$(1 + 2R)u_{i,j+1} = 2R(u_{i-1,j} + u_{i+1,j}) + (1 - 2R)u_{i,j-1}$$

This is called the *DuFort–Frankel formula*, which involves three time levels, as does the formula (2.10.13) derived for hyperbolic differential equations.

Show that (3.5.8) is an unconditionally stable numerical scheme.

Let us take a close look at the explicit formula (3.5.3). The solution at the grid point $(i, j + 1)$ is computed, using this formula, from the solutions evaluated at three grid points $(i-1, j)$, (i, j) , and $(i+1, j)$. These values, in turn, are computed from solutions in their neighborhood at the previous time step. In this way we can trace out the region of dependence of the point $(i, j + 1)$, which is confined between the two dashed lines shown in Fig. 3.5.1. This means that the disturbance created at any other height in the fluid reaches the height y_i with a finite speed h/τ . This contradicts the real situation in an incompressible fluid, in which a disturbance at any point is felt immediately by all parts throughout the fluid. Thus, to improve the accuracy of (3.5.3), we may reduce the size of τ or the value of R . In so doing the dashed lines will approach the horizontal grid line passing through $(i, j + 1)$ and, in the meantime, more time steps will be needed in the computation to reach the same time level. The improved accuracy in the explicit method is therefore obtained at the expense of an increased amount of computer time.

3.6 IMPLICIT METHODS FOR SOLVING PARABOLIC PARTIAL DIFFERENTIAL EQUATIONS – STARTING FLOW IN A CHANNEL

The deficiency associated with the explicit methods, that the solution computed at one point is not affected immediately by the conditions at all other points in the fluid, can be avoided by devising an alternative numerical scheme for solving the same diffusion equation (3.5.1). If we still use centered difference in space but use backward, instead of forward, difference in time, a finite-difference equation is obtained at (i, j) of the form

$$\frac{1}{\tau}(u_{i,j} - u_{i,j-1}) = \frac{\nu}{h^2}(u_{i-1,j} - 2u_{i,j} + u_{i+1,j}) \quad (3.6.1)$$

It becomes, after regrouping,

$$Ru_{i-1,j} - (1 + 2R)u_{i,j} + Ru_{i+1,j} = -u_{i,j-1} \quad (3.6.2)$$

where $R = \nu\tau/h^2$ is the same dimensionless parameter as that defined in Section 3.5.

The slight modification in approximating the time derivative causes a radical change in the procedure for obtaining a solution. Suppose the solution at $t = t_j$ is to be computed based on the solution known at the previous time step $t = t_{j-1}$; (3.6.2) shows that every three neighboring unknown values are interrelated through this linear algebraic equation. Applying (3.6.2) at all grid points interior to the boundaries at one time level gives a system of simultaneous equations that can be solved for all the unknowns at that time instant. In this way the velocities at different heights are not independent of one another; a change at one point will be felt immediately by all other points. Thus, this numerical scheme is more sound than the explicit scheme on physical grounds. By using the numerical

scheme the solution can no longer be computed explicitly as before, so (3.6.2) is called a formula for the *implicit method*.

The computational stability of (3.6.2) can be examined again with von Neumann's stability analysis by assuming the form already shown in (3.5.4) for the numerical solution. It can easily be verified that the resulting relationship from that analysis is

$$U_j = \frac{1}{1 + 2R(1 - \cos kh)} U_{j-1} = \lambda U_{j-1} \quad (3.6.3)$$

As $\cos kh$ varies from -1 to $+1$, the value of the amplification factor λ changes from $1/(1 + 4R)$ to 1 and can never exceed 1 . Therefore, this numerical scheme is stable for all positive values of R .

Although for computational stability there is no restriction on the magnitude of R as long as it is positive, a smaller value of R results in a more accurate numerical solution. The reason for this is that after multiplying (3.6.1) through by τ , the truncated higher-order terms on the right-hand side are all multiplied by R .

We now apply the implicit method to solve a problem concerning the development of a channel flow caused by the application of a constant pressure gradient. The initially stationary incompressible fluid contained between two parallel infinite plates is set in motion by a suddenly imposed pressure gradient dp/dx along the channel. Simplified for the present geometry, the equation of motion (3.1.7) becomes

$$\frac{\partial u}{\partial t} = -\frac{1}{\rho} \frac{dp}{dx} + \nu \frac{\partial^2 u}{\partial y^2} \quad (3.6.4)$$

If the distance between plates is $2L$ and the origin of the coordinate system is placed at the middle of the channel, the boundary and initial conditions are

$$u = 0 \quad \text{at} \quad y = \pm L \quad \text{for all} \quad t \quad (3.6.5)$$

$$u = 0 \quad \text{at} \quad t = 0 \quad \text{for} \quad -L \leq y \leq L \quad (3.6.6)$$

We know that as time increases, the velocity profile will approach its steady-state parabolic distribution

$$u_s = -\frac{1}{2\mu} \frac{dp}{dx} (L^2 - y^2) \quad (3.6.7)$$

which is a particular solution to (3.6.4) satisfying the boundary conditions (3.6.5). By introducing the dimensionless variables

$$T = \frac{t}{L^2/\nu}, \quad Y = \frac{y}{L}, \quad U = u \left/ \left(-\frac{L^2}{2\mu} \frac{dp}{dx} \right) \right. \quad (3.6.8)$$

and a dimensionless velocity difference

$$W = (u_s - u) \left/ \left(-\frac{L^2}{2\mu} \frac{dp}{dx} \right) \right. = (1 - Y^2) - U \quad (3.6.9)$$

the governing equation (3.6.4) is simplified to

$$\frac{\partial W}{\partial T} = \frac{\partial^2 W}{\partial Y^2} \quad (3.6.10)$$

with boundary and initial conditions

$$W = 0 \quad \text{at } Y = \pm 1 \quad \text{for all } T \quad (3.6.11)$$

$$W = 1 - Y^2 \quad \text{at } T = 0 \quad \text{for } -1 \leq Y \leq 1 \quad (3.6.12)$$

The implicit numerical scheme for solving (3.6.10) is, according to (3.6.2),

$$RW_{i-1,j} - (1 + 2R)W_{i,j} + RW_{i+1,j} = -W_{i,j-1} \quad (3.6.13)$$

where $R = \tau/h^2$, τ and h being the interval sizes in the nondimensionalized time and space coordinates, respectively. Equation (3.6.13) is, in fact, a special case of the finite-difference equation (2.2.10) with constant coefficients C_{ij} on the left-hand side, so that, after it is applied to all interior grid points, the resulting tridiagonal system of simultaneous equations can be solved by calling the subroutine TRID constructed in Program 2.1. Comparing (3.6.13) with the standard form (2.2.10) reveals that the coefficients are

$$C_{i1} = R, \quad C_{i2} = -1 - 2R, \quad C_{i3} = R, \quad C_{i4} = -W_{i,j-1}$$

The subscripts j and $j - 1$ in (3.6.13) can be dropped in the computer program if we compute the coefficients C_{i4} using the values of W_i at hand, call TRID to get the solution at the next time step that will be stored under the same name W_i , and then advance in time by repeating the same process. Moreover, because the flow is symmetric about the x axis, it suffices to find a solution only in the upper half of the channel. Accordingly, the conditions (3.6.11) and (3.6.12) are modified to

$$W = 0 \quad \text{at } Y = 1 \quad \text{for all } T \quad (3.6.14)$$

$$\frac{\partial W}{\partial Y} = 0 \quad \text{at } Y = 0 \quad \text{for all } T \quad (3.6.15)$$

$$W = 1 - Y^2 \quad \text{at } T = 0 \quad \text{for } 0 \leq Y \leq 1 \quad (3.6.16)$$

The derivative boundary condition (3.6.15) indicates that a fictitious grid point is needed below $Y = 0$. Thus, to use subroutine TRID, which solves n simultaneous equations, we divide the range $0 \leq Y \leq 1$ into n segments of equal width h , denote the grid points by Y_1, Y_2, \dots, Y_{n+1} , respectively, and finally add a fictitious point Y_0 at $Y = -h$. Equation (3.6.15) then becomes $W_0 = W_2$, and the boundary conditions are exactly analogous to those for the temperature profile on the flat-plate thermometer in Section 3.3. Following the discussion in that section, before TRID is called, the coefficient matrix must be modified using the

following assignment statements:

$$C_{13} \leftarrow (C_{11} + C_{13}) \quad (3.6.17)$$

$$C_{11} \leftarrow 0 \quad (3.6.18)$$

$$C_{n4} \leftarrow (C_{n4} - C_{n3} W_{n+1}) \quad (3.6.19)$$

$$C_{n3} \leftarrow 0 \quad (3.6.20)$$

The dimensionless velocity U at any time level is calculated from (3.6.9) once W becomes known for that time.

Velocity profiles are printed (Table 3.A.5) and plotted selectively in Program 3.5, computed for $n = 20$ and $R = 0.4$. In the plot the nondimensionalized steady-state velocity distribution U_s is added to compare with the profiles at other time instants.

One thousand time steps have been marched in the computation of Program 3.5 without encountering any instability, as expected of the implicit method. Figure 3.6.1 displays the development of the flow from a stationary state to the steady-state parabolic velocity profile as time approaches infinity. Right after the pressure gradient is applied, the flow acceleration is large, but the acceleration

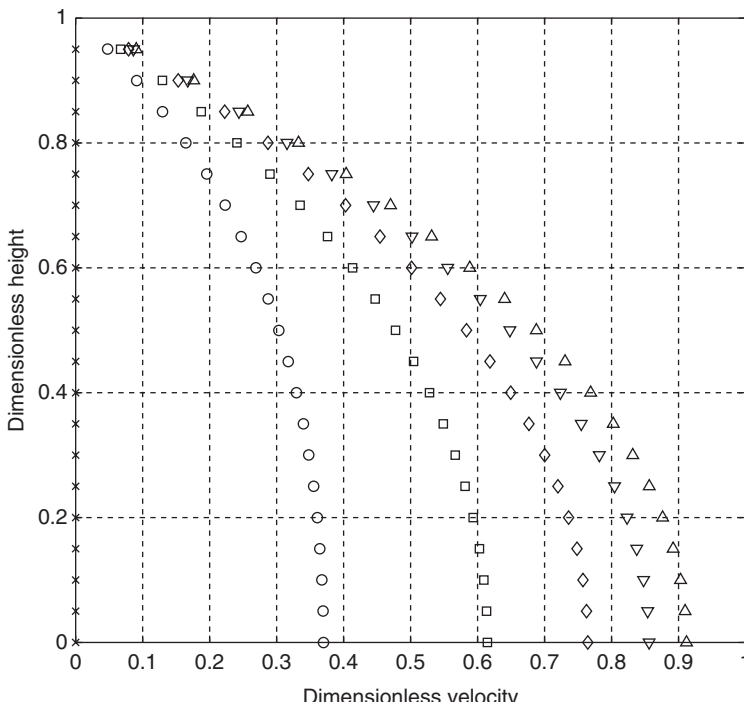


FIGURE 3.6.1 Velocity profiles. \times , $T = 0$; \circ , $T = 0.2$; \square , $T = 0.4$; \diamond ; $T = 0.6$; ∇ , $T = 0.8$; \triangle , steady state.

diminishes with increasing time. At $T = 1$ the velocity at the center of the channel is 91% the steady-state value. For water ($\nu = 1 \times 10^{-6} \text{ m}^2/\text{s}$) in a channel 2 cm high, this dimensionless time corresponds to 100 s in real time. The slow readjustment of the vorticity distribution is a characteristic of laminar flows with small kinematic viscosity.

The governing equation (3.6.10) and the boundary and initial conditions (3.6.11) and (3.6.12) for W show that $W(Y, T)$ describes the deceleration of a channel flow with a parabolic velocity profile when the pressure gradient used to sustain the flow is suddenly removed.

For the problem considered here, an analytical solution to (3.6.4) is possible by assuming

$$u = -\frac{1}{2\mu} \frac{dp}{dx} (L^2 - y^2) + \sum_{m=1}^{\infty} A_m \exp\left(-\lambda_m^2 \frac{vt}{L}\right) \cos\left(\lambda_m \frac{y}{L}\right)$$

The eigenvalues λ_m are to be determined from the boundary conditions (3.6.5), and the coefficients A_m are to be evaluated after substituting this expression into the initial condition (3.6.6) and using the orthogonal relationships among cosine functions.

The truncation error resulting from approximating the differential equation (3.5.1) by the implicit formula (3.6.2) is $O(\tau, h^2)$. Following a procedure very similar to that used to obtain the DuFort-Frankel formula (3.5.8) for improvement of the explicit method, we may derive an improved implicit scheme with a truncation error of $O(\tau^2, h^2)$. Let us replace the differential equation by a finite-difference equation at the midpoint $(i, j - \frac{1}{2})$ between grid points (i, j) and $(i, j - 1)$, as shown in Fig. 3.6.2. The time derivative in (3.5.1) is approximated by the central-difference formula (2.2.8) to give

$$\left(\frac{\partial u}{\partial t}\right)_{i,j-(1/2)} = \frac{u_{i,j} - u_{i,j-1}}{2(\tau/2)} + O\left[\left(\frac{\tau}{2}\right)^2\right]$$

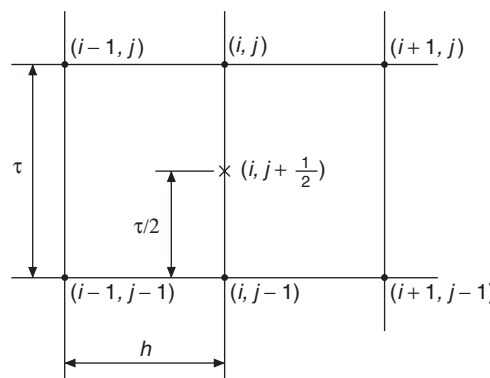


FIGURE 3.6.2 Crank-Nicolson method.

The second-order spatial derivative at $(i, j - \frac{1}{2})$ is approximated by the average of those at (i, j) and $(i, j - 1)$, each of which is expressed in the central-difference form. Thus, we have

$$\left(\frac{\partial^2 u}{\partial y^2}\right)_{i,j-(1/2)} = \frac{1}{2} \left(\frac{u_{i-1,j} - 2u_{i,j} + u_{i+1,j}}{h^2} + \frac{u_{i-1,j-1} - 2u_{i,j-1} + u_{i+1,j-1}}{h^2} \right) + O(h^2)$$

Substituting these two approximations into (3.5.1) yields, after rearranging and dropping terms $O(\tau^2)$ and $O(h^2)$,

$$Ru_{i-1,j} - 2(1 + R)u_{i,j} + Ru_{i+1,j} = -Ru_{i-1,j-1} - 2(1 - R)u_{i,j-1} - Ru_{i+1,j-1} \quad (3.6.21)$$

The form of this more accurate formula differs from the form of (3.6.2) in that it involves the evaluation of u at three grid points instead of at one on the right-hand side. The corresponding increase in computational work is merely in the evaluation of the coefficients C_{i4} , which is apparently an insignificant portion of the total computational effort. The numerical technique using (3.6.21) is called the *Crank-Nicolson method*. It can easily be shown that this is also an unconditionally stable scheme.

Problem 3.12 For the unsteady flow in an infinitely long tube of circular cross section along the x axis, the governing equation is

$$\frac{\partial u}{\partial t} = -\frac{1}{\rho} \frac{\partial p}{\partial x} + v \left(\frac{\partial^2 u}{\partial r^2} + \frac{1}{r} \frac{\partial u}{\partial r} \right) \quad (3.6.22)$$

Derive an implicit scheme for this differential equation in a form analogous to (3.6.2), examine its stability, and then use it to find the solution for the flow caused by the sudden application of a constant pressure gradient along a tube of radius A . The analytical solution of this problem can be found in Section 4.3 of Batchelor (1967), expressed in terms of a Fourier-Bessel series.

Project for Further Study: Find the solution for a flow in a tube of radius A caused by the application of an alternating pressure gradient

$$\frac{\partial p}{\partial x} = -K \cos \omega t$$

where K is the constant amplitude and ω is the circular frequency of the oscillation. For this problem it is more convenient to introduce dimensionless variables

$$T = \omega t, \quad R = \frac{r}{A}, \quad U = \frac{u}{KA^2/4\mu}$$

so that the governing equation (3.6.22) becomes, with $\Omega = \omega\rho A^2/\mu$,

$$\Omega \frac{\partial U}{\partial T} = 4 \cos T + \frac{\partial^2 U}{\partial R^2} + \frac{1}{R} \frac{\partial U}{\partial R}$$

Using the numerical scheme constructed in the previous problem, find $U(R, T)$ for $\Omega = 0.1, 7$, and 35 and compare them with the analytical solution plotted in Fig. 1 of Chow and Lai (1972).

3.7 NUMERICAL SOLUTION OF BIHARMONIC EQUATIONS – STOKES FLOWS

In the previous three sections, examples with special geometries were chosen so that the nonlinear terms contained in the substantial derivative on the left side of (3.1.7) disappeared. The same result can be achieved by requiring that the Reynolds number of the flow be small.

Assuming that the incompressible flow is characterized by a length L and a speed U , we may introduce the following dimensionless variables:

$$t' = \frac{t}{L/U}, \quad (x', y', z') = \left(\frac{x}{L}, \frac{y}{L}, \frac{z}{L} \right), \quad \mathbf{V}' = \frac{\mathbf{V}}{U}, \quad p' = \frac{p}{\rho U^2}$$

In terms of the new variables, the Navier-Stokes equation (3.1.7) becomes

$$\frac{D\mathbf{V}'}{Dt'} = -\nabla' p' + \frac{1}{\text{Re}} \nabla'^2 \mathbf{V}' \quad (3.7.1)$$

where the primed operators are those in dimensionless form and $\text{Re} = \rho UL/\mu$ is the Reynolds number.

As stated earlier in Section 2.1, the Reynolds number (Re) measures the relative importance of inertial force and viscous force in a flow. If Re is large, the viscous force terms, or the second group on the right side of (3.7.1), become small in comparison with the inertial force terms on the left. In this case the viscous force is important only in a thin region on the surface of a body in motion relative to the fluid. This thin region is the boundary layer considered in Sections 3.2 and 3.3. On the other hand, if Re is much smaller than unity, viscous force has a dominating influence on the fluid motion. By dropping the inertial force term and returning to dimensional notation, we obtain for the steady state the linear equation

$$\mu \nabla^2 \mathbf{V} = \nabla p \quad (3.7.2)$$

Flows for which $\text{Re} \ll 1$ are called the *Stokes flows* or *creeping flows*. The flow of molasses and the flow induced by the motion of a microorganism are examples. Taking the curl of (3.7.2) gives

$$\nabla^2 \boldsymbol{\zeta} = 0 \quad (3.7.3)$$

in which $\boldsymbol{\zeta} = \nabla \times \mathbf{V}$ is the vorticity vector. Alternatively, divergence of (3.7.2) yields, remembering that $\nabla \cdot \mathbf{V} = 0$ for incompressible fluids,

$$\nabla^2 p = 0 \quad (3.7.4)$$

This states that the pressure in an incompressible Stokes flow satisfies the Laplace equation.

Here we consider the special case of two-dimensional Stokes flows parallel to the x - y plane. If the stream function introduced in Section 2.1 is used so that

$$u = \frac{\partial \psi}{\partial y} \quad \text{and} \quad v = -\frac{\partial \psi}{\partial x} \quad (3.7.5)$$

the only nonvanishing vorticity component ζ in the z direction can be written, according to (2.8.16), as

$$\nabla^2 \psi = -\zeta \quad (3.7.6)$$

and the vector equation (3.7.3) reduces to a scalar equation

$$\nabla^2 \zeta = 0 \quad (3.7.7)$$

Combining (3.7.6) and (3.7.7) results in

$$\nabla^4 \psi = 0 \quad (3.7.8)$$

where the operator is defined as

$$\nabla^4 = \nabla^2 \nabla^2 = \frac{\partial^4}{\partial x^4} + 2 \frac{\partial^4}{\partial x^2 \partial y^2} + \frac{\partial^4}{\partial y^4} \quad (3.7.9)$$

Because the Laplace equation is also called the harmonic equation, (3.7.8) is usually referred to as the *biharmonic equation*.

Numerical solution of the biharmonic equation (3.7.8) seems to be simple. It may be treated as two simultaneous second-order equations (3.7.6) and (3.7.7) to each of which the numerical methods developed in Section 2.8 for solving elliptic equations may be applied. However, difficulties arise in specifying the boundary conditions for the vorticity equation (3.7.7). On the boundaries of a flow region we can only prescribe the velocity components and/or some of their derivatives or, equivalently, the stream function and/or some of its derivatives. Vorticity is to be computed from the velocity field, but it cannot be specified at the boundaries before the problem is solved. Thus, the numerical solution of the biharmonic equation is not as simple as it first appears to be, and special techniques are needed to utilize the numerical methods, devised originally for solving Poisson and Laplace equations, to solve the present boundary-value problem.

An example with an especially simple geometry is used here to demonstrate how such a problem is handled. A square cavity $DABC$ is shown in Fig. 3.7.1 within which a steady fluid motion is generated by sliding an infinitely long plate lying on top of the cavity. Suppose that all variables are normalized so that the size of the cavity is 1×1 and the sliding velocity is 1 in the positive x direction, and that the Reynolds number is so low that the induced motion can be classified as a Stokes flow.

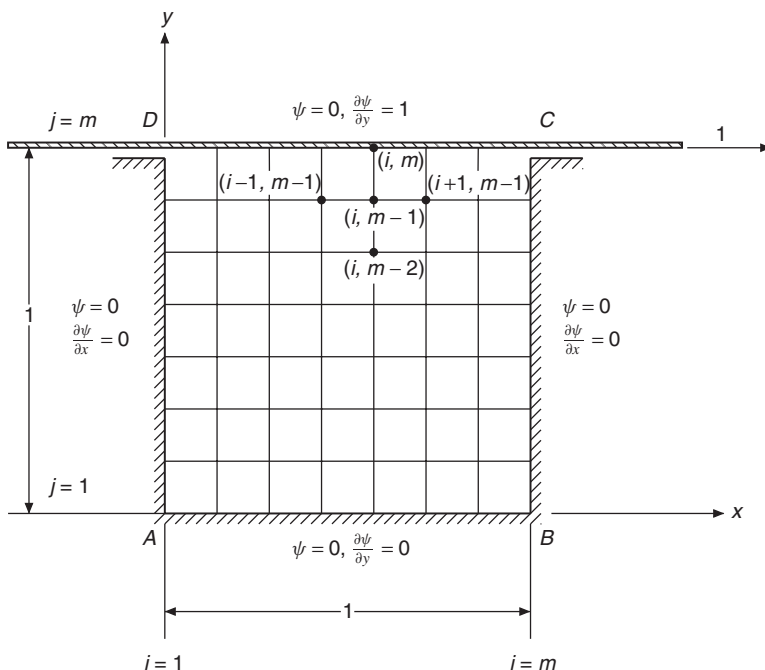


FIGURE 3.7.1 Cavity flow caused by a moving plate.

If no fluid is squeezed out of the cavity below the moving plate, the fluid motion forms closed paths within the cavity. The surfaces DA , AB , BC , and CD are then segments of the bounding streamline designated by $\psi = 0$. This is equivalent to specifying that the velocities normal to these four surfaces are all zero. To require that the tangential velocity be vanishing on all surfaces except on the top plate where it is 1, we obtain four additional boundary conditions in terms of derivatives of ψ , as indicated in Fig. 3.7.1, along the four sides. In summary, the boundary conditions are

$$\psi = 0 \quad \text{and} \quad \frac{\partial \psi}{\partial x} = 0 \quad \text{on } DA \quad (3.7.10)$$

$$\psi = 0 \quad \text{and} \quad \frac{\partial \psi}{\partial y} = 0 \quad \text{on } AB \quad (3.7.11)$$

$$\psi = 0 \quad \text{and} \quad \frac{\partial \psi}{\partial x} = 0 \quad \text{on } BC \quad (3.7.12)$$

$$\psi = 0 \quad \text{and} \quad \frac{\partial \psi}{\partial y} = 1 \quad \text{on } CD \quad (3.7.13)$$

This problem is similar to the one considered in Section 7.2 of Greenspan (1974), except in that analysis the inertial terms are retained. Furthermore, we will use a different procedure to compute the vorticity at the boundaries.

The fluid region is covered with a square mesh of size h having m horizontal grid lines and an equal number of vertical grid lines, as shown schematically in Fig. 3.7.1. Next, we derived expressions for boundary values of ζ in terms of ψ , which are needed for solving (3.7.7).

Let us first consider an arbitrary grid point (i, m) at the moving plate on top of the cavity. Our purpose is to calculate the vorticity at this point based on the local velocity and on the information of ψ at four neighboring grid points marked in Fig. 3.7.1. Similar to expression (2.9.4), we now assume the following form for vorticity at (i, m) :

$$\begin{aligned}\zeta_{i,m} &= - \left(\frac{\partial^2 \psi}{\partial x^2} + \frac{\partial^2 \psi}{\partial y^2} \right)_{i,m} \\ &= \alpha_1 \psi_{i-1,m-1} + \alpha_2 \psi_{i,m-1} + \alpha_3 \psi_{i+1,m-1} + \alpha_4 \psi_{i,m-2} + \alpha_5 \left(\frac{\partial \psi}{\partial y} \right)_{i,m}\end{aligned}\quad (3.7.14)$$

Substituting from the Taylor's series expansions,

$$\begin{aligned}\psi_{i \pm 1, m-1} &= \psi_{i,m} \pm h \left(\frac{\partial \psi}{\partial x} \right)_{i,m} + \frac{h^2}{2} \left(\frac{\partial^2 \psi}{\partial x^2} \right)_{i,m} - h \left(\frac{\partial \psi}{\partial y} \right)_{i,m} \\ &\quad + \frac{h^2}{2} \left(\frac{\partial^2 \psi}{\partial y^2} \right)_{i,m} + O(h^3) \\ \psi_{i,m-n} &= \psi_{i,m} - nh \left(\frac{\partial \psi}{\partial y} \right)_{i,m} + \frac{1}{2} n^2 h^2 \left(\frac{\partial^2 \psi}{\partial y^2} \right)_{i,m} + O(h^3)\end{aligned}$$

and retaining only terms up to $O(h^2)$, (3.7.14) becomes

$$\begin{aligned}- \left(\frac{\partial^2 \psi}{\partial x^2} + \frac{\partial^2 \psi}{\partial y^2} \right)_{i,m} &= (\alpha_1 + \alpha_2 + \alpha_3 + \alpha_4) \psi_{i,m} + (\alpha_3 - \alpha_1) h \left(\frac{\partial \psi}{\partial x} \right)_{i,m} \\ &\quad + \left(\frac{\alpha_5}{h} - \alpha_1 - \alpha_2 - \alpha_3 - 2\alpha_4 \right) h \left(\frac{\partial \psi}{\partial y} \right)_{i,m} \\ &\quad + (\alpha_1 + \alpha_3) \frac{h^2}{2} \left(\frac{\partial^2 \psi}{\partial x^2} \right)_{i,m} \\ &\quad + (\alpha_1 + \alpha_2 + \alpha_3 + 4\alpha_4) \frac{h^2}{2} \left(\frac{\partial^2 \psi}{\partial y^2} \right)_{i,m}\end{aligned}$$

The constants α 's are determined by equating the coefficients of like terms on the two sides of this equation. Substitution of these values into (3.7.14) gives

$$\zeta_{i,m} = \frac{1}{h^2} \left(-\psi_{i-1,m-1} + \frac{8}{3} \psi_{i,m-1} - \psi_{i+1,m-1} - \frac{2}{3} \psi_{i,m-2} \right) - \frac{2}{3h} \left(\frac{\partial \psi}{\partial y} \right)_{i,m}\quad (3.7.15)$$

where $(\partial\psi/\partial y)_{i,m}$ has the constant value of 1 according to the second boundary condition in (3.7.13). By analogy we can write down the expressions for vorticity at the three stationary boundaries as

$$\zeta_{1,j} = \frac{1}{h^2} \left(-\psi_{2,j-1} + \frac{8}{3}\psi_{2,j} - \psi_{2,j+1} - \frac{2}{3}\psi_{3,j} \right) \quad (3.7.16)$$

$$\zeta_{m,j} = \frac{1}{h^2} \left(-\psi_{m-1,j-1} + \frac{8}{3}\psi_{m-1,j} - \psi_{m-1,j+1} - \frac{2}{3}\psi_{m-2,j} \right) \quad (3.7.17)$$

$$\zeta_{i,1} = \frac{1}{h^2} \left(-\psi_{i-1,2} + \frac{8}{3}\psi_{i,2} - \psi_{i+1,2} - \frac{2}{3}\psi_{i,3} \right) \quad (3.7.18)$$

in which the derivative boundary conditions in (3.7.10) to (3.7.12) have been employed.

The vorticity boundary conditions just derived enable us to solve (3.7.7) provided ψ is known at some interior points. However, the determination of ψ from (3.7.6) depends on the distribution of vorticity within the bounded domain. Thus, ψ and ζ are coupled, and an iterative scheme will be constructed to find the solution.

A stationary state is first assumed so that $\psi = 0$ everywhere in the fluid region. Based on this initial assumption, the boundary values computed from (3.7.15) to (3.7.18) show that vorticity is initially generated at the moving plate. This concentrated vorticity starts to diffuse into the cavity, resulting in a temporary vorticity distribution that is the solution of (3.7.7) that satisfies the present boundary conditions. This computed vorticity distribution causes a modification to the assumed ψ after solving (3.7.6) subject to the restriction that $\psi = 0$ on the boundary. In this way we have completed the first iteration. To start the next iteration, the boundary values of vorticity are recomputed based on the modified stream function, and the same procedure is repeated to obtain a new solution for ψ and ζ . During each iteration the difference between the newly computed ζ and the previous value at every grid point is recorded as the local error, and the sum of absolute errors at all grid points is called ERZETA. The same is done for ψ , and the corresponding sum is called ERPSI. Iteration is terminated when both ERZETA and ERPSI are smaller than a specified small positive value EPSILON; the solution at this stage is then considered to be satisfactory, since it has the desired accuracy.

In Program 3.6 an iteration counter ITER is introduced whose value is printed only when the final result has been obtained. The Poisson equation (3.7.6) is solved by applying Liebmann's iterative formula (2.8.6) repeatedly at all interior points. The iteration method is programmed in a subroutine named LIEBMN for a square domain. The same subroutine is called to solve the Laplace equation (3.7.7), which is, in fact, a Poisson equation with a vanishing right-hand side.

When Liebmann's method is used, the values of vorticity at the corners A, B, C, and D of the cavity (Fig. 3.7.1) are not involved in the numerical computation for solving equations (3.7.6) and (3.7.7). These values are computed

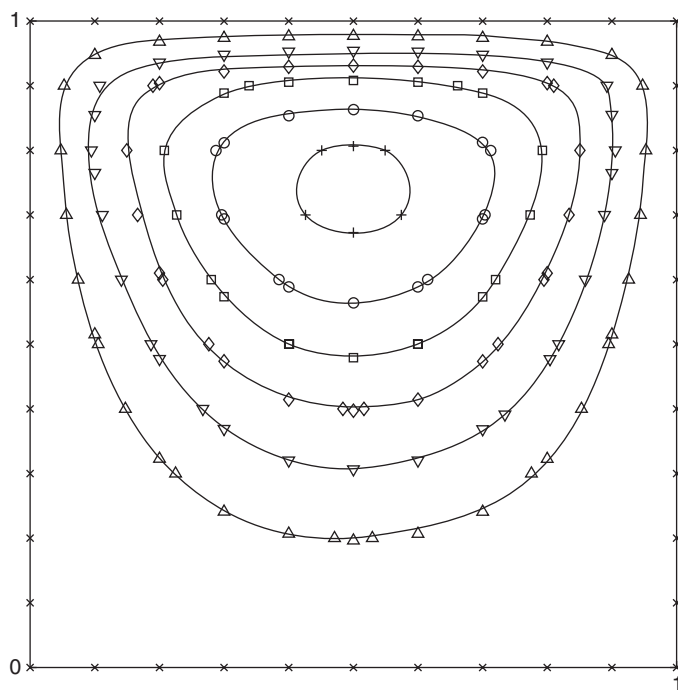


FIGURE 3.7.2 Stream function plot. +, $\text{PSI} = -0.09$; o, $\text{PSI} = -0.075$; □, $\text{PSI} = -0.06$; ◇, $\text{PSI} = -0.045$; ▽, $\text{PSI} = -0.03$; △, $\text{PSI} = -0.015$; ×, $\text{PSI} = 0$.

from the final vorticity distribution by taking the average of the values at two neighboring grid points.

After printing the numerical values ψ and ζ for the final solution (Table 3.A.6) the flow pattern is plotted in Fig. 3.7.2. It turns out that the stream function is either negative or zero in the present problem, so that the absolute value of ψ is used instead in determination of the plotting symbols for various ranges of the stream function.

The output of Program 3.6 shows that with $\text{EPSILON} = 0.001$, 109 iterations are needed to have the numerical result converge to the desired solution. During the last iteration, ERPSI , or the sum of absolute errors in the computation for ψ , is 0.00004, whereas ERZETA , the sum of absolute errors in the computation for ζ , is 0.00094. After being distributed among 121 grid points, the average error at each grid point is really a very small quantity.

The printed values of ψ show that stream function is symmetric about the vertical line passing through the center of the cavity, but a slight asymmetry in vorticity is detected at some locations. The errors, which appear only at the third decimal place, can be reduced by assigning a number smaller than 0.001 to ERRMAX when the subroutine `LIEBMN` is called. But to obtain a solution of higher accuracy requires a longer computer time. Program 3.6 is constructed for

demonstration, and the accuracy of the result is not a main consideration here. On the other hand, results of higher resolutions can be obtained by increasing the total number of grid points.

Problem 3.13 Solve for the Stokes flow in the square cavity shown in Fig. 3.7.1 with a free surface CD and a bottom surface AB moving at a constant unit velocity in the positive x direction.

3.8 FLOW STABILITY AND PSEUDO-SPECTRAL METHODS

In this section, we consider two problems that serve as examples of flow stability subject to different types of excitation. The first is the Rayleigh-Benard problem, in which a horizontal layer of fluid heated from below becomes unstable due to buoyancy forces lifting the hot fluid upward. Then, continuity requires fluid from the colder, upper region of the flow to move downward, thus setting up a pattern called *Benard* cells. A full account of this problem is offered in Section 4.3. Here, we will simply consider the same problem introduced in Section 4.3, but instead of solving the full nonlinear system, we will first linearize the governing equations, then apply separation of variables and convert the governing partial differential equations into a system of ordinary differential equations, and finally solve the resulting system using a MATLAB eigenvalue solver. The solution of this system will provide the conditions under which an otherwise quiescent horizontal layer of fluid will become unstable with respect to a certain scaling parameter of the system. Once a threshold value for this parameter is exceeded, then the system becomes unstable and a convective flow pattern is established. The characteristic nondimensional number for this problem is the *Rayleigh* number, defined as

$$\text{Ra} = \frac{g\alpha\Delta TH^3}{\kappa\nu} \quad (3.8.1)$$

Here, g is the gravitational acceleration, α is the thermal expansion coefficient, ΔT is the temperature difference between the lower (hot) surface and the upper (cold) surface, H is the height of the horizontal fluid layer, κ is the thermal diffusivity, and ν is the kinematic viscosity of the fluid. From (3.8.1), it is apparent that the Rayleigh number is the ratio, (buoyant energy production)/(energy diffusion).

We adopt the *Boussinesq* approximation (Section 4.3), and write the governing equations in the primitive variable form (see Section 4.5). For two-dimensional incompressible flows, the primitive variables of the problem are the velocity components u, w and the pressure p . In the presence of surface heating, as in the present problem, the energy equation must also be considered. Consequently, for this problem, the fourth dependent variable is temperature, T . The governing equations are the continuity equation, the x -momentum equation, the z -momentum equation (in the vertical direction, by convention), and the energy

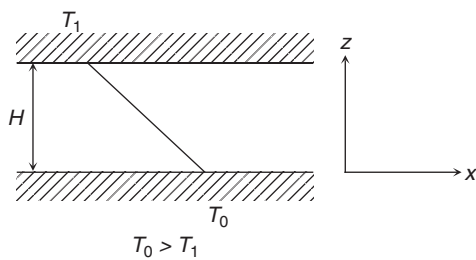


FIGURE 3.8.1 Schematic of the Benard problem.

equation written with respect to Fig. 3.8.1, viz.,

$$\frac{\partial u}{\partial x} + \frac{\partial w}{\partial z} = 0 \quad (3.8.2)$$

$$\frac{\partial u}{\partial t} + u \frac{\partial u}{\partial x} + w \frac{\partial u}{\partial z} = -\frac{\partial p}{\partial x} + \text{Pr} \nabla^2 u \quad (3.8.3)$$

$$\frac{\partial w}{\partial t} + u \frac{\partial w}{\partial x} + w \frac{\partial w}{\partial z} = -\frac{\partial p}{\partial z} + \text{Pr} \nabla^2 w + \text{Ra} \text{Pr} \theta \quad (3.8.4)$$

$$\frac{\partial \theta}{\partial t} + u \frac{\partial \theta}{\partial x} + w \frac{\partial \theta}{\partial z} = \nabla^2 \theta \quad (3.8.5)$$

In these equations, Pr is the Prandtl number expressing the ratio (viscous diffusion)/(thermal diffusion) and is given as $\text{Pr} = \nu/\kappa$. These equations have been nondimensionalized in the following manner:

$$\begin{aligned} u &= \frac{L}{\kappa} U, & w &= \frac{L}{\kappa} W, & x &= \frac{X}{H}, & z &= \frac{Z}{H} \\ \theta &= \frac{(T - T_o)}{(T_1 - T_o)}, & p &= \frac{H^2}{\kappa^2 \rho_o} P, & t &= \frac{\kappa}{H^2} \tau \end{aligned} \quad (3.8.6)$$

In these expressions, U , W , X , Z , T , P , and τ are dimensional quantities, and ρ_o is the reference fluid density (Section 4.3). We now assume that the instabilities due to buoyancy will have very small amplitudes, and the initial state of the fluid is quiescent so that the dependent variables can be separated into a mean component that represents the initial conditions (base state), and a time-dependent component that represents the perturbation field,

$$\begin{aligned} u &= 0 + \hat{u}(x, z, t) \\ w &= 0 + \hat{w}(x, z, t) \\ p &= \bar{p}(z) + \hat{p}(x, z, t) \\ \theta &= \bar{\theta}(z) + \hat{\theta}(x, z, t) \end{aligned} \quad (3.8.7)$$

The base state is satisfied by

$$\begin{aligned} u &= w = 0 \\ \hat{p} &= 0 \\ \hat{\theta} &= 0, \quad \frac{d\bar{\theta}}{dz} = -1 \end{aligned} \tag{3.8.8}$$

so that the z -momentum and energy equations for the base state become, respectively,

$$\frac{\partial \bar{p}}{\partial z} = \text{RaPr} \bar{\theta} \tag{3.8.9}$$

$$\frac{\partial \bar{\theta}}{\partial t} = \nabla^2 \bar{\theta} \tag{3.8.10}$$

Next, the governing equations (3.8.2)–(3.8.5) are linearized according to the following script:

- Substitute decomposed variables, (3.8.7), into (3.8.2)–(3.8.5).
- Subtract the base state, (3.8.9), (3.8.10) from these equations.
- Omit terms that are quadratic in the perturbation quantities.
- Eliminate \hat{p} and \hat{u} from the \hat{w} equation (z -momentum equation) by using continuity (3.8.2) and x -momentum (3.8.3) equations.

The resulting two equations for the perturbation variables \hat{w} and $\hat{\theta}$ are

$$\frac{\partial}{\partial t} (\nabla^2 \hat{w}) - \text{Pr} \nabla^2 (\nabla^2 \hat{w}) = \text{RaPr} \hat{\theta} \tag{3.8.11}$$

$$\frac{\partial \hat{\theta}}{\partial t} - \nabla^2 \hat{\theta} = \hat{w} \tag{3.8.12}$$

Because both equations (3.8.11) and (3.8.12) are linear, we can use separation of variables. For periodic solution in the x direction, we can assume

$$\begin{aligned} \hat{w}(x, z, t) &= w'(z) e^{\sigma t} e^{I k x} \\ \hat{\theta}(x, z, t) &= \theta'(z) e^{\sigma t} e^{I k x} \end{aligned} \tag{3.8.13}$$

In (3.8.13), σ is the amplification factor; it can be shown (Kundu and Cohen, 2008, p. 475) that it is a real number for $\text{Ra} > 0$ and $I^2 = -1$. The wave number k is also real if the solution is periodic as $x \rightarrow \infty$. We also note that if $\sigma = 0$, the disturbances remain neutral; if $\sigma < 0$, disturbances decay in time; and if $\sigma > 0$, disturbances amplify, resulting in the formation of Benard cells, which will be periodic in x with a wave number k . Then, w' gives the amplitude distribution of these cells in the z direction. With the substitution of (3.8.13) into (3.8.11)

and (3.8.12), we obtain

$$\left[\frac{\sigma}{\text{Pr}} - (D^2 - k^2) \right] (D^2 - k^2) w' = -k^2 (\text{Ra}) \theta' \\ D \equiv \frac{d}{dz} \quad (3.8.14)$$

$$[\sigma - (D^2 - k^2)] \theta' = w' \quad (3.8.15)$$

These equations are homogeneous ordinary differential equations, with the following homogeneous boundary conditions:

$$\begin{aligned} z = 0, 1 & \quad w' = 0 \\ z = 0, 1 & \quad D w' = 0 \\ z = 0, 1 & \quad \theta' = 0 \end{aligned} \quad (3.8.16)$$

The boundary condition $Dw' = 0$ follows directly from the incompressible continuity equation evaluated at the wall ($z = 0$) for a viscous fluid satisfying the no-slip boundary condition. Accordingly, at the wall $u'(0, t) = 0$ and therefore $(\partial u'/\partial x) = 0$. Hence, from continuity, $(\partial w'/\partial z) = 0$ and, consequently, $Dw' = 0$ must be satisfied.

We now have a coupled system of two homogeneous equations, the first fourth order and the other second order, both with homogeneous boundary conditions. Given Ra , Pr and the wave number k , these equations become an eigenvalue problem for σ . The eigenfunctions $w'(z)$ and $\theta'(z)$ give the amplitude distribution of the perturbations.

A very useful simplification of this problem is the search for neutral stability when $\sigma = 0$. For this case the governing equations (3.8.14) and (3.8.15) can be written as a coupled system of equations:

$$(D^2 - k^2) \theta' + w' = 0 \quad (3.8.17)$$

$$(D^2 - k^2)^2 w' - k^2 (\text{Ra}) \theta' = 0 \quad (3.8.18)$$

Writing these equations in vector-matrix form, with \mathbf{I} as the identity matrix, we obtain

$$\begin{bmatrix} [(\mathbf{D}^2 - k^2)\mathbf{I}] & \mathbf{I} \\ 0 & (\mathbf{D}^2 - k^2)\mathbf{I}^2 \end{bmatrix} - \text{Ra} \begin{bmatrix} 0 & 0 \\ k^2\mathbf{I} & 0 \end{bmatrix} \begin{bmatrix} \Theta' \\ w' \end{bmatrix} = 0 \quad (3.8.19)$$

Equation (3.8.19) with the homogeneous boundary conditions (3.8.16) comprises a generalized eigenvalue problem where for given wave number, k , the desired eigenvalue is the minimum Ra , and the solution vector $\{\Theta' \ w'\}$ contains the corresponding eigenfunctions.

A numerical solution for this problem can be obtained by discretizing the difference operator D by second-order central finite differences. At the boundary points corresponding to the solid plates placed at $z = 0, 1$, one-sided differences

will be used. Consequently, the following finite difference formulae are considered:

Operator	Derivative	Formula	Order
Forward	$\frac{dw'}{dz} \Big _i$	$\frac{-3w'_i + 4w'_{i+1} - w'_{i+2}}{2\Delta z}$	Δz^2
Backward	$\frac{dw'}{dz} \Big _i$	$\frac{3w'_i - 4w'_{i-1} + w'_{i-2}}{2\Delta z}$	Δz^2
Central	$\frac{d^2w'}{dz^2} \Big _i$	$\frac{w'_{i+1} - 2w'_i + w'_{i-1}}{\Delta z^2}$	Δz^2
Central	$\frac{d^4w'}{dz^4} \Big _i$	$\frac{w'_{i+2} - 4w'_{i+1} + 6w'_i - 4w'_{i-1} + w'_{i-2}}{\Delta z^4}$	Δz^2

(3.8.20)

Let us now consider the discrete form of (3.8.17), which is obtained using (3.8.20), with the homogeneous boundary conditions, assuming that the grid point index $i = 1$ corresponds to the lower wall and $i = imax$ corresponds to the upper wall. With $h = \Delta z$, these finite-difference equations are listed below:

$$\begin{aligned}\theta'_1 &= 0 \\ \frac{1}{h^2}\theta'_{i-1} - \left(\frac{2}{h^2} + k^2\right)\theta'_i + \frac{1}{h^2}\theta'_{i+1} + w'_i &= 0 \\ \theta'_{imax} &= 0\end{aligned}\quad (3.8.21)$$

We also define the following parameters for later use:

$$\begin{aligned}a_1 &\equiv \frac{1}{h^2} \\ a_2 &\equiv -\left(\frac{2}{h^2} + k^2\right)\end{aligned}$$

For (3.8.18), we obtain

$$\begin{aligned}w'_1 &= 0 \\ -\frac{3}{2h}w'_1 + \frac{2}{h}w'_2 - \frac{1}{2h}w'_3 &= 0 \text{ (for boundary condition } Dw = 0 \text{ at the lower plate)} \\ \frac{1}{h^4}w'_{i-2} - \left(\frac{4}{h^4} + \frac{2k^2}{h^2}\right)w'_{i-1} + \left(\frac{6}{h^4} + \frac{4k^2}{h^2} + k^4\right)w'_i - \left(\frac{4}{h^4} + \frac{2k^2}{h^2}\right)w'_{i+1} \\ &\quad + \frac{1}{h^4}w'_{i+2} - k^2(Ra)\theta'_i = 0 \\ \frac{3}{2h}w'_{imax} - \frac{2}{h}w'_{imax-1} + \frac{1}{2h}w'_{imax-2} &= 0 \text{ (for boundary condition } Dw = 0 \text{ at the upper plate)} \\ w'_{imax} &= 0\end{aligned}\quad (3.8.22)$$

Similarly, we define the following parameters:

$$\begin{aligned} b_1 &\equiv \frac{1}{h^4} \\ b_2 &\equiv -\left(\frac{4}{h^4} + \frac{2k^2}{h^2}\right) \\ b_3 &\equiv \left(\frac{6}{h^4} + \frac{4k^2}{h^2} + k^4\right) \end{aligned}$$

Considering a computational mesh of 7 grid points including the lower and upper boundaries, we write (3.8.21) and (3.8.22) in matrix form:

$$\left[\begin{array}{cccccc|c} 1 & 0 & & & & & 0 \\ a_1 & a_2 & a_1 & & & & 1 \\ a_1 & a_2 & a_1 & & & & 1 \\ a_1 & a_2 & a_1 & & & & 1 \\ a_1 & a_2 & a_1 & & & & 1 \\ a_1 & a_2 & a_1 & & & & 1 \\ 0 & 1 & & & & & 0 \end{array} \right] \left[\begin{array}{c} \theta_1 \\ \theta_2 \\ \theta_3 \\ \theta_4 \\ \theta_5 \\ \theta_6 \\ \theta_7 \end{array} \right]' = \left[\begin{array}{c} w_1 \\ w_2 \\ w_3 \\ w_4 \\ w_5 \\ w_6 \\ w_7 \end{array} \right]$$

$$\left[\begin{array}{ccccc|c} 1 & 0 & 0 & & & 0 \\ -3 & 2 & -1 & 0 & & 0 \\ \hline 2h & h & 2h & & & \\ b_1 & b_2 & b_3 & b_2 & b_1 & b_1 \\ b_1 & b_2 & b_3 & b_2 & b_1 & b_1 \\ b_1 & b_2 & b_3 & b_2 & b_1 & b_1 \\ 0 & \frac{1}{2h} & \frac{-2}{h} & \frac{3}{2h} & & 0 \end{array} \right] \left[\begin{array}{c} \theta_1 \\ \theta_2 \\ \theta_3 \\ \theta_4 \\ \theta_5 \\ \theta_6 \\ \theta_7 \end{array} \right]' = \left[\begin{array}{c} w_1 \\ w_2 \\ w_3 \\ w_4 \\ w_5 \\ w_6 \\ w_7 \end{array} \right]$$

$$\left[\begin{array}{ccccc|c} 0 & & & & & 0 \\ 0 & & & & & 0 \\ 0 & & & & & 0 \\ 0 & & & & & 0 \\ 0 & & & & & 0 \\ 0 & & & & & 0 \\ 0 & & & & & 0 \end{array} \right] \left[\begin{array}{c} \theta_1 \\ \theta_2 \\ \theta_3 \\ \theta_4 \\ \theta_5 \\ \theta_6 \\ \theta_7 \end{array} \right]' = \left[\begin{array}{c} w_1 \\ w_2 \\ w_3 \\ w_4 \\ w_5 \\ w_6 \\ w_7 \end{array} \right] = 0$$
(3.8.23)

which has the general form

$$[\mathbf{A} - \text{Ra} \cdot \mathbf{B}] \begin{bmatrix} \boldsymbol{\Theta}' \\ \mathbf{w}' \end{bmatrix} = 0 \quad (3.8.24)$$

$$\boldsymbol{\Theta}' = \{\theta'_1, \theta'_2, \dots, \theta'_7\}$$

$$\mathbf{w}' = \{w'_1, w'_2, \dots, w'_7\}$$

It is important to note that the 1st and the 7th rows of the coefficient matrices \mathbf{A} and \mathbf{B} in (3.8.23) have been modified to impose the boundary conditions on θ' at the lower and upper plates, respectively. The boundary conditions for w' at the lower plate are imposed by modifying rows 8, 9 in both coefficient matrices \mathbf{A} and \mathbf{B} ; the boundary conditions on w' at the upper plate are imposed by modifying rows 13 and 14 in \mathbf{A} and \mathbf{B} .

The generalized eigenvalue problem (3.8.24) can be very conveniently solved by the MATLAB command $eig(A, B)$ for \mathbf{A} and \mathbf{B} square matrices. For example, the command $[X, D] = eig(A, B)$ returns a diagonal matrix \mathbf{D} with the eigenvalues in the diagonal and a matrix \mathbf{X} with corresponding eigenvectors as columns.

Problem 3.14 Compute the neutral stability curve for Benard convection between rigid–rigid boundaries using the formulation given above to calculate the critical value Ra_c , and the corresponding wave number. It is important to note that a range of k values are specified, $0.5 \leq k \leq 10.0$, and a full set of eigenvalues are calculated for each value of k as the program is stepped up by an amount $\Delta k = 0.1$. For each k value, the minimum Ra is selected, and Ra_c corresponds to the minimum of these Ra values. The computation can start with about 30–40 grid points, but as the value of Ra_c is approached, the solution requires significantly higher mesh resolution of about 150 grid points. A closed form solution for this problem is given by Jeffreys (1928), which reads

$$\text{Ra}_c = \frac{(\pi^2 + k^2)^3}{\left(1 - \frac{\pi^2}{(\pi^2 + k^2)^2 \kappa}\right) k^2} \quad (3.8.25)$$

$$\kappa = \frac{1}{8k} \tanh \frac{k}{2} + \frac{1}{16} \left(\operatorname{sech} \frac{k}{2}\right)^2$$

- Plot the computed neutral stability curve.
- Find the critical Rayleigh number.
- Plot the corresponding eigenfunctions.
- Graphically compare your results with the analytic solution given by Jeffreys (3.8.25).

Next, we consider a canonical example concerning the hydrodynamic stability of plane channel flow formed by a pressure gradient between two parallel plates. We will again consider two-dimensional, unsteady, incompressible flow. The

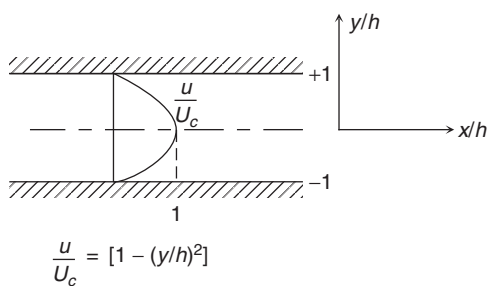


FIGURE 3.8.2 Schematic of plane Poiseuille flow.

problem will consist of perturbing the laminar, steady, fully developed flow in the channel (Figure 3.8.2) with small amplitude disturbances in the form of traveling waves and determining the conditions under which these disturbances (normal modes) will amplify and eventually drive the laminar base flow to a turbulent state. The steady-state solution (base flow) for this pressure-driven flow is called the *Poiseuille flow* and generates a parabolic velocity profile between the two plates (Figure 3.8.2). This solution is obtained from the governing equations written for the two-dimensional flow of an incompressible fluid. Note that, in compliance with customary notation, for this problem we define the vertical axis as the y axis and consequently the plates are located at $y = \pm h$, where h is the channel half-height. The continuity, x -momentum and the y -momentum equations are given as

$$\frac{\partial u}{\partial x} + \frac{\partial v}{\partial y} = 0 \quad (3.8.26)$$

$$\frac{\partial u}{\partial t} + u \frac{\partial u}{\partial x} + v \frac{\partial u}{\partial y} = -\frac{1}{\rho} \frac{\partial p}{\partial x} + \nu \nabla^2 u \quad (3.8.27)$$

$$\frac{\partial v}{\partial t} + u \frac{\partial v}{\partial x} + v \frac{\partial v}{\partial y} = -\frac{1}{\rho} \frac{\partial p}{\partial y} + \nu \nabla^2 v \quad (3.8.28)$$

We assume that the flow is driven by a constant mean pressure gradient along the x direction, where $u = u(y)$ only. Then, for steady flow, (3.8.26) and (3.8.28) are identically zero, and (3.8.27) reduces to

$$\nu \frac{d^2 u}{dy^2} = \frac{1}{\rho} \frac{dp}{dx} \quad (3.8.29)$$

$$y = \pm h, \quad u = 0$$

Integrating twice and imposing the boundary conditions, one obtains

$$U = (1 - y^2), \quad -1 \leq y \leq 1 \quad (3.8.30)$$

Here, U is nondimensionalized by the channel centerline velocity, $U_c = -(h^2/2\rho\nu)(dp/dx)$, and x and y are nondimensionalized by h . Equation (3.8.30) is the laminar base flow, which will be perturbed by the imposed disturbances. A similar solution is given in Section 3.6.

In a similar manner as in the previous example, it is assumed that the velocity components and the pressure can be written as a sum of a mean (base) component and a small amplitude fluctuating disturbance component:

$$\begin{aligned} u &= U(y) + \hat{u}(x, y, t), \\ v &= \hat{v}(x, y, t), \\ p &= P(x) + \hat{p}(x, y, t) \end{aligned} \quad (3.8.31)$$

Substituting (3.8.31) into (3.8.26)–(3.8.28) and subtracting the base flow (3.8.29), and, further, linearizing the equations with respect to the quadratic terms in the fluctuating components and scaling the pressure with density, one obtains

$$\frac{\partial \hat{u}}{\partial x} + \frac{\partial \hat{v}}{\partial y} = 0 \quad (3.8.32)$$

$$\frac{\partial \hat{u}}{\partial t} + U \frac{\partial \hat{u}}{\partial x} + v \frac{\partial U}{\partial y} + \frac{\partial \hat{p}}{\partial x} = \nu \left(\frac{\partial^2 \hat{u}}{\partial x^2} + \frac{\partial^2 \hat{u}}{\partial y^2} \right) \quad (3.8.33)$$

$$\frac{\partial \hat{v}}{\partial t} + U \frac{\partial \hat{v}}{\partial x} + \frac{\partial \hat{p}}{\partial y} = \nu \left(\frac{\partial^2 \hat{v}}{\partial x^2} + \frac{\partial^2 \hat{v}}{\partial y^2} \right) \quad (3.8.34)$$

where \hat{p} is *kinematic pressure*, or pressure divided by density, ρ . Noting that because these equations are linear, separation of variables can be used and a solution of the following form can be assumed:

$$\begin{aligned} \hat{u}(x, y, t) &= \tilde{u}(y) e^{I\alpha(x-ct)} \\ \hat{v}(x, y, t) &= \tilde{v}(y) e^{I\alpha(x-ct)} \\ \hat{p}(x, y, t) &= \tilde{p}(y) e^{I\alpha(x-ct)} \end{aligned} \quad (3.8.35)$$

In (3.8.35), assuming temporal growth of the disturbances, the wave number α is a real positive number but the wave velocity c is complex. The real part c_R corresponds to the phase velocity, and the imaginary part c_I is the growth rate of the disturbances. Hence, for $c_I < 0$, disturbances attenuate; $c_I = 0$ gives the neutral curve; and $c_I > 0$ corresponds to amplifying disturbances, which are called the Tollmien-Schlichting waves. Substituting (3.8.35) into (3.8.32)–(3.8.34), after elimination of the exponential factors, we obtain the following equations:

$$I\alpha \tilde{u} + \tilde{v}' = 0 \quad (3.8.36)$$

$$I\alpha(U - c)\tilde{u} + \tilde{v}U' + I\alpha\tilde{p} = \nu(\tilde{u}'' - \alpha^2\tilde{u}) \quad (3.8.37)$$

$$I\alpha(U - c)\tilde{v} + \tilde{p}' = \nu(\tilde{v}'' - \alpha^2\tilde{v}) \quad (3.8.38)$$

In these equations primes denote differentiation with respect to y . Next, \tilde{u} and \tilde{p} are eliminated from (3.8.38) by using (3.8.36) and (3.8.37), and the resulting equation is nondimensionalized by the channel half-height h and the channel

centerline velocity U_c . The resulting equation is the fourth-order, linear Orr-Sommerfeld equation, which governs the stability of parallel shear flows and reads (with all the variables in nondimensional form)

$$(U - c)(v'' - \alpha^2 v) - vU'' = -\frac{i}{\alpha \text{Re}}(v''' - 2\alpha^2 v'' + \alpha^4 v)$$

For Poiseuille flow,

$$\text{Re} = \frac{U_c h}{v}, \quad U = (1 - y^2), \quad U'' = -2, \quad v_{y=\pm 1} = 0, \quad v'_{y=\pm 1} = 0$$

Equation (3.8.39) shows that both the Orr-Sommerfeld equation and its boundary conditions are homogeneous, and the temporal problem is reduced to an eigenvalue problem with the following functional form:

$$f(\text{Re}, \alpha, c_R, c_I) = 0 \quad (3.8.40)$$

Then, for given real α and Re , the computational problem is to calculate the complex eigenvalue, c .

A very efficient and accurate method to solve the eigenvalue problem (3.8.39) is the use of spectral methods (or transform methods) with Chebyshev differentiation matrices. The use of these methods for linear stability problems and for the Navier-Stokes equations has been pioneered by Orszag's (1971) work on Poiseuille flow; practical aspects and applications have been exposed by two exceptionally well-written books by Trefethen (2000) and Moin (2001). Trefethen's book contains short and very efficiently written MATLAB codes, which will form the basis of the solution procedure that we will use in this section to solve (3.8.39). Comprehensive coverage of advanced methods based on spectral elements can be found in Karniadakis and Sherwin (2005).

For nonperiodic functions over an interval $[-1, 1]$, derivatives can be calculated by an interpolation polynomial at *Chebyshev* points obtained from

$$y_j = \cos(j\pi/N), \quad j = 0, 1, \dots, N \quad (3.8.41)$$

These points are unequally distributed within the computational domain and are clustered toward the boundaries at $y = \pm 1$ (with grid index $j = 0$ on $y = 1$, and the grid index $j = N$ on $y = -1$) and are particularly suitable for problems where gradients of the flow-field variables are very strong at the boundaries, such as in wall-bounded flows. We also note that these points correspond to the extrema of the Chebyshev polynomial, $T_k(y)$, where k indicates the degree of the polynomial. These polynomials can be used to approximate any function and its derivatives at the Chebyshev points (3.8.41). It is important to consider that spectral accuracy, which can be expressed in terms of the exponentially decreasing error, i.e., $\varepsilon \sim e^{-N}$, will be achieved with $k > 16$ for most problems.

The k th degree Chebyshev polynomial is defined as

$$T_k(y) = \cos(k \cos^{-1} y) \equiv \cos(k\theta) \quad (3.8.42)$$

Then, using trigonometric identities, we obtain

$$\begin{aligned} T_0(y) &= 1 \\ T_1(y) &= y \\ T_2(y) &= 2y^2 - 1 \\ T_3(y) &= 4y^3 - 3y \\ &\vdots \\ T_{k+1}(y) &= 2yT_k(y) - T_{k-1}(y) \quad k \geq 1 \end{aligned} \quad (3.8.43)$$

The Chebyshev polynomial $T_N(y)$ has N zeros in the interval $[-1, 1]$ located at

$$y_j = \cos\left[\frac{\pi(j - 1/2)}{N}\right], \quad j = 1, 2, \dots, N \quad (3.8.44)$$

In the same interval, it has $(N + 1)$ extrema at locations given by (3.8.41). From approximation theory, using the orthogonality of the polynomials (Moin, 2001, p. 180), any function can be expanded in terms of Chebyshev polynomials at collocation points given by (3.8.41), by a given set of coefficients,

$$u(y) = \sum_{k=0}^N a_k T_k(y), \quad (3.8.45)$$

where a_k is the coefficient for the k th Chebyshev polynomial.

As an example, let us consider the function $u(y) = y^2$. Using (3.8.45), we can write

$$\begin{aligned} u(y) &= a_0 T_0(y) + a_1 T_1(y) + a_2 T_2(y) + \dots \\ T_0(y) &= 1, \quad T_1(y) = y, \quad T_2(y) = 2y^2 - 1 \\ \therefore a_0 &= 0.5, \quad a_1 = 0, \quad a_2 = 0.5 \end{aligned} \quad (3.8.46)$$

Equation (3.8.45) can be written in discrete form such that

$$u_j = u(y_j) = \sum_{k=0}^N a_k T_k(y_j), \quad j = 0, 1, \dots, N \quad (3.8.47)$$

Similarly,

$$a_k = \frac{2}{Nc_k} \sum_{j=0}^N \frac{1}{c_j} T_k(y_j) u_j, \quad k = 0, 1, \dots, N \quad (3.8.48)$$

$$c_j = \begin{cases} 2 & j = 0, N \\ 1 & \text{otherwise} \end{cases}$$

We can write this expression in matrix form for the Chebyshev coefficient vector, \mathbf{a} :

$$\mathbf{a} = \hat{\mathbf{T}}\mathbf{u} \quad (3.8.49)$$

Here, the vector of unknowns contains the values of $u(y_j)$ at the Chebyshev collocation points. In a similar fashion, we can obtain the derivative

$$u'(y_j) = \sum_{k=0}^N b_k T_k(y_j) \quad (3.8.50)$$

Equation (3.8.50) can be written in vector-matrix form:

$$\mathbf{u}' = \mathbf{T}\mathbf{b} \quad (3.8.51)$$

Vectors \mathbf{a} and \mathbf{b} are related through the matrix \mathbf{G} (Moin, 2001, p. 187),

$$\mathbf{b} = \mathbf{G}\mathbf{a}$$

$$G_{kj} = \begin{cases} 0 & \text{if } k \geq j \text{ or } k + j \text{ even} \\ \frac{2j}{c_k} & \text{otherwise} \end{cases} \quad (3.8.52)$$

Hence, it follows that

$$\mathbf{u}' = \mathbf{T}\mathbf{G}\mathbf{a} = \mathbf{T}\mathbf{G}\hat{\mathbf{T}}\mathbf{u} = \mathbf{D}\mathbf{u} \quad (3.8.53)$$

Matrices \mathbf{T} and $\hat{\mathbf{T}}$ are functions of the Chebyshev polynomials, and the elements, d_{jk} , of the $(N+1) \times (N+1)$ Chebyshev collocation differentiation matrix \mathbf{D} are given by (Gottlieb, Hussaini, Orszag, 1984; Trefethen, 2000; Moin, 2001)

$$d_{00} = \frac{2N^2 + 1}{6}, \quad d_{NN} = -\frac{2N^2 + 1}{6}$$

$$d_{jj} = \frac{-y_j}{2(1 - y_j)^2}, \quad j = 1, 2, \dots, (N-1) \quad (3.8.54)$$

$$d_{jk} = \frac{c_j (-1)^{j+k}}{c_k (y_j - y_k)}, \quad j \neq k, \quad j, k = 0, 1, \dots, N$$

In (3.8.54), y_j are the collocations points (grid points) obtained from (3.8.41) and c_j are given as

$$c_j = \begin{cases} 2, & j = 0 \text{ or } N \\ 1, & \text{otherwise} \end{cases}$$

A remarkable feature of the Chebyshev differentiation matrix, \mathbf{D} , is that higher-order derivatives of the function $u(y)$ can be directly calculated from its corresponding powers:

$$\begin{aligned} \mathbf{u}'' &= \mathbf{D}^2 \mathbf{u} \\ \mathbf{u}''' &= \mathbf{D}^3 \mathbf{u} \\ \mathbf{u}^{iv} &= \mathbf{D}^4 \mathbf{u} \end{aligned} \quad (3.8.55)$$

Consider the boundary value problem,

$$u''(y) + \pi u(y) = \pi; \quad u(-1) = 0, \quad u(+1) = 1 \quad (3.8.56)$$

Evaluating $u(y)$ at the Chebyshev collocation points (3.8.41), and using (3.8.55), we get

$$\begin{aligned} \mathbf{A}\mathbf{u} &= \mathbf{c} \\ \mathbf{A} &\equiv (\mathbf{D}^2 + \pi \mathbf{I}) \\ \mathbf{c} &= \pi(\text{diag}\mathbf{I}) \end{aligned} \quad (3.8.57)$$

Note that the \mathbf{D} matrix and, consequently, the \mathbf{A} matrix are both written for all the collocation points, including the boundary points; i.e., the first and last rows corresponding to the boundary points. The boundary conditions at $y = \pm 1$ can be implemented by modifying these rows:

$$\underbrace{\left[\begin{array}{ccccc} 1 & 0 & \cdots & 0 & 0 \\ a_{1,0} & a_{1,1} & \cdots & & a_{1,N} \\ & \ddots & & & \\ a_{N-1,0} & \cdots & a_{N-1,N-1} & a_{N-1,N} & 1 \\ 0 & 0 & \cdots & 0 & 1 \end{array} \right]}_{\overline{\mathbf{A}}} \left[\begin{array}{c} u_0 \\ u_1 \\ \vdots \\ u_{N-1} \\ u_N \end{array} \right] = \left[\begin{array}{c} 1 \\ \pi \\ \vdots \\ \pi \\ 0 \end{array} \right] \quad (3.8.58)$$

In (3.8.58), $\overline{\mathbf{A}}$ is the \mathbf{A} matrix modified by the implementation of the boundary conditions. The solution of (3.8.57) can be obtained by the MATLAB backslash division:

$$\mathbf{u} = \overline{\mathbf{A}} \setminus \mathbf{c}' \quad (3.8.59)$$

The backslash indicates LU factorization with left division of $\overline{\mathbf{A}}$ into \mathbf{c}' and the apostrophe transposes the row vector \mathbf{c} into a column vector \mathbf{c}' . Program 3.7 is a MATLAB script that solves (3.8.56). In Fig. 3.8.3, computational results are compared with the exact solution for (3.8.56), and shows that even with only nine

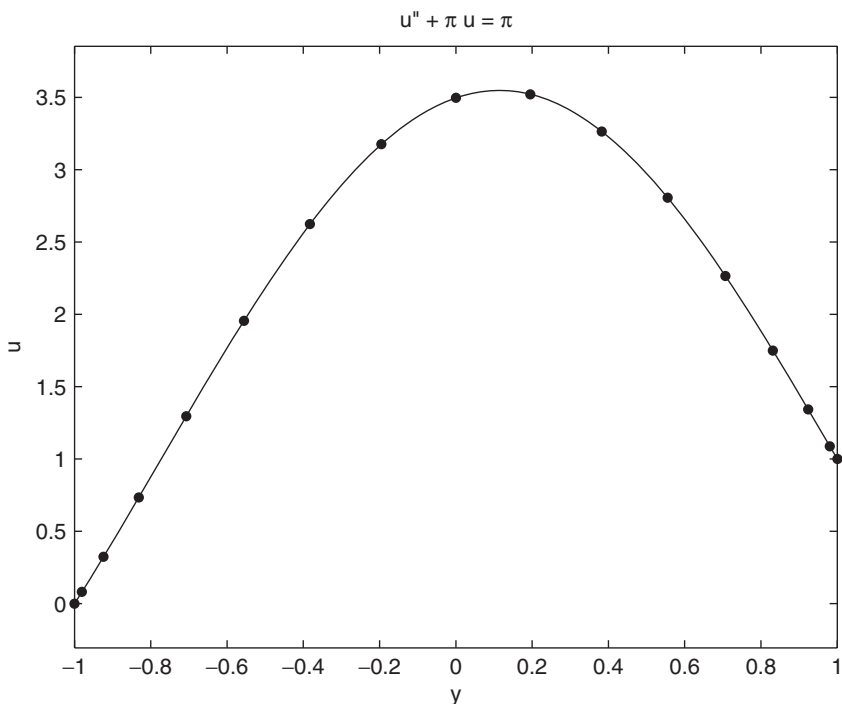


FIGURE 3.8.3 Solution of (3.8.56) using the Chebyshev matrix method with 9 collocation points. The solid line is the exact solution.

collocation points, the Chebyshev matrix method provides remarkably accurate results. We should also note that in the MATLAB program, the indices for the grid point locations run from 1 to $(N+1)$, not from zero to N as in (3.8.41).

The solution of the hydrodynamic stability problem outlined above and given by (3.8.39) and (3.8.40) can be obtained in a similar manner. For temporal eigenvalues, the wave number α , the Reynolds number Re , and the base velocity profile $U(y)$ are all real and given, so that the unknowns in the problem are the complex perturbation velocity, v , and the complex wave velocity, c

$$\begin{aligned} U(y) &= 1 - y^2, & U''(y) &= -2 \\ v(y) &= v_R + I v_I \\ c &= c_R + I c_I \end{aligned} \tag{3.8.60}$$

We can define the various derivatives appearing in (3.8.39) in terms of the Chebyshev matrix:

$$\begin{aligned} \mathbf{v}' &= \mathbf{D}\mathbf{v}, & \mathbf{v}'' &= \mathbf{D}^2\mathbf{v}, & \mathbf{v}''' &= \mathbf{D}^4\mathbf{v} \\ \mathbf{U} &= \text{diag}[U_{y_0} \cdots U_{y_N}], & y_0 &= +1, & y_N &= -1 \end{aligned} \tag{3.8.61}$$

Equation (3.8.39) can now be written as a generalized eigenvalue problem for the complex wave velocity $\lambda = -ic$, and defining \mathbf{I} as the identity matrix

$$\begin{aligned}\mathbf{A}\mathbf{v} &= \lambda\mathbf{B}\mathbf{v} \\ \mathbf{A} &= (\alpha\text{Re})^{-1} (\mathbf{D}^4 - 2\alpha^2\mathbf{D}^2 + \alpha^4\mathbf{I}) - 2\mathbf{II} - I\text{diag}(1 - y^2)(\mathbf{D}^2 - \alpha^2\mathbf{I}) \\ \mathbf{B} &= \mathbf{D}^2 - \alpha^2\mathbf{I}\end{aligned}\tag{3.8.62}$$

To implement the homogeneous boundary conditions, the first and last rows of the \mathbf{A} matrix are modified as before (3.8.58), and the zero derivative boundary condition (Neumann condition) at $y = 1$ is imposed by replacing the second row of the \mathbf{A} matrix with the first row of the \mathbf{D} matrix (Chebyshev matrix for the first derivative). We again note that in the MATLAB program, the indices for the grid point locations will run from 1 to $(N + 1)$, not from zero to N . Consequently, to impose the homogeneous Neumann boundary condition at $y = -1$, we replace the N th row of the \mathbf{A} matrix with the $(N + 1)$ th row (last row) of the \mathbf{D} matrix. If we denote the modified matrices as $\bar{\mathbf{A}}$ and $\bar{\mathbf{B}}$, for given α and Re , the resulting equation can be written as a generalized eigenvalue problem (3.8.62), where the complex eigenvalue is λ , and the corresponding complex eigenfunction is \mathbf{v} ; the solution will provide N eigenvalues and N corresponding eigenfunctions for each eigenvalue, and we note that $\lambda_R > 0$ indicates amplifying disturbance waves:

$$[\bar{\mathbf{A}} - \lambda\bar{\mathbf{B}}]\mathbf{v} = 0\tag{3.8.63}$$

The solution for (3.8.63) can be obtained by the MATLAB function *eig(A,B)*.

Program 3.8 is a MATLAB script that solves (3.8.62) for the full eigenvalue spectrum with $N = 100$, and given different values of Re and α . The elements of the \mathbf{D} matrix are calculated by using a compact MATLAB program from Trefethen (2000, p. 54). Figure 3.8.4 illustrates the eigenvalue spectrum for $\text{Re} = 5772$, $\alpha = 1.02$, which are the critical values for this flow as calculated by Orszag (1971). For this case $(\lambda_R)_{\max} = -0.0000004209 \approx 0$, representing a neutrally stable wave. If we increase the Reynolds number to $\text{Re} = 7500$, we obtain $(\lambda_R)_{\max} = 0.002029$ (Fig. 3.8.5), indicating that this disturbance wave will grow exponentially in time. It is apparent that within the bounds of a stability limit, certain combinations of Re and α will result in unstable (growing) waves. This limit is called the neutral stability curve and is calculated by setting $\lambda_R = 0$, as shown in Fig. 3.8.6 for Poiseuille flow obtained by modifying Program 3.8. For a given $\text{Re} \gtrsim 5800$, there is a narrow band of wave numbers (α values) that will resonate with the mean velocity profile and drive the laminar channel flow to instability and, eventually, to turbulence.

Problem 3.15 Modify Program 3.8. to obtain the neutral stability curve for the general Couette flow, which represents pressure-driven flow in a channel with the upper lid moving at a constant velocity, U_0 . The mean velocity profile,

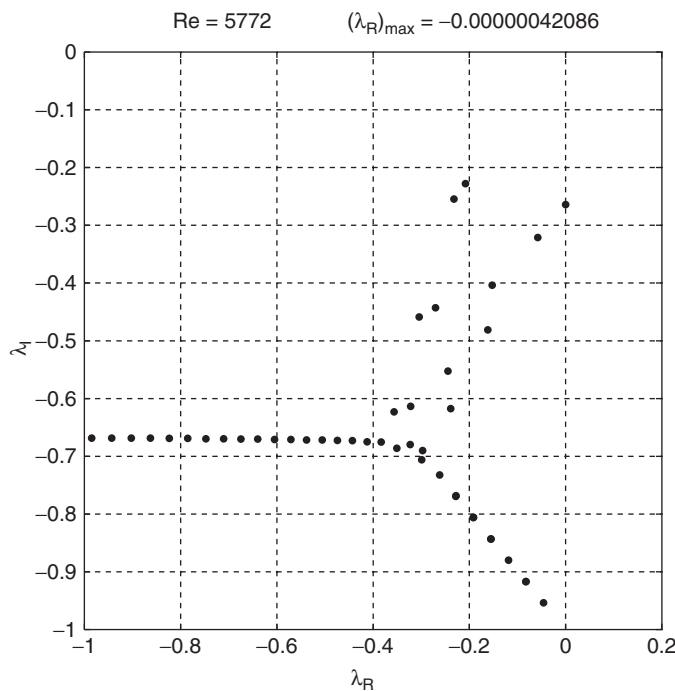


FIGURE 3.8.4 Eigenvalues for plane channel flow for $\alpha = 1.02$, $\text{Re} = 5772$.

nondimensionalized with the wall velocity can be written as

$$U(y) = \frac{1}{2}(1+y) + \frac{B}{2}(1-y^2), \quad u = 0 \quad y = \pm 1 \quad (3.8.64)$$

Obtain the neutral stability curves for $B = 1, 3, 7, 25, 100$. For larger B , does the curve approach that of the pressure-driven channel (Poiseuille) flow? Plot the critical Reynolds number, Re_c as a function of the Brinkman number B , and comment on if the flow becomes more or less stable when upper wall motion is added. When $B = 0$, are there any unstable modes? The neutral stability curves for different B should be obtained for $0 \leq \alpha \leq 1.2$, and $3.10^3 \leq \text{Re} \leq 10^5$.

Pseudo-spectral or transform methods can also be very effective for problems that are periodic in one or more space dimensions. Such problems occur in transitional or turbulent flow simulations; for example, in the pressure-driven channel flow, eigenfunctions obtained from the Orr-Sommerfeld solution can be used as initial conditions for the numerical simulation of the Navier-Stokes equation to investigate how the laminar flow will become turbulent as the disturbance amplitudes grow exponentially due to nonlinear interactions generated by the convective terms. It is often preferable to assume the flow to be periodic in the streamwise x direction, and simply observe the time evolution of one period of

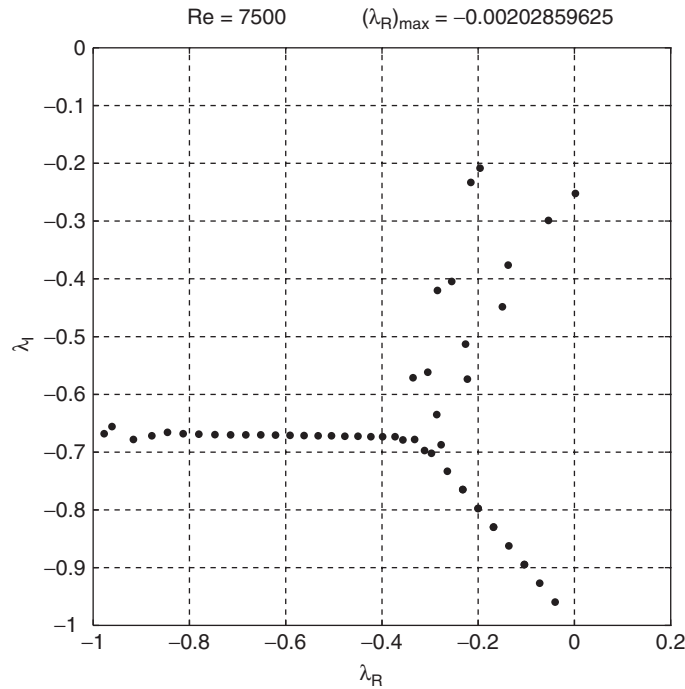


FIGURE 3.8.5 Eigenvalues for plane channel flow for $\alpha = 1.02$, $Re = 7500$.

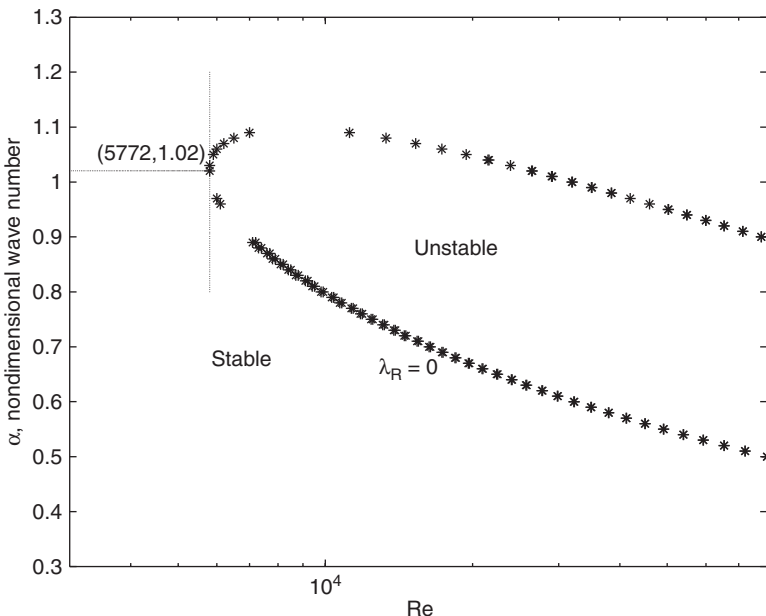


FIGURE 3.8.6 Neutral stability curve ($\lambda_R = 0$) for plane channel flow.

the disturbance in a reference frame moving with the wave speed. This enables us to deploy all available mesh resolution to capture the nonlinear evolution of one single wavelength of the disturbance. It is often sufficient to assume the spanwise z direction to be periodic as well. The assumption of periodicity enables the use of discrete Fourier transforms, which can be very efficiently computed by fast Fourier transform (FFT) algorithms.

Efficient FFT algorithms require that the periodic function, $u(x)$, is defined on N equidistant grid points, where N is an even number given as $N = 2^l$, where l is an integer. Generally, to resolve one period of a disturbance wave with minimum acceptable accuracy, $l = 4$ or $N = 16$. The discrete Fourier transform of $u(x)$ can be written as

$$u(x_m) = \sum_{n=-N/2}^{n=N/2-1} \hat{u}(k_n) e^{Ik_n x_m} \quad (3.8.65)$$

Making use of the discrete orthogonality of the Fourier series (e.g., Moin, 2001, p. 159), we can write the Fourier coefficients in (3.8.65) as

$$\hat{u}(k_n) = \frac{1}{N} \sum_{m=0}^{m=N-1} u(x_m) e^{-Ik_n x_m} \quad (3.8.66)$$

The discrete Fourier transform is computed at N equidistant points along the x direction over a computational distance L , separated by a constant grid size of Δx , and $L = N \cdot \Delta x$. We can then impose periodicity of the function $u(x)$ by making $u(x_o) = u(x_N)$ so that the period ends at x_{N-1} and the next period starts at x_N . Hence, we have

$$x_m = m \Delta x \quad (m = 0, 1, \dots, N - 1)$$

$$k_n = \frac{2\pi n}{L} \quad (\text{wave number}) \quad n = -N/2, -N/2 + 1, \dots, 0, \dots, N/2 - 1 \quad (3.8.67)$$

Derivatives along the x direction can also be easily calculated by the pseudo-spectral method (Orszag, 1972; Fox and Orszag, 1973) according to the following transforms:

$$\left. \frac{\partial u}{\partial x} \right|_m = \sum_{n=-N/2}^{n=N/2-1} I k_n \hat{u}(k_n) e^{Ik_n x_m} \quad (3.8.68)$$

where

$$\left. \frac{\partial \hat{u}}{\partial x} \right|_n = I k_n \hat{u}(k_n)$$

It follows that according to (3.8.68), the first derivative of $u(x)$ can be calculated by Fourier transforming $u(x)$ in the x direction, multiplying it by $I k_n$, and taking

the inverse transform. Similarly, the second derivative can be calculated from

$$\left. \frac{\partial^2 u}{\partial x^2} \right|_m = \sum_{n=-N/2}^{n=N/2-1} -k_n^2 \hat{u}(k_n) e^{ik_n x_m} \quad (3.8.69)$$

where

$$\left. \frac{\partial^2 \hat{u}}{\partial x^2} \right|_n = -k_n^2 \hat{u}(k_n)$$

In computing derivatives using (3.8.68) and (3.8.69), we note that for real $u(x)$ in the physical space, the Fourier coefficient of the derivative for $n = -N/2$ must be set to zero to avoid a the calculation of a “noisy” derivative.

As an example, let us consider the ordinary differential equation (Moin, 2001, p. 191),

$$\begin{aligned} u'' - u' - 2u &= 2 + 6 \sin x - 38 \cos 6x, \\ u(0) &= u(2\pi) = 0 \end{aligned} \quad (3.8.70)$$

We will solve this two-point boundary-value problem by the Fourier transform method. Writing the derivatives in the Fourier space for wave number k_n , we obtain

$$\begin{aligned} -k_n^2 \hat{u}(k_n) - ik_n \hat{u}(k_n) - 2\hat{u}(k_n) &= \hat{b}(k_n) \\ \hat{u}(k_n) &= \frac{\hat{b}(k_n)}{-k_n^2 - ik_n - 2}, \quad n = 1, \dots, N \end{aligned} \quad (3.8.71)$$

We note that $\hat{b}(k_n)$ is the Fourier coefficient of the right-hand-side of (3.8.70), and the solution will be obtained simply by back transforming (3.8.71). In Program 3.9, a MATLAB script is given that performs this integration, and the solution is compared with the exact solution,

$$u(x) = \cos(6x) - 1 \quad (3.8.72)$$

If this program is executed for different values of N , it becomes apparent that the number of grid points on which the function is evaluated has a very strong effect on the solution accuracy, and to have an acceptable solution one would have at least $N = 32$ grid points. Figure 3.8.7 presents the solution to (3.8.70) using 64 collocation points and compares it with the exact solution (3.8.72). As expected from the periodic nature of $u(x)$, the numerical solution is exact for this problem.

A more interesting application of the Fourier method can be illustrated by its application to the two-dimensional convection-diffusion equation,

$$\frac{\partial T}{\partial t} + u \frac{\partial T}{\partial x} + v \frac{\partial T}{\partial y} = \frac{1}{\text{Pr Re}} \left(\frac{\partial^2 T}{\partial x^2} + \frac{\partial^2 T}{\partial y^2} \right)$$

$$u = -\sin(\pi x) \cos(2\pi y), \quad v = \cos(\pi x) \cos(\pi y) \quad (\text{given velocity field}) \quad (3.8.73)$$

$$x = 0, \quad T = 0; \quad x = 1, \quad T = 1$$

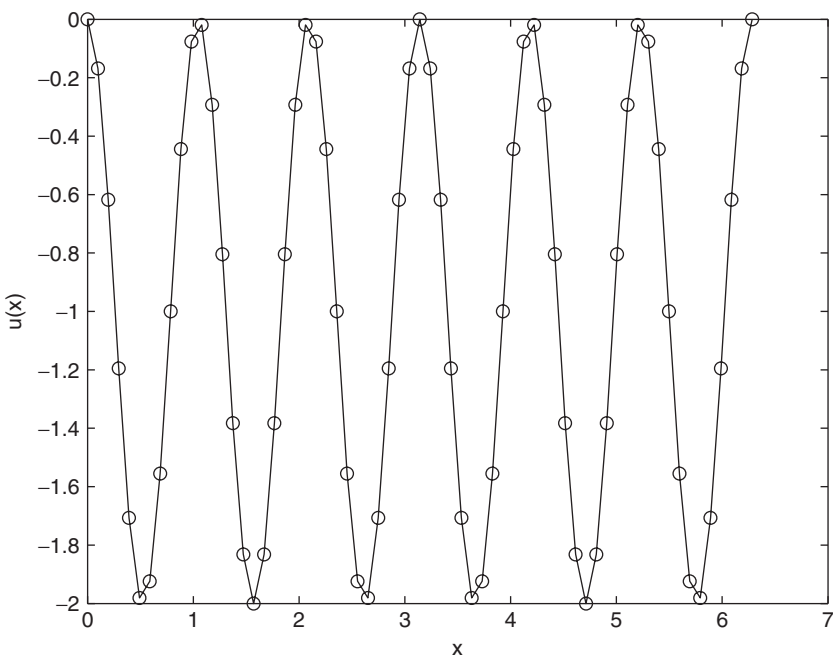


FIGURE 3.8.7 Solution of equation (3.8.70) by the Fourier transform method.

According to (3.8.73), temperature, $T(x, y)$ is a periodic function in y with a period, $L = 2$; also, Re is the Reynolds number and Pr is the Prandtl number. In the solution process, first, we advance the solution in time using the Euler explicit scheme and second-order central differences along the nonperiodic x direction. With \bar{n} representing the current time level, the resulting finite difference equation reads

$$\begin{aligned} T_{i,j}^{\bar{n}+1} &= T_{i,j}^{\bar{n}} - u_{i,j} \Delta t \left(\frac{T_{i+1,j}^{\bar{n}} - T_{i-1,j}^{\bar{n}}}{2\Delta x} \right) - v_{i,j} \Delta t \left(\frac{\partial T}{\partial y} \right)_{i,j}^{\bar{n}} \\ &\quad + \frac{\Delta t}{\text{Pr Re}} \left(\frac{T_{i+1,j}^{\bar{n}} - T_{i,j}^{\bar{n}} + T_{i-1,j}^{\bar{n}}}{\Delta x^2} \right) + \frac{\Delta t}{\text{Pr Re}} \left(\frac{\partial^2 T}{\partial y^2} \right)_{i,j}^{\bar{n}} \end{aligned} \quad (3.8.74)$$

The derivatives along the y direction will be calculated by the pseudo-spectral Fourier transform method. Program 3.10 presents a MATLAB script that integrates (3.8.74) until it meets the convergence criterion below:

$$\left| T_{i,j}^{n+1} - T_{i,j}^n \right|_{\max} \leq e^{-5} \quad (3.8.75)$$

Because the integration is explicit in time, the time step has to comply with both the diffusive and convective stability criteria. For $\text{Re} = 1$, and $\text{Pr} = 0.71$ (air),

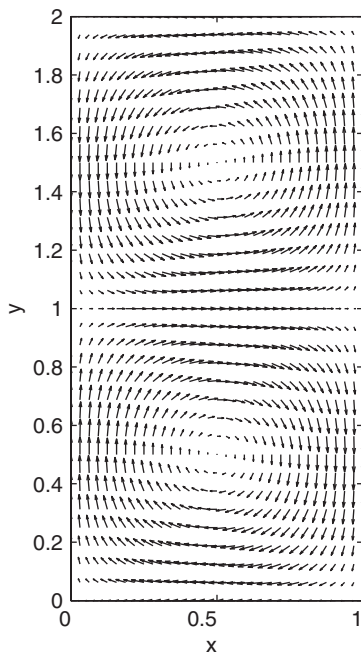


FIGURE 3.8.8 Velocity vectors given by u and v in (3.8.73).

$\Delta t = 0.0001$ was required to ensure numerical stability, whereas for $Re = 1$ and $Pr = 25$ (molten glass), $\Delta t = 0.001$ was sufficient to meet both stability criteria.

Figure 3.8.8 shows the velocity field, which is “frozen” in time, whereas in Fig. 3.8.9 temperature contours for $Pr = 0.71$ are presented. Comparing these with the temperature contours for $Pr = 25$ (Fig. 3.8.10) clearly indicates that with increasing Pr , temperature diffusion is much stronger, and high temperatures generated at the right boundary penetrate much farther toward the left (cold) boundary.

Problem 3.16 Solve equation (3.8.73) using the Euler scheme (forward in time) with explicit time advancement for the convective terms and implicit time advancement for the diffusion terms with first-order time advancement (forward in time). Use second-order central differences in space along the x direction. The problem is periodic in the y direction so that Fourier transforms can be used along y (see Program 3.10). Because the velocity components u and v are given (they are not solution dependent), the convective terms are linear. You can use any solver from Chapter 2, e.g., TRID from Program 2.1, for the solution of the tridiagonal system of equations resulting from the finite differences along the nonperiodic x direction. You can also use the MATLAB backslash operator to solve the resulting tridiagonal matrix equation.

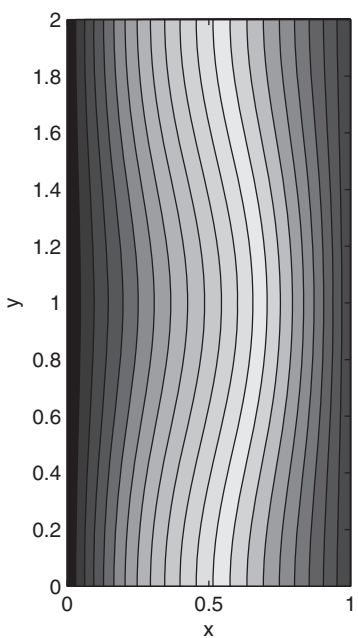


FIGURE 3.8.9 Temperature contours for $\text{Pr} = 0.71$. Right wall ($x = 1$) is “hot” and left wall is “cold.”

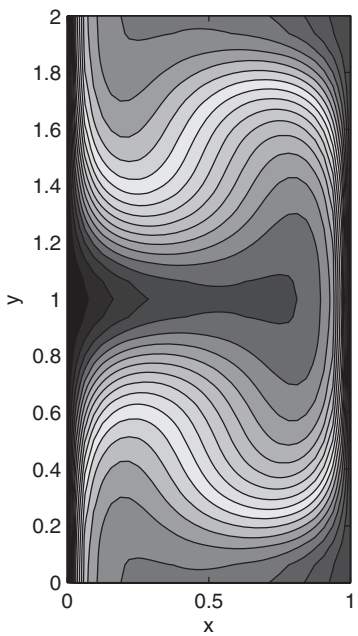


FIGURE 3.8.10 Temperature contours for $\text{Pr} = 25$. Right wall ($x = 1$) is “hot” and left wall is “cold.”

APPENDIX

TABLE 3.A.1 Tabulated Data for Program 3.1 (Number of Iterations = 31)

ETA	F	F*	F**
0	0	0	3.3206e-01
2.0000e-01	6.6410e-03	6.6408e-02	3.3198e-01
4.0000e-01	2.6560e-02	1.3276e-01	3.3147e-01
6.0000e-01	5.9735e-02	1.9894e-01	3.3008e-01
8.0000e-01	1.0611e-01	2.6471e-01	3.2739e-01
1.0000e+00	1.6557e-01	3.2978e-01	3.2301e-01
1.2000e+00	2.3795e-01	3.9378e-01	3.1659e-01
1.4000e+00	3.2298e-01	4.5626e-01	3.0787e-01
1.6000e+00	4.2032e-01	5.1676e-01	2.9666e-01
1.8000e+00	5.2952e-01	5.7476e-01	2.8293e-01
2.0000e+00	6.5002e-01	6.2977e-01	2.6675e-01
2.2000e+00	7.8119e-01	6.8131e-01	2.4835e-01
2.4000e+00	9.2229e-01	7.2898e-01	2.2809e-01
2.6000e+00	1.0725e+00	7.7245e-01	2.0645e-01
2.8000e+00	1.2310e+00	8.1151e-01	1.8401e-01
3.0000e+00	1.3968e+00	8.4604e-01	1.6136e-01
3.2000e+00	1.5691e+00	8.7608e-01	1.3913e-01
3.4000e+00	1.7469e+00	9.0176e-01	1.1788e-01
3.6000e+00	1.9295e+00	9.2333e-01	9.8086e-02
3.8000e+00	2.1160e+00	9.4112e-01	8.0126e-02
4.0000e+00	2.3057e+00	9.5552e-01	6.4234e-02
4.2000e+00	2.4980e+00	9.6696e-01	5.0520e-02
4.4000e+00	2.6924e+00	9.7587e-01	3.8973e-02
4.6000e+00	2.8882e+00	9.8268e-01	2.9484e-02
4.8000e+00	3.0853e+00	9.8779e-01	2.1871e-02
5.0000e+00	3.2833e+00	9.9154e-01	1.5907e-02
5.2000e+00	3.4819e+00	9.9425e-01	1.1342e-02
5.4000e+00	3.6809e+00	9.9615e-01	7.9278e-03
5.6000e+00	3.8803e+00	9.9748e-01	5.4321e-03
5.8000e+00	4.0799e+00	9.9838e-01	3.6485e-03
6.0000e+00	4.2796e+00	9.9897e-01	2.4021e-03
6.2000e+00	4.4795e+00	9.9936e-01	1.5502e-03
6.4000e+00	4.6794e+00	9.9961e-01	9.8067e-04
6.6000e+00	4.8793e+00	9.9977e-01	6.0809e-04
6.8000e+00	5.0793e+00	9.9986e-01	3.6960e-04
7.0000e+00	5.2792e+00	9.9992e-01	2.2019e-04
7.2000e+00	5.4792e+00	9.9996e-01	1.2859e-04
7.4000e+00	5.6792e+00	9.9998e-01	7.3606e-05
7.6000e+00	5.8792e+00	9.9999e-01	4.1300e-05
7.8000e+00	6.0792e+00	9.9999e-01	2.2714e-05
8.0000e+00	6.2792e+00	1.0000e+00	1.2245e-05
8.2000e+00	6.4792e+00	1.0000e+00	6.4706e-06

(continues)

TABLE 3.A.1 (continued)

ETA	F	F*	F**
8.4000e+00	6.6792e+00	1.0000e+00	3.3516e-06
8.6000e+00	6.8792e+00	1.0000e+00	1.7017e-06
8.8000e+00	7.0792e+00	1.0000e+00	8.4688e-07
9.0000e+00	7.2792e+00	1.0000e+00	4.1314e-07
9.2000e+00	7.4792e+00	1.0000e+00	1.9755e-07
9.4000e+00	7.6792e+00	1.0000e+00	9.2598e-08
9.6000e+00	7.8792e+00	1.0000e+00	4.2545e-08
9.8000e+00	8.0792e+00	1.0000e+00	1.9161e-08
1.0000e+01	8.2792e+00	1.0000e+00	8.4589e-09

TABLE 3.A.2 Tabulated Data for Program 3.2

ETA	THETA (WATER)	THETA (AIR)	THETA (MERCURY)
0	2.4877e+00	8.4428e-01	1.5900e-01
1.0000e-01	2.4802e+00	8.4349e-01	1.5895e-01
2.0000e-01	2.4579e+00	8.4113e-01	1.5880e-01
3.0000e-01	2.4208e+00	8.3719e-01	1.5856e-01
4.0000e-01	2.3690e+00	8.3169e-01	1.5822e-01
5.0000e-01	2.3029e+00	8.2462e-01	1.5779e-01
6.0000e-01	2.2231e+00	8.1600e-01	1.5725e-01
7.0000e-01	2.1303e+00	8.0585e-01	1.5663e-01
8.0000e-01	2.0256e+00	7.9418e-01	1.5590e-01
9.0000e-01	1.9104e+00	7.8103e-01	1.5508e-01
1.0000e+00	1.7862e+00	7.6643e-01	1.5417e-01
1.1000e+00	1.6552e+00	7.5043e-01	1.5317e-01
1.2000e+00	1.5193e+00	7.3309e-01	1.5208e-01
1.3000e+00	1.3809e+00	7.1447e-01	1.5090e-01
1.4000e+00	1.2424e+00	6.9465e-01	1.4964e-01
1.5000e+00	1.1060e+00	6.7371e-01	1.4829e-01
1.6000e+00	9.7404e-01	6.5174e-01	1.4686e-01
1.7000e+00	8.4847e-01	6.2885e-01	1.4536e-01
1.8000e+00	7.3095e-01	6.0516e-01	1.4379e-01
1.9000e+00	6.2280e-01	5.8078e-01	1.4214e-01
2.0000e+00	5.2488e-01	5.5583e-01	1.4044e-01
2.1000e+00	4.3767e-01	5.3045e-01	1.3867e-01
2.2000e+00	3.6121e-01	5.0478e-01	1.3684e-01
2.3000e+00	2.9521e-01	4.7894e-01	1.3497e-01
2.4000e+00	2.3906e-01	4.5307e-01	1.3305e-01
2.5000e+00	1.9196e-01	4.2732e-01	1.3109e-01
2.6000e+00	1.5296e-01	4.0179e-01	1.2909e-01
2.7000e+00	1.2104e-01	3.7663e-01	1.2705e-01
2.8000e+00	9.5183e-02	3.5195e-01	1.2499e-01

(continues)

TABLE 3.A.2 (continued)

ETA	THETA (WATER)	THETA (AIR)	THETA (MERCURY)
2.9000e+00	7.4440e-02	3.2786e-01	1.2291e-01
3.0000e+00	5.7926e-02	3.0446e-01	1.2080e-01
3.1000e+00	4.4868e-02	2.8183e-01	1.1868e-01
3.2000e+00	3.4600e-02	2.6005e-01	1.1654e-01
3.3000e+00	2.6566e-02	2.3919e-01	1.1440e-01
3.4000e+00	2.0305e-02	2.1931e-01	1.1225e-01
3.5000e+00	1.5447e-02	2.0043e-01	1.1009e-01
3.6000e+00	1.1692e-02	1.8259e-01	1.0793e-01
3.7000e+00	8.8015e-03	1.6580e-01	1.0578e-01
3.8000e+00	6.5873e-03	1.5008e-01	1.0362e-01
3.9000e+00	4.8996e-03	1.3541e-01	1.0148e-01
4.0000e+00	3.6205e-03	1.2179e-01	9.9332e-02
4.1000e+00	2.6570e-03	1.0918e-01	9.7196e-02
4.2000e+00	1.9360e-03	9.7572e-02	9.5068e-02
4.3000e+00	1.4002e-03	8.6916e-02	9.2950e-02
4.4000e+00	1.0050e-03	7.7177e-02	9.0842e-02
4.5000e+00	7.1570e-04	6.8310e-02	8.8745e-02
4.6000e+00	5.0565e-04	6.0268e-02	8.6660e-02
4.7000e+00	3.5436e-04	5.3004e-02	8.4588e-02
4.8000e+00	2.4629e-04	4.6466e-02	8.2528e-02
4.9000e+00	1.6976e-04	4.0603e-02	8.0482e-02
5.0000e+00	1.1603e-04	3.5367e-02	7.8450e-02
5.1000e+00	7.8628e-05	3.0707e-02	7.6433e-02
5.2000e+00	5.2826e-05	2.6576e-02	7.4430e-02
5.3000e+00	3.5184e-05	2.2926e-02	7.2442e-02
5.4000e+00	2.3229e-05	1.9713e-02	7.0470e-02
5.5000e+00	1.5202e-05	1.6896e-02	6.8514e-02
5.6000e+00	9.8606e-06	1.4435e-02	6.6573e-02
5.7000e+00	6.3391e-06	1.2292e-02	6.4650e-02
5.8000e+00	4.0388e-06	1.0433e-02	6.2743e-02
5.9000e+00	2.5501e-06	8.8259e-03	6.0853e-02
6.0000e+00	1.5956e-06	7.4421e-03	5.8980e-02
6.1000e+00	9.8933e-07	6.2546e-03	5.7125e-02
6.2000e+00	6.0782e-07	5.2393e-03	5.5288e-02
6.3000e+00	3.7002e-07	4.3743e-03	5.3469e-02
6.4000e+00	2.2319e-07	3.6400e-03	5.1668e-02
6.5000e+00	1.3338e-07	3.0189e-03	4.9885e-02

(continues)

TABLE 3.A.2 (continued)

ETA	THETA (WATER)	THETA (AIR)	THETA (MERCURY)
6.6000e+00	7.8976e-08	2.4954e-03	4.8121e-02
6.7000e+00	4.6329e-08	2.0558e-03	4.6376e-02
6.8000e+00	2.6925e-08	1.6880e-03	4.4650e-02
6.9000e+00	1.5503e-08	1.3813e-03	4.2943e-02
7.0000e+00	8.8425e-09	1.1265e-03	4.1256e-02
7.1000e+00	4.9964e-09	9.1565e-04	3.9588e-02
7.2000e+00	2.7967e-09	7.4171e-04	3.7939e-02
7.3000e+00	1.5508e-09	5.9876e-04	3.6310e-02
7.4000e+00	8.5179e-10	4.8171e-04	3.4702e-02
7.5000e+00	4.6344e-10	3.8620e-04	3.3113e-02
7.6000e+00	2.4977e-10	3.0855e-04	3.1544e-02
7.7000e+00	1.3334e-10	2.4566e-04	2.9995e-02
7.8000e+00	7.0506e-11	1.9489e-04	2.8467e-02
7.9000e+00	3.6928e-11	1.5407e-04	2.6959e-02
8.0000e+00	1.9157e-11	1.2135e-04	2.5471e-02
8.1000e+00	9.8438e-12	9.5233e-05	2.4004e-02
8.2000e+00	5.0098e-12	7.4453e-05	2.2557e-02
8.3000e+00	2.5253e-12	5.7982e-05	2.1131e-02
8.4000e+00	1.2608e-12	4.4972e-05	1.9725e-02
8.5000e+00	6.2343e-13	3.4735e-05	1.8339e-02
8.6000e+00	3.0531e-13	2.6707e-05	1.6974e-02
8.7000e+00	1.4809e-13	2.0435e-05	1.5630e-02
8.8000e+00	7.1137e-14	1.5553e-05	1.4306e-02
8.9000e+00	3.3842e-14	1.1767e-05	1.3003e-02
9.0000e+00	1.5943e-14	8.8403e-06	1.1720e-02
9.1000e+00	7.4374e-15	6.5869e-06	1.0457e-02
9.2000e+00	3.4346e-15	4.8580e-06	9.2149e-03
9.3000e+00	1.5693e-15	3.5364e-06	7.9929e-03
9.4000e+00	7.0857e-16	2.5298e-06	6.7911e-03
9.5000e+00	3.1530e-16	1.7659e-06	5.6094e-03
9.6000e+00	1.3737e-16	1.1883e-06	4.4478e-03
9.7000e+00	5.7655e-17	7.5308e-07	3.3062e-03
9.8000e+00	2.2291e-17	4.2640e-07	2.1844e-03
9.9000e+00	6.7570e-18	1.8207e-07	1.0824e-03
1.0000e+01	0	0	0

TABLE 3.A.3 Tabulated Data for Program 3.3 (Velocity Distribution across the Channel Based on 60 Iterations, Volume Flow Rate = 0.056392

0	4.1527e-02	7.3396e-02	9.5915e-02	1.0932e-01	1.1378e-01	1.0933e-0	9.5925e-02	7.3407e-02	4.1534e-02	0
0	4.1353e-02	7.3067e-02	9.5463e-02	1.0879e-01	1.1322e-01	1.0880e-01	9.5474e-02	7.3079e-02	4.1362e-02	0
0	4.0819e-02	7.2053e-02	9.4069e-02	1.0716e-01	1.1150e-01	1.0716e-01	9.4080e-02	7.2066e-02	4.0828e-02	0
0	3.9870e-02	7.0251e-02	9.1593e-02	1.0425e-01	1.0845e-01	1.0426e-01	9.1606e-02	7.0265e-02	3.9880e-02	0
0	3.8410e-02	6.7481e-02	8.7792e-02	9.9793e-02	1.0376e-01	9.9800e-02	8.7805e-02	6.7495e-02	3.8421e-02	0
0	3.6287e-02	6.3459e-02	8.2285e-02	9.3345e-02	9.6995e-02	9.3553e-02	8.2298e-02	6.3473e-02	3.6297e-02	0
0	3.3269e-02	5.7765e-02	7.4521e-02	8.4283e-02	8.7492e-02	8.4290e-0	7.4533e-02	5.7779e-02	3.3279e-02	0
0	2.9007e-02	4.9781e-02	6.3718e-02	7.1743e-02	7.4367e-02	7.1750e-02	6.3729e-02	4.9793e-02	2.9015e-02	0
0	2.2930e-02	3.8579e-02	4.8782e-02	5.4568e-02	5.6447e-02	5.4573e-02	4.8790e-02	3.8589e-02	2.2956e-02	0
0	1.4007e-02	2.2730e-02	2.8205e-02	3.1261e-02	3.2248e-02	3.1264e-02	2.8210e-02	2.2735e-02	1.4011e-02	0
0	0.0000	0.0000	0.0000	0.0000	0.0000	0.0000	0.0000	0.0000	0.0000	0

TABLE 3.A.4 Tabulated Data for Program 3.4

Time (Seconds)	Velocities at Different Heights (Meters/Second)					
0	0	0	0	0	0	0
1.2500e+04	0	7.8398e-10	1.0258e-07	4.8739e-06	1.1222e-04	1.4505e-03
2.5000e+04	0	4.7178e-05	3.1728e-04	1.6888e-03	7.2755e-03	2.5654e-02
3.7500e+04	0	9.3036e-04	3.4411e-03	1.0610e-02	2.8703e-02	6.8594e-02
5.0000e+04	0	3.9165e-03	1.1298e-02	2.6988e-02	5.8216e-02	1.469e-01
6.2500e+04	0	9.0859e-03	2.3089e-02	4.7775e-02	9.0168e-02	1.5815e-01
7.5000e+04	0	1.5713e-02	3.7126e-02	7.0292e-02	1.2164e-01	1.9743e-01
8.7500e+04	0	2.3011e-02	5.1964e-02	9.2806e-02	1.5129e-01	2.3244e-01
1.0000e+05	0	3.0405e-02	6.6637e-02	1.1432e-01	1.7857e-01	2.6348e-01
1.1250e+05	0	3.7535e-02	8.0580e-02	1.3433e-01	2.0332e-01	2.9094e-01
1.2500e+05	0	4.4206e-02	9.3505e-02	1.5263e-01	2.2558e-01	3.1523e-01
1.3750e+05	0	5.0331e-02	1.0530e-01	1.6917e-01	2.4548e-01	3.3669e-01
1.5000e+05	0	5.5883e-02	1.1595e-01	1.8401e-01	2.6321e-01	3.5566e-01
1.6250e+05	0	6.0875e-02	1.2550e-01	1.9727e-01	2.7897e-01	3.7243e-01
1.7500e+05	0	6.5339e-02	1.3402e-01	2.0908e-01	2.9295e-01	3.8725e-01
1.8750e+05	0	6.9316e-02	1.4161e-01	2.1956e-01	3.0534e-01	4.0035e-01
2.0000e+05	0	7.2851e-02	1.4834e-01	2.2886e-01	3.1630e-01	4.1193e-01
2.1250e+05	0	7.5987e-02	1.5431e-01	2.3709e-01	3.2601e-01	4.2216e-01
2.2500e+05	0	7.8765e-02	1.5960e-01	2.4438e-01	3.3459e-01	4.3120e-01
2.3750e+05	0	8.1225e-02	1.6428e-01	2.5083e-01	3.4219e-01	4.3920e-01
2.5000e+05	0	8.3402e-02	1.6843e-01	2.5654e-01	3.4890e-01	4.4626e-01
						5.4888e-01
						6.5651e-01
						7.6840e-01
						8.8338e-01
						1.0000e+00

TABLE 3.A.5 Tabulated Data for Program 3.5

Time (Seconds)	Velocities at Different Heights (Meters/Second)								
	0	0	0	0	0	0	0	0	0
5.0000e-02	9.9930e-02	9.9888e-02	9.9720e-02	9.9287e-02	9.8270e-02	9.6045e-02	9.1495e-02	8.2796e-02	6.7231e-02
1.0000e-01	1.9754e-01	1.9701e-01	1.9528e-01	1.9188e-01	1.8604e-01	1.7653e-01	1.6173e-01	1.3949e-01	1.0721e-01
1.5000e-01	2.8818e-01	2.8681e-01	2.8250e-01	2.7471e-01	2.6252e-01	2.4464e-01	2.1939e-01	1.8477e-01	1.3843e-01
2.0000e-01	3.6988e-01	3.6759e-01	3.6054e-01	3.4820e-01	3.2968e-01	3.0375e-01	2.6888e-01	2.2323e-01	1.6474e-01
2.5000e-01	4.4263e-01	4.3947e-01	4.2985e-01	4.1326e-01	3.8889e-01	3.5563e-01	3.1213e-01	2.5672e-01	1.8758e-01
3.0000e-01	5.0712e-01	5.0318e-01	4.9123e-01	4.7080e-01	4.4119e-01	4.0141e-01	3.5021e-01	2.8616e-01	2.0763e-01
3.5000e-01	5.6420e-01	5.5957e-01	5.4553e-01	5.2169e-01	4.8741e-01	4.4182e-01	3.8382e-01	3.1213e-01	2.2531e-01
4.0000e-01	6.1469e-01	6.0943e-01	5.9355e-01	5.6668e-01	5.2827e-01	4.7754e-01	4.1351e-01	3.3506e-01	2.4093e-01
4.5000e-01	6.5933e-01	6.5333e-01	6.3601e-01	6.0464e-01	5.6439e-01	5.0911e-01	4.3976e-01	3.5534e-01	2.5473e-01
5.0000e-01	6.9881e-01	6.9252e-01	6.7355e-01	6.4163e-01	5.9633e-01	5.3702e-01	4.6296e-01	3.7326e-01	2.6693e-01
5.5000e-01	7.3371e-01	7.2699e-01	7.0674e-01	6.7273e-01	6.2456e-01	5.6170e-01	4.8348e-01	3.8911e-01	2.7771e-01
6.0000e-01	7.6456e-01	7.5746e-01	7.3609e-01	7.0022e-01	6.4953e-01	5.8352e-01	5.0161e-01	4.0311e-01	1.5317e-01
6.5000e-01	7.9184e-01	7.8441e-01	7.6203e-01	7.2453e-01	6.7160e-01	6.0281e-01	5.1765e-01	4.1550e-01	1.5744e-01
7.0000e-01	8.1596e-01	8.0822e-01	7.8497e-01	7.4602e-01	6.9111e-01	6.1987e-01	5.3183e-01	4.2645e-01	3.0313e-01
7.5000e-01	8.3729e-01	8.2929e-01	8.0525e-01	7.6502e-01	7.0836e-01	6.3495e-01	5.4436e-01	4.3613e-01	3.0972e-01
8.0000e-01	8.5614e-01	8.4791e-01	8.2318e-01	7.8182e-01	7.2362e-01	6.4828e-01	5.5544e-01	4.4469e-01	3.1555e-01
8.5000e-01	8.7281e-01	8.6438e-01	8.3904e-01	7.9667e-01	7.3710e-01	6.6006e-01	5.6524e-01	4.5226e-01	3.2070e-01
9.0000e-01	8.8755e-01	8.7892e-01	8.5305e-01	8.0981e-01	7.4903e-01	6.7049e-01	5.7390e-01	4.5895e-01	3.2525e-01
9.5000e-01	9.0058e-01	8.9180e-01	8.6545e-01	8.2142e-01	7.5957e-01	6.7970e-01	5.8156e-01	4.6486e-01	3.2928e-01
1.0000e+00	9.1210e-01	9.0318e-01	8.7640e-01	8.3168e-01	7.6889e-01	6.8785e-01	5.8833e-01	4.7009e-01	3.3284e-01

TABLE 3.A.6 Tabulated Data for Program 3.6

Stream Function Based on 109 Iterations, ERPSI = 4.0726e-05											
Vorticity Distribution ERZETA = 0.000094498											
0	0	0	0	0	0	0	0	0	0	0	0
-2.8594e-02	-4.6621e-02	-5.7761e-02	-6.3540e-02	-6.5342e-02	-6.3544e-02	-5.7768e-02	-4.6829e-02	-2.8600e-02	-4.6829e-02	-2.8600e-02	0
-3.1696e-02	-5.8577e-02	-7.7377e-02	-8.820e-02	-9.1721e-02	-8.8214e-02	-7.7392e-02	-5.8594e-02	-3.1707e-02	-5.8594e-02	-3.1707e-02	0
-2.6830e-02	-5.4292e-02	-7.5701e-02	-8.8852e-02	-9.3256e-02	-8.8866e-02	-7.5724e-02	-5.4316e-02	-2.6847e-02	-5.4316e-02	-2.6847e-02	0
-2.0234e-02	-4.3955e-02	-6.3987e-02	-7.6907e-02	-8.1337e-02	-7.6924e-02	-6.4016e-02	-4.3986e-02	-2.0256e-02	-4.3986e-02	-2.0256e-02	0
-1.4049e-02	-3.2407e-02	-4.8905e-02	-5.9960e-02	-6.3821e-02	-5.9979e-02	-4.8938e-02	-3.2442e-02	-1.4073e-02	-3.2442e-02	-1.4073e-02	0
-8.9047e-03	-2.1801e-02	-3.4029e-02	-4.2485e-02	-4.5485e-02	-4.2505e-02	-3.4062e-02	-2.1837e-02	-8.9292e-03	-2.1837e-02	-8.9292e-03	0
-4.8927e-03	-1.2978e-02	-2.1073e-02	-2.6836e-02	-2.8908e-02	-2.6853e-02	-2.1103e-02	-1.3010e-02	-4.9148e-03	-1.3010e-02	-4.9148e-03	0
-1.9761e-03	-6.2333e-03	-1.0796e-02	-1.4137e-02	-1.5354e-02	-1.4150e-02	-1.0818e-02	-6.2575e-03	-1.9929e-03	-6.2575e-03	-1.9929e-03	0
-2.1939e-04	-1.7756e-03	-3.6111e-03	-4.9898e-03	-5.4960e-03	-4.9967e-03	-3.6230e-03	-1.7887e-03	-2.2870e-04	-1.7887e-03	-2.2870e-04	0
0	0	0	0	0	0	0	0	0	0	0	0

4

NUMERICAL SOLUTION OF THE INCOMPRESSIBLE NAVIER-STOKES EQUATION

The nonlinear behavior of fluid flow is emphasized in this chapter. Here we examine the phenomena of secondary flow and flow instability through illustrative examples.

In the numerical methods that we have used so far, a solution is computed only at a set of selected grid points in the flow region. The Galerkin method introduced in Section 4.1 takes a different approach, in which the solution is approximated by a continuous function expressed in the form of a polynomial with arbitrary coefficients. After distributing the resultant error throughout the entire fluid domain, the problem of solving nonlinear partial differential equations is simplified to that of solving a set of nonlinear algebraic equations. The solution of nonlinear algebraic equations can be found iteratively by using the Newton-Raphson method. The solution procedure is illustrated by considering the flow of a viscous incompressible fluid past a sphere. Secondary flow is found to appear in the wake when the Reynolds number exceeds a critical value.

To construct an effective numerical scheme for handling the nonlinear substantial derivative, which will be used repeatedly in later sections, a simplified one-dimensional model equation is considered in Section 4.4. Analyses show that only the upwind differencing scheme can give computational stability.

An upwind differencing formula suitable for approximating the substantial derivative in axisymmetric flow is introduced in Section 4.2. The same method works as well in other coordinate systems. It is applied in Section 4.3 to find the planar convective motion of a fluid layer under an unstable arrangement of heating from below. The method can be extended to study the behavior of rotating flows. In the remaining three sections 4.4–4.6, examples for the numerical integration

of the time-dependent Navier-Stokes equation in both primitive variable form and vorticity-stream function form are given.

4.1 FLOW AROUND A SPHERE AT FINITE REYNOLDS NUMBERS – GALERKIN METHOD

The Stokes flows considered in Section 3.7 rarely occur in practical flow problems. For example, Fig. 1.2.5 shows that the Reynolds number of a free-falling water droplet of 0.5 mm diameter is 59, which is already far beyond the Stokes flow range. If the geometry of a body is not as simple as those described in Sections 3.4 to 3.6, the inertial terms in the Navier-Stokes equation do not drop out, and the equation remains nonlinear for finite Reynolds numbers. Similar to the linearized equations, the full Navier-Stokes equation can also be solved using finite difference techniques that will be developed later in this chapter. However, in this section a completely different approach is taken in which the solution is expressed in the form of a continuous function instead of the form of numerical values at discrete points. The essence of this method, often called the *Galerkin method*, is revealed here by considering a special problem of incompressible flow past a sphere.

Let (r, θ, φ) be the spherical coordinates with the origin at the center of the sphere of radius a (Fig. 4.1.1). Far away from the sphere the flow is of a constant speed U along the x axis. Because of the axisymmetric configuration, the flow field is independent of the azimuthal coordinate φ . For such a flow a *Stokes stream function* ψ can be introduced, from which the r and θ components of the velocity are derived from the relationships

$$u_r = \frac{1}{r^2 \sin \theta} \frac{\partial \psi}{\partial \theta}, \quad u_\theta = -\frac{1}{r \sin \theta} \frac{\partial \psi}{\partial r} \quad (4.1.1)$$

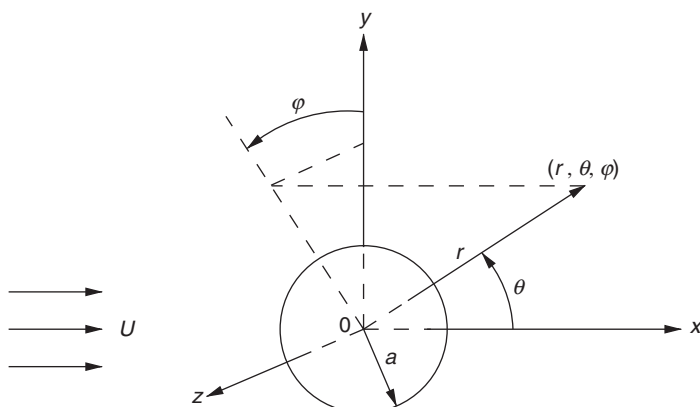


FIGURE 4.1.1 Uniform flow past a sphere.

To be generalized for curvilinear coordinates, the incompressible Navier-Stokes equation (3.1.7) is first rewritten in the form (Hughes and Gaylord, 1964, p. 24)

$$\rho \left[\frac{\partial \mathbf{V}}{\partial t} - \mathbf{V} \times (\nabla \times \mathbf{V}) \right] = -\nabla(p + \frac{1}{2}\rho V^2) - \mu \nabla \times \nabla \times \mathbf{V} \quad (4.1.2)$$

After taking the curl of this equation, the leading terms on both sides disappear under the assumption of a steady flow. Upon substitution from (4.1.1), the resultant equation becomes

$$\frac{1}{r^2 \sin \theta} \left(\frac{\partial \psi}{\partial \theta} \frac{\partial}{\partial r} - \frac{\partial \psi}{\partial r} \frac{\partial}{\partial \theta} + 2 \cot \theta \frac{\partial \psi}{\partial r} - \frac{2}{r} \frac{\partial \psi}{\partial \theta} \right) D^2 \psi = \frac{2}{Re} D^4 \psi \quad (4.1.3)$$

in which $Re = 2\rho Ua/\mu$ is the Reynolds number based on the diameter of the sphere, ψ and r are the stream function and radial coordinate made nondimensionalized by reference to Ua^2 and a , respectively, and the operator D^2 is defined as

$$D^2 \equiv \frac{\partial^2}{\partial r^2} + \frac{\sin \theta}{r^2} \frac{\partial}{\partial \theta} \left(\frac{1}{\sin \theta} \frac{\partial}{\partial \theta} \right) \quad (4.1.4)$$

The boundary conditions are that the fluid velocity components u_r and u_θ are both zero on the sphere, or

$$\psi(1, \theta) = 0 \quad (4.1.5)$$

$$\frac{\partial \psi}{\partial r}(1, \theta) = 0 \quad (4.1.6)$$

and the flow far away from the body is uniform, or

$$\psi(r, \theta) = \frac{1}{2}r^2 \sin^2 \theta \quad \text{as } r \rightarrow \infty \quad (4.1.7)$$

To facilitate mathematical manipulations, it is more convenient to introduce a new variable $\zeta \equiv \cos \theta$ instead of θ , so that (4.1.3) becomes

$$\frac{2}{Re} D^4 \psi + \frac{1}{r^2} \left(\frac{\partial \psi}{\partial \zeta} \frac{\partial}{\partial r} - \frac{\partial \psi}{\partial r} \frac{\partial}{\partial \zeta} - \frac{2\zeta}{1-\zeta^2} \frac{\partial \psi}{\partial r} - \frac{2}{r} \frac{\partial \psi}{\partial \zeta} \right) D^2 \psi = 0 \quad (4.1.8)$$

where

$$D^2 \equiv \frac{\partial^2}{\partial r^2} + \frac{1-\zeta^2}{r^2} \frac{\partial^2}{\partial \zeta^2} \quad (4.1.9)$$

and the boundary condition (4.1.7) becomes

$$\psi(r, \zeta) = \frac{1}{2}r^2(1-\zeta^2) \quad \text{as } r \rightarrow \infty \quad (4.1.10)$$

Conditions (4.1.5) and (4.1.6) remain in the same form, except θ is replaced by ζ .

According to the Galerkin method, the solution to (4.1.8) is approximated by a polynomial formed by a linear combination of a basic set of functions Φ_i :

$$\psi = \sum_{i=1}^n \Phi_i(r, \zeta) \quad (4.1.11)$$

The functions Φ_i must be linearly independent in the flow domain and must be differentiable to the extent that all terms in the differential equation and boundary conditions can be obtained. These functions are so chosen that all boundary conditions are satisfied exactly, although the solution (4.1.11) itself is only approximate. If Φ_i are the first n members of a complete set of orthogonal functions, the approximate solution is expected to approach the exact solution as $n \rightarrow \infty$.

For the problem at hand, let us choose for Φ_i the following form:

$$\Phi_i(r, \zeta) = f_i(r)[P_{i-1}(\zeta) - P_{i+1}(\zeta)], \quad i = 1, 2, \dots \quad (4.1.12)$$

where $P_m(\zeta)$ are the Legendre polynomials defined by Rodrigues' formula

$$P_m(\zeta) = \frac{1}{2^m m!} \frac{d^m}{d\zeta^m} (\zeta^2 - 1)^m \quad (4.1.13)$$

of which the first four are

$$P_0(\zeta) = 1$$

$$P_1(\zeta) = \zeta$$

$$P_2(\zeta) = \frac{1}{2}(3\zeta^2 - 1)$$

$$P_3(\zeta) = \frac{1}{2}\zeta(5\zeta^2 - 3)$$

Φ_i defined in (4.1.12) form a complete set of independent functions in the sense that the integrals

$$\int_{-1}^1 \Phi_i(r, \zeta) \Phi_j(r, \zeta) d\zeta$$

vanish for all i and j except when $i = j$, which follows from the orthogonal property of the Legendre polynomials.

Any appropriately chosen trial functions $f_i(r)$ may be used. As an example, we follow Kawaguti (1955) by choosing $n = 2$ and letting

$$\begin{aligned} \psi = & \left(\frac{1}{2}r^2 + \frac{A_1}{r} + \frac{A_2}{r^2} + \frac{A_3}{r^3} + \frac{A_4}{r^4} \right) (1 - \zeta^2) \\ & + \left(\frac{B_1}{r} + \frac{B_2}{r^2} + \frac{B_3}{r^3} + \frac{B_4}{r^4} \right) \zeta (1 - \zeta^2) \end{aligned} \quad (4.1.14)$$

which automatically satisfies the boundary condition (4.1.10) of uniform flow at infinity. The coefficients A and B are constants to be determined. The no-slip

conditions (4.1.5) and (4.1.6) at the surface require

$$A_1 + A_2 + A_3 + A_4 = -\frac{1}{2} \quad (4.1.15)$$

$$A_1 + 2A_2 + 3A_3 + 4A_4 = 1 \quad (4.1.16)$$

$$B_1 + B_2 + B_3 + B_4 = 0 \quad (4.1.17)$$

$$B_1 + 2B_2 + 3B_3 + 4B_4 = 0 \quad (4.1.18)$$

When the stream function is approximated by the trial function (4.1.14), an error or residual (NS) results on the left-hand side of the Navier-Stokes equation (4.1.8), which reads

$$\begin{aligned} (\text{NS}) = & g_1(r)(1 - \zeta^2) + g_2(r)\zeta(1 - \zeta^2) + g_3(r)\zeta^2(1 - \zeta^2) \\ & + g_4(r)(1 - \zeta^2)(1 - 3\zeta^2) + g_5(r)\zeta(1 - \zeta^2)(1 - 3\zeta^2) \\ & + g_6(r)\zeta^3(1 - \zeta^2) \end{aligned} \quad (4.1.19)$$

With the notations that

$$\alpha_m \equiv \frac{A_m}{r^m} \quad \text{and} \quad \beta_m \equiv \frac{B_m}{r^m}$$

the functions in (4.1.19) are defined as

$$g_1(r) = \frac{4}{r^5} \left[\frac{2}{\text{Re}} r(9\alpha_2 + 35\alpha_3 + 90\alpha_4) - (2\alpha_2 + 5\alpha_3 + 9\alpha_4)(\beta_1 + \beta_2 + \beta_3 + \beta_4) \right]$$

$$\begin{aligned} g_2(r) = & \frac{4}{r^5} \left[-\frac{6}{\text{Re}} r(\beta_1 - 6\beta_3 - 21\beta_4) + \left(\frac{1}{2}r^2 + \alpha_1 + \alpha_2 + \alpha_3 + \alpha_4 \right) \right. \\ & \times (12\alpha_2 + 35\alpha_3 + 73\alpha_4) + (\beta_1 + \beta_2 + \beta_3 + \beta_4)(2\beta_1 - 3\beta_3 - 7\beta_4) \left. \right] \end{aligned}$$

$$\begin{aligned} g_3(r) = & \frac{4}{r^5} \left[\left(\frac{1}{2}r^2 + \alpha_1 + \alpha_2 + \alpha_3 + \alpha_4 \right) (-6\beta_1 + 15\beta_3 + 42\beta_4) \right. \\ & + (3\alpha_1 + 4\alpha_2 + 5\alpha_3 + 6\alpha_4)(-2\beta_1 + 3\beta_3 + 7\beta_4) \\ & \left. + 3(2\alpha_2 + 5\alpha_3 + 9\alpha_4)(\beta_1 + \beta_2 + \beta_3 + \beta_4) \right] \end{aligned}$$

$$\begin{aligned} g_4(r) = & \frac{2}{r^5} \left[(r^2 - \alpha_1 - 2\alpha_2 - 3\alpha_3 - 4\alpha_4)(2\beta_1 - 3\beta_3 - 7\beta_4) \right. \\ & \left. - (8\alpha_2 + 25\alpha_3 + 54\alpha_4)(\beta_1 + \beta_2 + \beta_3 + \beta_4) \right] \end{aligned}$$

$$\begin{aligned} g_5(r) = & \frac{2}{r^5} \left[(\beta_1 + \beta_2 + \beta_3 + \beta_4)(6\beta_1 - 15\beta_3 - 42\beta_4) \right. \\ & \left. - (\beta_1 + 2\beta_2 + 3\beta_3 + 4\beta_4)(2\beta_1 - 3\beta_3 - 7\beta_4) \right] \end{aligned}$$

$$g_6(r) = -\frac{4}{r^5} [(4\beta_1 + 5\beta_2 + 6\beta_3 + 7\beta_4)(2\beta_1 - 3\beta_3 - 7\beta_4)]$$

We require that the Navier-Stokes equation be satisfied exactly on the sphere by the trial function; that is, $(\text{NS}) = 0$ at $r = 1$, which leads to

$$9A_2 + 35A_3 + 90A_4 = 0 \quad (4.1.20)$$

$$B_1 - 6B_3 - 21B_4 = 0 \quad (4.1.21)$$

Away from the sphere the error is generally not zero. It is distributed throughout the flow field in the following manner:

$$\int_1^\infty \int_{-1}^1 \frac{1}{r} (\text{NS}) [P_0(\zeta) - P_2(\zeta)] d\zeta dr = 0 \quad (4.1.22)$$

$$\int_1^\infty \int_{-1}^1 \frac{1}{r^2} (\text{NS}) [P_1(\zeta) - P_3(\zeta)] d\zeta dr = 0 \quad (4.1.23)$$

from which we obtain

$$\begin{aligned} & \frac{32}{\text{Re}} \left(\frac{6}{5}A_2 + 4A_3 + 9A_4 \right) + \frac{8}{35}(B_1 + B_3 + 4B_4) \\ & - \frac{512}{245}A_1B_1 - \frac{184}{35}A_2B_1 - \frac{448}{45}A_3B_1 - \frac{2848}{175}A_4B_1 - \frac{256}{105}A_2B_2 \\ & - \frac{32}{5}A_3B_2 - \frac{4608}{385}A_4B_2 + \frac{64}{21}A_1B_3 + \frac{48}{35}A_2B_3 - \frac{704}{385}A_3B_3 \\ & - \frac{232}{35}A_4B_3 + \frac{176}{25}A_1B_4 + \frac{2368}{385}A_2B_4 + \frac{392}{105}A_3B_4 - \frac{128}{455}A_4B_4 = 0 \end{aligned} \quad (4.1.24)$$

$$\begin{aligned} & \frac{32}{21\text{Re}}(-2B_1 + 9B_3 + 28B_4) + \frac{16}{21}(2A_2 + 5A_3 + 9A_4) \\ & + \frac{128}{63}A_1A_2 + \frac{16}{3}A_1A_3 + \frac{768}{77}A_1A_4 + \frac{64}{35}A_2^2 + \frac{1504}{231}A_2A_3 \\ & + \frac{32}{3}A_2A_4 + \frac{40}{9}A_3^2 + \frac{3424}{273}A_3A_4 + \frac{384}{49}A_4^2 - \frac{8}{63}B_1^2 \\ & - \frac{128}{567}B_1B_2 - \frac{16}{105}B_1B_3 - \frac{32}{693}B_1B_4 + \frac{64}{231}B_2B_3 + \frac{16}{27}B_2B_4 \\ & + \frac{8}{21}B_3^2 + \frac{352}{273}B_3B_4 + \frac{64}{63}B_4^2 = 0 \end{aligned} \quad (4.1.25)$$

Thus, we have eight algebraic equations, (4.1.15) to (4.1.18), (4.1.20), (4.1.21), (4.1.24), and (4.1.25), which can be solved simultaneously for the eight unknown coefficients that appeared in the trial stream function described by (4.1.14). The

first six equations enable us to express six of the unknowns in terms of the remaining two.

$$\begin{aligned} A_2 &= -\frac{15}{29}(8 + 5A_1), & B_2 &= -\frac{23}{9}B_1 \\ A_3 &= \frac{9}{29}(17 + 7A_1), & B_3 &= \frac{19}{9}B_1 \\ A_4 &= -\frac{1}{58}(95 + 34A_1), & B_4 &= -\frac{5}{9}B_1 \end{aligned} \quad (4.1.26)$$

Substituting these expressions into (4.1.24) and (4.1.25) yields

$$\frac{9.931035}{\text{Re}}A_1 + 0.011713B_1 - 0.002546A_1B_1 + \frac{44.689656}{\text{Re}} = 0 \quad (4.1.27)$$

$$0.050148A_1 + \frac{2.201058}{\text{Re}}B_1 + 0.002421A_1^2 - 0.000376B_1^2 + 0.379018 = 0 \quad (4.1.28)$$

The solution of simultaneous nonlinear algebraic equations are be discussed later in this section. After we manage to obtain the values of A_1 and B_1 , the values of the other coefficients are immediately computed from (4.1.26), so that the approximated ψ in (4.1.14) becomes a known function of r and θ .

Once the stream function becomes known, the flow pattern can be plotted and any other properties of the flow can be deduced. For example, substituting ψ into (4.1.1), we obtain the following expressions for velocity components:

$$\begin{aligned} \frac{u_r}{U} &= \left(1 + 2\frac{A_1}{r^3} + 2\frac{A_2}{r^4} + 2\frac{A_3}{r^5} + 2\frac{A_4}{r^6} \right) \cos \theta \\ &\quad + \left(\frac{B_1}{r^3} + \frac{B_2}{r^4} + \frac{B_3}{r^5} + \frac{B_4}{r^6} \right) (3 \cos^2 \theta - 1) \end{aligned} \quad (4.1.29)$$

$$\begin{aligned} \frac{u_\theta}{U} &= \left(-1 + \frac{A_1}{r^3} + 2\frac{A_2}{r^4} + 3\frac{A_3}{r^5} + 4\frac{A_4}{r^6} \right) \sin \theta \\ &\quad + \left(\frac{B_1}{r^3} + 2\frac{B_2}{r^4} + 3\frac{B_3}{r^5} + 4\frac{B_4}{r^6} \right) \sin \theta \cos \theta \end{aligned} \quad (4.1.30)$$

where u_r and u_θ are dimensional velocities and r is in dimensionless form.

One of the most important tasks is to compute the drag of the sphere. Let $(\tau_{rr})_{r=a}$ and $(\tau_{r\theta})_{r=a}$ be the normal and shear stresses, respectively, acting on an elementary surface area that is axisymmetric about the x -axis, as shown in Fig. 4.1.2. They are components of the *stress tensor* in spherical coordinates; the first index denotes the outward normal direction of the surface on which the stress is acting, and the second index denotes the direction of the stress.

The total drag of the sphere consists of two parts.

$$\text{Drag} = D_p + D_s \quad (4.1.31)$$

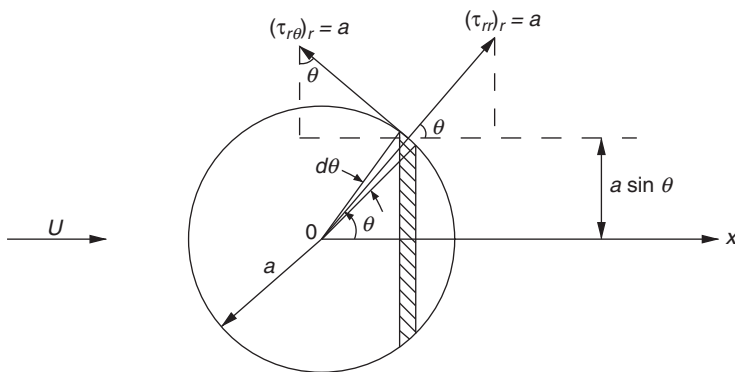


FIGURE 4.1.2 Stresses on a sphere.

where D_p is the pressure or form drag caused by normal stresses, and D_s is the skin friction caused by shear stresses on the body surface. They have the following expressions, derived by observing Fig. 4.1.2:

$$D_p = \int_0^\pi (\tau_{rr})_{r=a} \cos \theta \cdot 2\pi a \sin \theta \cdot a \ d\theta \quad (4.1.32)$$

$$D_s = - \int_0^\pi (\tau_{r\theta})_{r=a} \sin \theta \cdot 2\pi a \sin \theta \cdot a \ d\theta \quad (4.1.33)$$

The *dimensional* expressions for these two stress tensor components are (Hughes and Gaylord, 1964, p. 8)

$$\tau_{rr} = -p + 2\mu \frac{\partial u_r}{\partial r} \quad (4.1.34)$$

$$\tau_{r\theta} = \mu \left[r \frac{\partial}{\partial r} \left(\frac{u_\theta}{r} \right) + \frac{1}{r} \frac{\partial u_r}{\partial \theta} \right] \quad (4.1.35)$$

It can easily be shown by substituting from the dimensionless equations (4.1.29) and (4.1.30) that

$$\left(\frac{\partial u_r}{\partial r} \right)_{r=a} = 0 \quad (4.1.36)$$

$$\begin{aligned} (\tau_{r\theta})_{r=a} &= \frac{2\mu U}{a} [(2A_2 + 5A_3 + 9A_4) \sin \theta \\ &\quad + (2B_2 + 3B_3 + 3B_4) \sin \theta \cos \theta] \end{aligned} \quad (4.1.37)$$

We now need to find an expression for the pressure. The lengthy derivation is briefly stated as follows. We start from the θ component of the vector equation of motion (4.1.2). It can be integrated immediately after substituting velocity components from (4.1.29) and (4.1.30). When evaluated at the surface, many

terms drop out, and the expression is simplified to

$$(p)_{r=a} = P + \frac{\mu U}{a} \left[-2(8A_2 + 25A_3 + 54A_4) \cos \theta + 3(2B_2 + 7B_3 + 16B_4) \sin^2 \theta \right] \quad (4.1.38)$$

where P is the constant of integration. Since the constant term and the terms containing $\sin^2 \theta$ or $\sin \theta \cos \theta$ do not contribute to the integrals in (4.1.32) and (4.1.33), we obtain

$$D_p = \frac{8}{3}\pi\mu aU(8A_2 + 25A_3 + 54A_4) \quad (4.1.39)$$

$$D_s = \frac{16}{3}\pi\mu aU(2A_2 + 5A_3 + 9A_4) \quad (4.1.40)$$

The drag coefficient is defined as the drag force divided by $\frac{1}{2}\rho U^2 \cdot \pi a^2$, the product of the free-stream dynamic pressure and the projected area of the sphere. Based on this definition, we can compute the pressure drag coefficient, the drag coefficient from skin friction, and the total drag coefficient to arrive at the following expressions:

$$c_{dp} = \frac{32}{3Re}(8A_2 + 25A_3 + 54A_4) \quad (4.1.41)$$

$$c_{ds} = \frac{64}{3Re}(2A_2 + 5A_3 + 9A_4) \quad (4.1.42)$$

$$c_d = c_{dp} + c_{ds} \quad (4.1.43)$$

As the Reynolds number increases, the flow may become separated from the rear part of the sphere, and a secondary flow may appear in the form of a standing eddy. If the Reynolds number is not too large, the recirculating wake remains laminar and is confined within the streamline $\psi = 0$, as sketched in Fig. 4.1.3. The dimensionless radial distance r_s of the tip of the eddy, where the velocity

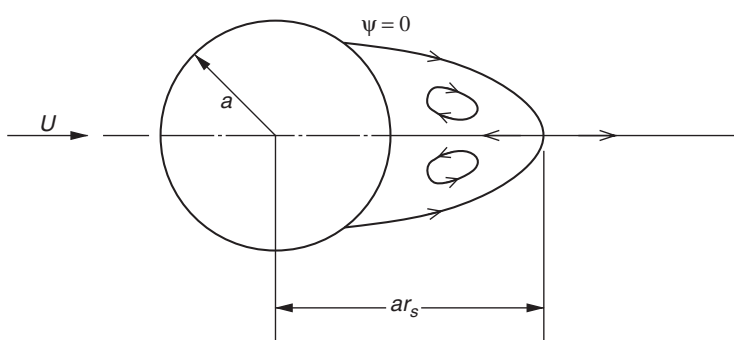


FIGURE 4.1.3 Secondary flow behind a sphere.

vanishes, is a root of the equation

$$\frac{1}{2} + \frac{A_1 + B_1}{r^3} + \frac{A_2 + B_2}{r^4} + \frac{A_3 + B_3}{r^5} + \frac{A_4 + B_4}{r^6} = 0 \quad (4.1.44)$$

which is obtained from (4.1.29) by letting $u_r = 0$ at $\theta = 0$.

To find the root of this nonlinear algebraic equation, we will use the *Newton-Raphson method*. This method is first applied to find the root of a single equation and will be extended later to find the roots of a system of simultaneous equations.

Consider a function $f(x)$ intersecting the x axis at a point x , which is a root of the equation

$$f(x) = 0 \quad (4.1.45)$$

According to the Newton-Raphson method, an arbitrary value x_1 is first guessed for the solution of (4.1.45). The function evaluated at x_1 is f_1 , which is generally not zero, as shown in Fig. 4.1.4. To improve the solution, the tangent to $f(x)$ is drawn at $x = x_1$ intersecting the x axis at x_2 . Since $\tan \theta_1 = f'(x_1) = f_1/(x_1 - x_2)$, where f' represents df/dx , we have

$$x_2 = x_1 - \frac{f(x_1)}{f'(x_1)}$$

which is closer than x_1 to the exact solution. By repeating the same procedure, successive improvements x_3, x_4, \dots of the root are computed from the generalized iterative formula

$$x_{k+1} = x_k - \frac{f(x_k)}{f'(x_k)} \quad (4.1.46)$$

The iteration is terminated when the absolute value of the difference between two consecutive approximations is less than a designated small positive quantity ϵ ;

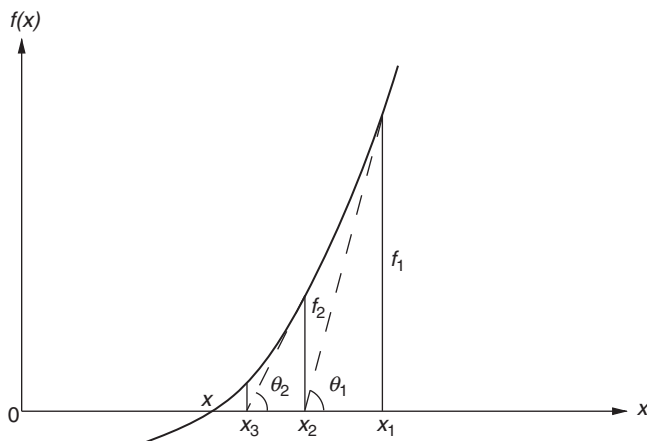


FIGURE 4.1.4 Newton-Raphson method.

that is, when

$$|x_{k+1} - x_k| < \epsilon \quad (4.1.47)$$

The Newton-Raphson method for finding the root of a single algebraic equation is programmed in the function subprogram NEWTN1 that is attached to Program 4.1; by calling this subroutine, the roots of (4.1.44) are found for various Reynolds numbers.

At the final stage of the Galerkin method, the values of A_1 and B_1 must be calculated by solving simultaneously the nonlinear algebraic equations (4.1.27) and (4.1.28), which are represented in the following general form:

$$g(x, y) = 0 \quad \text{and} \quad h(x, y) = 0 \quad (4.1.48)$$

The solution to the system of two equations may again be found using the Newton-Raphson method by first guessing arbitrary initial values x_1, y_1 and then applying successively the modified iterative formulas:

$$x_{k+1} = x_k - \frac{g(x_k, y_k)}{(\partial g / \partial x)(x_k, y_k)} \quad (4.1.49)$$

$$y_{k+1} = y_k - \frac{h(x_{k+1}, y_k)}{(\partial h / \partial y)(x_{k+1}, y_k)} \quad (4.1.50)$$

Notice that the value of x obtained from the first formula is used on the right-hand side of the second formula in computing the improved value for y . The approximate solution is considered satisfactory when both

$$|x_{k+1} - x_k| < \epsilon \quad \text{and} \quad |y_{k+1} - y_k| < \epsilon \quad (4.1.51)$$

The subroutine NEWTN2 is constructed for such a purpose.

Now we are ready to write a computer program for computing flow properties at various Reynold numbers based on the result deduced from the Galerkin method. The procedure is outlined in the listing for Program 4.1. Computations were performed for 20 different Reynolds numbers ranging from 5 to 1000. Three flow patterns were plotted respectively for $\text{Re} = 10, 100$, and 300. Points along stream lines are obtained by calling SEARCH (or by using MATLAB plotting commands, given as an option in the program); their images are plotted in the way described Section 2.6. The result is shown in Figs. 4.1.5 to 4.1.7.

The computed drag coefficient c_d agrees well with the measured curve within the same Reynolds number range, as plotted in Fig. 1.2.2. The printed data (Table 4.A.1) reveal the important fact that at low Reynolds numbers, the drag of a sphere is attributed mainly to the skin friction, whereas the pressure drag becomes more important for $\text{Re} > 90$. This suggests an efficient method for drag reduction at high Reynolds numbers by reducing the size of the separated flow region behind a body, because the pressure drag is caused primarily by the low pressure associated with the secondary flow in the wake.

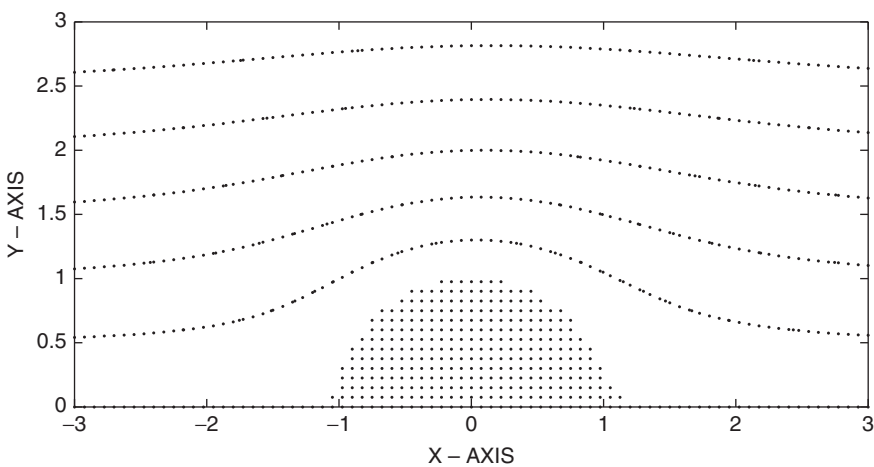


FIGURE 4.1.5 Flow about a sphere at $Re = 10$. Only the upper half of the sphere is shown.

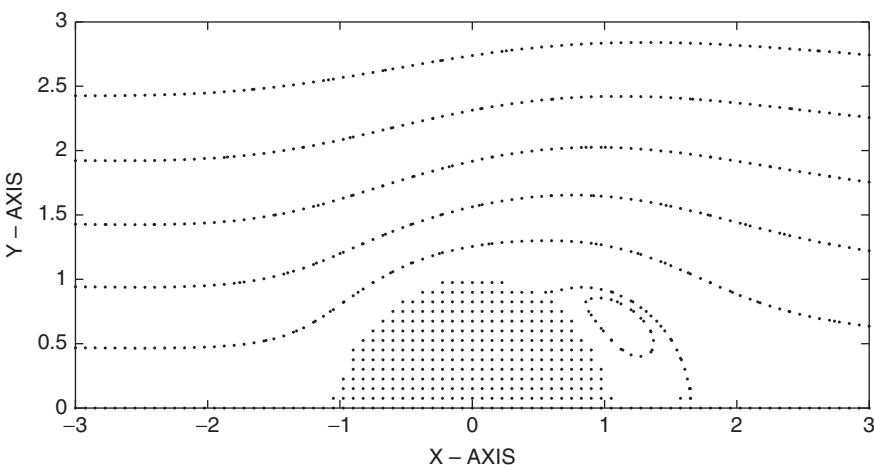


FIGURE 4.1.6 Flow about a sphere at $Re = 100$. Only the upper half of the sphere is shown.

According to the result of the Galerkin method, the boundary layer on a sphere separates at a Reynolds number slightly lower than 40 when r_s first becomes greater than unity. This is higher than the value of 24 measured by Taneda (1956). The lengths r_s at all the considered Reynolds numbers are shorter than those observed in the same experiment. Streamline plots show an almost fore-aft symmetric flow pattern at $Re = 10$. The expansion in the separated flow region as the Reynolds number increases from 100 to 300 can also be seen.

Kawaguti (1955) claimed that the trial stream function shown in (4.1.14) is appropriate for the regime $10 < Re < 80$ as far as drag is concerned. For Re less

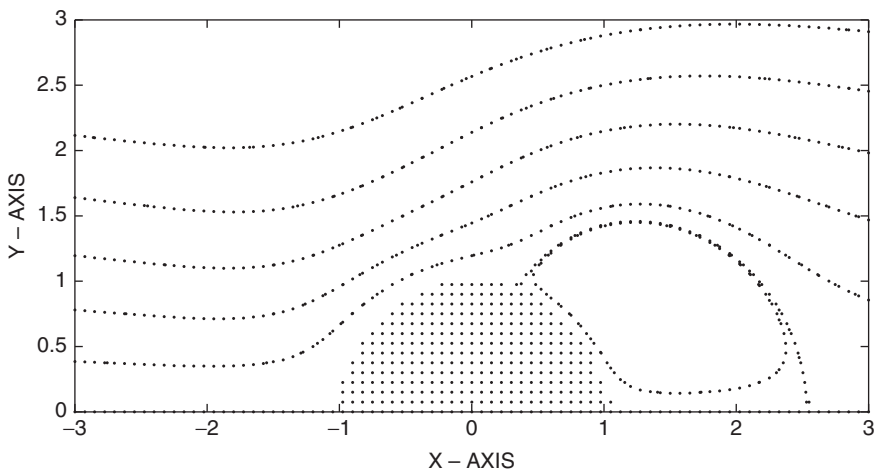


FIGURE 4.1.7 Flow about a sphere at $\text{Re} = 300$. Only the upper half of the sphere is shown.

than 2, he used another trial function:

$$\begin{aligned}\psi = & \left(\frac{1}{2}r^2 + A_1 r + A_2 + \frac{A_3}{r} + \frac{A_4}{r^2} \right) (1 - \xi^2) \\ & + \left(B_1 r + B_2 + \frac{B_3}{r} + \frac{B_4}{r^2} \right) \xi (1 - \xi^2)\end{aligned}\quad (4.1.52)$$

and the drag coefficient so computed agrees very well with that measured in that Reynolds number regime. It can be shown that (4.1.52) reduces to the Stokes approximation as the Reynolds number tends to zero.

In the present example we choose a trial stream function that satisfies boundary conditions exactly but the governing differential equation only approximately. The resultant error is distributed throughout the flow region and is set to zero on the body surface. On the other hand, the trial function may be so chosen that the governing equation is satisfied exactly but the boundary conditions are fulfilled approximately. The errors resulting from the boundary conditions are then distributed over some appropriate regions. However, the latter method can hardly be used in problems whose governing differential equations are nonlinear, such as the one considered presently.

Many other flow problems involving spherical geometry have been solved using the Galerkin method. For example, Hamielec, Storey, and Whitehead (1963) computed the drag of an undeformed fluid sphere moving through another fluid medium at various Reynolds numbers. A rigid sphere with a radial mass efflux was examined by Hamielec, Hoffman, and Ross (1967), and a sphere made of an electrically conducting material moving through a fluid carrying an electric current was studied by Chow and Halat (1969).

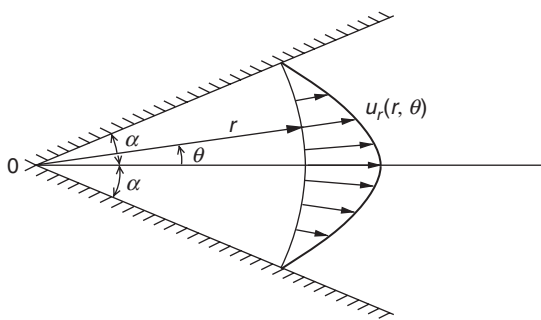


FIGURE 4.1.8 Radial flow between inclined walls.

Let us now apply the Galerkin method to solve a problem that is not related to flows about a spherical body. Consider the steady two-dimensional flow of an incompressible fluid between two inclined plane walls meeting at an angle 2α , as shown in Fig. 4.1.8. The flow is assumed to be radial, so that $u_r(r, \theta)$ is the only component of the velocity vector. The simplified Navier-Stokes equation may be written in the following component form (Hughes and Gaylord, 1964, p. 25):

$$\rho u_r \frac{\partial u_r}{\partial r} + \frac{\partial p}{\partial r} - \mu \left\{ \frac{\partial}{\partial r} \left[\frac{1}{r} \frac{\partial}{\partial r} (ru_r) \right] + \frac{1}{r^2} \frac{\partial^2 u_r}{\partial \theta^2} \right\} = 0 \quad (4.1.53)$$

$$-\frac{1}{r} \frac{\partial p}{\partial \theta} + \frac{2\mu}{r^2} \frac{\partial u_r}{\partial \theta} = 0 \quad (4.1.54)$$

If Q represents the specified mass flow rate per unit width of the channel, the equation of continuity can be written as

$$2\rho \int_0^\alpha u_r r d\theta = Q \quad (4.1.55)$$

Boundary conditions are that on the walls the velocity must be zero, or

$$u_r = 0 \quad \text{at} \quad \theta = \pm\alpha \quad (4.1.56)$$

Snyder, Spriggs, and Stewart (1964) considered a number of trial functions and found that the set

$$u_r = \sum_{j=1}^n \frac{Q}{\rho r} C_j (\alpha^2 - \theta^2)^j \quad (4.1.57)$$

$$p - p_0 = \frac{Q\mu}{\rho r^2} \left[C_0 + 2 \sum_{j=1}^n C_j (\alpha^2 - \theta^2)^j \right] \quad (4.1.58)$$

yielded the best approximate solution when only the three leading terms were used in solving the problem. These trial functions already satisfy the θ component

of the equation of motion, (4.1.54), and the boundary conditions (4.1.56). Upon substitution from (4.1.57), the continuity equation (4.1.55) becomes

$$2 \sum_{j=1}^n \int_0^\alpha C_j (\alpha^2 - \theta^2)^j d\theta = 1 \quad (4.1.59)$$

When the trial functions are substituted into the r component of the equation of motion, (4.1.53), an error $E(\theta)$ instead of zero is obtained on the left-hand side:

$$\begin{aligned} E(\theta) &= \sum_{i=1}^n \sum_{j=1}^n \operatorname{Re} C_i C_j (\alpha^2 - \theta^2)^{i+j} + 2C_0 \\ &\quad + 4 \sum_{j=1}^n C_j (\alpha^2 - \theta^2)^j + \sum_{j=1}^n C_j \frac{d^2}{d\theta^2} (\alpha^2 - \theta^2)^j \end{aligned} \quad (4.1.60)$$

where Re is the Reynolds number defined as Q/μ . The error is then distributed throughout the flow region by making it orthogonal to $(\alpha^2 - \theta^2)^k$ in the following manner:

$$\int_0^\alpha E(\theta) (\alpha^2 - \theta^2)^k d\theta = 0 \quad \text{for } k = 1, \dots, n \quad (4.1.61)$$

The linear equations (4.1.59) and n quadratic equations (4.1.61) are solved simultaneously for the $n + 1$ unknowns C_0 and C_j .

Project for Further Study: Evaluate analytically the integrals in (4.1.59) and (4.1.61) for $n = 2$, and write a computer program for $\operatorname{Re} = 14.164$ and $\alpha = 0.36$ rad. After the coefficients C_0 , C_1 and C_2 have been obtained, the dimensionless velocity $u_r \rho r / Q$ and the dimensionless pressure difference $(p - p_0) \rho r^2 / Q \mu$ are computed as functions of θ . The velocity distribution for this case, as plotted by Snyder et al. (1964), is found to be in excellent agreement with the exact solution found by Rosenhead (1940). The same problem was also studied analytically by Landau and Lifshitz (1959, p. 81) with the exact solution expressed in terms of elliptic integrals.

4.2 UPWIND DIFFERENCING AND ARTIFICIAL VISCOSITY

One of the main difficulties encountered in solving fluid dynamic problems is caused by the nonlinear substantial derivative that appears, for example, in the Euler equation (2.1.5), the Navier-Stokes equation (3.1.2), and the energy equation (3.1.3). Special care must be taken in approximating a substantial derivative by a finite difference expression. To prepare for the subsequent numerical computations in this chapter, in which the nonlinear terms in the Navier-Stokes equation are retained, we derive here a numerical scheme suitable for handling such terms by considering a simplified one-dimensional model equation:

$$\frac{\partial \zeta}{\partial t} + u \frac{\partial \zeta}{\partial x} = 0 \quad (4.2.1)$$

where ζ is the vorticity. This equation is obtained by taking the curl of the Euler equation (2.1.5) and then assuming a one-dimensional configuration (see Section 4.6). It describes the conservation of vorticity in an inviscid fluid moving parallel to the x axis. For illustration let us assume the velocity u to be a positive constant.

To replace the differential equation by a finite-difference one, the time-space plane is subdivided into small meshes of size $h \times \tau$. Using the forward-differencing formula (2.2.6) for the time derivative and the backward-differencing formula (2.2.7) for the spatial derivative, (4.2.1) at grid point (x_i, t_j) is approximated by

$$\frac{\zeta_{i,j+1} - \zeta_{i,j}}{\tau} = -u \frac{\zeta_{i,j} - \zeta_{i-1,j}}{h} \quad (4.2.2)$$

having truncation errors of $O(\tau, h)$. Because of its special appearance [i.e., the spatial difference is on the upwind side of the point indexed (i, j)], the numerical scheme (4.2.2) is said to be in the *upwind differencing form* (see Fig. 4.2.1). Rearranging terms in (4.2.2) gives

$$\zeta_{i,j+1} = (1 - C)\zeta_{i,j} + C\zeta_{i-1,j} \quad (4.2.3)$$

in which $C = u\tau/h$ is the Courant number defined in (2.10.5). Equation (4.2.3) enables us to compute vorticity at any time level based on the distribution of vorticity at the previous time step.

It is important to know whether the numerical scheme so constructed is computationally stable. Its behavior will be examined here using a method called the *discrete perturbation stability analysis*, which is conceptually different from von Neumann's stability analysis, introduced in Section 2.10. The method was first used by Thom and Apelt (1961), and it was further developed by Thoman and Szewczyk (1966). To apply this method, a steady-state solution that $\zeta_{i,j} = 0$ for all i is assumed at time level t_j . If a disturbance ϵ is introduced at x_m , its influence at the next time step will be shown at two points located at x_m and x_{m+1} . The disturbances there are computed according to (4.2.3), and have the following form:

$$\zeta_{m,j+1} = (1 - C)\epsilon \quad (4.2.4)$$

$$\zeta_{m+1,j+1} = C\epsilon \quad (4.2.5)$$

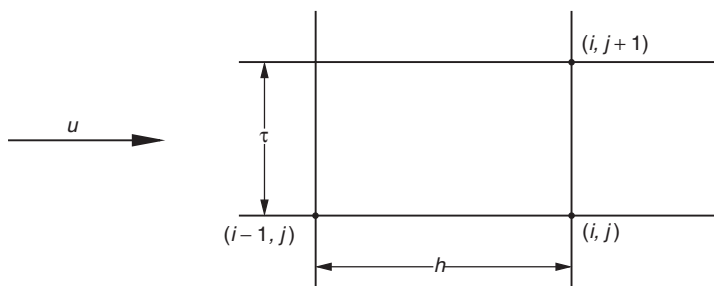


FIGURE 4.2.1 Upwind differencing scheme.

For stability it is required that both

$$|\zeta_{m,j+1}/\epsilon| \leq 1 \quad \text{and} \quad |\zeta_{m+1,j+1}/\epsilon| \leq 1 \quad (4.2.6)$$

so that these disturbances will not grow in time. From the first of (4.2.6) we have

$$-1 \leq (1 - C) \leq +1 \quad (4.2.7)$$

The inequality on the right-hand side is automatically satisfied by the upwind differencing scheme in which C is positive. To satisfy the left-hand inequality, a restriction on the magnitude of C is obtained that

$$C \leq 2 \quad (4.2.8)$$

However, the second part of (4.2.6) puts a more restrictive condition on C that

$$C \leq 1 \quad (4.2.9)$$

Thus, for a positive C satisfying (4.2.9), the computation at the first time step is stable. In a similar manner, the disturbances at the second time step can be calculated:

$$\zeta_{m,j+2} = (1 - C)^2 \epsilon \quad (4.2.10)$$

$$\zeta_{m+1,j+2} = 2C(1 - C)\epsilon \quad (4.2.11)$$

$$\zeta_{m+2,j+2} = C^2 \epsilon \quad (4.2.12)$$

It can easily be shown that the previous requirements for C also insure the computational stability at the second time step, and that the amplitudes of disturbances will decrease with increasing time steps if the perturbations at succeeding time steps are explicitly written out. Therefore, the condition that

$$0 < C \leq 1 \quad (4.2.13)$$

is the stability criterion for the numerical scheme (4.2.3).

Problem 4.1 Show that the same stability criterion (4.2.13) results if von Neumann's stability analysis is used.

If the spatial derivative in (4.2.1) were approximated by the forward (or downwind) differencing form, a finite-difference equation would be obtained having the same appearance as that of (4.2.3), but with a negative value of C . Such a numerical scheme can never satisfy one of the stability requirements, as shown on the right side of the inequality (4.2.7). Thus, a downwind differencing scheme is numerically unstable.

One of the salient features of the upwind differencing scheme is that it possesses the *transportive property* that a perturbation is advected only in the direction of the fluid motion. Suppose at x_m a disturbance ϵ is introduced at time t_j , when the trivial solution that $\zeta_{i,j} = 0$ for all i is assumed. The change

of vorticity at x_m during a time period τ is, according to (4.2.2),

$$\zeta_{m,j+1} - \zeta_{m,j} = -\frac{u\tau}{h}(\epsilon - 0) = -\frac{u\tau}{h}\epsilon \quad (4.2.14)$$

The change at x_{m+1} , which is a point one grid downstream from x_m , during the same period is calculated also from (4.2.2) as

$$\zeta_{m+1,j+1} - \zeta_{m+1,j} = -\frac{u\tau}{h}(0 - \epsilon) = +\frac{u\tau}{h}\epsilon \quad (4.2.15)$$

The result shows that the perturbation is transported, as it should be, from one point to another in the downstream direction. It is also concluded that the numerical solution to the differential equation (4.2.1) based on (4.2.3) is exact if $u\tau/h$, or C , is chosen to be unity.

Problem 4.2 Using an approximation with forward differencing in time and central differencing in space, (4.2.1) is replaced by the finite-difference equation

$$\zeta_{i,j+1} = \zeta_{i,j} - \frac{1}{2}C(\zeta_{i+1,j} - \zeta_{i-1,j}) \quad (4.2.16)$$

Use the discrete perturbation stability analysis to show that stability of this numerical scheme can be achieved only when $C \rightarrow 0$. Show also that (4.2.16) does not possess the transportive property.

The upwind differencing scheme (4.2.2) is now reexamined from a different point of view. Expanding its first and last terms in the form of a Taylor series about the value of $\zeta_{i,j}$ we obtain

$$\zeta_{i,j+1} = \zeta_{i,j} + \tau \left(\frac{\partial \zeta}{\partial t} \right)_{i,j} + \frac{1}{2}\tau^2 \left(\frac{\partial^2 \zeta}{\partial t^2} \right)_{i,j} + O(\tau^3) \quad (4.2.17)$$

$$\zeta_{i-1,j} = \zeta_{i,j} - h \left(\frac{\partial \zeta}{\partial x} \right)_{i,j} + \frac{1}{2}h^2 \left(\frac{\partial^2 \zeta}{\partial x^2} \right)_{i,j} + O(h^3) \quad (4.2.18)$$

Substituting into (4.2.2) and dropping the subscripts i and j gives

$$\frac{\partial \zeta}{\partial t} + \frac{\tau}{2} \frac{\partial^2 \zeta}{\partial t^2} + O(\tau^2) = -u \frac{\partial \zeta}{\partial x} + \frac{1}{2}uh \frac{\partial^2 \zeta}{\partial x^2} + O(h^2) \quad (4.2.19)$$

The second term on the left side can be evaluated for constant u from (4.2.1) as

$$\frac{\partial^2 \zeta}{\partial t^2} = \frac{\partial}{\partial t} \left(-u \frac{\partial \zeta}{\partial x} \right) = -u \frac{\partial}{\partial x} \left(\frac{\partial \zeta}{\partial t} \right) = u^2 \frac{\partial^2 \zeta}{\partial x^2} \quad (4.2.20)$$

Upon substitution of this expression in (4.2.19) and with terms up to the first order in τ and h retained, the differential equation

$$\frac{\partial \zeta}{\partial t} + u \frac{\partial \zeta}{\partial x} = \mu_e \frac{\partial^2 \zeta}{\partial x^2} \quad (4.2.21)$$

is obtained in which

$$\mu_e = \frac{1}{2}uh(1 - C) \quad (4.2.22)$$

is a constant determined by the grid size τ and h . Because the term on the right-hand side of (4.2.21) is caused by the errors inherited when (4.2.1) is replaced by (4.2.2), and because this term is analogous to the diffusive viscous force term in the Navier-Stokes equation (3.1.7), the coefficient μ_e is called the *artificial viscosity*. Its effect is to introduce artificial damping and diffusion in the numerical solution. μ_e vanishes when either $C = 1$ or both τ and h approach zero. Under that condition, (4.2.21) reverts to the original differential equation (4.2.1).

Hirt (1968) argued that the effect of a diffusion term is to smear out a disturbance in ζ so that a negative diffusion coefficient is physically impossible, or otherwise the opposite would happen. The requirement that $\mu_e \geq 0$ results in $C \leq 1$, which is the stability criterion (4.2.13) derived previously for the upwind numerical scheme (4.2.3). The present procedure for determining the stability, based on a differential equation constructed from the finite-difference equation through Taylor series expansion, is called *Hirt's stability analysis*.

Problem 4.3 Applying Hirt's stability analysis to the explicit formula (3.5.3) for solving parabolic equation (3.5.1), show that the resulting differential equation is

$$\frac{\partial u}{\partial t} = v \frac{\partial^2 u}{\partial y^2} + \frac{1}{2}v h^2 \left(\frac{1}{6} - R \right) \frac{\partial^4 u}{\partial y^4} \quad (4.2.23)$$

by retaining terms up to $O(\tau, h^2)$, in which $R = v\tau/h^2$. Positive terms of even derivatives, like the second-order derivative term, cause damping. Thus, the stability condition $R \leq \frac{1}{6}$ so obtained is more restrictive than the condition $R \leq \frac{1}{2}$ obtained in Section 3.5 using von Neumann's stability analysis.

Show also that when Hirt's stability analysis is applied to the implicit formula (3.6.1), the same conclusion is deduced that the numerical scheme is stable for any positive value of R .

Problem 4.4 Show that by using the discrete perturbation stability analysis, the condition $R \leq \frac{1}{2}$ is obtained for (3.5.3) in agreement with von Neumann's method.

The results stated in Problems 4.4 and 4.5 indicate that a stability criterion deduced from the discrete perturbation stability analysis or from Hirt's stability analysis may or may not agree with that deduced from von Neumann's analysis. The reason for the disagreement is that the condition for computational stability in each analysis is derived based on a different physical argument. Both von Neumann's and the discrete perturbation analyses require that the amplitude of a disturbance should not grow with time. But the former is concerned with a distribution of disturbances that can be synthesized by a Fourier series, whereas the latter traces only the influence of a point perturbation. Hirt's stability condition is based on the fact that a diffusion coefficient cannot be negative. Despite the

fact that von Neumann's stability analysis is most commonly used, each method has its own advantages as well as limitations. A comparison and evaluation of these three methods can be found in Chapter 3, Section A-5, of Roache (1972).

By using a model equation (4.2.1), we have shown that the substantial derivative may be approximated by the upwind differencing scheme, which is computationally stable if the ratio τ/h is chosen appropriate for the local fluid velocity. Furthermore, the upwind differencing scheme introduces, in addition to the truncation errors, an artificial diffusion whose effect is to smear out perturbations in the numerical solution. For thorough referencing and a more detailed discussion on the subject and its related topics, Sections A-8 to A-11 in Chapter 3 of Roache (1972) are recommended.

4.3 BÉNARD AND TAYLOR INSTABILITIES

When a horizontal layer of fluid is heated from below in a gravitational field, the density of the fluid at any location becomes smaller than the fluid just above it. If a fluid parcel is displaced slightly upward into the region of higher density, a buoyant force will assist it to move further upward. Similarly, if the fluid parcel is displaced downward into a region of smaller density, it will keep moving in the same direction. Without a sufficiently large, viscous, retarding force, this situation is said to be unstable, and the instability appears in the form of a net of hexagonal convection cells.

Lord Rayleigh (1916) made the first theoretical analysis of the so-called *Bénard problem* concerning the stability of a fluid layer in the presence of a temperature gradient parallel to the gravitational force. An extensive treatment on this subject based on linearized theories can be found in the book by Chandrasekhar (1961). An example of a solution procedure for the linearized equations for his problem was presented in Section 3.8 of this book. As we have observed there, the linearized theory predicts only the onset of instabilities. Once the flow becomes unstable, the initially small disturbances will grow with time, and the subsequent fluid motion will be governed by the nonlinear Navier-Stokes equation. Now that we already have a successful upwind-difference numerical scheme for approximating the nonlinear terms in that equation, the method used in Section 4.2 will be adopted here to study the Bénard problem numerically on the computer.

The governing equations for the fluid motion are (3.1.1) to (3.1.3), the continuity, the Navier-Stokes (adding the buoyant force), the energy equations, and, also, the equation of state. For the last equation we use, instead of (3.1.5), the following form:

$$\rho = \rho_0[1 - \alpha(T - T_0)] \quad (4.3.1)$$

where α is the coefficient of volume expansion and T_0 is the temperature at which the fluid density is ρ_0 . For ordinary gases or liquids, α is of the order of 10^{-3} or 10^{-4} . Based on this fact, considerable simplifications can be made by using the *Boussinesq approximation* that, if temperature variations are not too large, ρ

can be considered constant everywhere except in the buoyant force term. Under further assumption of constant physical properties of the fluid, (3.1.1) and (3.1.2) become

$$\nabla \cdot \mathbf{V} = 0 \quad (4.3.2)$$

$$\rho_0 \frac{D\mathbf{V}}{Dt} = -\mathbf{j}(\rho - \rho_0)g - \nabla p + \mu \nabla^2 \mathbf{V} \quad (4.3.3)$$

in which \mathbf{j} is the unit vector along the y -axis opposite to the direction of the gravitational acceleration g . It can be shown (see Section II.8, Chandrasekhar, 1961) that the energy equation (3.1.3) reduces to

$$\frac{DT}{Dt} = \kappa \nabla^2 T \quad (4.3.4)$$

where $\kappa (= k/\rho_0 c_v)$ is the coefficient of thermometric conductivity, and c_v is the constant-volume specific heat. Note that the dissipation function drops out completely from the energy equation in the present approximation.

We consider a two-dimensional flow in the x - y plane contained between two flat plates at $y = 0$ and $y = H$, respectively. The fluid originally at a uniform temperature T_0 is heated from below by increasing the temperature of the lower plate suddenly to T_1 . Being perpendicular to the fluid motion, the vorticity is in the z direction and its magnitude is designated ζ . Again, a stream function ψ can be introduced to satisfy (4.3.2).

For this problem H is a reference length, $\mu/\rho_0 H$ is a reference velocity, and $T_1 - T_0$ is a reference temperature difference. Based on these reference quantities, the following dimensionless variables are constructed:

$$\begin{aligned} X &= \frac{x}{H}, & Y &= \frac{y}{H}, & T &= \frac{t}{\rho_0 H^2 / \mu} \\ U &= \frac{u}{\mu / \rho_0 H}, & V &= \frac{v}{\mu / \rho_0 H}, & \Psi &= \frac{\psi}{\mu / \rho_0} \\ \Omega &= \frac{\zeta}{\mu / \rho_0 H^2}, & \theta &= \frac{T - T_0}{T_1 - T_0} \end{aligned} \quad (4.3.5)$$

From now on T is used to designate the dimensionless time, and θ is used to designate the dimensionless temperature difference.

Density difference in (4.3.3) is first replaced by temperature difference, with substitution from (4.3.1). Then the pressure gradient term is eliminated after taking the curl of the resulting equation of motion. When expressed in dimensionless form, the governing equations are

$$U = \frac{\partial \Psi}{\partial Y} \quad (4.3.6)$$

$$V = -\frac{\partial \Psi}{\partial X} \quad (4.3.7)$$

$$\Omega = - \left(\frac{\partial^2}{\partial X^2} + \frac{\partial^2}{\partial Y^2} \right) \Psi \quad (4.3.8)$$

$$\frac{\partial \Omega}{\partial T} + \frac{\partial(U\Omega)}{\partial X} + \frac{\partial(V\Omega)}{\partial Y} = \text{Gr} \frac{\partial \theta}{\partial X} + \left(\frac{\partial^2}{\partial X^2} + \frac{\partial^2}{\partial Y^2} \right) \Omega \quad (4.3.9)$$

$$\frac{\partial \theta}{\partial T} + \frac{\partial(U\theta)}{\partial X} + \frac{\partial(V\theta)}{\partial Y} = \text{Pr}^{-1} \left(\frac{\partial^2}{\partial X^2} + \frac{\partial^2}{\partial Y^2} \right) \theta \quad (4.3.10)$$

in which $\text{Gr} = \alpha g H^3 (T_1 - T_0) / v^2$ is the *Grashof number* and $\text{Pr} = \nu/\kappa$ is the *Prandtl number*, $\nu (= \mu/\rho_0)$ being the kinematic viscosity coefficient. In some analyses the Rayleigh number instead of the Grashof number is used, which is defined as the product of Gr and Pr . The nonlinear terms in (4.3.9) and (4.3.10) are written in the same form, so that both equations can be solved by using the same numerical technique.

In Program 4.2 we consider water ($\text{Pr} = 6.75$) enclosed by a rectangular box, shown schematically in Fig. 4.3.1. Because of the symmetry about the Y axis, only the left half of the flow needs to be computed, thus resulting in large savings in computational efforts. Square meshes of size $h \times h$ are chosen for the numerical work, and the concerned fluid region is covered with m vertical and n horizontal grid lines. Since the dimensionless distance between parallel plates is unity, the grid size h has the value of $1/(n-1)$. The values $m = 21$ and $n = 9$ are assumed for the present example.

At time $T = 0$, the temperature distribution is such that $\theta = 0$ everywhere, except $\theta = 1$ on the lower plate. As time increases, fluid temperature changes, but the values at solid walls are kept always at the initial condition. The boundary condition along the Y axis is $\partial \theta / \partial X = 0$, as required by the symmetry of the temperature field. The temperature boundary conditions are indicated in Fig. 4.3.1.

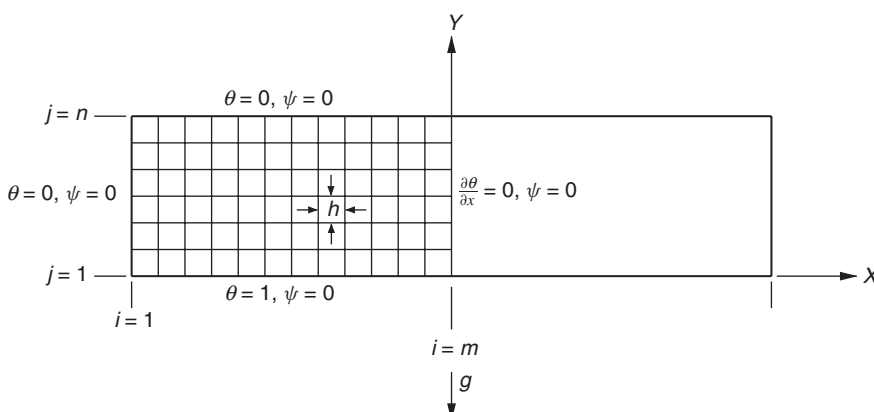


FIGURE 4.3.1 Schematic representation of the problem considered in Program 4.2.

Except the nonlinear terms, all spatial derivatives in the governing differential equations are approximated at the interior grid points using the central-difference formula. The finite-difference forms of (4.3.6) and (4.3.7) are

$$U_{i,j} = \frac{\Psi_{i,j+1} - \Psi_{i,j-1}}{2h} \quad (4.3.11)$$

$$V_{i,j} = -\frac{\Psi_{i+1,j} - \Psi_{i-1,j}}{2h} \quad (4.3.12)$$

Equation (4.3.8) conforms with the generalized Poisson equation (2.8.1) if Ψ is replaced by f and $-\Omega$ by q . The successive overrelaxation method represented by the iterative scheme (2.8.13) is programmed in the subroutine SORLX, which is used to find the stream function for a certain known vorticity distribution. The maximum error ERRMAX allowed in our program for the SOR method is 0.0001. The boundary conditions for Ψ stated in this subroutine are those shown in Fig. 4.3.1, specified particularly for the present problem. The condition that $\Psi = 0$ on the three solid walls comes from the fact that there is no net flow across these boundaries. Ψ must also vanish along the Y axis to make the fluid motion to its right the mirror image of that to its left. When the same subroutine is used elsewhere, care must be taken to check whether the boundary conditions need to be modified accordingly.

The symmetric distribution of θ and the antisymmetric distribution of Ψ about the Y axis result in the following boundary conditions for all values of j :

$$\theta_{m+1,j} = \theta_{m-1,j} \quad (4.3.13)$$

$$\Psi_{m,j} = 0 \quad (4.3.14)$$

$$\Psi_{m+1,j} = -\Psi_{m-1,j} \quad (4.3.15)$$

$$U_{m+1,j} = -U_{m-1,j} \quad (4.3.16)$$

$$U_{m,j} = 0 \quad (4.3.17)$$

$$V_{m,j} = \frac{\Psi_{m-1,j}}{h} \quad (4.3.18)$$

$$\Omega_{m,j} = 0 \quad (4.3.19)$$

The last three conditions are deduced from (4.3.11), (4.3.12), and (4.3.8), respectively, by using (4.3.14) and (4.3.15).

To solve both (4.3.9) and (4.3.10), a function subprogram named PNEW is constructed for handling a generalized equation of the form

$$\frac{\partial P}{\partial T} = -\frac{\partial(UP)}{\partial X} - \frac{\partial(VP)}{\partial Y} + A \frac{\partial Q}{\partial X} + B \left(\frac{\partial^2 P}{\partial X^2} + \frac{\partial^2 P}{\partial Y^2} \right) \quad (4.3.20)$$

The computationally stable upwind-differencing scheme of the previous section is used to approximate the first two terms on the right-hand side of this equation.

Here, we adopt a solution method developed by Torrance (1968) for solving natural convection (Torrance and Rockett, 1969) and rotating flow (Kopecky and Torrance, 1973) problems. We first define U_f and U_b as the average x -directional velocities evaluated, respectively, at half a grid point forward and backward from the point (X_i, Y_j) in the x direction, given as

$$\begin{aligned} U_f &= \frac{1}{2}(U_{i+1,j} + U_{i,j}) \\ U_b &= \frac{1}{2}(U_{i,j} + U_{i-1,j}) \end{aligned} \quad (4.3.21)$$

and, similarly, for V

$$\begin{aligned} V_f &= \frac{1}{2}(V_{i,j+1} + V_{i,j}) \\ V_b &= \frac{1}{2}(V_{i,j} + V_{i,j-1}) \end{aligned} \quad (4.3.22)$$

Further defining,

$$\begin{aligned} P1 &= (U_f - |U_f|)P_{i+1,j} + (U_f + |U_f| - U_b + |U_b|)P_{i,j} \\ &\quad - (U_b + |U_b|)P_{i-1,j} \end{aligned} \quad (4.3.23)$$

$$\begin{aligned} P2 &= (V_f - |V_f|)P_{i,j+1} + (V_f + |V_f| - V_b + |V_b|)P_{i,j} \\ &\quad - (V_b + |V_b|)P_{i,j-1} \end{aligned} \quad (4.3.24)$$

the upwind differencing form is preserved. The terms multiplied by A and B are approximated by central-differencing schemes. For them we let

$$P3 = Q_{i+1,j} - Q_{i-1,j} \quad (4.3.25)$$

$$P4 = P_{i+1,j} + P_{i-1,j} + P_{i,j+1} + P_{i,j-1} - 4P_{i,j} \quad (4.3.26)$$

Finally, a forward-differencing scheme is used to approximate the time derivative, so that

$$\left(\frac{\partial P}{\partial T} \right)_{i,j} = \frac{1}{\Delta T} (P'_{i,j} - P_{i,j}) \quad (4.3.27)$$

in which ΔT is the size of the time increment and a prime is used to denote the value of a variable evaluated at time $T + \Delta T$. Thus, after rearranging terms, (4.3.20) becomes

$$P'_{i,j} = P_{i,j} + \frac{\Delta T}{2h} \left(-P1 - P2 + A \cdot P3 + 2B \frac{P4}{h} \right) \quad (4.3.28)$$

When (4.3.28) is used to integrate (4.3.9) at an interior grid point, we replace P by Ω , Q by θ , and let $A = \text{Gr}$ and $B = 1$. The value evaluated from the right-hand side of (4.3.28) is stored temporarily as an element of a two-dimensional array named OMNEW. Similarly, for integrating (4.3.10), $A = 0$, $B = \text{Pr}^{-1}$, and

P is replaced by θ . Since Q is multiplied by zero in this case, it cannot have any influence on the computation. Q is arbitrarily replaced by θ in Program 4.2. The newly computed value for θ is assigned to the array THNEW. After computations have been done at all grid points, OMNEW and THNEW represent the updated vorticity and temperature distributions at $T + \Delta T$. Their elements are then assigned respectively back to OMEGA and THETA, which are the variable names used in the program for Ω and θ . The data may be printed or plotted before proceeding to the next time step.

The function PNEW is used to compute Ω and θ at all interior points except those on the Y axis, along which vorticity vanishes according to (4.3.19). Temperature along that axis is computed separately by again applying (4.3.28), but with the symmetric boundary condition (4.3.13) incorporated.

Vorticities at solid walls are computed according to (4.3.8). On the vertical surface at $i = 1$, $U = 0$ and $\partial U / \partial Y = 0$, so that

$$\Omega_{1,j} = \left(\frac{\partial V}{\partial X} \right)_{1,j} = \frac{1}{2h} (4V_{2,j} - V_{3,j}) \quad (4.3.29)$$

This approximation is obtained by using a three-point forward differencing scheme having a truncation error $O(h^2)$, and the fact that $V_{i,j} = 0$. Similarly, on the top and bottom walls where $V = 0$, $\partial V / \partial X = 0$, and $U = 0$, the boundary values of vorticity are approximated by

$$\Omega_{i,1} = \frac{1}{2h} (-4U_{i,2} + U_{i,3}) \quad (4.3.30)$$

$$\Omega_{i,n} = \frac{1}{2h} (4U_{i,n-1} - U_{i,n-2}) \quad (4.3.31)$$

In summary, the procedure for our numerical computations is outlined as follows. At any time instant the vorticity and temperature distributions are obtained from the conditions at the previous time step; however, at the initial instant they are prescribed by the initial conditions. Stream function is computed based on the vorticity distribution by solving (4.3.8) with the help of the subroutine SORLX. Velocity components are calculated from (4.3.11) and (4.3.12) once Ψ becomes known. By using the function subprogram PNEW, (4.3.9) and (4.3.10) are integrated to find the vorticity and temperature in the interior region at the next time step. Their boundary values are either fixed by the boundary conditions or updated appropriately in the way just described. The same process is repeated for each of the following time steps until the time step counter NSTEP reaches a specified value MAXSTP.

Problem 4.5 The computational stability of the numerical scheme (4.3.28) is to be examined. When it is applied to integrate the energy equation (4.3.10), it can be written as

$$\theta'_{i,j} = a_1\theta_{i+1,j} + a_2\theta_{i-1,j} + a_3\theta_{i,j} + a_4\theta_{i,j+1} + a_5\theta_{i,j-1} \quad (4.3.32)$$

Show that except for a_3 , all the coefficients are positive, no matter what the flow direction is. According to the quasilinear analysis of Lax and Richtmyer (1956), the scheme is stable if every coefficient in (4.3.32) is positive or, equivalently, if $a_3 \geq 0$. Show that this requirement gives the stability criterion that

$$\Delta T \leq \left[\frac{1}{2h} (U_f + |U_f| - U_b + |U_b| + V_f + |V_f| - V_b + |V_b|) + \frac{4}{h^2 \text{Pr}} \right]^{-1} \quad (4.3.33)$$

A similar inequality may be derived from (4.3.9), which puts an additional constraint on the time step size ΔT . These relations, however, show that ΔT is dependent on the velocity field as well as on h , Pr , and Gr ; its size will therefore vary as fluid motion gradually develops. A program can be written in such a way that the maximum allowable size of ΔT at every time step is determined to satisfy all stability criteria at every grid point. To make it simple, we use a constant value of 0.0025 for ΔT in Program 4.2, which is obtained after several trial runs with larger and smaller step sizes for $\text{Pr} = 6.75$ and $\text{Gr} = 1000$.

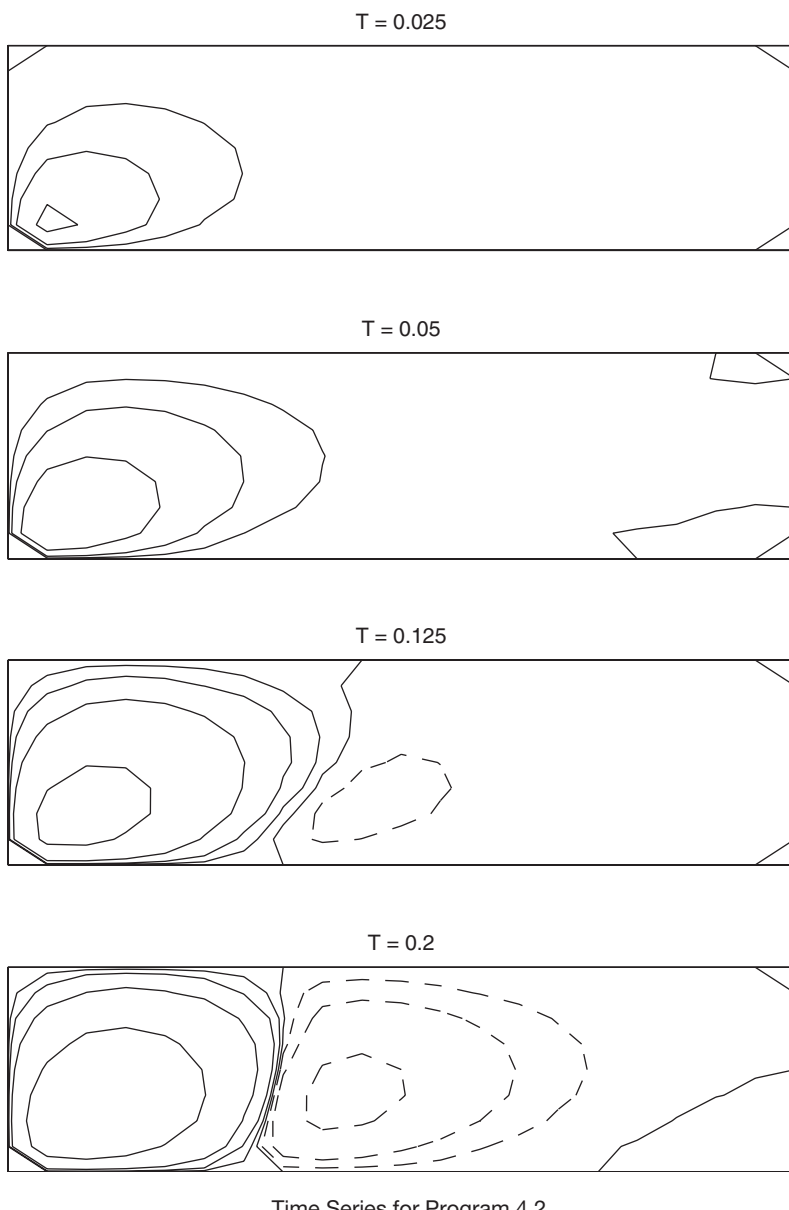
Having determined the appropriate time step size, we first run the program for a long period of time with $\text{MAXSTP} = 2000$ and print out numerical results at some selected time instants. The output reveals that no drastic change in flow pattern occurs after the step counter NSTEP is beyond 400. In Program 4.2, we finally use $\text{MAXSTP} = 400$ and plot some representative stream patterns at several critical stages of the flow development.

Program 4.2 computes for the originally stationary flow confined within a rectangular region bounded by cold top and side walls and a hot bottom plate. Shown in the output is the time history of the flow pattern in the left half of the fluid region.

Flow pattern is plotted only at particular time steps using MATLAB contour plotting programs, where solid lines indicate positive contour levels and dashed lines indicate negative contour levels.

At an early stage when $T = 0.025$, a weak convective motion develops in the fluid at the corner where the cold and hot walls intersect and the stream function is positive everywhere. Elsewhere the fluid is practically motionless. Along a closed streamline assuming a positive value of Ψ , the fluid motion is in the counterclockwise direction. Conversely, the motion is clockwise along closed streamlines of negative Ψ . Thus, the fluid descends along the cold vertical wall and then rises after flowing over the hot surface. This motion becomes stronger at $T = 0.05$, but two bubbles containing clockwise fluid motions are forming on the top and bottom plates at the midplane.

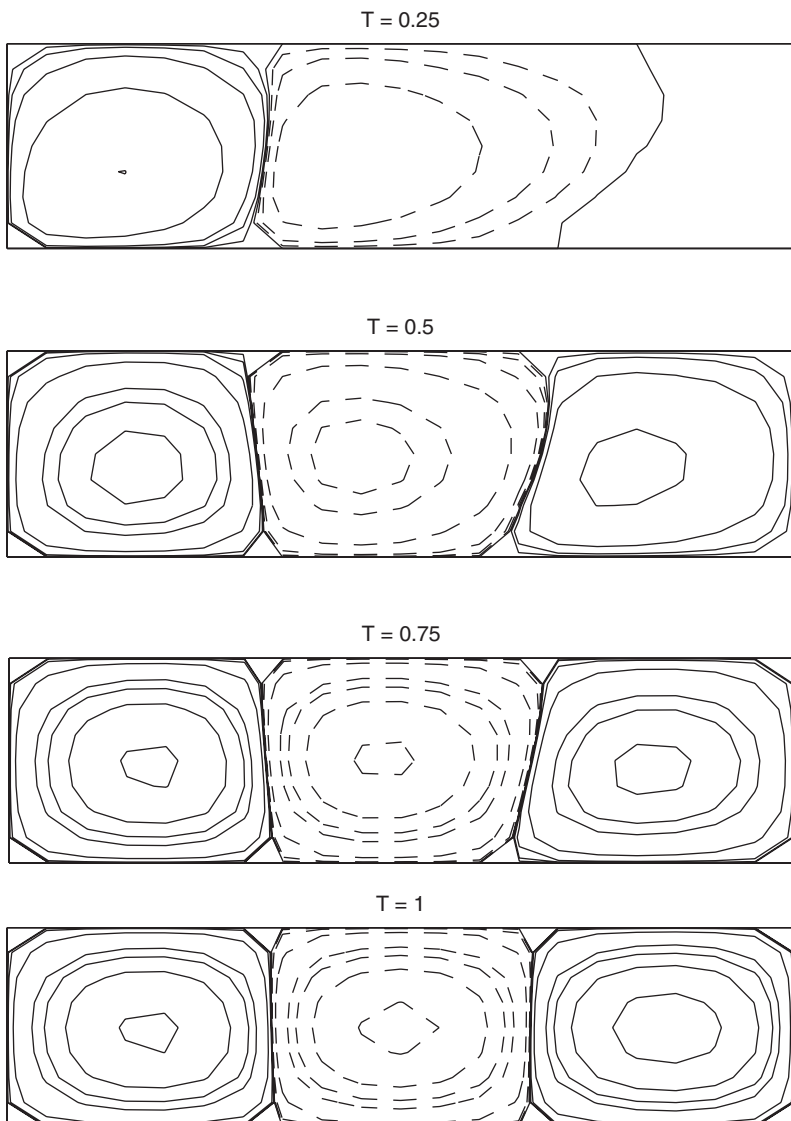
Very soon these two bubbles are connected. The region of negative Ψ expands from the middle and pushes gradually toward the side wall, as revealed by the plot showing two convective cells at $T = 0.125$. In the meantime, the motion near the side wall is intensified. While this trend continues, a small bubble containing



Time Series for Program 4.2.

counterclockwise motion starts to appear at the center of the bottom plate, as shown at $T = 0.2$. The plots for $T = 0.25, 0.5$, and 0.75 describe the expansion of this bubble and the continuing intensification of the motion in all three cells.

At $T = 1.0$, when $\text{NSTEP} = 400$, the sizes of all three cells are approximately equal. Printed numerical data disclose that at this instant the strongest motion



Time Series for Program 4.2. (continued)

occurs in the cell on the right, and the cell on the left is the weakest. This situation is not always true, however. Subsequent data show that as time increases, the motion in the left cell is strengthened, whereas those in the other two are weakened. At $T = 5.0$ the cell on the left becomes the strongest and the middle one the weakest. The differences in peak velocities among the cells are within 20% of the value in the left cell.

After $T = 1.0$ the changes in stream pattern are not drastic. At $T = 5.0$ the left boundary of the middle cell has shifted to the right from its position shown in the plot for $T = 1.0$. The displacement of the lower portion of that boundary is a little longer than that of the upper portion, resulting in a curved interface. Although a steady state has not been reached yet at $T = 5.0$, the flow does not seem to have any further significant changes.

Temperature profiles are not plotted in the output because of their slow variation with respect to time. In general, the isothermal lines, except those for $\theta = 0$ and 1, have the shape of the cutaway view of an opened umbrella.

Since the pictures shown in the output describe only the behavior of half of the flow, the total number of convective cells to appear in the channel under the present arrangement is two at the beginning, changes to four later, and finally becomes six as the flow continuously evolves. Thus, we start from an unstable situation of the fluid system having a density inversion; the numerical solution of the governing equations leads us to a final state, at which the system may be said to be most stable under the imposed temperature boundary conditions. Once the computer program has been written, we can easily change the dimensions of the channel, try different fluid media by varying the Prandtl number, or examine the effect of temperature gradient by assigning various values to the Grashof number, and we observe the results of our numerical experiments on the computer.

There are many advantages to using numerical methods to examine the stability of a fluid flow. If a linearized analytic method, as in Section 3.8, were used to study the problem considered in this section, a certain number of cells might be predicted for the onset of instability. However, this prediction may not be valid at later stages, when the ignored inertial force becomes important, as revealed by our numerical result that the number of cells is changing with time. It seems there is no guarantee that the most unstable condition predicted by a linearized theory will show up in the final state. Furthermore, the inequality in cell size and the curved cell boundaries are all nonlinear phenomena and cannot be predicted using linearized theories. Higher-order analyses are generally tedious and are usually formulated based on the linearized result. The validity of the result so obtained is also uncertain.

The numerical solution in Program 4.2 is obtained under the assumption of a two-dimensional flow. The result is unrealistic by virtue of the fact that the observed convection cells are hexagonal when looking from the top, so that the actual fluid motion is three dimensional.

Project for Further Study: Perform a numerical experiment on the fluid system shown in Fig. 4.3.1, but with some of the boundary conditions changed. It is now assumed that at the initial instant, $\theta = 0$ everywhere, except $\theta = 1$ on the upper surface. Thereafter, the temperatures at all bounding surfaces will be kept at their initial values. The upper surface is considered to be a rigid free surface where both vorticity and shear stress vanish. Assume that there is no initial motion in the water layer. The situation stated in this problem is somewhat

similar to that in an ocean region bounded by two large icebergs, when the upper surface is heated by the sun.

Project for Further Study: The general circulation of the earth's atmosphere is the result of temperature gradients parallel to the earth's surface caused by differential solar heating between polar and equatorial regions, even if the vertical stratification of the atmosphere is considered stable. The global horizontal temperature gradients may cause convective motions in the core of the earth as well as in the ocean. To study the effect of a horizontal temperature gradient, we consider a two-dimensional flow contained between two infinitely long parallel plates whose surfaces are normal to the direction of the gravitational acceleration. Using the distance H between plates as the reference length and introducing dimensionless variables defined in (4.3.5), we obtain the same set of governing equations as shown in (4.3.6) to (4.3.10).

For the initial condition we assume that $\theta = 0$ everywhere except that on the upper plate a periodic temperature distribution

$$\theta = 1 + 0.5 \sin\left(2\pi \frac{X}{\lambda}\right)$$

is imposed and is kept unchanged thereafter. The temperature on the bottom plate is also maintained always at $\theta = 0$.

Because the fluid motion driven by this periodic temperature gradient is also periodical, we only need to consider the region $0 \leq X \leq \lambda$. *Periodic boundary conditions* are applied at these two ends. More specifically, if these two vertical surfaces are represented in index notation by $i = 1$ and m , respectively, and if we let S be any scalar variable, the periodic condition for S requires that

$$\begin{aligned} S_{1,j} &= S_{m,j} \\ S_{0,j} &= S_{m-1,j} \\ S_{2,j} &= S_{m+1,j} \end{aligned}$$

Thus, in computing the vertical velocities on the left surface by a central-differencing scheme, for example, we write

$$\begin{aligned} V_{1,j} &= -\frac{1}{2h}(\Psi_{2,j} - \Psi_{0,j}) \\ &= -\frac{1}{2h}(\Psi_{2,j} - \Psi_{m-1,j}) \end{aligned}$$

so that it can be evaluated from the stream function within the concerned fluid domain. For numerical computation let $\text{Pr} = 6.75$, $\text{Gr} = 1000$, and $\lambda = 2.5$. Plot flow pattern and isothermal contours at several representative time steps.

A flow may become unstable when going along a curved path. This phenomenon can be observed, for example, in the fluid contained between two

concentric cylinders rotating at different speeds. When the two speeds are in a right combination, the flow cannot maintain its purely angular motion and becomes unstable. The instability, shown in the form of a series of donut-shaped ring vortices, was first examined by Taylor (1923) using a linearized analysis and is usually referred to as the *Taylor instability*. It turns out that the governing equations and therefore the analysis for this problem are very similar to those for the Bénard problem just considered.

For such problems, governed by the equations for an incompressible fluid, we let r_i and ω_i be the radius and angular speed of the inner cylinder and r_0 and ω_0 those of the outer. By choosing ω_i^{-1} as the reference time, r_i as the reference length, and $r_i\omega_i$ as the reference speed, a set of dimensionless variables can be defined, in which Ω is the nondimensional form of the θ -component of vorticity, whose magnitude is ζ :

$$\begin{aligned} R &= \frac{r}{r_i}, & Z &= \frac{z}{r_i}, & U &= \frac{u_z}{r_i\omega_i}, & V &= \frac{u_r}{r_i\omega_i} \\ T &= \frac{t}{\omega_i^{-1}}, & \Psi &= \frac{\psi}{r_i^2(r_i\omega_i)}, & \Omega &= \frac{-\zeta}{(r_i\omega_i)/r_i} \end{aligned} \quad (4.3.34)$$

In addition, because of the presence of the angular velocity u_θ , a new variable is defined as

$$W = \frac{ru_\theta}{r_i^2\omega_i} \quad (4.3.35)$$

which is the angular momentum expressed in dimensionless form. If the motion is still assumed to be axisymmetric, the system of nondimensionalized governing equations consists of

$$U = \frac{1}{R} \frac{\partial \Psi}{\partial R} \quad (4.3.36)$$

$$V = -\frac{1}{R} \frac{\partial \Psi}{\partial Z} \quad (4.3.37)$$

$$\left(\frac{\partial^2}{\partial R^2} - \frac{1}{R} \frac{\partial}{\partial R} + \frac{\partial^2}{\partial Z^2} \right) \Psi = R\Omega \quad (4.3.38)$$

$$\frac{\partial \Omega}{\partial T} = -\frac{\partial(U\Omega)}{\partial Z} - \frac{\partial(V\Omega)}{\partial R} - 2\frac{W}{R^3} \frac{\partial W}{\partial Z} + \frac{1}{Re} \left(\frac{\partial^2}{\partial R^2} + \frac{1}{R} \frac{\partial}{\partial R} - \frac{1}{R^2} + \frac{\partial^2}{\partial Z^2} \right) \Omega \quad (4.3.39)$$

$$\frac{\partial W}{\partial T} = -\frac{\partial(UW)}{\partial Z} - \frac{\partial(VW)}{\partial R} - \frac{VW}{R} + \frac{1}{Re} \left(\frac{\partial^2}{\partial R^2} - \frac{1}{R} \frac{\partial}{\partial R} + \frac{\partial^2}{\partial Z^2} \right) W \quad (4.3.40)$$

in which $Re = r_i^2\omega_i/v$ is the characteristic Reynolds number, and (4.3.40) is the θ component of the Navier-Stokes equation. The nonlinear terms in these equations are expressed purposely in the same form.

A computational procedure can be set up for solving the rotating flow problem that is analogous to that used for solving the convection problem. You are then ready to make numerical studies of the stability and other nonlinear features of rotating flows through the following suggested problems.

Project for Further Study: Consider an already established steady flow between infinitely long concentric cylinders, whose boundary conditions are

$$W = 1 \quad \text{at} \quad R = 1 \quad (4.3.41)$$

$$W = \frac{r_0^2 \omega_0}{r_i^2 \omega_i} \quad \text{at} \quad R = \frac{r_0}{r_i} \quad (4.3.42)$$

Since there is no motion in the meridian plane, $U = V = 0$, so the angular motion is described by

$$W = [(A^2 B - 1)R^2 + A^2(1 - B)]/(A^2 - 1) \quad (4.3.43)$$

which is the steady-state solution of (4.3.40) satisfying boundary conditions (4.3.41) and (4.3.42). The parameters

$$A = \frac{r_0}{r_i} \quad \text{and} \quad B = \frac{\omega_0}{\omega_i} \quad (4.3.44)$$

are, respectively, the ratio of the radii and that of the angular speeds; they are given constants.

The purely angular flow is then perturbed slightly in the meridian plane at time $T = 0$. The small perturbation is represented by a weak periodic vorticity distribution

$$\Omega = 0.01 \sin\left(2\pi \frac{Z}{\lambda}\right) \quad (4.3.45)$$

where λ is the dimensionless wavelength. The meridian motion associated with this vorticity is computed from (4.3.36) and (4.3.37) after the stream function has been obtained by solving the equation (4.3.38). Consequently, the angular motion will be modified according to (4.3.40), causing Ω to change. The time history of the flow variation is then traced by progressing in T .

On solid walls both U and V vanish for all times. Responding to a periodic disturbance, the resultant fluid motion is also periodic, so that only an axial length of λ is needed in the computation. The periodic boundary conditions stated in the Project for Further Study on page 244 are applied at the ends of this fluid region.

For numerical computation we assume that $A = 2, B = 0$ (for a stationary outer cylinder), $\lambda = 4$, and $Re = 1000$. Suggested intervals are $h = 0.125$ and $\Delta T = 0.02$. The result should show the development of Taylor ring vortices between the cylinders. Similar flow patterns can be found in the work by Strawbridge and Hooper (1968), obtained using a slightly different numerical scheme.

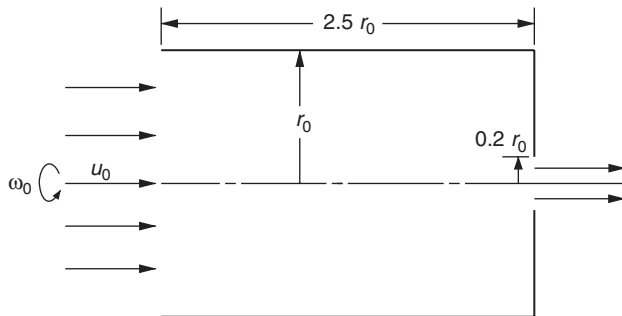


FIGURE 4.3.2 Rotating tube flow through a constriction.

Project for Further Study: Find the steady-state solution for a flow through a rotating tube having an abrupt contraction, as shown in Fig. 4.3.2. At the entrance the flow is in rigid body rotation with the same angular speed ω_0 as that of the tube, and the axial motion is uniform of speed u_0 .

In this problem it is natural to choose the tube radius r_0 as the reference length and u_0 the reference speed. The dimensionless variables are defined similar to (4.3.34). Instead of (4.3.35), the dimensionless angular momentum is redefined as

$$W = \frac{ru\theta}{r_0^2\omega_0} \quad (4.3.46)$$

After they are nondimensionalized, the governing equations are the same as those for the previous problem, except that (4.3.39) is now replaced by

$$\begin{aligned} \frac{\partial \Omega}{\partial T} &= -\frac{\partial(U\Omega)}{\partial Z} - \frac{\partial(V\Omega)}{\partial R} - \frac{1}{2Ro^2} \frac{W}{R^3} \frac{\partial W}{\partial Z} \\ &+ \frac{1}{Re} \left(\frac{\partial^2}{\partial R^2} + \frac{1}{R} \frac{\partial}{\partial R} - \frac{1}{R^2} + \frac{\partial^2}{\partial Z^2} \right) \Omega \end{aligned} \quad (4.3.47)$$

in which $Re = u_0 r_0 / v$ is the Reynolds number and $Ro = u_0 / 2r_0 \omega_0$ is the *Rossby number*, whose value indicates the relative magnitude between the axial and angular motions of the flow.

Boundary conditions at the entrance have already been specified. For the remaining boundaries we assume no-slip conditions on the rotating tube wall, and we require that $V = 0$ at the exit. Those boundary conditions concerning stream function are specifically stated as follows: $\Psi = 0$ along the tube axis, $\Psi = \frac{1}{2}$ on the wall, $\Psi = \frac{1}{2}R^2$ at the entrance and, finally, $\partial\Psi/\partial Z = 0$ at the exit. Note that the velocity along the tube axis is calculated from

$$U_{i,1} = \frac{2\psi_{i,2}}{h^2} \quad (4.3.48)$$

For a fixed value $Re = 50$, plot the flow pattern in the meridian plane for $Ro = 2, 1, 0.5$, and 0.2 .

According to a computation (Yih, 1965, p. 260) for an inviscid rotating flow into a sink (which can be formed by letting the cross-sectional area of our exit approach zero), at small Rossby numbers the flow is found to separate from the axis, forming a secondary flow upstream from the sink.

Project for Further Study: In the book by Scorer (1958), the author used a cartoon as the last problem for discussion. It shows a woman having arrived at the bottom of a long helical stairway with a tray, serving coffee to two gentlemen. The caption states: "You'll find it's already stirred." Let us check on the computer to see if what was said by the woman is correct. An idealized coffee cup is shown in Fig. 4.3.3. The motion of the cup can be decomposed into a translation and a rotation. Only the rotation has an effect on the fluid motion inside the cup. At the initial instant when the woman starts to come down the stairway, there is no motion in the coffee, and the cup is suddenly given an angular velocity ω_0 . Suppose the woman is moving at a constant pace so that the angular velocity is maintained at the same value. The upper surface of the liquid is assumed to be horizontal and free of shear stresses.

In this problem there is no net axial flow, the dimensionless governing equations are exactly the same as (4.3.41)–(4.3.45), except that the reference length and speed are now r_0 and $r_0\omega_0$, respectively, and the dimensionless angular momentum is redefined as $W = ru_\theta/r_0^2\omega_0$. We assume $r_0 = 0.04$ m and $\omega_0 = 0.1\pi$ rad/s (computed for 3 revolutions/min). In spite of lacking data on the physical properties of hot coffee, we use the value of 10^{-6} m²/s for kinematic viscosity, which is approximately that of water. The characteristic Reynolds number, $r_0^2\omega_0/\nu$, is 500 after rounded off.

Derive two expressions for ΔT , in a form similar to that of (4.3.33), by applying the quasilinear analysis of Lax and Richtmyer on the governing equations (4.3.47) and (4.3.40). In your program, at every time step the lowest value of

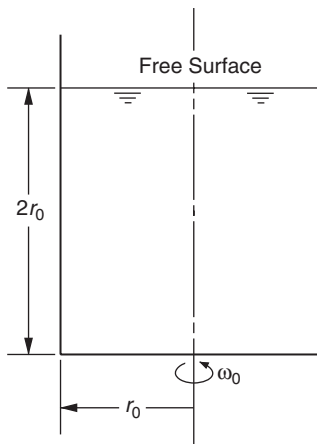


FIGURE 4.3.3 Spin-up in a coffee cup.

ΔT , which is obtained by searching through the values at all grid points, is to be used for numerical computations. Selectively plot the flow pattern until the dimensionless time reaches the value 8. The reference time in this problem is $1/\omega_0$.

This is a simplified *spin-up problem*, studying the secondary flows and the development of boundary layers on surfaces in a rotating fluid. The spin-up problems that interest geophysicists and astrophysicists are usually concerned with more complex geometries and may include other effects, such as buoyancy and electromagnetic forces. A general description of the spin up phenomenon can be found in Greenspan (1968).

4.4 PRIMITIVE VARIABLE FORMULATION: ALGORITHMIC CONSIDERATIONS

We consider the numerical solution of the two-dimensional, incompressible, time-dependent Navier-Stokes equation written in primitive variable form, where the unknowns are the two velocity components and the pressure. As we have seen in Chapter 3, the governing equations, i.e., the (scalar) continuity equation (3.1.6) and the (vector) equation of motion (3.1.7) are obtained from mass conservation and momentum conservation laws. We also recall that in incompressible flows density is constant, and the energy equation is important only when there is surface heating as in the Benard problem. It was also shown in Chapter 3 that as opposed to the primitive variables, in the vorticity-stream function formulation of the governing equations, the pressure gradient term does not explicitly appear. In this section, we will first reexamine several second-order accurate finite difference formulas that have been widely used for the solution of incompressible flow problems in primitive variable form. We will then introduce efficient numerical algorithms for the solution of tridiagonal systems of linear equations that result from implicit time advancement of the viscous terms. The solution for pressure, staggered mesh arrangements, time advancement will be introduced in Section 4.5, where we also consider a canonical model problem consisting of the flow in a lid-driven square cavity.

Generally, finite difference formulas with second-order accuracy in space and first-order in time are sufficiently accurate for a large number of problems, especially when the transients in the solution are not of particular interest. However, there are situations where the time dependency of the solution is important, such as in turbulent and transitional flows. Also, if the flow has a rapid mean transient, time accuracy will be of interest. We will explore two popular and efficient methods that are second-order accurate in both time and space that have been used frequently for the computation of time-dependent, low-speed, incompressible flows. To introduce these methods, we will first consider the model convection (hyperbolic) and the model diffusion (parabolic) equations. Subsequently, we will apply these methods to the numerical integration of the primitive variable form of the governing equations.

From (2.13.8), the one-dimensional nonlinear convection equation is written as

$$\frac{\partial u}{\partial t} + u \frac{\partial u}{\partial x} = 0 \quad (4.4.1)$$

where u is the velocity, t is time, and x is the spatial coordinate. Let us use Taylor series expansion around the grid point (i, n) with respect to the coordinates (x, t) , with $u_t = \partial u / \partial t$, $u_{tt} = \partial^2 u / \partial t^2$:

$$u_i^{n+1} = u_i^n + (u_t)_i^n \Delta t + (u_{tt})_i^n \frac{\Delta t^2}{2} + O(\Delta t^3) \quad (4.4.2)$$

As in Section 2.13, the superscript n will denote the time level and the subscripts i, j are the spatial indices representing coordinates x and y , respectively; the x increment will be denoted Δx , the y increment Δy , and the time step as Δt . Using one-sided differences,

$$(u_{tt})_i^n = \frac{(u_t)_i^n - (u_t)_i^{n-1}}{\Delta t} + O(\Delta t) \quad (4.4.3)$$

and substituting (4.4.3) into (4.4.2), we obtain

$$u_i^{n+1} = u_i^n + (u_t)_i^n \Delta t + \frac{1}{2} [(u_t)_i^n \Delta t - (u_t)_i^{n-1} \Delta t] + O(\Delta t) \Delta t^2 \quad (4.4.4)$$

and after dividing by Δt

$$\frac{u_i^{n+1} - u_i^n}{\Delta t} = \frac{3}{2} \left(\frac{\partial u}{\partial t} \right)_i^n - \frac{1}{2} \left(\frac{\partial u}{\partial t} \right)_i^{n-1} + O(\Delta t^2) \quad (4.4.5)$$

Now, from (4.4.1) let us define

$$\frac{\partial u}{\partial t} = -u \frac{\partial u}{\partial x} \equiv H \quad (4.4.6)$$

Substituting into (4.4.5), we obtain

$$\frac{u_i^{n+1} - u_i^n}{\Delta t} = \frac{3}{2} H_i^n - \frac{1}{2} H_i^{n-1} + O(\Delta t^2) \quad (4.4.7)$$

Equation (4.4.7) is called the Adams-Bashforth method, and with second-order central differences in space, the spatial accuracy of this scheme becomes $O(\Delta x^2)$. Linear stability analysis indicates that this method is mildly but unconditionally unstable, and the amplification factor can be written as

$$\lambda = 1 + O(\Delta t^2) \quad (4.4.8)$$

In long-term time-accurate calculations, this instability remains bounded if the time step is subject to the Courant number restriction, i.e.,

$$C \equiv \frac{u_{\max} \Delta t}{\Delta x} \leq 1 \quad (4.4.9)$$

As shown in Section 2.10, this condition is obtained from the von Neumann analysis, which assumes the error function to be periodic (nonperiodic boundary conditions are not taken into account) and the equation to be locally linear. Therefore, for nonlinear equations such as (4.4.1), it is generally required to choose Δt (generally by trial and error) such that C is considerably less than one. We note that although the convective term is nonlinear (quasi-linear), (4.4.7) can be solved algebraically because explicit finite difference formulas used for the nonlinear terms do not result in nonlinear difference equations, whereas implicit formulas used on the nonlinear convective terms will result in nonlinear difference equations. The solution of such nonlinear difference equations will necessitate local linearization or iterative improvement, which will increase computer resource requirements (Tannehill, Anderson, and Pletcher, 1997, p. 449). Generally, the inclusion of a diffusive term improves the stability of the Adams-Bashforth (AB) method.

We also note that to advance the velocity field to time level $(n + 1)$ using (4.4.7), we need two levels of initial data, at time level n and at time level $(n - 1)$. This can be accomplished by initially using a one-step method, such as the Euler explicit method for the first time step, and then using that result and the given initial conditions as the initial data for the second time step to start the AB solution process. The Euler explicit method for the convection-diffusion equation can be written as

$$\frac{u_i^{n+1} - u_i^n}{\Delta t} = H_i^n + O(\Delta t) \quad (4.4.10)$$

Thus, for the first time step only, the time accuracy of the AB method is first order.

Let us now consider the one-dimensional nonlinear Burgers equation (nonlinear convection-diffusion equation), which is a more realistic model for the Navier-Stokes equation,

$$\frac{\partial u}{\partial t} + u \frac{\partial u}{\partial x} = v \frac{\partial^2 u}{\partial x^2} \quad (4.4.11)$$

where v is some transport coefficient, for example, the kinematic viscosity of the fluid. Rewriting (4.4.6) as

$$\frac{\partial u}{\partial t} = v \frac{\partial^2 u}{\partial x^2} - u \frac{\partial u}{\partial x} \equiv H \quad (4.4.12)$$

and using the Adams-Bashforth formula (4.4.7) with central differences in space, we obtain

$$\frac{u_i^{n+1} - u_i^n}{\Delta t} = \frac{3}{2} H_i^n - \frac{1}{2} H_i^{n-1} + O(\Delta t^2, \Delta x^2) \quad (4.4.13)$$

For this equation, both the convective and diffusive stability requirements must be satisfied. Obtained from the von Neumann analysis, these two conditions are, respectively,

$$C = \frac{u_{\max} \Delta t}{\Delta x} \leq 1 \quad (4.4.14)$$

$$d \equiv \nu \frac{\Delta t}{\Delta x^2} \leq \frac{1}{2} \quad (4.4.15)$$

For practical purposes, we choose Δt from the smaller of the two. It is interesting to note that Δt obtained from (4.4.15) decreases quadratically with Δx , whereas according to (4.4.14), Δt decreases linearly with Δx . Therefore, in regions of the flow where field variables rapidly vary, and where it would be necessary to use very fine mesh with small Δx , the time step restrictions imposed by (4.4.15) will be much more severe. To relax the Δt restriction due to the explicit differencing of the diffusion term, it is generally preferred to use an implicit scheme. For the linear diffusion term with constant viscosity, implicit finite differences result in a banded system of linear equations that can be solved very efficiently by direct elimination methods.

In Section 3.6, the implicit Crank-Nicolson (CN) method was introduced as a second-order accurate (in time and in space) formula for solving parabolic partial difference equations. This method is unconditionally stable (in the von Neumann sense) for both advective and diffusive equations. To recapitulate the derivation in Section 3.6, let us consider the model diffusion equation with constant transport coefficient ν ,

$$\frac{\partial u}{\partial t} = \nu \frac{\partial^2 u}{\partial x^2} \quad (4.4.16)$$

Using “trapezoidal” differencing with Taylor series,

$$u_i^{n+1} = u_i^n + (u_t)_i^n \Delta t + (u_{tt})_i^n \frac{\Delta t^2}{2} + (u_{ttt})_i^n \frac{\Delta t^3}{6} + \dots \quad (4.4.17)$$

$$u_i^n = u_i^{n+1} - (u_t)_i^{n+1} \Delta t + (u_{tt})_i^{n+1} \frac{\Delta t^2}{2} - (u_{ttt})_i^{n+1} \frac{\Delta t^3}{6} + \dots \quad (4.4.18)$$

Subtracting (4.4.18) from (4.4.17), we obtain

$$\begin{aligned} u_i^{n+1} - u_i^n &= u_i^n - u_i^{n+1} + (u_t)_i^n \Delta t + (u_t)_i^{n+1} \Delta t + (u_{tt})_i^n \frac{\Delta t^2}{2} \\ &\quad - (u_{tt})_i^{n+1} \frac{\Delta t^2}{2} + O(\Delta t^3) \end{aligned} \quad (4.4.19)$$

Again using Taylor series,

$$(u_{tt})_i^{n+1} = (u_{tt})_i^n + \Delta t (u_{ttt})_i^n + O(\Delta t^2) \quad (4.4.20)$$

can be obtained. Substitution of (4.4.20) into (4.4.19) gives

$$2(u_i^{n+1} - u_i^n) = (u_t)_i^n \Delta t + (u_t)_i^{n+1} \Delta t + (u_{tt})_i^n \frac{\Delta t^2}{2} - (u_{tt})_i^n \frac{\Delta t^2}{2} - (u_{ttt})_i^n \frac{\Delta t^3}{2} \quad (4.4.21)$$

After canceling and dividing by Δt , equation (4.4.21) can be written as

$$\frac{u_i^{n+1} - u_i^n}{\Delta t} = \frac{1}{2}(u_t)_i^{n+1} + \frac{1}{2}(u_t)_i^n + O(\Delta t^2) \quad (4.4.22)$$

Substituting directly from (4.4.16) for $u_t = vu_{xx}$,

$$\frac{u_i^{n+1} - u_i^n}{\Delta t} = \frac{1}{2} \left(v \frac{\partial^2 u}{\partial x^2} \right)^{n+1} + \frac{1}{2} \left(v \frac{\partial^2 u}{\partial x^2} \right)^n + O(\Delta t^2, \Delta x^2) \quad (4.4.23)$$

Spatial derivatives will be replaced by second-order central differences to maintain second-order accuracy in both space and time:

$$\begin{aligned} \frac{u_i^{n+1} - u_i^n}{\Delta t} &= \frac{1}{2} \frac{v}{\Delta x^2} \left(u_{i+1}^{n+1} - 2u_i^{n+1} + u_{i-1}^{n+1} + u_{i+1}^n - 2u_i^n + u_{i-1}^n \right) \\ &\quad + O(\Delta t^2, \Delta x^2) \end{aligned} \quad (4.4.24)$$

Simplifying this expression, we obtain

$$-\frac{d}{2}u_{i+1}^{n+1} + (1+d)u_i^{n+1} - \frac{d}{2}u_{i-1}^{n+1} = \frac{d}{2}u_{i+1}^n - (d-1)u_i^{n+1} + \frac{d}{2}u_{i-1}^n \quad (4.4.25)$$

with the diffusion coefficient defined as $d = v\Delta t/\Delta x^2$. Equation (4.4.25) shows that the finite difference formula leads to a tridiagonal matrix equation which can be solved by an efficient direct solver.

Now let us apply the Crank-Nicolson method to the convection–diffusion equation (4.4.11):

$$\frac{u_i^{n+1} - u_i^n}{\Delta t} + \frac{1}{2} \left(u \frac{\partial u}{\partial x} \right)^{n+1} - \frac{1}{2} v \frac{\partial^2 u}{\partial x^2}^{n+1} = \frac{1}{2} v \frac{\partial^2 u}{\partial x^2}^n - \frac{1}{2} \left(u \frac{\partial u}{\partial x} \right)^n \quad (4.4.26)$$

The second term on the left-hand side of this equation is the nonlinear convective term discretized at the advanced time level ($n + 1$) and, with central differences, can be written as

$$\frac{1}{2} \left(u \frac{\partial u}{\partial x} \right)^{n+1} = \frac{1}{4\Delta x} u_i^{n+1} (u_{i+1}^{n+1} - u_{i-1}^{n+1}) \quad (4.4.27)$$

resulting in a nonlinear difference equation. The solution of such an equation requires local linearization, which can be obtained by lagging the coefficient term u_i^{n+1} (predictor step), and using the new value in the coefficient during the

corrector step; one iteration step is generally sufficient (Tannehill et al., 1997). It is apparent that because the predictor step has to go through the whole computation cycle, this linearization will be accomplished at increasing computational cost, which can be significant for multidimensional large-scale problems. We also note that in the von Neumann sense, the Crank-Nicolson method is unconditionally stable for the convection–diffusion equation.

A very useful and highly popular scheme for the incompressible Navier-Stokes equation is the semi-implicit AB-CN method, which uses the explicit Adams-Bashforth (AB) method on the nonlinear convective terms, and the implicit Crank-Nicolson (CN) method on the diffusion terms. One important advantage of this approach is that due to the explicit AB method on the nonlinear convective terms, no iteration (or linearization) is required, as the resulting finite-difference equation is linear; hence, the calculation is considerably cheaper than with fully implicit methods. The AB-CN method is especially suitable for viscous wall-bounded problems, in which the implicit CN method on the viscous diffusion terms relaxes the viscous stability time-step restriction.

Considering (4.4.11), we write the convective term in conservative form, and define a function H ,

$$H = -u \frac{\partial u}{\partial x} = -\frac{1}{2} \frac{\partial u^2}{\partial x} \quad (4.4.28)$$

so that (4.4.11) can be written as

$$\frac{\partial u}{\partial t} = H + v \frac{\partial^2 u}{\partial x^2} \quad (4.4.29)$$

Using the AB method for H , we obtain

$$\frac{u_i^{n+1} - u_i^n}{\Delta t} = \frac{3}{2} H_i^n - \frac{1}{2} H_i^{n-1} \quad (4.4.30)$$

For the diffusion term we use the CN method such that

$$\frac{u_i^{n+1} - u_i^n}{\Delta t} = \left(v \frac{\partial^2 u}{\partial x^2} \right)^{n+1/2} = \frac{1}{2} v \frac{\partial^2 u}{\partial x^2}^{n+1} + \frac{1}{2} v \frac{\partial^2 u}{\partial x^2}^n \quad (4.4.31)$$

Now we can advance (4.4.29) in time, which obtains

$$\frac{u_i^{n+1} - u_i^n}{\Delta t} = \frac{3}{2} H_i^n - \frac{1}{2} H_i^{n-1} + \frac{1}{2} v \frac{\partial^2 u}{\partial x^2}^{n+1} + \frac{1}{2} v \frac{\partial^2 u}{\partial x^2}^n + O(\Delta t^2, \Delta x^2) \quad (4.4.32)$$

Rearranging (4.4.32),

$$u_i^{n+1} - \frac{1}{2} v \Delta t \frac{\partial^2 u}{\partial x^2}^{n+1} = u_i^n + \frac{3}{2} \Delta t H_i^n - \frac{1}{2} \Delta t H_i^{n-1} + \frac{1}{2} v \Delta t \frac{\partial^2 u}{\partial x^2}^n \equiv \text{RHS}_i^n \quad (4.4.33)$$

Using central differences, and defining the numerical diffusion coefficient as $d = v\Delta t/\Delta x^2$ as before, we obtain

$$-\frac{1}{2}du_{i-1}^{n+1} + (d + 1)u_i^{n+1} - \frac{1}{2}du_{i+1}^{n+1} = \text{RHS}_i^n \quad (4.4.34)$$

Now we calculate the RHS term:

$$\text{RHS}_i^n = \frac{1}{2}d(u_{i-1}^n + u_{i+1}^n) + u_i^n(1 - d) + \frac{1}{2}\Delta t(3H_i^n - H_i^{n-1})$$

with

$$\begin{aligned} H_i^n &= -\frac{1}{2} \left[\frac{(u^2)_{i+1}^n - (u^2)_{i-1}^n}{2\Delta x} \right] \\ H_i^{n-1} &= -\frac{1}{2} \left[\frac{(u^2)_{i+1}^{n-1} - (u^2)_{i-1}^{n-1}}{2\Delta x} \right] \end{aligned} \quad (4.4.35)$$

The solution proceeds as follows:

1. Generate the second level initial data at time level n by using the explicit Euler method on the convective term; the CN method can be used for the diffusion term.
2. Evaluate H_i^n and H_i^{n-1} using second-order central differences.
3. Evaluate RHS_i^n from (4.4.35).
4. Calculate the coefficients of the left-hand-side of (4.4.34).
5. Impose the boundary conditions.
6. Solve the resulting tridiagonal matrix equation.
7. Go back to step 2; continue to advance the solution in time.
8. In assigning the allowable time step, the only restriction is the convective restriction. Therefore, Δt must be chosen to ensure that the Courant number, $C \leq 1$, is strictly obeyed as in (4.4.14).

As we have observed in Sections (2.2) and (3.3), discretization of the diffusion term by second-order central finite differences results in a linear system of equations where the coefficient matrix is tridiagonal. The subroutine TRID solves this system of equations using an efficient adaptation of Gaussian elimination exploiting the sparseness of the matrix. Here we will introduce a similar algorithm called the *Thomas algorithm*, which also requires only $3n$ storage, where n is the number of the unknowns in the problem (that is, the number of grid points). We will also provide an algorithm for the LU decomposition method for tridiagonal matrices, which is more efficient when one solves many linear equations in sequence with the same coefficient matrix, such as in time-dependent solutions of the parabolic diffusion equation.

Thomas Algorithm

We consider the following generic system of linear equations, where the coefficient matrix \mathbf{A} is tridiagonal:

$$\mathbf{Ax} = \mathbf{f} \quad (4.4.36)$$

In this equation, \mathbf{x} is the solution vector and \mathbf{f} is the right-hand-side vector.

As we have seen in Section 2.2, the coefficient matrix \mathbf{A} can be written as

$$\mathbf{A} = \begin{bmatrix} a_1 & c_1 & 0 & 0 & \cdots & 0 & 0 \\ b_2 & a_2 & c_2 & 0 & \cdots & 0 & 0 \\ 0 & b_3 & a_3 & c_3 & \cdots & 0 & 0 \\ 0 & 0 & \ddots & \ddots & \ddots & 0 & 0 \\ \vdots & \vdots & \ddots & \ddots & \ddots & \ddots & 0 \\ 0 & 0 & \cdots & 0 & b_{n-1} & a_{n-1} & c_{n-1} \\ 0 & 0 & \cdots & \cdots & 0 & b_n & a_n \end{bmatrix} \quad (4.4.37)$$

The Thomas algorithm, which is an efficient adaptation of Gaussian elimination to tridiagonal matrices, can be written as follows.

Forward elimination:

$$a_j = a_j - \frac{b_j}{a_{j-1}}c_{j-1} \quad (4.4.38)$$

$$f_j = f_j - \frac{b_j}{a_{j-1}}f_{j-1} \quad j = 2, \dots, n \quad (4.4.39)$$

Back substitution:

$$x_n = f_n/a_n \quad (4.4.40)$$

$$x_{n-j} = (f_{n-j} - c_{n-j}x_{n-j+1})/a_{n-j} \quad j = 1, \dots, n-1 \quad (4.4.41)$$

The number of operations is proportional to n , and is much more computationally efficient than Gaussian elimination on a full matrix where the number of operations is proportional to n^3 (Ferziger, 1998). Also, during forward elimination, the diagonal elements of the original coefficient matrix are overwritten, and, unless the algorithm is modified to preserve the diagonal, at each step the diagonal (a_j) has to be redefined.

LU Decomposition

Another efficient way of solving the tridiagonal system (4.4.36) is by LU decomposition. Let us consider a 4×4 tridiagonal coefficient matrix, \mathbf{A} :

$$\mathbf{A} = \begin{bmatrix} a_1 & c_1 & 0 & 0 \\ b_2 & a_2 & c_2 & 0 \\ 0 & b_3 & a_3 & c_3 \\ 0 & 0 & b_4 & a_4 \end{bmatrix} \quad (4.4.42)$$

We intend to decompose the \mathbf{A} matrix into two matrices, \mathbf{L} and \mathbf{U} as defined below:

$$\mathbf{L} = \begin{bmatrix} l_1 & 0 & 0 & 0 \\ b_2 & l_2 & 0 & 0 \\ 0 & b_3 & l_3 & 0 \\ 0 & b_4 & l_4 & \end{bmatrix}, \quad \mathbf{U} = \begin{bmatrix} 1 & u_1 & 0 & 0 \\ 0 & 1 & u_2 & 0 \\ 0 & 0 & 1 & u_3 \\ 0 & 0 & 0 & 1 \end{bmatrix} \quad (4.4.43)$$

$$\mathbf{LU} = \begin{bmatrix} l_1 & l_1 u_1 & 0 & 0 \\ b_2 & b_2 u_1 + l_2 & l_2 u_2 & 0 \\ 0 & b_3 & b_3 u_2 + l_3 & l_3 u_3 \\ b_4 & b_4 u_3 + l_4 & \end{bmatrix}$$

Comparing \mathbf{LU} element by element with the \mathbf{A} matrix, we solve for u_j and l_j . Noting that the subdiagonal b_j is the same in \mathbf{A} and \mathbf{L} matrices, \mathbf{L} and \mathbf{U} can be obtained from the following algorithm:

$$\begin{aligned} l_1 &= a_1 \\ u_{j-1} &= c_{j-1}/l_{j-1} \\ l_j &= a_j - b_j u_{j-1}, \quad j = 2, 3, \dots, n-1, n \end{aligned} \quad (4.4.44)$$

The solution of (4.4.36) can then be obtained as

$$\begin{aligned} \mathbf{Ax} &= \mathbf{f} \\ \mathbf{A} &= \mathbf{LU} \rightarrow \text{find } \mathbf{L} \text{ and } \mathbf{U} \end{aligned} \quad (4.4.45)$$

Once \mathbf{L} and \mathbf{U} are calculated by using (4.4.44), the solution proceeds:

$$\begin{aligned} \mathbf{LUx} &= \mathbf{f} \\ \mathbf{Lz} &= \mathbf{f} \rightarrow \text{find } \mathbf{z} \\ \mathbf{Ux} &= \mathbf{z} \rightarrow \text{find } \mathbf{x} \end{aligned} \quad (4.4.46)$$

The last two steps of (4.4.46) can be written in algorithmic form as

$$\begin{aligned} z_1 &= f_1/l_1 \\ z_j &= (f_j - b_j z_{j-1})/l_j \quad j = 2, 3, \dots, n \end{aligned} \quad (4.4.47)$$

From which one can obtain the solution vector, \mathbf{x} :

$$\begin{aligned} x_n &= z_n \\ x_j &= z_j - u_j x_{j+1}, \quad j = n-1, n-2, \dots, 1 \end{aligned} \quad (4.4.48)$$

The LU decomposition will be especially efficient when the system has constant coefficients so that the decomposition will be done only once during the solution. The \mathbf{L} and \mathbf{U} matrices can be stored at the first time step, and during the subsequent steps only the back-substitution steps (4.4.47) and (4.4.48) will be performed, thus decreasing computer time necessary to obtain the solution.

Problem 4.6 MATLAB script 4.3 solves the one-dimensional, nonlinear, viscous Burgers equation using the AB-CN semi-implicit method; the tridiagonal linear system of finite-difference equations resulting from the implicit time advancement of the viscous diffusion term is solved using the Thomas algorithm, with the same initial/boundary conditions as described in Problem 2.12. Solve the same problem using LU decomposition instead of the Thomas algorithm.

4.5 PRIMITIVE VARIABLE FORMULATION: NUMERICAL INTEGRATION OF THE NAVIER-STOKES EQUATION

In this section, we apply the methods developed in Section 4.4 to the numerical integration of the two-dimensional, incompressible, time-dependent Navier-Stokes equation written in terms of primitive variables on a uniform grid. We will introduce the fractional time-step algorithm and staggered mesh systems and outline a method for solving for the pressure (gradient) that satisfies mass conservation to machine accuracy at the advanced time level. Putting all these together, we will develop an efficient solver for the driven cavity problem.

Let us consider the two-dimensional, time-dependent, incompressible Navier-Stokes and the continuity equations nondimensionalized by the characteristic length and velocity scales, L and U_0 , respectively:

$$\nabla \cdot \mathbf{V} = 0 \quad (4.5.1)$$

$$\frac{\partial \mathbf{V}}{\partial t} + \mathbf{V} \cdot \nabla \mathbf{V} = -\nabla P + \text{Re}^{-1} \nabla^2 \mathbf{V} \quad (4.5.2)$$

Here, $P = p/\rho$, where p is thermodynamic pressure, and using (4.5.1) we define

$$\mathbf{H} = \mathbf{V} \cdot \nabla \mathbf{V} = \nabla \cdot (\mathbf{V}\mathbf{V}) \quad (4.5.3)$$

The Reynolds number Re is defined as

$$\text{Re} = \frac{U_o L}{\nu} \quad (4.5.4)$$

When integrating (4.5.1) and (4.5.2), it is imperative that mass conservation equation (4.5.1) is satisfied to machine zero at every point in the integration domain. An efficient way to ensure this constraint is by the use of the *time-splitting* (or the *fractional time step*) method. Of the several variants of this method (Chorin, 1968; Orszag and Kells, 1981; Kim and Moin, 1985), we will adopt the one used by Huser and Biringen (1992) in their simulations of shear-driven cavity flows. Another predictor–corrector algorithm for incompressible flows is the SIMPLE algorithm (semi-implicit method for pressure-linked equations) advanced by Patankar and Spalding (1972) and Patankar (1980). This method is based on a finite-volume discretization on a staggered grid, and has been widely used in computational fluid mechanics and heat transfer.

According to the time-splitting method, in the first step (*predictor step*) from t^n to \hat{t} , the pressure gradient is neglected and the resulting equation is solved:

$$\frac{\hat{\mathbf{V}} - \mathbf{V}^n}{\Delta t} = -\frac{3}{2}\mathbf{H}^n + \frac{1}{2}\mathbf{H}^{n-1} + \frac{1}{2\text{Re}}\nabla^2(\hat{\mathbf{V}} + \mathbf{V}^n) \quad (4.5.5)$$

We note that in (4.5.5) temporal discretization is done with the Crank-Nicolson scheme on the viscous diffusion terms and with the Adams-Basforth method on the convective terms. Next, advancing (4.5.2) from t^n to t^{n+1} , we obtain

$$\frac{\mathbf{V}^{n+1} - \mathbf{V}^n}{\Delta t} = -\frac{3}{2}\mathbf{H}^n + \frac{1}{2}\mathbf{H}^{n-1} + \frac{1}{2\text{Re}}(\nabla^2\mathbf{V}^{n+1} + \nabla^2\mathbf{V}^n) - \nabla P^{n+1} \quad (4.5.6)$$

Subtracting (4.5.5) from (4.5.6) gives the *corrector step* for updating \mathbf{V}^{n+1} :

$$\frac{\mathbf{V}^{n+1} - \hat{\mathbf{V}}}{\Delta t} = \frac{1}{2\text{Re}}(\nabla^2\mathbf{V}^{n+1} - \nabla^2\hat{\mathbf{V}}) - \nabla P^{n+1} \doteq -\nabla\phi^{n+1} \quad (4.5.7)$$

The term $\nabla\phi^{n+1}$, which is the gradient of the scalar quantity ϕ^{n+1} , contains the pressure gradient term as well as the residual viscous terms, and simply is used as an operator to ensure zero divergence of the velocity field at time level $(n+1)$. This is accomplished by taking the divergence of (4.5.7):

$$\frac{\nabla \cdot \mathbf{V}^{n+1} - \nabla \cdot \hat{\mathbf{V}}}{\Delta t} = -\nabla^2\phi^{n+1} \quad (4.5.8)$$

Now, enforcing continuity at time level $(n+1)$,

$$\nabla \cdot \mathbf{V}^{n+1} = 0 \quad (4.5.9)$$

equation (4.5.8) gives

$$\frac{\nabla \cdot \hat{\mathbf{V}}}{\Delta t} = \nabla^2\phi^{n+1} \quad (4.5.10)$$

The solution process can be constructed as follows.

Step 1. Solve for $\hat{\mathbf{V}}$ from (4.5.5):

$$\frac{\hat{\mathbf{V}}}{\Delta t} - \frac{1}{2\text{Re}}\nabla^2\hat{\mathbf{V}} = -\frac{3}{2}\mathbf{H}^n + \frac{1}{2}\mathbf{H}^{n-1} + \frac{1}{2\text{Re}}\nabla^2\mathbf{V}^n + \frac{\mathbf{V}^n}{\Delta t} \quad (4.5.11)$$

Multiplying through by Δt , the x component of (4.5.11) can be written in Cartesian coordinates (x, y, z) :

$$\hat{u}_{i,j} - \frac{\Delta t}{2\text{Re}}\nabla^2\hat{u}_{i,j} = -\frac{3\Delta t}{2}(H_u^n)_{i,j} + \frac{\Delta t}{2}(H_u^{n-1})_{i,j} + \frac{\Delta t}{2\text{Re}}\nabla^2u_{i,j}^n + u_{i,j}^n \quad (4.5.12)$$

The subscript u (or v) indicates that the quantity appears in the u (or v)-momentum equation. Now using second-order central differences with $\Delta x = \Delta y = h$, we obtain

$$\begin{aligned} \beta_1 \hat{u}_{i,j} - (\hat{u}_{i+1,j} - 2\hat{u}_{i,j} + \hat{u}_{i-1,j}) - (\hat{u}_{i,j+1} - 2\hat{u}_{i,j} + \hat{u}_{i,j-1}) \\ = (\text{RHS}_u^n)_{i,j} \end{aligned} \quad (4.5.13)$$

The quantities β_1 and (RHS_u^n) are defined as

$$\begin{aligned} \beta_1^{-1} &\equiv \frac{\Delta t}{2\text{Re } h^2} \\ (\text{RHS}_u^n)_{i,j} &= -\frac{3\Delta t \beta_1}{2} (H_u^n)_{i,j} + \frac{\Delta t \beta_1}{2} (H_u^{n-1})_{i,j} \\ &\quad + \left(u_{i+1,j}^n - 2u_{i,j}^n + u_{i-1,j}^n \right) + \left(u_{i,j+1}^n - 2u_{i,j}^n + u_{i,j-1}^n \right) \\ &\quad + \beta_1 u_{i,j}^n \end{aligned} \quad (4.5.14)$$

Equation (4.5.13) can be written in compact form:

$$-\hat{u}_{i+1,j} - \hat{u}_{i-1,j} - \hat{u}_{i,j+1} - \hat{u}_{i,j-1} + (4 + \beta_1) \hat{u}_{i,j} = (\text{RHS}_u^n)_{i,j} \quad (4.5.15)$$

We note that this is an elliptic (*Helmholtz*) equation in space, and can be solved with any of the methods introduced previously in Section 2.8. For small mesh sizes, around 100×100 or so, direct methods based on Gaussian elimination (for example, the LU decomposition method) can be used efficiently.

A similar elliptic equation will be solved for the v component of equation (4.5.11).

- Step 2. Solve for ϕ^{n+1} using (4.5.10) with second-order central differences. This equation is written as

$$\left(\phi_{i+1,j}^{n+1} + \phi_{i-1,j}^{n+1} + \phi_{i,j+1}^{n+1} + \phi_{i,j-1}^{n+1} - 4\phi_{i,j}^{n+1} \right) = \frac{h^2}{\Delta t} \left(\frac{\partial \hat{u}}{\partial x} + \frac{\partial \hat{v}}{\partial y} \right) \quad (4.5.16)$$

The right-hand side of this elliptic equation involves the evaluation of the divergence of the velocity field at the intermediate time step, which will be done in conjunction with the *staggered mesh* system that will be introduced later in this section. Equation (4.5.16) can be solved with any of the iterative elliptic solvers mentioned in Section 2.8 as well as with a direct solver. Special care must be devoted to the solution of this equation, as all the boundary conditions are of Neumann type; that is, they are imposed on the normal gradients of ϕ , thus making the system of equations (4.5.16) linearly dependent. We will explore how to alleviate this problem later in this section.

Step 3. The velocity field will be updated using (4.5.7):

$$\frac{\mathbf{V}^{n+1} - \hat{\mathbf{V}}}{\Delta t} = -\nabla \phi^{n+1} \quad (4.5.17)$$

Accordingly, the velocity components at the advanced time level are given as

$$\begin{aligned} \mathbf{V}^{n+1} &= \hat{\mathbf{V}} - (\Delta t) \nabla \phi^{n+1} \\ u_{i+1/2,j}^{n+1} &= \hat{u}_{i+1/2,j}^n - (\Delta t) \left. \frac{\partial \phi}{\partial x} \right|_{i,j}^{n+1} \\ v_{i,j+1/2}^{n+1} &= \hat{v}_{i,j+1/2}^n - (\Delta t) \left. \frac{\partial \phi}{\partial y} \right|_{i,j}^{n+1} \end{aligned} \quad (4.5.18)$$

The indices $i + 1/2$ and $j + 1/2$ refer to the u and v grids in the staggered mesh system. Spatial discretization will be done on a staggered mesh, following the marker-and-cell (MAC) method of Harlow and Welch (1965). It was shown by Bernard and Thompson (1984) that staggered mesh arrangements provide a stronger coupling between velocity and pressure thus eliminating some high frequency oscillations that may exist at high Reynolds number computations. In addition, mass conservation is satisfied across a grid not at a grid point, and finally, pressure boundary conditions are obtained from the velocity boundary conditions. One should also recall that because of the staggered arrangement, velocity boundary conditions require specification of velocities at one grid point outside of the boundary.

To illustrate the pressure–velocity coupling, we will consider the one-dimensional equation of motion, retaining only the temporal term and the pressure gradient term:

$$\frac{\partial u}{\partial t} = -\frac{\partial P}{\partial x} \quad (4.5.19)$$

and also the one-dimensional continuity equation:

$$\frac{\partial u}{\partial x} = 0 \quad (4.5.20)$$

Using implicit time integration on a collocated grid (Figure 4.5.1) to calculate P at time level $(n + 1)$, and with second-order central differences in space, we obtain

$$u_i^{n+1} = u_i^n - \frac{\Delta t}{2\Delta x} (P_{i+1}^{n+1} - P_{i-1}^{n+1}) \quad (4.5.21)$$

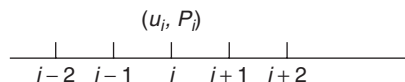


FIGURE 4.5.1 Velocity and pressure nodes on a collocated grid.

Now taking the x derivative of (4.5.21) and imposing $(\partial u / \partial x)_i^{n+1} = 0$, we get

$$\Delta t \frac{\partial^2 P_i^{n+1}}{\partial x^2} = \frac{\partial u_i^n}{\partial x} \quad (4.5.22)$$

With second-order central differences we obtain

$$P_{i+1}^{n+1} - 2P_i^{n+1} + P_{i-1}^{n+1} = \frac{\Delta x}{2\Delta t} (u_{i+1}^n - u_{i-1}^n) \quad (4.5.23)$$

We note that in (4.5.23) P_i^{n+1} is not influenced by u_i^{n+1} , and in (4.5.21), u_i^{n+1} is not influenced by P_i^{n+1} . Therefore, pressure and velocity are decoupled at odd–even points. This can lead to high-frequency oscillations necessitating the use of artificial viscosity to smoothen the solutions.

Let us now consider a staggered grid arrangement as shown in Fig. 4.5.2.

Again, with second-order central differences about grid point $(i + \frac{1}{2})$, (4.5.19) is written as

$$u_{i+1/2}^{n+1} = u_{i+1/2}^n - \frac{\Delta t}{\Delta x} (P_{i+1}^{n+1} - P_i^{n+1}) \quad (4.5.24)$$

Taking the x derivative of (4.5.24), and setting

$$\left(\frac{\partial u}{\partial x} \right)_{i+1/2}^{n+1} = 0 \quad (4.5.25)$$

satisfying mass conservation (4.5.20) at time level $(n + 1)$, we obtain in discretized form

$$P_{i+1}^{n+1} - 2P_i^{n+1} + P_{i-1}^{n+1} = \frac{\Delta x}{\Delta t} (u_{i+1/2}^n - u_{i-1/2}^n) \quad (4.5.26)$$

For the staggered mesh, an examination of (4.5.24) and (4.5.26) reveals that the P nodes at grid location i and the u nodes at grid location $(i + \frac{1}{2})$ are always coupled. At high-Reynolds numbers, with central differences, high-frequency oscillations may still persist, but these generally will have lower amplitudes and occur at higher Reynolds numbers than those on collocated grids. In such cases, staggered grids with high-order upwind or upwind biased differences may be preferable (Rai and Moin, 1991).

We will now consider the full two-dimensional, time dependent Navier-Stokes (momentum conservation equation) and continuity equations for incompressible flows in x - y rectangular coordinates. The convective terms will be written in

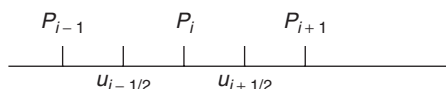


FIGURE 4.5.2 Velocity and pressure nodes on a staggered grid.

conservative form which preserves mass and momentum in the discrete form of the equations (Roache, 1972). The conservative form of the convective terms are obtained from equation (4.5.2):

$$\mathbf{V} \cdot \nabla \mathbf{V} = \nabla \cdot (\mathbf{V}\mathbf{V}) - \mathbf{V}\nabla \cdot \mathbf{V} \quad (4.5.27)$$

Noting that by continuity (4.5.1),

$$\mathbf{V}\nabla \cdot \mathbf{V} = \mathbf{0} \quad (4.5.28)$$

it then follows that for the x momentum equation of motion, we obtain

$$\mathbf{V} \cdot \nabla \mathbf{V} = \frac{\partial u^2}{\partial x} + \frac{\partial uv}{\partial y} \quad (4.5.29)$$

and for the y momentum equation, the conservative form of the convective term is

$$\mathbf{V} \cdot \nabla \mathbf{V} = \frac{\partial uv}{\partial x} + \frac{\partial v^2}{\partial y} \quad (4.5.30)$$

The x and y components of the equation of motion in nondimensional form can now be written respectively as

$$\frac{\partial u}{\partial t} + \frac{\partial u^2}{\partial x} + \frac{\partial uv}{\partial y} = \text{Re}^{-1} \left(\frac{\partial^2 u}{\partial x^2} + \frac{\partial^2 u}{\partial y^2} \right) - \frac{\partial P}{\partial x} \quad (4.5.31)$$

$$\frac{\partial v}{\partial t} + \frac{\partial uv}{\partial x} + \frac{\partial v^2}{\partial y} = \text{Re}^{-1} \left(\frac{\partial^2 v}{\partial x^2} + \frac{\partial^2 v}{\partial y^2} \right) - \frac{\partial P}{\partial y} \quad (4.5.32)$$

Considering the P , u , and the v nodes in the MAC configuration (Fig. 4.5.3), the x -momentum equation is written at the u nodes, and the y -momentum equation is written at the v nodes. Accordingly, the various derivatives in the x -momentum equation (4.5.31) are calculated as follows:

$$\left(\frac{\partial u}{\partial t} \right)_{i+1/2,j}^{n+1} = \left(u_{i+1/2,j}^{n+1} - u_{i+1/2,j}^n \right) / \Delta t \quad (4.5.33)$$

$$\left(\frac{\partial^2 u}{\partial x^2} \right)_{i+1/2,j}^{n+1} = \left(u_{i-1/2,j}^{n+1} - 2u_{i+1/2,j}^{n+1} + u_{i+3/2,j}^{n+1} \right) / \Delta x^2 \quad (4.5.34)$$

$$\left(\frac{\partial P}{\partial x} \right)_{i+1/2,j}^{n+1} = \left(P_{i+1,j}^{n+1} - P_{i,j}^{n+1} \right) / \Delta x \quad (4.5.35)$$

Using the MAC method, the other terms in the u -momentum equation (4.5.31) are written as

$$\left(\frac{\partial u^2}{\partial x} \right)_{i+1/2,j}^n = \left(u_{i+1,j}^2 - u_{i,j}^2 \right)^n / \Delta x \quad (4.5.36)$$

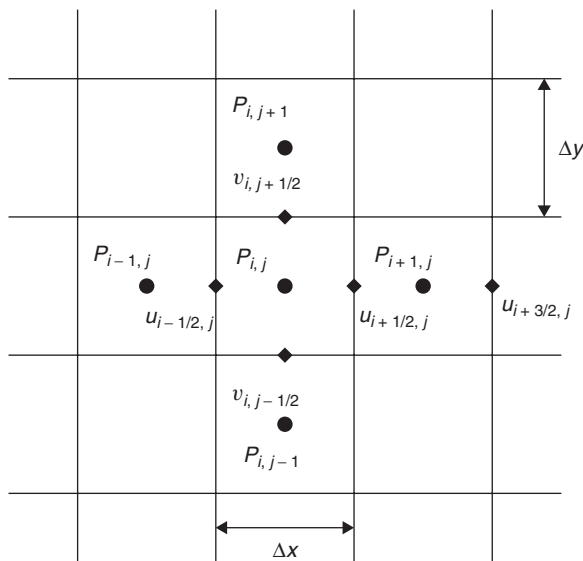


FIGURE 4.5.3 MAC staggered grid system.

But we note that $u_{i+1,j}$ is not defined on a u node, so that to obtain this quantity, we use averaging such that

$$u_{i+1,j} = \frac{1}{2} (u_{i+1/2,j} + u_{i+3/2,j}) \quad (4.5.37)$$

Finally, the product term $\partial uv / \partial y$ will be evaluated as the product of averages, not as the average of the products, so that

$$\begin{aligned} \left(\frac{\partial uv}{\partial y} \right)_{i+1/2,j} &= [(uv)_{i+1/2,j+1/2} - (uv)_{i+1/2,j-1/2}] / \Delta y \\ &= \frac{1}{\Delta y} [(u_{i+1/2,j+1/2})(v_{i+1/2,j+1/2}) - (u_{i+1/2,j-1/2})(v_{i+1/2,j-1/2})] \\ (u_{i+1/2,j+1/2}) &= \frac{1}{2} (u_{i+1/2,j} + u_{i+1/2,j+1}) \\ (v_{i+1/2,j+1/2}) &= \frac{1}{2} (v_{i,j+1/2} + v_{i+1,j+1/2}) \\ (u_{i+1/2,j-1/2}) &= \frac{1}{2} (u_{i+1/2,j-1} + u_{i+1/2,j}) \\ (v_{i+1/2,j-1/2}) &= \frac{1}{2} (v_{i,j-1/2} + v_{i+1,j-1/2}) \end{aligned} \quad (4.5.38)$$

For simplicity, we will implement a fully explicit version of the time-splitting (fractional time-step) method described by (4.5.5)–(4.5.18) using the Euler explicit scheme (4.4.10) for both the viscous and the diffusion terms. This method is $O(\Delta t, \Delta x^2)$ with second-order central differences in space, and when

applied to the x -momentum equation on the staggered grid from time level t to \hat{t} yields the following equation at the intermediate step:

$$\begin{aligned} \frac{\hat{u}_{i+1/2,j} - u_{i+1/2,j}^n}{\Delta t} &= \frac{(u_{i,j}^n)^2 - (u_{i+1,j}^n)^2}{\Delta x} + \frac{(uv)_{i+1/2,j-1/2}^n - (uv)_{i+1/2,j+1/2}^n}{\Delta y} \\ &\quad + \frac{1}{\text{Re } \Delta x^2} (u_{i+3/2,j}^n - 2u_{i+1/2,j}^n + u_{i-1/2,j}^n) \\ &\quad + \frac{1}{\text{Re } \Delta y^2} (u_{i+1/2,j+1}^n - 2u_{i+1/2,j}^n + u_{i+1/2,j-1}^n) \end{aligned} \quad (4.5.39)$$

Similarly for the y -momentum equation we obtain the following equation:

$$\begin{aligned} \frac{\hat{v}_{i,j+1/2} - v_{i,j+1/2}^n}{\Delta t} &= \frac{(uv)_{i-1/2,j+1/2}^n - (uv)_{i+1/2,j+1/2}^n}{\Delta x} + \frac{(v_{i,j}^n)^2 - (v_{i,j+1}^n)^2}{\Delta y} \\ &\quad + \frac{1}{\text{Re } \Delta x^2} (v_{i+1,j+1/2}^n - 2v_{i,j+1/2}^n + v_{i-1,j+1/2}^n) \\ &\quad + \frac{1}{\text{Re } \Delta y^2} (v_{i,j+3/2}^n - 2v_{i,j+1/2}^n + v_{i,j-1/2}^n) \end{aligned} \quad (4.5.40)$$

Practical stability requirements obtained from the von Neumann analysis for the Euler explicit solver are given by Peyret and Taylor (1983, p. 148) as follows:

$$\begin{aligned} 0.25(|u| + |v|)^2 \Delta t \text{ Re} &\leq 1 \\ \frac{\Delta t}{\text{Re } \Delta x^2} &\leq 0.25, \text{ assuming that } \Delta x = \Delta y \end{aligned} \quad (4.5.41)$$

It is also possible to maintain stability considering the values of the following quantities (Moin et al., 1978; Huser and Biringen, 1992),

$$\begin{aligned} c_1(t) &= \max_{i,j} [(|u_{i,j}|/\Delta x_i + |v_{i,j}|/\Delta y_j) \Delta t] \\ c_2(t) &= \max_{i,j} \left[\frac{\Delta t}{\text{Re}} \left(\frac{1}{(\Delta x_i)^2} + \frac{1}{(\Delta y_j)^2} \right) \right] \end{aligned} \quad (4.5.42)$$

In general, a stable solution will be obtained for $c_1(t)$ less than about 0.5 and $c_2(t)$ less than about 0.1. However, in actual computations, these values are determined by trial and error.

In the MAC grid, explicit boundary condition (Fig. 4.5.4) on the pressure are not needed with the time-splitting method, but the implementation of boundary conditions on the velocity components is more complicated than in collocated grids. At a horizontal wall, boundary conditions for the velocities parallel to the

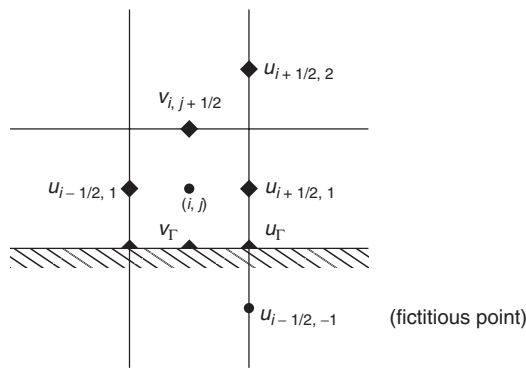


FIGURE 4.5.4 MAC grid boundary conditions for the u velocity near a horizontal wall.

walls are obtained using averaging, which gives

$$\begin{aligned} u_\Gamma &= \frac{1}{2}(u_{i+1/2,1} + u_{i+1/2,-1}) \\ u_{i+1/2,-1} &= 2u_\Gamma - u_{i+1/2,1} \end{aligned} \quad (4.5.43)$$

We note that (4.5.43) is equivalent to linear extrapolation and $u_{i+1/2,-1}$ is the velocity at the first u node outside the physical boundary (fictitious point). Higher-order extrapolations are also possible as given by Peyret and Taylor (1983, p. 150), such as

$$u_{i+1/2,-1} = \frac{1}{3}(u_{i+1/2,2} - 6u_{i+1/2,1} + 8u_\Gamma) \quad (4.5.44)$$

The velocity u_Γ in (4.5.43) and (4.5.44) is the specified wall velocity; for example, as $u_\Gamma = 0$ for a stationary wall and $u_\Gamma = 1$ for a horizontal wall moving from left to right when the velocity scale is chosen as u_Γ . On the horizontal wall v nodes exist, so that the no-slip boundary condition $v_\Gamma = 0$ (stationary wall) can be directly imposed. On a vertical wall, where u nodes exist and v nodes do not, similar boundary conditions as in (4.5.43) and (4.5.44) can be obtained for v .

It should be noted that the second step of the time-splitting procedure with the Euler explicit method cancels the convective and viscous terms exactly as shown below. Advancing (4.5.2) from time step t^n to \hat{t} gives

$$\frac{\hat{\mathbf{V}} - \mathbf{V}^n}{\Delta t} = -\mathbf{H}^n + \frac{1}{\text{Re}} \nabla^2 \mathbf{V}^n \quad (4.5.45)$$

Now, advancing (4.5.2) from time step t^n to t^{n+1} , we obtain

$$\frac{\mathbf{V}^{n+1} - \mathbf{V}^n}{\Delta t} = -\mathbf{H}^n + \frac{1}{\text{Re}} \nabla^2 \mathbf{V}^n - \nabla P^{n+1} \quad (4.5.46)$$

Subtracting (4.5.45) from (4.5.46), we find

$$\frac{\mathbf{V}^{n+1} - \hat{\mathbf{V}}}{\Delta t} = -\nabla P^{n+1} \quad (4.5.47)$$

We now impose zero divergence of the velocity field at time level $(n + 1)$, $\nabla \cdot \mathbf{V}^{n+1} = 0$, so that taking the divergence of (4.5.47), one obtains the elliptic pressure equation:

$$\frac{\nabla \cdot \hat{\mathbf{V}}}{\Delta t} = \nabla^2 P^{n+1} \quad (4.5.48)$$

From (4.5.48), we infer that the scalar quantity that projects zero divergence of the velocity field at time level $(n + 1)$ is the thermodynamic pressure (normalized by the constant density); hence, with the fully explicit methods there is no need to extract pressure from ϕ , which is required for semi-implicit time advancement if the pressure solution is desired.

Pressure boundary conditions are all homogeneous Neumann boundary conditions, given by $\partial P^{n+1} / \partial n = 0$, where $\partial / \partial n$ denotes differentiation along the normal to the boundary. This boundary condition is derived from (4.5.47) with $\mathbf{V}^{n+1} = \mathbf{V}^n = \hat{\mathbf{V}}$ at the boundaries, provided that $\partial P / \partial n = 0$ at the first time step. The accuracy of these boundary conditions have been documented by Gresho (1991) and Kim and Moin (1985).

To demonstrate how pressure boundary conditions are implemented, consider the computational cell adjacent to a horizontal wall (Fig. 4.5.5). Writing the pressure equation (4.5.48) at grid location (i, j) , for an impermeable wall gives

$$\begin{aligned} & \frac{P_{i,2}^{n+1} - 2P_{i,1}^{n+1} + P_{i,-1}^{n+1}}{\Delta y^2} + \frac{P_{i+1,1}^{n+1} - 2P_{i,1}^{n+1} + P_{i-1,1}^{n+1}}{\Delta x^2} \\ &= \frac{1}{\Delta t} \left[\frac{\hat{u}_{i+1/2,1} - \hat{u}_{i-1/2,1}}{\Delta x} + \frac{\hat{v}_{i,1+1/2} - \hat{v}_\Gamma}{\Delta y} \right] \\ P_{i,-1}^{n+1} &= P_{i,1}^{n+1} \left(\text{from } \frac{\partial P^{n+1}}{\partial n} \Big|_\Gamma = 0 \right) \quad (4.5.49) \\ \hat{v}_\Gamma &= v_\Gamma^{n+1} = 0 \quad (\text{stationary wall}) \end{aligned}$$

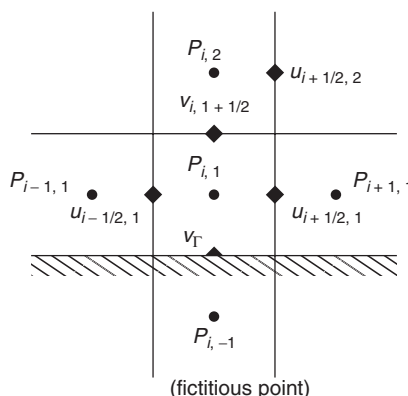


FIGURE 4.5.5 Computational cell adjacent to a horizontal wall, pressure boundary conditions.

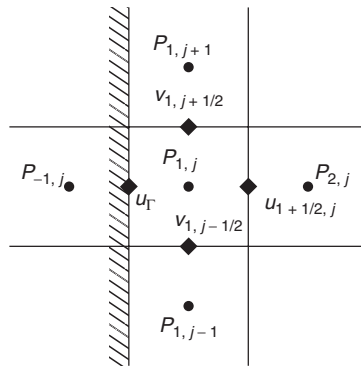


FIGURE 4.5.6 Computational cell adjacent to a vertical wall, pressure boundary conditions.

With similar boundary conditions for a vertical wall as in Figure 4.5.6, the pressure equation becomes

$$\begin{aligned} & \frac{P_{2,j}^{n+1} - 2P_{1,j}^{n+1} + P_{-1,j}^{n+1}}{\Delta x^2} + \frac{P_{1,j+1}^{n+1} - 2P_{1,j}^{n+1} + P_{1,j-1}^{n+1}}{\Delta y^2} \\ &= \frac{1}{\Delta t} \left[\frac{\hat{u}_{1+1/2,j} - \hat{u}_\Gamma}{\Delta x} + \frac{\hat{v}_{1,j+1/2} - \hat{v}_{1,j-1/2}}{\Delta y} \right] \\ & P_{-1,j}^{n+1} = P_{1,j}^{n+1} \quad (4.5.50) \\ & \hat{u}_\Gamma = u_\Gamma^{n+1} = 0 \quad (\text{stationary wall}) \end{aligned}$$

It is important to recognize that the moving wall boundary conditions will be imposed on the solution during the calculation of the viscous terms (also by the convective terms through averaging). Consider the y -directional viscous term in the x -momentum equation (4.5.39). Referring to Fig. 4.5.7 we obtain

$$\left(\frac{\partial^2 u}{\partial y^2} \right)_{i+1/2,j}^n = \frac{u_{i+1/2,j-1}^n - 2u_{i+1/2,j}^n + u_{i+1/2,+1}^n}{\Delta y^2} \quad (4.5.51)$$

The velocity outside of the computational domain, $u_{i+1/2,+1}^n$, is calculated by averaging:

$$\frac{1}{2} (u_{i+1/2,+1}^n + u_{i+1/2,j}^n) = u_\Gamma^n \quad (4.5.52)$$

From this expression one can obtain $u_{i+1/2,+1}^n$ considering that for the stationary wall $u_\Gamma^n = 0$, and for the wall moving with constant velocity normalized by itself (which is the maximum velocity in the computational domain), $u_\Gamma^n = 1$.

For the y -directional viscous term in the y -momentum equation, we obtain

$$\left(\frac{\partial^2 v}{\partial y^2} \right)_{i,j-1/2}^n = \frac{v_{i,j-3/2}^n - 2v_{i,j-1/2}^n + v_{i,j+1/2}^n}{\Delta y^2} \quad (4.5.53)$$

At the upper (impermeable) wall, we define $v_{i,j+1/2}^n = v_\Gamma^n = 0$.

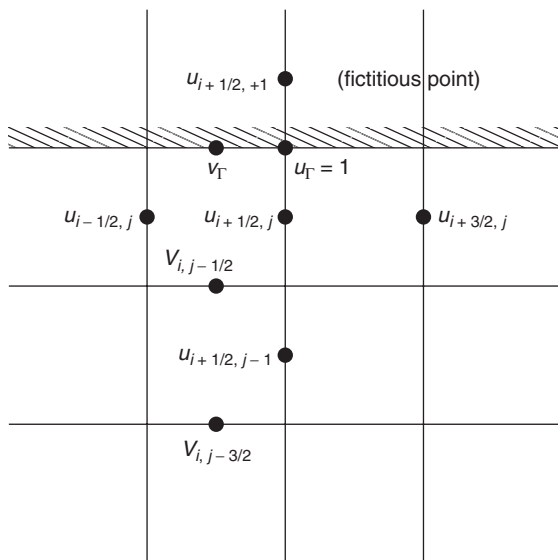


FIGURE 4.5.7 Evaluation of the viscous terms at the horizontal upper wall.

Elliptic equations with Neumann boundary conditions on all boundaries, such as the pressure equation (4.5.48), present an indeterminate problem, as the coefficient matrix of the finite-difference representation of the equation has one zero eigenvalue. Consequently, the resulting system of equations is linearly dependent and cannot be solved uniquely (Mitchell, 1969, p. 118). This can be alleviated by assigning a constant value to pressure at one reference point in the solution domain. The resulting equations will be linearly independent, and will have a unique solution for an arbitrary value of the constant. Thus, the pressure solution will be off by this constant, but the pressure gradient, which is the actual term that exists in the equation of motion, will be correctly calculated. In the Neumann problem for elliptic equations, the other issue is to globally satisfy an integral constraint. Consider the following Laplace equation:

$$\nabla^2 \phi = 0 \quad (4.5.54)$$

subject to the boundary conditions

$$\frac{\partial \phi}{\partial n} = g(x_1, x_2) \quad (4.5.55)$$

These boundary conditions will be applied on the boundary of the unit square, $0 \leq x_1, x_2 \leq 1$, where $\partial/\partial n$ is the normal derivative. Using the divergence theorem, we get

$$\int_S (\nabla^2 \phi) dS = \int_L \frac{\partial \phi}{\partial n} dl = 0 \quad (4.5.56)$$

In (4.5.56), S is the surface of the unit square, and L is the perimeter. Accordingly, dS is the element of area in S , and dl is the element of length along L . Substituting from the right-hand side of (4.5.55), we obtain

$$\int_L \frac{\partial \phi}{\partial n} dl = \int_L g(x_1, x_2) dl = 0 \quad (4.5.57)$$

$$\int_L g(x_1, x_2) dl = 0$$

Similarly for the elliptic Poisson equation,

$$\nabla^2 \phi = f(x_1, x_2) \quad (4.5.58)$$

with the boundary conditions as before, the integral constraint becomes

$$\int_S f(x_1, x_2) dS = \int_L \frac{\partial \phi}{\partial n} dl = \int_L g(x_1, x_2) dl \quad (4.5.59)$$

$$\int_L g(x_1, x_2) dl = \int_S f(x_1, x_2) dS$$

For all elliptic equations with Neumann boundary conditions, (4.5.57) or (4.5.59) must be satisfied by the discrete form of the equations. It is very important to note that in the MAC staggered grid system, the discretized form of the pressure Poisson equation automatically satisfies the discrete form of (4.5.59), obviating the need for any adjustments to the right-hand side of the Poisson equation (Fletcher, 2006), which is required in collocated mesh systems.

Let us again consider Poisson's equation (4.5.58) with the Neumann boundary conditions (4.5.55). Using second-order central differences and with $\Delta x = \Delta y = h$, at a grid point (i, j) (4.5.58) can be written as

$$\frac{\phi_{i+1,j} - 2\phi_{i,j} + \phi_{i-1,j}}{h^2} + \frac{\phi_{i,j+1} - 2\phi_{i,j} + \phi_{i,j-1}}{h^2} = f(x_i, y_j) \quad (4.5.60)$$

For the interior points, simplifying (4.5.60) leads to

$$\phi_{i+1,j} + \phi_{i-1,j} + \phi_{i,j+1} + \phi_{i,j-1} - 4\phi_{i,j} = h^2 f_{ij}$$

$$i = 1, 2, \dots, N \quad (4.5.61)$$

$$j = 1, 2, \dots, N$$

We evaluate this equation in the computational domain comprising a unit square as shown in Fig. 4.5.8, with $N = 2$, i.e., with 4 interior grid points. Writing

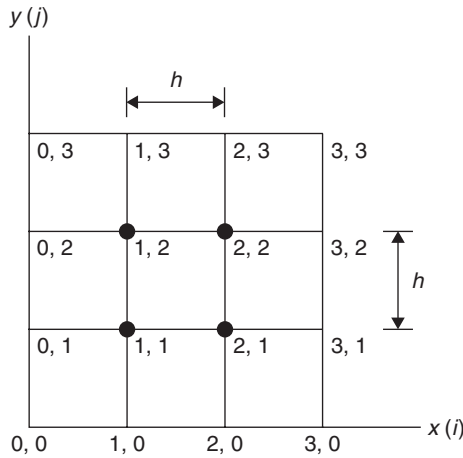


FIGURE 4.5.8 Schematic for the Poisson equation (4.5.62).

(4.5.61) for each node, the following system of linear equations is obtained:

$$\begin{aligned}\phi_{21} + \phi_{01} + \phi_{10} + \phi_{12} - 4\phi_{11} &= h^2 f_{11} \quad (1,1) \\ \phi_{31} + \phi_{11} + \phi_{20} + \phi_{22} - 4\phi_{21} &= h^2 f_{21} \quad (2,1) \\ \phi_{22} + \phi_{02} + \phi_{11} + \phi_{13} - 4\phi_{12} &= h^2 f_{12} \quad (1,2) \\ \phi_{32} + \phi_{12} + \phi_{21} + \phi_{23} - 4\phi_{22} &= h^2 f_{22} \quad (2,2)\end{aligned}\quad (4.5.62)$$

The boundary points ϕ_{i0} , ϕ_{0j} , ϕ_{i3} , ϕ_{3j} will be approximated by using first-order differences directed away from the interior of the square, for example, at $i = 1, j = 0$:

$$\left(\frac{\partial \phi}{\partial n}\right)_{1,0} = \left(\frac{\partial \phi}{\partial y}\right)_{1,0} = \frac{\phi_{11} - \phi_{10}}{h} = g_{10} \quad (4.5.63)$$

$$\phi_{10} = \phi_{11} - hg_{10}$$

Using (4.5.63) to eliminate ϕ_{10} , the finite difference equation at node (1,1) simplifies to

$$\phi_{21} + \phi_{12} - 2\phi_{11} = h^2 f_{11} + hg_{01} + hg_{10} = r_{11} \quad (4.5.64)$$

Similarly, for the other interior nodes the corresponding finite difference equations are

$$\phi_{11} + \phi_{22} - 2\phi_{21} = h^2 f_{21} + hg_{31} + hg_{20} = r_{21} \quad (4.5.65)$$

$$\phi_{11} + \phi_{22} - 2\phi_{12} = h^2 f_{12} + hg_{02} + hg_{13} = r_{12} \quad (4.5.66)$$

$$\phi_{21} + \phi_{12} - 2\phi_{22} = h^2 f_{22} + hg_{32} + hg_{23} = r_{22} \quad (4.5.67)$$

Writing (4.5.59)–(4.5.62) in matrix form, we obtain

$$\mathbf{A}\Phi = \mathbf{G}$$

$$\begin{bmatrix} -2 & 1 & 1 & 0 \\ 1 & -2 & 0 & 1 \\ 1 & 0 & -2 & 1 \\ 0 & 1 & 1 & -2 \end{bmatrix} \begin{bmatrix} \phi_{11} \\ \phi_{12} \\ \phi_{21} \\ \phi_{22} \end{bmatrix} = \begin{bmatrix} r_{11} \\ r_{12} \\ r_{21} \\ r_{22} \end{bmatrix} \quad (4.5.68)$$

We can calculate the eigenvalues λ_{1-4} of the coefficient matrix, \mathbf{A} , using the MATLAB function *eig(A)*, which gives

$$\lambda_1 = -4.0, \quad \lambda_{2,3} = -4.0, \quad \lambda_4 = 0.0 \quad (4.5.69)$$

From (4.5.69), we observe that there is an eigenvalue whose value is zero; therefore, the matrix \mathbf{A} is singular, cannot be inverted, and (4.5.68) does not have a solution. We can now use the MATLAB function *rcond(A)*, which calculates the reciprocal of the condition number of matrix \mathbf{A} based on the maximum column sum of the matrix. If the output *rcond(A)* is close to zero, the input matrix \mathbf{A} is badly conditioned or singular. If the output is close to 1, then the input matrix is well conditioned. For the \mathbf{A} matrix in (4.5.68), the value of *rcond* is $1.39e^{-17}$, confirming that the matrix is singular. Mitchell (1969, p. 121) shows that the singularity of the coefficient matrix of the Neumann problem in elliptic equations is because the system of equations (4.5.62) is linearly dependent; i.e., the number of independent equations is one less than the number of unknowns. Thus, one remedy is to assign a value to one of the unknowns eliminating one variable so that the number of linearly independent equations will be equal to the number of remaining unknowns. In this context, let us assign an arbitrary constant value, $\phi_{11} = 0$. Then the remaining equations can be solved in terms of this constant. In this case, the matrix equation (4.5.68) becomes

$$\mathbf{A}_1\Phi_1 = \mathbf{G}_1$$

$$\begin{bmatrix} 0 & 0 & 0 \\ -2 & 0 & 1 \\ 0 & -2 & 1 \\ 0 & 1 & -2 \end{bmatrix} \begin{bmatrix} \phi_{11} \\ \phi_{12} \\ \phi_{21} \\ \phi_{22} \end{bmatrix} = \begin{bmatrix} 0 \\ r_{12} \\ r_{21} \\ r_{22} \end{bmatrix} \quad (4.5.70)$$

Here, \mathbf{A}_1 and \mathbf{G}_1 are the modified coefficient matrix and the modified right-hand side vector, respectively. The eigenvalues of \mathbf{A}_1 are

$$\lambda_1 = -0.5858, \quad \lambda_2 = -3.4142, \quad \lambda_3 = -2.0, \quad (4.5.71)$$

All the eigenvalues are nonzero; therefore, equations (4.5.65) will have a unique solution for given values of the right-hand side vector. However, the condition number of the coefficient matrix \mathbf{A}_1 is 0.1250 so the system is linearly independent but still ill-conditioned. Consequently, iterative solutions of this system will be slower to converge than with Dirichlet-type boundary conditions. Because

of the slow convergence, for moderate-size problems, direct solutions based on LU decomposition will be very efficient. This can be accomplished by using the MATLAB operation $\Phi = \mathbf{A}_1 \backslash \mathbf{G}_1$.

Projects for Further Study

1. Numerically integrate the incompressible the continuity equation (4.5.1) and the Navier-Stokes equation (4.5.2) for a square cavity with a lid moving at a velocity, U , to the right (Figure 4.5.9). Solve the problem for Reynolds numbers $Re = 100$ and $Re = 400$. For this problem, $Re = UL/\nu$, where L is the cavity height and ν is the kinematic viscosity of the fluid. You can incorporate one of the following methods:

- a. Crank-Nicolson (or Euler implicit), Adams-Bashforth (or Euler explicit) semi-implicit scheme with the fractional step algorithm
- b. Fully explicit Euler (or Adams-Bashforth) scheme with the fractional step algorithm

As the mesh system, use the MAC staggered mesh arrangement. Note that for the viscous terms the Euler implicit scheme can be written as

$$\begin{aligned} \frac{\partial \zeta}{\partial t} &= \nu \frac{\partial^2 \zeta}{\partial x^2} \\ \frac{\zeta_i^{n+1} - \zeta_i^n}{\Delta t} &= \nu \frac{\zeta_{i+1}^{n+1} - 2\zeta_i^{n+1} + \zeta_{i-1}^{n+1}}{\Delta x^2} + O(\Delta t, \Delta x^2) \end{aligned} \quad (4.5.72)$$

For the explicit portions of the time step, the diffusive and convective stability criteria must be obeyed. Generally, the full Neumann boundary conditions of the pressure equation will require a direct solver (see Section 4.6 for more on direct solvers). At these values of Re , a 21×21 uniform mesh should be sufficient. Plot the stream function and vorticity contours and compare the values of ψ

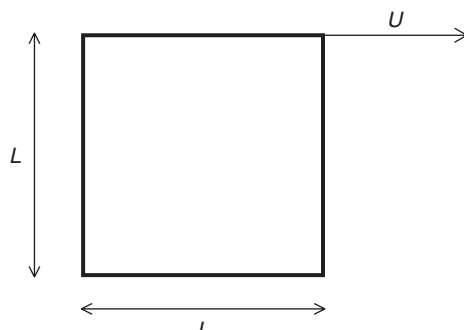


FIGURE 4.5.9 Schematic of the driven-cavity problem.

and ω at the center of the primary vortex with published data (Ghia, Ghia, and Shin, 1982; Kim and Moin, 1985). Because the Neumann problem for elliptic equations is singular (one zero eigenvalue), we must set a reference value for the pressure; say, on a boundary point set $P = 0$. This will eliminate one unknown from the problem (and the related equation also has to be eliminated from the system as explained in this section, so that the remaining equations will comprise a linearly independent system of equations. The solution of the system will be off by a constant, but the pressure gradient will be correctly calculated.

Assume steady state when the error in the solution is reduced by three orders of magnitude from its initial value. We can use either the maximum magnitude error norm or the Frobenius error norm for this purpose (Gerald and Wheatley, 1997, p. 156). For example, we define the error between successive iterates (or time levels) and the corresponding error norms below:

$$\begin{aligned} f_{i,j}^{n+1} &= u_{i+1/2,j}^{n+1} - u_{i+1/2,j}^n \\ \|\mathbf{F}\|_\infty &= \max_{1 \leq i \leq M} \sum_{j=1}^N |f_{i,j}^{n+1}| = \text{maximum magnitude norm (row sum)} \quad (4.5.73) \\ \|\mathbf{F}\|_f &= \left(\sum_{i=1}^M \sum_{j=1}^N \left(f_{i,j}^{n+1} \right)^2 \right)^{1/2} = \text{Frobenius norm (Euclidean norm)} \end{aligned}$$

These quantities can be readily calculated by MATLAB basic commands `norm(F, inf)` and `norm(A, 'fro')`, respectively.

Calculate the stream function (ψ) and vorticity (ω) values at the pressure-node points using the following equations:

$$\begin{aligned} \omega &= \frac{\partial v}{\partial x} - \frac{\partial u}{\partial y} \\ \psi_{ij} &= \psi_{i,j-1} + \Delta y (u_{i,j-1/2}) \end{aligned} \quad (4.5.74)$$

Note that ψ calculation requires an integration and the ψ equation above is the discrete form for the staggered mesh. The integration can start from the lower wall where $\psi = 0$ and continue along the vertical direction. To calculate u at pressure nodes, averaging will be required. Assume $\psi = 0$ on all the solid boundaries.

In Program 4.3 the governing equations are numerically integrated for the driven-cavity problem with the explicit Euler method; the divergence of the converged velocity field was on the order of machine zero (about e-14). We note that the flow is time dependent as it starts from a quiescent initial state when the upper lid moves to the right, and it requires many iterations until the flow reaches steady state. The solution efficiency can be significantly enhanced if the coefficient matrix of the linear system of the elliptic equations (either resulting from the implicit time advancement of the viscous terms in the momentum equations, or as in the present case resulting from the discretization of the “pressure” equation)

is declared as sparse; for example,

$$\mathbf{A} = \text{sparse}(\mathbf{B})$$

returns the matrix \mathbf{B} in compact form storing all nonzero elements together with information for the location of each nonzero element in the matrix (row and column numbers). Operations such as LU decomposition (backslash operation) will be performed in sparse form if \mathbf{A} is a sparse matrix.

A more efficient way of accomplishing the same computational efficiency with less storage will be to define the \mathbf{A} matrix (the coefficient matrix of the linear system),

$$\mathbf{A} = \text{sparse}(L, L)$$

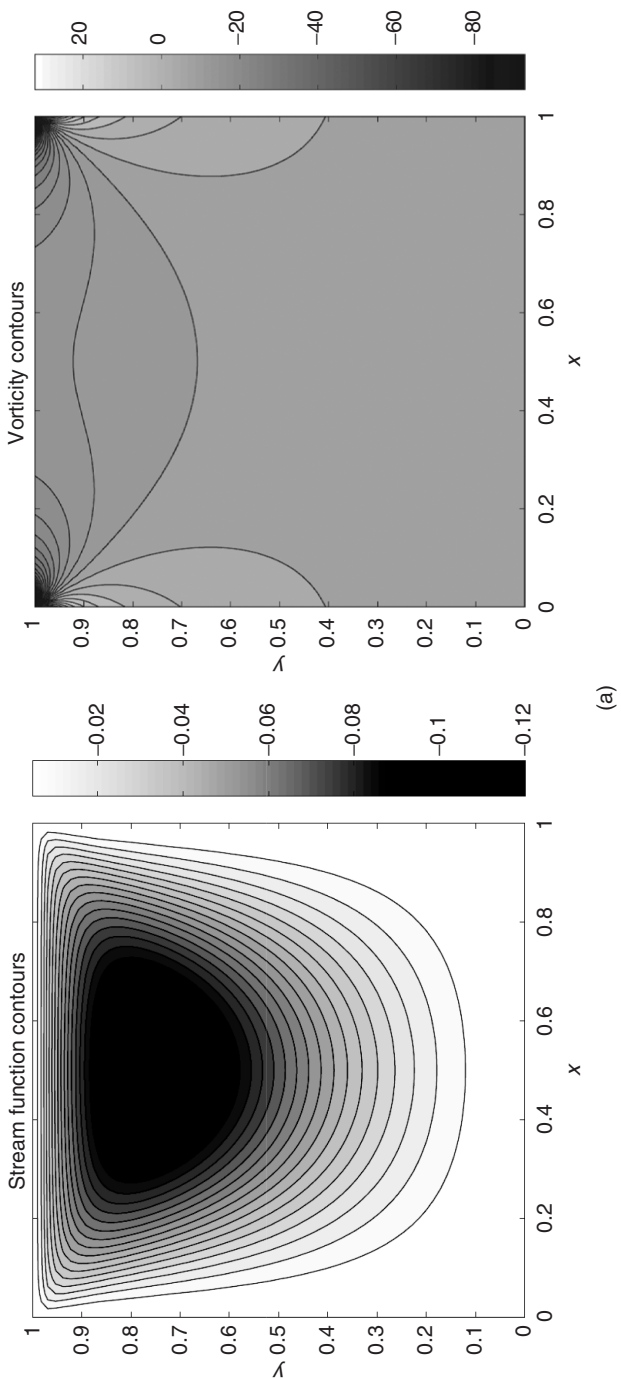
where L is the dimension of \mathbf{A} . This statement defines a zero $L \times L$ matrix without allocating any storage. When the nonzero components of \mathbf{A} are defined, \mathbf{A} is stored and returned in compact form.

Solutions for the cavity problem for various Reynolds numbers are presented in Fig. 4.5.10. For $\text{Re} = 1$, the solution has vertical symmetry, as displayed by the stream function and vorticity contours, and the vorticity is concentrated close to the upper corners where the problem is singular due to the double value (0 and 1) of the u velocity at these locations. As the Re increases to $\text{Re} = 100$, y symmetry is broken and the vortex center moves toward the right upper corner; a substantial increase to $\text{Re} = 4000$ results in the formation of secondary vortices in three corners of the cavity. Vorticity is concentrated on the upper and the right walls, and a vorticity tongue extends deeply into the cavity from the right wall. Table 4.5.1 summarizes vorticity and stream function values at the center of the primary vortex for various Reynolds numbers. These values compare favorably with previous work concerning this flow (see, e.g., Kim and Moin, 1985) for the comparable number of grid points employed.

2. The shear-driven cavity flow is of interest because of its similarity to wind-driven flows and can be useful to assess momentum transport from air to water when the effect of waves on the interface is neglected. Let us assume that at the air–water interface the shear stress $\tau = \rho_a u_*^2$ is constant. The governing equations (4.5.1) and (4.5.2) are nondimensionalized by the friction velocity u_* and the cavity height L , so that $\text{Re} = u_* L / v$. The physical constants used in

TABLE 4.5.1 Stream Function (ψ_c) and Vorticity (ω_c) at the Center of the Primary Vortices; N_x and N_y Are the Number of Grid Points along x and y Directions

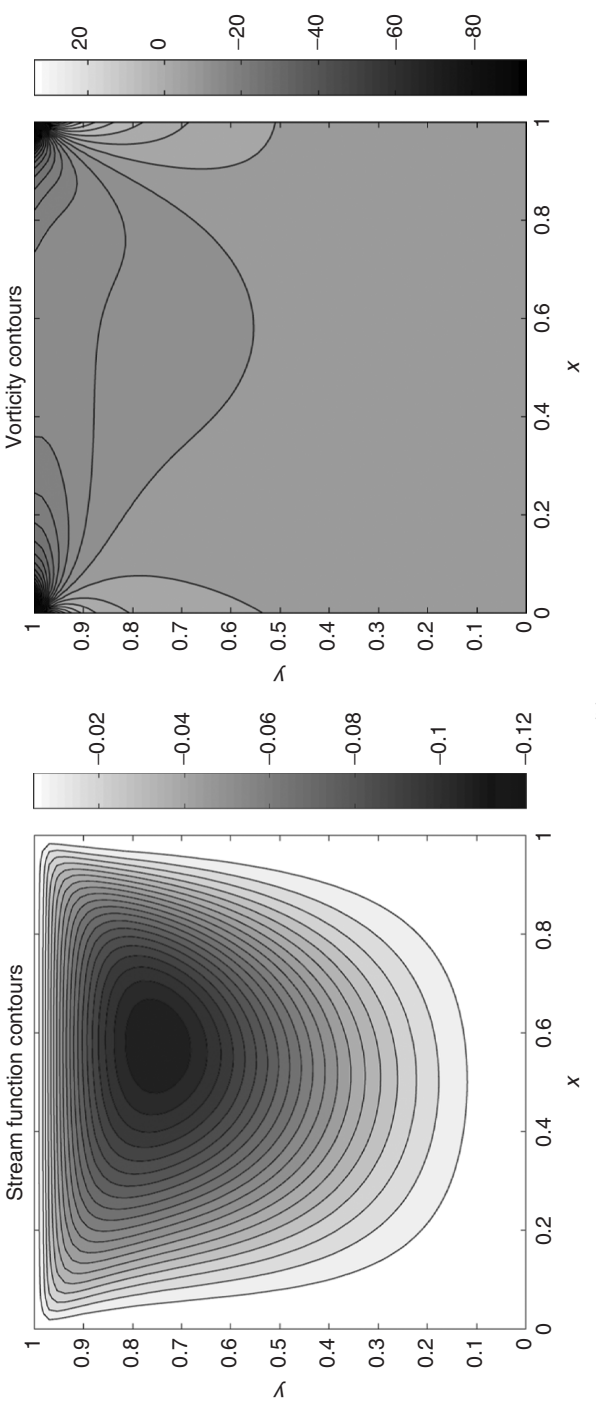
Re	ψ_c	ω_c	$N_x \times N_y$
1	-0.099	-3.207	65×65
100	-0.101	-3.157	65×65
400	-0.107	-2.609	65×65
1000	-0.113	-2.191	81×81
4000	-0.113	-1.842	81×81



(a)

FIGURE 4.5.10 Streamlines and vorticity contours for the driven cavity. (a) $Re = 1$, (b) $Re = 100$, (c) $Re = 4000$.

FIGURE 4.5.10 (continued)



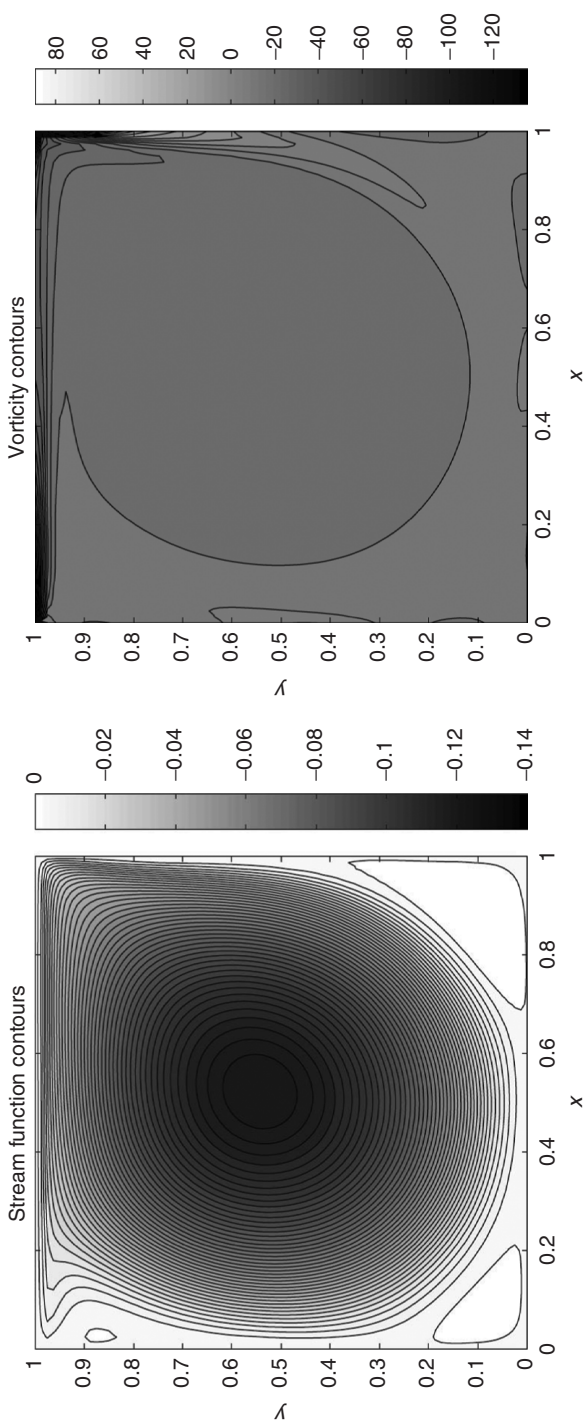


FIGURE 4.5.10 (continued)

(c)

the problem are the kinematic viscosity of water $\nu = 10^{-6} \text{ m}^2 \text{ s}^{-1}$, the density of water $\rho = 1000 \text{ kg m}^{-3}$, and the density of air $\rho_a = 1 \text{ kg m}^{-3}$. The governing equations are solved with the following boundary conditions:

At the air water interface (top wall moving from right to left):

$$\frac{\partial u}{\partial y} = -\frac{\rho_a}{\rho} \text{ Re} \quad \text{and} \quad v = 0$$

At the solid walls: $u = v = 0$

Calculate the resulting flow field for $\text{Re} = 100$ and for $\text{Re} = 2000$; plot the stream function and vorticity contours for each value of Re . Also plot u -velocity profiles as a function of the y coordinate at $x = 0.5$. Finally calculate the values of $\Delta\psi = \psi_{\max} - \psi_{\min}$ and compare your results with the published results of Huser and Biringen (1992). For these steady-state calculations a 41×41 uniform mesh should be adequate.

In summary, the integration of the two-dimensional, unsteady, incompressible continuity and momentum equations on a rectangular, staggered grid arrangement using the fractional step Euler explicit method can be accomplished by the following procedure.

Step 1. Prediction step:

- Using (4.5.39) and (4.5.40), calculate \hat{u} and \hat{v} at their respective grid point locations.
- Apply the boundary conditions as described by (4.5.43) or (4.5.44). Generally, (4.5.43) will be sufficient as the computation sweeps along the x and y directions.
- These equations will be solved algebraically because time advancement is fully explicit. Quantities that are not evaluated at their respective nodes will be evaluated by averaging, as in (4.5.33)–(4.5.38).
- Linear stability conditions (4.5.41) and (4.5.42) must be obeyed; in fact, because the equations are nonlinear, especially at higher Reynolds numbers, these restrictions will have to be multiplied by a safety factor on the order of 10^{-1} and even smaller.
- Divergence of the velocity field must be calculated at every time step, using the velocity field at the advanced time level, $(n + 1)$,

$$\nabla \cdot \mathbf{u} = \frac{u_{i+1/2,j}^{n+1} - u_{i-1/2,j}^{n+1}}{\Delta x} - \frac{v_{i,j+1/2}^{n+1} - v_{i,j-1/2}^{n+1}}{\Delta y} \quad (4.5.75)$$

The sum of the divergence magnitude at all grid points should be satisfied to machine zero at each time step. If this quantity increases, the calculation should be terminated and restarted with a smaller time step.

Step 2. Pressure calculation:

- Calculate the pressure form the pressure-Poisson equation (4.5.48),

$$\begin{aligned} & \frac{P_{i,j+1}^{n+1} - 2P_{i,j}^{n+1} + P_{i,j-1}^{n+1}}{\Delta y^2} + \frac{P_{i+1,j}^{n+1} - 2P_{i,j}^{n+1} + P_{i-1,j}^{n+1}}{\Delta x^2} \\ &= \frac{1}{\Delta t} \left[\frac{\hat{u}_{i+1/2,j} - \hat{u}_{i-1/2,j}}{\Delta x} + \frac{\hat{v}_{i,j+1/2} - \hat{v}_{i,j-1/2}}{\Delta y} \right] \quad (4.5.76) \end{aligned}$$

A direct solver with LU decomposition can be used for the solution of this equation. This is illustrated in greater in greater detail in Section 4.6.

- Boundary condition applied to the pressure equation at all boundaries is the homogeneous Neumann boundary conditions (4.5.49) and (4.5.50). This equation is solved at the pressure nodes (i, j) (Fig. 4.5.3). Note that the Euler explicit time-advancement calculates the actual thermodynamic pressure (scaled by the constant density) and not a pseudo-pressure.
- The Neumann problem for the elliptic pressure equation results in a singular coefficient matrix. To remove this singularity (and obtain a system of linearly independent equations), it is necessary to assign a constant value (for example, $P = 0$) to the pressure at one pressure node. The resulting solution will be off by a constant, but the pressure gradient will be correctly calculated. A smoother solution can be obtained by setting the average value of the solution vector to zero and by imposing this condition in place of one of the nodal equations.

Step 3. Velocity correction:

- Obtain the velocity field at the advanced time level ($n + 1$) from (4.5.47); for each velocity component, this equation gives

$$u_{i+1/2,j}^{n+1} = \hat{u}_{i+1/2,j} - \frac{\Delta t}{\Delta x} (P_{i+1,j}^{n+1} - P_{i,j}^{n+1}) \quad (4.5.77)$$

$$v_{i,j+1/2}^{n+1} = \hat{v}_{i,j+1/2} - \frac{\Delta t}{\Delta x} (P_{i,j+1}^{n+1} - P_{i,j}^{n+1}) \quad (4.5.78)$$

- Steady-state solution at low Reynolds numbers should be assumed converged when one of the error norms (4.5.73) will decrease by at least three orders of magnitude.

4.6 FLOW PAST A CIRCULAR CYLINDER: AN EXAMPLE FOR THE VORTICITY-STREAM FUNCTION FORMULATION

As we have seen in Section 4.3, an alternate formulation of the governing equations for two-dimensional, steady and unsteady incompressible equations is the vorticity-stream function formulation where pressure does not appear as

a dependent variable. We can obtain the vorticity transport equation from the Navier-Stokes equation as follows. First we write the Navier-Stokes equation as a vector equation:

$$\frac{\partial \mathbf{V}}{\partial t} + (\mathbf{V} \cdot \nabla) \mathbf{V} = -\nabla \left(\frac{p}{\rho} \right) + \nu \nabla^2 \mathbf{V} \quad (4.6.1)$$

where \mathbf{V} is the velocity vector, ν is the kinematic viscosity, p is thermodynamic pressure, and ρ is the fluid density. Using vector identities for the convection term, we obtain

$$(\mathbf{V} \cdot \nabla) \mathbf{V} = \nabla \left(\frac{1}{2} \mathbf{V} \cdot \mathbf{V} \right) - \mathbf{V} \times (\nabla \times \mathbf{V}) \quad (4.6.2)$$

Substitution of (4.6.2) into (4.6.1) yields

$$\frac{\partial \mathbf{V}}{\partial t} + \nabla \left(\frac{1}{2} \mathbf{V} \cdot \mathbf{V} \right) - \mathbf{V} \times (\nabla \times \mathbf{V}) = -\nabla \left(\frac{p}{\rho} \right) + \nu \nabla^2 \mathbf{V} \quad (4.6.3)$$

Defining the vorticity vector

$$\boldsymbol{\omega} = \nabla \times \mathbf{V} \quad (4.6.4)$$

and noting that the scalar quantity (p/ρ)

$$\nabla \times \nabla \left(\frac{p}{\rho} \right) = 0 \quad (4.6.5)$$

then from vector identities we can write

$$\mathbf{V} \times (\nabla \times \mathbf{V}) = \mathbf{V} \times \boldsymbol{\omega} \quad (4.6.6)$$

With (4.6.4)–(4.6.6), after taking the curl equation (4.6.3) becomes

$$\frac{\partial \boldsymbol{\omega}}{\partial t} - \nabla \times (\mathbf{V} \times \boldsymbol{\omega}) = \nu \nabla^2 \boldsymbol{\omega} \quad (4.6.7)$$

Again, using vector identities, we obtain

$$\begin{aligned} \nabla \times (\mathbf{V} \times \boldsymbol{\omega}) &= \mathbf{V}(\nabla \cdot \boldsymbol{\omega}) - \boldsymbol{\omega}(\nabla \cdot \mathbf{V}) - (\mathbf{V} \cdot \nabla) \boldsymbol{\omega} + (\boldsymbol{\omega} \cdot \nabla) \mathbf{V} \\ \nabla \cdot \boldsymbol{\omega} &= \nabla \cdot (\nabla \times \mathbf{V}) = 0 \text{ (divergence of the curl of any vector is zero)} \\ \nabla \cdot \mathbf{V} &= 0 \text{ (satisfies mass conservation for incompressible flow)} \\ (\boldsymbol{\omega} \cdot \nabla) \mathbf{V} &= 0 \text{ (for two-dimensional flow)} \end{aligned} \quad (4.6.8)$$

The substitution of (4.6.8) into (4.6.7) results in

$$\frac{\partial \boldsymbol{\omega}}{\partial t} + (\mathbf{V} \cdot \nabla) \boldsymbol{\omega} = \nu \nabla^2 \boldsymbol{\omega} \quad (4.6.9)$$

Equation (4.6.9) is the vorticity transport equation, in which the vorticity and the velocity vectors are the unknowns. In two-dimensional flows the only nonzero component of the vorticity is along the z direction, so that equation (4.6.9) is written only for the z component of the vorticity, ω

$$\frac{\partial \omega}{\partial t} + u \frac{\partial \omega}{\partial x} + v \frac{\partial \omega}{\partial y} = \nu \nabla^2 \omega \quad (4.6.10)$$

The velocities can be written in terms of the stream function

$$u = \frac{\partial \psi}{\partial y}, \quad v = -\frac{\partial \psi}{\partial x} \quad (4.6.11)$$

The substitution of (4.6.11) into the definition of vorticity, $\omega = \partial v / \partial x - \partial u / \partial y$, yields the elliptic stream function equation,

$$\nabla^2 \psi = -\omega \quad (4.6.12)$$

The system of equations (4.6.10) and (4.6.12) will be integrated for the two unknowns, ω and ψ . Velocities can be updated by using (4.6.11). We discretize these equations using the Euler explicit scheme for simplicity. Other integration formulas, such as the implicit or semi-implicit time stepping schemes, can be easily substituted for this scheme.

Let us now consider the wall-driven cavity problem outlined in Section 4.5. We will use the vorticity/stream-function approach to obtain a solution for this problem. It is possible to use a collocated mesh because the elimination of the pressure gradient term obviates the use of a staggered mesh to strengthen pressure–velocity coupling as in the primitive variable system (Section 2.5). With second-order central differences and Euler-explicit time-advancement, the finite-difference form of (4.6.10) is written as

$$\begin{aligned} & \frac{\omega_{i,j}^{n+1} - \omega_{i,j}^n}{\Delta t} + u_{i,j}^n \frac{\omega_{i+1,j}^n - \omega_{i-1,j}^n}{2h} + v_{i,j}^n \frac{\omega_{i,j+1}^n - \omega_{i,j-1}^n}{2h} \\ &= \frac{1}{h^2 \text{Re}} (\omega_{i+1,j}^n + \omega_{i-1,j}^n + \omega_{i,j+1}^n + \omega_{i,j-1}^n - 4\omega_{i,j}^n) \end{aligned} \quad (4.6.13)$$

We will assume that the variables have been nondimensionalized by U and L , the lid velocity and the cavity height, respectively, so that $\text{Re} = UL/\nu$; also, $h = \Delta x = \Delta y$. Using the vorticity at the advanced time level ($n + 1$), the stream function is calculated from the finite-difference form of (4.6.12):

$$\frac{\psi_{i+1,j}^{n+1} - 2\psi_{i,j}^{n+1} + \psi_{i-1,j}^{n+1}}{h^2} + \frac{\psi_{i,j+1}^{n+1} - 2\psi_{i,j}^{n+1} + \psi_{i,j-1}^{n+1}}{h^2} = -\omega_{i,j}^{n+1} \quad (4.6.14)$$

Equation (4.6.14) can be solved either by an iterative method or by a direct method (LU decomposition). The velocity components are updated from (4.6.11):

$$u_{i,j}^{n+1} = \frac{\psi_{i,j+1}^{n+1} - \psi_{i,j-1}^{n+1}}{2h}, \quad v_{i,j}^{n+1} = -\frac{\psi_{i+1,j}^{n+1} - \psi_{i-1,j}^{n+1}}{2h} \quad (4.6.15)$$

The numerical integration is done according to the following sequence:

1. Set initial conditions at $t = 0$ (e.g., at all interior points set $\omega_{i,j}^n = 0$).
2. Calculate $\omega_{i,j}^{n+1}$ at time level $t + \Delta t$ from (4.6.13).
3. Obtain $\psi_{i,j}^{n+1}$ by solving (4.6.14) either by a direct method or iteratively.
4. Update velocities by calculating $u_{i,j}^{n+1}$ and $v_{i,j}^{n+1}$ from (4.6.15).
5. Boundary values for $\omega_{i,j}$ are solution-dependent and must be updated at every time step using $\psi_{i,j}^{n+1}$. We suggest a way of doing that below.
6. If the computation has reached the desired time, or if a prescribed convergence criterion is reached, terminate the calculation; otherwise, go back to step 2.
7. Monitor the Courant number (which is solution-dependent) and if it starts to increase rapidly, terminate the calculation and start over with half the original time step.

For the driven-cavity problem, all boundary conditions are prescribed on impermeable solid boundaries. Higher-order boundary conditions for vorticity were developed in Section 3.7, equations (3.7.14) and (3.7.15). Here we provide an alternative way of writing the boundary conditions for vorticity obtained from the interior values of the stream function only in the wall-normal direction. Consider Fig. 4.6.1, which shows the vertical grid layout close to the lower stationary wall, where $\psi_{i,1}^{n+1}$ is the value of the stream function on the wall and $\psi_{i,2}^{n+1}$ is the value of the stream function at the first point away from the wall; $h = \Delta y$ is the grid length. Using Taylor series up to second order, assuming Δy is small:

$$\psi_{i,2}^{n+1} = \psi_{i,1}^{n+1} + \left(\frac{\partial \psi}{\partial y} \right)_{i,1}^{n+1} \Delta y + \left(\frac{\partial^2 \psi}{\partial y^2} \right)_{i,1}^{n+1} \frac{\Delta y^2}{2} + \dots \quad (4.6.16)$$

We now note that when there is no through flow, the boundary condition for the stream function on solid wall is prescribed as

$$\psi_{i,1}^{n+1} = 0$$

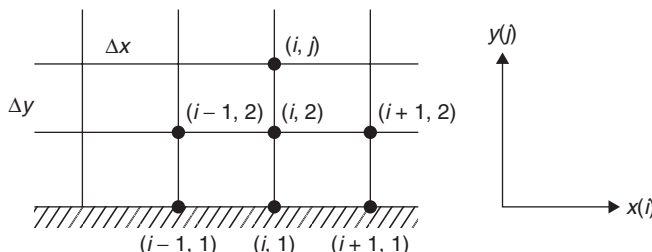


FIGURE 4.6.1 Grid arrangement close to the stationary lower wall.

Also,

$$\left(\frac{\partial \psi}{\partial y}\right)_{i,1}^{n+1} = u_{i,1}^{n+1} = 0 \text{ (stationary wall, no slip boundary)}$$

From the definition of vorticity,

$$\omega_{i,1}^{n+1} = \left(\frac{\partial v}{\partial x}\right)_{i,1}^{n+1} - \left(\frac{\partial u}{\partial y}\right)_{i,1}^{n+1} \quad (4.6.17)$$

Imposing a no-slip boundary condition, we get

$$v_{i,1}^{n+1} = 0 \quad \text{so that} \quad \left(\frac{\partial v}{\partial x}\right)_{i,1}^{n+1} = 0 \quad (4.6.18)$$

It then follows from (4.6.17) that

$$\omega_{i,1}^{n+1} = -\left(\frac{\partial u}{\partial y}\right)_{i,1}^{n+1} \quad (4.6.19)$$

Hence, (4.6.16) can be written as

$$\psi_{i,2}^{n+1} = \left(\frac{\partial^2 \psi}{\partial y^2}\right)_{i,1}^{n+1} \frac{\Delta y^2}{2} = \frac{\partial}{\partial y} \left(\frac{\partial \psi}{\partial y}\right)_{i,1}^{n+1} \frac{\Delta y^2}{2} = \left(\frac{\partial u}{\partial y}\right)_{i,1}^{n+1} \frac{\Delta y^2}{2} = -\omega_{i,1}^{n+1} \frac{\Delta y^2}{2} \quad (4.6.20)$$

which leads to the boundary condition for vorticity on the stationary lower wall of the cavity:

$$\omega_{i,1}^{n+1} = -\frac{\psi_{i,2}^{n+1}}{\Delta y^2/2} \quad (4.6.21)$$

Now, considering the upper wall (Fig. 4.6.2), where the grid index $j = J$, and using Taylor series as before, we have

$$\psi_{i,J-1}^{n+1} = \psi_{i,J}^{n+1} - \left(\frac{\partial \psi}{\partial y}\right)_{i,J}^{n+1} \Delta y + \left(\frac{\partial^2 \psi}{\partial y^2}\right)_{i,J}^{n+1} \frac{\Delta y^2}{2} + \dots \quad (4.6.22)$$

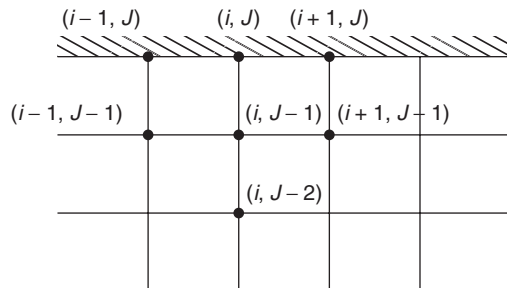


FIGURE 4.6.2 Grid arrangement close to the moving upper wall.

Using the same arguments as before, on solid boundaries with no flow through, $\psi_{i,J}^{n+1} = 0$, and

$$\left(\frac{\partial \psi}{\partial y}\right)_{i,J}^{n+1} = u_{i,J}^{n+1} = u_W = 1 \text{ (moving wall, no slip boundary)} \quad (4.6.23)$$

Using (4.6.17)–(4.6.19), (4.6.22) can be written as

$$\psi_{i,J-1}^{n+1} = -\left(\frac{\partial \psi}{\partial y}\right)_{i,J}^{n+1} \Delta y + \left(\frac{\partial^2 \psi}{\partial y^2}\right)_{i,J}^{n+1} \frac{\Delta y^2}{2} = -u_W \Delta y - \omega_{i,J}^{n+1} \frac{\Delta y^2}{2} \quad (4.6.24)$$

from which we obtain

$$\omega_{i,J}^{n+1} = \frac{-\psi_{i,J-1}^{n+1} - u_W \Delta y}{\Delta y^2/2}, \quad u_W = 1 \quad (4.6.25)$$

Let us now consider the stream function equation (4.6.14) on a grid with 3×3 interior points shown in Fig. 4.6.3:

$$\begin{aligned} \psi_{i+1,j} + \psi_{i-1,j} + \psi_{i,j+1} + \psi_{i,j-1} - 4\psi_{i,j} &= -h^2 \omega_{ij} \\ i = 1, 2, \dots, N \\ j = 1, 2, \dots, N \quad N = 3 \end{aligned} \quad (4.6.26)$$

Here, the first subscript is the column index along the x direction, and the second subscript is the row index along the y direction. We can write (4.6.26) for each internal node:

$$\begin{aligned} \psi_{21} + \psi_{01} + \psi_{10} + \psi_{12} - 4\psi_{11} &= -h^2 \omega_{11} & (1,1) \\ \psi_{31} + \psi_{11} + \psi_{20} + \psi_{22} - 4\psi_{21} &= -h^2 \omega_{21} & (2,1) \\ \psi_{41} + \psi_{21} + \psi_{30} + \psi_{32} - 4\psi_{31} &= -h^2 \omega_{31} & (3,1) \\ \psi_{22} + \psi_{02} + \psi_{11} + \psi_{13} - 4\psi_{12} &= -h^2 \omega_{12} & (1,2) \\ \psi_{32} + \psi_{12} + \psi_{21} + \psi_{23} - 4\psi_{22} &= -h^2 \omega_{22} & (2,2) \\ \psi_{42} + \psi_{22} + \psi_{31} + \psi_{33} - 4\psi_{32} &= -h^2 \omega_{32} & (3,2) \\ \psi_{23} + \psi_{03} + \psi_{12} + \psi_{14} - 4\psi_{13} &= -h^2 \omega_{13} & (1,3) \\ \psi_{33} + \psi_{13} + \psi_{22} + \psi_{24} - 4\psi_{23} &= -h^2 \omega_{23} & (2,3) \\ \psi_{43} + \psi_{23} + \psi_{32} + \psi_{34} - 4\psi_{33} &= -h^2 \omega_{33} & (3,3) \end{aligned} \quad (4.6.27)$$

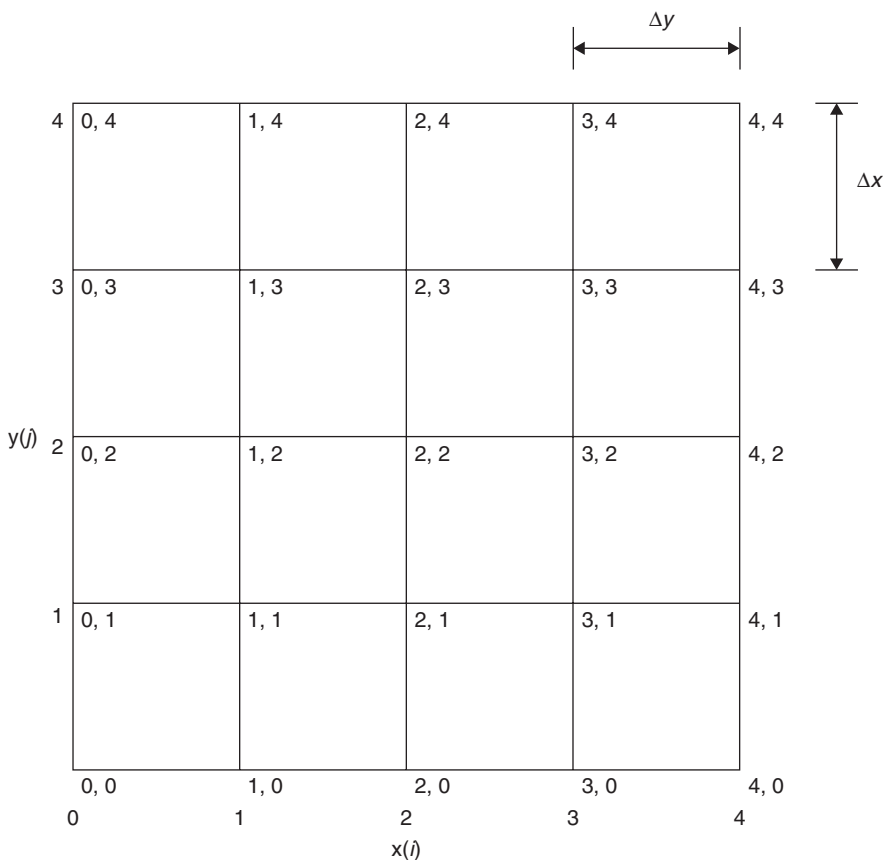


FIGURE 4.6.3 Computational grid for the ψ equation (4.6.26).

And in vector-matrix form,

$$\left[\begin{array}{cccccc|cccccc} 4 & -1 & 0 & -1 & 0 & 0 & 0 & 0 & 0 & 0 \\ -1 & 4 & -1 & 0 & -1 & 0 & 0 & 0 & 0 & 0 \\ 0 & -1 & 4 & 0 & 0 & -1 & 0 & 0 & 0 & 0 \\ \hline -1 & 0 & 0 & 4 & -1 & 0 & -1 & 0 & 0 & 0 \\ 0 & -1 & 0 & -1 & 4 & -1 & 0 & -1 & 0 & 0 \\ 0 & 0 & -1 & 0 & -1 & 4 & 0 & 0 & -1 & 0 \\ \hline 0 & 0 & 0 & -1 & 0 & 0 & 4 & -1 & 0 & 0 \\ 0 & 0 & 0 & 0 & -1 & 0 & -1 & 4 & -1 & 0 \\ 0 & 0 & 0 & 0 & 0 & -1 & 0 & -1 & 4 & -1 \\ \hline 0 & 0 & 0 & 0 & 0 & -1 & 0 & -1 & 4 & 0 \end{array} \right] \begin{bmatrix} \psi_{11} \\ \psi_{21} \\ \psi_{31} \\ \hline \psi_{12} \\ \psi_{22} \\ \psi_{32} \\ \hline \psi_{13} \\ \psi_{23} \\ \psi_{33} \end{bmatrix}^{n+1} = - \begin{bmatrix} -h^2\omega_{11} + \psi_{01} + \psi_{10} \\ -h^2\omega_{21} + \psi_{20} \\ -h^2\omega_{31} + \psi_{30} + \psi_{41} \\ \hline -h^2\omega_{12} + \psi_{02} \\ -h^2\omega_{22} \\ -h^2\omega_{32} + \psi_{42} \\ \hline -h^2\omega_{13} + \psi_{03} + \psi_{14} \\ -h^2\omega_{23} + \psi_{24} \\ -h^2\omega_{33} + \psi_{43} + \psi_{34} \end{bmatrix}^{n+1} \quad (4.6.28)$$

The problem again reduces to the solution of the linear equation:

$$\mathbf{A}\Psi = \mathbf{f}$$

where \mathbf{A} is the banded $N^2 \times N^2$ (9×9) coefficient matrix; the number of nonzero bands is $2N + 1$. We can also write (4.6.28) as follows:

$$\begin{bmatrix} \mathbf{B} & \mathbf{I} & \mathbf{0} \\ \mathbf{I} & \mathbf{B} & \mathbf{I} \\ \mathbf{0} & \mathbf{I} & \mathbf{B} \end{bmatrix} \begin{bmatrix} \boldsymbol{\psi}_{i1} \\ \boldsymbol{\psi}_{i2} \\ \boldsymbol{\psi}_{i3} \end{bmatrix} = \begin{bmatrix} \mathbf{f}_{i1} \\ \mathbf{f}_{i2} \\ \mathbf{f}_{i3} \end{bmatrix}, \quad i = 1, 2, 3$$

where we define \mathbf{I} as the 3×3 identity matrix and \mathbf{B} is the partitioned diagonal matrix of \mathbf{A} . The direct solution of the linear system $\mathbf{A}\boldsymbol{\Psi} = \mathbf{f}$ can be efficiently done by the LU decomposition method, where we decompose \mathbf{A} into a special upper triangular matrix \mathbf{U} and a lower triangular matrix \mathbf{L} with the diagonal equal to unity. The sequential solution of this system is the same as the solution of the tridiagonal matrix equation given by (4.4.45)–(4.4.46). In a similar fashion, when the problem requires successive solutions of the elliptic equation, the LU decomposition can be done only once and storing the \mathbf{L} and \mathbf{U} matrices, the back substitution can be performed as many times as needed, thus reducing the required computational effort. These savings are possible because the cost of the solution of an n system of linear equations by the LU decomposition method is $n^3/2$ operations, the same as in Gaussian elimination, but the backsubstitution part is only n^2 operations (Ferziger, 1998, p. 5). We also note that for the $\omega-\psi$ formulation of the governing equations, there is no singularity in both the coefficient matrix of the spatially elliptic ω equation and the coefficient matrix of the elliptic ψ equation, so that both can be solved by iterative methods, such as the successive overrelaxation (SOR) method outlined in Section 2.8, (2.8.13)–(2.8.14).

Another iterative method that can be efficiently employed for the solution of elliptic equations is the alternating-direction implicit (ADI) method. Let us consider the elliptic Laplace equation for a generic variable T , in a rectangle $0 < x, y < 1$, with Dirichlet boundary conditions on all the sides:

$$\frac{\partial^2 T}{\partial x^2} + \frac{\partial^2 T}{\partial y^2} = 0 \quad (4.6.29)$$

The ADI method assumes a pseudo time derivative, so that the equation becomes elliptic in space and parabolic in time, e.g.,

$$\frac{\partial T}{\partial t} = \frac{\partial^2 T}{\partial x^2} + \frac{\partial^2 T}{\partial y^2} \quad (4.6.30)$$

and seeks steady-state solutions for this problem as $t \rightarrow \infty$.

Thus, the use of the ADI method for elliptic problems implies that

- Physical significance and the accuracy of the transient solution are not of interest.
- As steady state is approached, that is, when $t \rightarrow \infty$, the solution approaches that of the elliptic Laplace (or Poisson) equation.

As the transient solution is not important, it is generally sufficient to advance the solution in time using the fully implicit Euler scheme, so that the two-step procedure of this method can be written as (Peaceman and Rachford, 1955)

$$\begin{aligned} \frac{T_{i,j}^{n+1/2} - T_{i,j}^n}{\Delta t_1} &= \frac{1}{\Delta x^2} \left[T_{i+1,j}^{n+1/2} - 2T_{i,j}^{n+1/2} + T_{i-1,j}^{n+1/2} \right] \\ &\quad + \frac{1}{\Delta y^2} \left[T_{i,j+1}^n - 2T_{i,j}^n + T_{i,j-1}^n \right] \\ \frac{T_{i,j}^{n+1} - T_{i,j}^{n+1/2}}{\Delta t_1} &= \frac{1}{\Delta x^2} \left[T_{i+1,j}^{n+1/2} - 2T_{i,j}^{n+1/2} + T_{i-1,j}^{n+1/2} \right] \\ &\quad + \frac{1}{\Delta y^2} \left[T_{i,j+1}^{n+1} - 2T_{i,j}^{n+1} + T_{i,j-1}^{n+1} \right] \end{aligned} \quad (4.6.31)$$

Defining

$$\beta_r = \Delta x / \Delta y, \quad \bar{\rho} = \Delta x^2 / \Delta t$$

the iteration sequence can be written as

$$\begin{aligned} T_{i+1,j}^{n+1/2} - (2 + \bar{\rho})T_{i,j}^{n+1/2} + T_{i-1,j}^{n+1/2} &= \beta_r^2 \left[-T_{i,j+1}^n + \left(2 - \frac{\bar{\rho}}{\beta_r^2} \right) T_{i,j}^n - T_{i,j-1}^n \right] \\ T_{i,j+1}^{n+1} - (2 + \frac{\bar{\rho}}{\beta_r^2})T_{i,j}^{n+1} + T_{i,j-1}^{n+1} &= \frac{1}{\beta_r^2} \left[-T_{i+1,j}^{n+1/2} + (2 - \bar{\rho})T_{i,j}^{n+1/2} - T_{i-1,j}^{n+1/2} \right] \end{aligned} \quad (4.6.32)$$

Now considering the Poisson equation,

$$\frac{\partial T}{\partial t} = \nabla^2 T - \xi(x, y) \quad (4.6.33)$$

where $\xi(x, y)$ is the source term. For $\Delta x = \Delta y$ ($\beta_r = 1$), the ADI sequence can be written as

$$\begin{aligned} T_{i+1,j}^{n+1/2} - (2 + \bar{\rho})T_{i,j}^{n+1/2} + T_{i-1,j}^{n+1/2} &= -T_{i,j+1}^n + (2 - \bar{\rho})T_{i,j}^n - T_{i,j-1}^n - \Delta x^2 \xi_{i,j} \\ T_{i,j+1}^{n+1} - (2 + \bar{\rho})T_{i,j}^{n+1} + T_{i,j-1}^{n+1} &= -T_{i+1,j}^{n+1/2} + (2 - \bar{\rho})T_{i,j}^{n+1/2} \\ &\quad - T_{i-1,j}^{n+1/2} - \Delta y^2 \xi_{i,j} \end{aligned} \quad (4.6.34)$$

Both set of equations (4.6.32) and (4.6.34) are solved first along rows and next by columns. In both steps, the resulting system of linear equations has tridiagonal coefficient matrices so that either the Thomas algorithm or the LU decomposition can be very efficiently implemented. It is important to recognize that the speed of solution convergence depends strongly on the choice of the iteration parameter, ρ . This method will converge for any fixed value of $\bar{\rho}$ for Laplace's

equation in a square, provided that the same value is used in the two half-steps. More information concerning different formulations of the ADI method and the selection of the iteration parameter are given in Mitchell (1969).

Project for Further Study: Program 4.4 is a MATLAB script that numerically integrates (4.6.10) and (4.6.12) with the Euler explicit scheme on a uniform mesh with $\Delta x = \Delta y$. The solution of the elliptic stream function (ψ) equation (4.6.12) is obtained by the SOR method. Modify the program and solve (4.6.12) using the Peaceman-Rachford ADI method outlined above for a grid of 31×31 interior grid points at Reynolds numbers $Re = 1, 100$, and 400 . Note that this equation has to reach a converged state at every time step during the integration process and the rate of convergence strongly depends on the proper choice of the iteration parameter, ρ ; for practical purposes, setting $\rho \approx 8/N$ is sufficient (Ferziger, 1998, p. 265). A parameter sequence for the Peaceman-Rachford method is given by Wachpress (1957) and summarized by Mitchell (1969, p. 111), which reads

$$r_{k+1} = (1/\bar{\rho}_{k+1}) = \frac{1}{2 \cos^2(\pi/2M)} \left(\cot^2 \frac{\pi}{2M} \right)^{k/(k_0-1)} \quad (k = 0, 1, \dots, k_0 - 1) \quad (4.6.35)$$

In (4.6.35), M is the number of grid divisions so that $(M-1)$ is the number of interior grid points in one direction. Also, k_0 is the smallest integer greater than or equal to 2, obtained from

$$\left(\sqrt{2} - 1 \right)^{(k_0-1)} \leq \tan \frac{\pi}{2M} \quad (4.6.36)$$

It is important to use the same value of $\bar{\rho}_k$ in each half step of the integration process. Assuming a 10×10 grid of interior points, $M = 11$, and from (4.6.36) one obtains $k_0 = 4$, which leads to the following sequence of r -values: 0.51033610, 1.85949096, 6.77535187, and 24.68707504. The parameter sequence can be applied as many times as needed until the imposed convergence criterion (for example, three orders of magnitude decrease on the amplitude of the initial error norm) is satisfied.

Compare the convergence rates of the solution at different Re , when using these two convergence criteria.

Flow Past a Circular Cylinder

As a final example, we will consider uniform flow, U_∞ , past a circular cylinder with radius a as shown in Figure 4.6.4. We follow the formulation of this problem outlined by Peyret and Taylor (1983, pp. 207–212) and, defining the diameter-based Reynolds number, $Re = 2Ua/v$, we write (4.6.12) and (4.6.9), respectively,

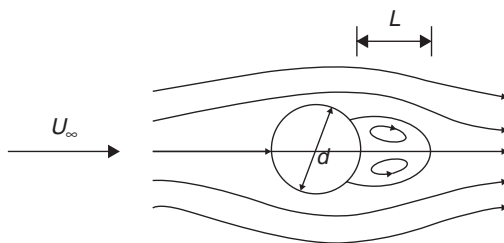


FIGURE 4.6.4 Geometry of flow past a circular cylinder, where d is the cylinder diameter, and L is the separation bubble length.

in cylindrical coordinates:

$$\frac{\partial^2 \psi}{\partial r^2} + \frac{1}{r} \frac{\partial \psi}{\partial r} + \frac{1}{r^2} \frac{\partial^2 \psi}{\partial \theta^2} = -\omega \quad (4.6.37)$$

$$\frac{\partial \omega}{\partial t} + v_r \frac{\partial \omega}{\partial r} + \frac{v_\theta}{r} \frac{\partial \omega}{\partial \theta} = \frac{2}{\text{Re}} \left(\frac{\partial^2 \omega}{\partial r^2} + \frac{1}{r} \frac{\partial \omega}{\partial r} + \frac{1}{r^2} \frac{\partial^2 \omega}{\partial \theta^2} \right) \quad (4.6.38)$$

where v_r and v_θ are the velocity components along the radial (r) and tangential (θ) directions, respectively.

The problem consists of the cylinder in quiescent air for time $t < 0$. At time $t \geq 0$, a uniform velocity U_∞ is applied. The unsteady Navier-Stokes equations are solved with no-slip boundary conditions on the surface boundary, Γ , and the boundary $r \rightarrow \infty$ has uniform flow. The flow remains symmetrical with respect to the centerline for low Reynolds numbers, $\text{Re} < 40$. For higher values of Re , the solution rapidly bifurcates into an oscillatory regime. We will consider low Re cases exploiting the symmetry of the solution, and investigate the effects of increasing values of Re on the separation bubble length (L/d) and the drag force on the cylinder.

It is apparent from the above statements that one major difficulty of this problem is the unbounded physical domain. This difficulty can be resolved by mapping the infinite extent of the physical domain in the r coordinate into a finite computational domain by an algebraic transformation given by Ta Phuoc Loc (1980), such that

$$r = \frac{\bar{r}}{a} = e^{\pi\xi} \quad (4.6.39)$$

$$\theta = \pi\eta$$

In (4.6.39), \bar{r} is the dimensional radius. Because of the symmetry of the solution at low $\text{Re} < 40$, it is sufficient to calculate the flow field in the upper half of the computational domain, i.e., for $0 \leq \theta \leq \pi$, so that $0 \leq \eta \leq 1$. Also, the computational domain is limited to a finite value $\xi_\infty \simeq 1$, which is equivalent to $r_\infty = 22$, sufficiently removed from the surface of the cylinder (Figure 4.6.5).

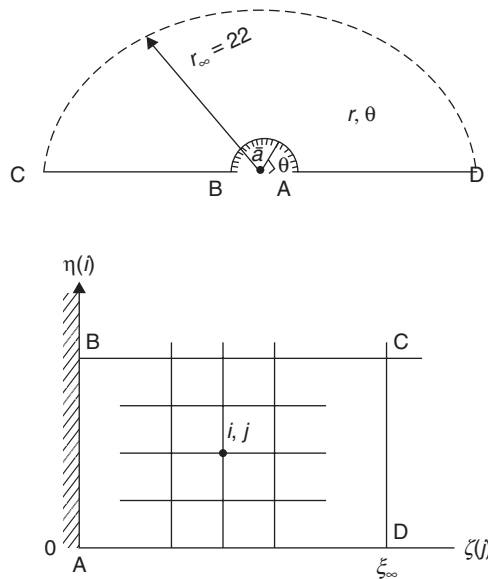


FIGURE 4.6.5 Cylinder in uniform flow in transformed coordinates.

In cylindrical coordinates, velocity components are given as

$$\begin{aligned} v_r &= \frac{1}{r} \frac{\partial \psi}{\partial \theta}, \\ v_\theta &= -\frac{\partial \psi}{\partial r} \end{aligned} \quad (4.6.40)$$

Also noting that

$$\frac{\partial \eta}{\partial \theta} = \frac{1}{\pi}, \quad \frac{\partial \xi}{\partial r} = \frac{1}{\pi r} = \frac{e^{-\pi \xi}}{\pi} \quad (4.6.41)$$

(4.6.40) can be transformed into the new variables by (4.6.41):

$$v_r = \frac{1}{r} \frac{\partial \psi}{\partial \eta} \frac{\partial \eta}{\partial \theta} = \frac{1}{r} \frac{\partial \psi}{\partial \eta} \frac{1}{\pi} = \frac{1}{\pi e^{\pi \xi}} \frac{\partial \psi}{\partial \eta} \quad (4.6.42)$$

$$v_\theta = -\frac{\partial \psi}{\partial r} = -\frac{\partial \psi}{\partial \xi} \frac{\partial \xi}{\partial r} = -\frac{1}{\pi r} = -\frac{1}{\pi e^{\pi \xi}} \frac{\partial \psi}{\partial \xi} \quad (4.6.43)$$

Substituting (4.6.39)–(4.6.43) into (4.6.37) and (4.6.38), we obtain the governing equations in the transformed $\xi - \eta$ coordinates:

$$\frac{\partial \omega}{\partial t} + \frac{1}{g(\xi)} \left[\frac{\partial \psi}{\partial \eta} \frac{\partial \omega}{\partial \xi} - \frac{\partial \psi}{\partial \xi} \frac{\partial \omega}{\partial \eta} \right] = \frac{2}{Re} \frac{1}{g(\xi)} \left(\frac{\partial^2 \omega}{\partial \xi^2} + \frac{\partial^2 \omega}{\partial \eta^2} \right) \quad (4.6.44)$$

$$\frac{\partial^2 \psi}{\partial \xi^2} + \frac{\partial^2 \psi}{\partial \eta^2} = -g(\xi)\omega \quad (4.6.45)$$

$$g(\xi) = \pi^2 e^{2\pi\xi} \quad (4.6.46)$$

Equation (4.6.44) is parabolic in time and elliptic in space, and (4.6.45) is an elliptic Poisson type equation. Because some of the boundary conditions imposed on these equations are Dirichlet type, both equations can be efficiently solved by iterative methods. The problem description will be complete with the definition of boundary conditions on all sides of the computational domain.

Referring to Fig. 4.6.5, we impose the following boundary conditions on the various boundaries of the computational domain.

a. Solid surface, A-B On an impermeable solid wall where $\psi = 0$, no slip boundary conditions will be applied. This implies that on the surface of the cylinder, $v_r = v_\theta = 0$, from which we can infer

$$\begin{aligned} v_r &= \frac{\partial \psi}{\partial \theta} = 0 \text{ (in the physical plane)} \\ \frac{\partial \psi}{\partial \eta} &= \frac{\partial^2 \psi}{\partial \eta^2} = 0 \text{ (in the transformed plane)} \\ g(\xi)|_{\xi=0} &= \pi^2 \end{aligned} \quad (4.6.47)$$

With these considerations, (4.6.45) reduces to

$$\omega = -\frac{1}{\pi^2} \frac{\partial^2 \psi}{\partial \xi^2} \quad (4.6.48)$$

Similar to the driven cavity problem, we can obtain a simple approximation to (4.6.48) by the use of Taylor series,

$$\psi_{i,2}^{n+1} = \psi_{i,1} + \left. \frac{\partial \psi}{\partial \xi} \right|_{i,1}^{n+1} \Delta \xi + \left. \frac{1}{2} \frac{\partial^2 \psi}{\partial \xi^2} \right|_{i,1}^{n+1} \Delta \xi^2 + \dots \quad (4.6.49)$$

Noting that on the wall ($j = 1$)

$$\psi_{i,1} = 0, \quad v_\theta = 0, \quad \left. \frac{\partial \psi}{\partial \xi} \right|_{i,1} = 0 \quad (4.6.50)$$

(4.6.49) can be written as

$$\psi_{i,2}^{n+1} = \left. \frac{1}{2} \frac{\partial^2 \psi}{\partial \xi^2} \right|_{i,1}^{n+1} \Delta \xi \quad (4.6.51)$$

Substituting (4.6.51) into (4.6.48), we obtain the boundary condition for ω in the wall. Assuming that $j = 1$ when $\xi = 0(r = 1)$, we obtain

$$\omega_{i,1}^{n+1} = -\frac{2\psi_{2,j}^{n+1}}{\pi^2 \Delta\xi^2}, \quad \psi_{i,1} = 0 \quad (4.6.52)$$

This first-order boundary condition, which calculates the current vorticity on the wall ($\omega_{i,1}^{n+1}$) from the current value of the stream function one grid point above the cylinder surface ($\psi_{i,2}^{n+1}$), has been used and generally provides results as accurate as higher-order forms (Roache, 1972, p. 141).

b. Symmetry line, C-B and A-D On these boundaries, it is sufficient to impose

$$\psi = 0, \quad \omega = 0 \quad (4.6.53)$$

c. Outer boundary, C-D Sufficiently removed from the solid wall, we assume the flow to be irrotational at the outer boundary. It is adequate to place the outer boundary at $\xi_\infty = 1$, which corresponds to $r = 23.14$. For irrotational flow, vorticity is zero; thus, assuming $j = J$ when $\xi = \xi_\infty$ (outer boundary),

$$\omega_{i,J} = 0 \quad (4.6.54)$$

The condition on ψ is obtained from the potential flow solution for inviscid flow around a circular cylinder (Kuethe and Chow, 1998, p. 102)

$$\psi = r \sin \theta \left(1 - \frac{1}{r^2} \right) \quad (4.6.55)$$

Substituting the definitions of r and θ in the transformed plane, we obtain

$$\psi = \sin(\pi \eta) e^{\pi \xi} \left(1 - \frac{1}{e^{2\pi \xi}} \right) \quad (4.6.56)$$

from which

$$\psi = \sin(\pi \eta) (e^{\pi \eta} - e^{-\pi \eta}) = 2 \sin(\pi \eta) \sinh(\pi \eta) \quad (4.6.57)$$

Hence, as $r \rightarrow r_\infty$, $\xi \rightarrow \xi_\infty$ and with $j = J$ on the outer boundary,

$$\psi_{i,J} = 2 \sin(\pi \eta) \sinh(\pi \xi_\infty) \quad (4.6.58)$$

Project for Further Study: Solve (4.6.44)–(4.6.46) for the problem of flow past a circular cylinder with the boundary conditions (Fig. 4.6.5) given by (4.6.52), (4.6.53), (4.6.54), and (4.6.58) using a time-differencing method of your choice.

A detailed description of this flow is given by Panton (1984, pp. 384–401), with a summary of the computational results of Formberg (1980). Calculate the flow field and determine the Reynolds number (based on the diameter) at which the flow separates from the surface of the cylinder; experiments indicate that this critical Reynolds number is around 5–7; determine the separation bubble length as a function of Re and compare with the values given in Panton (1984). Also calculate the drag on the cylinder surface as a function of the Reynolds number (for $2 \leq Re \leq 38$) and compare with available data (Panton, 1984, Fig. 15-15, p. 387). The drag on the cylinder can be calculated as a sum of (a) skin friction drag, D_s and (b) form drag resulting from flow separation, D_P . Consequently, for unit axial length the drag coefficient on the cylinder can be written as

$$C_D = \frac{D}{0.5\rho U_\infty^2 d} = \frac{D_s + D_P}{\rho U_\infty^2 a} \quad (4.6.59)$$

In (4.6.59), d is the cylinder diameter, and D is the drag force given as

$$\frac{D_s}{\rho U_\infty^2 a} + \frac{D_P}{\rho U_\infty^2 a} = -\frac{4\pi}{Re} \int_0^1 \omega \sin(\pi\eta) d\eta - 2\pi \int_0^1 P \cos(\pi\eta) d\eta \quad (4.6.60)$$

The only unknown in (4.6.60) is the nondimensional pressure, P , which can be obtained from the azimuthal (θ) component of the momentum equation written in terms of the vorticity, ω , evaluated at the cylinder surface, i.e.,

$$\left. \frac{\partial P}{\partial \eta} \right|_{i,1} = \frac{2}{Re} \left. \frac{\partial \omega}{\partial \xi} \right|_{i,1} \quad (4.6.61)$$

Equation (4.6.61) can be evaluated to second-order accuracy by applying the trapezoidal rule:

$$P_{i,1} = P_{i-1,1} + \frac{\Delta\eta}{Re} \left(\left. \frac{\partial \omega}{\partial \xi} \right|_{i,1} + \left. \frac{\partial \omega}{\partial \xi} \right|_{i-1,1} \right) \quad (4.6.62)$$

The evaluation of this integral requires an initial condition specified as the value of pressure at the grid node (1,1). For this purpose, it is plausible to assume that the pressure at the computational node (1,1) is equal to the stagnation value so that the nondimensional pressure is given as

$$\frac{P_{1,1}}{0.5\rho U_\infty^2} = 1 \quad (4.6.63)$$

Also, derive (4.6.60) evaluating the normal and azimuthal components of the momentum equation on the surface of the cylinder, and transforming them into the $\xi-\eta$ coordinates.

A MATLAB code was written to solve the cylinder problem using the finite-difference method described above and the results are displayed in Fig. 4.6.6

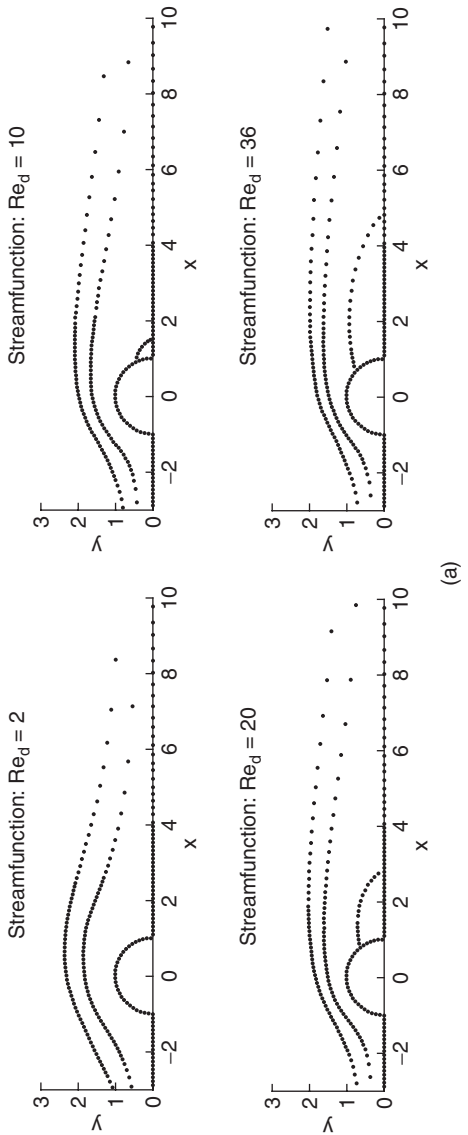


FIGURE 4.6.6 Streamlines (a) and vorticity contours (b) for flow over a cylinder for various Reynolds numbers, Re .

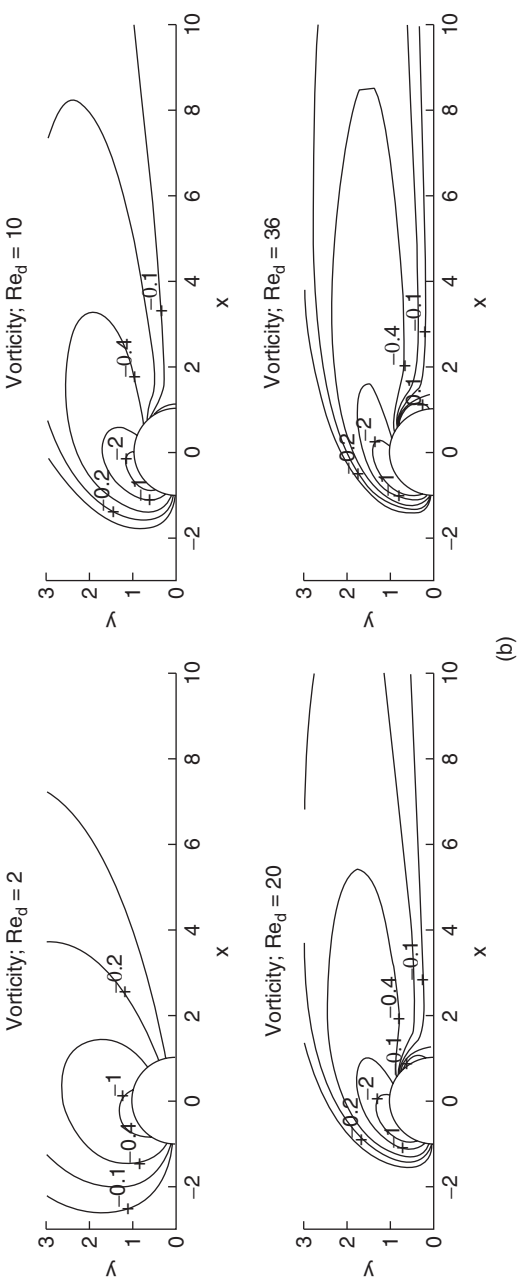


FIGURE 4.6.6 (continued)
(b)

for several Reynolds numbers within the symmetric flow range. In Fig. 4.6.6a, the streamlines display that the separation point moves forward with increasing Re. As shown in Fig. 4.6.6b, the vorticity that is concentrated on the cylinder surface is diffused deeper into the wake when Re increases. Another expected result of higher Re is the increasing asymmetry with the y axis, which is clearly observed in both figures.

APPENDIX

TABLE 4.A.1 Result of Galerkin Method for Flow Past a Sphere

RE	A1	B1	CDP	CDS	CD	RS
5.0000e+00	-4.4946e+00	-4.5989e-01	3.2225e+00	6.4095e+00	9.6319e+00	1.0000e+00
1.0000e+01	-4.4786e+00	-9.2077e-01	1.6449e+00	3.2189e+00	4.8639e+00	1.0000e+00
2.0000e+01	-4.4145e+00	-1.8494e+00	8.8961e-01	1.6377e+00	2.5273e+00	1.0000e+00
3.0000e+01	-4.3086e+00	-2.7936e+00	6.6711e-01	1.1230e+00	1.7901e+00	1.0000e+00
4.0000e+01	-4.1621e+00	-3.7604e+00	5.7711e-01	8.7457e-01	1.4517e+00	1.0144e+00
5.0000e+01	-3.9771e+00	-4.7560e+00	5.3927e-01	7.3232e-01	1.2716e+00	1.1574e+00
6.0000e+01	-3.7563e+00	-5.7851e+00	5.2652e-01	6.4274e-01	1.1693e+00	1.2759e+00
7.0000e+01	-3.5037e+00	-6.8500e+00	5.2696e-01	5.8278e-01	1.1097e+00	1.3813e+00
8.0000e+01	-3.2242e+00	-7.9502e+00	5.3436e-01	5.4078e-01	1.0751e+00	1.4779e+00
9.0000e+01	-2.9235e+00	-9.0813e+00	5.4503e-01	5.1019e-01	1.0552e+00	1.5681e+00
1.0000e+02	-2.6083e+00	-1.0236e+01	5.5660e-01	4.8699e-01	1.0436e+00	1.6529e+00
2.0000e+02	1.8308e-01	-2.0676e+01	5.7092e-01	3.6670e-01	9.3762e-01	2.2526e+00
3.0000e+02	1.6289e+00	-2.6816e+01	4.8165e-01	2.8701e-01	7.6866e-01	2.5321e+00
4.0000e+02	2.3858e+00	-3.0318e+01	4.0091e-01	2.3196e-01	6.3287e-01	2.6770e+00
5.0000e+02	2.8401e+00	-3.2526e+01	3.3978e-01	1.9359e-01	5.3337e-01	2.7640e+00
6.0000e+02	3.1410e+00	-3.4036e+01	2.9366e-01	1.6575e-01	4.5942e-01	2.8216e+00
7.0000e+02	3.3546e+00	-3.5130e+01	2.5811e-01	1.4477e-01	4.0288e-01	2.8626e+00
8.0000e+02	3.5139e+00	-3.5959e+01	2.3002e-01	1.2843e-01	3.5845e-01	2.8932e+00
9.0000e+02	3.6372e+00	-3.6609e+01	2.0733e-01	1.1537e-01	3.2270e-01	2.9168e+00

BIBLIOGRAPHY

- Abbott, I. H., and von Doenhoff, A. E. (1949), *Theory of Wing Sections*, McGraw-Hill, New York. Paperback edition, Dover, New York, 1959.
- Akman, O. E., Biringen, S., and Waggy, S. (2011), “Analysis of Signal Propagation in an Elastic Tube Flow Model,” *Med. Eng. Phys.* (in press).
- Anderson, J. D., Jr. (1995), *Computational Fluid Dynamics*, McGraw- Hill, New York.
- Anliker, M., Rockwell, R. L., and Ogden, E. (1971), “Nonlinear Analysis of Flow Pulses and Shock Waves in Arteries, Part I: Derivation and Properties of Mathematical Model,” *Z. Angew. Math. Phys.*, Vol. 22, 217–246.
- Batchelor, G. K. (1967), *An Introduction to Fluid Dynamics*, Cambridge University Press, Cambridge, England.
- Beam, R. M., and Warming, R. F. (1976), “An Implicit Finite-Difference Algorithm For Hyperbolic Systems in Conservation Law Form,” *J. Comput. Phys.*, Vol. 22, 87–110.
- Beaton, E. R., and Platzman, G. W. (1972), “A Table of Solutions of the One-Dimensional Burgers Equation,” *Quart. Appl. Math.*, Vol. 30, 195–212.
- Bernard, R. S., and Thompson, J. F. (1984), “Mass Conservation on Regular Grids for Incompressible Flow,” *AIAA Paper 84-1669*, Snowmass, Colorado.
- Biringen, S., and Danabasoglu, G. (1989), “Oscillatory Flow with Heat Transfer in a Square Cavity,” *Phys. Fluids A*, Vol. 1, 1796–1812.
- Birkhoff, G. D., and Fisher, J. (1959), “Do Vortex Sheets Roll Up?” *Rendi. Circ. Mat. Palermo*, Ser. 2, Vol. 8, 77–90.
- Bisplinghoff, R. L., and Ashley, H. (1962), *Principles of Aeroelasticity*, Wiley, New York.
- Blanchard, D. C. (1967), *From Raindrops to Volcanoes*, Doubleday, Garden City, New York.
- Blasius, H. (1908), “Grenzschichten in Flüssigkeiten mit kleiner Reibung,” *Z. Angew. Math. Phys.*, Vol. 56, 1. Available in English translation as NACA TM 1256.
- Carnahan, B., Luther, H. A., and Wilkes, J. O. (1969), *Applied Numerical Methods*, Wiley, New York.
- Chandrasekhar, S. (1961), *Hydrodynamic and Hydromagnetic Stability*, Oxford University Press, London.
- Chorin, A. J. (1967), “A Numerical Method for Solving Incompressible Viscous Flow Problems,” *J. Comput. Phys.*, Vol. 2, 12–26.
- Chorin, A. J. (1968), “Numerical Solution of the Navier-Stokes Equations,” *Math. Comput.*, Vol. 22, 745–762.

- Chow, C.-Y., and Halat, J. A. (1969), "Drag of a Sphere of Arbitrary Conductivity in a Current-Carrying Fluid," *Phys. Fluids*, Vol. 12, 2317–2322.
- Chow, C.-Y., and Lai, Y.-C. (1972), "Alternating Flow in Trachea," *Resp. Physiol.*, Vol. 16, 22–32.
- Churchill, R. V. (1948), *Introduction to Complex Variables and Applications*, McGraw-Hill, New York.
- Courant, R., Isaacson, E., and Rees, M. (1952), "On the Solution of Nonlinear Hyperbolic Differential Equations by Finite Differences," *Commun. Pure Appl. Math.*, Vol. 5, 243–255.
- Falkner, V. M., and Skan, S. W. (1930), *Some Approximate Solutions of the Boundary Layer Equations*, British Aeronautical Research Committee Reports & Memo 1314.
- Ferziger, J. H. (1998), *Numerical Methods for Engineering Application*, 2nd edition, Wiley-Interscience, New York.
- Fletcher, C. A. J. (2006), *Computational Techniques for Fluid Dynamics*, Vols. I and II, Springer-Verlag, New York.
- Fornberg, B. (1980), "A Numerical Study of Steady Viscous Flow past a Circular Cylinder," *J. Fluid Mech.*, Vol. 98, 819–855.
- Fornberg, B. (1996), *A Practical Guide to Pseudospectral Methods*, Cambridge University Press, New York.
- Fox, D. G., and Orszag, S. A. (1973) "Pseudospectral Approximation to Two-Dimensional Turbulence," *J. Comput. Phys.*, Vol. 11, 612–619.
- Gerald, C. F., and Wheatley, P. O. (1997) *Applied Numerical Analysis*, 6th edition, Addison Wesley, New York.
- Ghia, U., Ghia, K., and Shin, C. T. (1982), "High-Re Solutions for Incompressible Flow Using the Navier-Stokes Equations and a Multigrid Method", *J. Comput. Phys.*, Vol. 48, 387–411.
- Goldstein, S., Ed. (1938), *Modern Developments in Fluid Dynamics*, Vol. 1, Clarendon Press, Oxford, England.
- Gottlieb, D., and Turkel, E. (1976), "Dissipative Two-Four Methods for Time-Dependent Problems," *Math. Comput.*, Vol. 30, No. 136, 703–723.
- Gottlieb, D., Hussaini, M. Y., and Orszag, S. A. (1984), "Introduction: Theory and Applications of Spectral Methods," in R. G. Voight, D. Gottlieb, and M. Y. Hussani, Eds., *Spectral Methods for Partial Differential Equations*, SIAM, Philadelphia.
- Grad, H. (1952), "The Profile of a Steady Plane Shock Wave," *Commun. Pure Appl. Math.*, Vol. 5, 257–300.
- Greenspan, H. P. (1968), *The Theory of Rotating Fluids*, Cambridge University Press, Cambridge, England.
- Greenspan, D. (1974), *Discrete Numerical Methods in Physics and Engineering*, Academic Press, New York.
- Gresho, P. M. (1991), "Some Current CFD Issues Relevant to the Incompressible Navier-Stokes Equations," *Comput. Methods in Appl. Mech. Eng.*, Vol. 87, 201–252.
- Hamielec, A. E., Hoffman, T. W., and Ross, L. L. (1967), "Numerical Solution of the Navier-Stokes Equation for Flow past Spheres: Part 1. Viscous Flow around Spheres with and without Radial Mass Efflux," *A.I.Ch.E. J.*, Vol. 13, 212–219.

- Hamielec, A. E., Storey, S. H., and Whitehead, J. M. (1963), "Viscous Flow Around Fluid Spheres at Intermediate Reynolds Numbers (II)," *Can. J. Chem. Eng.*, Vol. 41, 246–251.
- Happel, J., and Brenner, H. (1965), *Low Reynolds Number Hydrodynamics*, Prentice-Hall, Englewood Cliffs, New Jersey.
- Harlow, F. H., and Welch, J. E. (1965), "Numerical Calculation of Time-Dependent Viscous Incompressible Flow of Fluids with Free Surface," *Phys. Fluids*, Vol. 8, 2182–2189.
- Harman, T. L., Dabney, J., and Richert, N. (2000), *Advanced Engineering Mathematics with MATLAB*, Brooks/Cole, Pacific Grove, California.
- Hartree, D. R. (1958), *Numerical Analysis*, 2nd edition, Oxford University Press, London.
- Hirt, C. W. (1968), "Heuristic Stability Theory for Finite-Difference Equations," *J. Comput. Phys.*, Vol. 2, 339–355.
- Hoffmann, K. A., and Chiang, S. T. (1993), *Computational Fluid Dynamics for Engineers*, Vol. I, Engineering Education System, Kansas.
- Howarth, L. (1938), "On the Solution of the Laminar Boundary Layer Equations," *Proc. R. Soc. London A*, Vol. 164, 547–579.
- Hughes, W. F., and Gaylord, E. W. (1964), *Basic Equations of Engineering Science*, Schaum, New York.
- Huser, A., and Biringen, S. (1992), "Calculation of Wind-Driven Flow at High Reynolds Numbers," *Int. J. Numer. Methods Fluids*, Vol. 14, 1087–1109.
- Jeffreys, H. (1928), "Some Cases of Instability in Fluid Motion," *Proc. R. Soc. London A*, Vol. 118, 195–208.
- Karniadakis, G., and Sherwin, S. (2005), *Spectral Element Methods for Computational Fluid Dynamics*, 2nd ed., Oxford Science, Oxford, England.
- Kawaguti, M. (1955), "The Critical Reynolds Number for the Flow past a Sphere," *J. Phys. Soc. Jpn.*, Vol. 10, 694–699.
- Kim, J., and Moin, P. (1985), "Application of a Fractional-Step Method to Incompressible Navier-Stokes Equations," *J. Comput. Phys.*, Vol. 59, 308–323.
- Kopecky, R. M., and Torrance, K. E., (1973), "Initiation and Structure of Axisymmetric Eddies in a Rotating Stream," *Comput. Fluids*, Vol. 1, 289–300.
- Kuethe, A. M., and Chow, C.-Y. (1998), *Foundations of Aerodynamics: Bases of Aerodynamic Design*, 5th edition, Wiley, New York.
- Kundu, P. K., and Cohen, I. M. (2008), *Fluid Mechanics*, 4th edition, Academic Press, Burlington, Massachusetts.
- Kuo, S. S. (1972), *Computer Applications of Numerical Methods*, Addison-Wesley, Reading, Massachusetts.
- Lamb, H. (1932), *Hydrodynamics*, 6th edition, Cambridge University Press, Cambridge, England.
- Landau, L. D., and Lifshitz, E. M. (1959), *Fluid Mechanics*, Addison-Wesley, Reading, Massachusetts.
- Laney, C. B. (1998), *Computational Gas Dynamics*, Cambridge University Press, Cambridge, England.
- Lax, P. D., and Richtmyer, R. D. (1956), "Survey of the Stability of Linear Finite Difference Equations," *Commun. Pure Appl. Math.*, Vol. 9, 267–293.

- Liepmann, H. W., and Roshko, A. (1957), *Elements of Gas Dynamics*, Wiley, New York.
- Lin, C. C. (1955), *The Theory of Hydrodynamic Stability*, Cambridge University Press, Cambridge, England.
- Lindsey, W. F. (1938), *Drag of Cylinders of Simple Shapes*, NACA Report 619.
- MacCormack, R. W. (1969), "The Effect of Viscosity in Hypervelocity Impact Cratering," *AIAA Paper 69-354*, Cincinnati, Ohio.
- McCormick, J. M., and Salvadori, M. G. (1964), *Numerical Methods in FORTRAN*, Prentice-Hall, Englewood Cliffs, New Jersey.
- Mitchell, A. R. (1969), *Computational Methods in Partial Differential Equations*, Wiley, New York.
- Moin, P. (2001), *Fundamentals of Engineering Numerical Analysis*, Cambridge University Press, Cambridge, England.
- Moin, P., Reynolds, W. C., and Ferziger, J. H. (1978), *Large Eddy Simulation of Incompressible Turbulent Channel Flow*, Technical Report TF-12, Thermosciences Division, Department of Mechanical Engineering, Stanford University, Stanford, California.
- Moore, D. W. (1974), "A Numerical Study of the Roll-Up of a Finite Vortex Sheet," *J. Fluid Mech.*, Vol. 63, 225–235.
- Orszag, S. A. (1971), "Accurate Solution of the Orr-Sommerfeld Stability Equation," *J. Fluid Mech.*, Vol. 50, 689–703.
- Orszag, S. A. (1972), "Comparison of Pseudospectral and Spectral Approximation," *Studies Appl. Math.*, Vol. 51, 253–259.
- Orszag, S. A., and Kells, L. C. (1981), "Transition to Turbulence in Plane Poiseuille Flow and in Plane Couette Flow," *J. Fluid Mech.*, Vol. 96, 159–205.
- Orszag, S. A., and Patera, A. T. (1983), "Secondary Instability of Wall-Bounded Shear Flows," *J. Fluid Mech.*, Vol. 128, 347–385.
- Panton, R. L. (1984), *Incompressible Flow*, Wiley, New York.
- Patankar, S. V. (1980), *Numerical Heat Transfer and Fluid Flow*, Hemisphere, Washington, D.C.
- Patankar, S. V., and Spalding, D. B. (1972), "A Calculation Procedure for Heat, Mass and Momentum Transfer in Three-Dimensional Parabolic Flows," *Int. J. Heat Mass Transfer*, Vol. 15, 1787–1806.
- Peaceman, D. W., and Rachford, H. H. (1955) "The Numerical Solution of Parabolic and Elliptic Differential Equations," *J. Soc. Ind. Appl. Math.*, Vol. 3, 28–41.
- Peyret, R., and Taylor, T. D. (1983), *Computational Methods for Fluid Flow*, Springer-Verlag, New York.
- Pohlhausen, E. (1921), "Der Warmeaustausch zwischen festen Körpern und Flüssigkeiten mit kleiner Reibung und kleiner Warmeleitung," *Z. Angew. Math. Mech.*, Vol. 1, 115.
- Prandtl, L. (1904), "Über Flüssigkeitsbewegung bei sehr kleiner Reibung," *Proc. III Intern. Math. Congr.*, Heidelberg, Germany.
- Rai, M. M., and Moin, P. (1991), "Direct Simulations of Turbulent Flow Using Finite-Difference Schemes," *J. Comput. Phys.*, Vol. 96, 15–33.
- Rayleigh, Lord (1911), "On the Motion of Solid Bodies through Viscous Liquid," *Philos. Mag.*, Ser. VI, Vol. 21, 697–711.
- Rayleigh, Lord (1916), "On Convective Currents in a Horizontal Layer of Fluid When the Higher Temperature Is on the Under Side," *Philos. Mag.*, Ser. VI, Vol. 32, 529–546.

- Roache, P. J. (1972), *Computational Fluid Dynamics*, Hermosa, Albuquerque, New Mexico.
- Rosenhead, L. (1940), "The Steady Two-Dimensional Radial Flow of Viscous Fluid Between Two Inclined Walls," *Proc. R. Soc. London A*, Vol. 175, 436–467.
- Rumberger, J. A., and Nerem, R. T. (1977), "A method-of-Characteristic Calculation of Coronary Blood Flow," *J. Fluid Mech.*, Vol. 82, No. 3, 429–448.
- Schlichting, H. (1968), *Boundary Layer Theory*, 6th edition, McGraw-Hill, New York.
- Scorer, R. S. (1958), *Natural Aerodynamics*, Pergamon, London.
- Snyder, L. J., Spriggs, T. W., and Stewart, W. E. (1964), "Solution of the Equations of Change by Galerkin's Method," *A.I.Ch.E. J.*, Vol. 10, 535–540.
- Stoker, J. J. (1957), *Water Waves*, Wiley-Interscience, New York.
- Strawbridge, D. R., and Hooper, G. T. J. (1968), "Numerical Solution of the Navier-Stokes Equations for Axisymmetric Flows," *J. Mech. Eng. Sci.*, Vol. 10, 389–401.
- Ta Phuoc Loc (1980), "Numerical Analysis of Unsteady Secondary Vortices Generated by an Impulsively Started Circular Cylinder," *J. Fluid Mech.*, Vol. 100, 111–128.
- Taneda, S. (1956), "Studies on Wake Vortices (III). Experimental Investigation of the Wake behind a Sphere at Low Reynolds Numbers," *Rep. Res. Inst. Appl. Mech. Kyushu Univ.*, Vol. 4, 99–105.
- Tannehill, J. C., Anderson, D. A., and Pletcher, R. H. (1997), *Computational Fluid Mechanics and Heat Transfer*, 2nd ed., Taylor & Francis, Washington, D.C.
- Taylor, G. I. (1923), "Stability of a Viscous Liquid Contained between Two Rotating Cylinders," *Philos. Trans. R. Soc., London A*, Vol. 223, 289–343.
- Taylor, T. D., and Acrivos, A. (1964), "On the Deformation and Drag of a Falling Viscous Drop at Low Reynolds Number," *J. Fluid Mech.*, Vol. 18, 466–476.
- Theodorsen, T. (1935), *General Theory of Aerodynamic Instability and the Mechanism of Flutter*, NACA Report 496.
- Thom, A., and Apelt, C. J. (1961), *Field Computations in Engineering and Physics*, Van Nostrand, New York.
- Thoman, D. C., and Szewczyk, A. A. (1966), *Numerical Solutions of Time Dependent Two-Dimensional Flow of a Viscous, Incompressible Fluid over Stationary and Rotating Cylinders*, Technical Report 66-14, Heat Transfer and Fluid Mechanics Laboratory, Department of Mechanical Engineering, University of Notre Dame, Notre Dame, Indiana.
- Torrance, K. E. (1968), "Comparison of Finite-Difference Computations of Natural Convection," *J. Res. Nat. Bur. Stand.*, Vol. 72B, 281–301.
- Torrance, K. E., and Rockett, J. A. (1969), "Numerical Study of Natural Convection in an Enclosure with Localized Heating from Below-Creeping Flow to the Onset of Laminar Instability," *J. Fluid Mech.*, Vol. 36, 33–54.
- Trefethen, L. N. (2000), *Spectral Methods in MATLAB*, SIAM, Philadelphia.
- von Karman, T. (1927), *Calculation of Pressure Distribution on Airship Hulls*, NACA TM 574.
- Wachpress, E. L. (1957), *A Generalized Two Space Dimension Multigroup Coding for the IBM 704*, CURE report KAPL-1724, General Electric Co., Schenectady, New York.
- Yih, C.-S. (1965), *Dynamics of Nonhomogeneous Fluids*, Macmillan, New York.
- Yih, C.-S. (1969), *Fluid Mechanics*, McGraw-Hill, New York.
- Zucrow, M. J., and Hoffman, J. D. (1977), *Gas Dynamics*, Vol. 2, Wiley, New York.

INDEX

- AB-CN semi-implicit method, 254–255, 258
 Accelerating body, force on, 6
 Adams-Basforth method, 250
 Added mass (free-falling spherical bodies), 7
 Adiabatic temperature, 157
 Adverse pressure gradient, 156
 Alternating-direction implicit (ADI) method, 287–289
 Amplification factor, 107
 Analytic functions, 77–78
 Archimedes' principle, 5
 Artificial viscosity, 233
 Atmospheric circulation, 244–246
 Axisymmetric flows:
 incompressible, 53–54
 through tube with repeated partitions, 103–105
 von Kármán's method, 69–75
 Backward-difference formula, 57
 Ballistics of spherical projectile, 24–31
 Beam and Warming method, 130–133, 135, 136, 138
 Benard cells, 185
 Bénard problem, 234–249. *See also*
 Rayleigh-Benard problem
 governing equations, 234–235
 water enclosed by rectangular box, 236–243
 Bender-Schmidt recurrence equation, 170
 Bernoulli constant, 52
 Bernoulli equation, 52
 Biharmonic equation, 179–185
 Biological fluid flow, in elastic tube, 138–143
 Biot-Savart law, 38
 Blasius problem, 148–150, 156
 Blood flow, 138–143
 Bodies of revolution, flow past (von Kármán's method), 69–75
 Boundary conditions:
 channel flow past circular cylinder, 99–103
 irregular and derivative, 96–105
 periodic, 244
 rectangular chamber with blocked corner, 97–98
 Boundary-layer equations, 148
 Boundary-layer flows:
 governing equations for, 147–148
 inviscid, 51–52
 in presence of injection, 154–155
 viscous:
 self-similar laminar, 147–158
 thermal, 157–163
 velocity, 147–158
 Boundary-value problems:
 defined, 55
 direct methods, 62
 inverse methods:
 conformal mapping, 76–87
 superposition of elementary flows, 61–69
 numerical solution, 55–61
 radial flow caused by distributed sources and sinks, 60–61
 Bound vortex:
 finite wing, 36
 infinitely long, 35
 Boussinesq approximation, 185, 234–235
 Buoyant force, of free-falling spherical body, 5–6
 Burgers equation, 131, 135–137, 251
 Cannon, range of, 30–31
 Cauchy-Riemann conditions, 77
 Cavity flow, caused by moving surface, 180–185, 273–280, 282–289
 Central-difference formula, 57
 Channel flow:
 hydrodynamic stability of, 191–194, 198–199
 open-channel, 163–168
 past circular cylinder, 99–103
 past rectangular cylinder, 103, 104

- Channel flow: (*Continued*)
 square-cross-section channel, 167
 starting flow in viscous fluid flows, 173–179
- Characteristics, 88, 121, 124
- Characteristics, method of, 121–124, 128
- Chebyshev differentiation matrices, 194–199
- Chebyshev polynomials, 194–195
- Circular cylinder. *See also* Tube(s)
 flow past:
 channel flow, 99–103
 superposition of elementary flows, 67
 uniform flow, 289–297
 vorticity-stream function formulation, 289–297
- fluid motion around, 162–163, 171
- incompressible flow through pipe, 163–164, 167–168
- power transmission line in time-varying winds, 21–22
- Circulation (vortex flow), 63
- Complex potential, 77
- Compressive waves, 119
- Concentric cylinders, flows between, 170, 246
- Conformal mapping, 76–87
- Continuity equation, 52
 incompressible flows, 53–55
 viscous flows, 146
 boundary-layer, 148
 simplified in Cartesian coordinates, 147
- Convection–diffusion equation, 251
- Convection equation, 250–251
- Courant number, 106
- Crank–Nicolson method, 177–178, 252–255
- Creeping flows, 179. *See also* Stokes flows
- Derivative boundary conditions:
 in ordinary boundary-value problems, 157–163
 potential flows in ducts or around bodies, 96–105
- Dirigible, flow around, 69–75
- Discrete Fourier transform, 202
- Discrete perturbation stability analysis, 230–234
- Discrete vortices, 44
- Dissipation function (viscous flows), 146
- Distributed sources, radial flow caused by, 60–61
- Doublet, 62–64, 66–68
- Drag:
 flight path of glider, 33–34
 flow around sphere at finite Reynolds numbers, 221–227
- free-falling spherical body:
 form drag, 6, 13
 liquid vs. rigid spheres, 13
 wave drag, 6, 7
- Drag coefficient:
 flow around sphere at finite Reynolds numbers, 223–225, 227
- free-falling spherical body, 6, 8
- long circular cylinder, 21
- spherical projectile, 25, 30
- Ducts, potential flows in, 96–105
- DuFort–Frankel formula, 172
- Egg-shaped bodies (superposition of elementary flows), 67, 68
- Elastically restrained wing, vibration of, 16–22
- Elastic tube, flow in, 138–143
- Elementary flows:
 high Reynolds number flow past streamlined body, 51
 stream functions and flow patterns, 62–64, 66
 streamlines, 63–66
 superposition of, 61–69
- Elliptic cylinder, mapping flow about, 80–87
- Elliptic partial differential equations, 90–96
 Liebmann's method, 92, 94–96
 Richardson's iterative (Jacobi) formula, 93–94
 solving in rectangular space, 90–92
 successive overrelaxation method, 94
- Energy equation, 146–148
- Equation of motion, 146, 147
- Equation of state:
 boundary-layer, 148
 for ideal gas, 146
- Equipotential lines, 76
- Euler equation, 52
- Euler's method, 205
- Expansive waves, 119
- Explicit method, defined, 169
- Falkner–Skan problem, 156–157
- Fast Fourier transform (FFT) algorithms, 202–205
- Finite-amplitude wave, propagation of, 120–128
- First-order ordinary differential equations, numerical solution, 1–4
- Flat plate:
 boundary layer on, 148–149
 flat-plate thermometer problem, 157–163
 generalized Rayleigh problem, 168–173
 Kutta condition, 87
 pressure distribution along upper surface, 69

- semi-infinite:
 boundary layer on, 148–149
 injecting uniform flow into boundary layer,
 155–156
- Flight:
 of a rocket, 34–35
 trajectory of a glider, 32–35
- Flow stability. *See also* Stability analysis
 Rayleigh-Benard problem:
 incompressible Navier-Stokes equations,
 234–249
 viscous fluid flows, 185–188
 viscous fluid flows, 185–206
 hydrodynamic stability of plane channel
 flow, 191–194, 198–199
 neutral stability, 188–191, 199–201
 pseudo-spectral methods, 200, 202–206
 Rayleigh-Benard problem, 185–188
- Form drag (free-falling spherical body), 6, 13
- Forward-difference formula, 57
- Fractional time step method, 258–261
- Free-falling sphere, 5–14
- Galerkin method, 216–229
 flow around a sphere at finite Reynolds
 numbers, 216–228
 radial flow between inclined walls, 228–229
- Gaussian elimination method, 59
- Gauss-Seidel formula, 92
- Generalized Rayleigh problem, 168–173
- Glider, flight path of, 32–35
- Global horizontal temperature gradients,
 244–246
- Grashof number, 236
- Half-interval method:
 boundary-layer flows, 151, 156
 optimum shooting angle for spherical
 projectile, 28–29, 31
- Helmholtz equation, 260
- Helmholtz vortex laws, 36
- Higher-order ordinary differential equations,
 Runge-Kutta methods for, 4
- High Reynolds number flow past streamlined
 body, 51, 52, 147
- Hirt's stability analysis, 233
- Horseshoe vortex, 36
- Hydrodynamic stability, of plane channel flow,
 191–194, 198–199
- Hyperbolic partial differential equations, 89–90
 linear:
 numerical solution, 105–110
 propagation of finite-amplitude wave,
 120–128
- nonlinear:
 flow in an elastic tube, 138–143
 propagation of a small-amplitude wave,
 110–119
- Ideal gas, equation of state for, 146
- Images, method of, 68–69
- Implicit method, defined, 174
- Inclined walls, radial flow between, 228–229
- Incompressible Navier-Stokes equations,
 215–297
 Bénard and Taylor instabilities, 234–249
 flow around a sphere at finite Reynolds
 numbers, 216–228
 flow past a circular cylinder, 289–297
 Galerkin method, 216–229
 primitive variable formulation:
 algorithmic considerations, 249–258
 numerical integration of equation, 258–280
 upwind differencing and artificial viscosity,
 229–234
 vorticity-stream function formulation,
 280–297
- Incompressible potential flows, 51–55
- Initial value problems, 1–44
 ballistics of spherical projectile, 24–31
 computer simulation of restrained motions,
 13–22
 defined, 1–2
 flight path of a glider, 32–35
 free falling of a spherical body, 5–13
 numerical solution, 1–4
 two-dimensional motions of a body through a
 fluid, 22–24
 vortex sheet trailing behind a finite wing,
 35–44
- Interval halving method:
 boundary-layer flows, 151
 optimum shooting angle for spherical
 projectile, 28–29, 31
- Inviscid fluid flows, 50–143
 biological fluid flow in an elastic tube,
 138–143
- boundary-value problems:
 conformal mapping, 76–87
 inverse methods, 61–69, 76–87
 with linear second-order ordinary
 differential equations, 55–59
 radial flow caused by distributed sources
 and sinks, 60–61
 superposition of elementary flows, 61–69
 elliptic partial differential equations, 90–96
 flow in an elastic tube, 138–143

- Inviscid fluid flows, (*Continued*)
 hyperbolic partial differential equations, 105–110
 incompressible potential flows, 51–55
 potential flows in ducts or around bodies, 96–105
 propagation and reflection of small-amplitude wave, 105, 110–119
 propagation of finite-amplitude wave, 120–128
 second-order partial differential equations:
 classification of, 87–90
 elliptic, 90–96
 hyperbolic, 105–110
 irregular and derivative boundary conditions, 96–105
 propagation and reflection of small-amplitude wave, 105, 110–119
 propagation of finite-amplitude wave, 120–128
 von Kármán's method for flow past bodies of revolution, 69–75
 Irregular boundary conditions, potential flows in, 96–105
 Irrotational flows, 51. *See also* Potential flows
 Jacobi formula, 93–94
 Joukowski airfoil, 80, 82–87
 Joukowski transformation, 80–82
 Kinematic pressure, 193
 Kutta condition, 83, 87
 Kutta-Joukowskii theorem, 35
 Laminar boundary-layer flows, self-similar, 147–157
 Laplace equation, 52, 55, 61–62
 Laplacian operator, 52
 Leapfrog method, 108–109
 Liebmann's iterative formula, 92, 94–96
 Liebmann's method, 92
 Lift:
 finite wing, 36
 flight path of glider, 33–34
 wing of infinite span, 35
 Lift coefficient, elastically restrained wing, 17, 19–20
 Linear convection equation, 129
 Linear second-order ordinary differential equations:
 boundary-value problems, 55–60
 hyperbolic:
 numerical solution, 105–110
 propagation of finite-amplitude wave, 120–128
 Linearized shock tube problem, 119
 Line source (sink), 62–64
 radial flow caused by, 60–61
 stream functions and flow patterns, 62–64
 Line vortex, 62–64, 95–96
 LU decomposition:
 flow past a circular cylinder, 255, 287, 288
 incompressible Navier-Stokes equations:
 primitive variable formulation, 256–258
 vorticity-stream function formulation, 287, 288
 MacCormack explicit method, 106, 128–134, 137, 138
 Mach lines, 88
 Mach number, 88
 MAC method, 261–273
 Mapping, 79. *See also* Conformal mapping
 Marker-and-cell (MAC) method, 261–273
 Mass, added, 7
 MATLAB, vii. *See also* specific topics
 Mean value theorem, 91
 Method of characteristics, 121, 123, 128
 Method of conformal mapping, *see* Conformal mapping
 Method of images, 68–69
 Motion, equation of, 146, 147
 Navier-Stokes equations:
 boundary-layer flows, 147–148
 incompressible, 215–297
 algorithmic considerations, 249–258
 Bénard and Taylor instabilities, 234–249
 flow around a sphere at finite Reynolds numbers, 216–228
 flow past a circular cylinder, 289–297
 Galerkin method, 216–229
 numerical integration of equation, 258–280
 primitive variable formulation, 249–280
 upwind differencing and artificial viscosity, 229–234
 vorticity-stream function formulation, 280–297
 viscous flows, 146
 Neutral stability, 188–191
 Benard convection between rigid–rigid boundaries, 191–199
 general Couette flow, 199–201
 Newton-Raphson method, 224–225
 Newton's law of motion, 7
 Nonlinear convection equation, 129–136

- Nonlinear hyperbolic partial differential equations:
propagation of a small-amplitude wave, 110–119
- Nonlinear substantial derivative (upwind differencing), 229–234
- Open-channel flows, 163–168
- Ordinary differential equations:
first-order, numerical solution, 1–4
higher-order, Runge-Kutta methods, 4
initial value problems, 1–44
ballistics of spherical projectile, 24–31
computer simulation of restrained motions, 13–22
flight path of a glider, 32–35
free falling of a spherical body, 5–13
numerical solution, 1–4
two-dimensional motions of a body through a fluid, 22–24
vortex sheet trailing behind a finite wing, 35–44
- second-order:
boundary-value problems, 55–60
hyperbolic, 105–110, 120–128
Runge-Kutta methods, 4
- Oval bodies (superposition of elementary flows), 67, 68
- Parabolic partial differential equations, 90
explicit methods, 168–173
implicit methods, 173–179
- Partial differential equations:
elliptic, 90–96
hyperbolic, 89–90
flow in an elastic tube, 138–143
propagation of a finite-amplitude wave, 110–119
second-order, 105–110
- parabolic, 90
explicit methods, 168–173
implicit methods, 173–179
- second-order:
classification of, 87–90
elliptic, 90–96
hyperbolic, 105–110
irregular and derivative boundary conditions, 96–105
propagation and reflection of small-amplitude wave, 105, 110–119
propagation of finite-amplitude wave, 120–128
- Peaceman-Rachford ADI method, 287–289
- Pendulum, simulated motion of, 14–16
- Periodic boundary conditions, 244
- Pipe, incompressible flow through, 163–164, 167–168
- Planar flows:
generalized Rayleigh problem, 168–173
incompressible, 53–54
von Kármán's method, 69–75
- Poiseuille flow, 164, 192
- Poisson equation, 55
- Potential flows:
in ducts or around bodies, 96–105
incompressible, 51–55
- Power transmission line, in time-varying winds, 21–22
- Prandtl numbers, 160–161, 236
- Prandtl's boundary-layer theory, 148
- Prandtl's postulation, 51, 52
- Predictor step (time-splitting method), 259
- Pressure:
free-falling spherical body, 6
on Joukowski airfoil, 84–87
in thin boundary layer, 148
- Pressure coefficient, 73
- Pressure gradient:
alternating, flow in tube caused by, 178–179
self-similar boundary-layer flows in presence of, 156–157
- Primitive variable formulation (incompressible Navier-Stokes equations):
algorithmic considerations, 249–258
LU decomposition, 256–258
numerical integration of equation, 258–280
Thomas algorithm, 255, 256
- Projectile, spherical, 24–31
- Pseudo-spectral methods (viscous fluid flows), 200, 202–206
- Radial flow:
caused by distributed sources and sinks, 60–61
between inclined walls, 228–229
- Range of a projectile, 26–31
- Rayleigh-Bénard problem, 185–188. *See also* Bénard problem
- Rayleigh number, 236
- Recovery factor, 160–161
- Recovery temperature, 157
- Rectangular cylinder, channel flow past, 103, 104
- Rectangular space:
flow pattern within, 64–66
solving elliptic partial differential equation in, 90–96
water enclosed in, 236–243
- Reflection, of small-amplitude wave, 110–119

- Restrained body motions:
 computer simulation of, 13–22
 pendulum, 14–16
 vibration of elastically restrained wing, 16–22
- Reynolds numbers, 51
 finite, flow around a sphere at, 216–228
 free-falling spherical body, 6–13
 high-Reynolds number flow past streamlined body, 51, 52, 147
 for validation of boundary-layer theory, 153
- Richardson's iterative formula, 93–94
- Riemann invariants, 121
- Rocket, flight of, 34–35
- Rossby number, 247
- Rotating (rotational) flow:
 boundary-layer, 51
 fluid around rotating circular cylinder, 162–163, 171
 incompressible Navier-Stokes equations, 238–239
- Rotating tube, having abrupt contraction, 247–248
- Runge-Kutta methods, 3–4
 fourth-order, 3–4
 boundary-layer flows, 150–151
 flight path of a glider, 33
 pendulum, 15
 roll-up of trailing vortex sheet, 39–40
 two-dimensional motions of body through fluid, 22–24
- free-falling spherical body, 5–11
 second-order, 2, 3
- Second-order differential equations:
 ordinary:
 boundary-value problems, 55–60
 hyperbolic, 105–110, 120–128
 Runge-Kutta methods, 4
- partial:
 classification of, 87–90
 elliptic, 90–96
 hyperbolic, 105–128
 irregular and derivative boundary conditions, 96–105
 propagation and reflection of
 small-amplitude wave, 105, 110–119
 propagation of finite-amplitude wave, 120–128
- Self-similarity, 149
 high Reynolds number flow past streamlined body, 51, 52
 laminar boundary-layer flows, 147–158
- Semi-implicit AB-CN method, 254–255, 258
- Similarity solution, 149
 Similarity variable, 149
 SIMPLE algorithm, 258
- Simulated motion:
 of free-falling sphere, 13–14
 pendulum, 14–16
 real motion vs., 13–14
 vibration of elastically restrained wing, 16–22
- Singularities, 64
- Sink, *see* Line source (sink)
- Skin friction (free-falling spherical body), 6
- Small-amplitude wave, propagation and reflection of, 105, 110–119
- S.O.R. method, *see* Successive overrelaxation method
- Sound waves:
 finite-amplitude wave, propagation of, 120–128
 small-amplitude wave, propagation and reflection of, 105, 110–119
- Spectral methods, with Chebyshev differentiation matrices, 194–199
- Sphere/spherical body:
 drag of, at finite Reynolds numbers, 221–227
 flow around, at finite Reynolds numbers, 216–228
 free falling of, 5–13
 restrained motion, 16
- Spherical projectile:
 ballistics of, 24–31
 range of, 26–31
- Spin-up problem, 248–249
- Square cavity:
 flow caused by moving plate, 180–185
 with lid moving, 273–280, 282–289
- Square-cross-section channel, viscous flow through, 167
- Stability analysis:
 Bénard problem, 234–249
 discrete perturbation, 230–234
 Hirt's, 233
 von Neumann's, 106–107
 and discrete perturbation stability analysis, 233–234
 upwind differencing, 231–232
- Staggered mesh system, 260–273
- Starting flow in channel, 173–179
- Stokes flows, 216
 caused by moving plate in square cavity, 180–185
 defined, 179
 two-dimensional, parallel to x - y plane, 180
 viscous fluid flows, 179–185
- Stokes formula (free-falling spherical bodies), 7

- Stokes stream function (flow around a sphere), 216–221
- Stream function:
 elementary flows, 62–64, 66
 incompressible flows, 53–54
 steady incompressible flow, 69–73
- Streamlines, 53, 76
 elementary flows, 63–66
 of line vortex within a finite domain, 95–96
- Streamlined body:
 high Reynolds number flow past, 51, 52, 147
 superposition of, 65–69
- Stress tensor (drag of sphere), 221–223
- Substantial derivative:
 Euler equation, 52
 upwind differencing, 229–234
- Successive overrelaxation (S.O.R.) method:
 elliptic stream function equation, 289
 irregular spaces, 97–98
 rectangular spaces, 94, 96
- Superposition of elementary flows, 61–69
- Supersonic flow, 87–88
- Taylor instability, 245–246
- Taylor's series expansion:
 if f has complicated derivatives, 3
 initial value problem, 2
- Terminal velocity, of body falling through a fluid, 10–13
- Thermal boundary layer, 157–163
- Thin-airfoil theory, 17
- Thomas algorithm, 255, 256
- Time-dependent incompressible flows, 249
 in primitive variable form, 249–280
 algorithmic considerations, 249–258
 numerical integration of Navier-Stokes equation, 258–280
 in vorticity-stream function form, 280–297
- Time-splitting method, 258–261
- Total derivative (Euler equation), 52
- Trailing vortices, behind a finite wing, 35–44
- Transform methods:
 with Chebyshev differentiation matrices, 194–199
 viscous fluid flows, 200, 202–206
- Transportive property (upwind differencing), 231–232
- Tridiagonal matrix:
 defined, 59
 Gaussian elimination method, 59
 LU decomposition, 256–258
 Thomas algorithm, 256
- Truncation errors, 3, 57
- Tube(s):
 flow in:
 caused by alternating pressure gradient, 178–179
 elastic tubes, 128–143
 incompressible flow with various cross-sections, 167–168
 infinitely long, unsteady flow, 178
 through rotating tube having abrupt contraction, 247–248
- propagation and reflection of small-amplitude wave, 119
- propagation of finite-amplitude wave, 124–128
- Two-dimensional motions of a body through a fluid, Runge-Kutta method for, 22–24
- Uniform flow, 62–64
 conformal mapping, 78–87
 injected into boundary layer, 155–156
 past circular cylinder, 289–297
 von Karman's method, 69–75
- Upwind differencing, 229–234
- Upwind differencing form, 230
- Velocity, terminal, 10–13
- Velocity boundary layer, 147–158
- Velocity potential, 51
- Velocity profiles, 176–177
- Viscosity:
 artificial, 233
 cause of, 51
 forces caused by, 6
- Viscous fluid flows, 145–206
 biharmonic equations, 179–185
 flat-plate thermometer problem, 157–163
 flow stability, 185–206
 generalized Rayleigh problem, 168–173
 governing equations for, 145–147
 parabolic partial differential equations:
 explicit methods, 168–173
 implicit methods, 173–179
 pipe and open-channel flows, 163–168
 pseudo-spectral or transform methods, 200–206
- Rayleigh-Benard problem, 185–188
 self-similar laminar boundary-layer flows, 147–158
- starting flow in channel, 173–179
- Stokes flows, 179–185
 thermal boundary layer, 157–163
 velocity boundary layer, 147–158
- Viscous forces, 51

- Von Kármán's method, 69–75
Von Neumann's stability analysis, 106–107
and discrete perturbation stability analysis,
233–234
upwind differencing, 231–232
- Vortices:
bound:
finite wing, 36
infinitely long, 35
discrete, 44
horseshoe, 36
- Vortex sheet:
trailing behind a finite wing, 35–44
wing of infinite span, 35
- Vorticity-stream function formulation, 280–297
Vorticity transport equation, 281–282
- Waves:
finite-amplitude, 120–128
small-amplitude, 105, 110–119
- Wave drag (free-falling spherical body), 6, 7
- Wave motions, 105
- Wing:
elastically restrained, vibration of, 16–22
of infinite span, lift for, 35
von Karman's method for uniform flow, 75
vortex sheet trailing behind a finite wing,
35–44